Autocompaction of mineralogenic intertidal sediments

Brain, Matthew James

Autocompaction of Mineralogenic Intertidal Sediments

Volume two: Figures and appendices

Matthew James Brain

Thesis submitted for the degree of Doctor of Philosophy

Department of Geography
Durham University

September 2006

CONTENTS

CONTENTS OF VOLUME II

LIST OF FIGURES

LIST OF APPENDICES

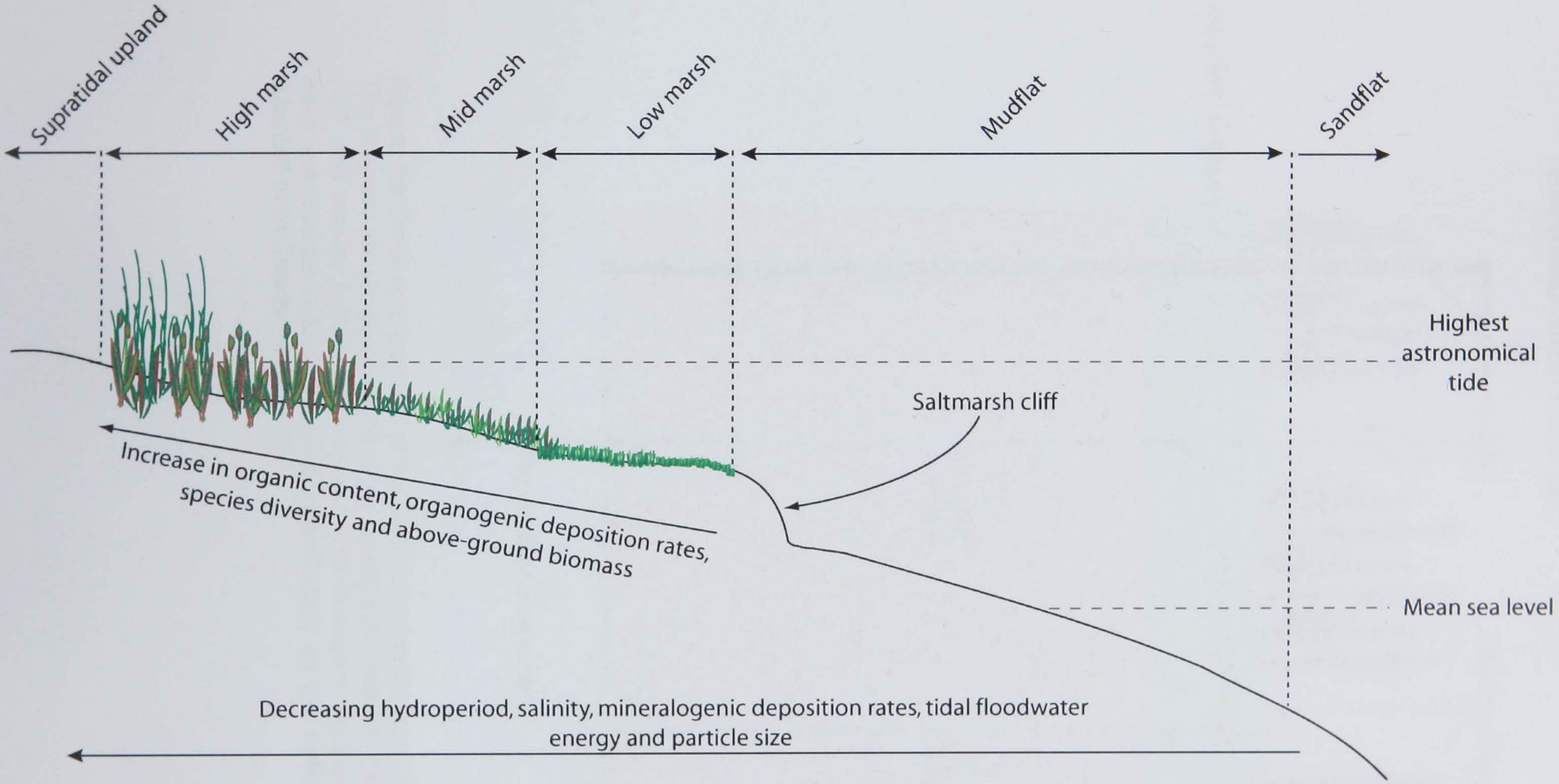

Figure 2.1 Schematic diagram displaying the relationship between elevation relative to mean sea level, floral zone, energy conditions, organic content and hydrographic characteristics. Such a sequence is typical of northwest European low energy intertidal environments. Distance and elevation are not drawn to scale.

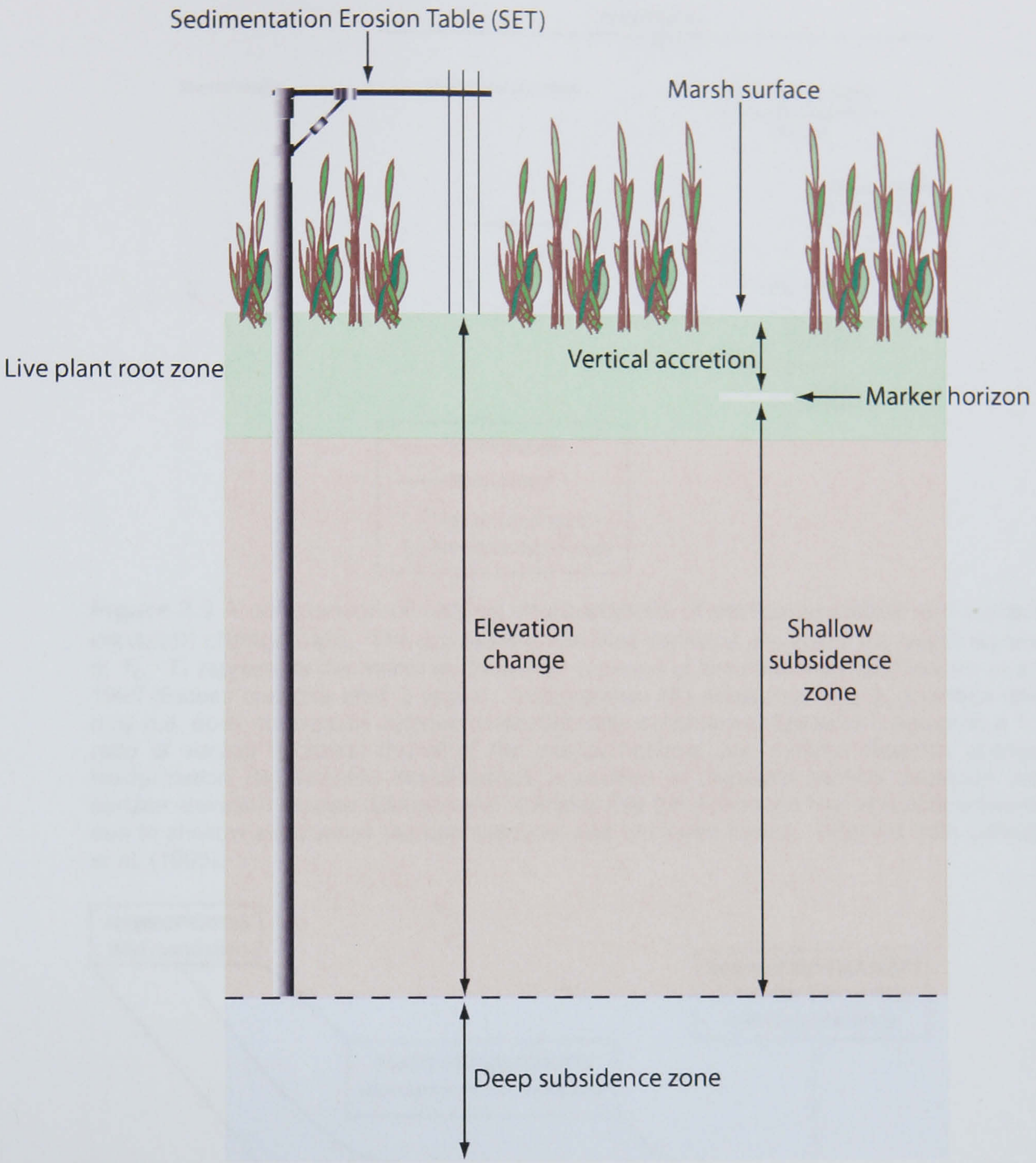

Figure 2.2 Schematic diagram of the Sedimentation Erosion Table (not to scale). The diagram shows the portions of the stratigraphic column being measured by the SET and marker horizon techniques. The boundary separating the shallow and deep subsidence zones is defined operationally by the bottom of the SET pipe. Adapted from Cahoon *et al.* (1995).

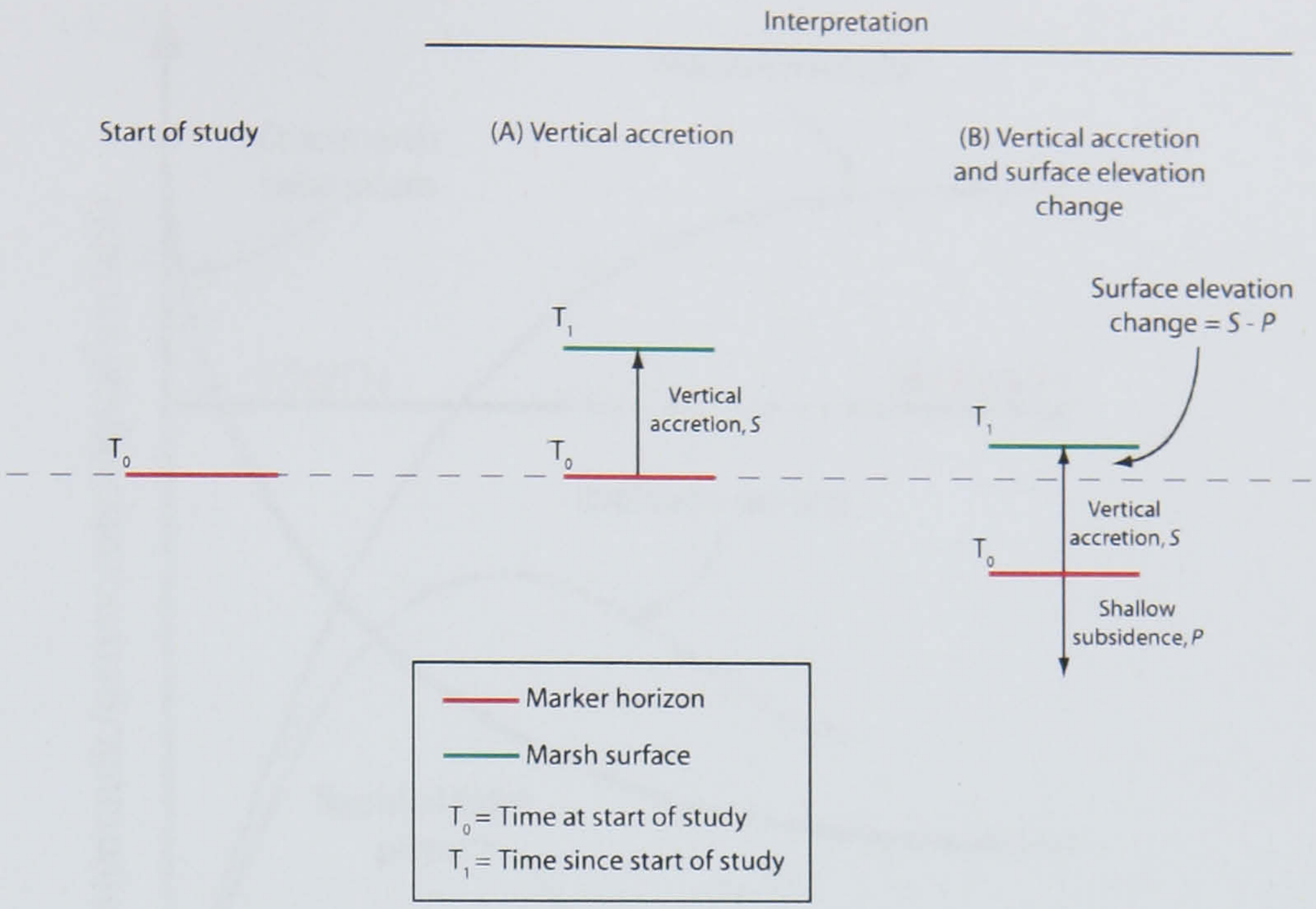

Figure 2.3 A comparison of varying interpretations of vertical accretion and surface elevation change data. The dashed line indicates the initial position of the marsh surface at T_0. T_1 represents the marsh surface after a period of time has elapsed (Cahoon *et al.*, 1995 discuss changes after 2 years). Interpretation (A) measures vertical accretion data only (i.e. does not include autocompaction/shallow subsidence) because it assumes a 1:1 ratio of vertical accretion (burial of the marker horizon) and surface elevation change. Interpretation (B) includes simultaneous evaluation of separate vertical accretion and surface elevation change datasets and indicates that the T_0 horizon has moved downwards due to shallow subsidence (autocompaction) and has been buried. Adapted from Cahoon *et al.* (1995).

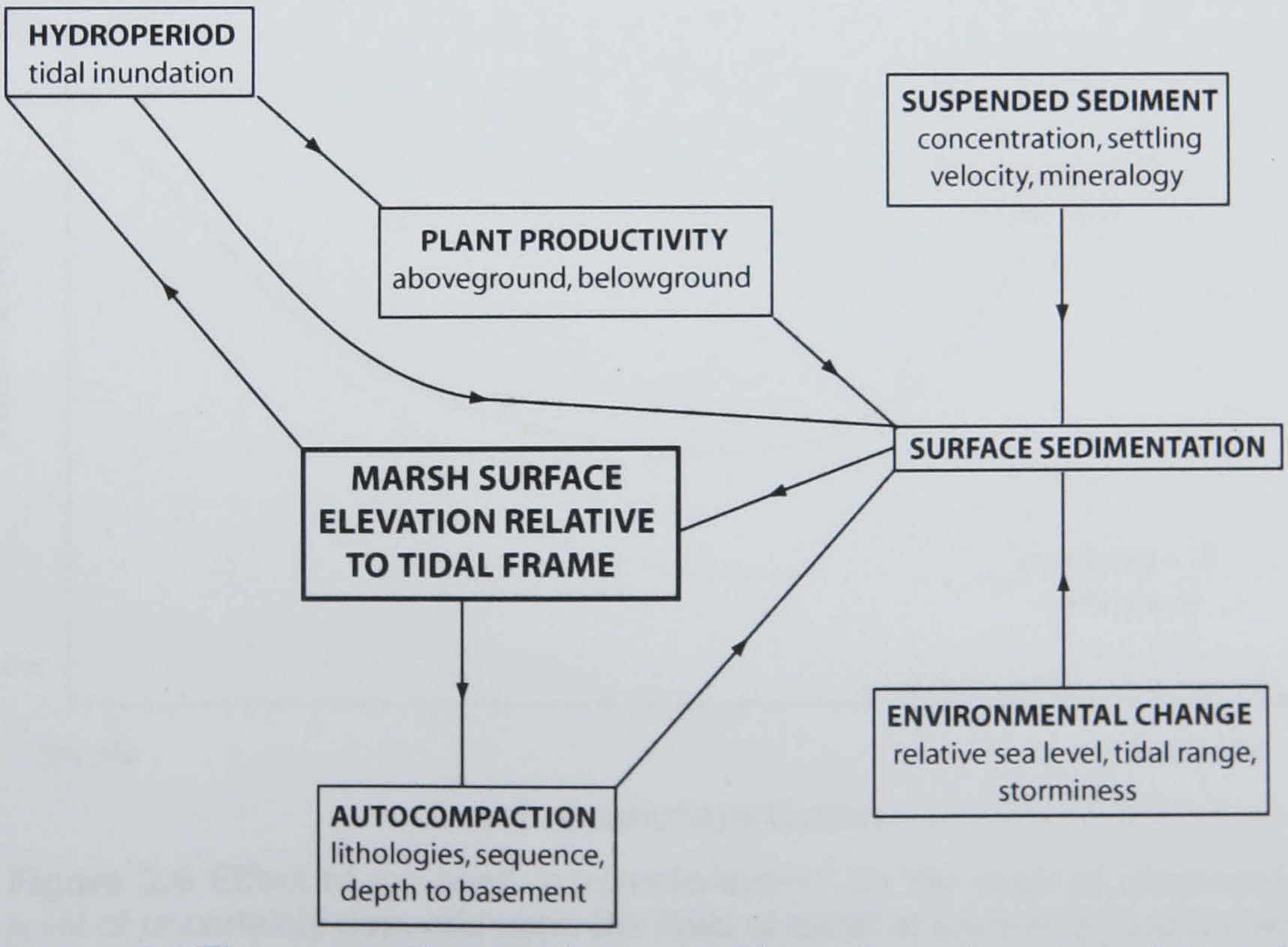

Figure 2.4 The composition and linkages of the saltmarsh system. Adapted from Allen (2000).

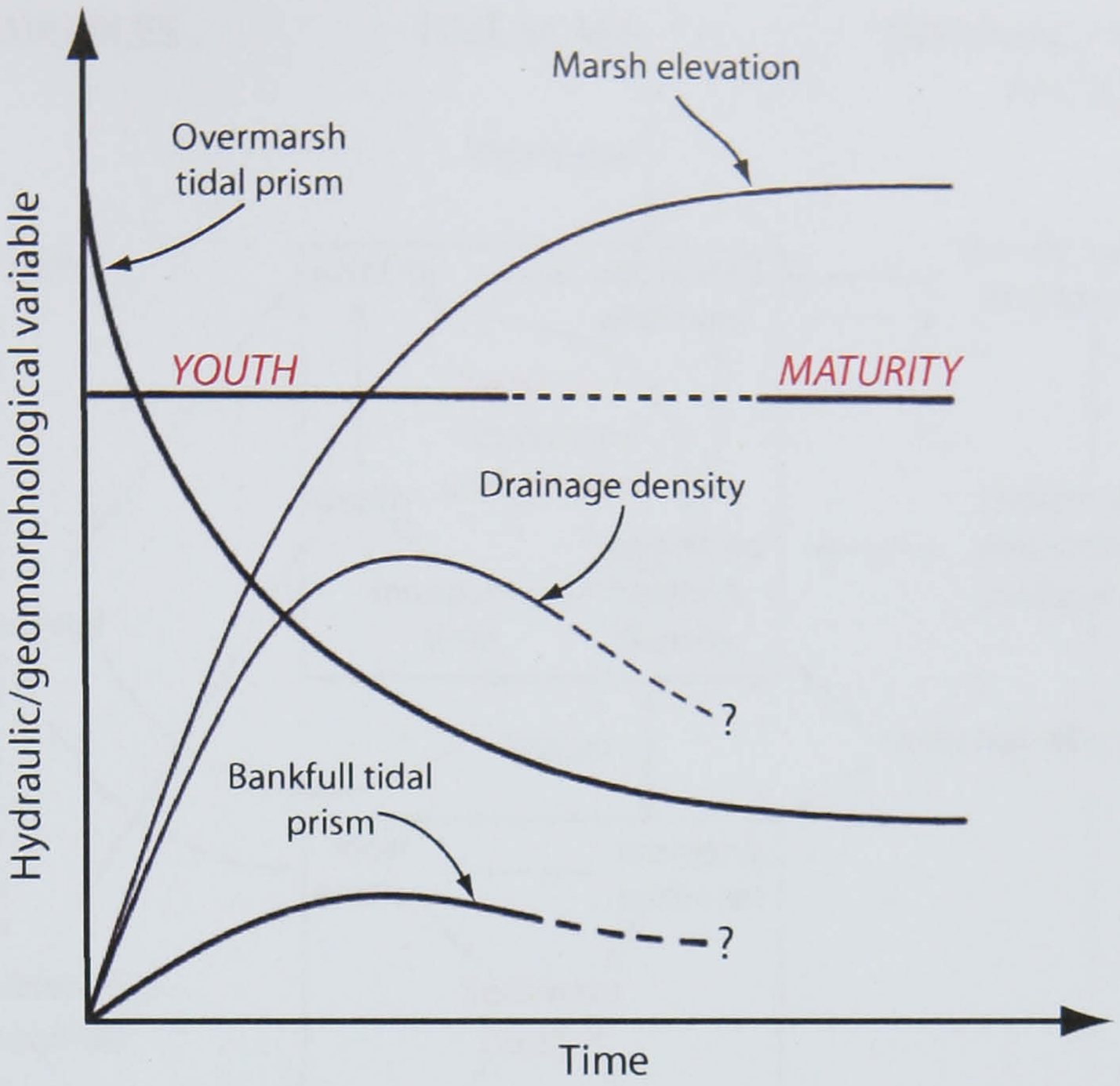

Figure 2.5 A model for the possible hydraulic and geomorphological evolution of saltmarsh in northwest Europe. The behaviour of sea level is likely to influence the absolute and relative amounts of the tidal prism. Redrawn from Allen (2000).

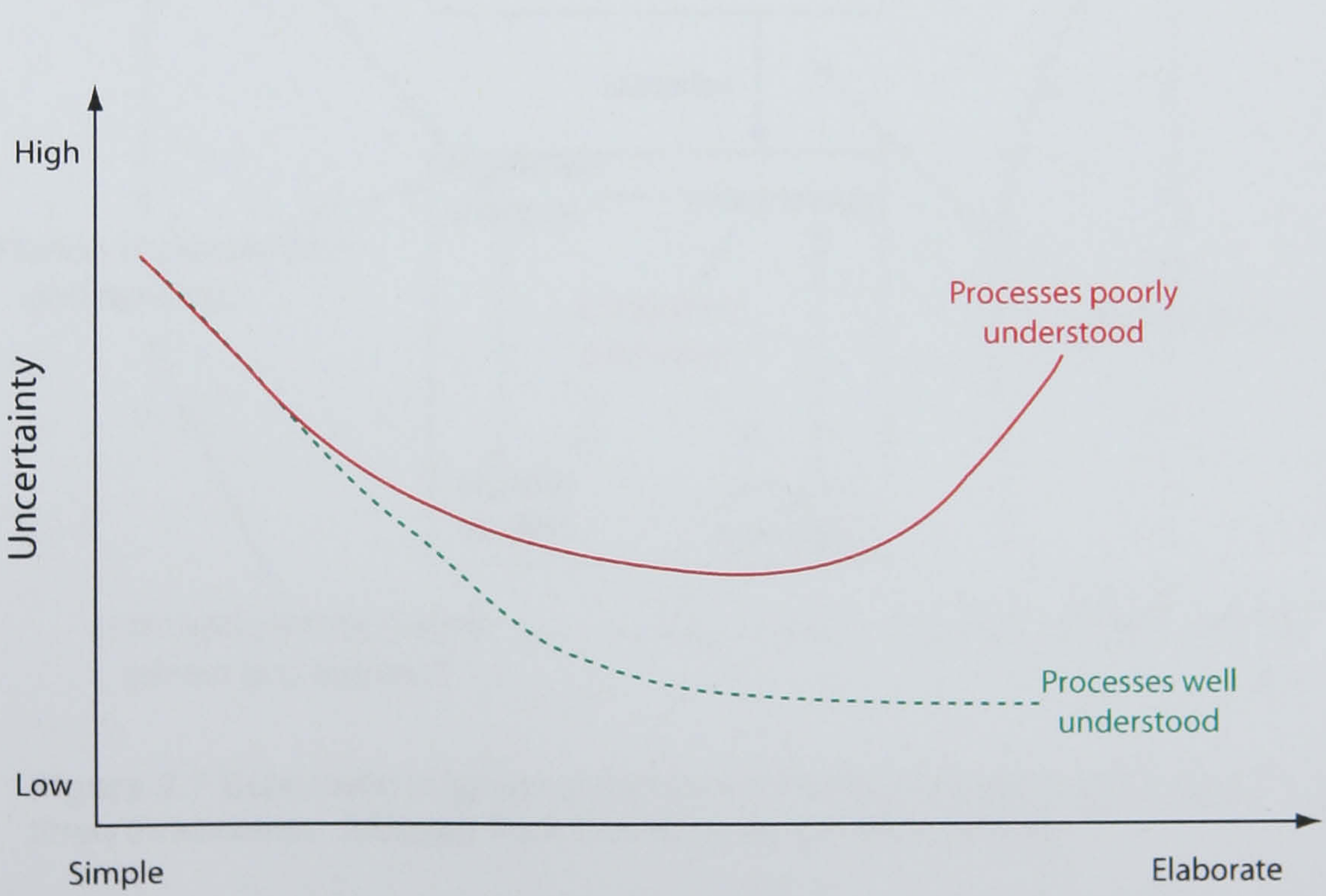

Figure 2.6 Effect of the level 'parameterisation' on the level of uncertainty. The level of uncertainty depends upon the level of detail in the model and the degree to which processes are understood. Adapted from GESAMP (1991).

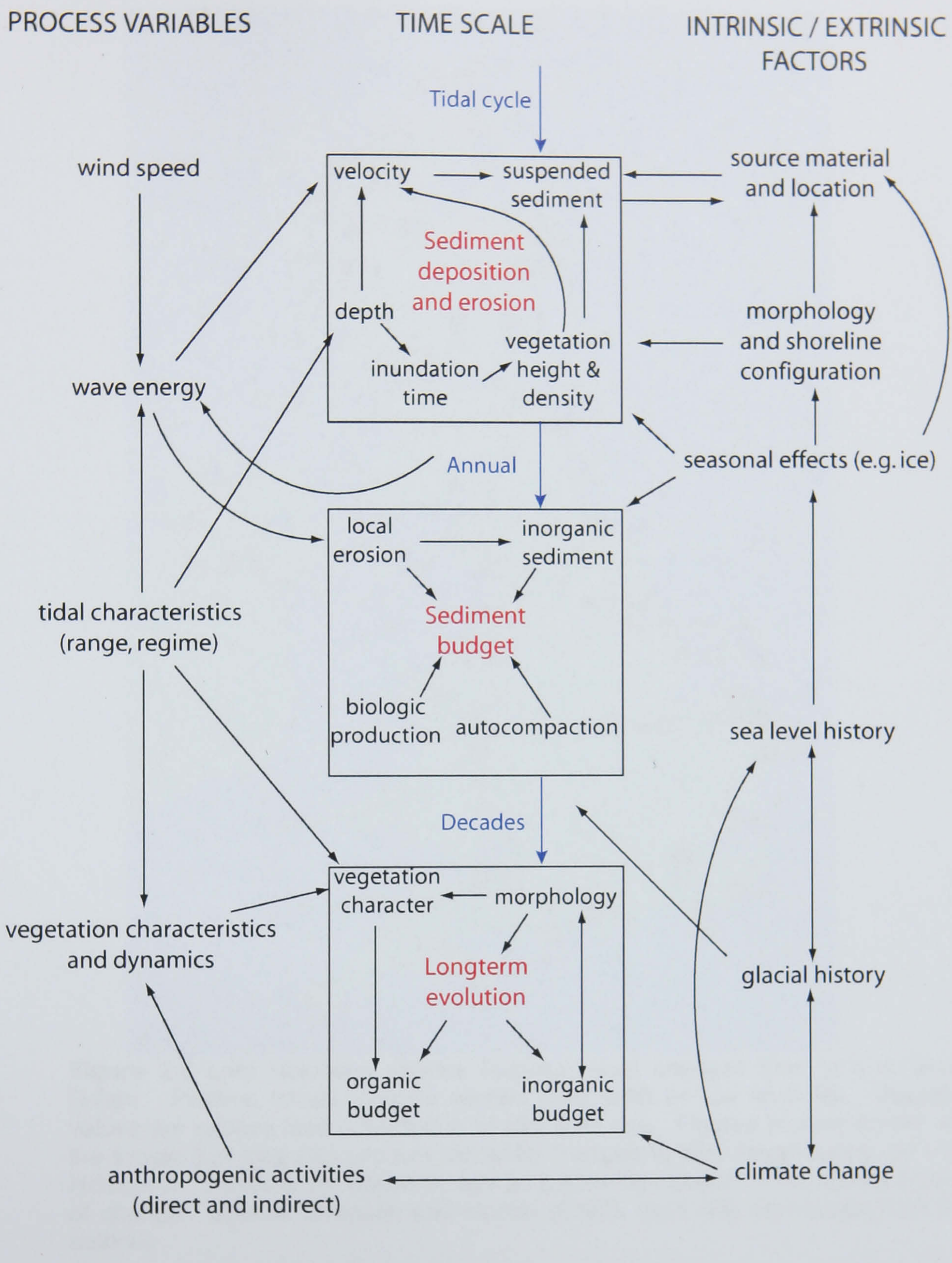

Figure 2.7 Schematic diagram of factors controlling saltmarsh sedimentation on three timescales. Adapted from Davidson-Arnott *et al*. (2002).

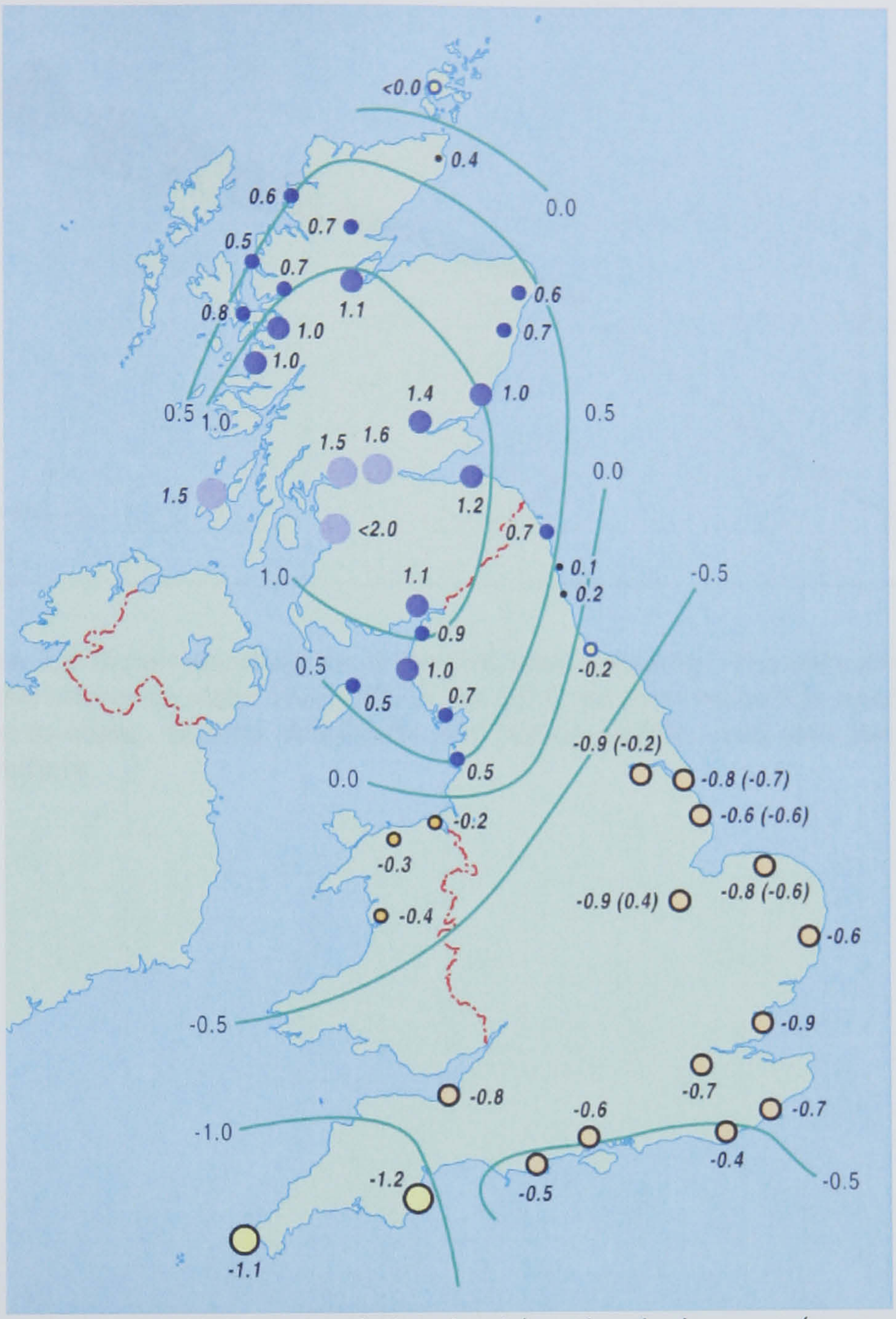

Figure 2.8 Late Holocene relative land-/sea-level changes (mm yr^{-1}) in Great Britain. Positive values indicate relative land uplift or sea level fall. Negative values are relative land subsidence of sea level rise. Figures in parentheses are the trends that take into account modelled changes in tidal range during the Late Holocene. Contours are drawn by eye as a summary sketch of the spatial pattern of change. Source: Shennan and Horton (2002), used with permission from the authors.

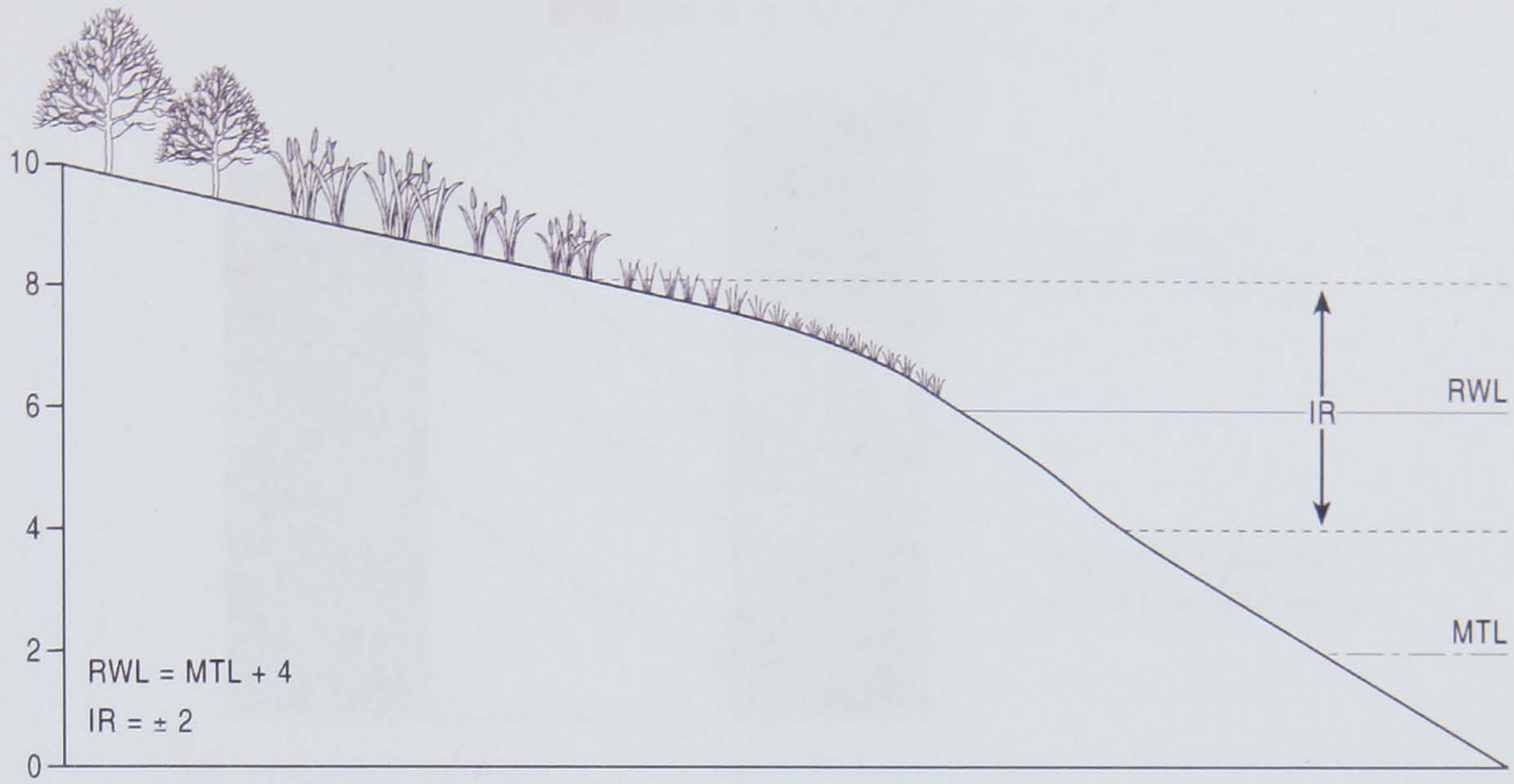

Figure 2.9 Schematic diagram of the indicative meaning. The indicative range (IR) and the reference water level (RWL) are obtained from mean tide level (MTL). Not drawn to scale. Source: Woodroffe and Horton (2005), used with permission from the authors.

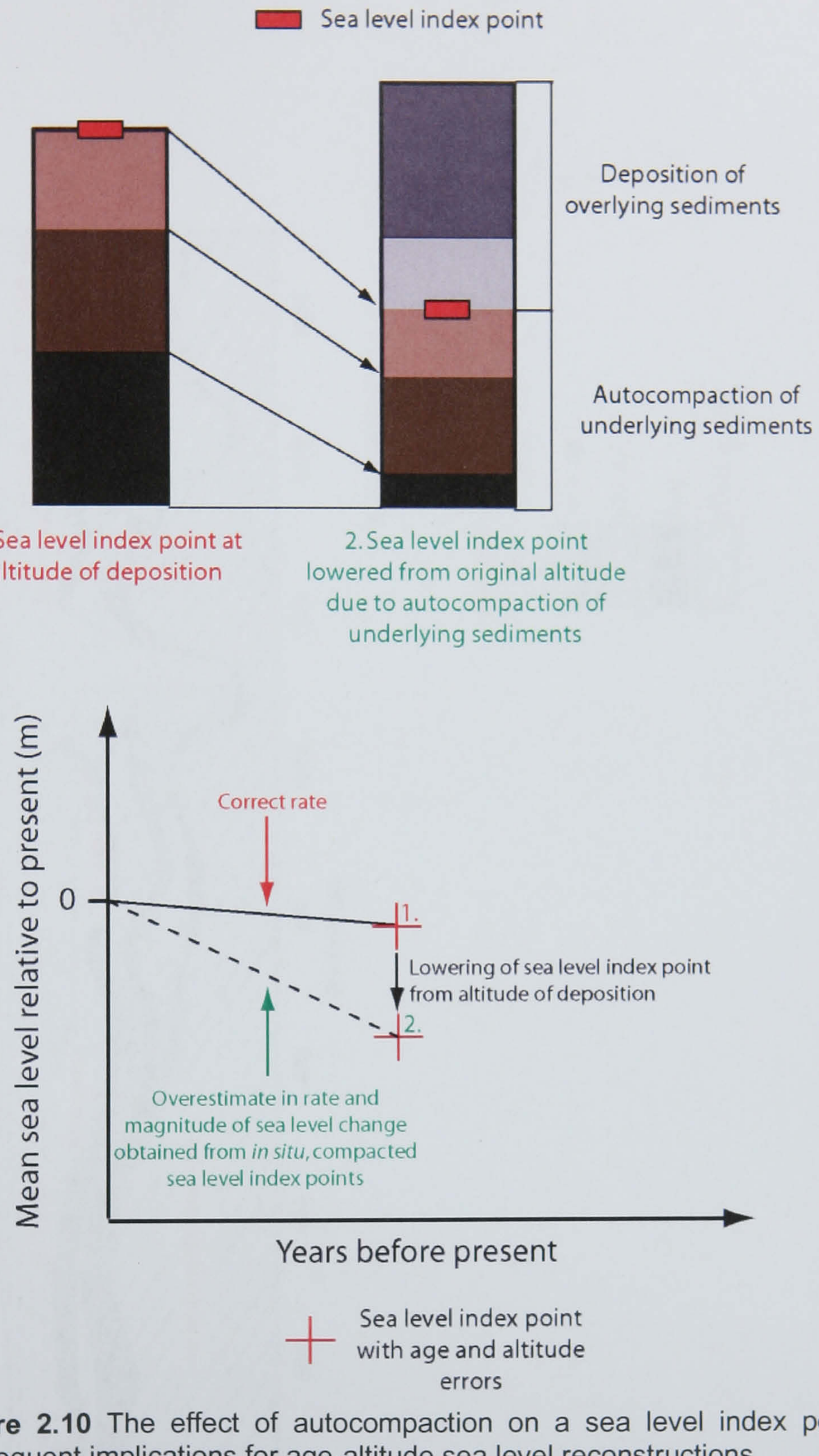

Figure 2.10 The effect of autocompaction on a sea level index point and the consequent implications for age-altitude sea level reconstructions.

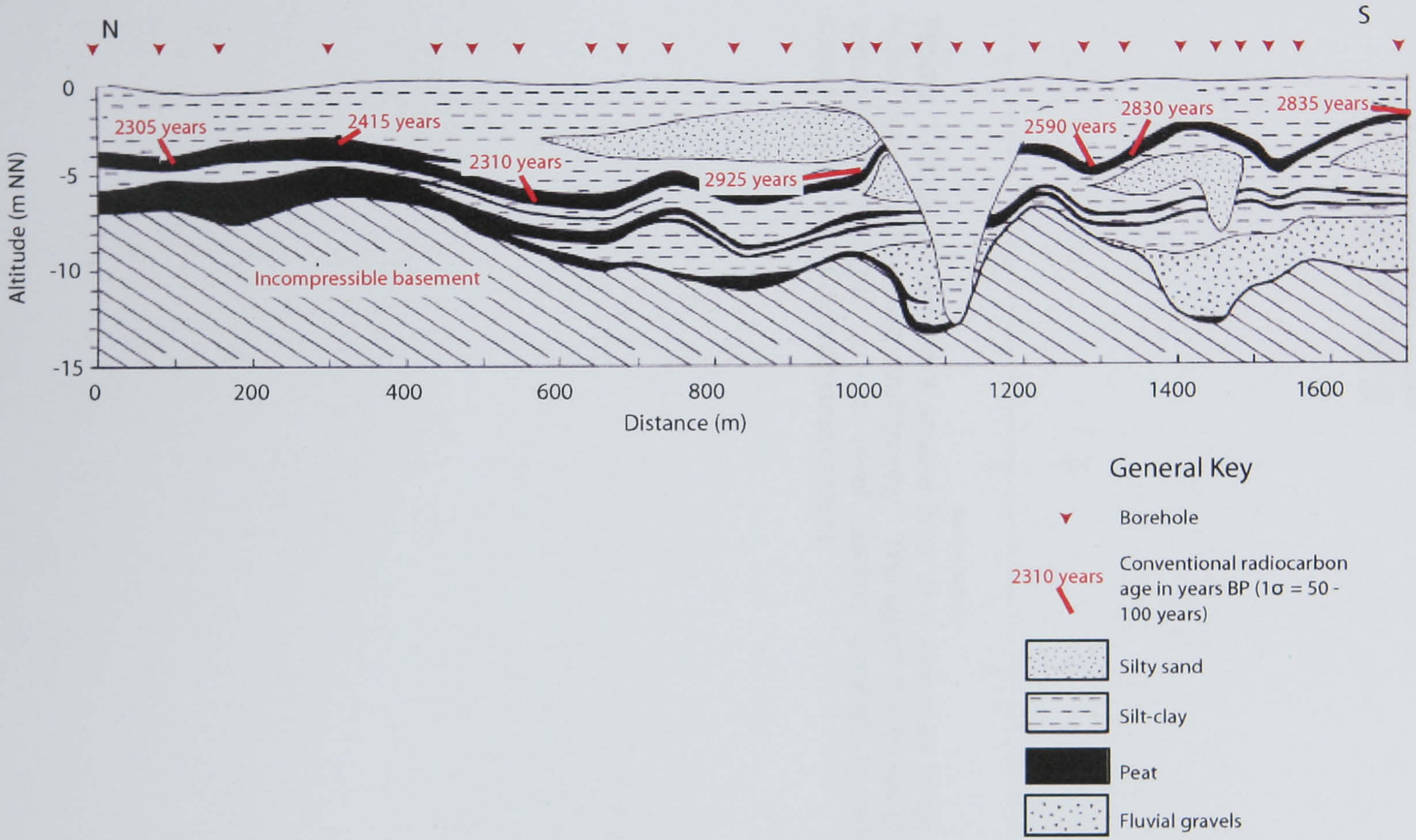

Figure 2.11 Stratigraphic cross-section at Woltzeten in the Ems marshes, northwest Germany. Stratigraphic distortion of isochronous beds is illustrated. Adapted from Allen (2000).

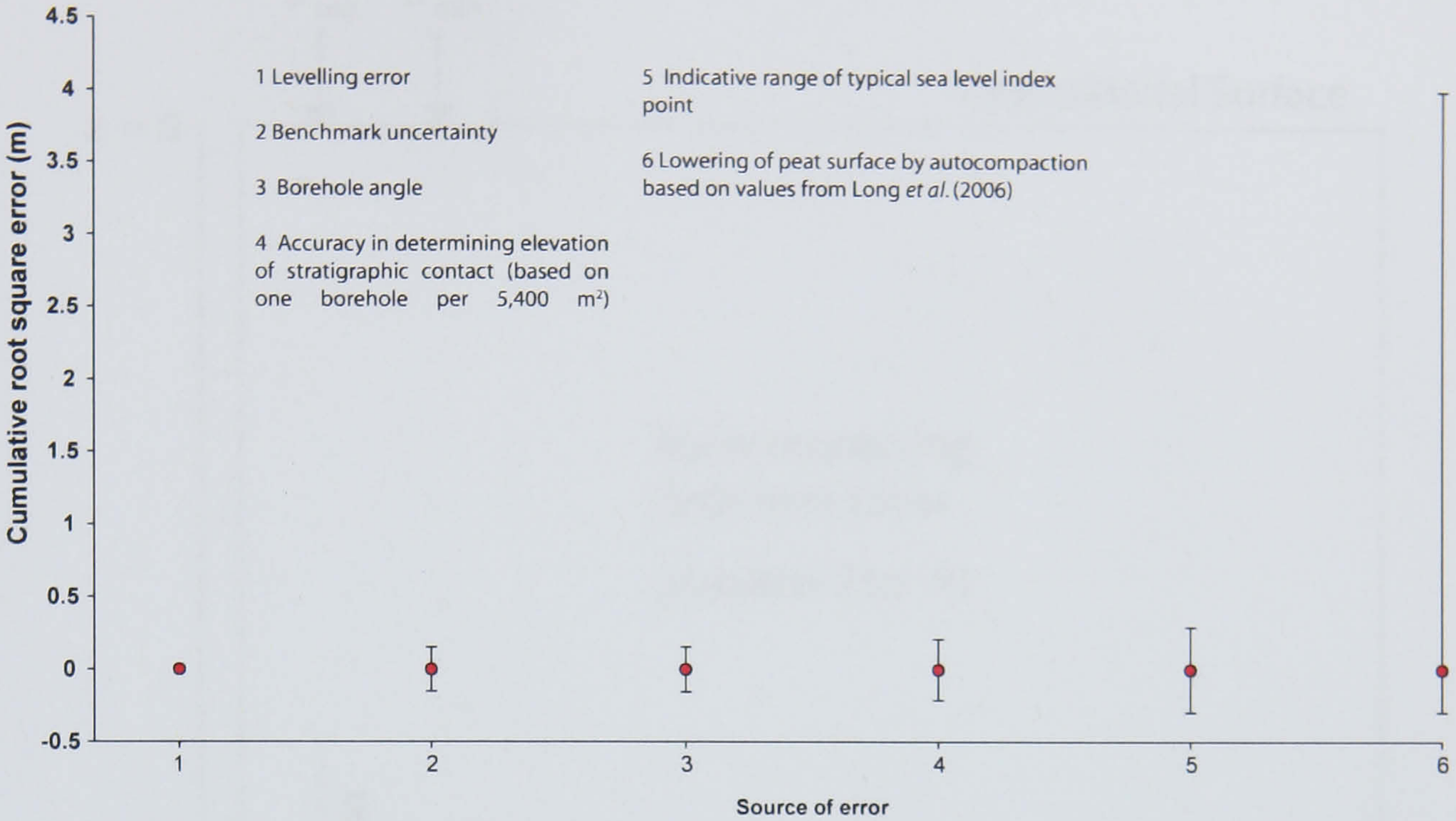

Figure 2.12 Cumulative root square error of a sea level index point underlain by highly compressible peat stratigraphy. The figure illustrates the magnitude of the autocompaction error in sea level studies, particularly those obtained from stratigraphies with a high organic content.

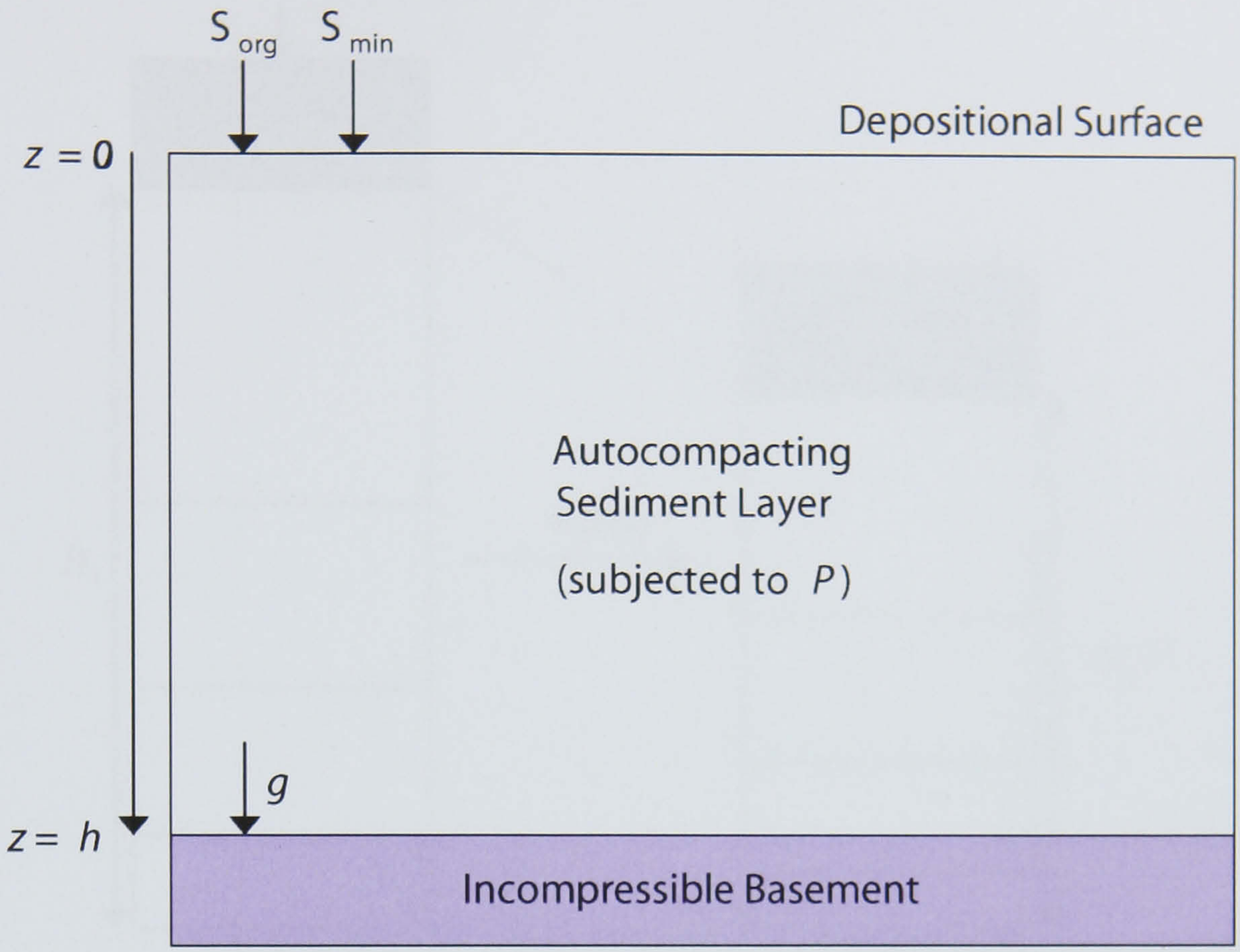

h = total thickness of the sediment column

z = height co-ordinate

g = gravitational force

S_{min} = tidally imported mineralogenic sediment

S_{org} = *in situ* organogenic growth

P = autocompaction processes

Figure 3.1 Diagram of an autocompacting sediment column. See text for explanation.

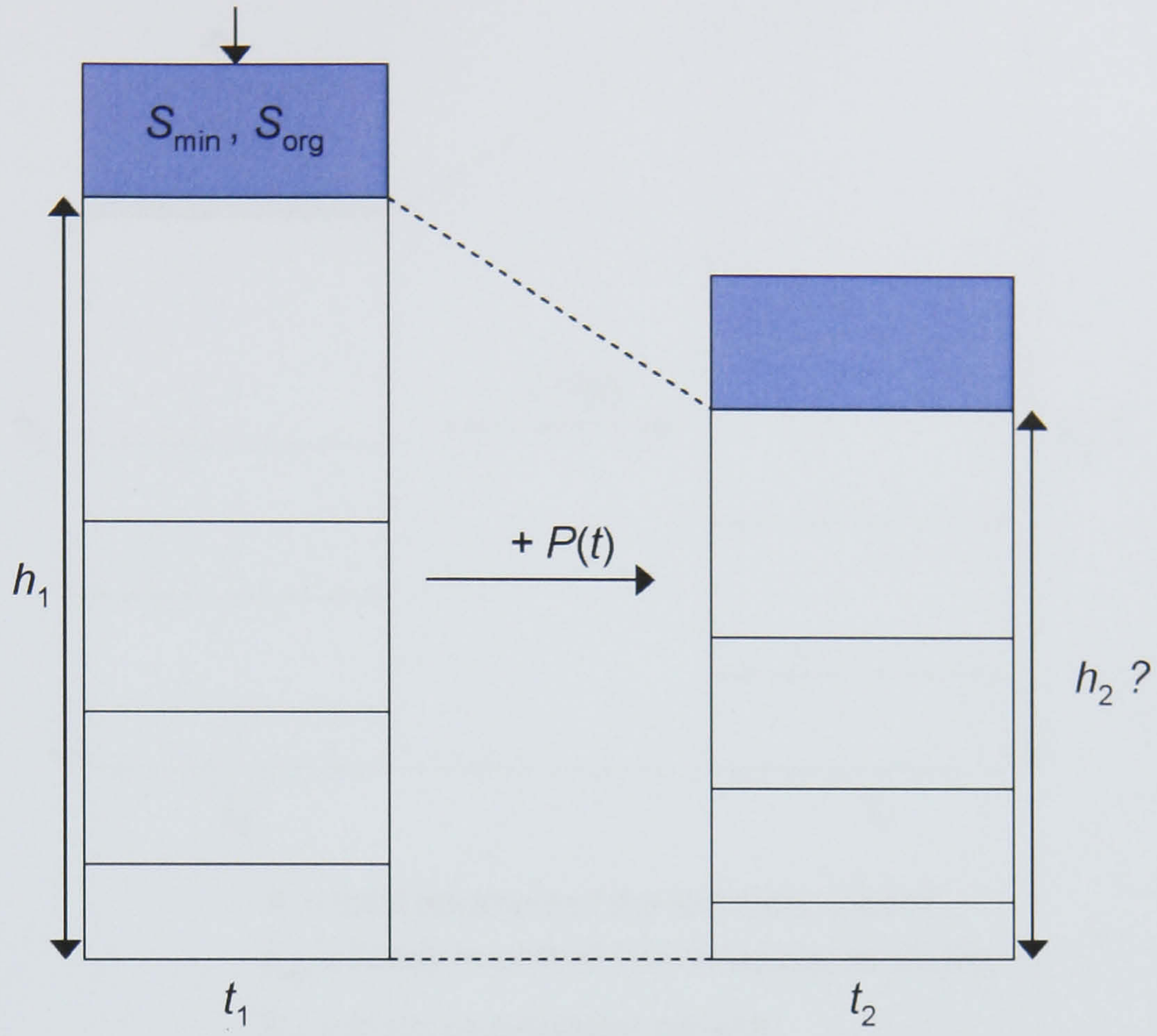

h = total thickness of the sediment column

S_{min} = tidally imported mineralogenic sediment

S_{org} = *in situ* organogenic growth

P = autocompaction processes

t = time

Figure 3.2 Schematic diagram of the effect of autocompaction on layer thickness and surface elevation changes.

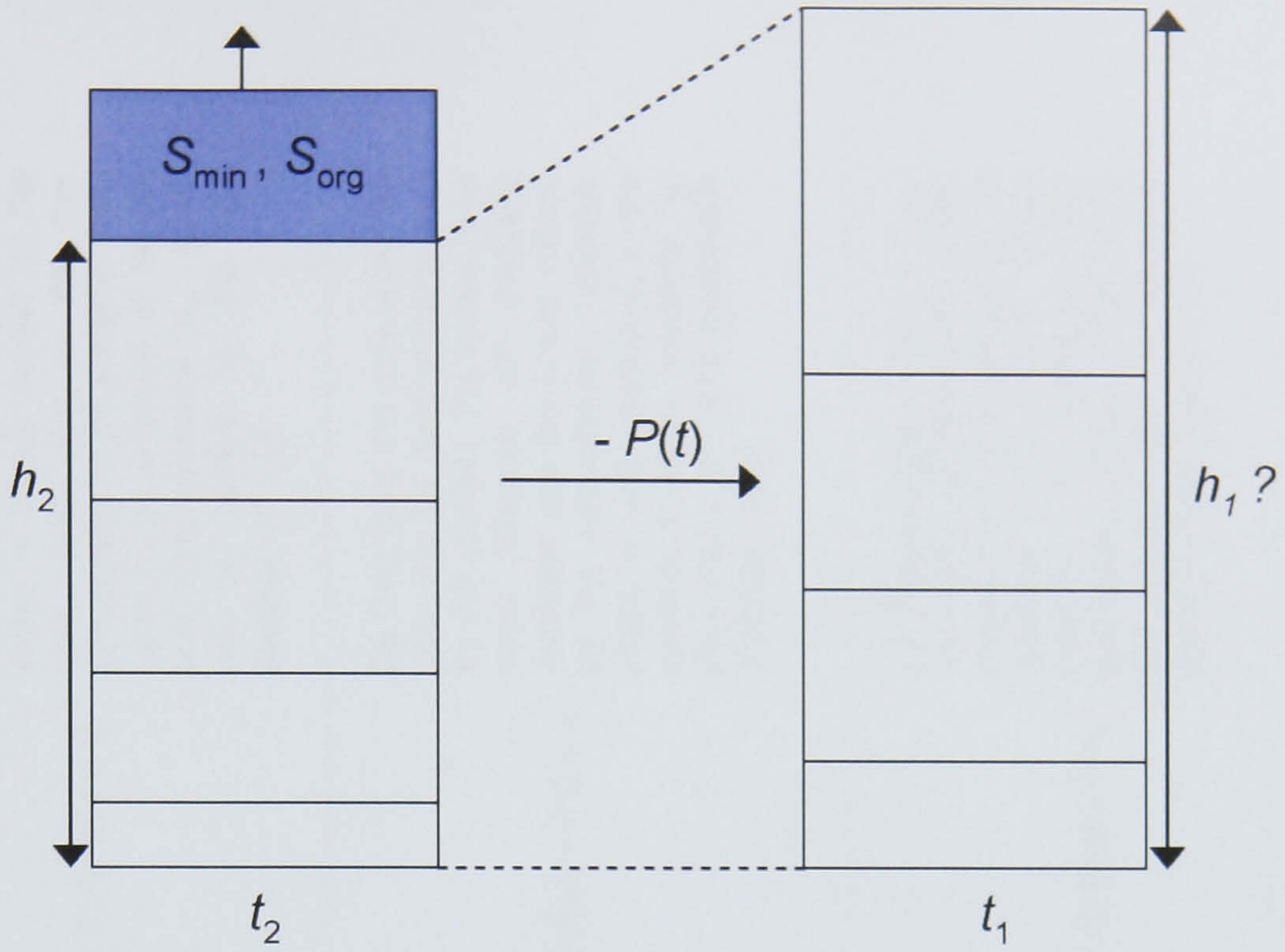

h = total thickness of the sediment column

S_{min} = tidally imported mineralogenic sediment

S_{org} = *in situ* organogenic growth

P = autocompaction processes

t = time

Figure 3.3 Schematic diagram illustrating the 'decompaction' process.

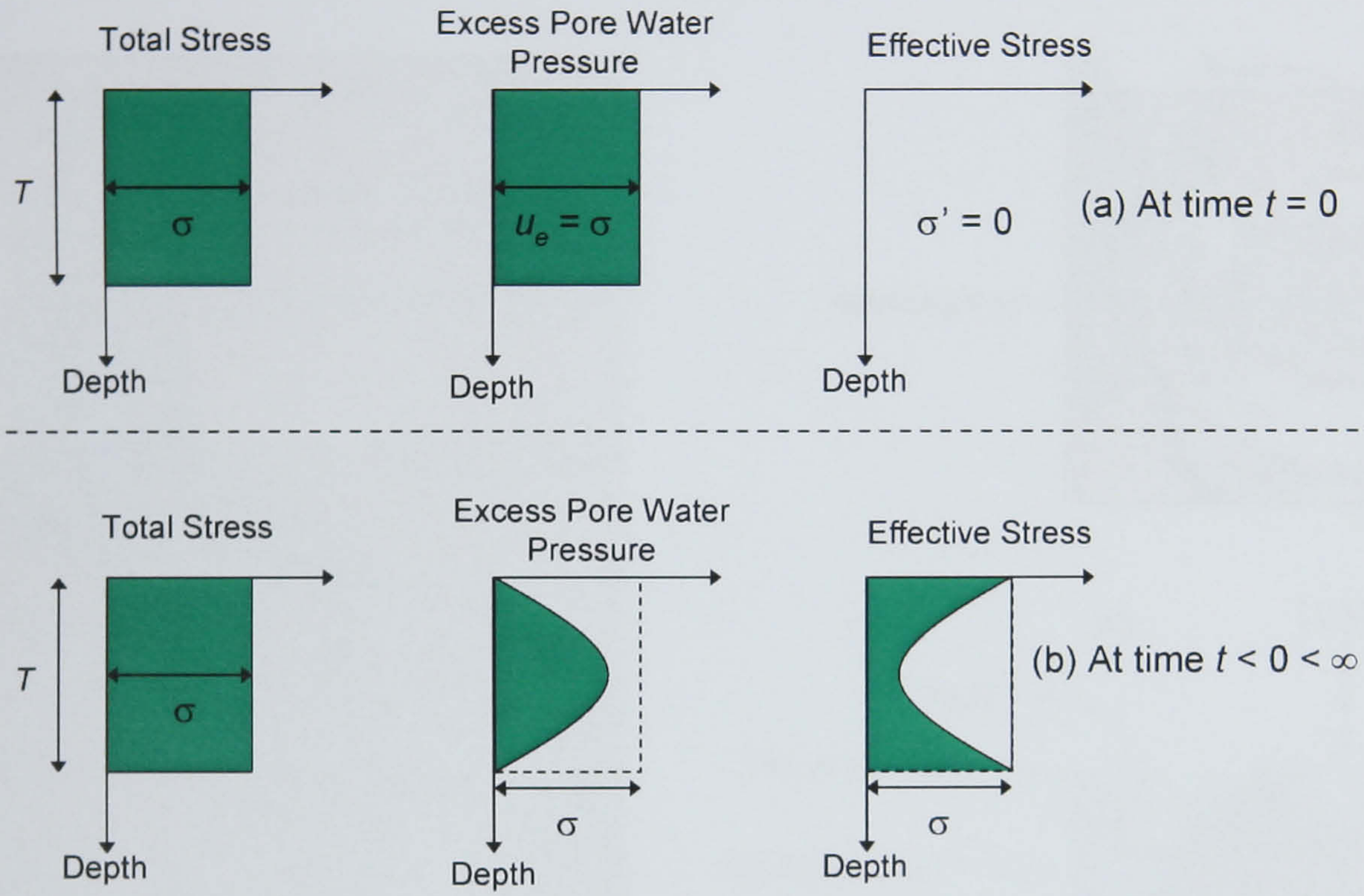

(a) When a saturated clay layer of thickness T is subjected to a compressive total stress, σ, the stress is initially carried by the pore water due to the low permeability of the material. This leads to an increase in excess pore water pressure, u_e. None will be carried by the soil skeleton (σ' = 0).

(b) Over time, the pore water will drain into the surrounding layers. By this process, the excess pore water pressure will gradually decrease and the stress carried by the soil skeleton (effective stress, σ') will increase at a rate dependent upon proximity to over- and under-lying permeable drainage layers.

(c) Theoretically, at time $t = \infty$, the entire excess pore water pressure will have dissipated by drainage from all points of the layer ($u_e = 0$). At this time, the total stress will be carried by the soil skeleton and so effective stress is equal to total stress.

Adapted from Das (1998).

Figure 3.4 The transfer of total to effective stress in a fine-grained material.

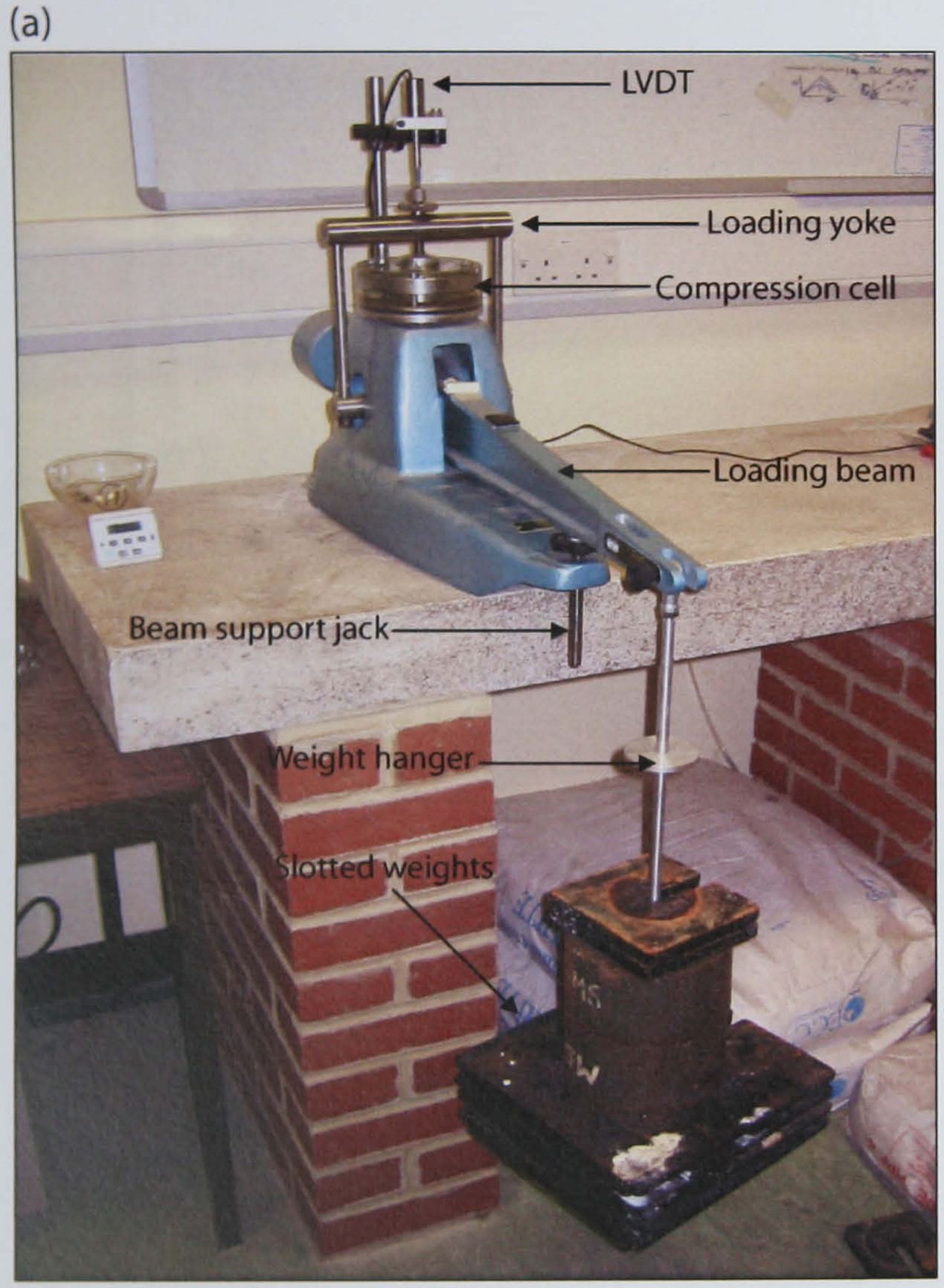

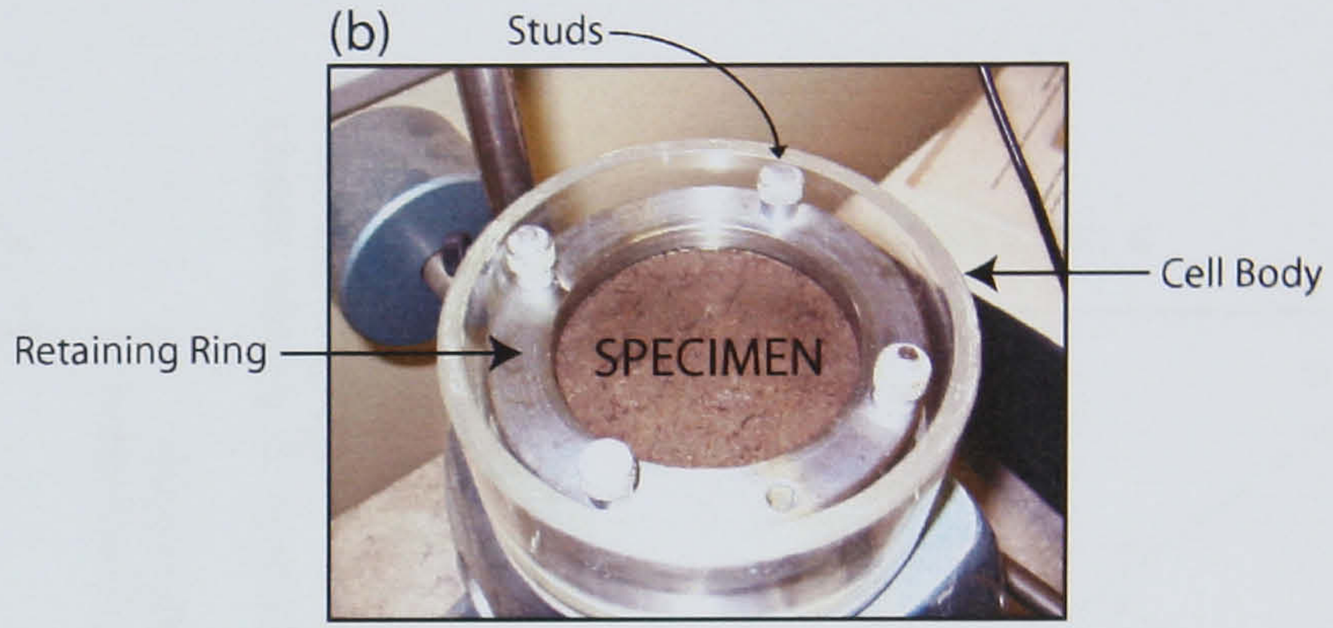

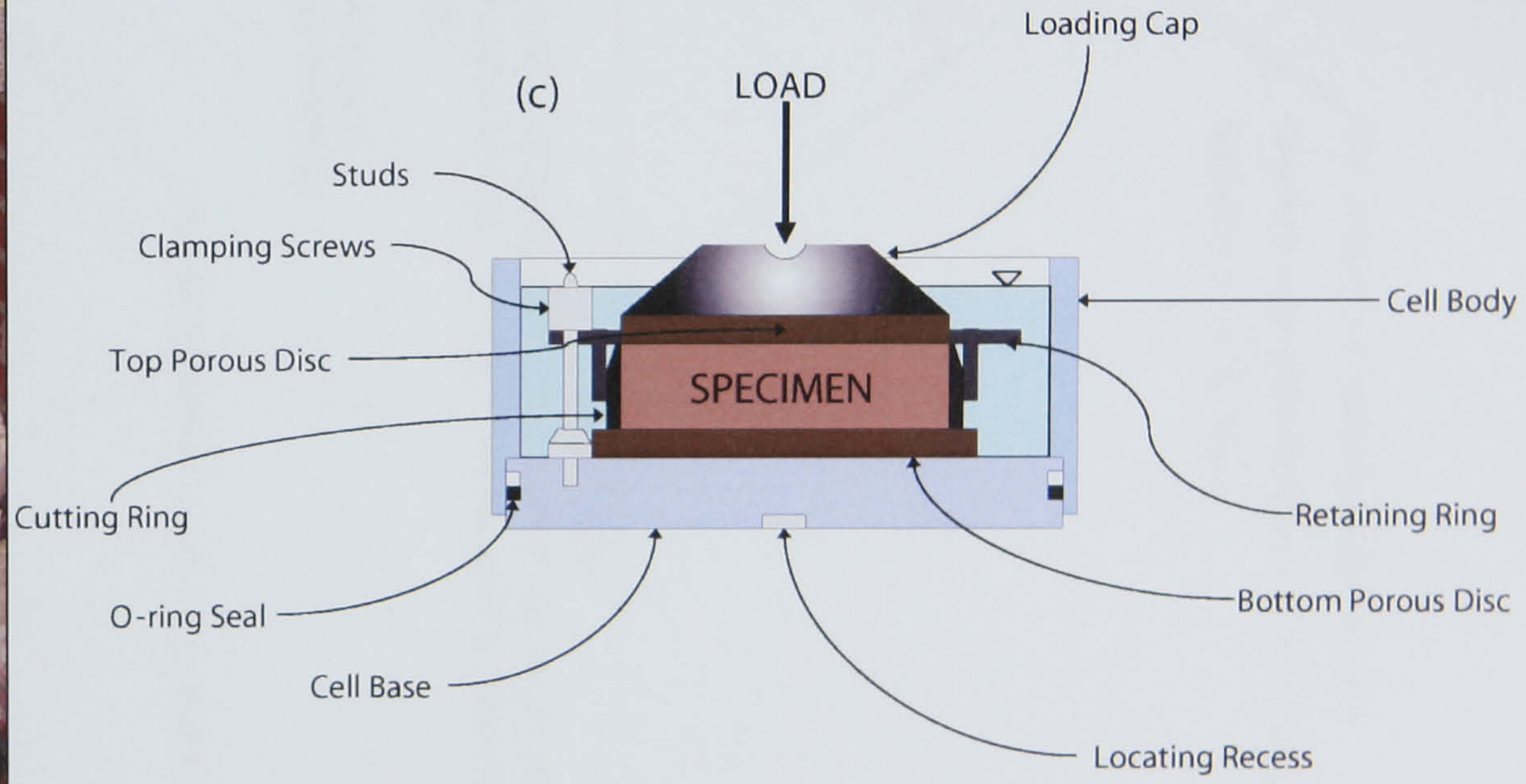

Figure 3.5 The oedometer compression apparatus. (a) laboratory set-up. (b) location of the specimen within the compression cell. (c) cross-section of a typical oedometer compression cell; the specimen is usually 20 mm high and 75 mm diameter and is restrained from deforming laterally by the cutting ring. The sample is flooded (indicated by the blue shading) and load is applied vertically.

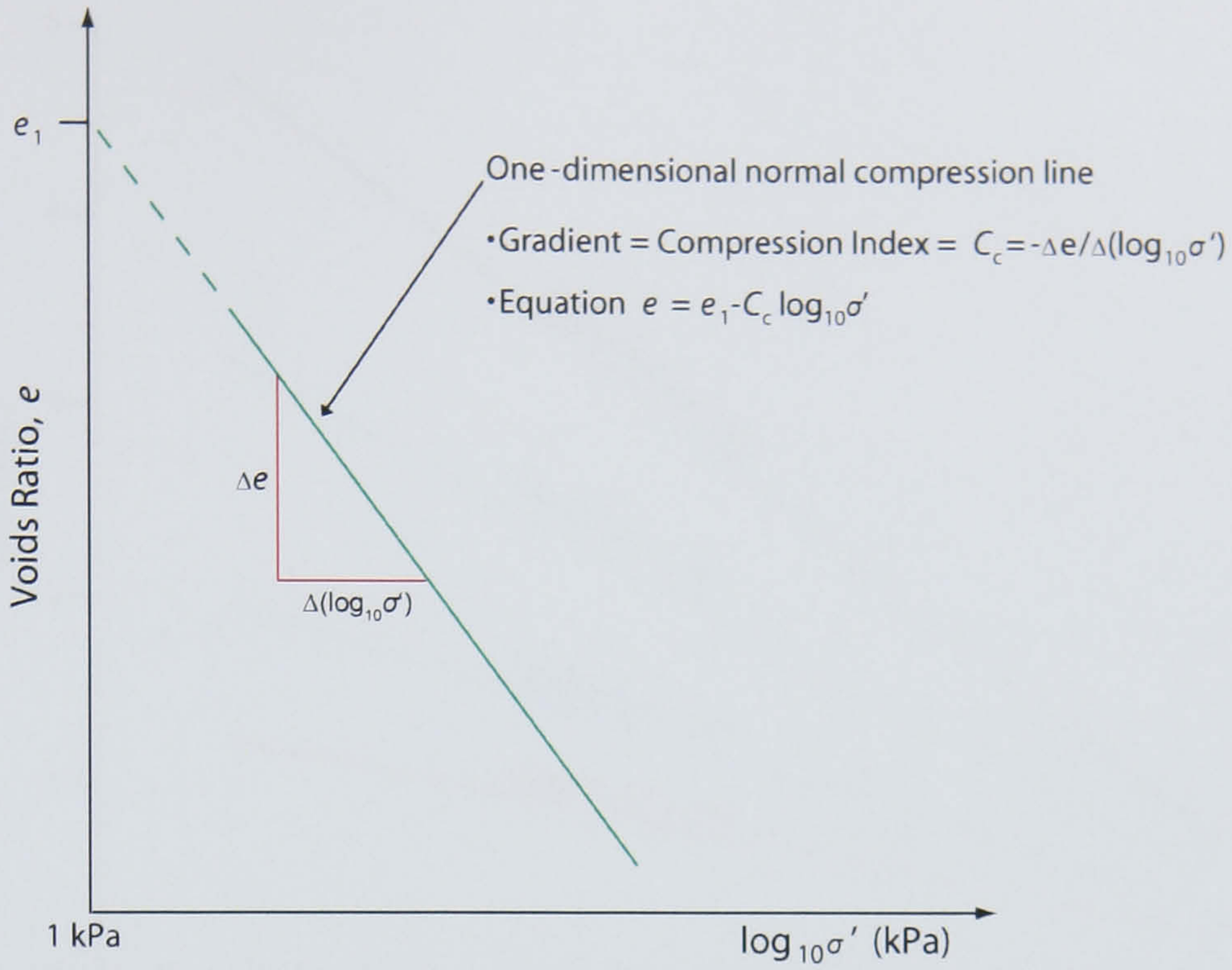

Figure 3.6 One-dimensional compression data plotted as voids ratio against the common logarithm of effective stress. A clay material with a normally consolidated stress history is illustrated.

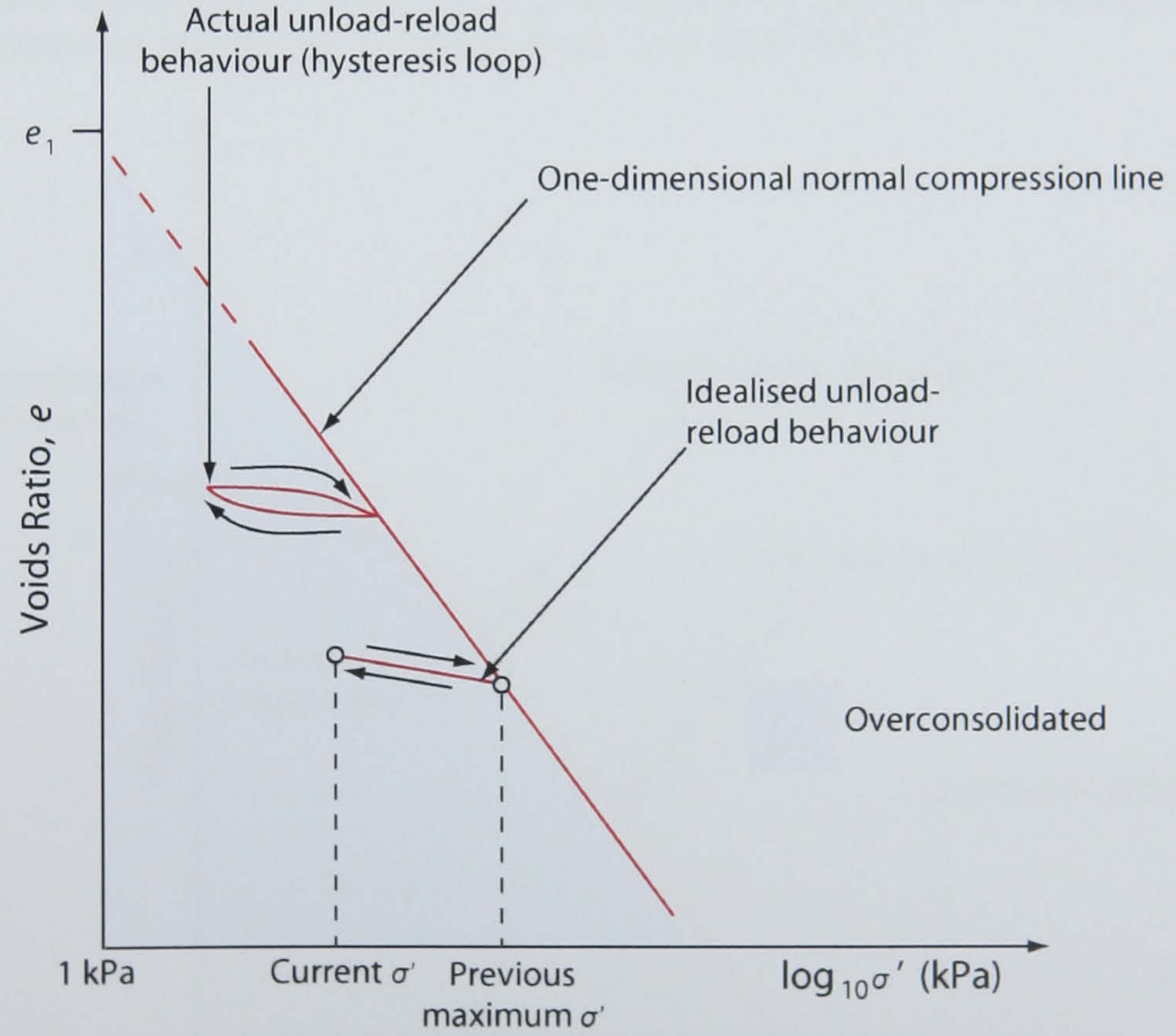

Figure 3.7 Behaviour of overconsolidated sediments in $e\log_{10}\sigma'$ space. If the effective stress acting on a material is decreased, a material becomes overconsolidated. Such materials follow an elastic unload-reload hysteresis loop unless the previous maximum effective stress is reached.

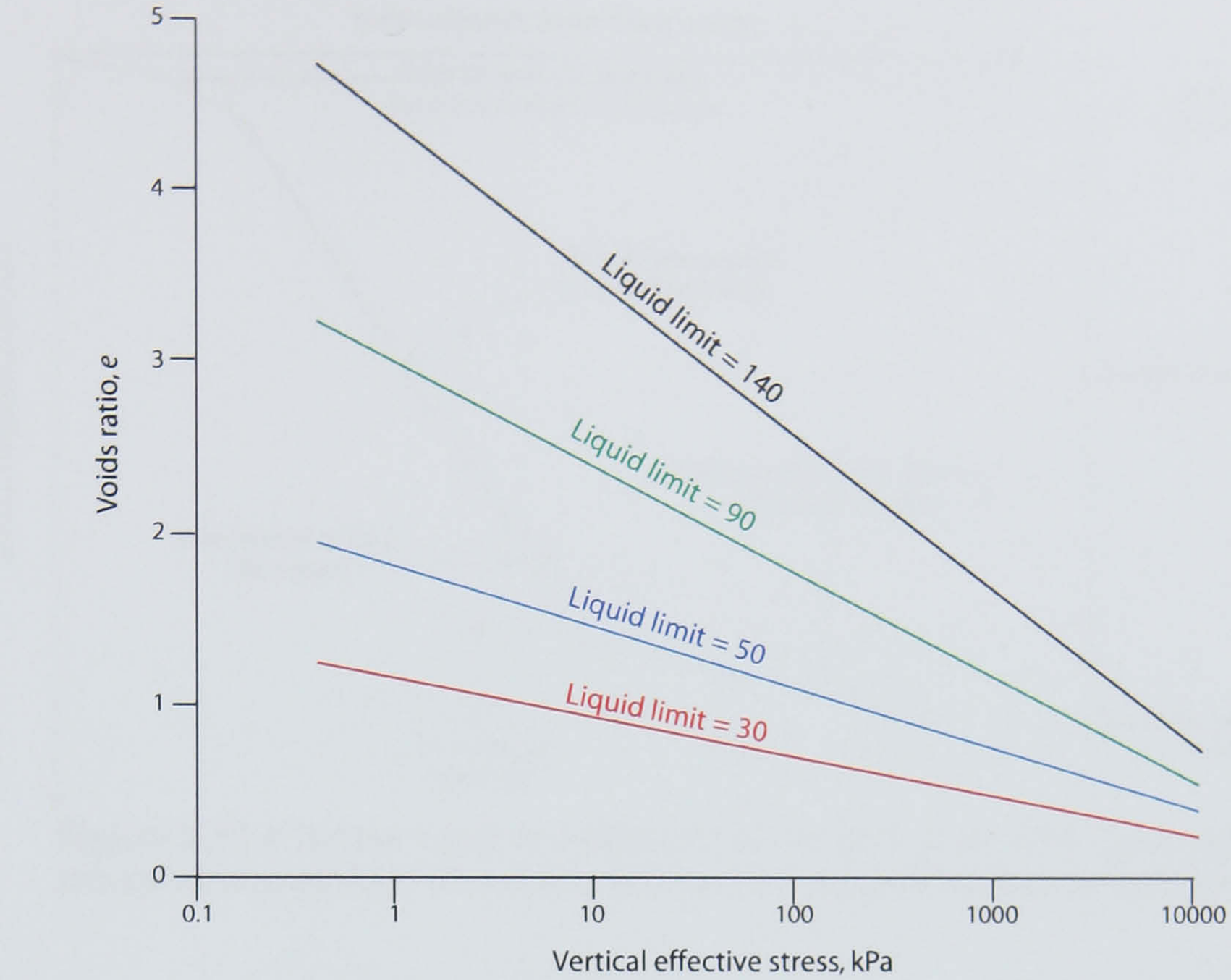

Figure 3.8 Simplified sedimentation compression curves for normally consolidated argillaceous sediments. Adapted from Skempton (1970).

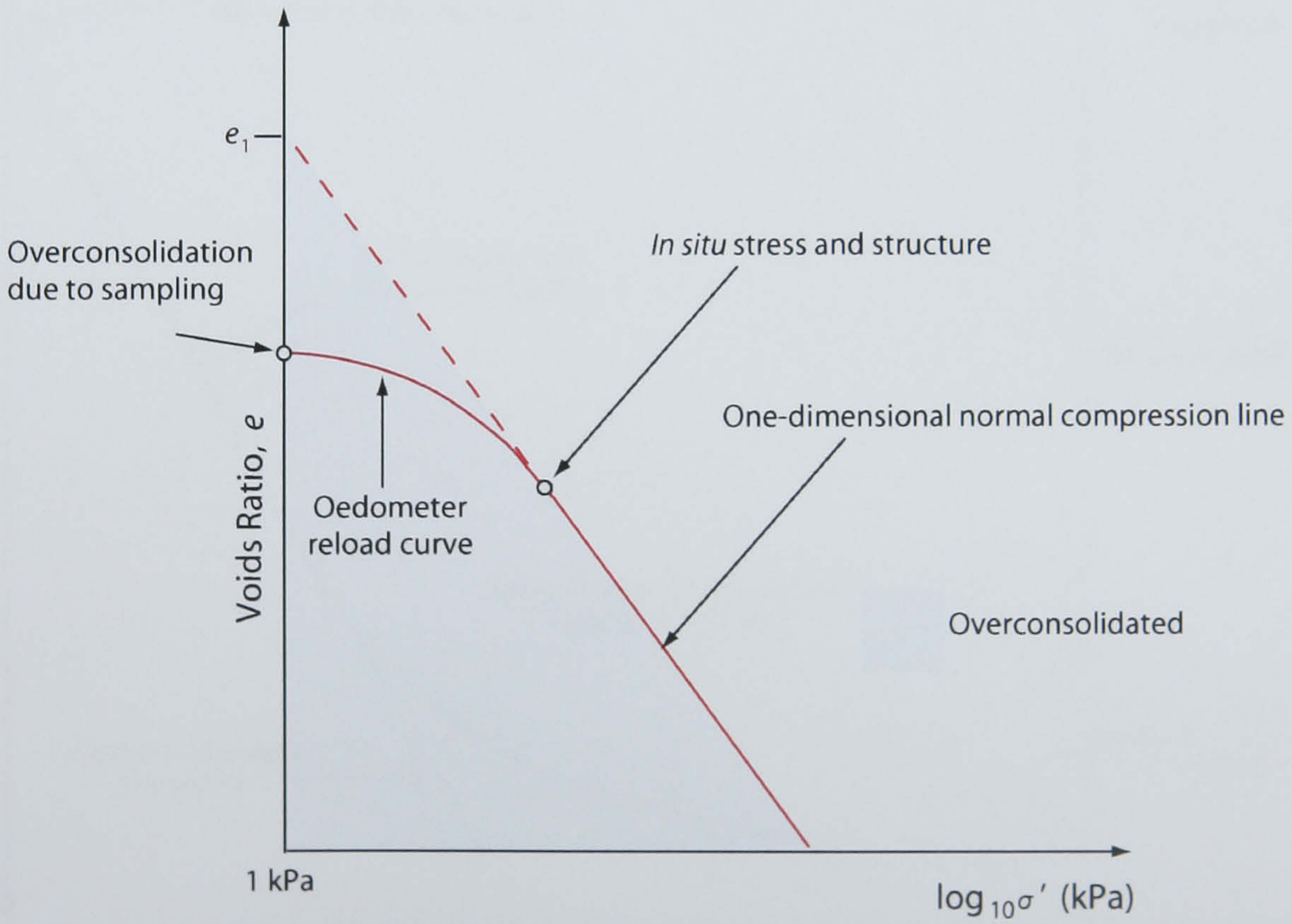

Figure 3.9 Backwards projection of the normal compression line. This procedure allows an estimate of the initial voids ratio, e_1, to be made.

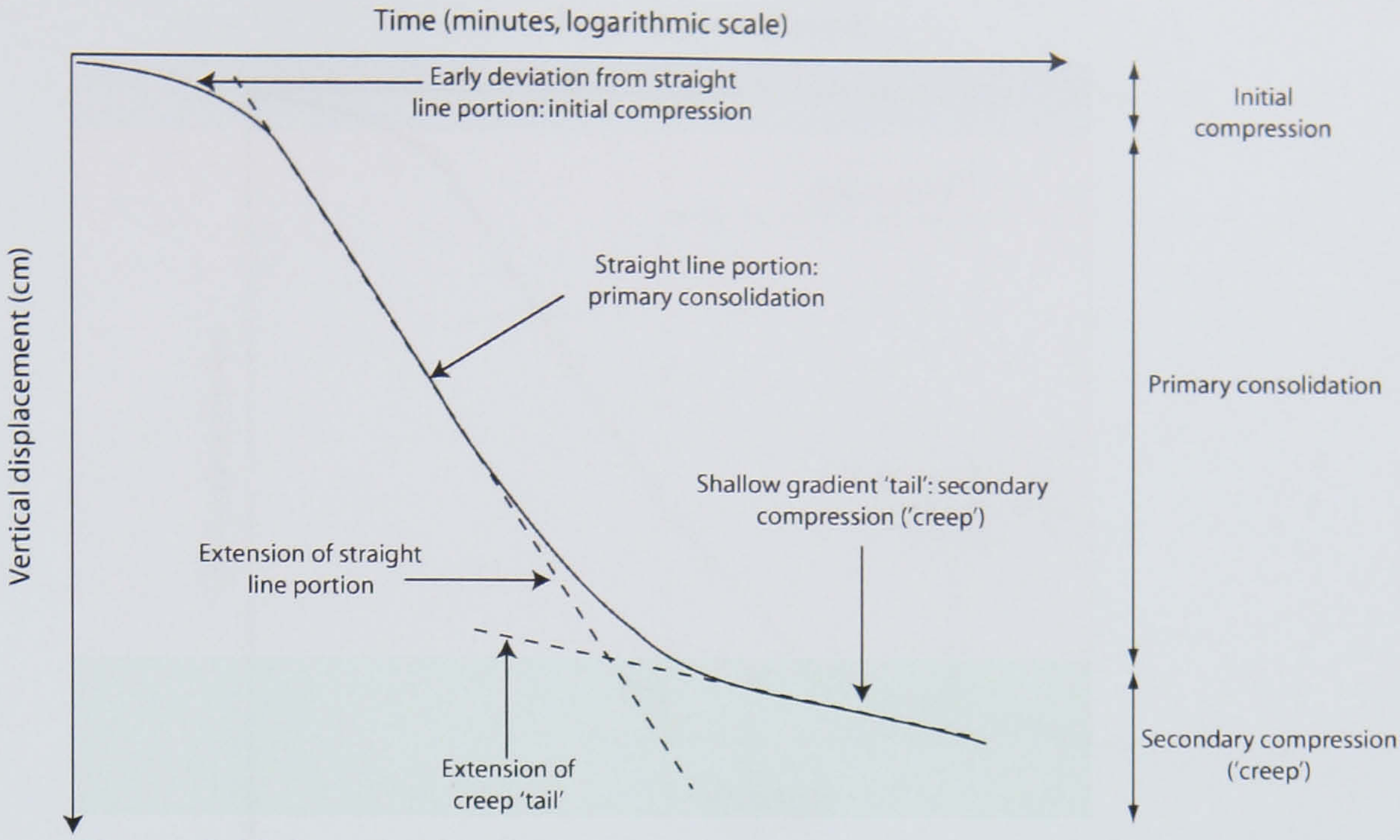

Figure 3.10 A typical log-time settlement curve for a given load increment on a saturated argillaceous material subjected to one-dimensional compression.

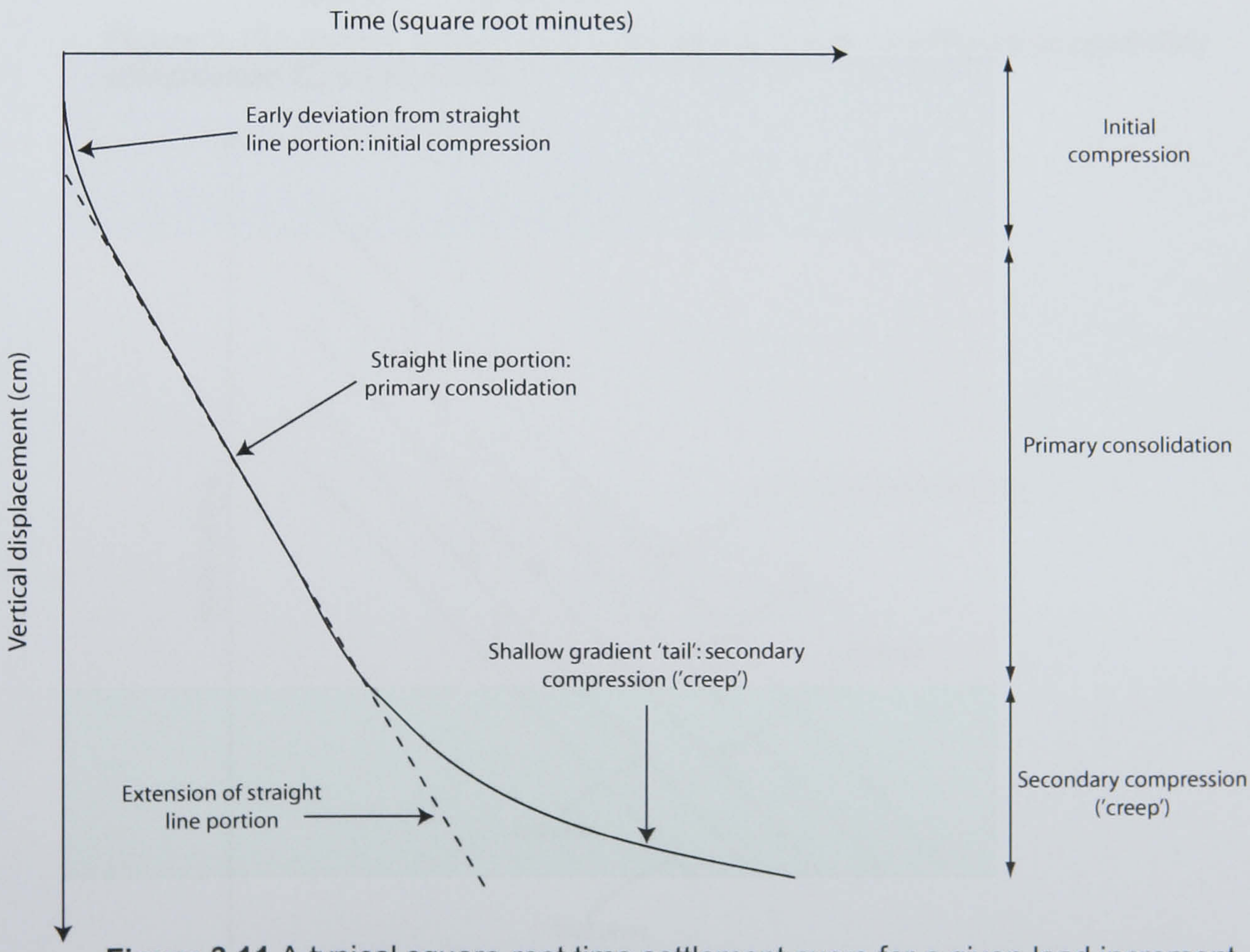

Figure 3.11 A typical square-root time settlement curve for a given load increment on a saturated argillaceous material subjected to one-dimensional compression.

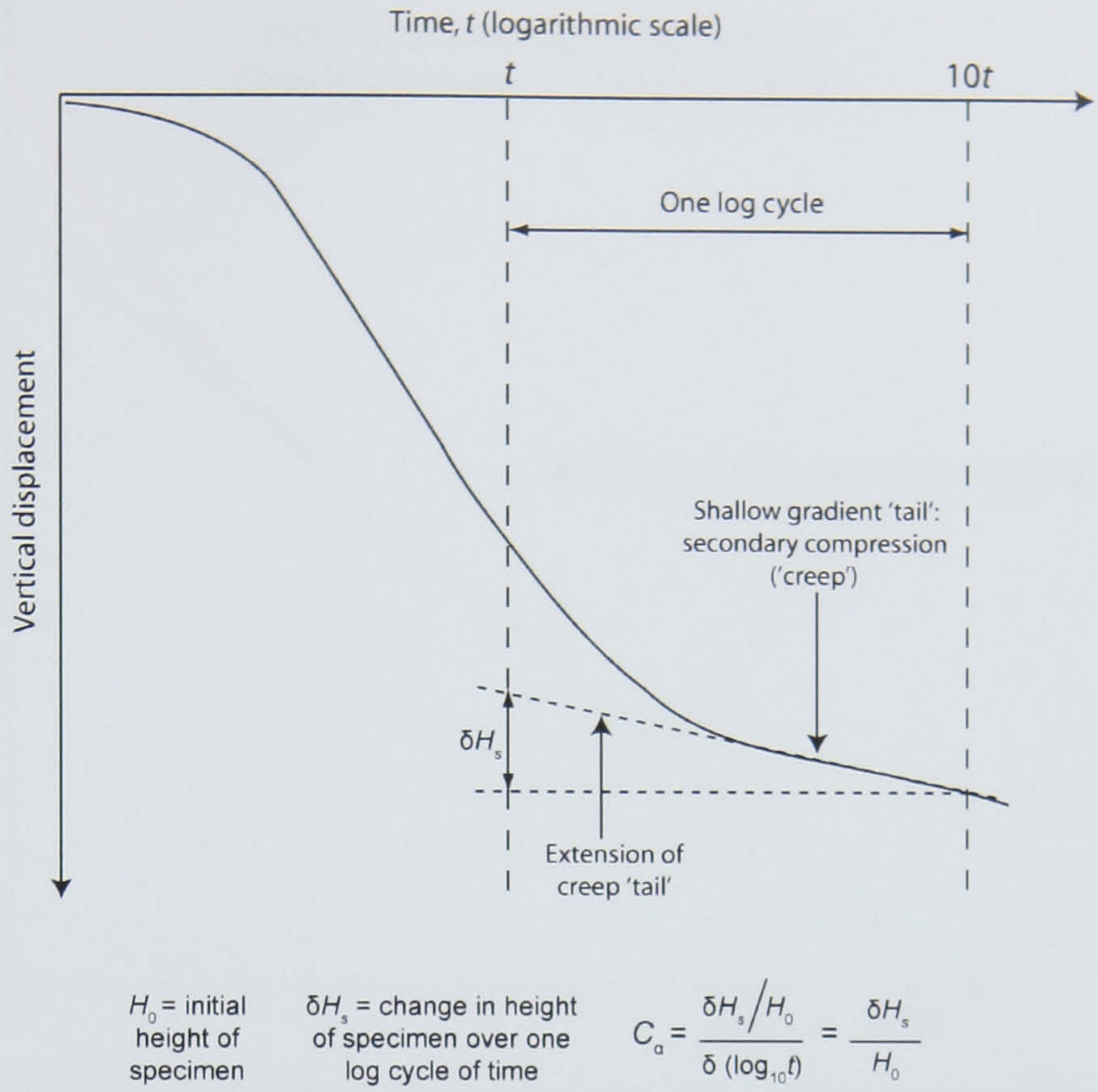

Figure 3.12 Log-time settlement plot displaying how the coefficient of secondary compression C_α is calculated.

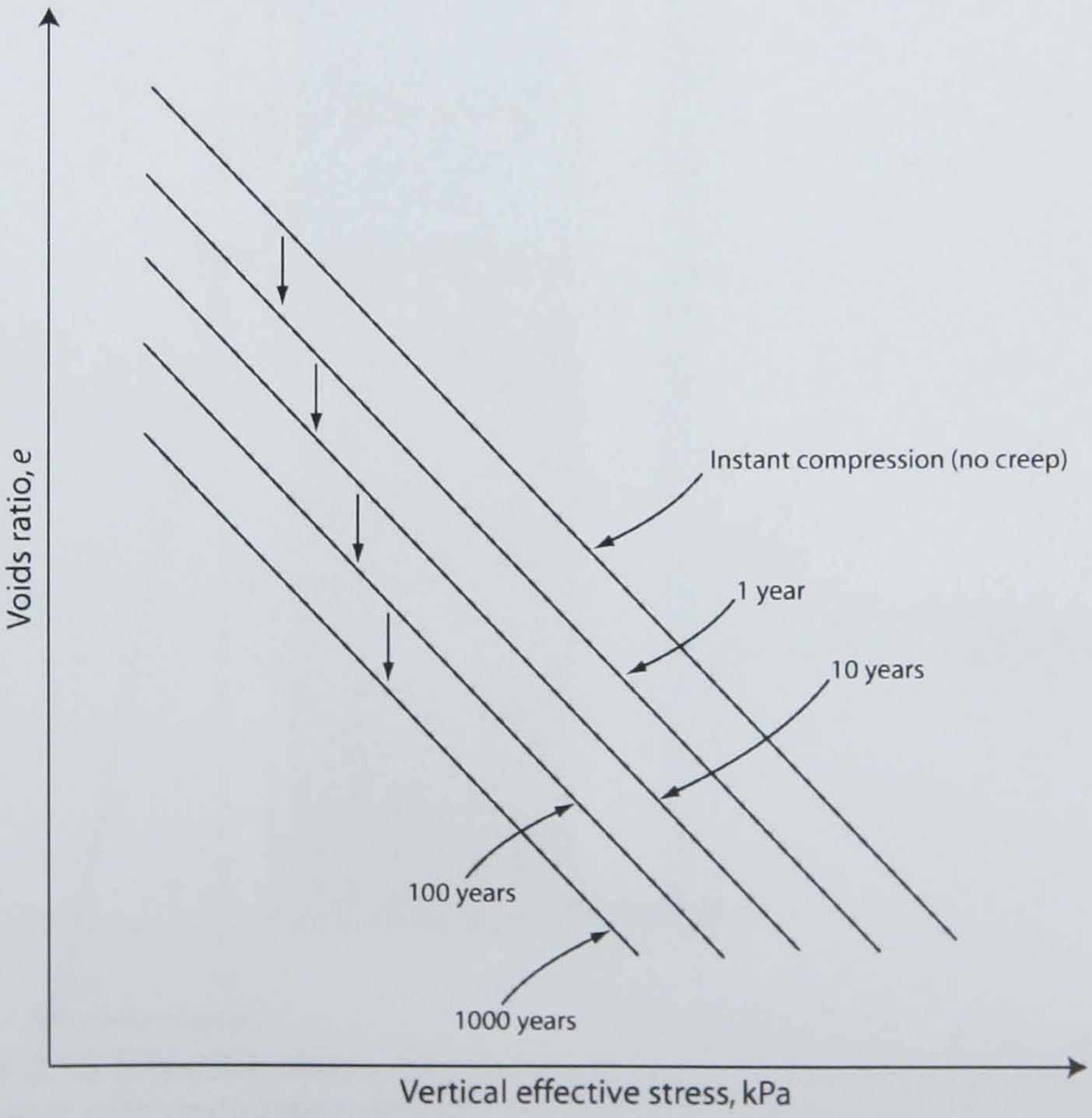

Figure 3.13 Conceptual representation of the relationship between voids ratio, effective stress and time of sustained loading. After Bjerrum (1967).

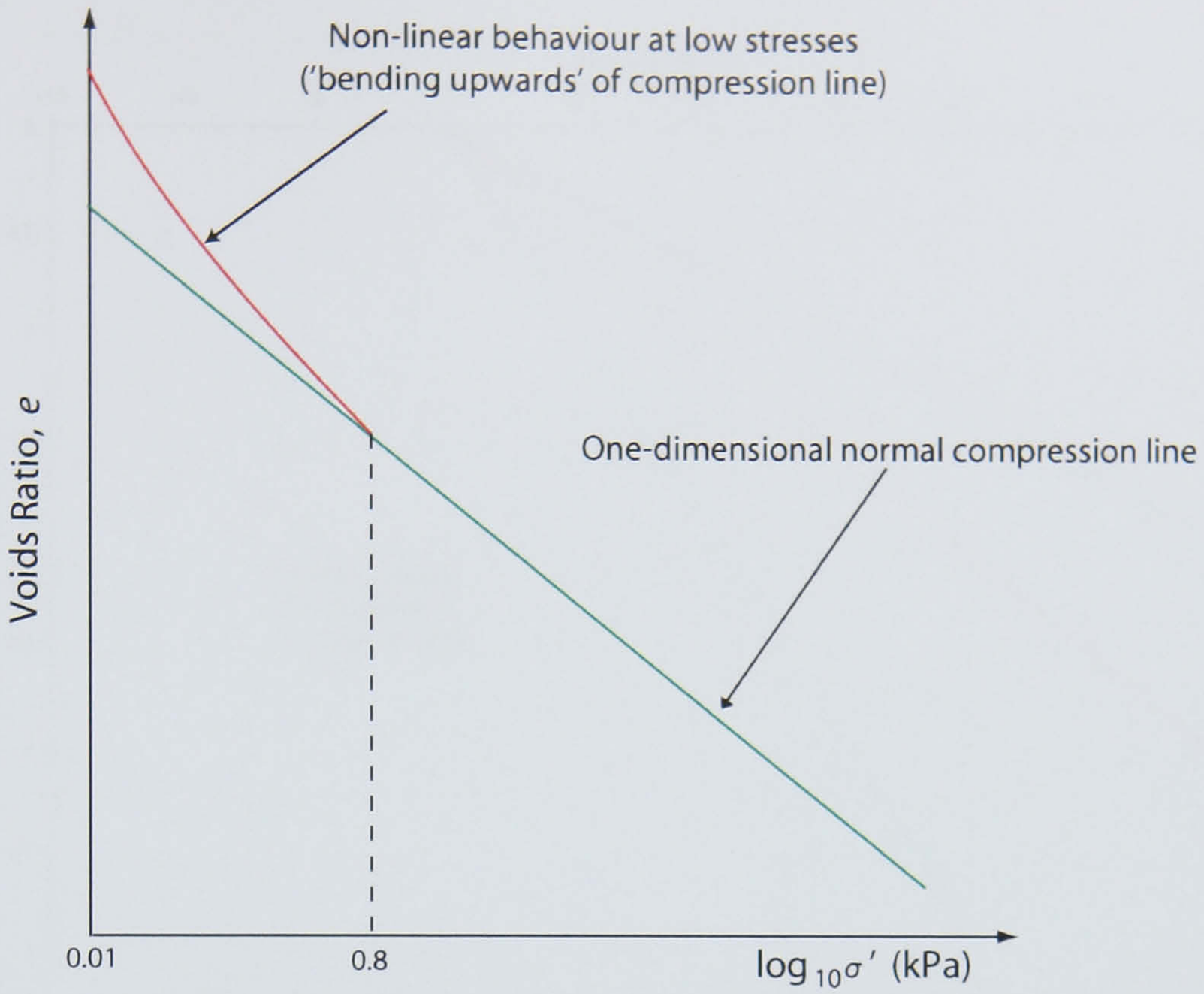

Figure 3.14 $e\log_{10}\sigma'$ plot displaying the low stress compression behaviour of an argillaceous deposit settling from a suspension. After Been and Sills (1981).

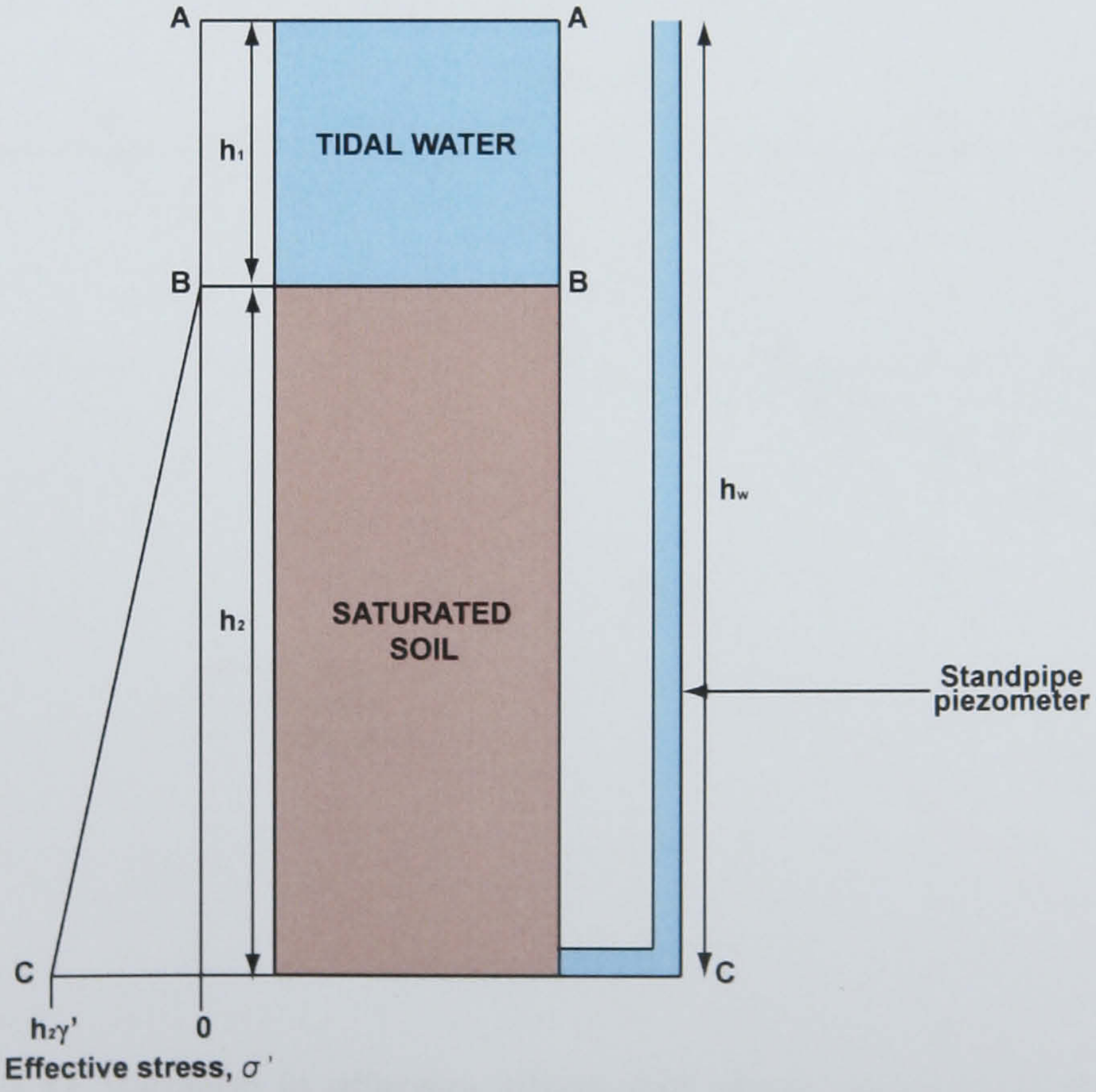

Figure 3.15 Effective stress distribution in a saturated soil mass submerged by tidal water with complete hydraulic connectivity between the overlying water mass and the soil. Adapted from Punmia (1994)

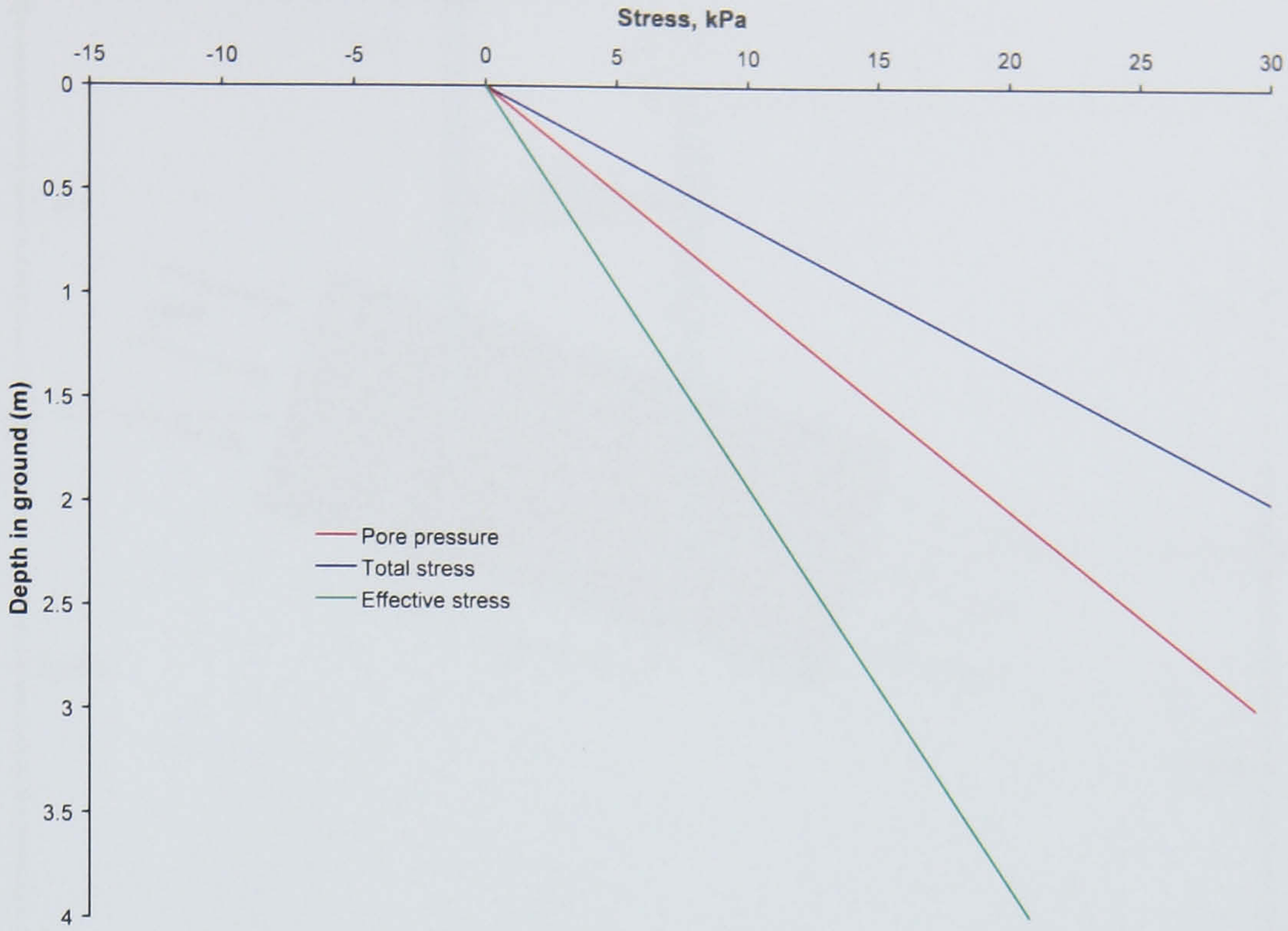

Figure 3.16 Variation in effective stress with depth under hydrostatic conditions when the groundwater level is at the depositional surface.

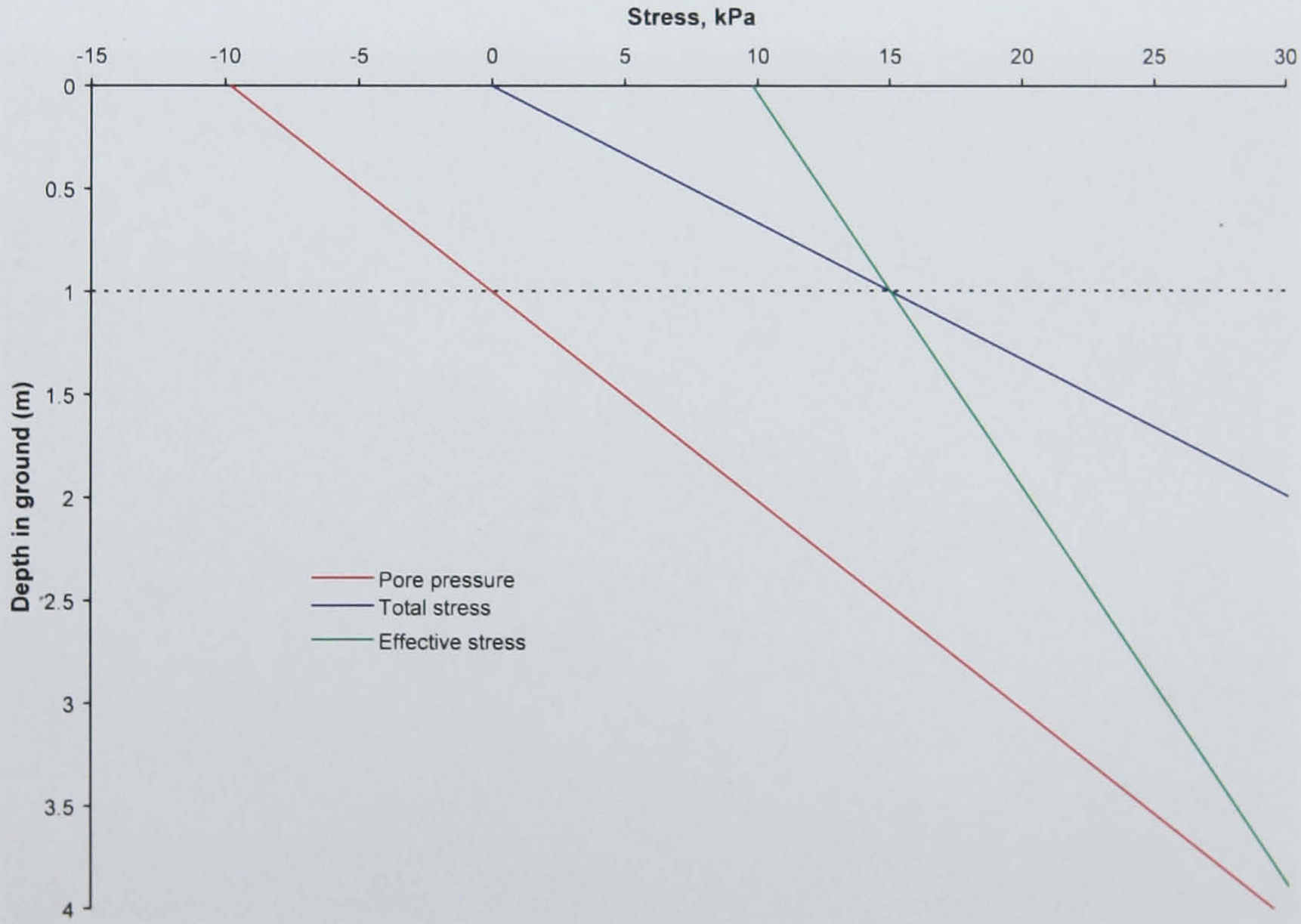

Figure 3.17 Variation in effective stress with depth under hydrostatic conditions when the groundwater level falls to 1 metre beneath the depositional surface.

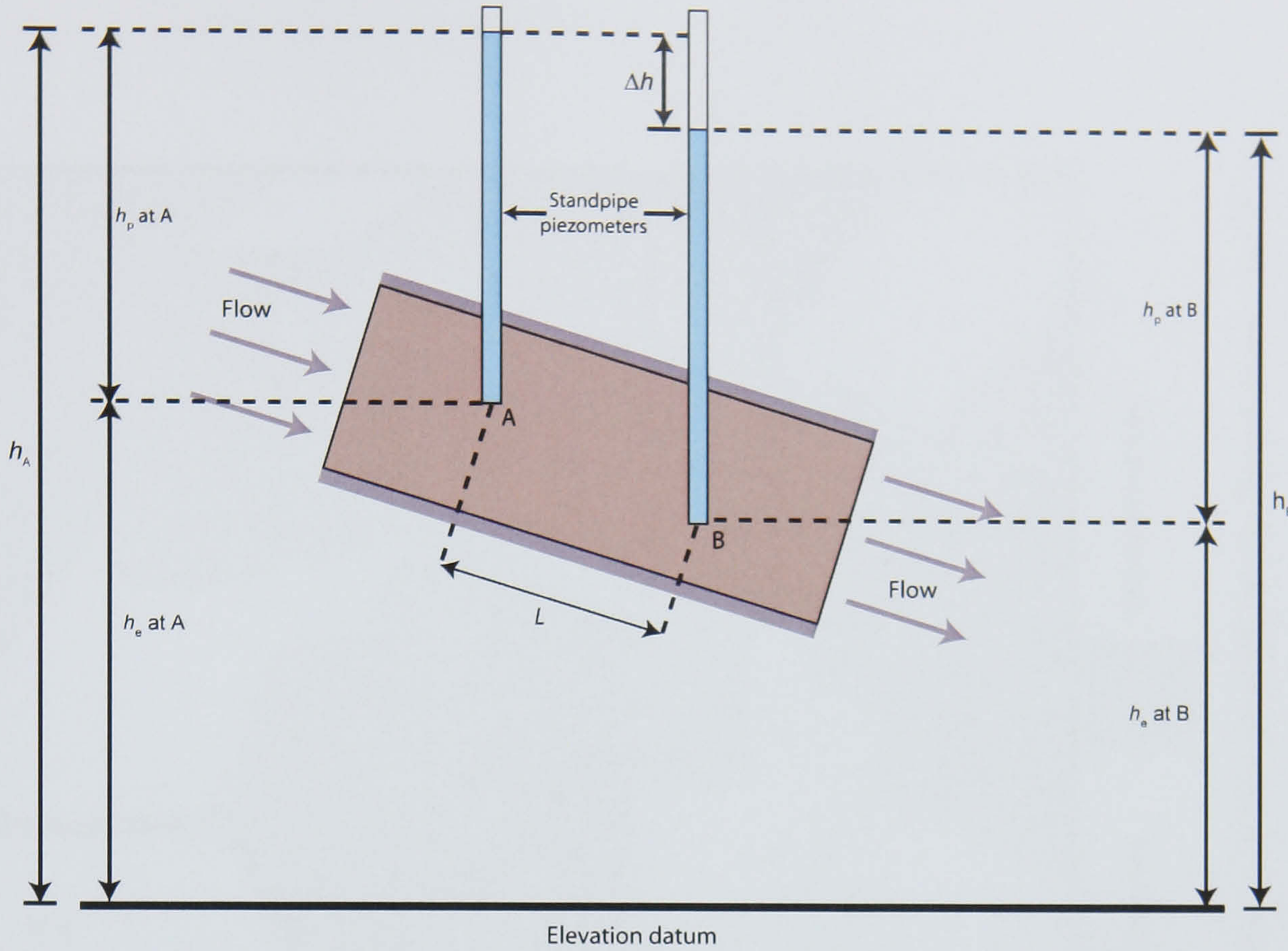

Figure 3.18 Pressure, elevation and total heads for laminar flow through a saturated soil. See text for description. Adapted from Das (1998).

Figure 3.19 Photograph of a low marsh sediment displaying iron(III)oxide concretations as a result of diagenetic remobilisation. The long (horizontal) axis of the sediment is approximately 0.4 m.

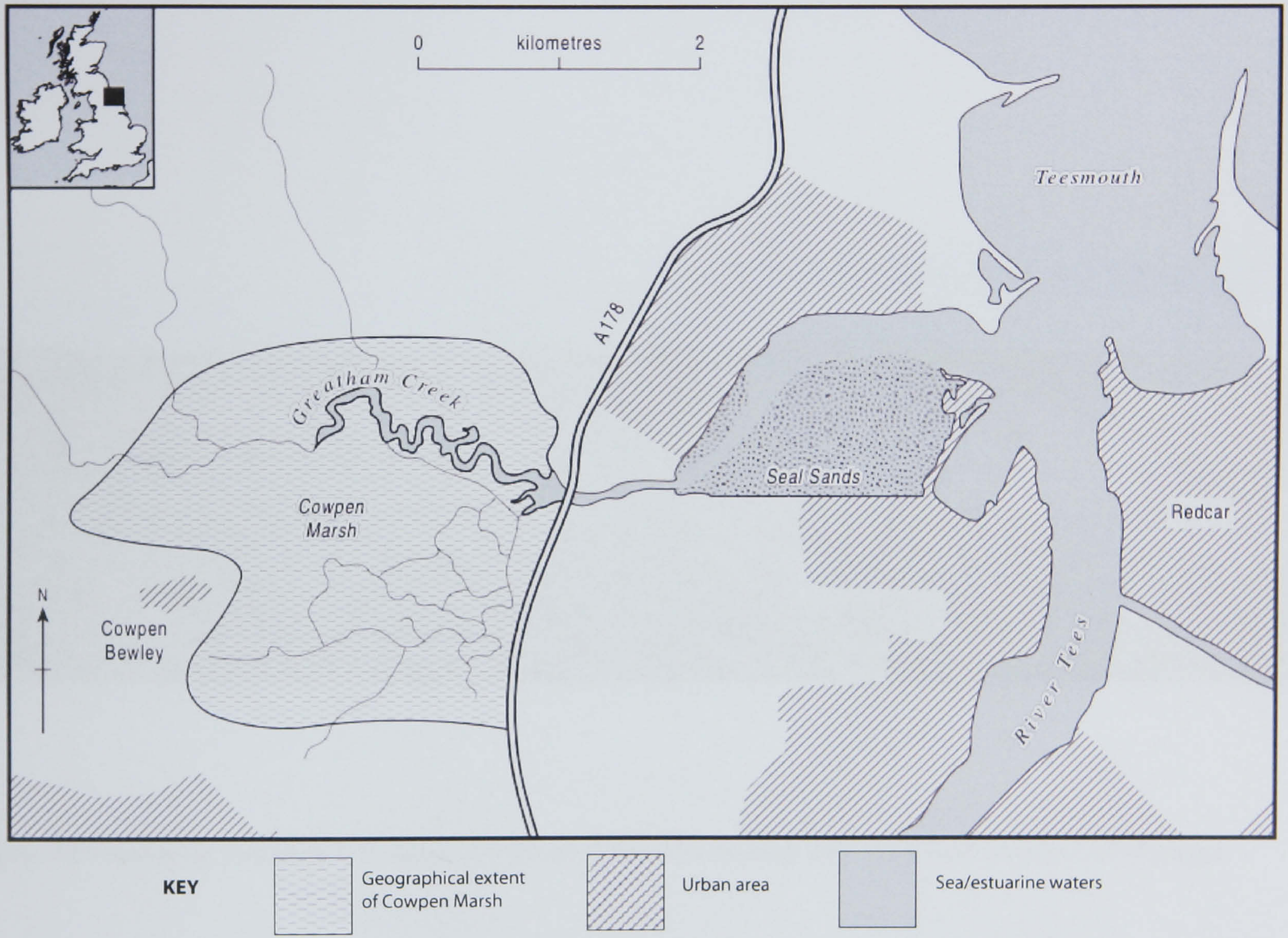

Figure 4.1 Locational map of Cowpen Marsh and Greatham Creek and their proximity to the Tees Estuary proper.

Figure 4.2 Panoramic photograph of Greatham Creek at low tide, looking west-northwest from the A178 bridge.

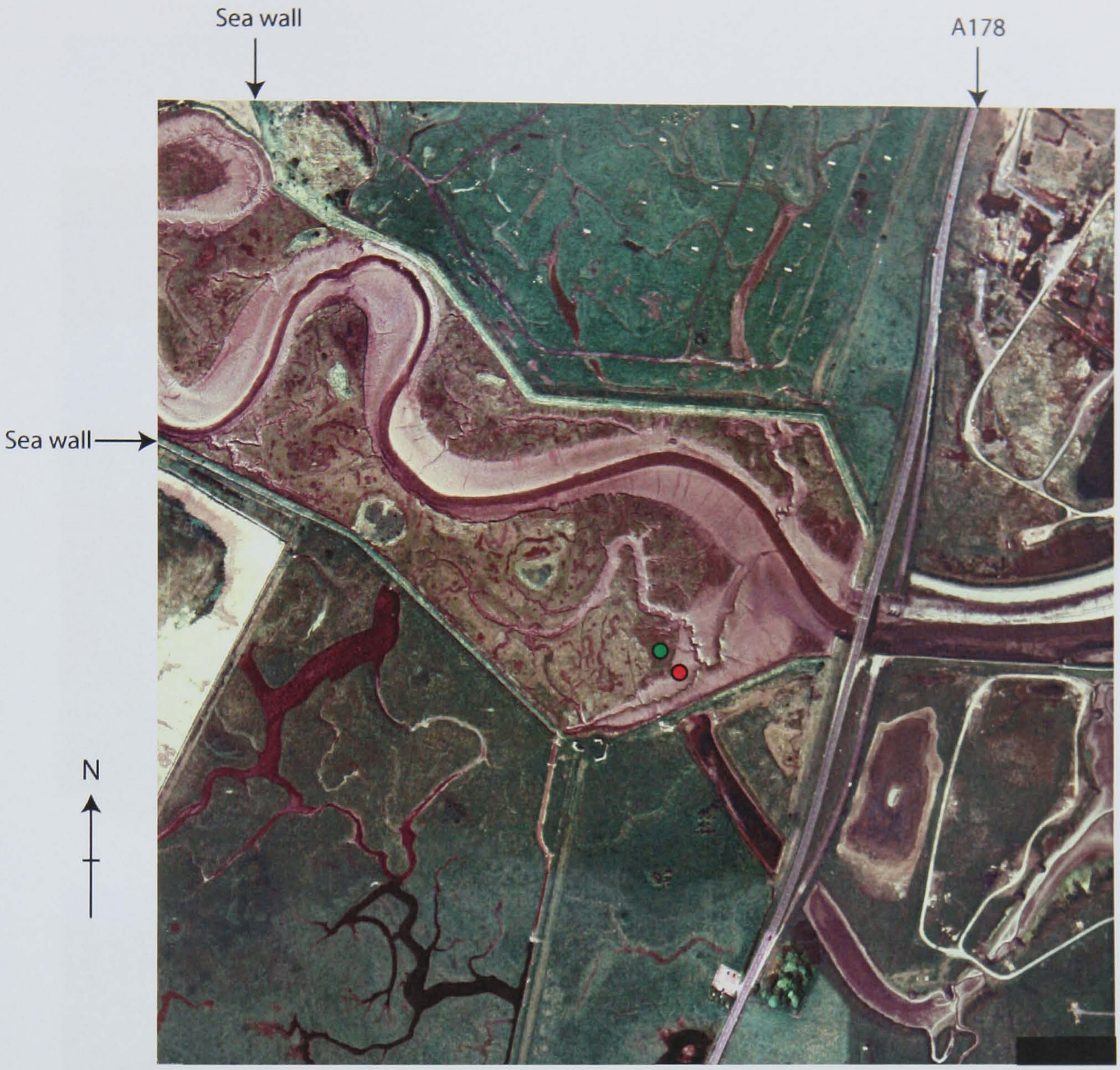

Figure 4.3 Aerial photograph of Cowpen Marsh. The north and south sea walls separate the reclaimed marsh from the active intertidal zone of Greatham Creek. Scale: 1 km × 1 km.

Figure 4.4 Photograph of the low marsh sampling site (*c*. 2.26 m OD).

Figure 4.5 Photograph of the mudflat sampling site (*c* 1.06 m OD).

Figure 4.6 Photographs of cohesive block samples obtained from saltmarsh sediments. Samples obtained for geotechnical testing remained in the confining 'box' sampler before use in the laboratory.

Figure 4.7 Photograph illustrating the use of a machete to carefully excavate a pit for removal of an undisturbed sediment core.

Figure 4.8 Photograph displaying 'hand-driving' of plastic core tubing into the sediment. The surrounding excavation is also evident.

Figure 4.9 Collection of undisturbed sediment cores from the mudflat sampling site. In this photograph, a duplicate sample has been obtained from the same depths (bottom left of photograph).

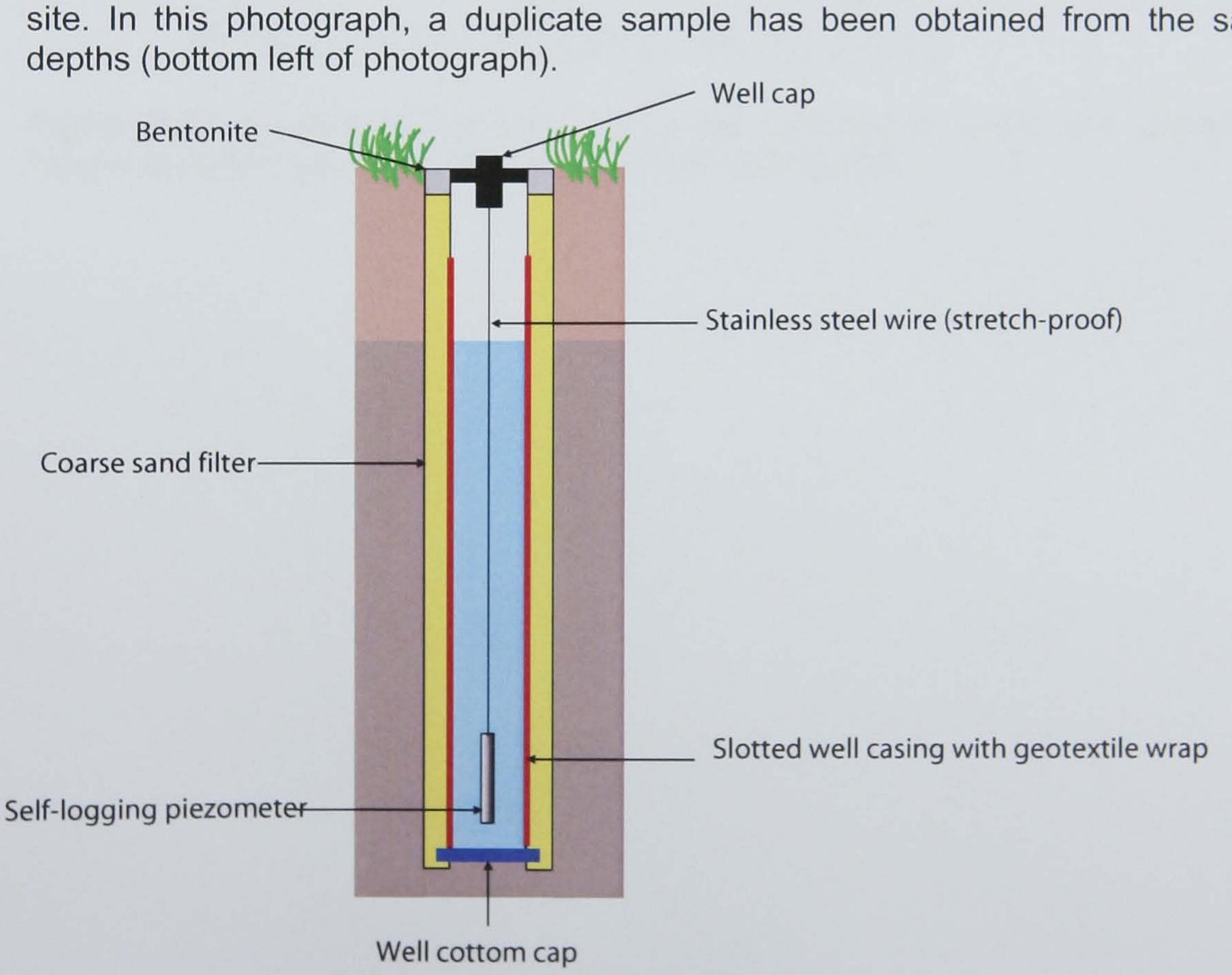

Figure 4.10 Schematic diagram of the piezometer well installation in the low marsh substrate.

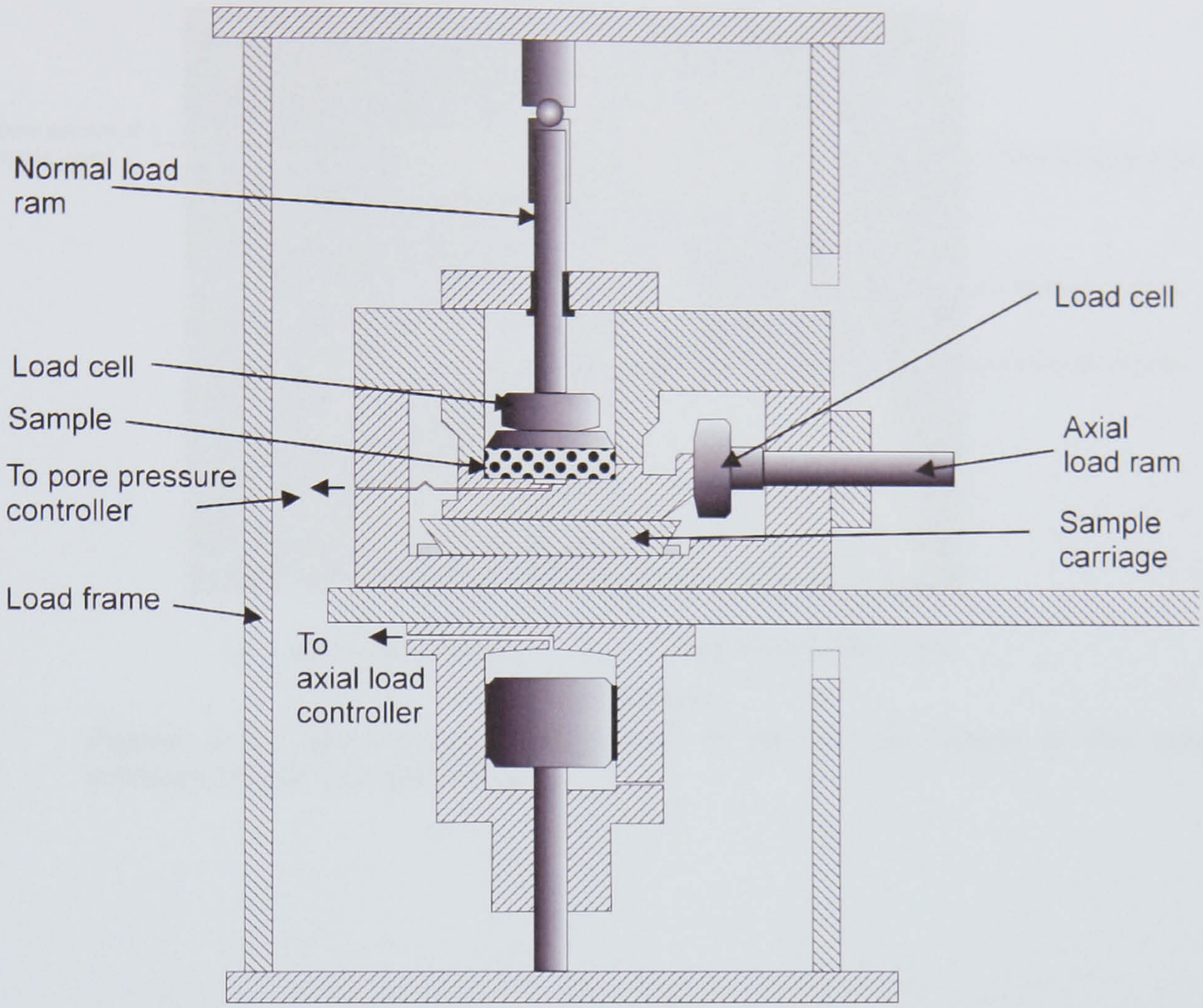

Figure 4.11 Cross-sectional view of the back-pressured shear box apparatus. Figure obtained from D. Petley and used with permission.

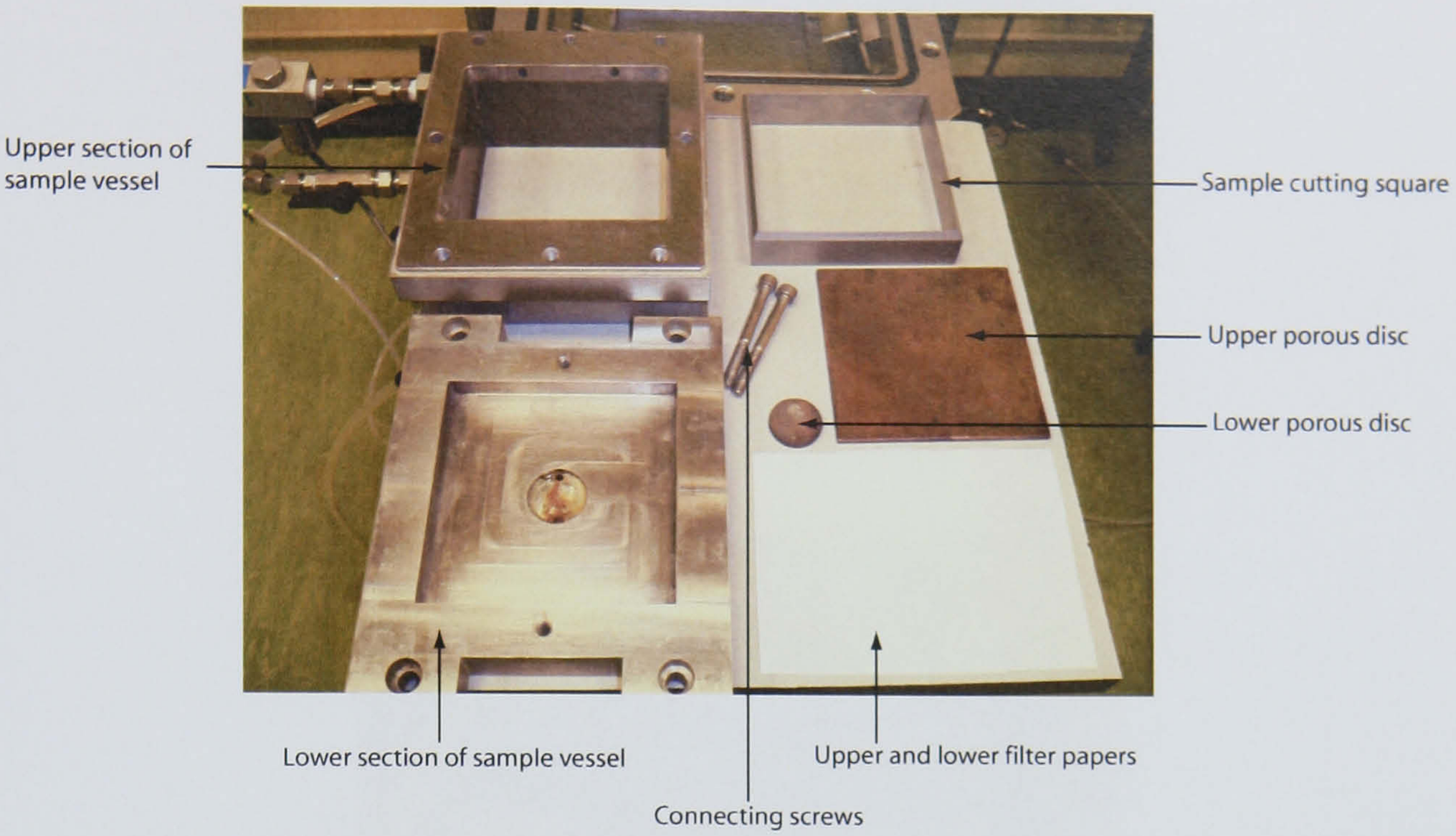

Figure 4.12 Disassembled components of the sample vessel of the back-pressured shear box apparatus.

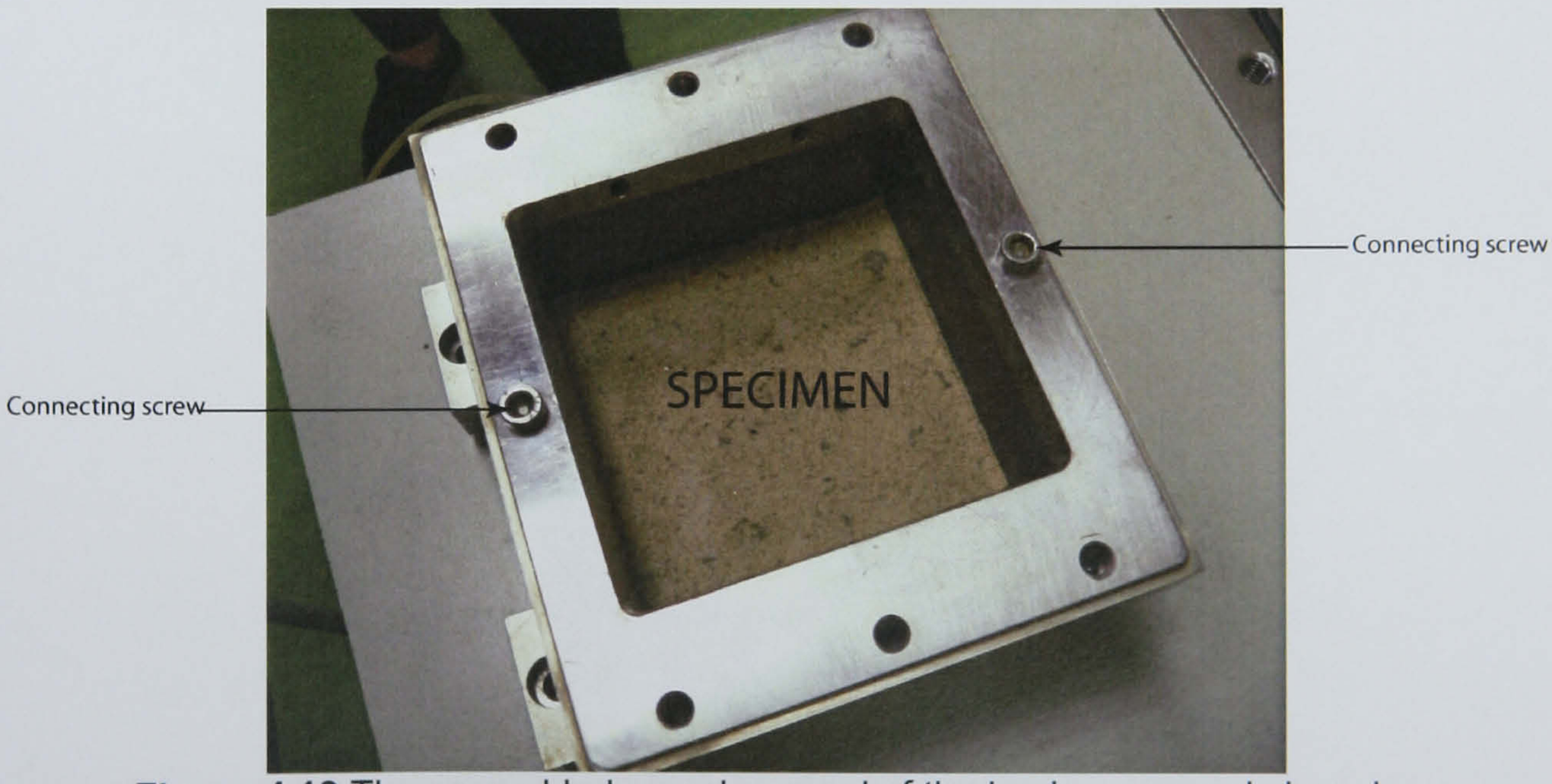

Figure 4.13 The assembled sample vessel of the back-pressured shear box.

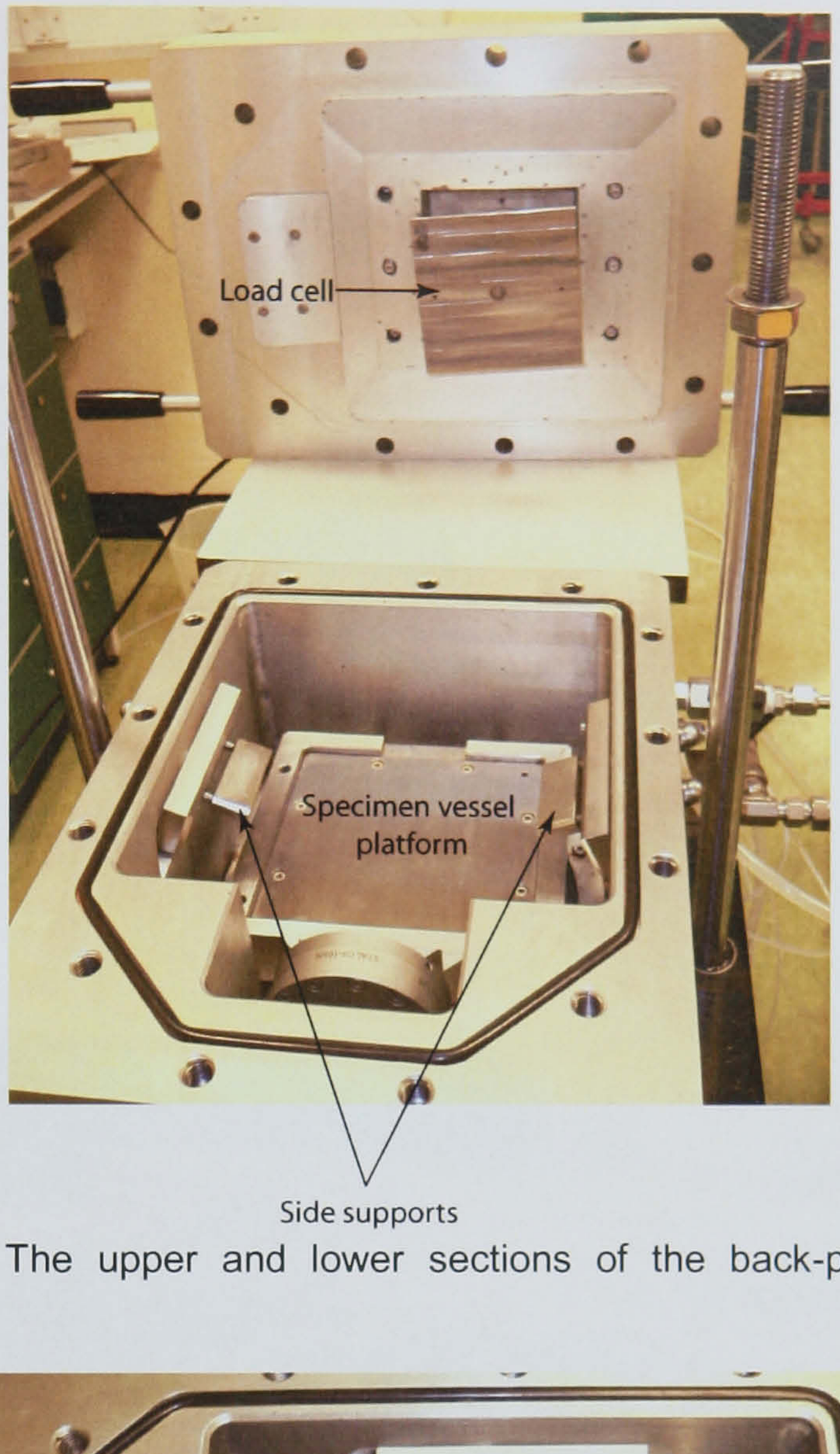

Figure 4.14 The upper and lower sections of the back-pressured shear box apparatus.

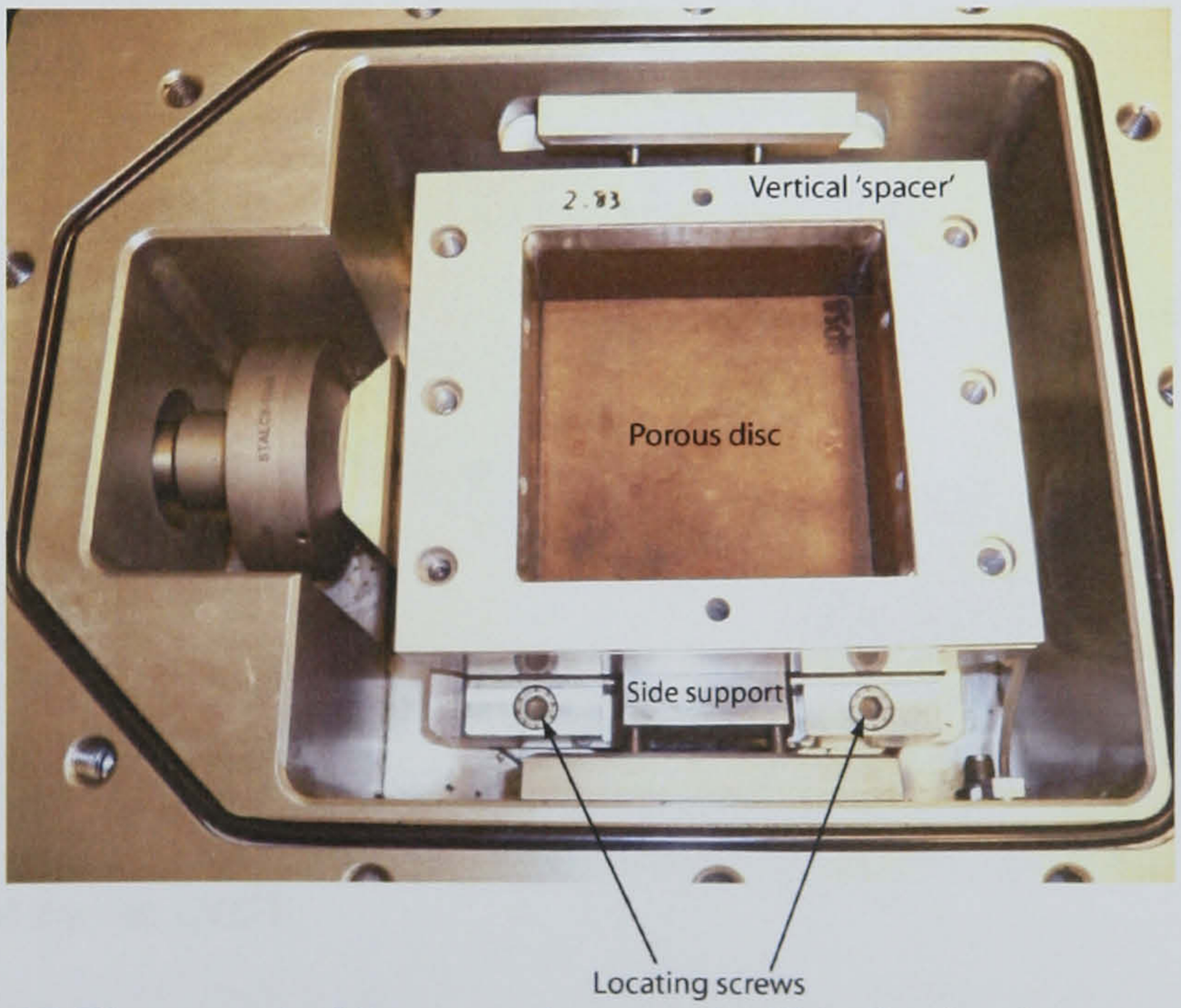

Figure 4.15 Placement of the sample vessel within the back-pressured shearbox apparatus.

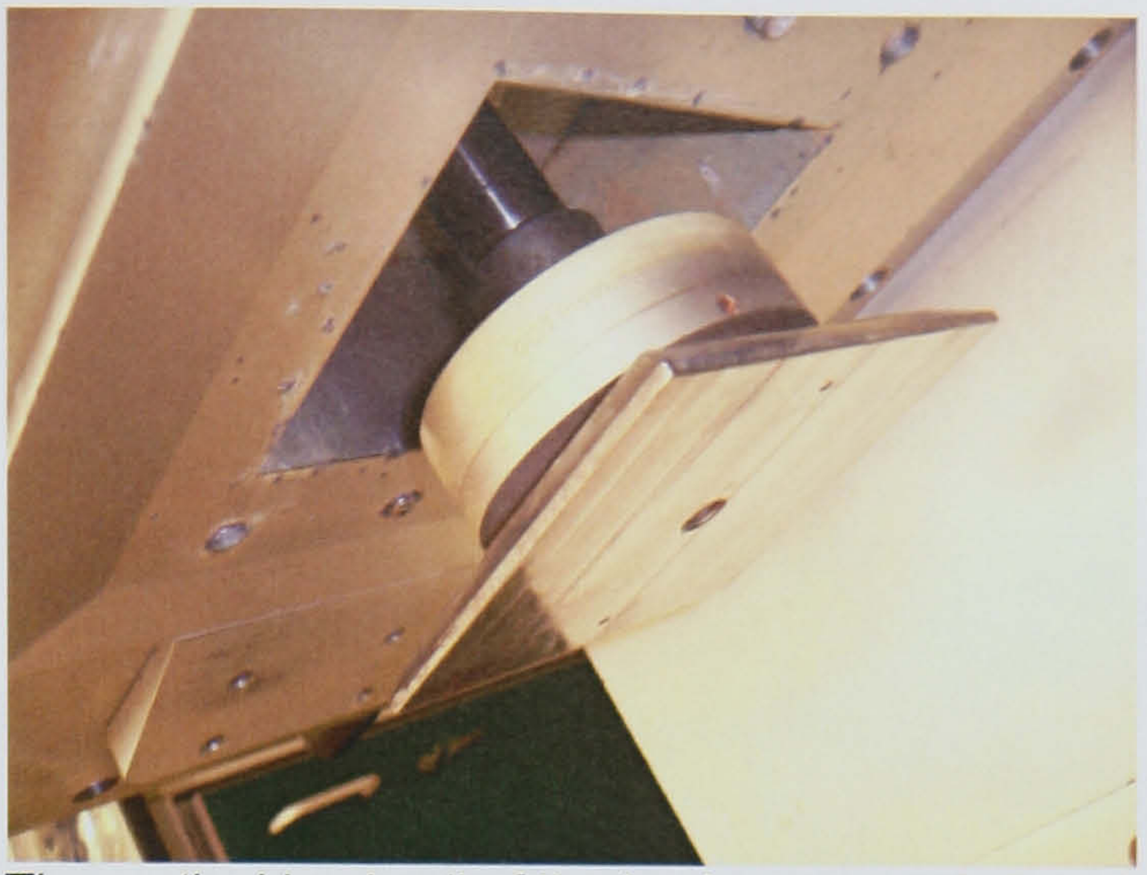

Figure 4.16 The vertical load cell of the back-pressured shear box apparatus.

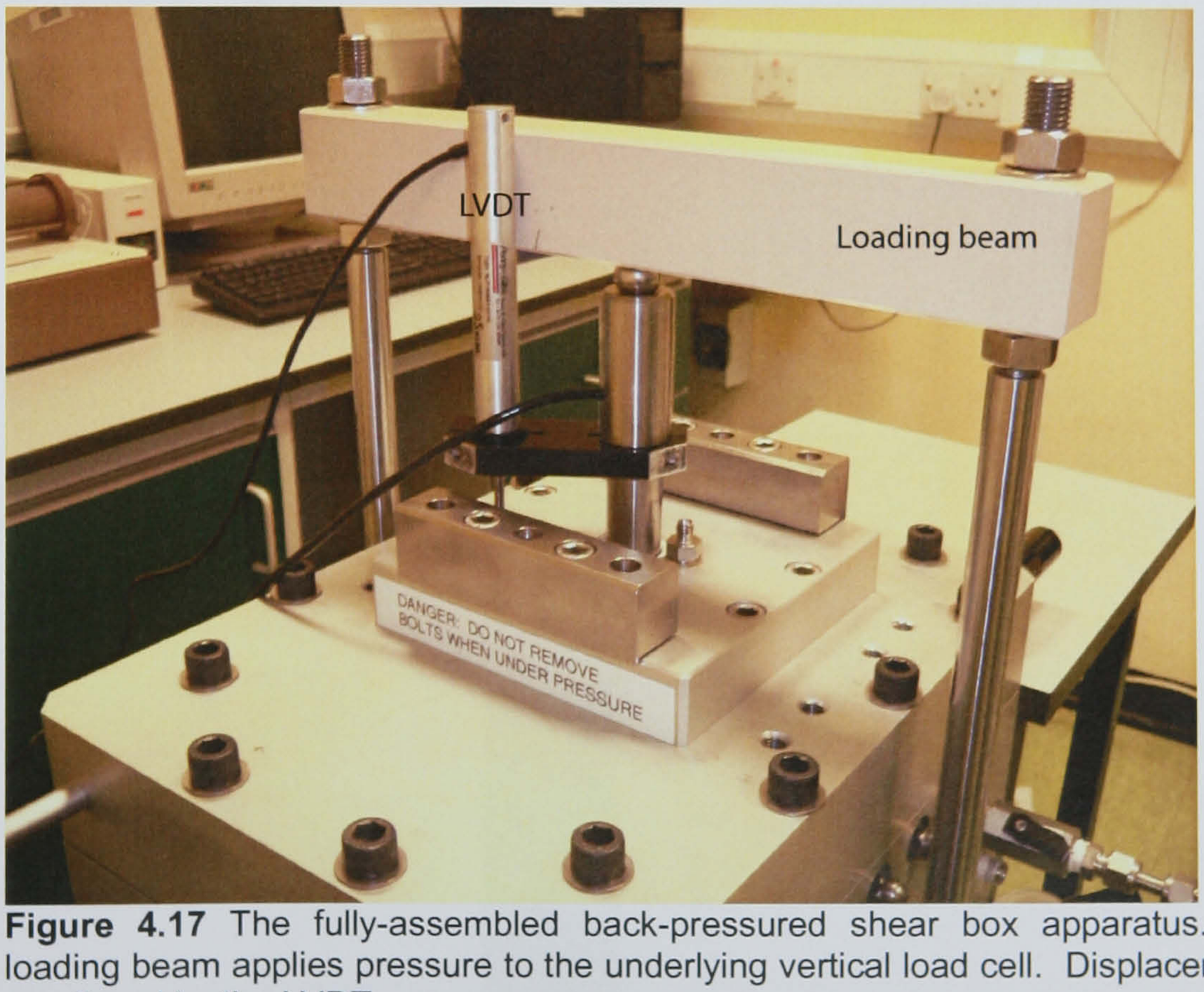

Figure 4.17 The fully-assembled back-pressured shear box apparatus. The loading beam applies pressure to the underlying vertical load cell. Displacement is monitored by the LVDT.

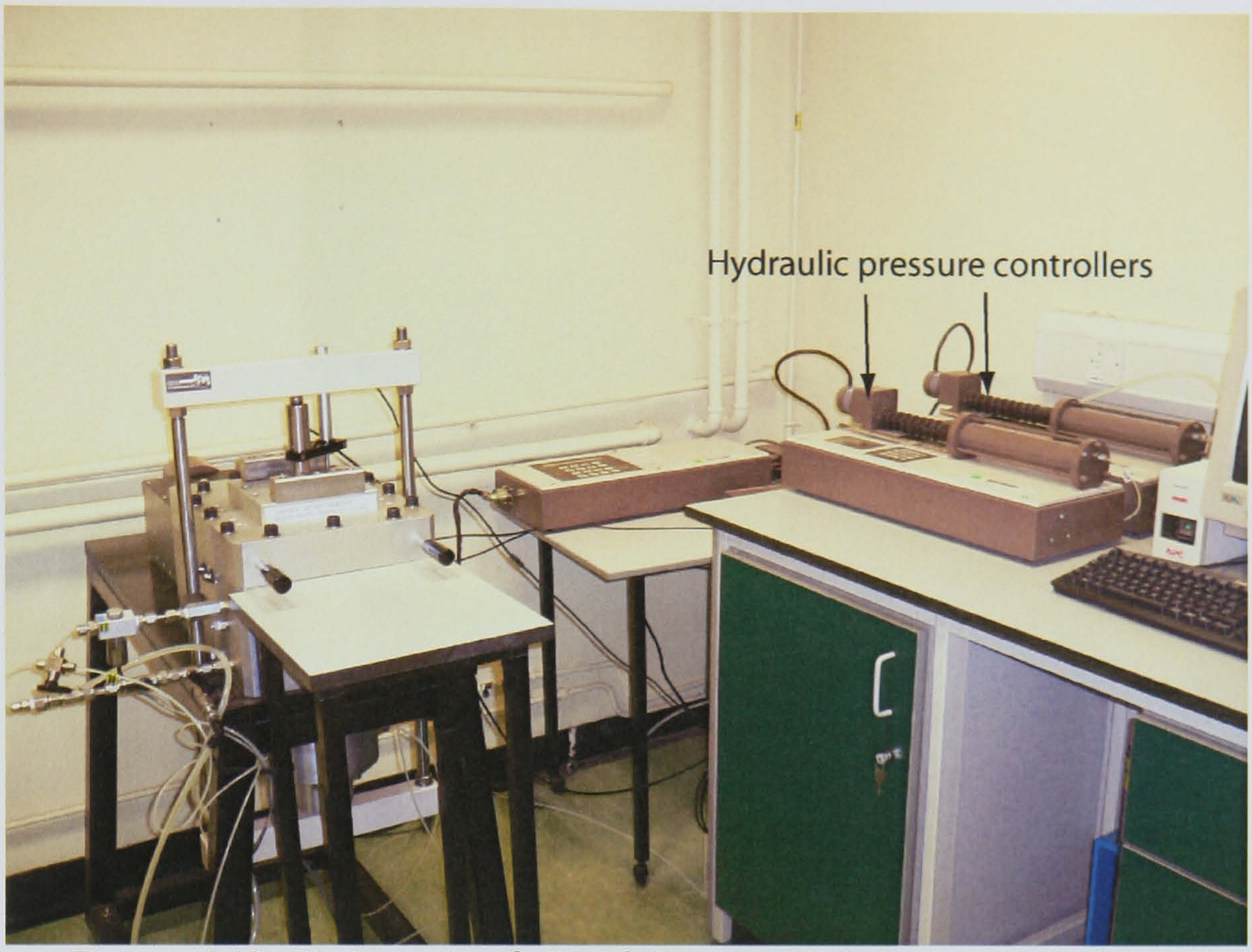

Figure 4.18 Photograph of the fully-assembled back-pressured shear box apparatus and the hydraulic pressure controllers.

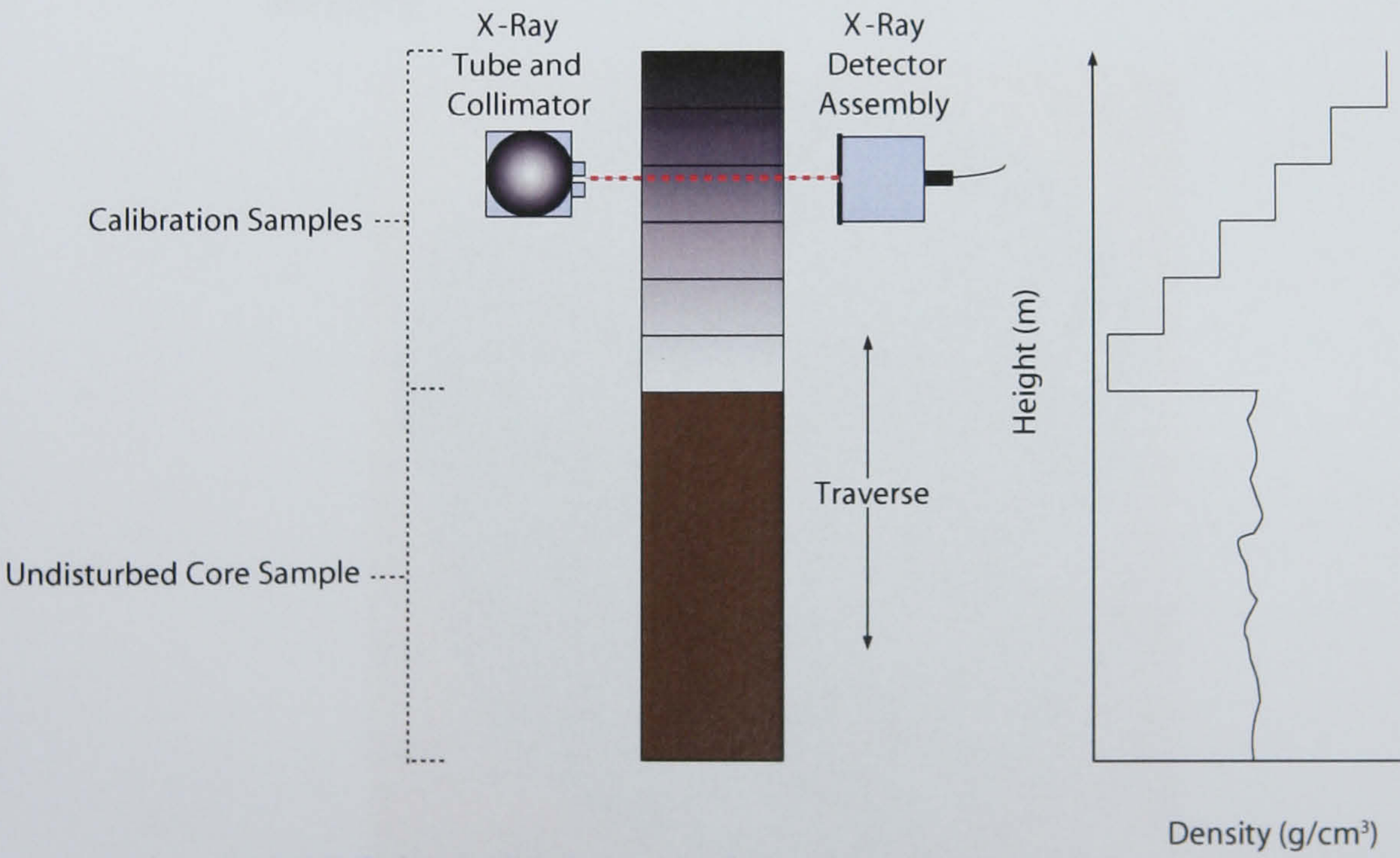

Figure 4.19 Schematic diagram of the x-ray core scanning apparatus for density determination.

Figure 4.20 Photograph of the x-ray collimator at the x-ray tube.

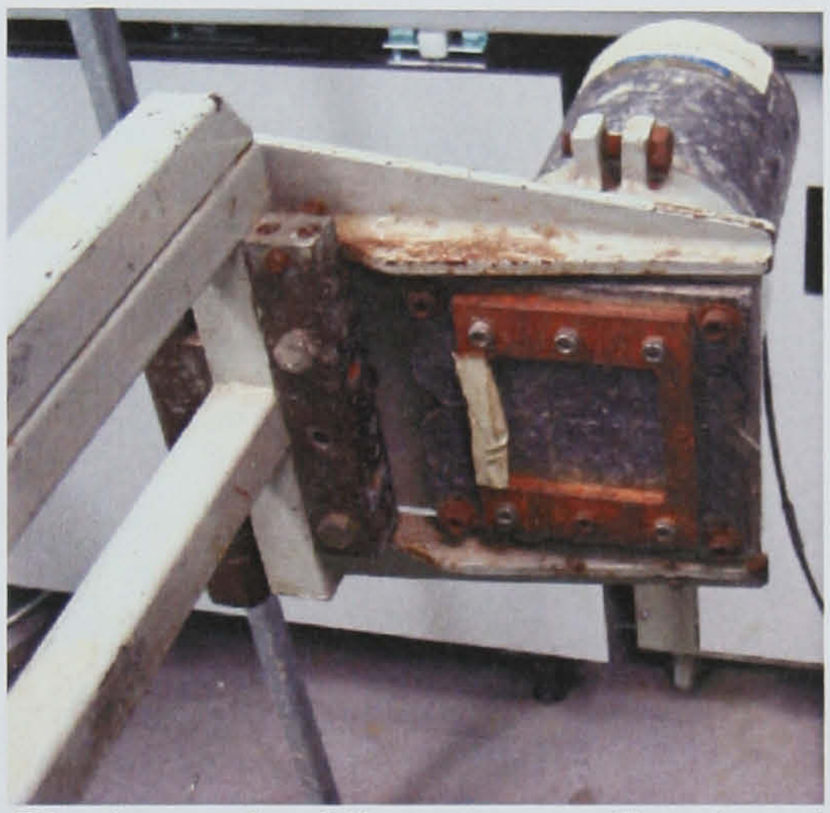

Figure 4.21 Photograph of the x-ray collimator at the x-ray detector assembly.

Figure 4.22 Photograph of a calibration sample for use in x-ray density determination.

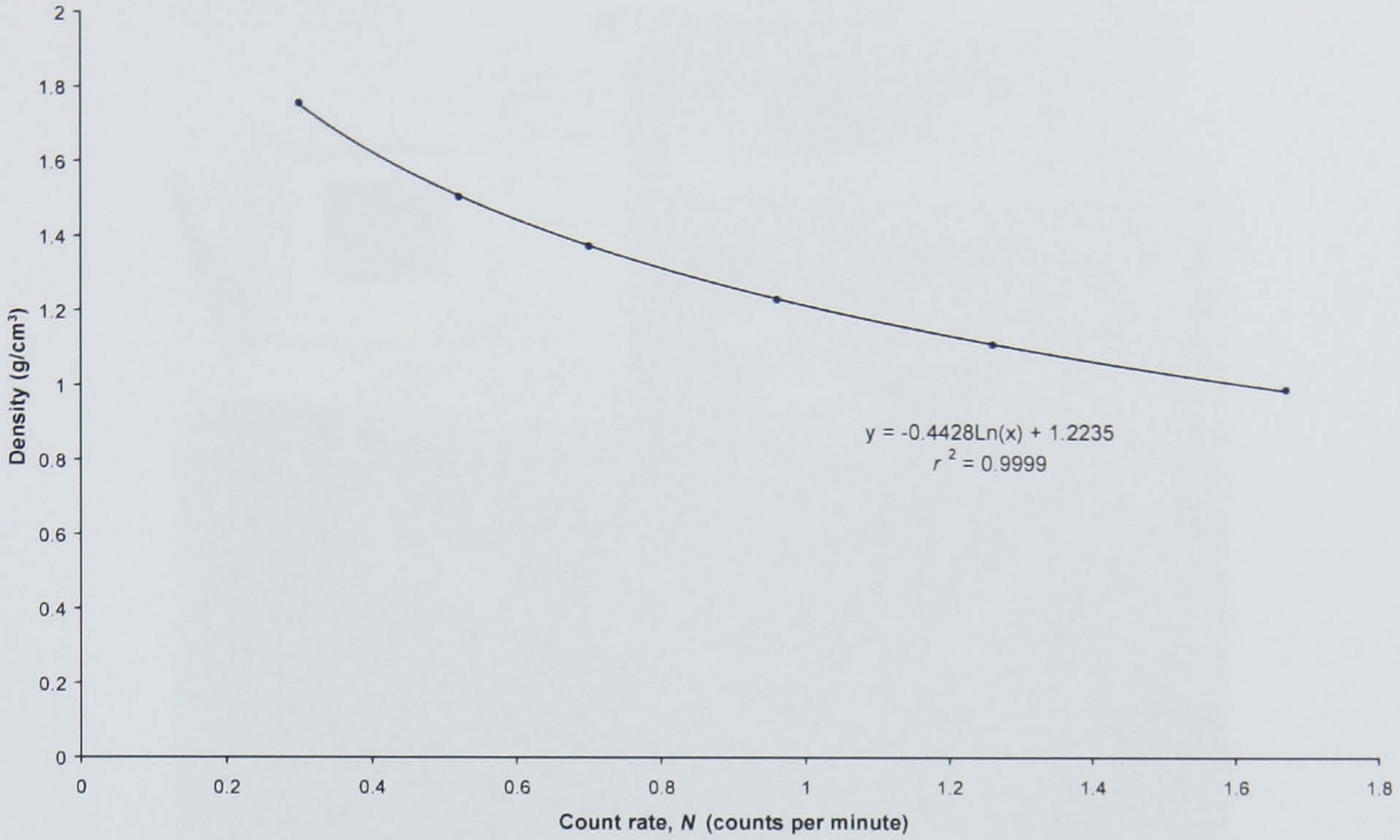

Figure 4.23 A typical x-ray calibration curve. Calibration samples of known density are scanned using the x-ray apparatus. Using the equation of the curve, the density profiles of undisturbed core samples of known count rate can be calculated.

Figure 4.24 Photograph displaying the sediment 'mixing' procedure for use in the calibration samples.

Figure 4.25 Photograph of the computer control unit of the x-ray scanning apparatus.

Figure 4.26 Photograph of the x-ray scanning density determination apparatus.

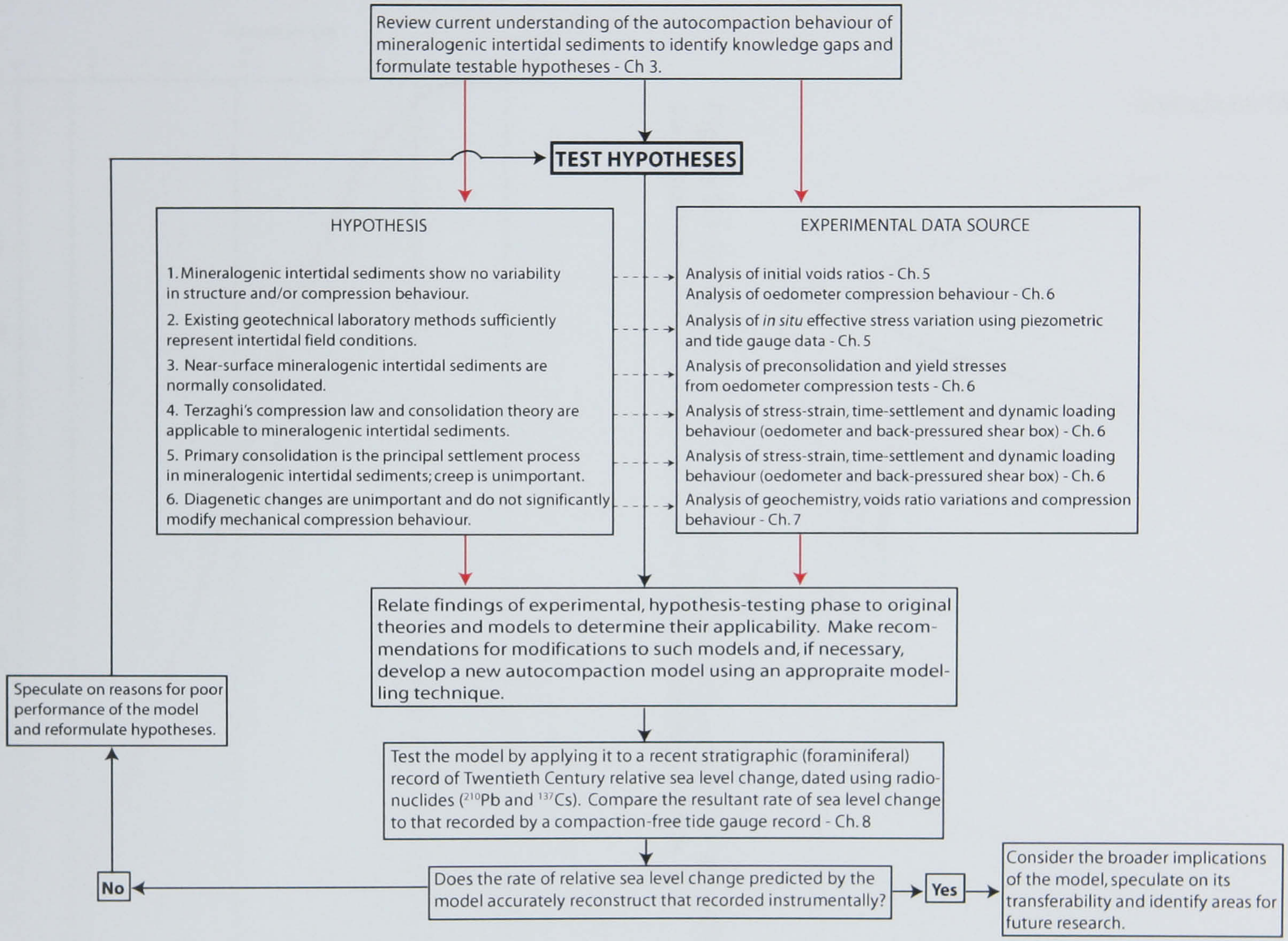

Figure 4.27 Flowchart summarising the overall research framework, the main information sources used in the study, how these relate to the overall objectives and their interrelations.

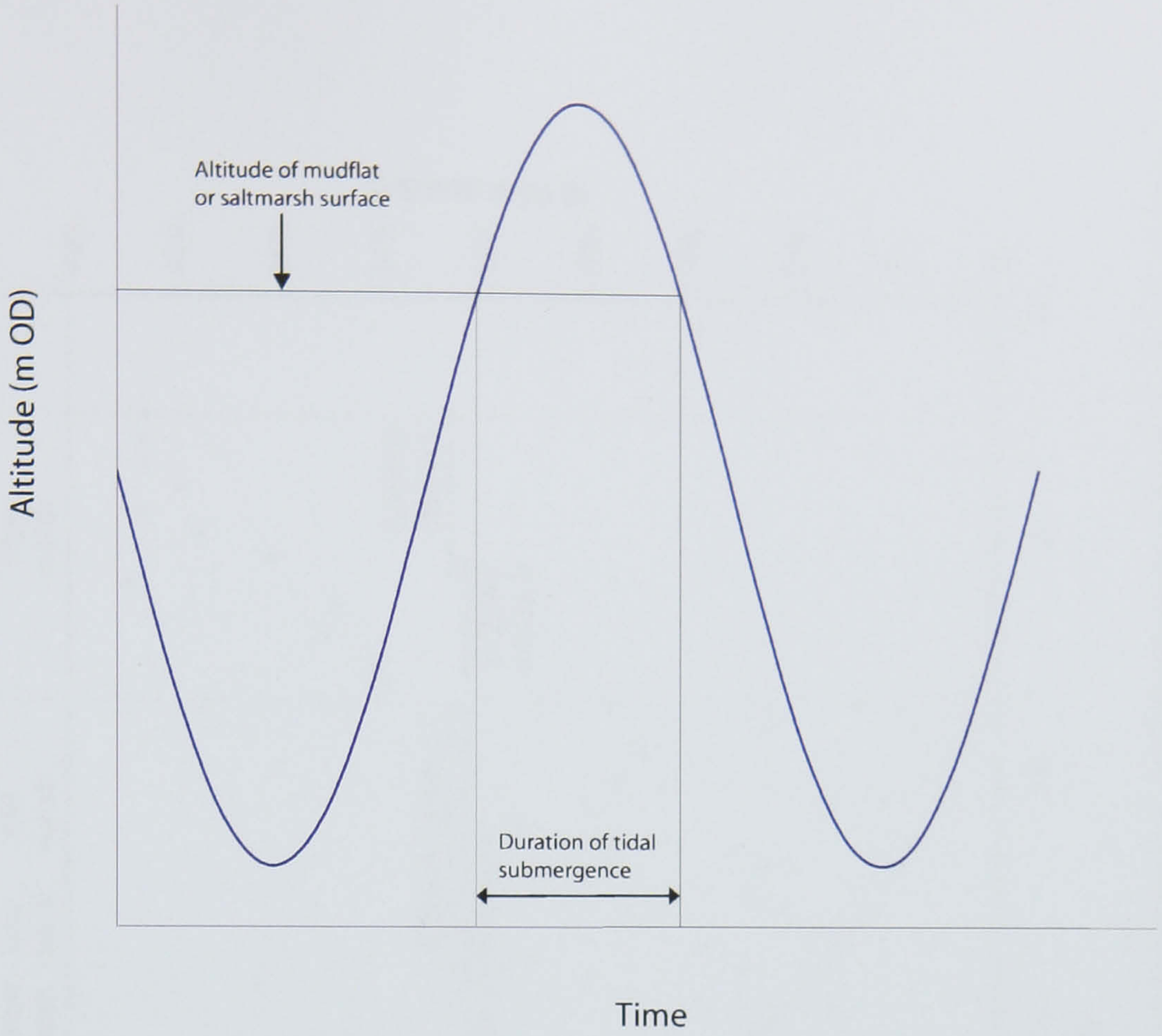

Figure 5.1 Schematic illustration defining flooding duration of an arbitrary saltmarsh or mudflat surface at a given altitude during a single tide.

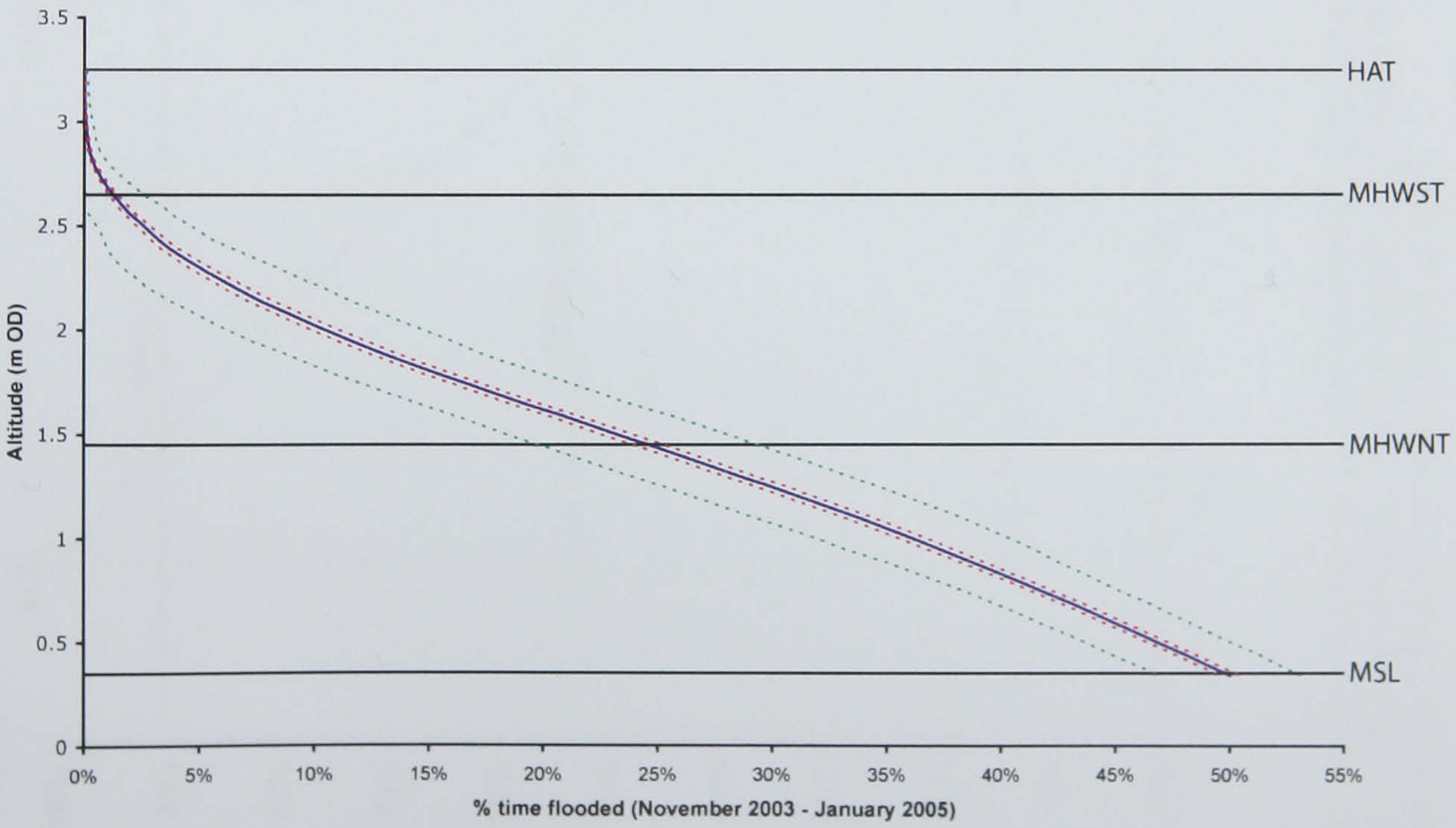

Figure 5.2 The relationship between flooding duration, expressed as a percentage of total time, and altitude (m OD) at Greatham Creek. The blue line represents the mean value calculated from 14 months of tidal gauge data. The dashed green line represents the standard deviation of the mean and the dashed red line is the standard error.

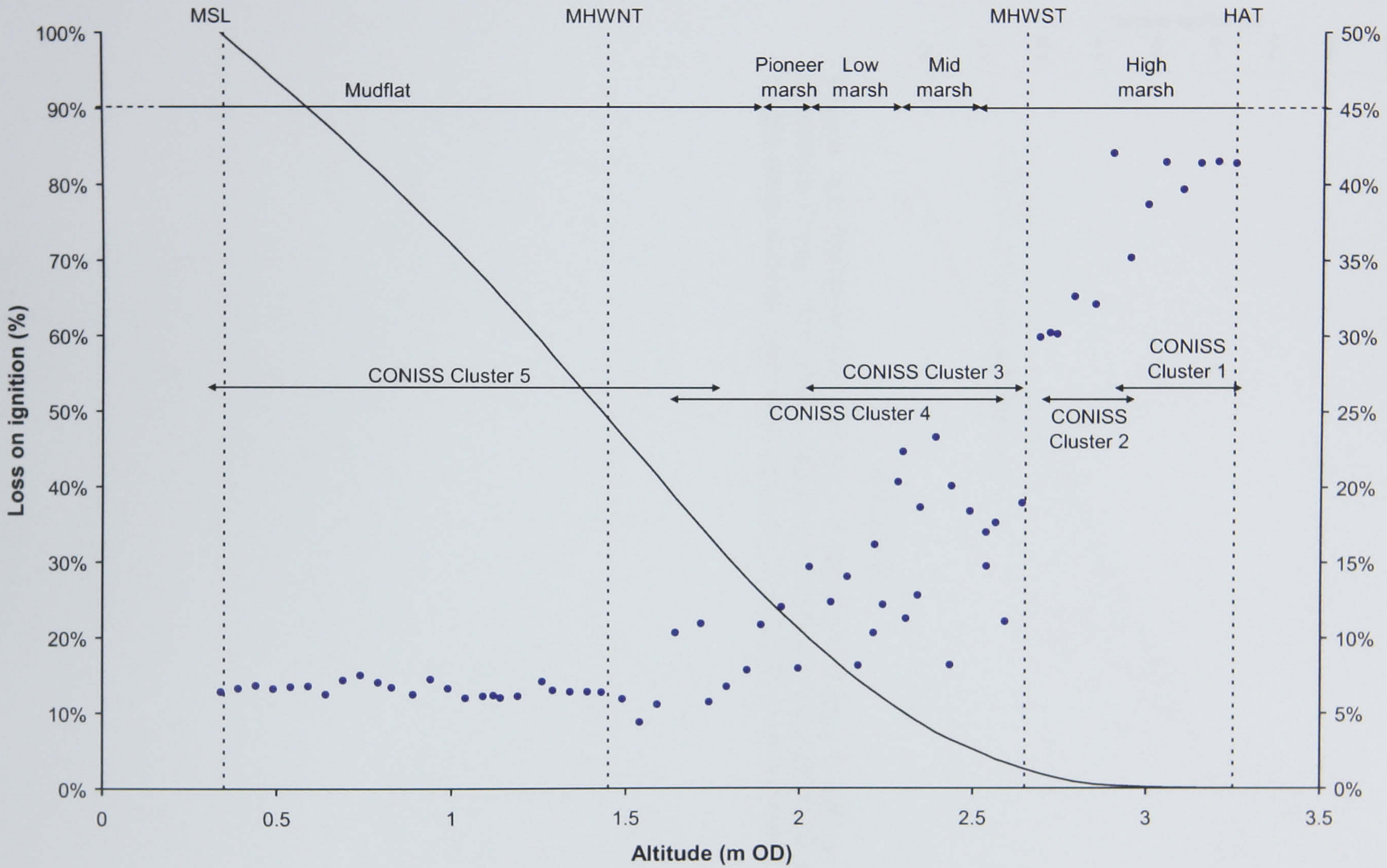

Figure 5.3 Variations in loss on ignition (blue data points, corresponding to the left-hand y-axis), an indirect measurement of organic content, in relation to altitude, flooding duration (continuous black data series, corresponding to the right-hand y-axis), reference water levels, approximate marsh floral zones and CONISS clusters.

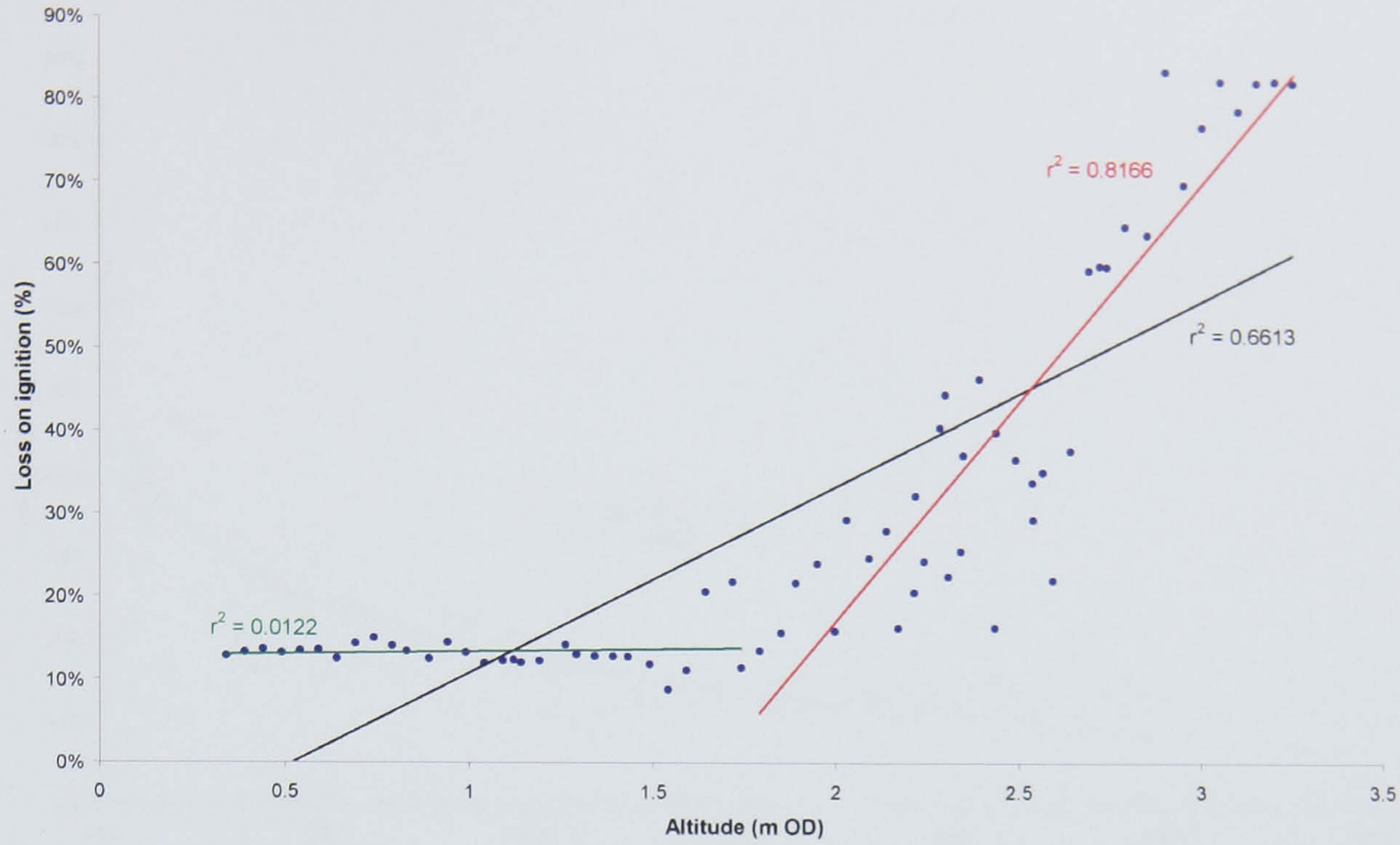

Figure 5.4 Relationships between altitude and loss on ignition content at Greatham Creek. The black, green and red linear regression lines are based on the entire dataset, saltmarsh data and mudflat data respectively.

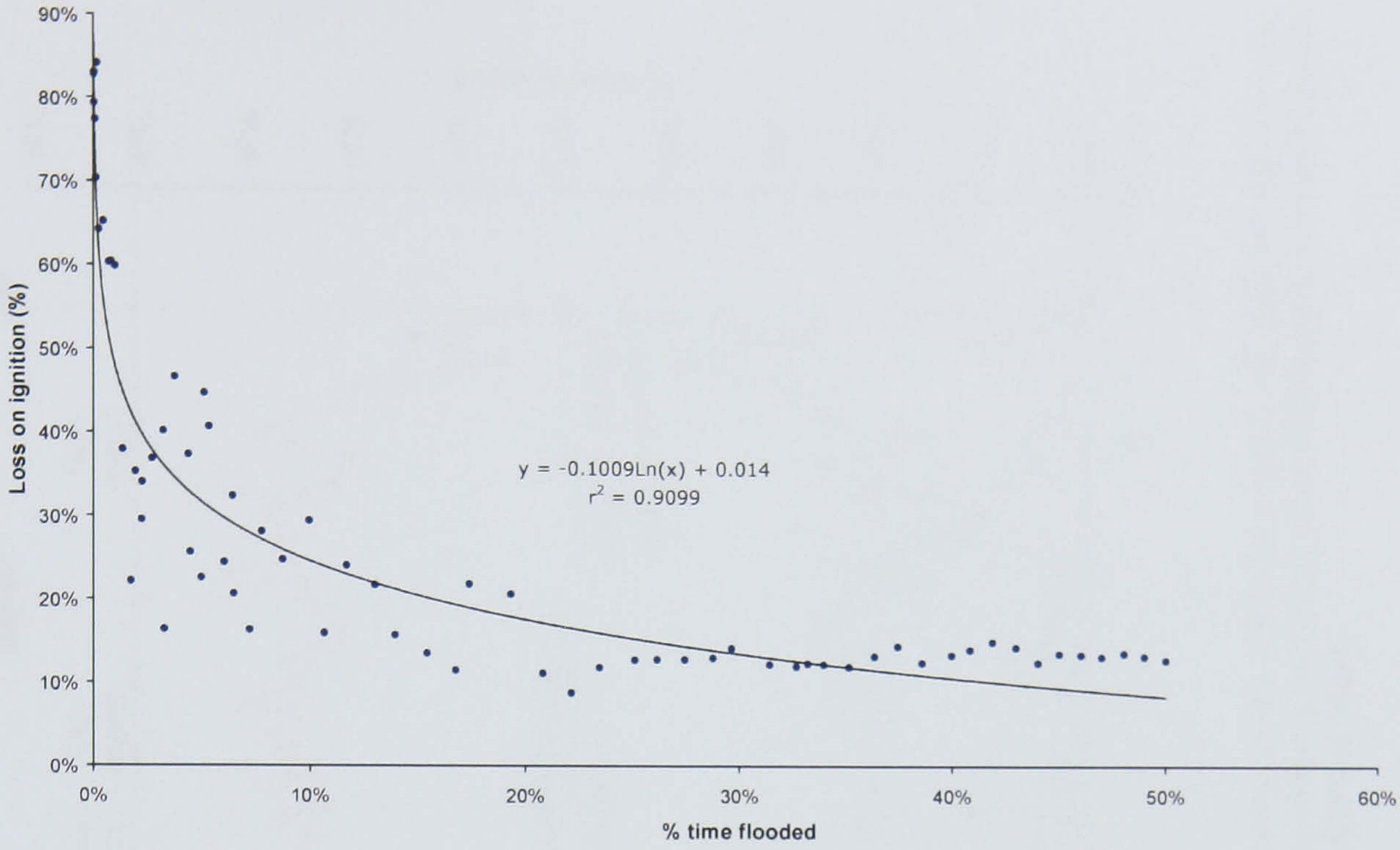

(a)

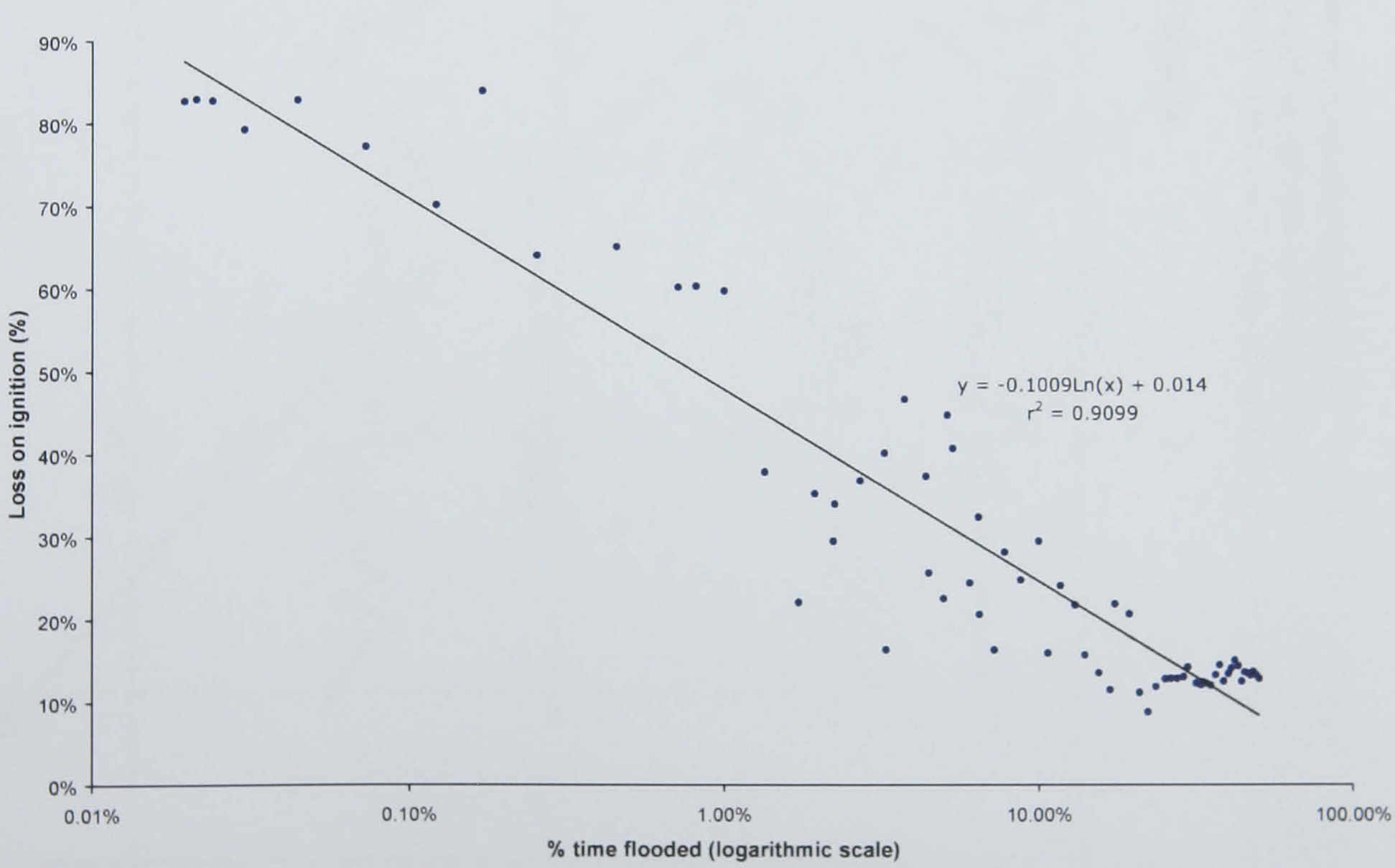

(b)

Figure 5.5 Relationship between flooding duration (% of total time) and loss on ignition content at Greatham Creek (a) natural x-axis scale (b) logarithmic x-axis scale.

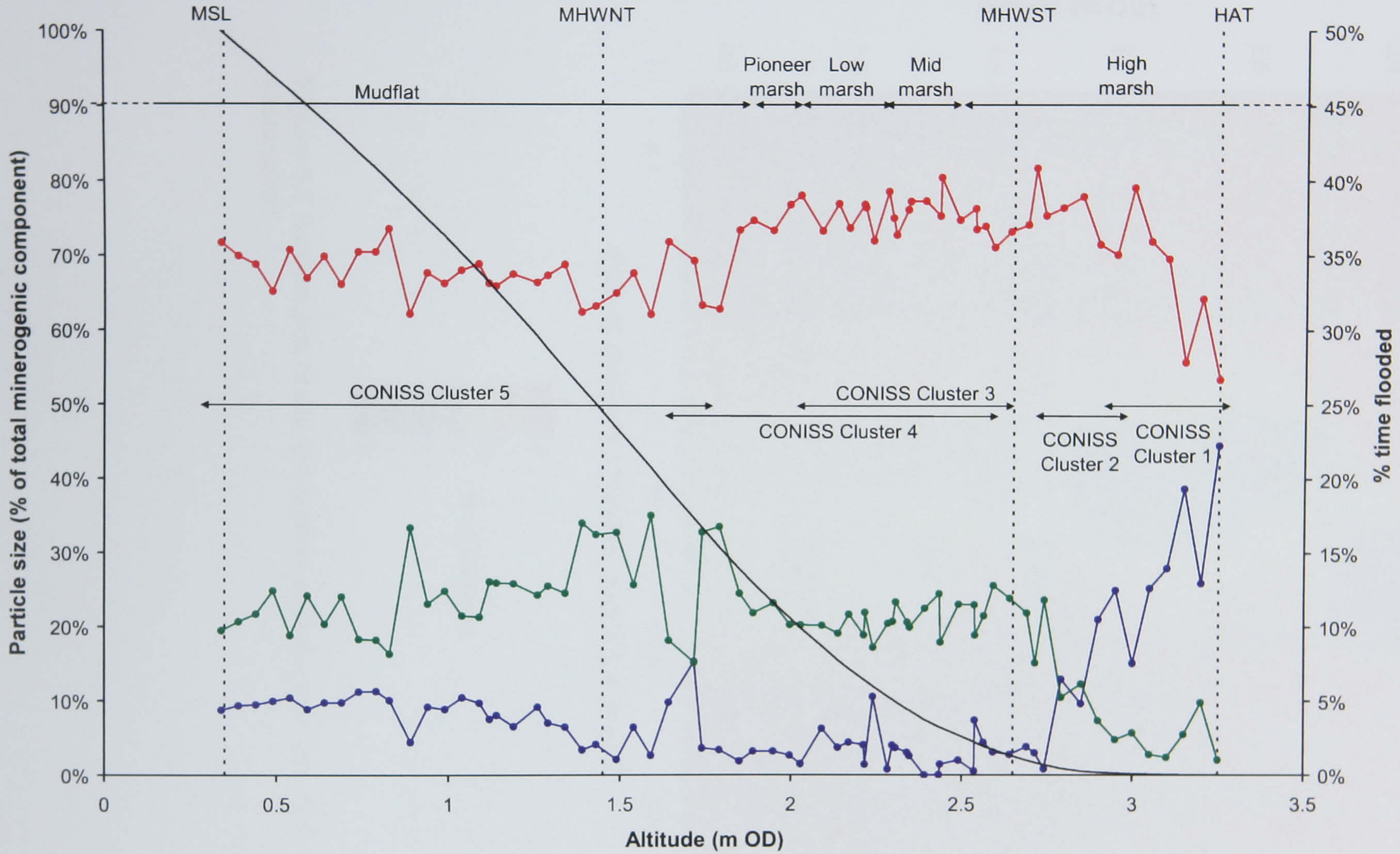

Figure 5.6 Variations in the relative abundance of sand (blue data series, corresponding to the left-hand y-axis), silt (red, left-hand y-axis) and clay (green, left-hand y-axis) particle size fractions in relation to altitude, flooding duration (continuous black data series, corresponding to the right-hand y-axis), reference water levels, approximate marsh floral zones and CONISS clusters.

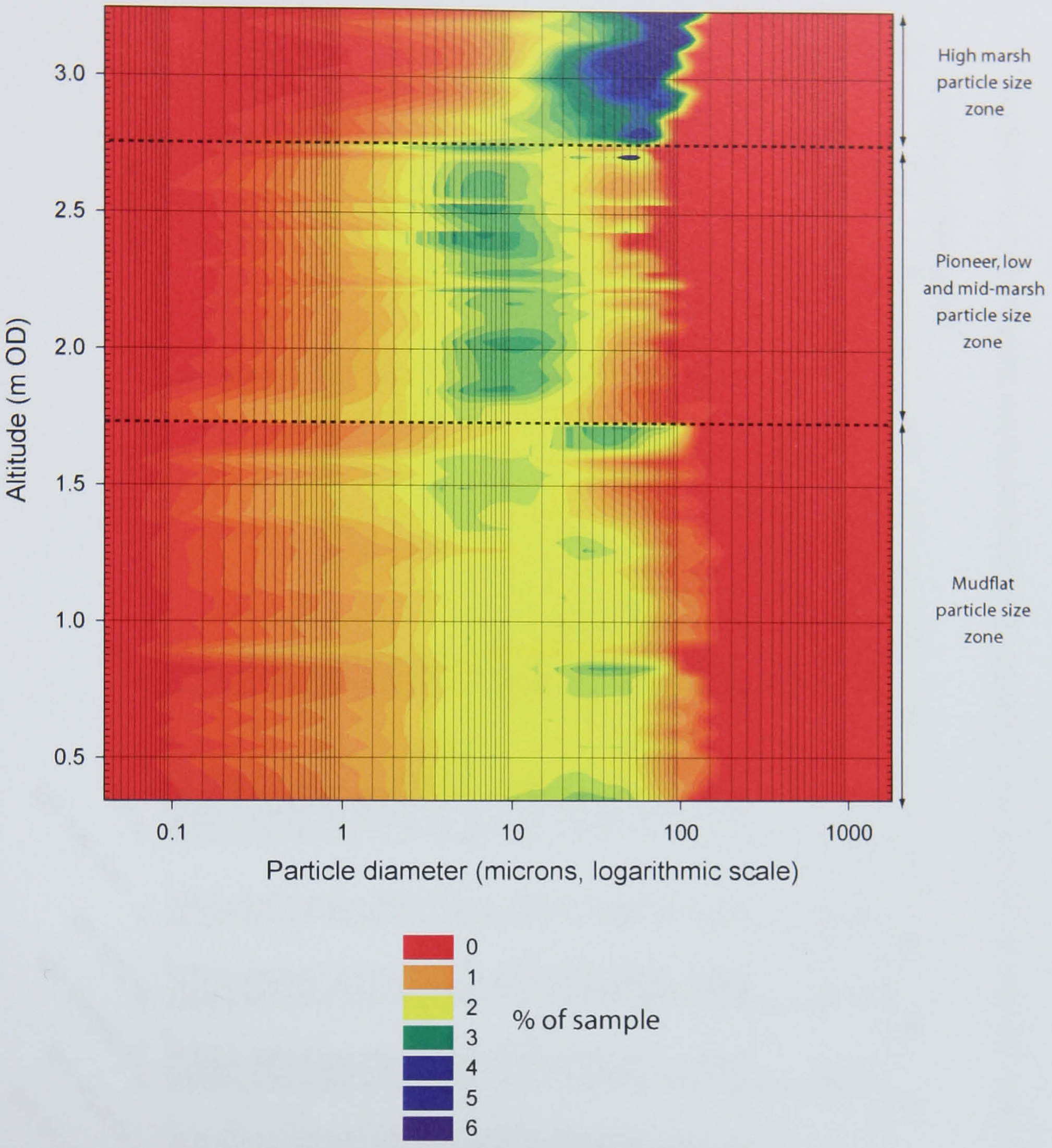

Figure 5.7 Surface plot of altitude against particle diameter. See text for explanation.

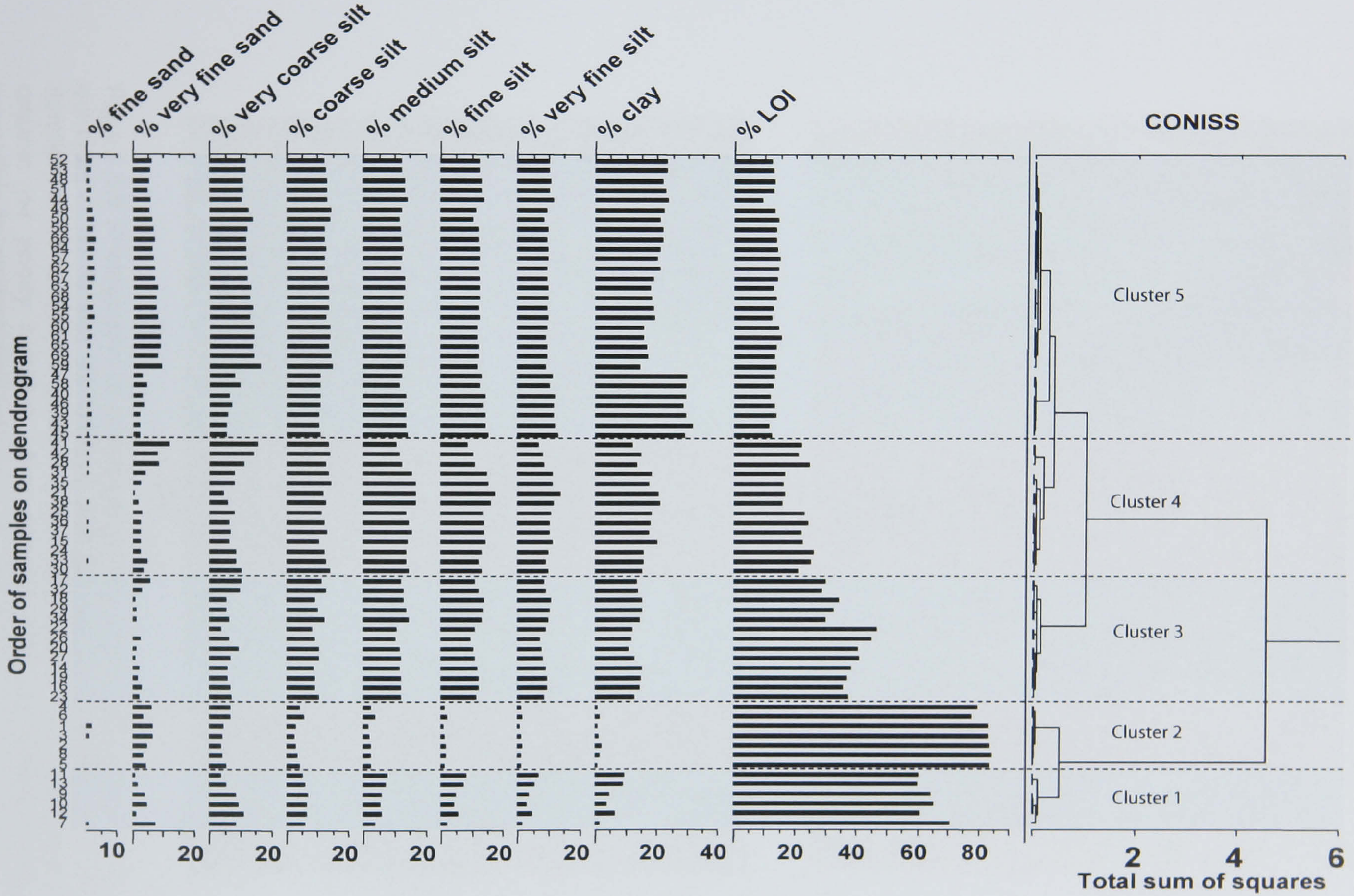

Figure 5.8 Output of unconstrained cluster analysis using CONISS, illustrating assigned lithostratigraphic clusters.

(a)

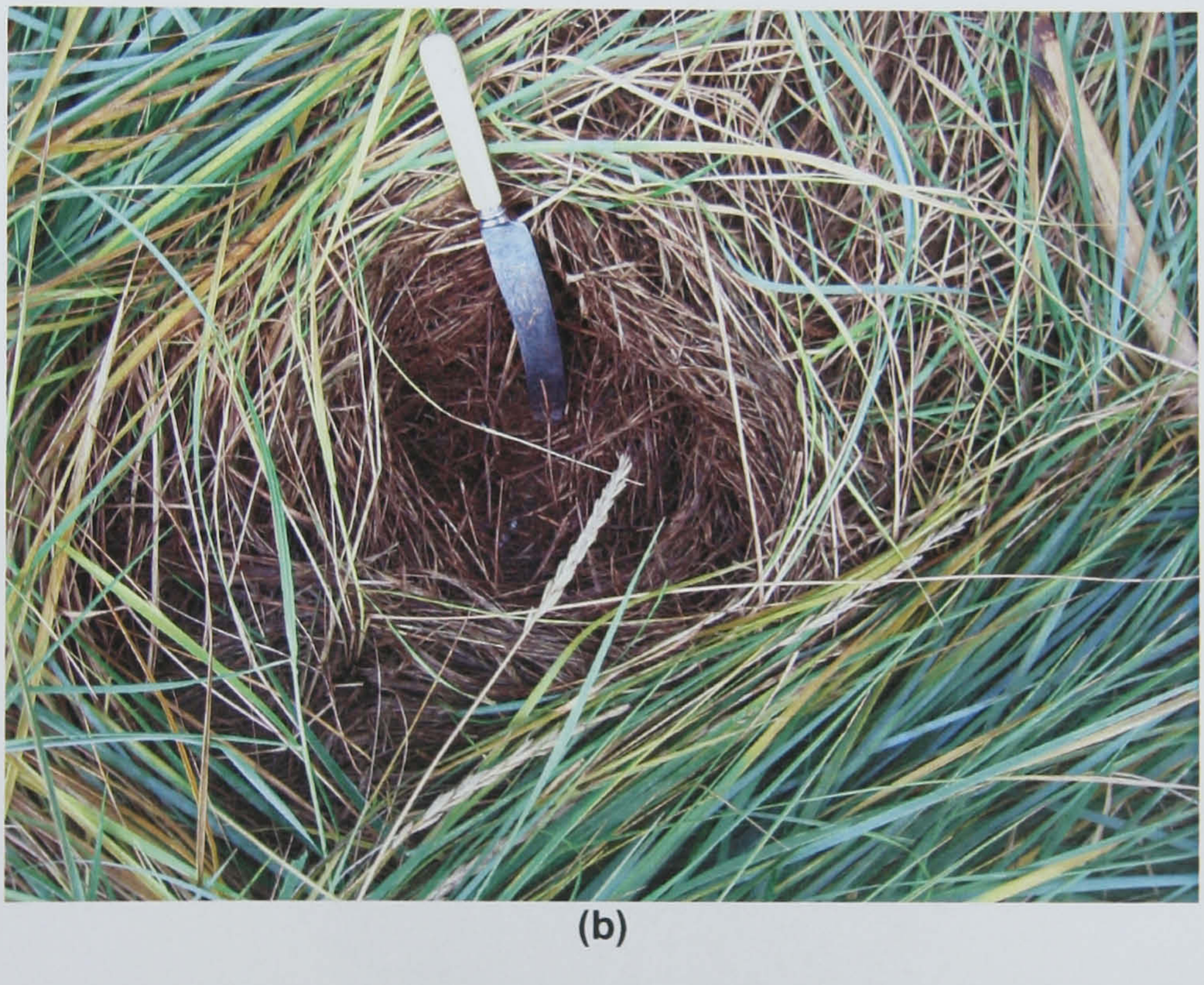

(b)

Figure 5.9 Photographs of contemporary (a) high (3.10 m OD, < 2% flooding duration, *c.* 85 % loss on ignition) and (b) mid (2.40 m OD, *c.* 5 % flooding duration, *c.* 40 % loss on ignition) marsh substrates. The sediments are highly organic yet poorly humified plant remains with no cohesion and so are unsuitable for geotechnical testing.

Figure 5.10 Photograph of newly sampled mudflat material, displaying evidence of bioturbation.

Figure 5.11 Photograph of low marsh material within an oedometer cutting ring. Note the presence of rootlets and unsaturated air pockets.

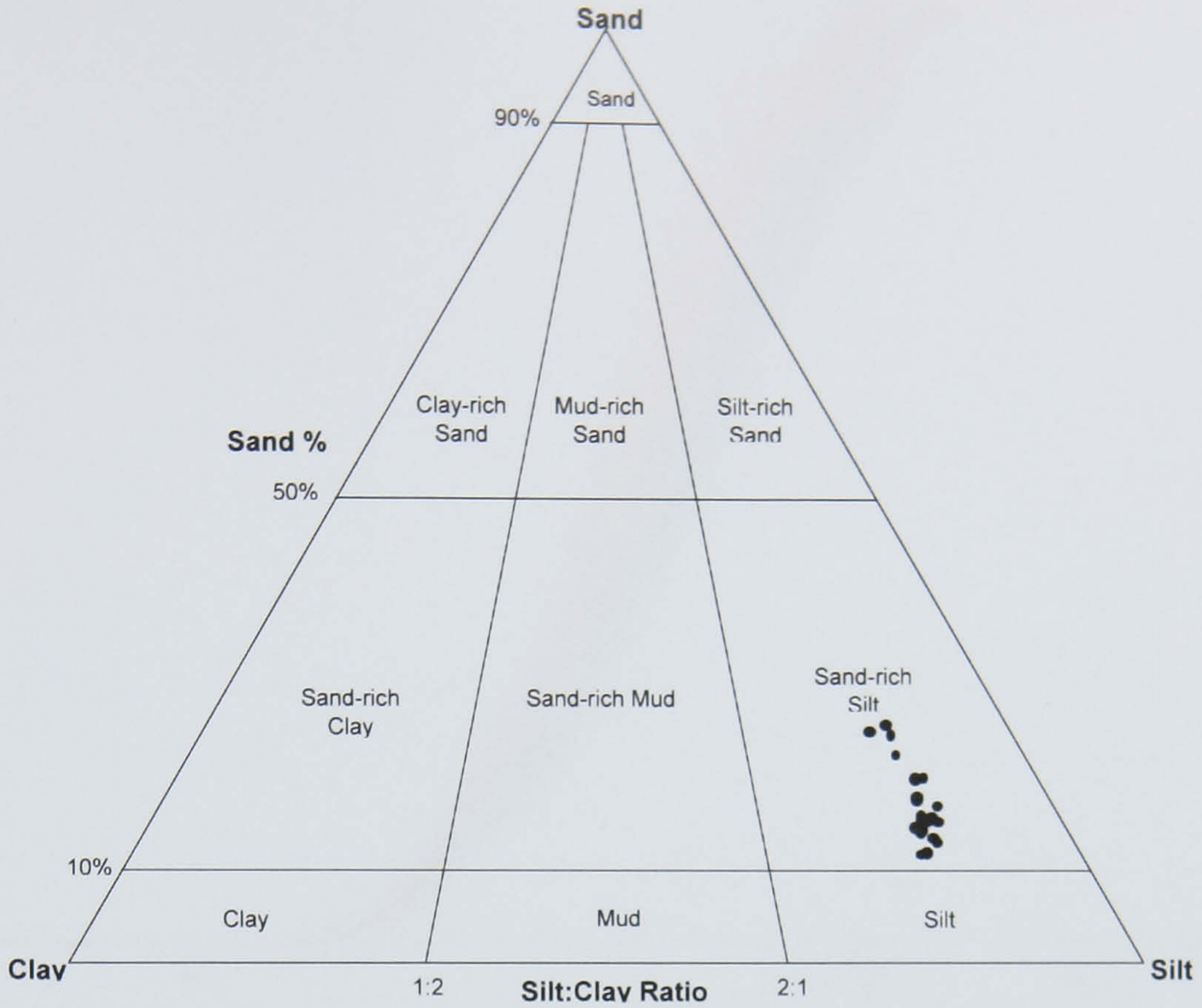

Figure 5.12 Ternary plot of the clastic components of the mudflat material.

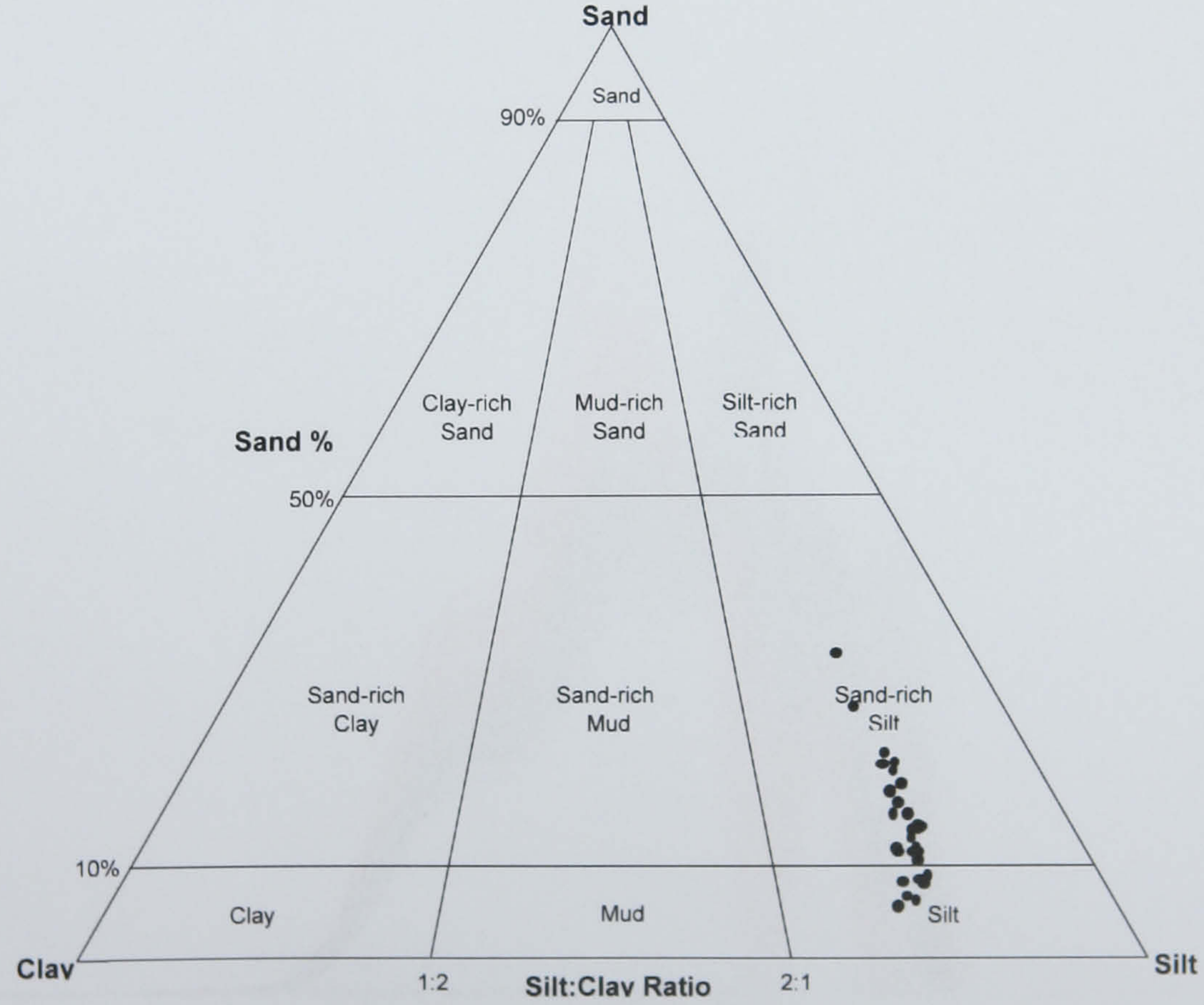

Figure 5.13 Ternary plot of the clastic components of the low marsh material.

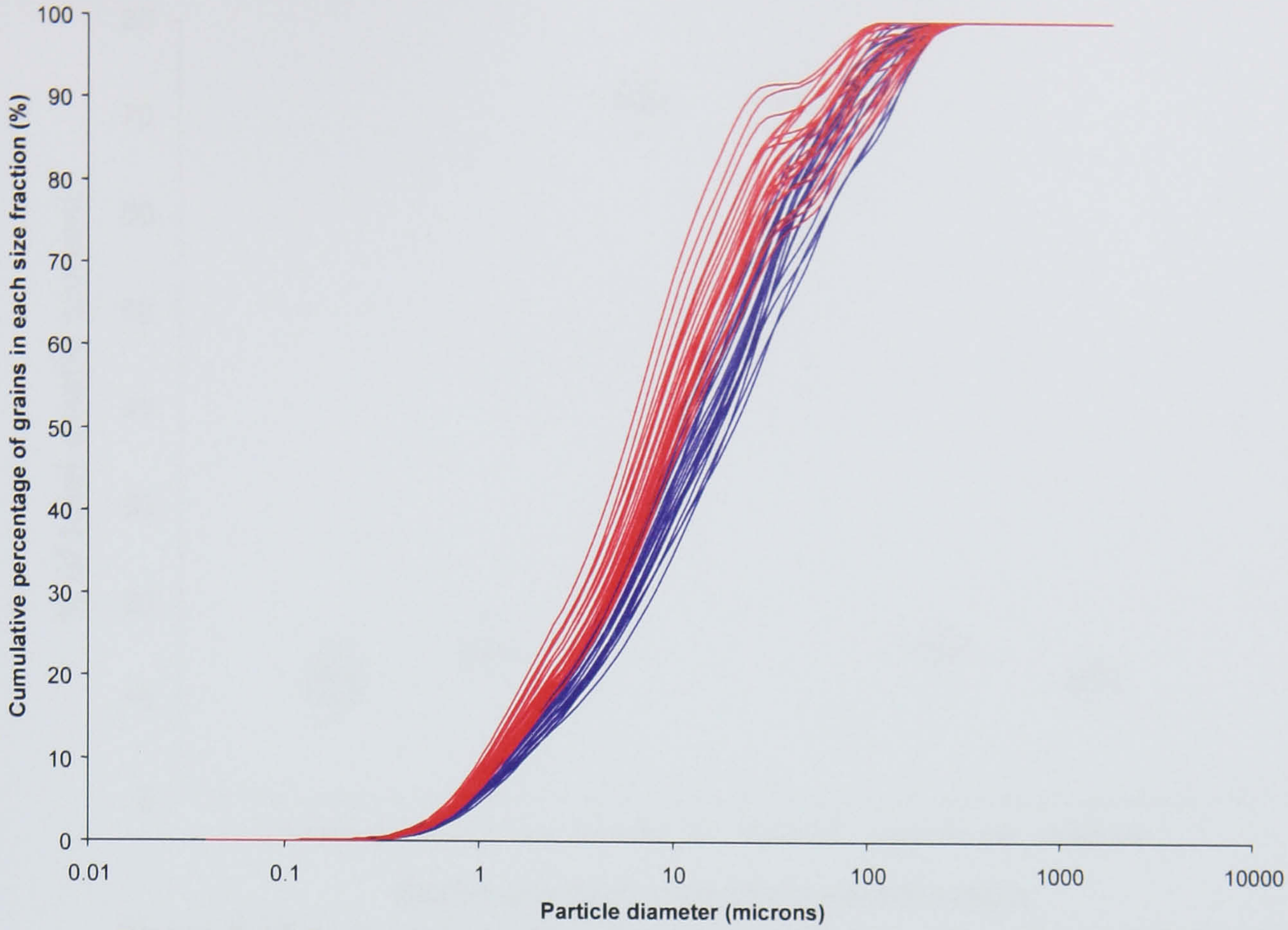

Figure 5.14 Cumulative particle size distribution for mudflat (blue) and low marsh (red) samples.

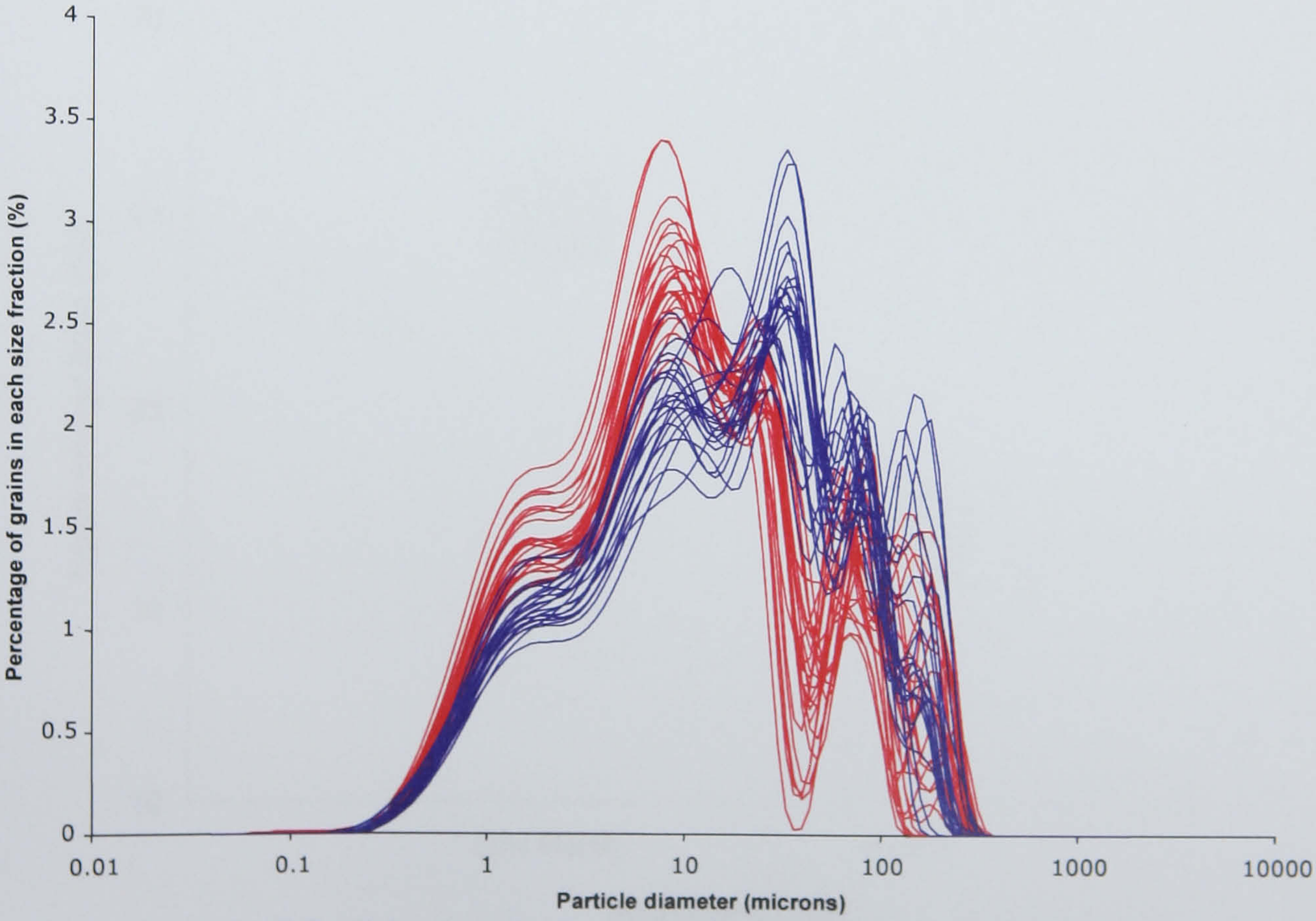

Figure 5.15 Particle size distributions of mudflat (blue) and low marsh (red) samples.

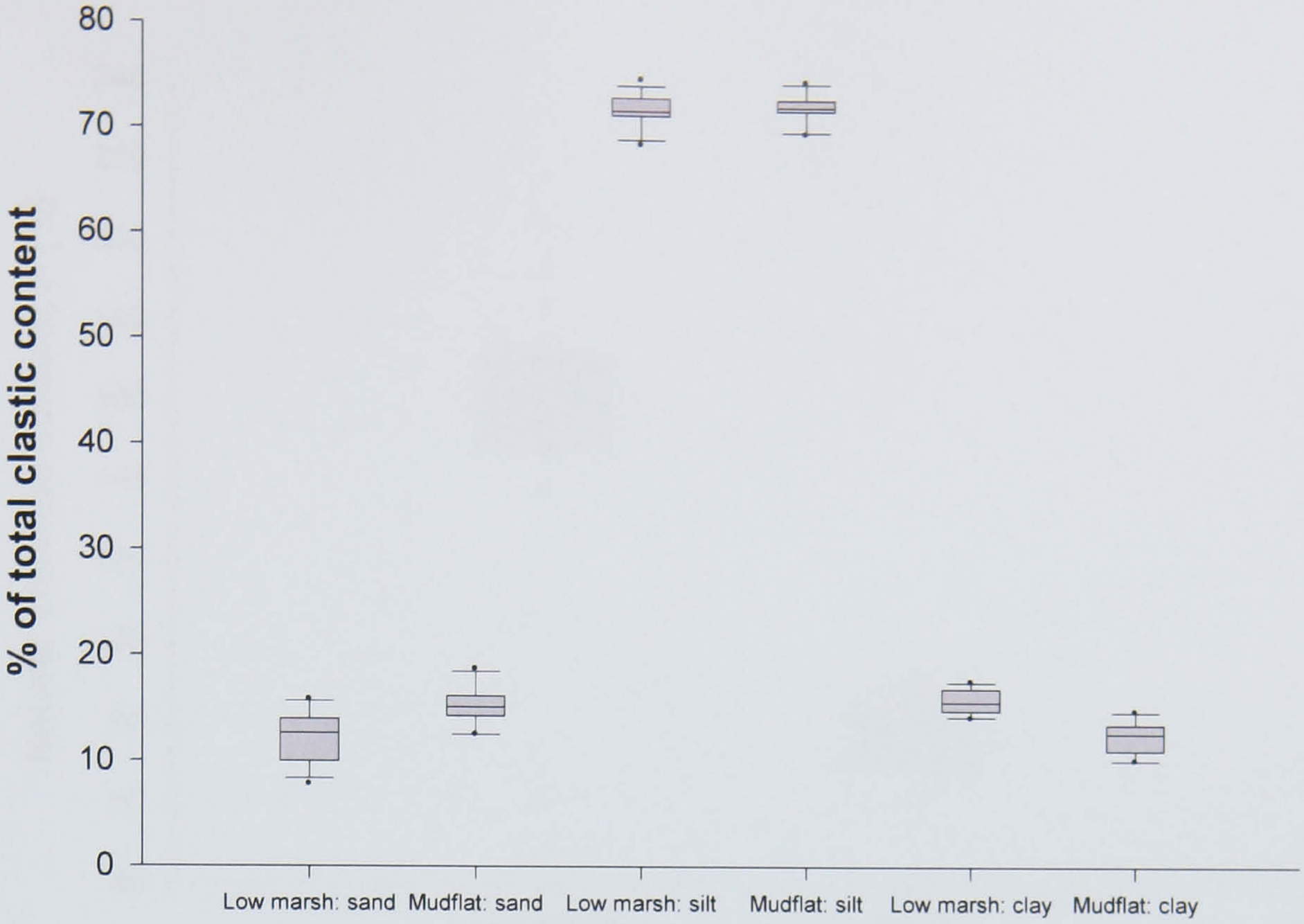

Figure 5.16 Boxplots illustrating frequency distributions of particle size fractions for low marsh and mudflat samples. Boxplot 'tails' represent 10th and 90th percentiles; outliers are represented by individual data points.

Figure 5.17 Boxplots illustrating frequency distributions of loss on ignition contents for low marsh and mudflat samples. Boxplot 'tails' represent 10th and 90th percentiles; outliers are represented by individual data points.

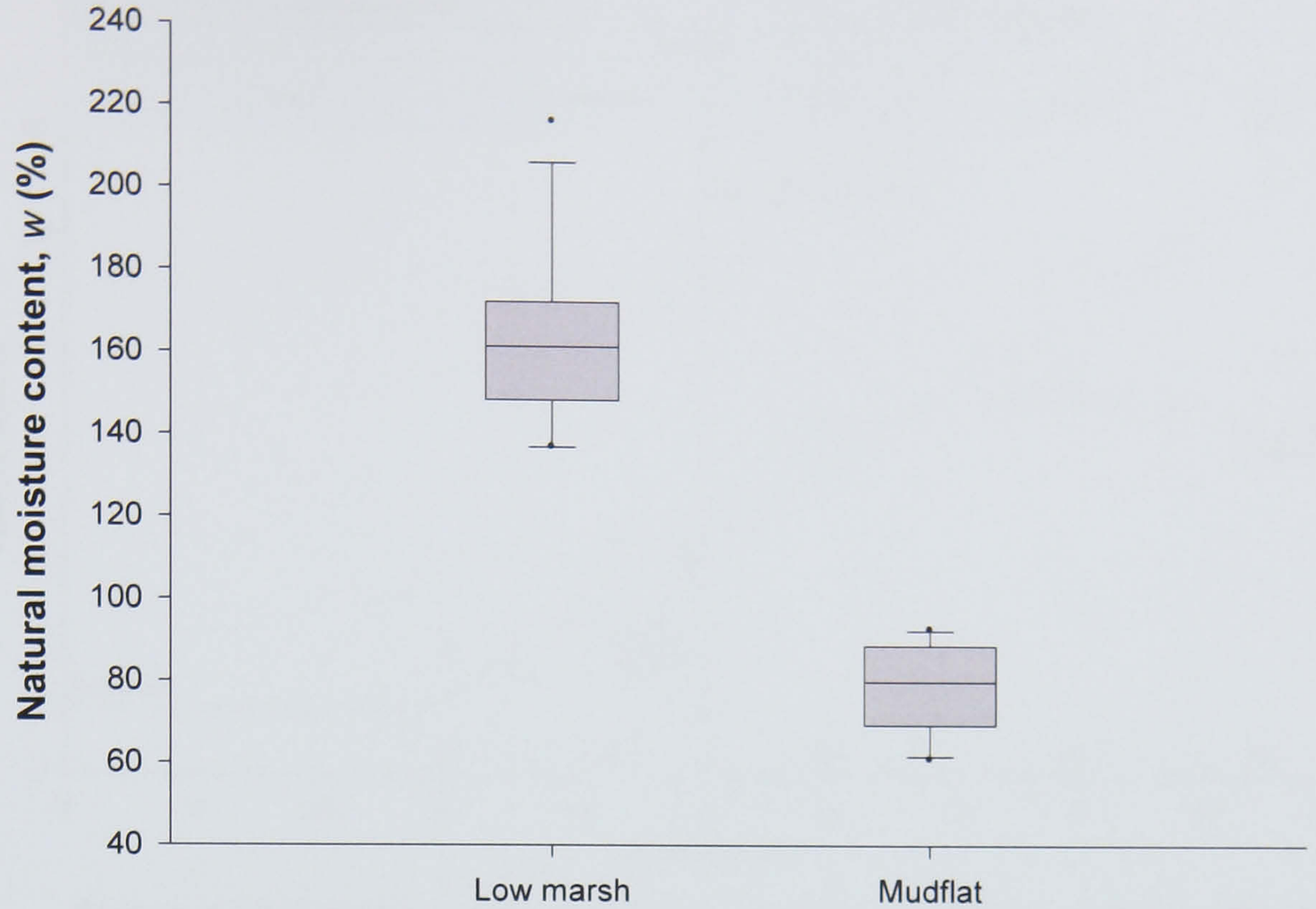

Figure 5.18 Boxplots illustrating frequency distributions of values of natural moisture contents for low marsh and mudflat samples. Boxplot 'tails' represent 10th and 90th percentiles; outliers are represented by individual data points.

Figure 5.19 Boxplots illustrating frequency distributions of values of *in situ* degree of saturation for low marsh and mudflat samples. Boxplot 'tails' represent 10th and 90th percentiles; outliers are represented by individual data points.

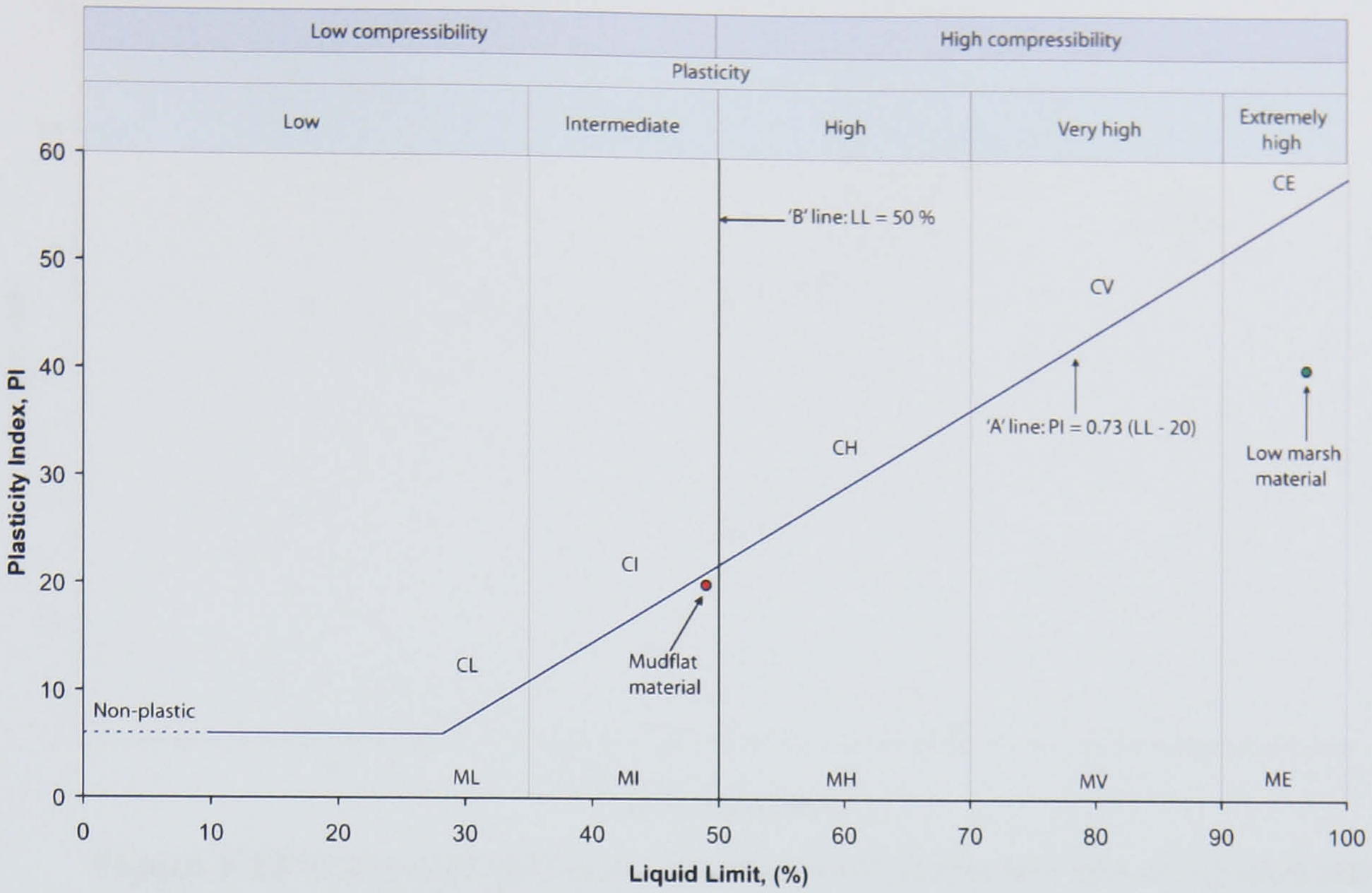

Figure 5.20 Plasticity chart showing the plasticity properties of the mudflat and low marsh samples.

Figure 5.21 Boxplots illustrating frequency distributions of values of initial voids ratio for low marsh and mudflat samples. Boxplot 'tails' represent 10th and 90th percentiles; outliers are represented by individual data points.

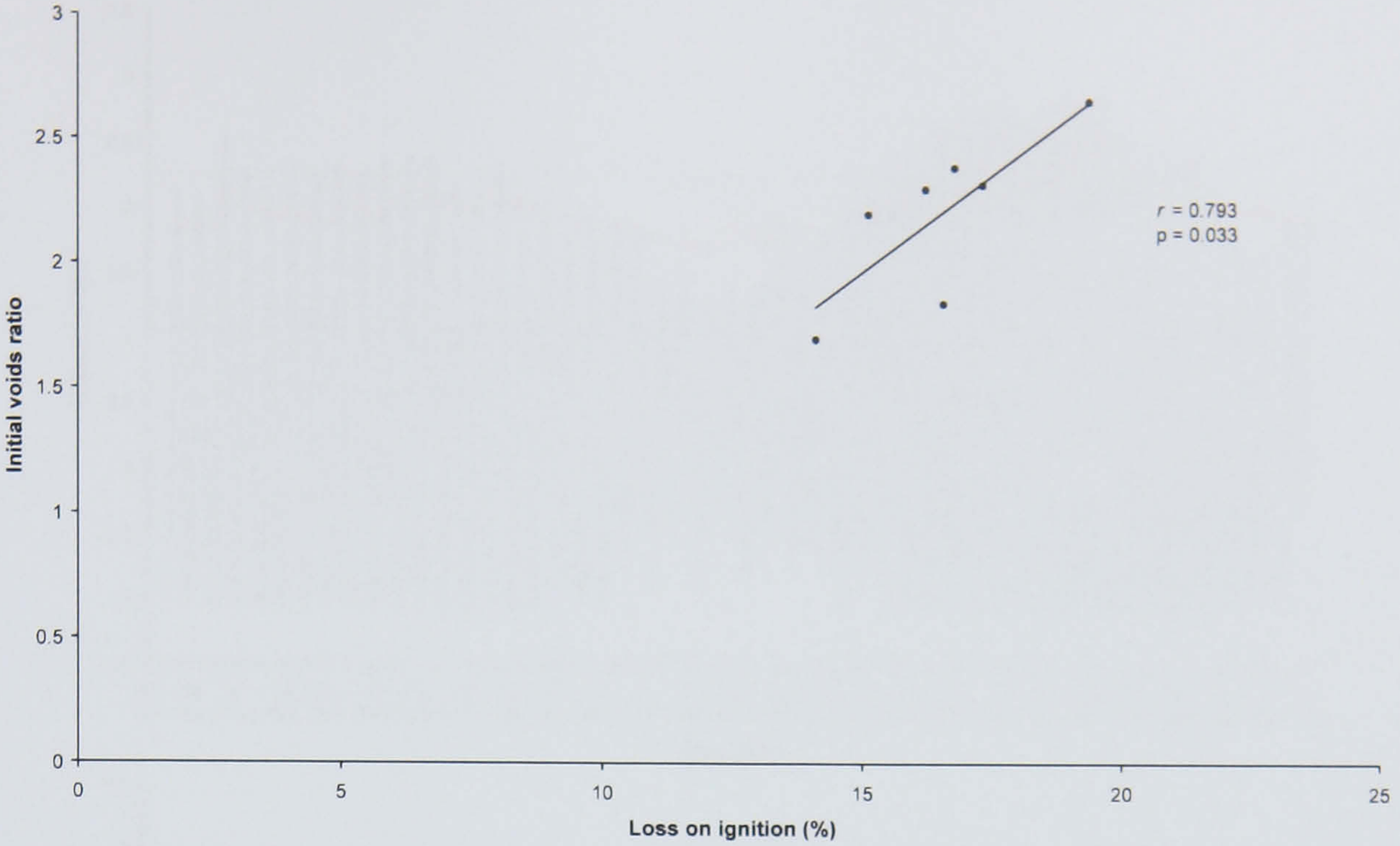

Figure 5.22 Scatterplot displaying the relationship between loss on ignition and the initial voids ratio for the mudflat samples.

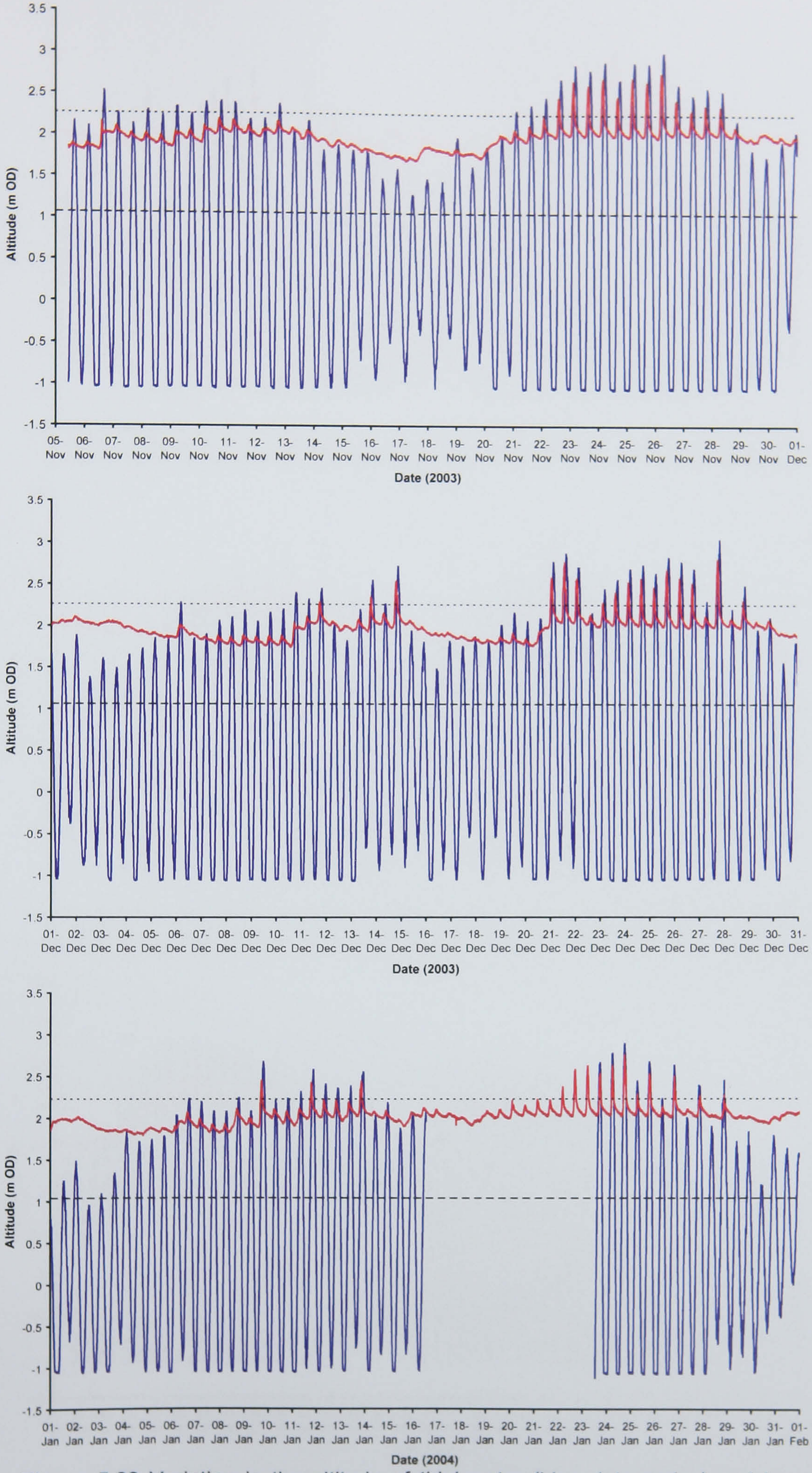

Figure 5.23 Variation in the altitude of tidal water (blue data series) and low marsh groundwater (red data series) through time. The upper horizontal line (2.26 m OD, fine dash) indicates the altitude of the low marsh sampling surface. The lower horizontal line (1.06 m OD, thicker dash) indicates the altitude of the mudflat sampling surface.

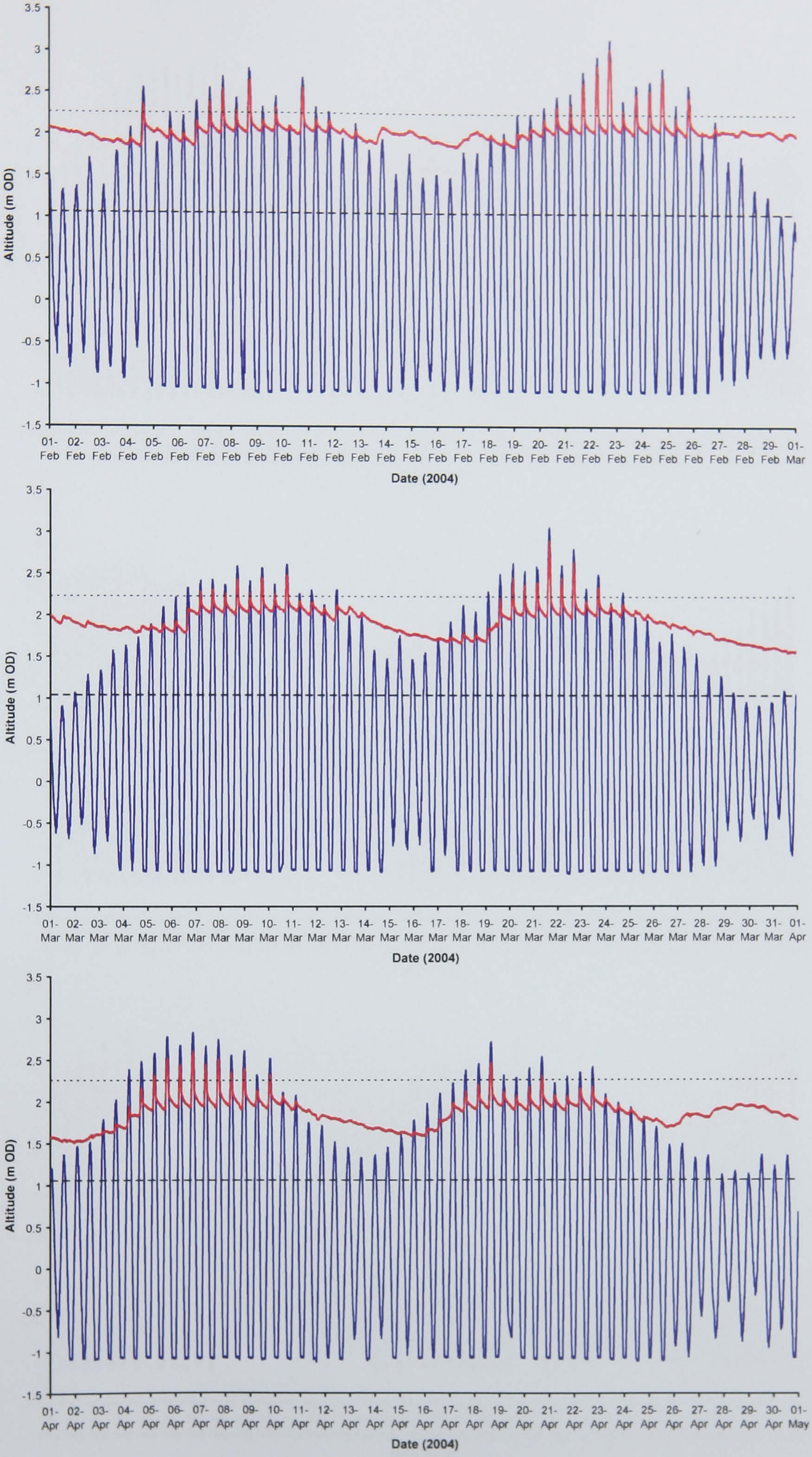

Figure 5.23 continued.

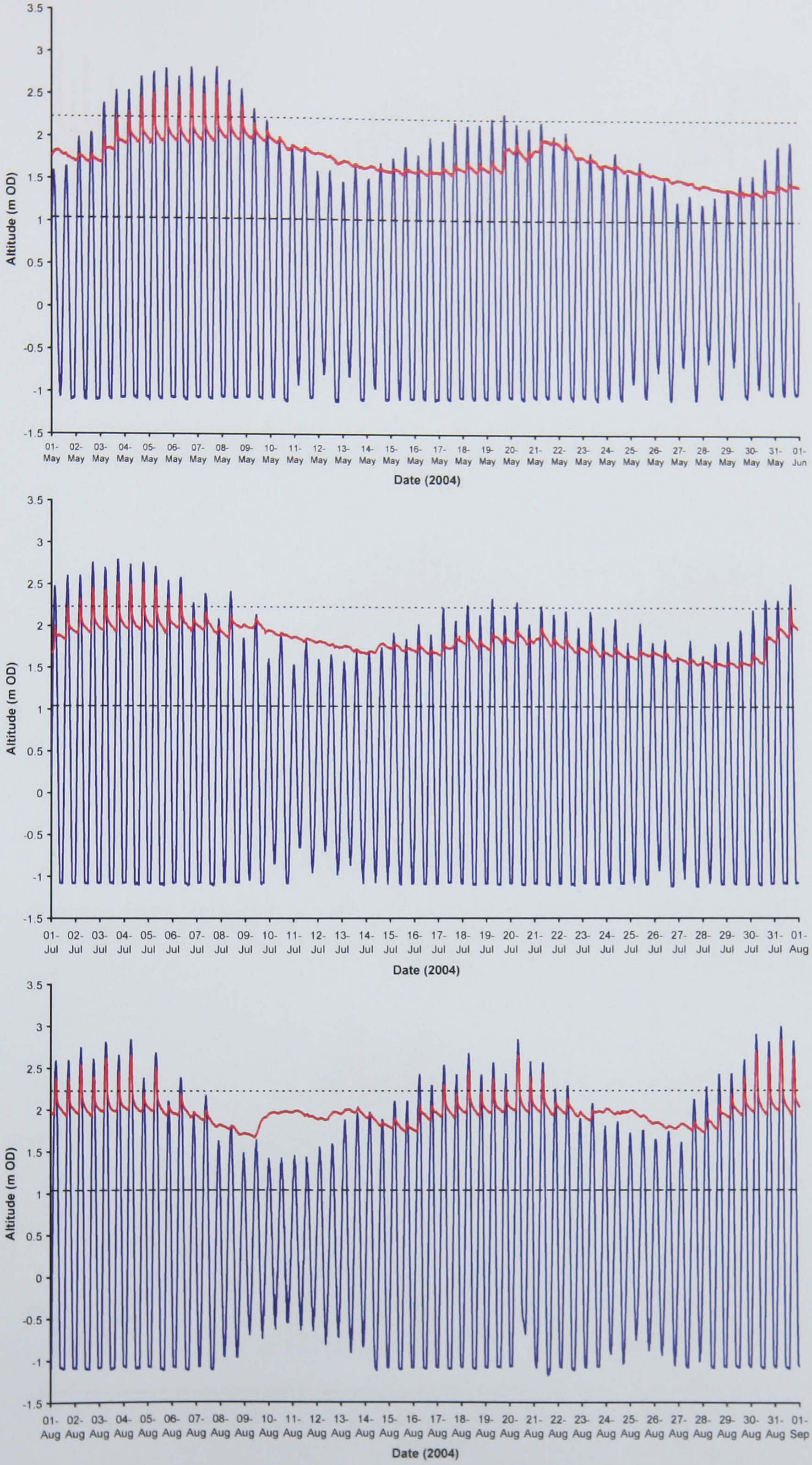

Figure 5.23 continued.

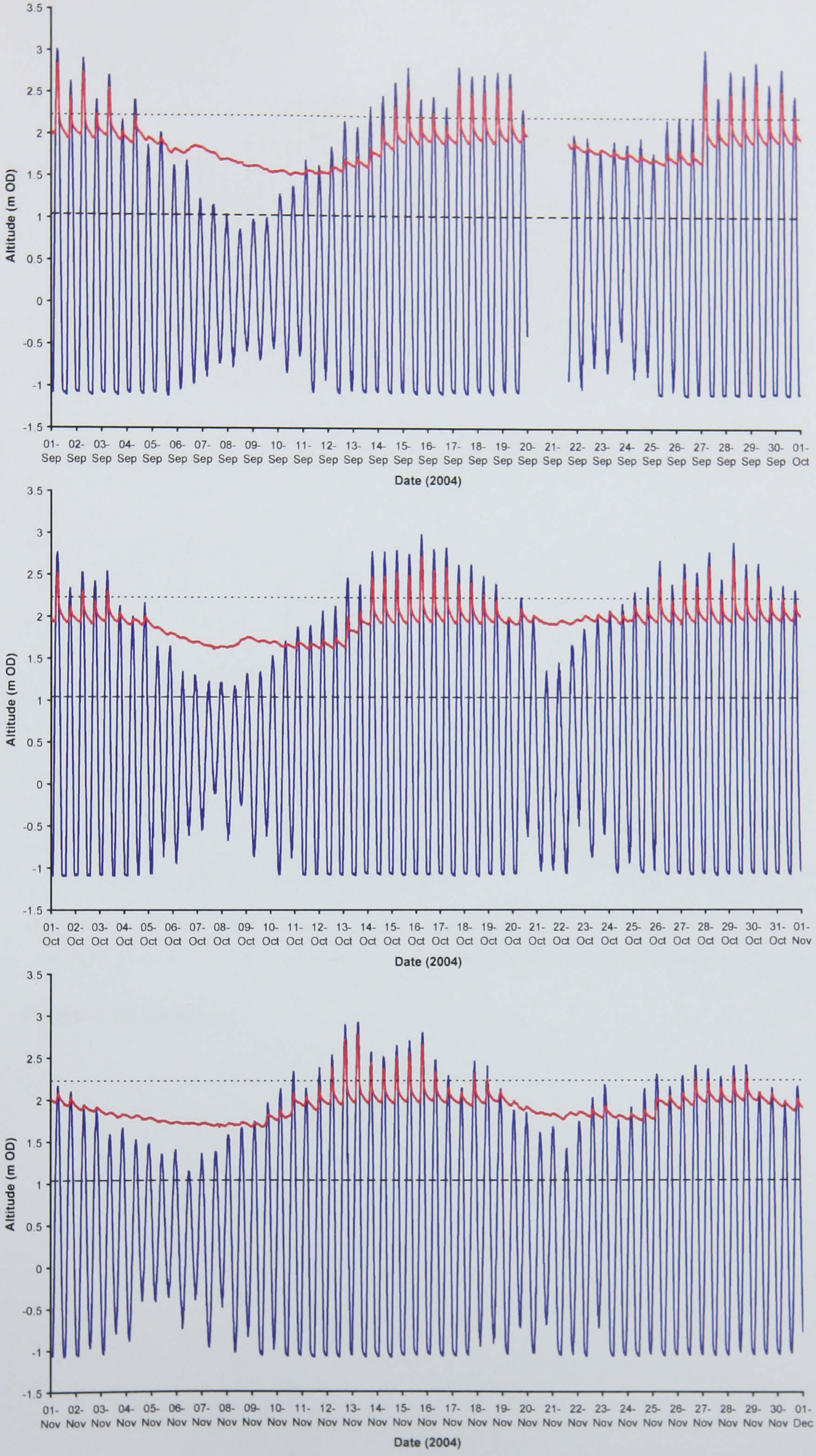

Figure 5.23 continued.

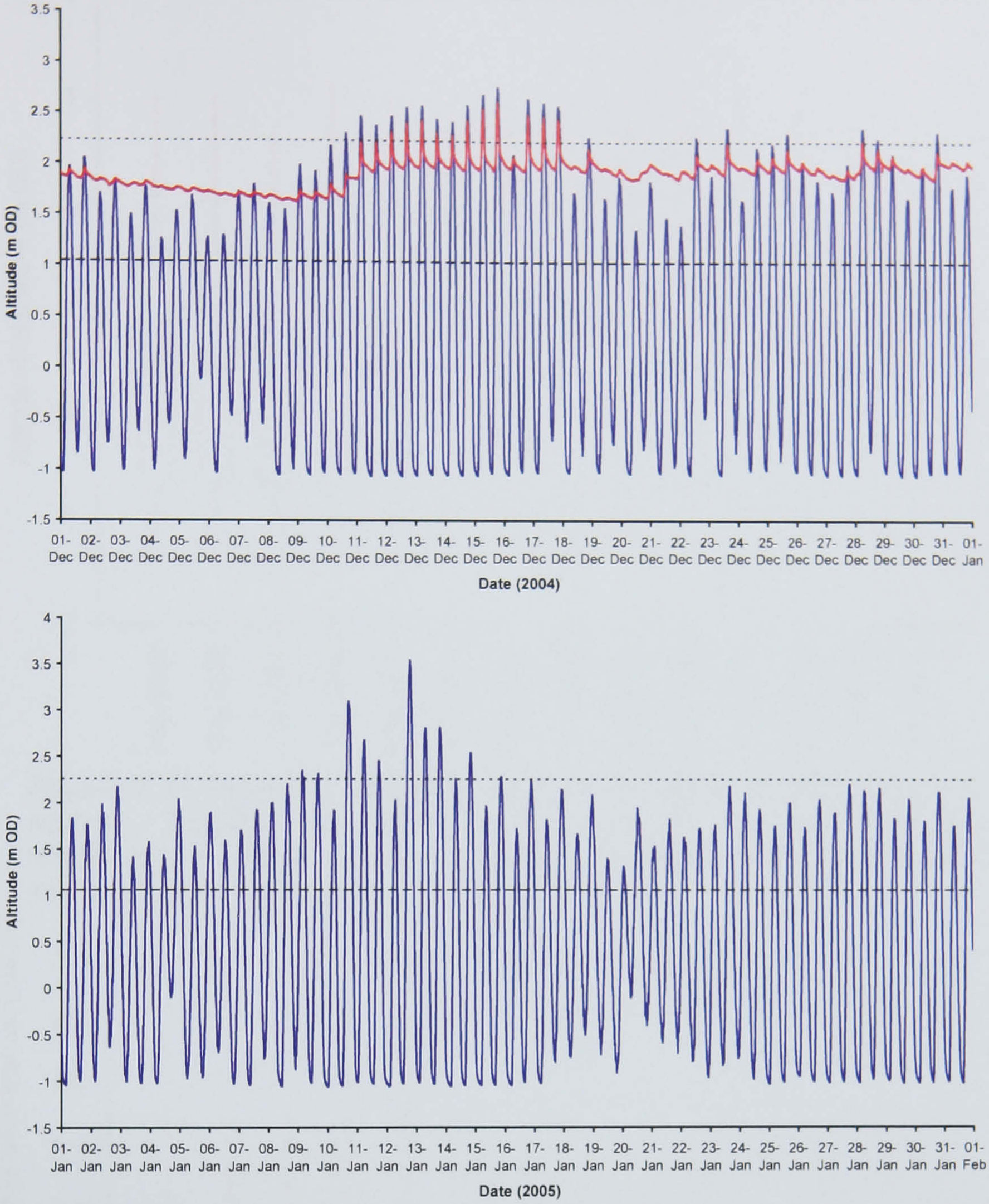

Figure 5.23 continued.

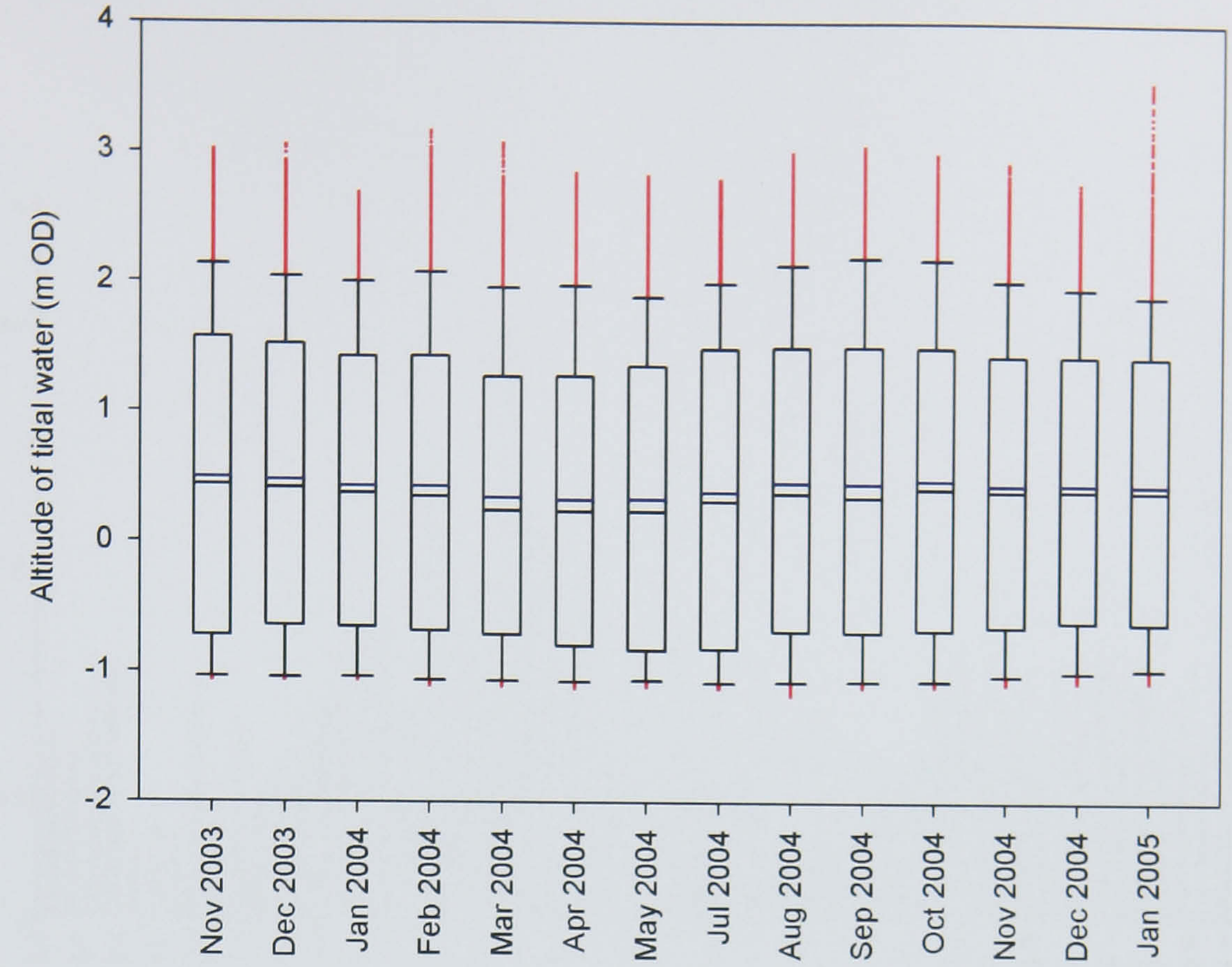

Figure 5.24 Boxplots illustrating monthly variations in the altitude of tidal waters. Boxplot 'tails' represent 10th and 90th percentiles; outliers are represented by individual red data points. The median (black) and mean (blue) values are also illustrated.

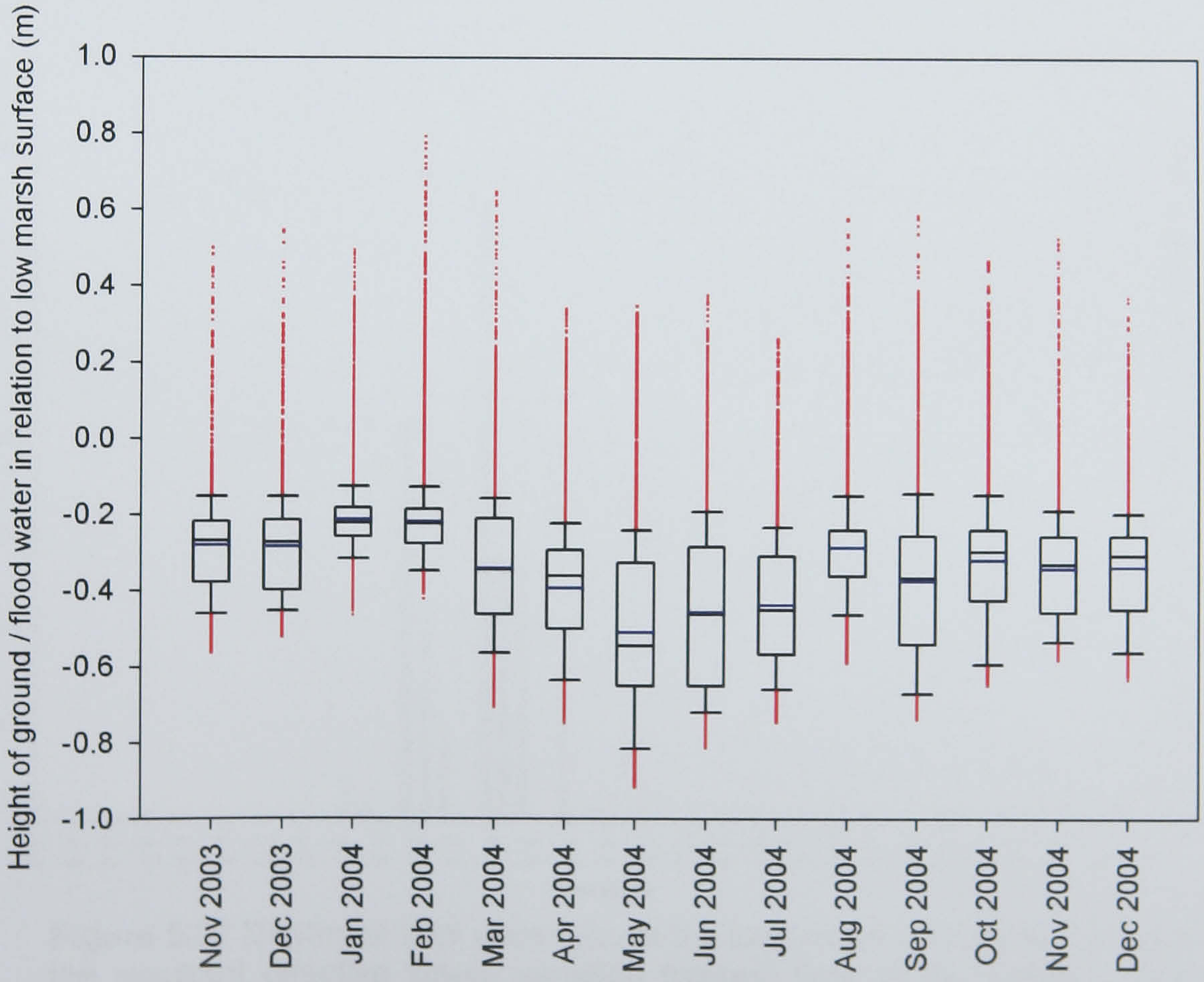

Figure 5.25 Boxplots illustrating monthly variations in the depth of the groundwater level in relation to the low marsh depositional surface. Boxplot 'tails' represent 10th and 90th percentiles; outliers are represented by individual red data points. The median (black) and mean (blue) values are also illustrated.

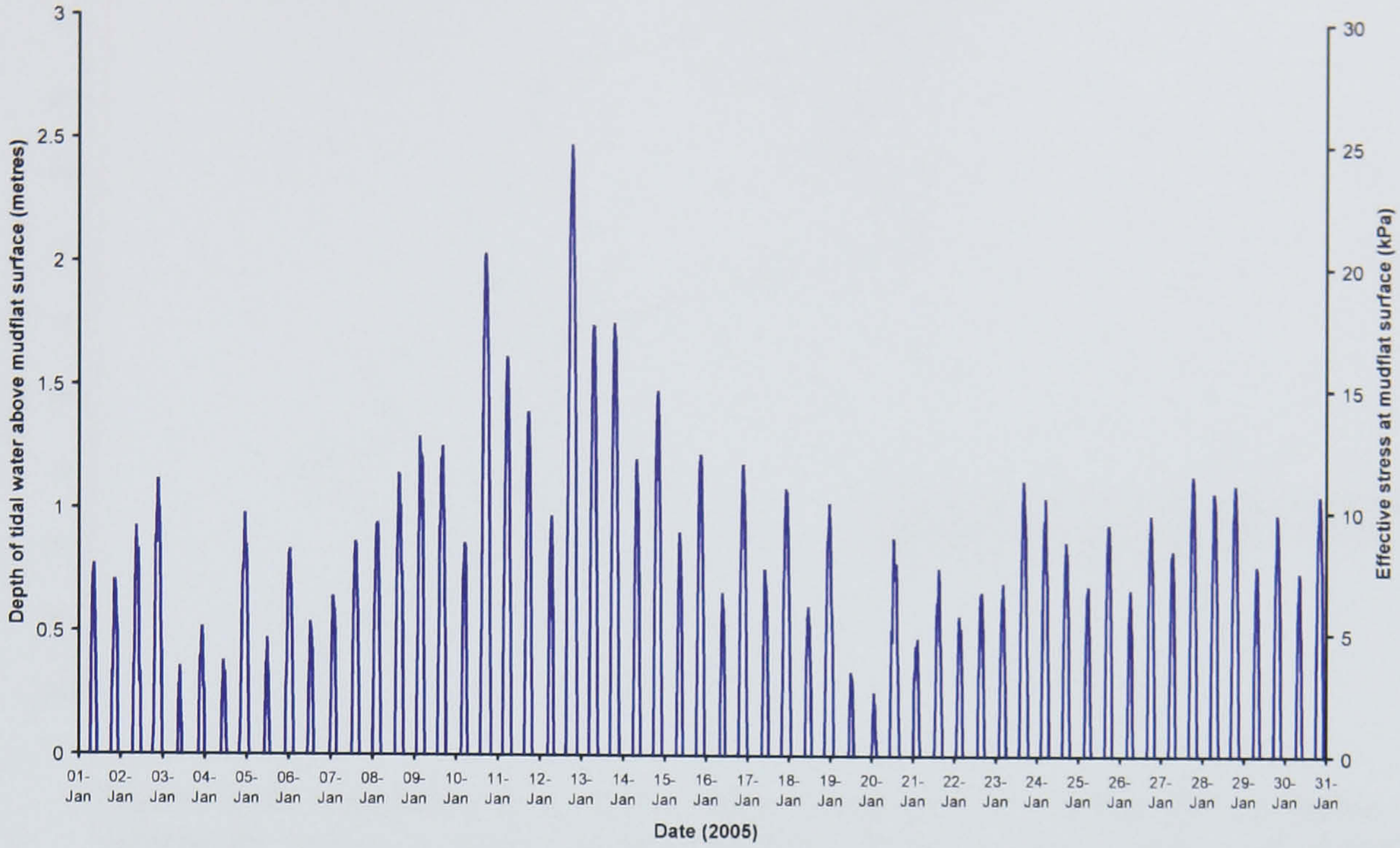

Figure 5.26 Depths of tidal water above the mudflat depositional surface and the resultant effective stress variation through time at the surface, assuming hydraulic disconnectivity.

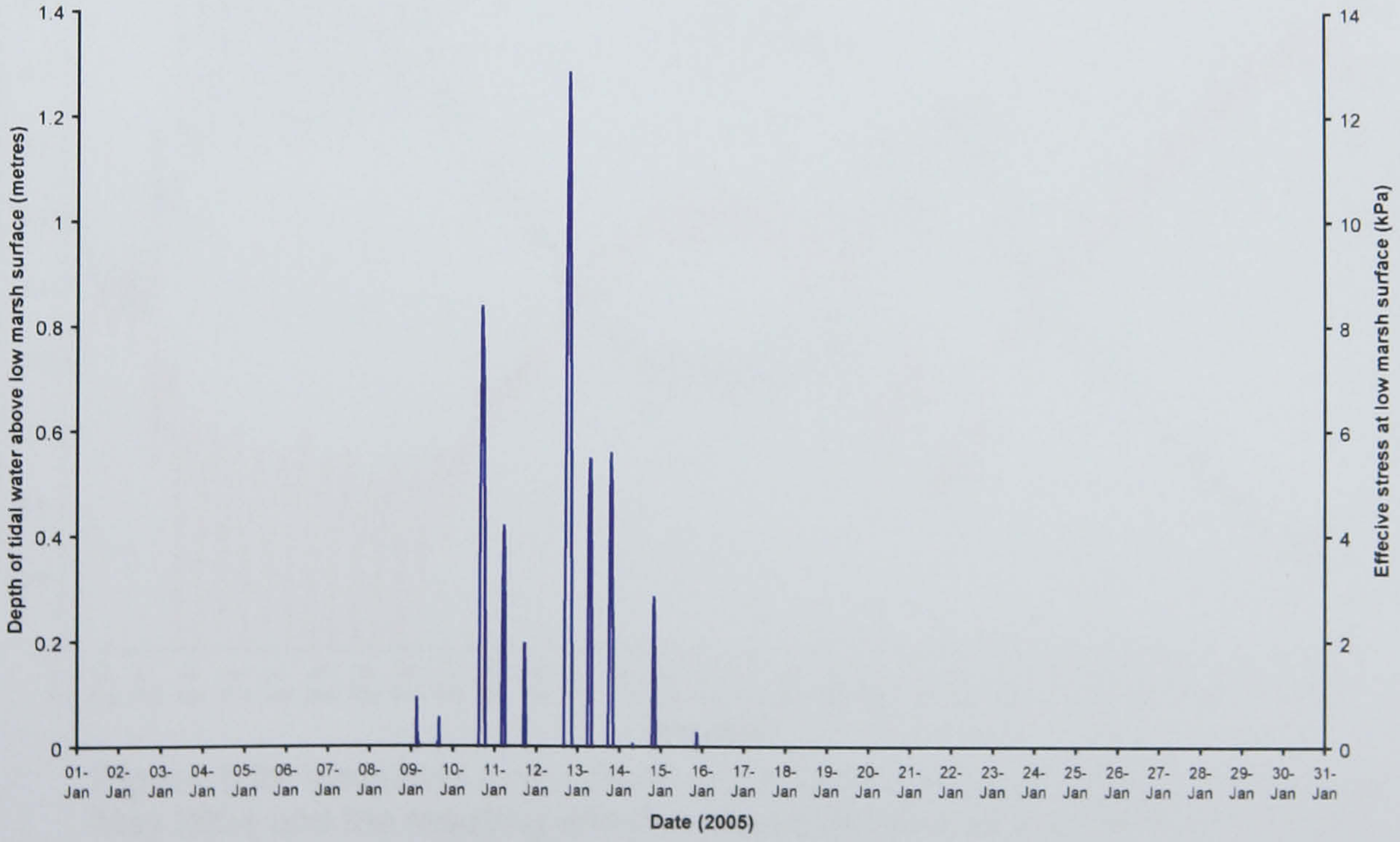

Figure 5.27 Depths of tidal water above the low marsh depositional surface and the resultant effective stress variation through time at the surface, assuming hydraulic disconnectivity.

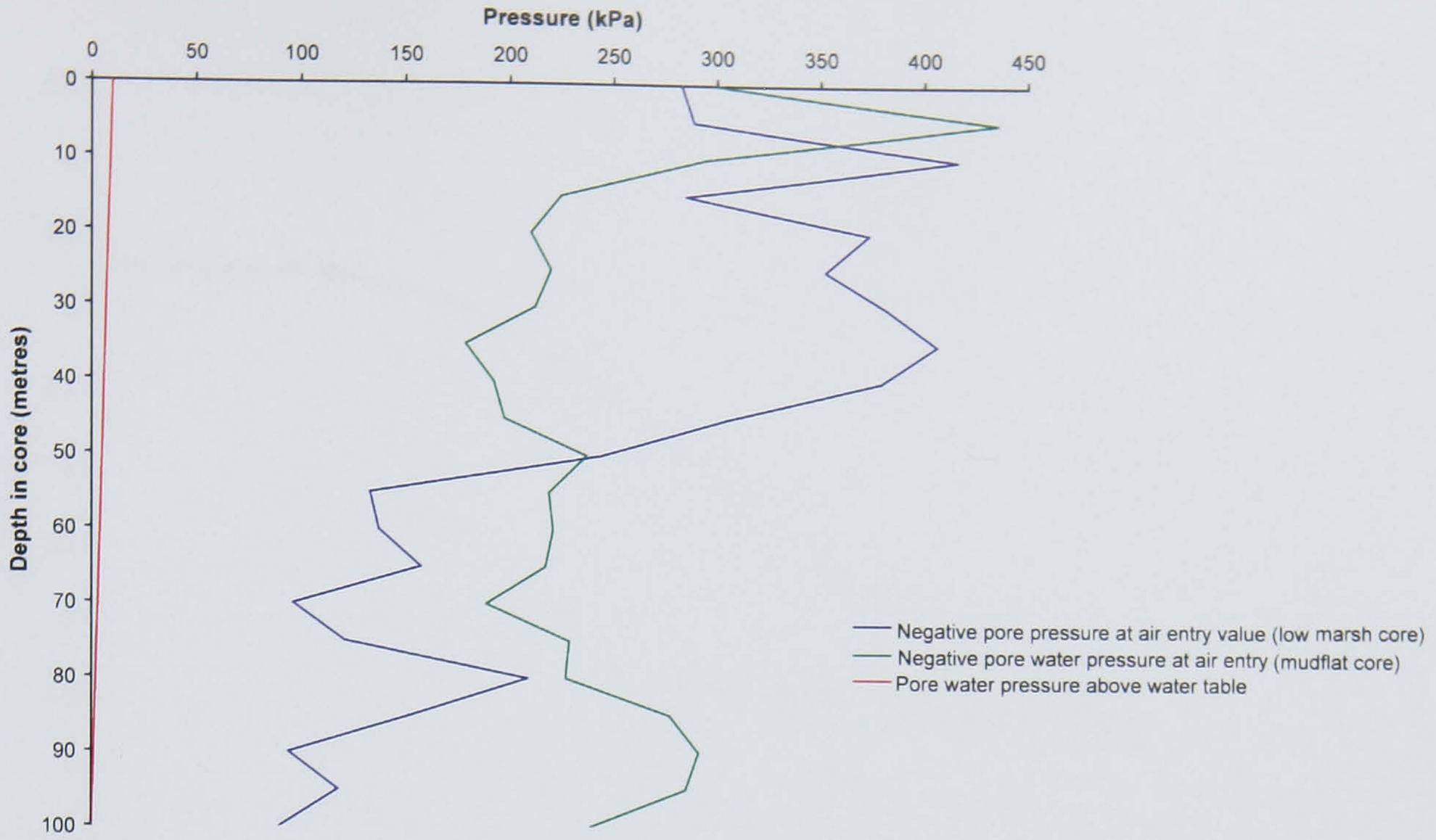

Figure 5.28 Variations in air entry value obtained from particle size analysis of sediments cores (1 metre length) collected from the low marsh and mudflat sampling altitudes. Capillary suction pressures associated with a drop in the water table of 1 metre are also displayed.

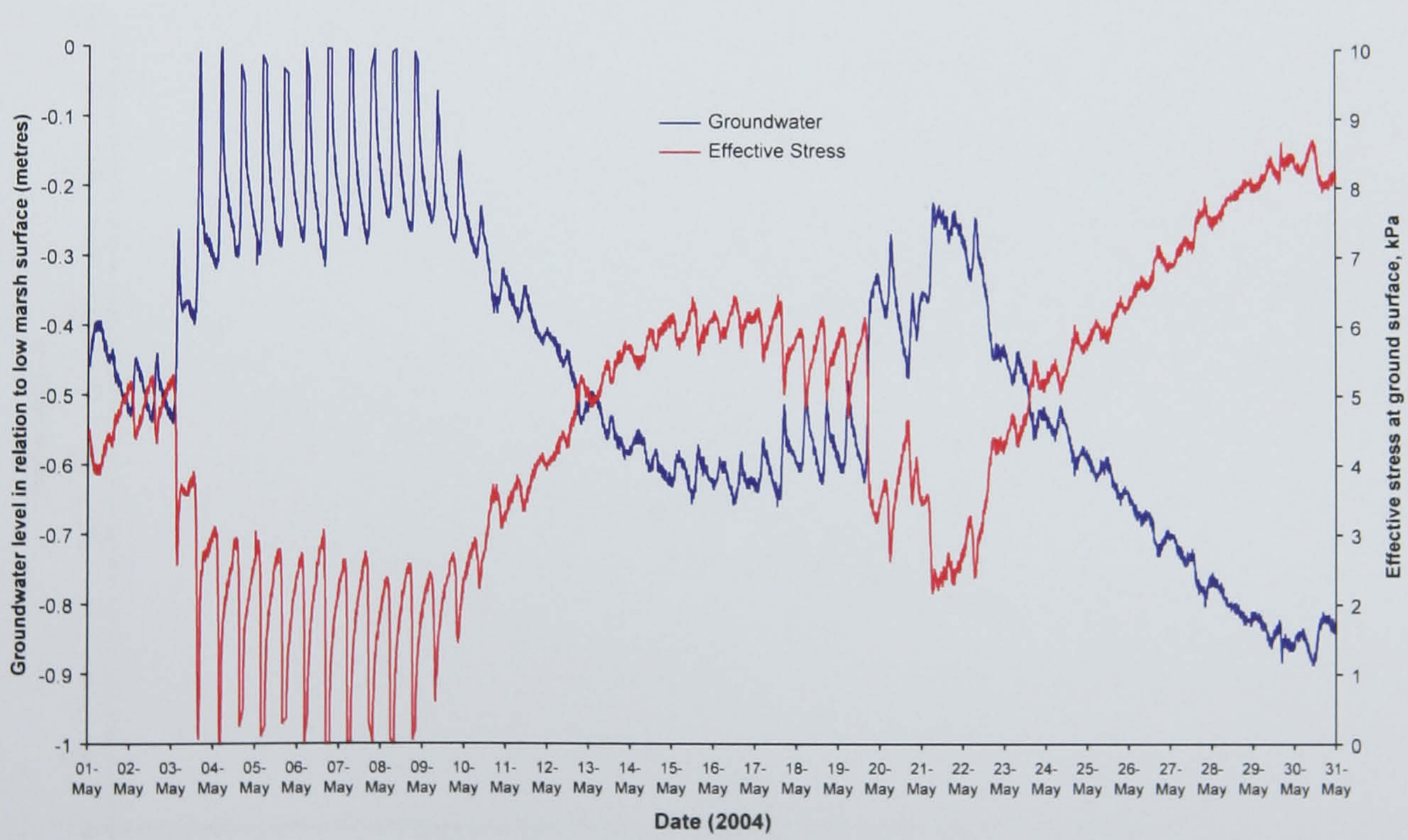

Figure 5.29 Variations in the depth of the low marsh groundwater table during May 2004 and the resulting effective stress variation at the low marsh ground surface.

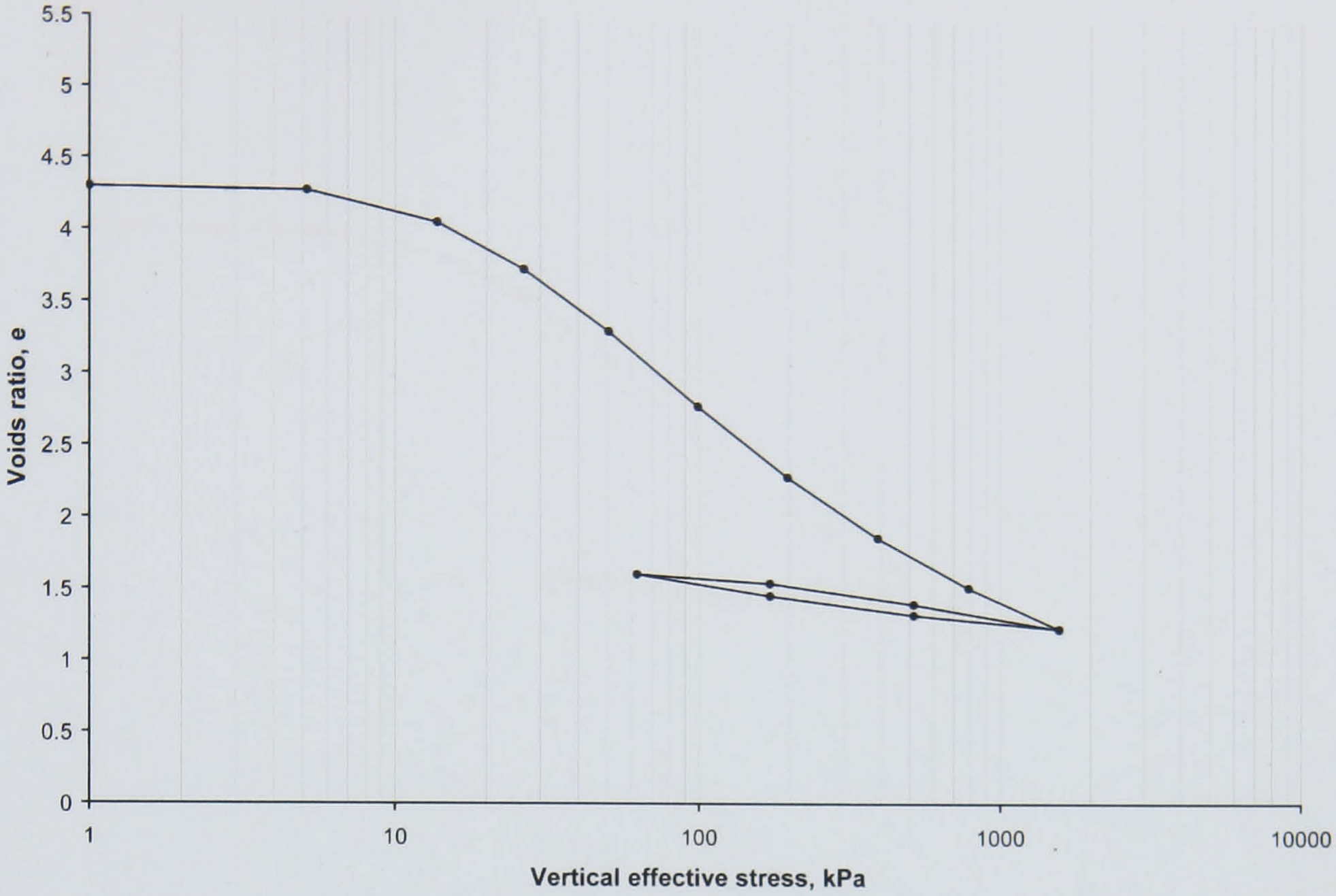

Figure 6.1 $e\log_{10}\sigma'$ plot of sample LM-1-S-OED-24.

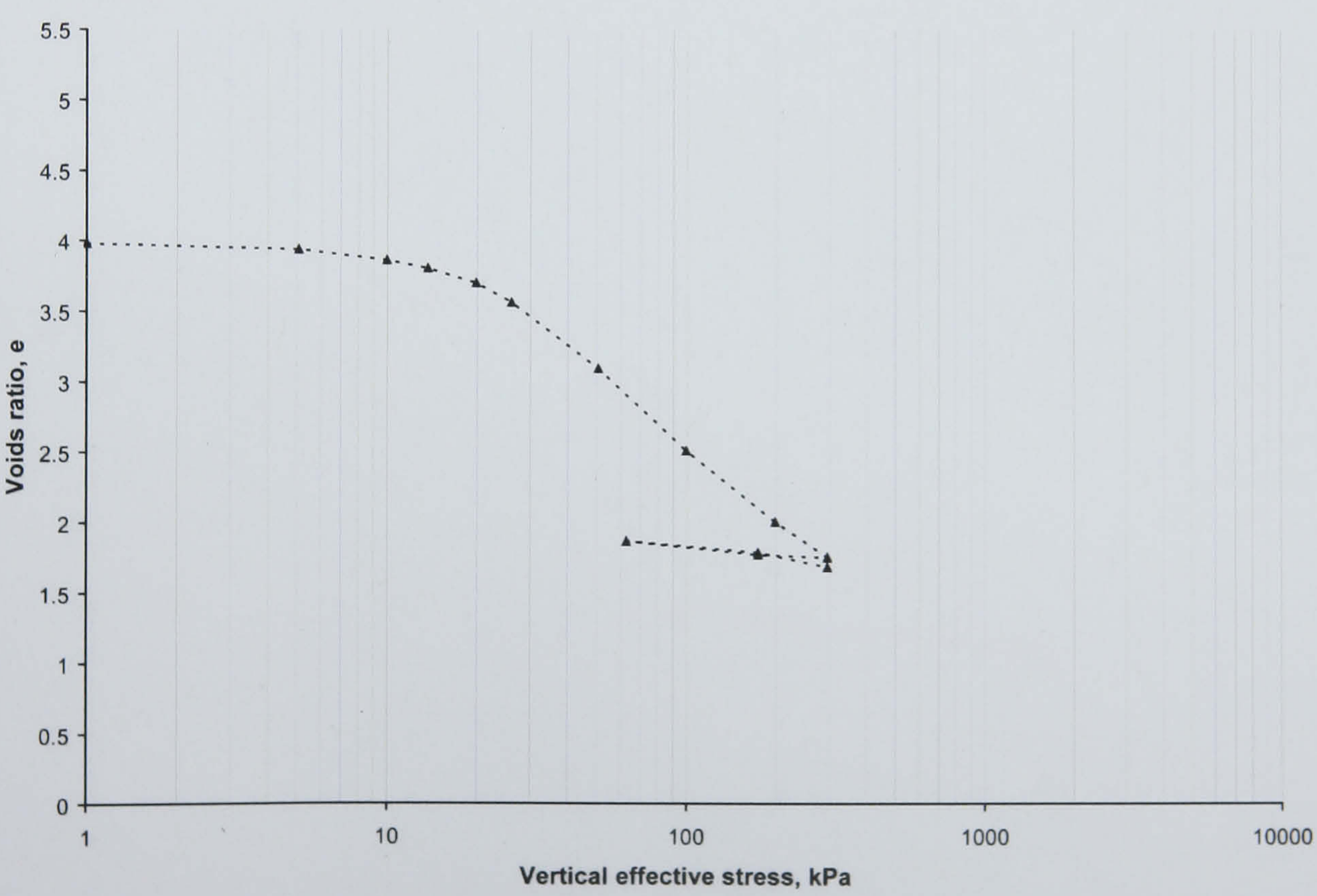

Figure 6.2 $e\log_{10}\sigma'$ plot of sample LM-2-S-OED-24.

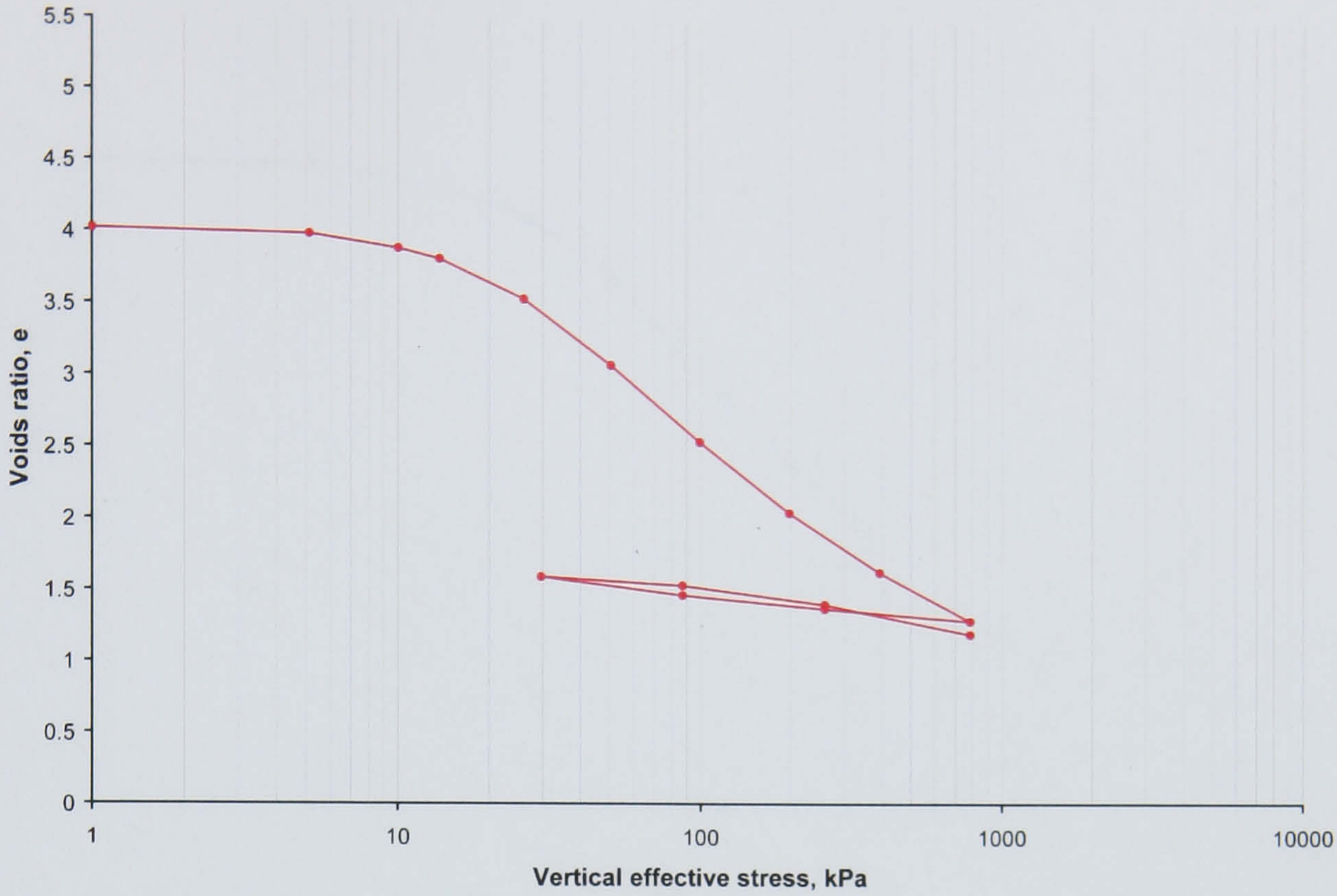

Figure 6.3 $e\log_{10}\sigma'$ of sample LM-3-S-OED-24.

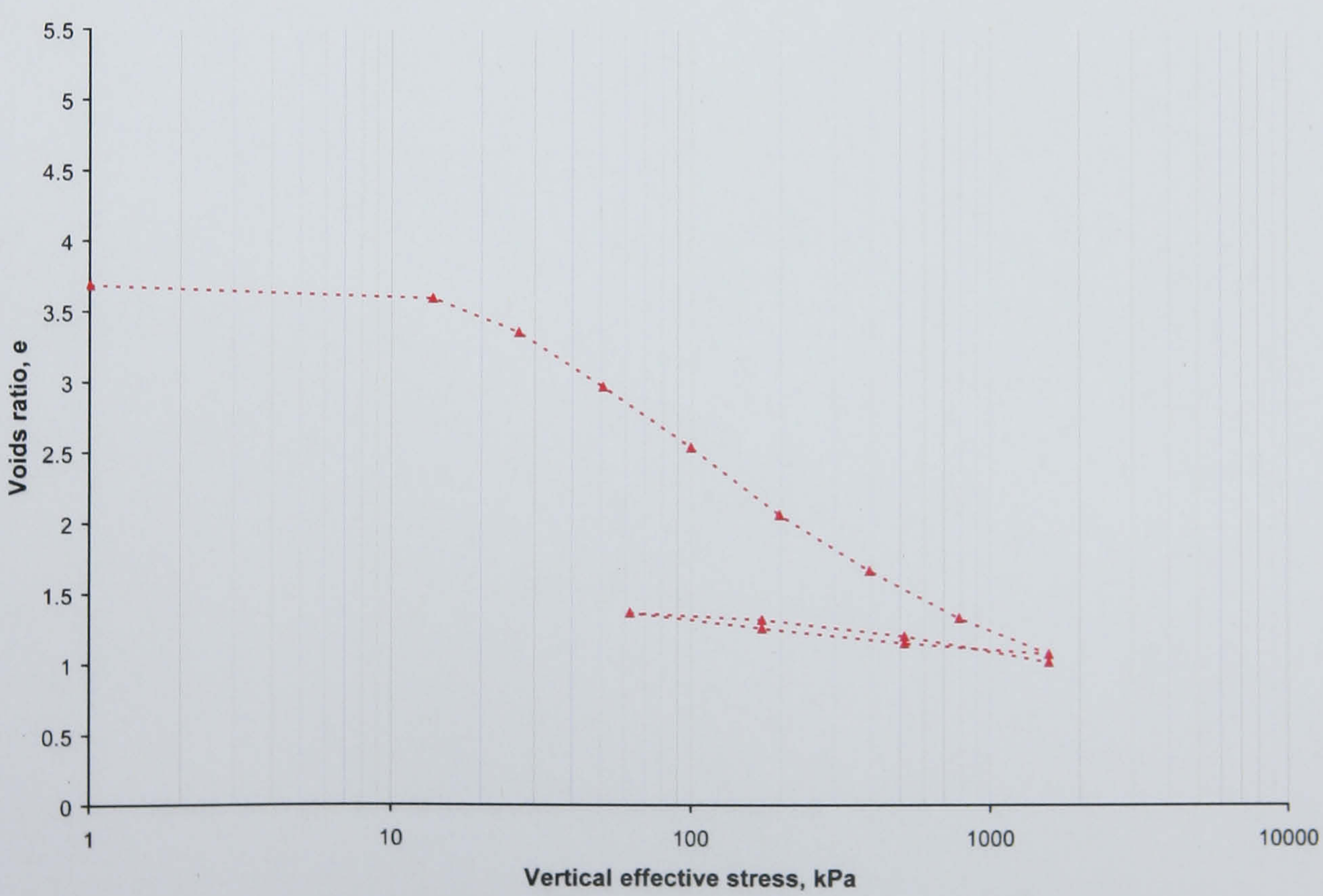

Figure 6.4 $e\log_{10}\sigma'$ of sample LM-4-S-OED-68.

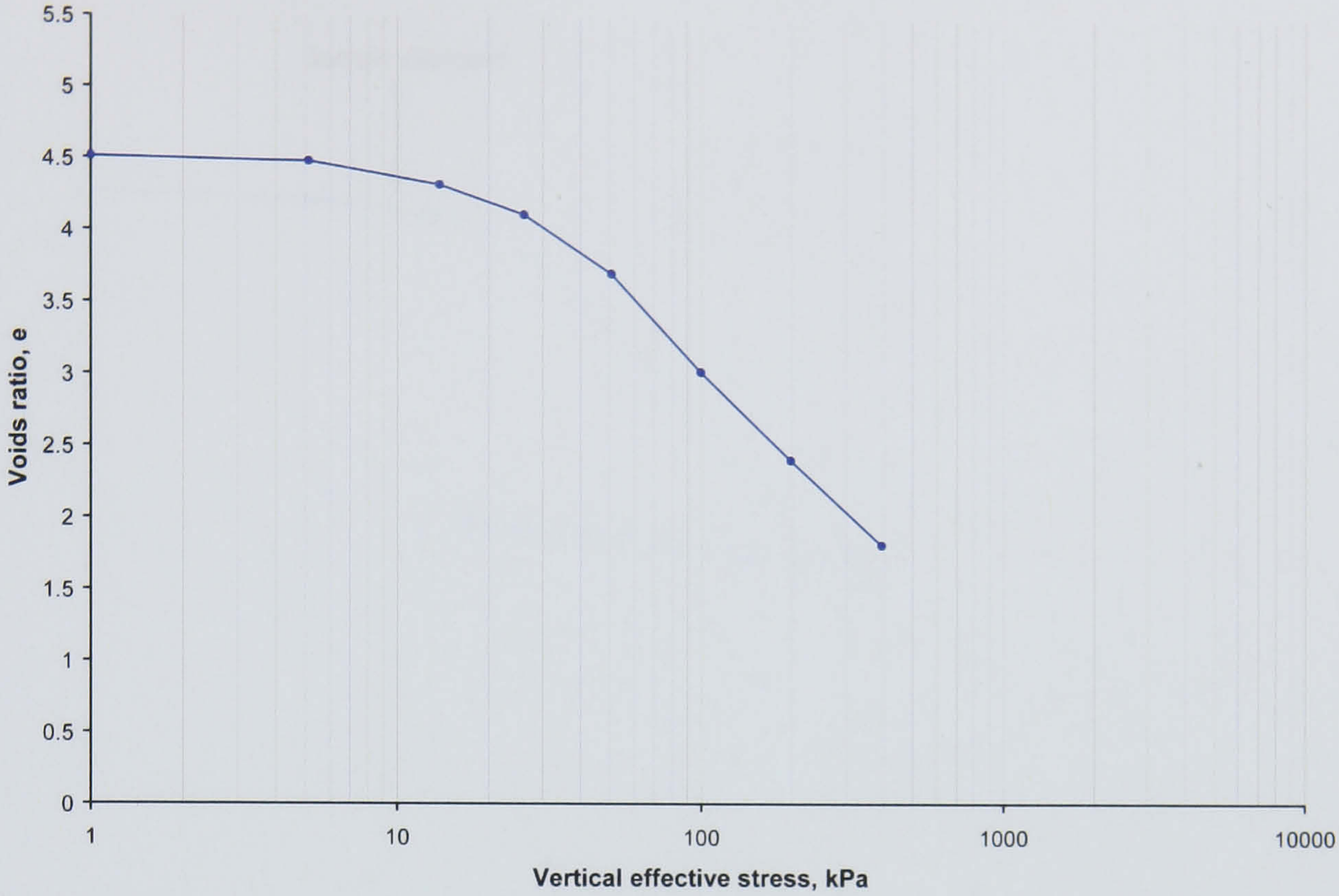

Figure 6.5 $e\log_{10}\sigma'$ of sample LM-5-S-OED-NC.

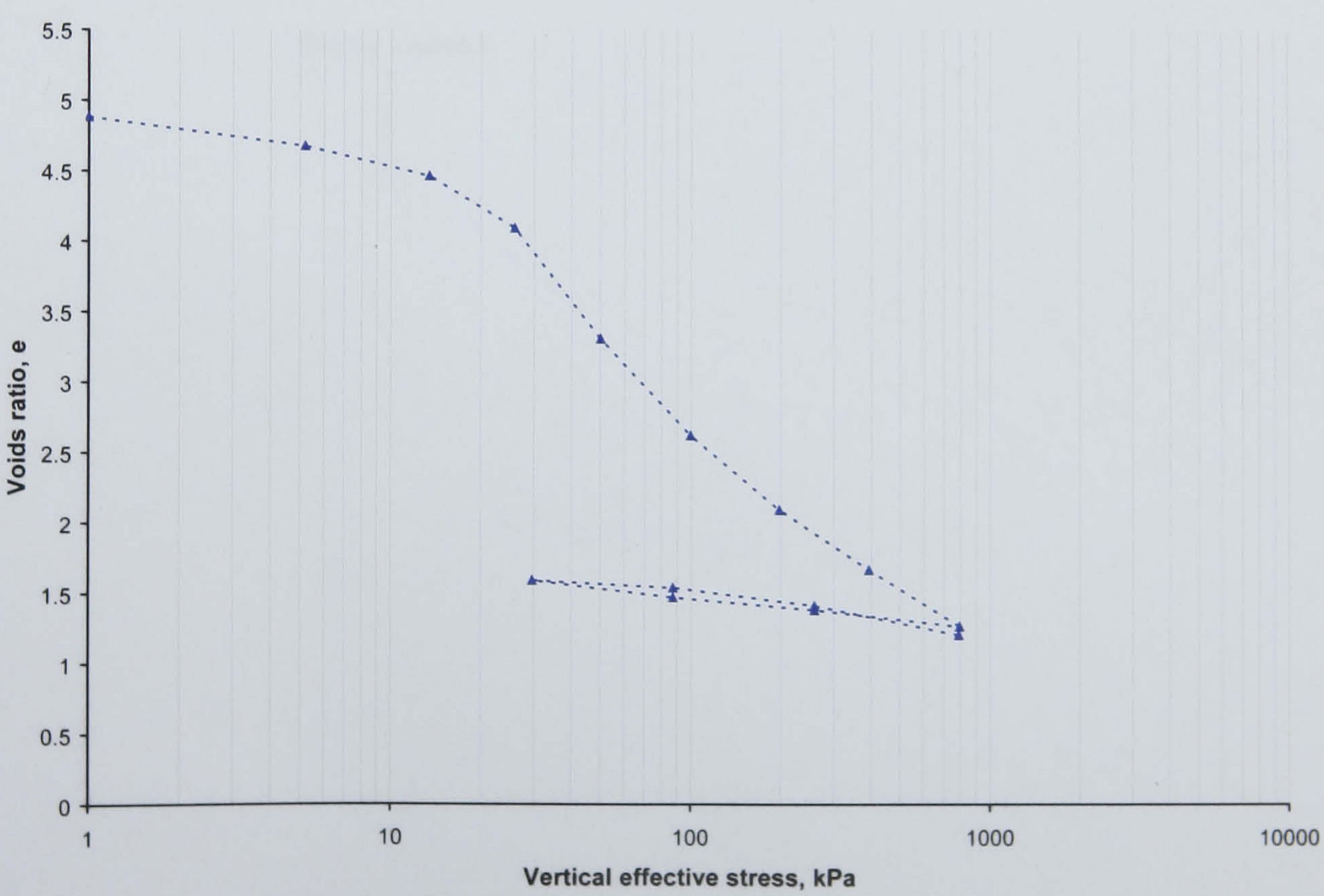

Figure 6.6 $e\log_{10}\sigma'$ of sample LM-6-S-BPS-24.

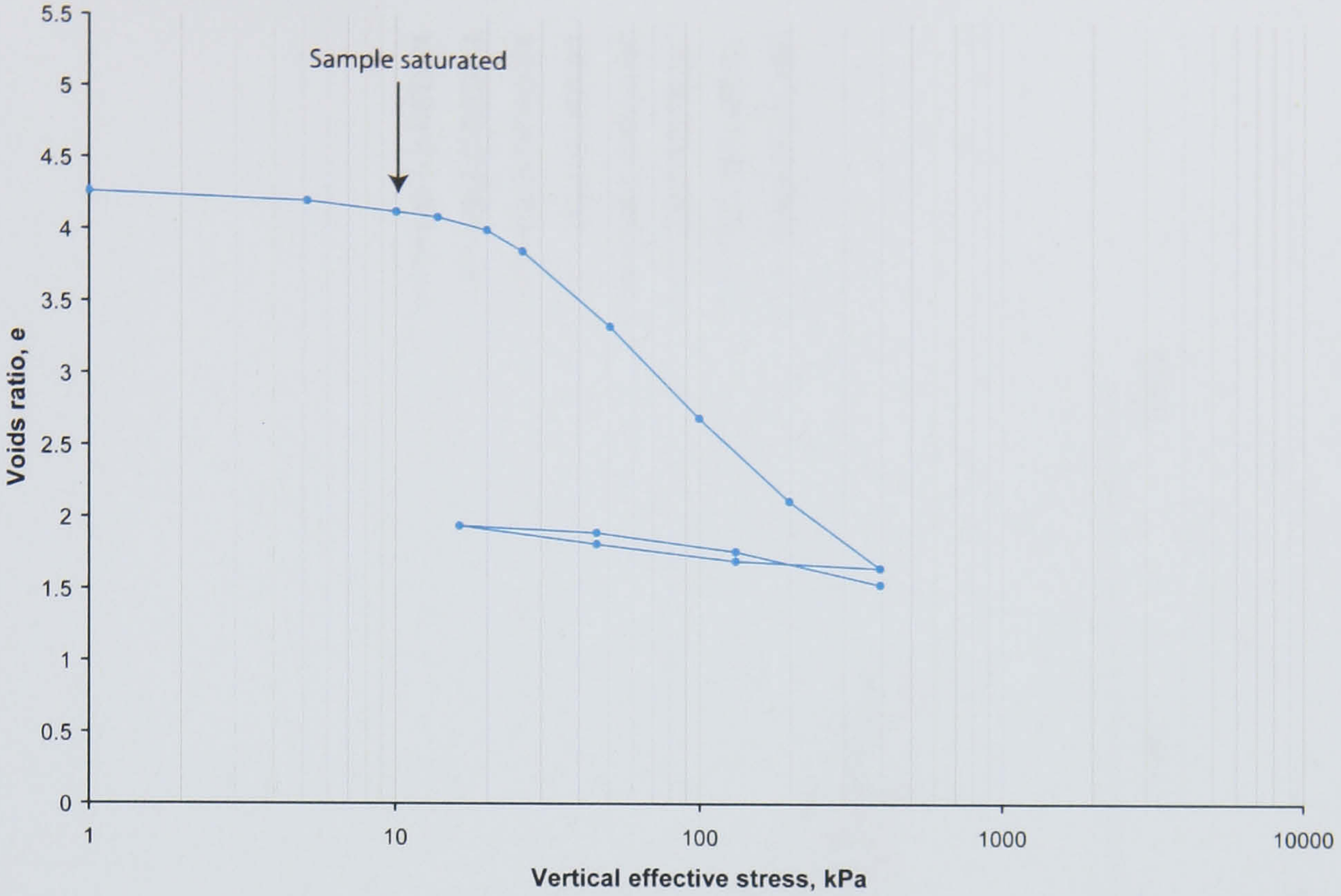

Figure 6.7 $e\log_{10}\sigma'$ of sample LM-7-N-OED-24.

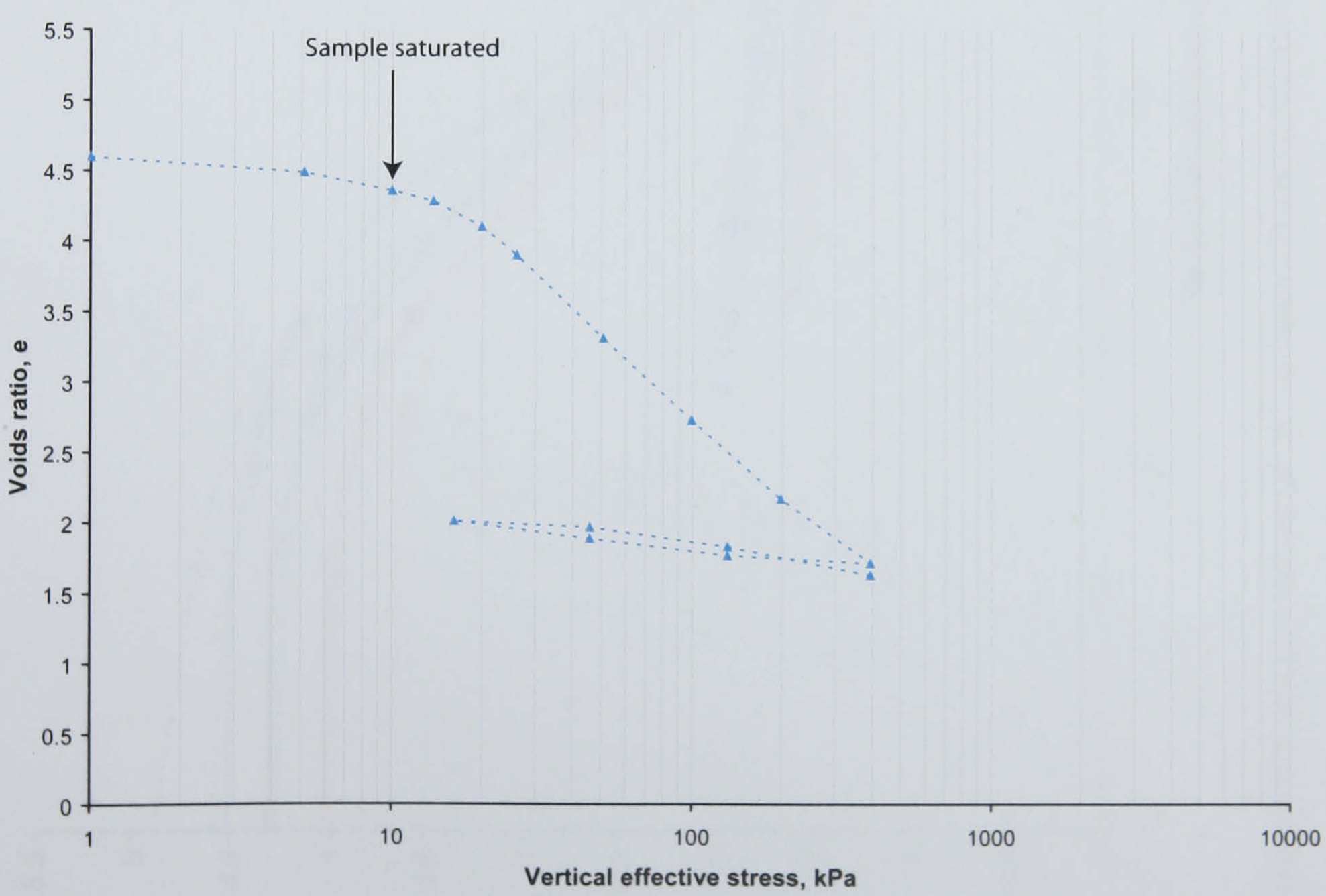

Figure 6.8 $e\log_{10}\sigma'$ of sample LM-8-N-OED-24.

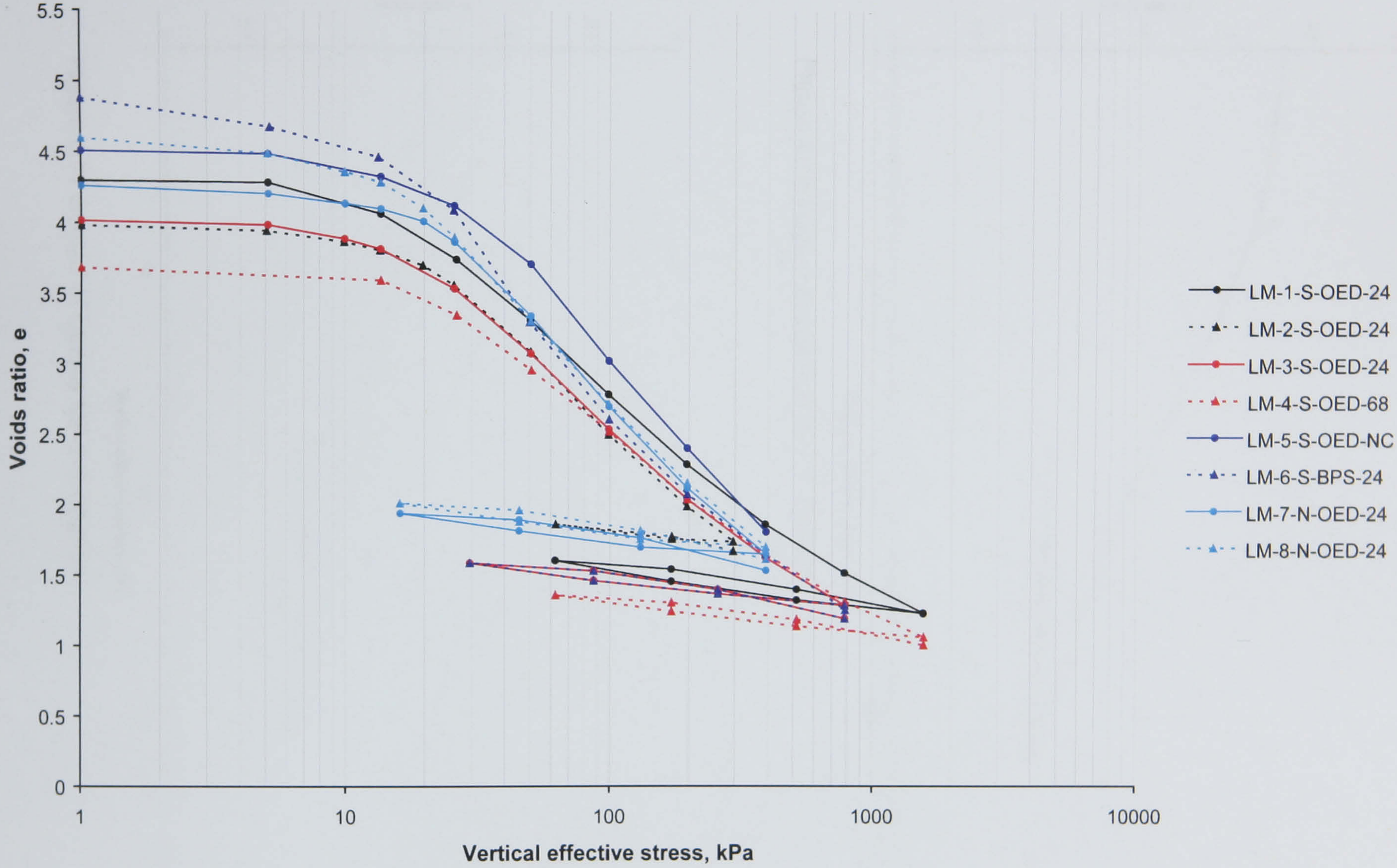

Figure 6.9 $e\log_{10}\sigma'$ curves of all low marsh incremental loading tests.

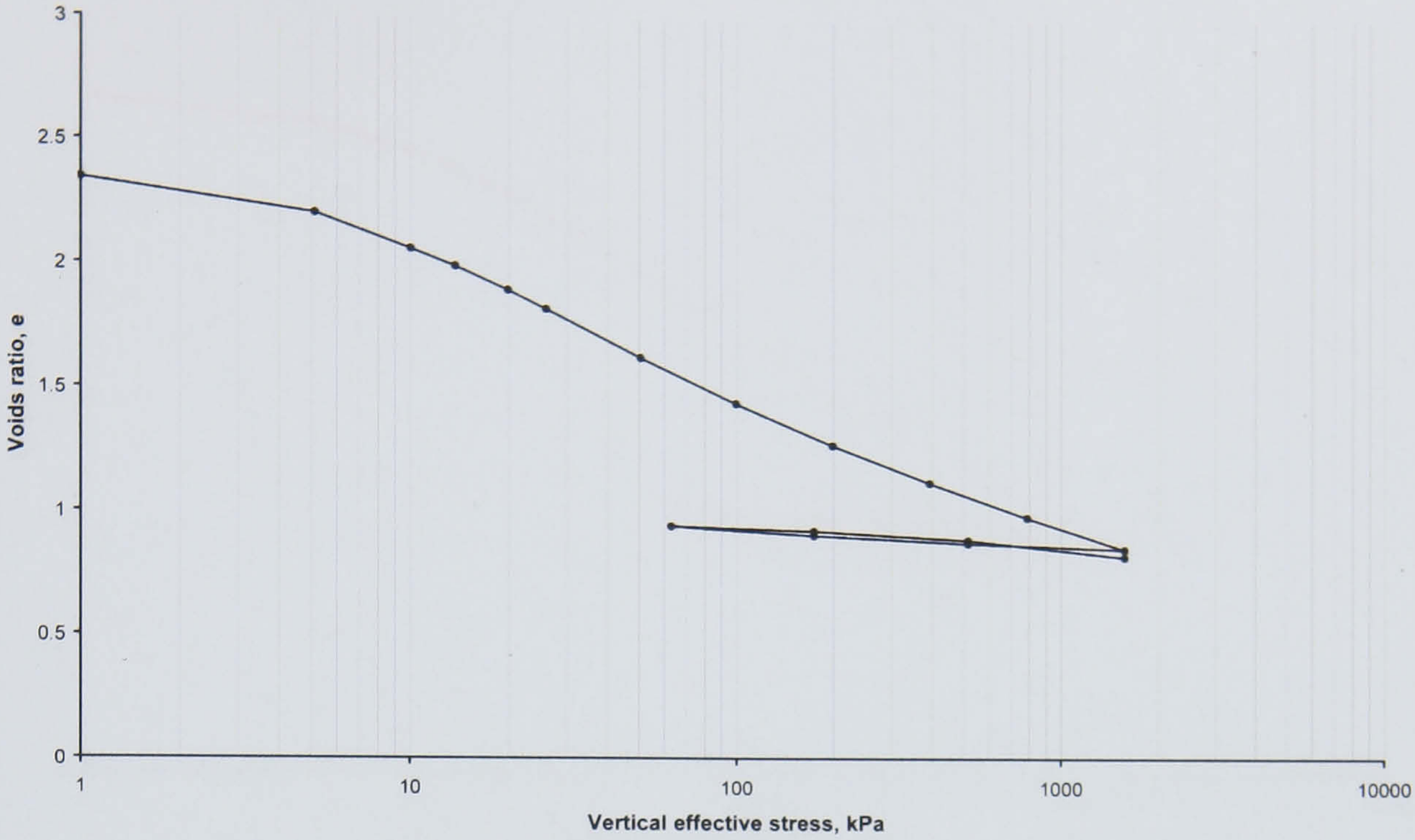

Figure 6.10 $e\log_{10}\sigma'$ of sample MF-1-S-OED-24.

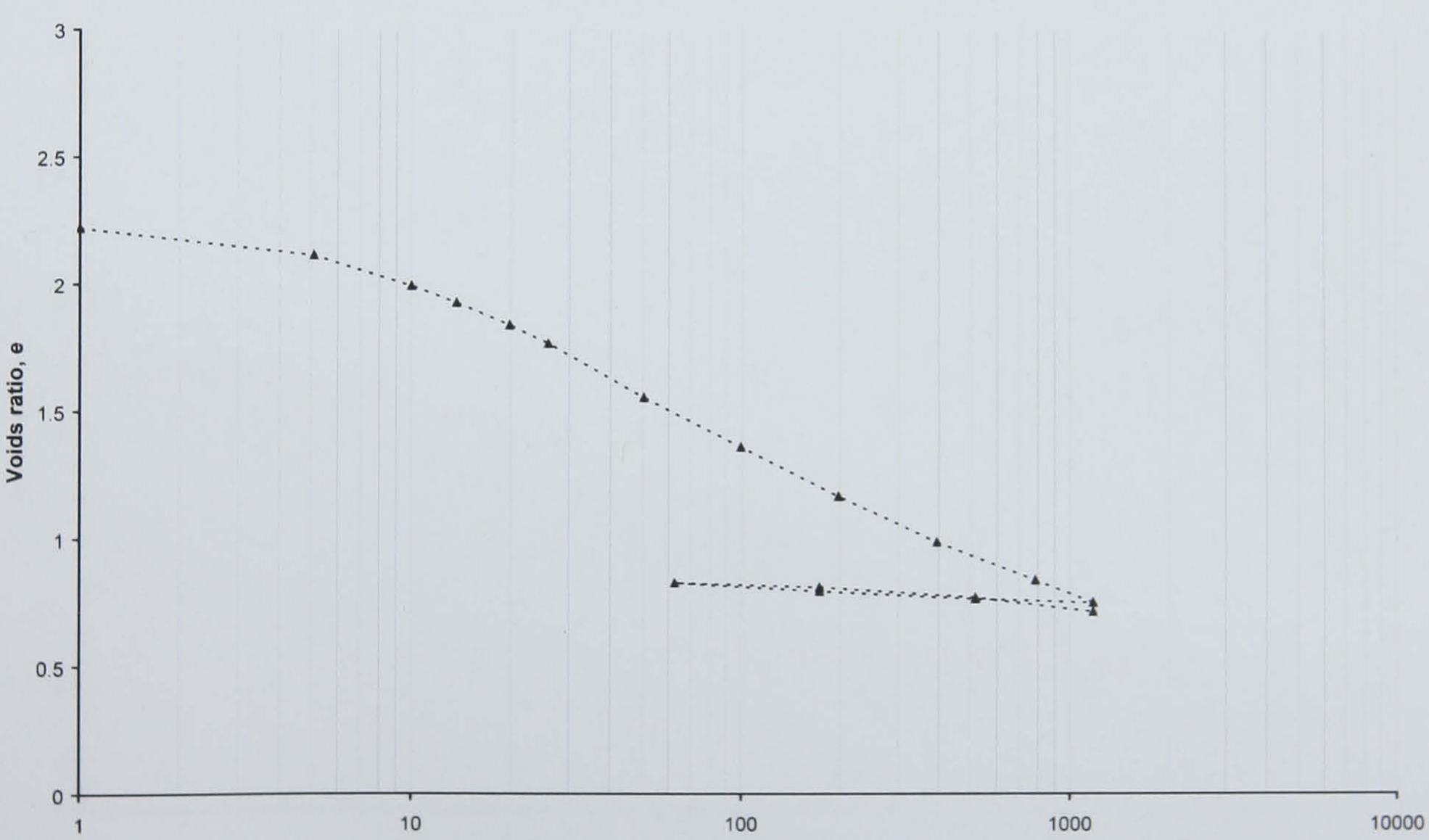

Figure 6.11 $e\log_{10}\sigma'$ of sample MF-2-S-OED-24.

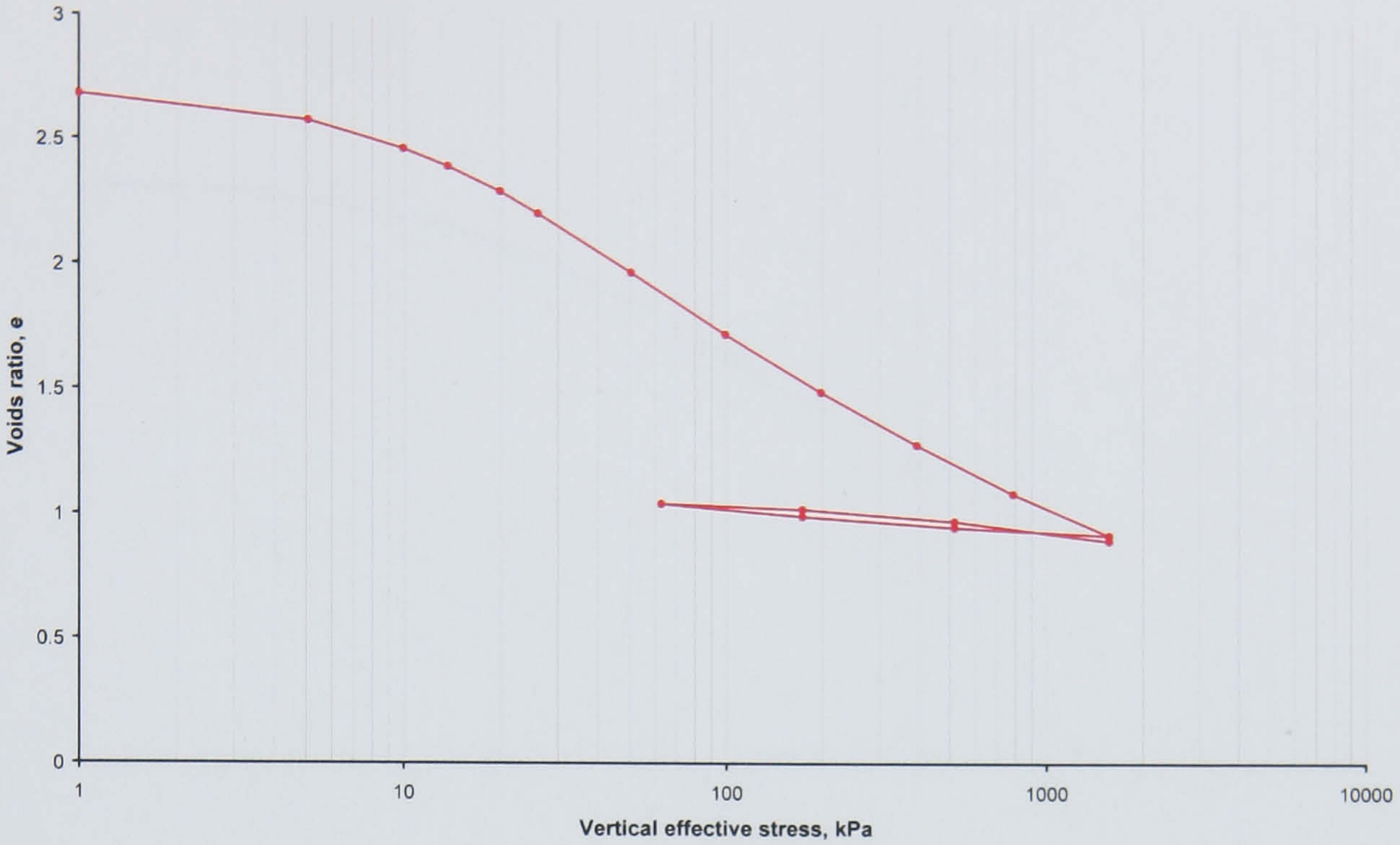

Figure 6.12 $e\log_{10}\sigma'$ of sample MF-3-S-OED-24.

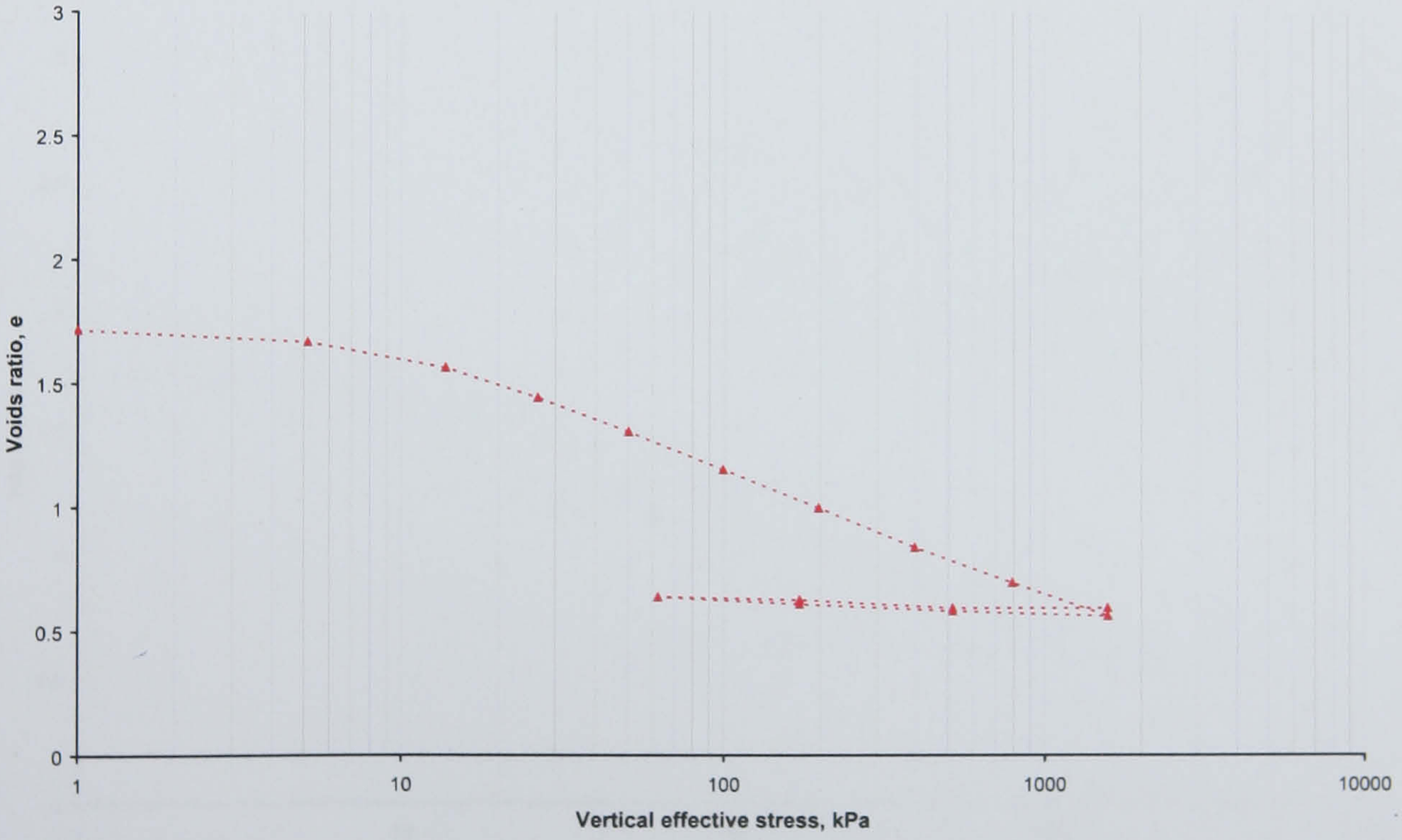

Figure 6.13 $e\log_{10}\sigma'$ of sample MF-4-S-OED-68.

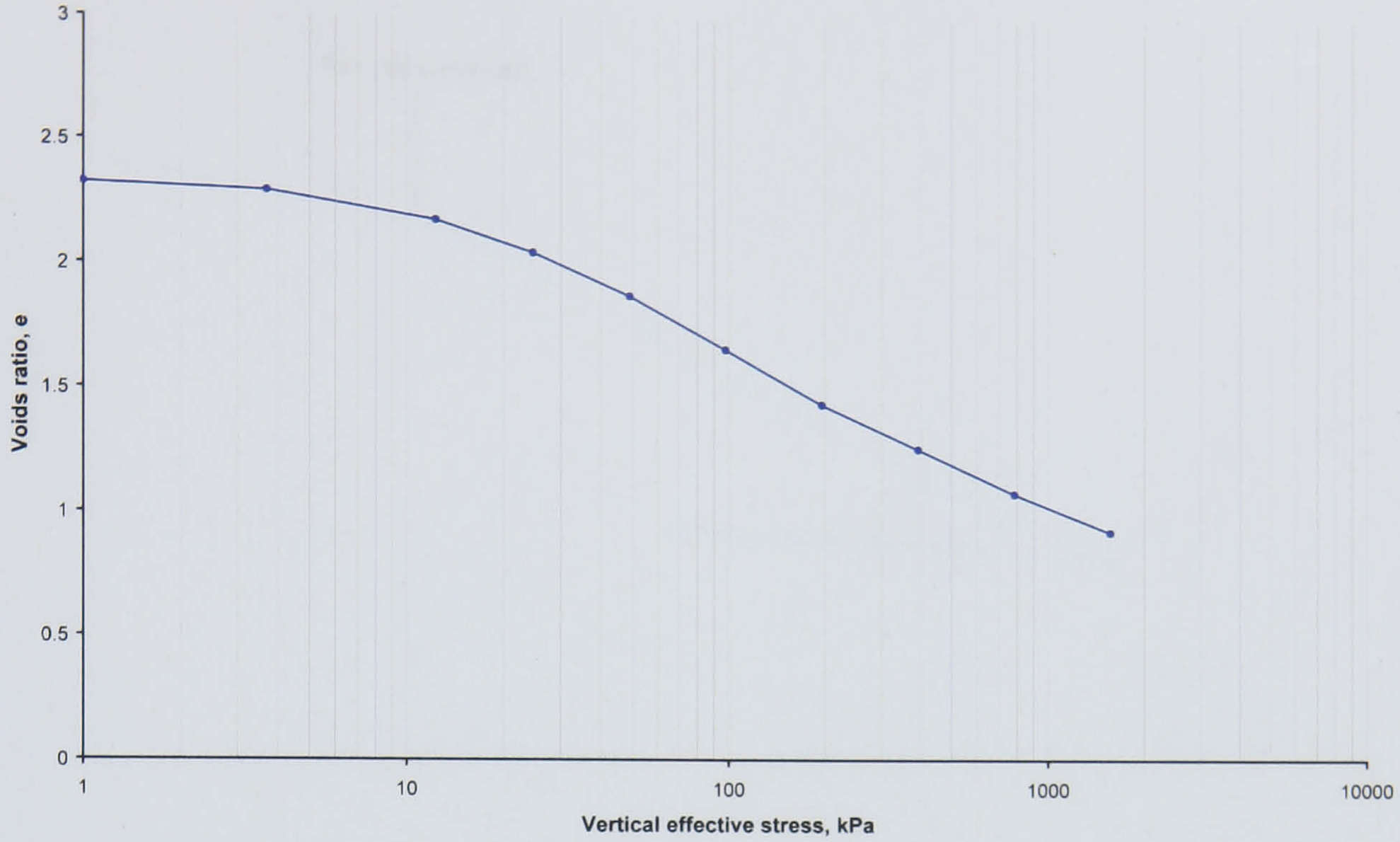

Figure 6.14 $e\log_{10}\sigma'$ of sample MF-5-S-OED-NC.

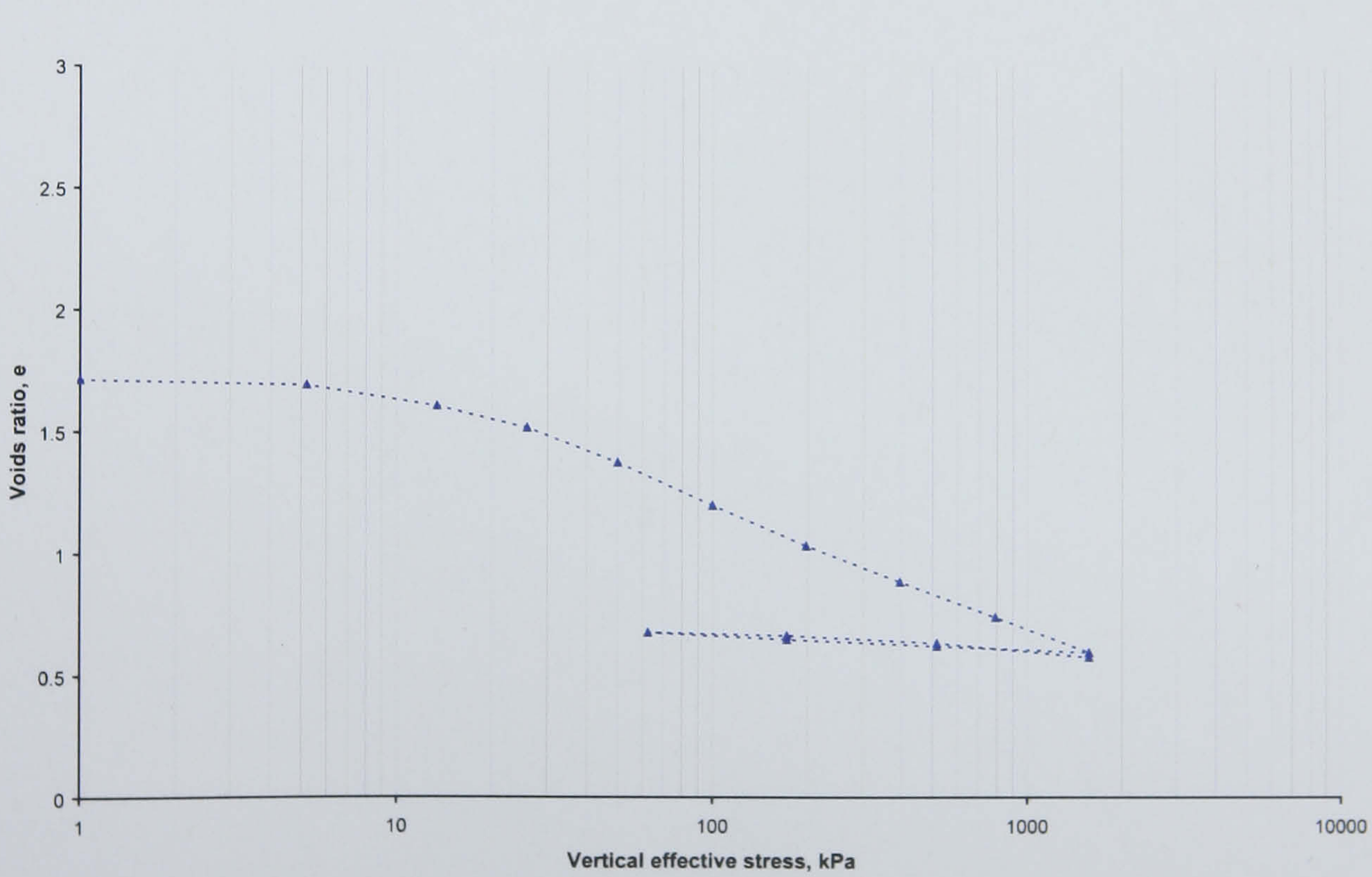

Figure 6.15 $e\log_{10}\sigma'$ of sample MF-6-S-BPS-24.

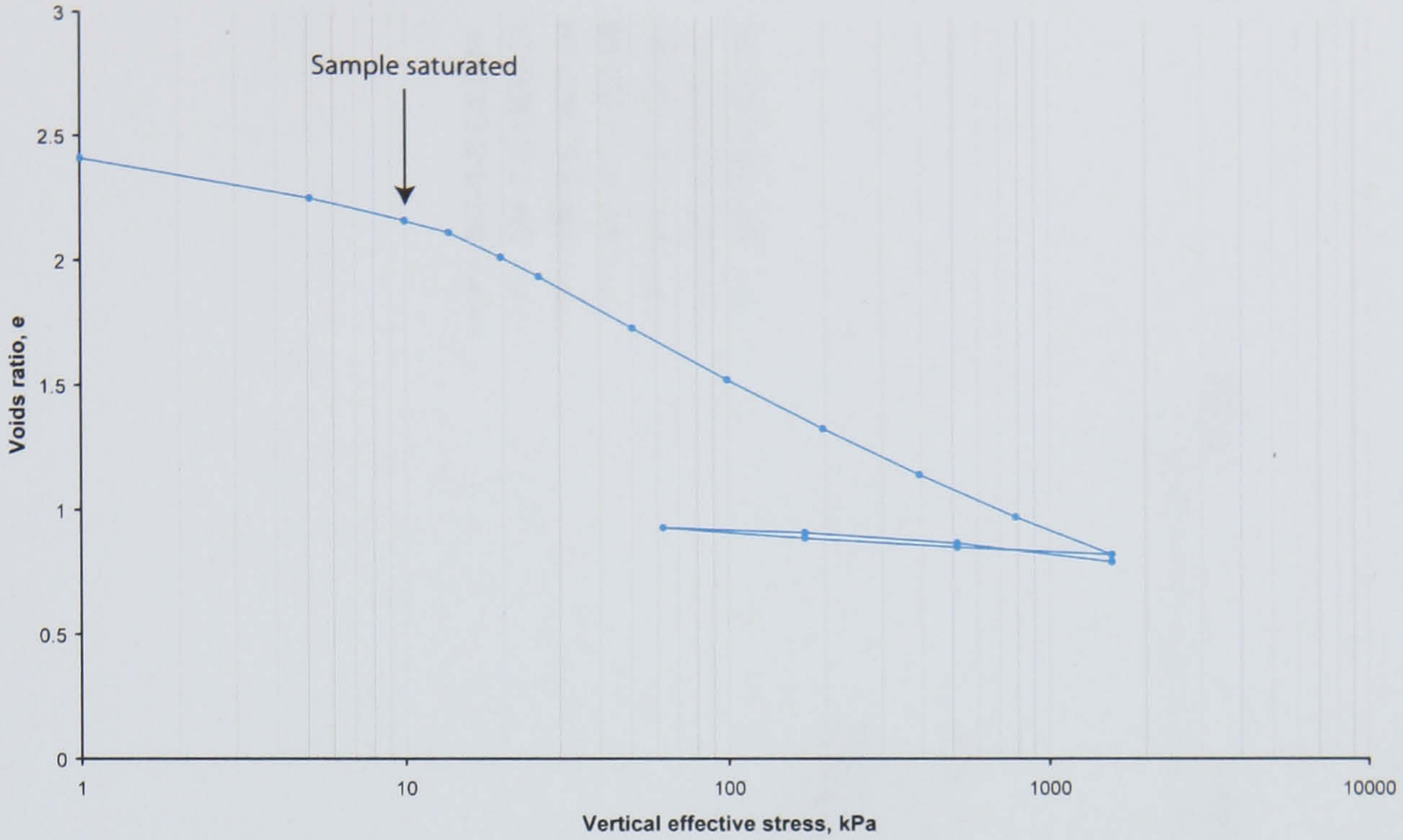

Figure 6.16 $e\log_{10}\sigma'$ of sample MF-7-N-OED-24.

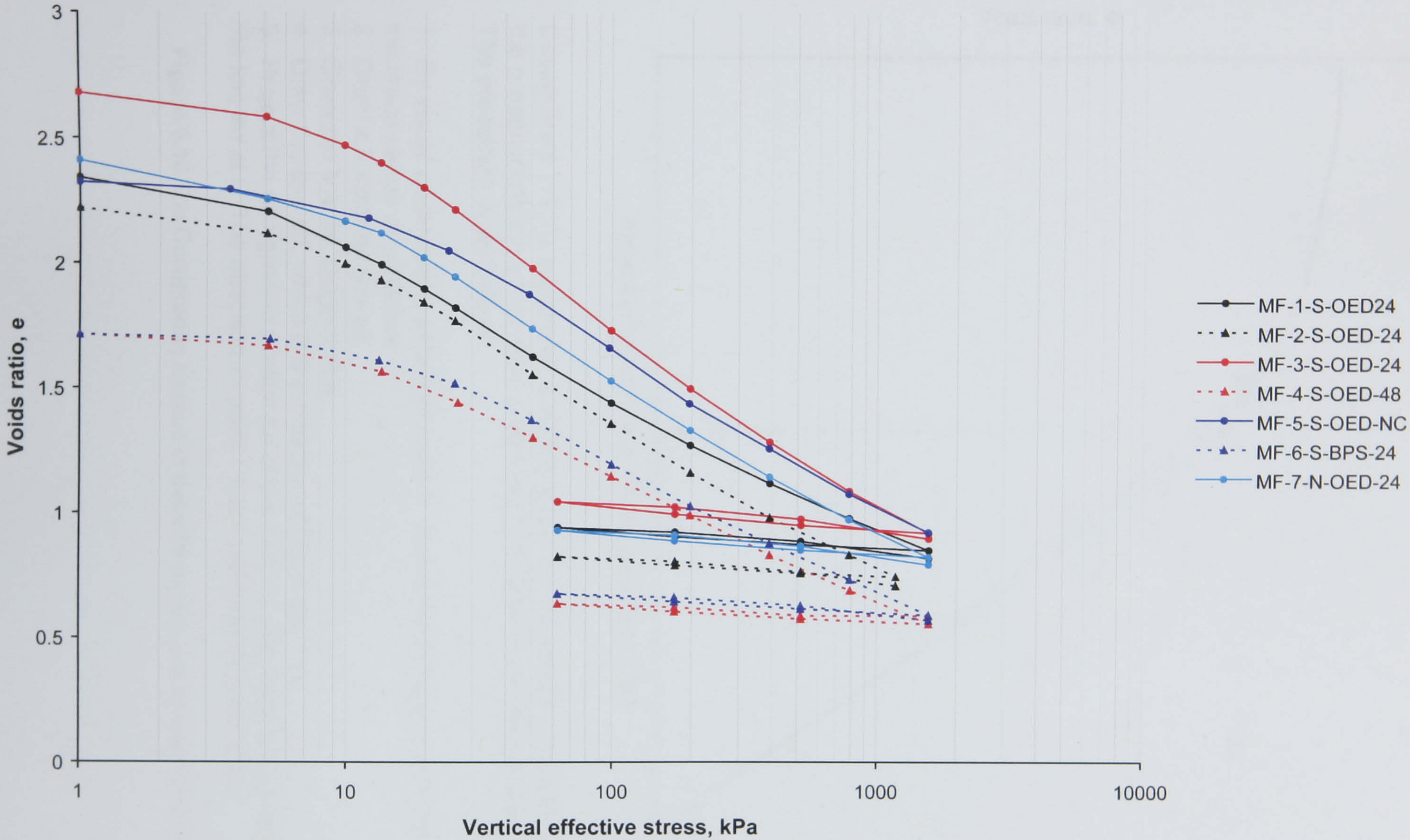

Figure 6.17 $e \log_{10} \sigma'$ curves of all mudflat incremental loading tests.

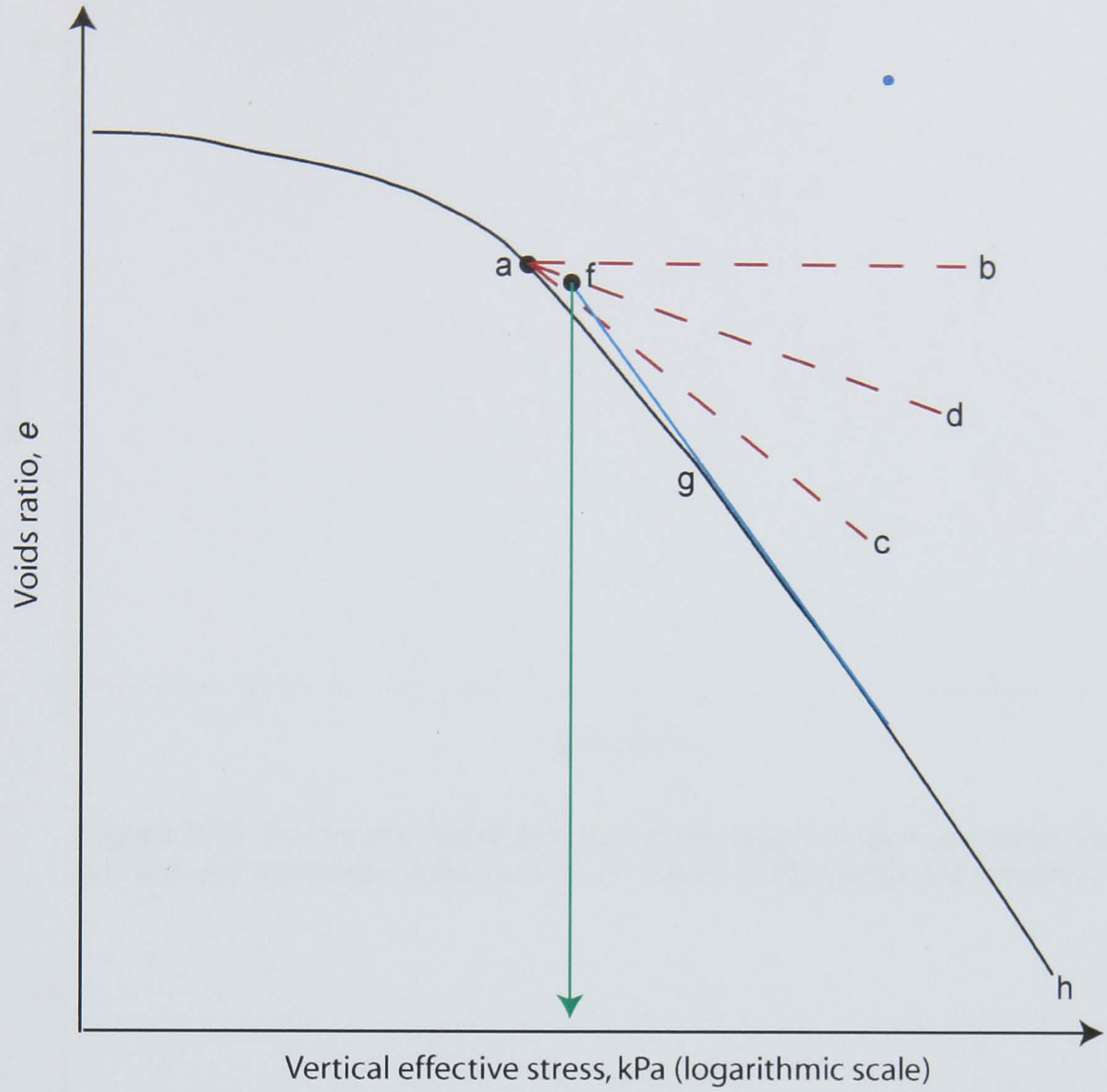

Casagrande (1936) suggested a simple graphical construction to determine the preconsolidation stress from a conventional laboratory $e\log_{10}\sigma'$ plot. The procedure is as follows:

1. By visual observation, establish point *a*, at which the $e\log_{10}\sigma'$plot has a minimum radius of curvature.
2. Draw a horizontal line *ab*.
3. Draw the line *ac*, tangent at *a*.
4. Draw the line *ad*, which is the bisector of the angle *bac*.
5. Project the straight-line portion *gh* of the $e\log_{10}\sigma'$ plot back to intersect the line *ad* at *f*. The abscissa of point *f* is the preconsolidation stress.

Figure 6.18 The Casagrande method of determining the preconsolidation stress.

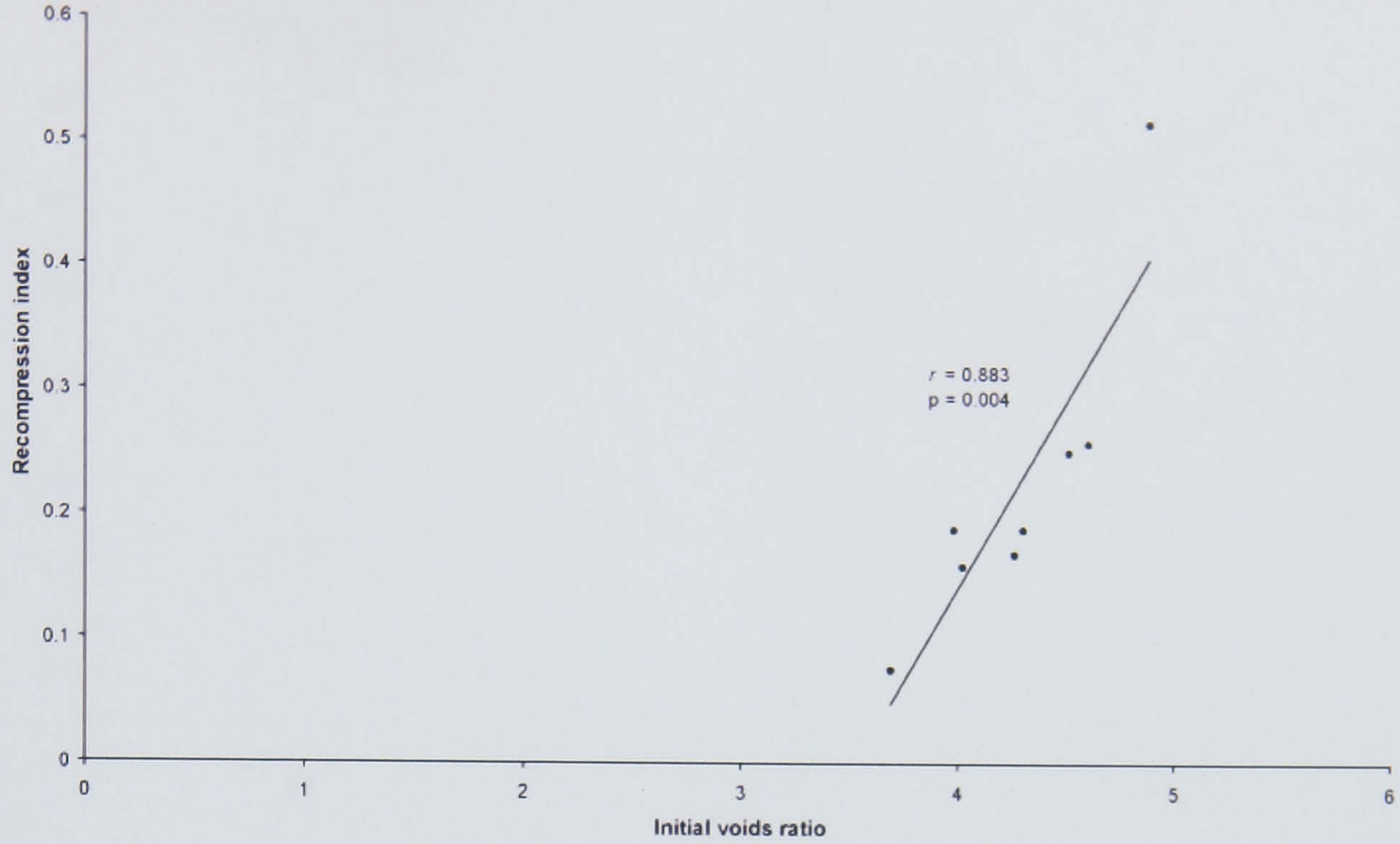

Figure 6.19 Scatterplot displaying the relationship between the initial voids ratio and the recompression index for the low marsh compression test samples.

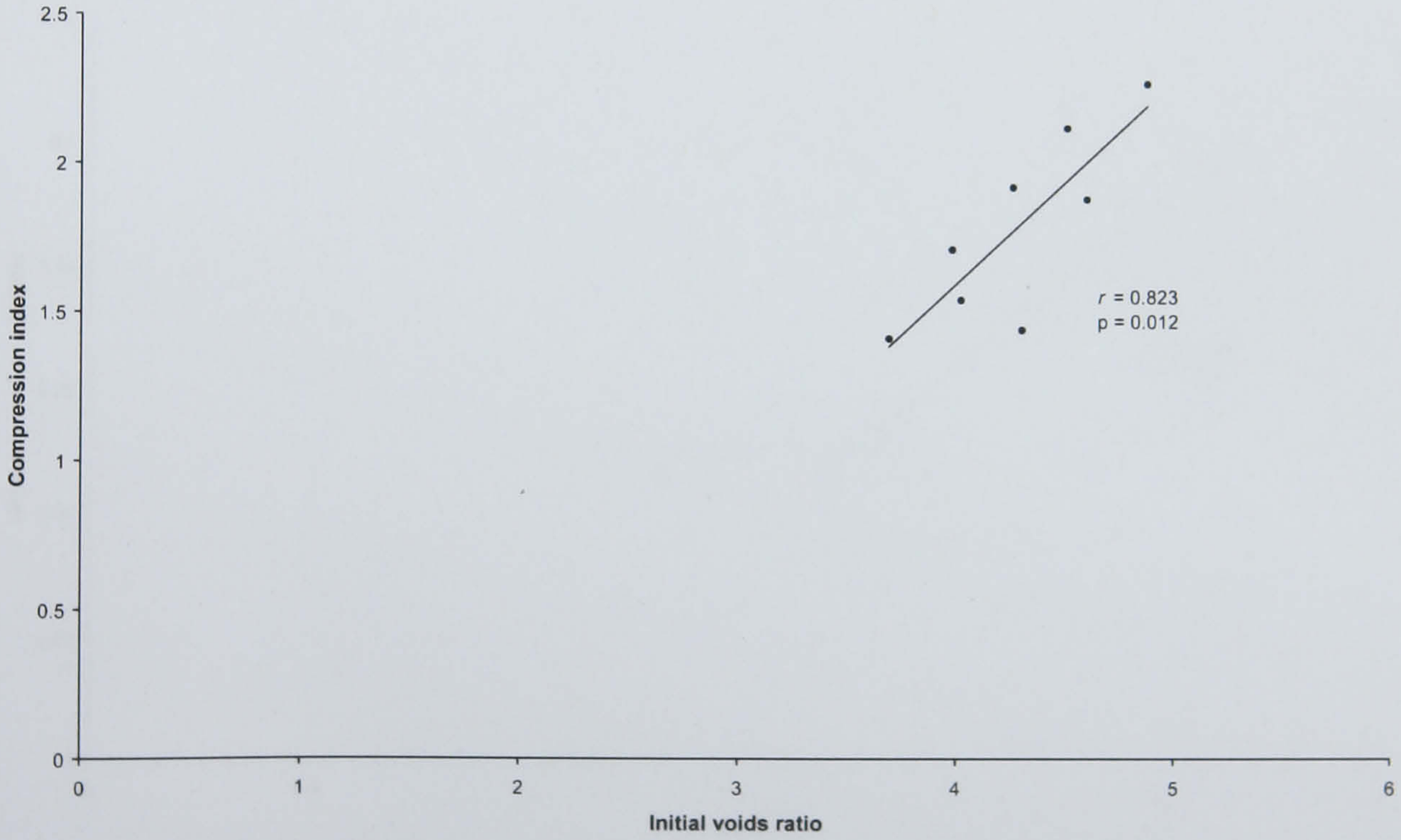

Figure 6.20 Scatterplot displaying the relationship between the initial voids ratio and the compression index for the low marsh compression test samples.

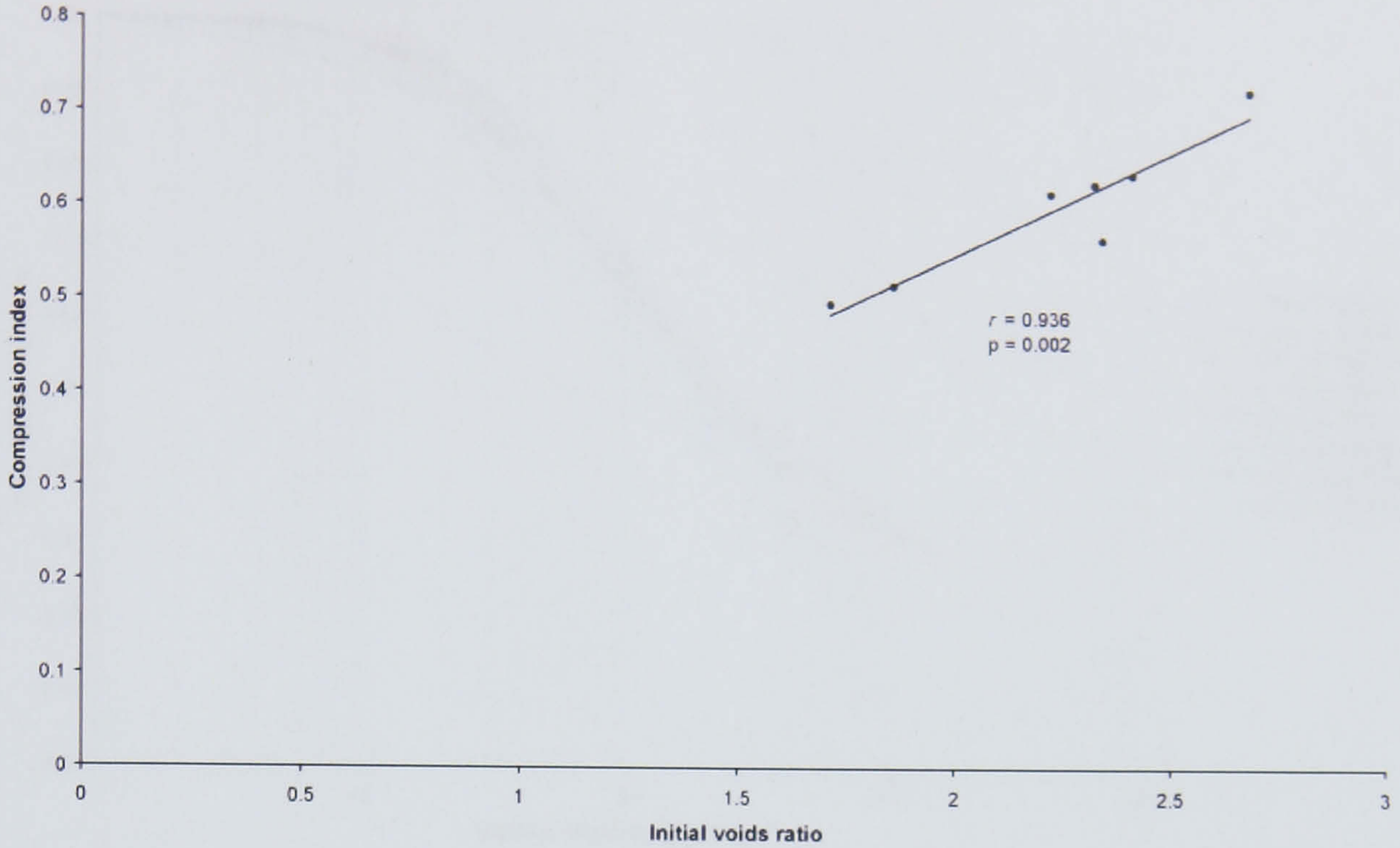

Figure 6.21 Scatterplot displaying the relationship between the initial voids ratio and the compression index for the mudflat compression test samples.

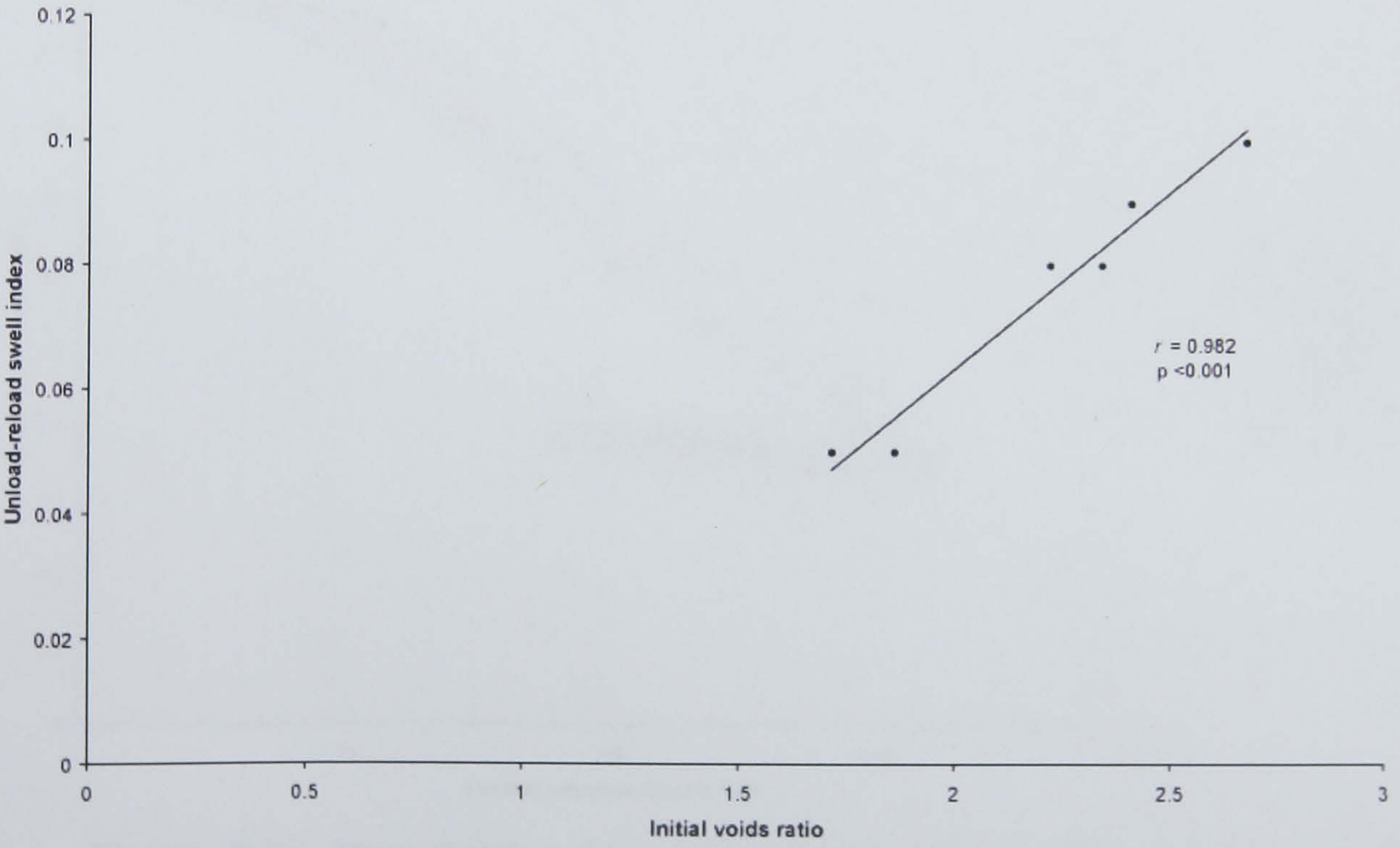

Figure 6.22 Scatterplot displaying the relationship between the initial voids ratio and the unload-reload swell index for the mudflat compression test samples.

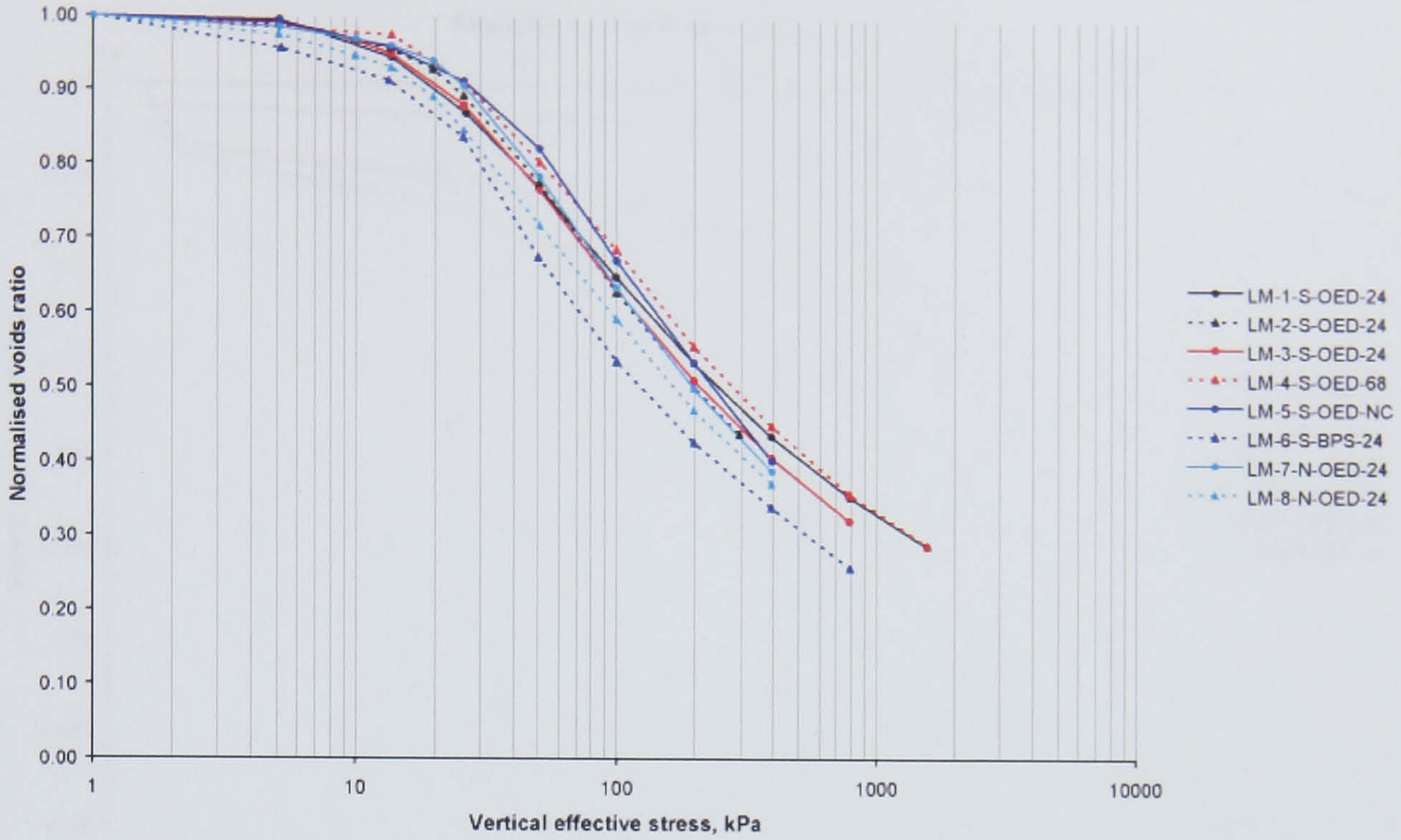

Figure 6.23 Normalised voids ratio against $\log_{10}\sigma'$ plots for the low marsh compression tests.

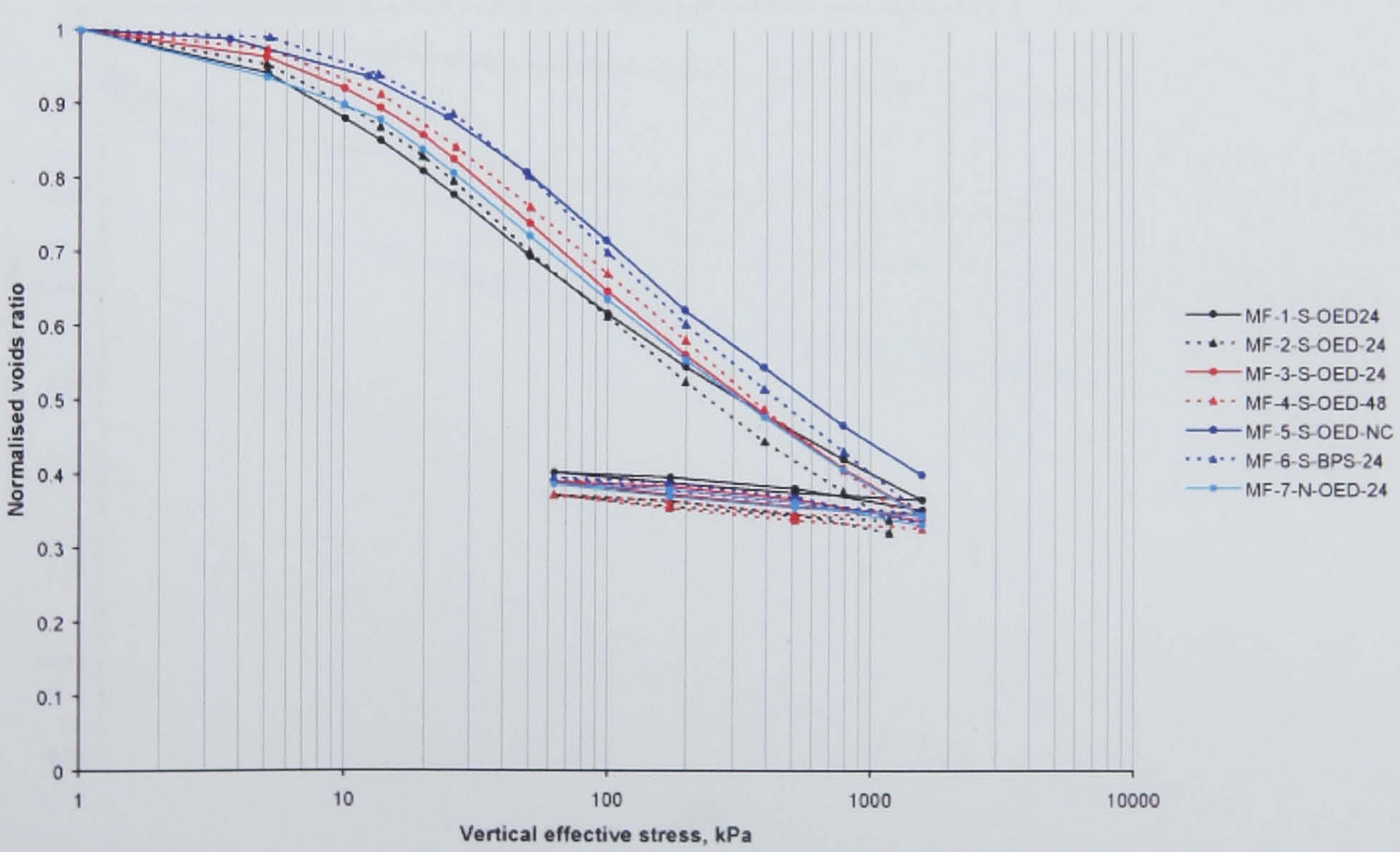

Figure 6.24 Normalised voids ratio against $\log_{10}\sigma'$ plots for the mudflat compression tests.

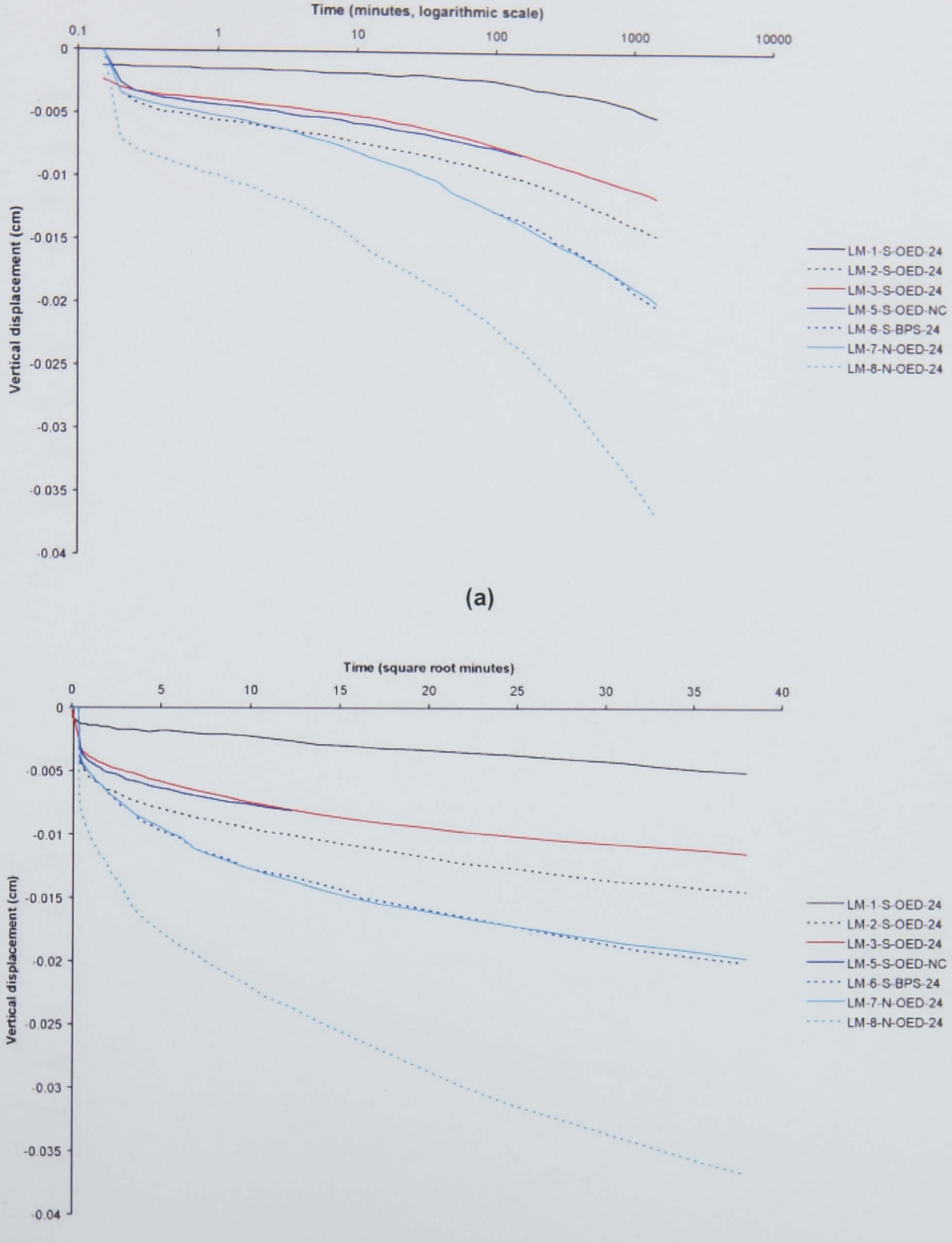

Figure 6.25 Time-vertical displacement plots for low marsh samples at an applied stress of 5.1 kPa (loading). (a) logarithmic time-vertical displacement (b) square-root time-vertical displacement.

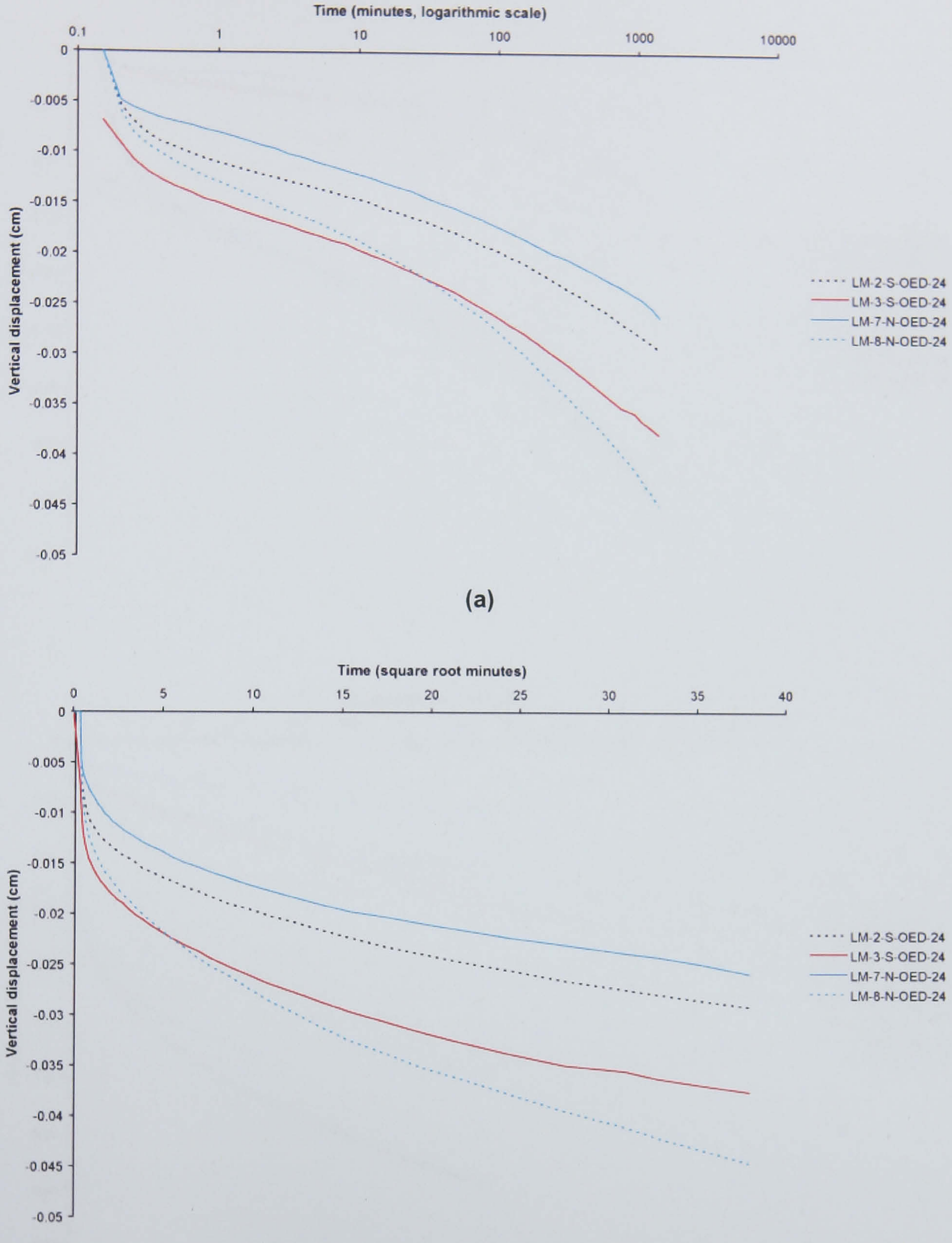

Figure 6.26 Time-vertical displacement plots for low marsh samples at an applied stress of 10 kPa (loading). (a) logarithmic time-vertical displacement (b) square-root time-vertical displacement.

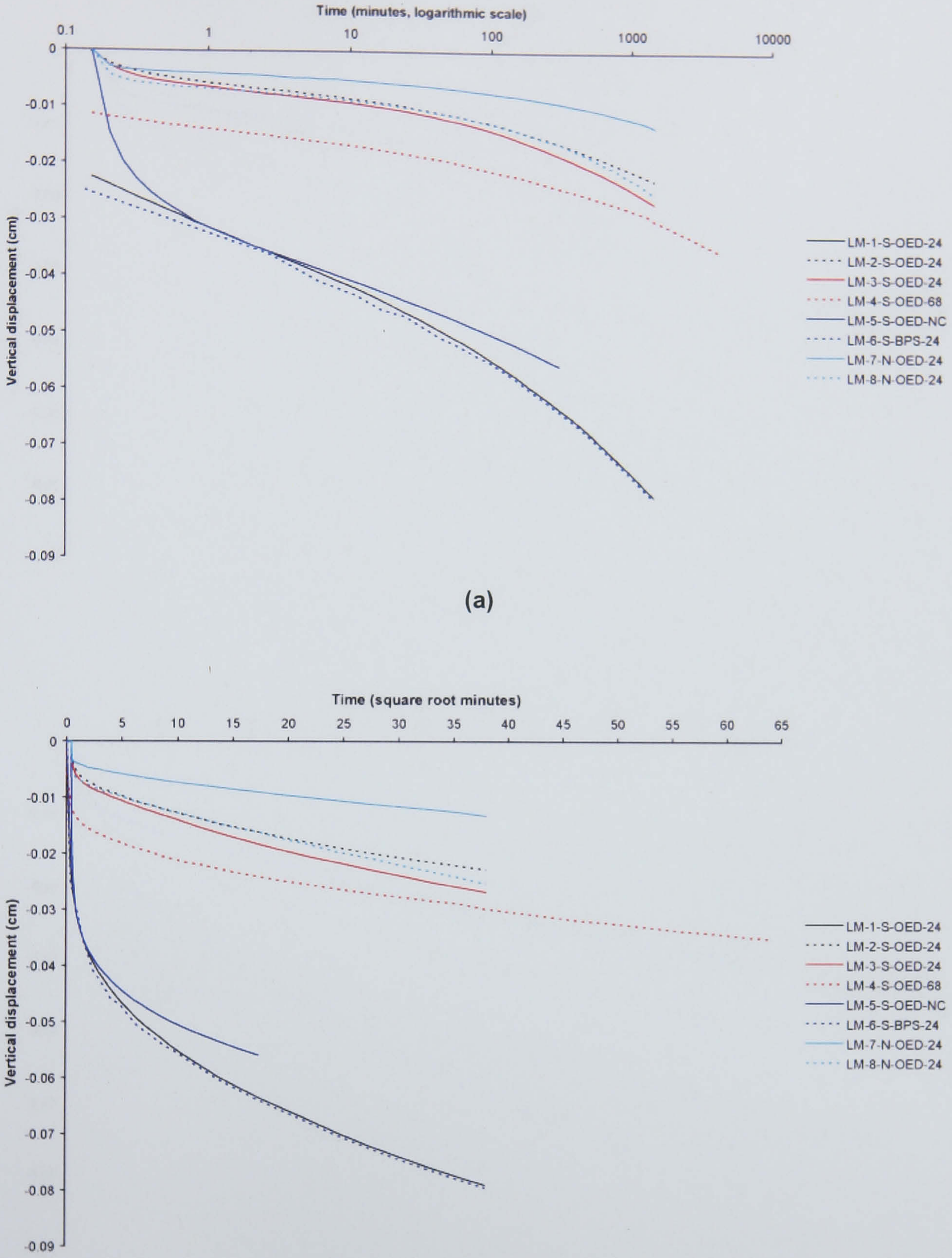

Figure 6.27 Time-vertical displacement plots for low marsh samples at an applied stress of 14 kPa (loading). (a) logarithmic time-vertical displacement (b) square-root time-vertical displacement.

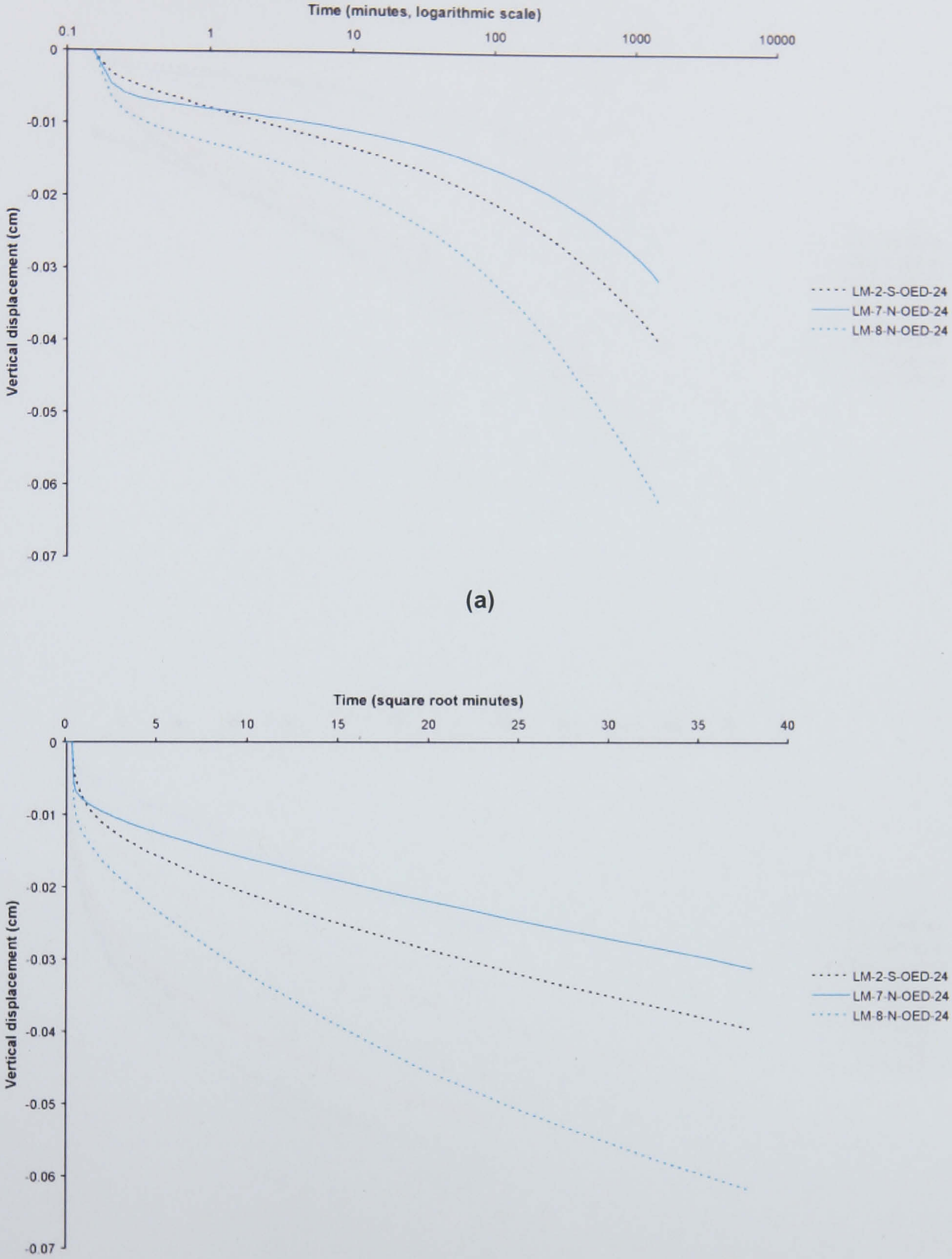

Figure 6.28 Time-vertical displacement plots for low marsh samples at an applied stress of 20 kPa (loading). (a) logarithmic time-vertical displacement (b) square-root time-vertical displacement.

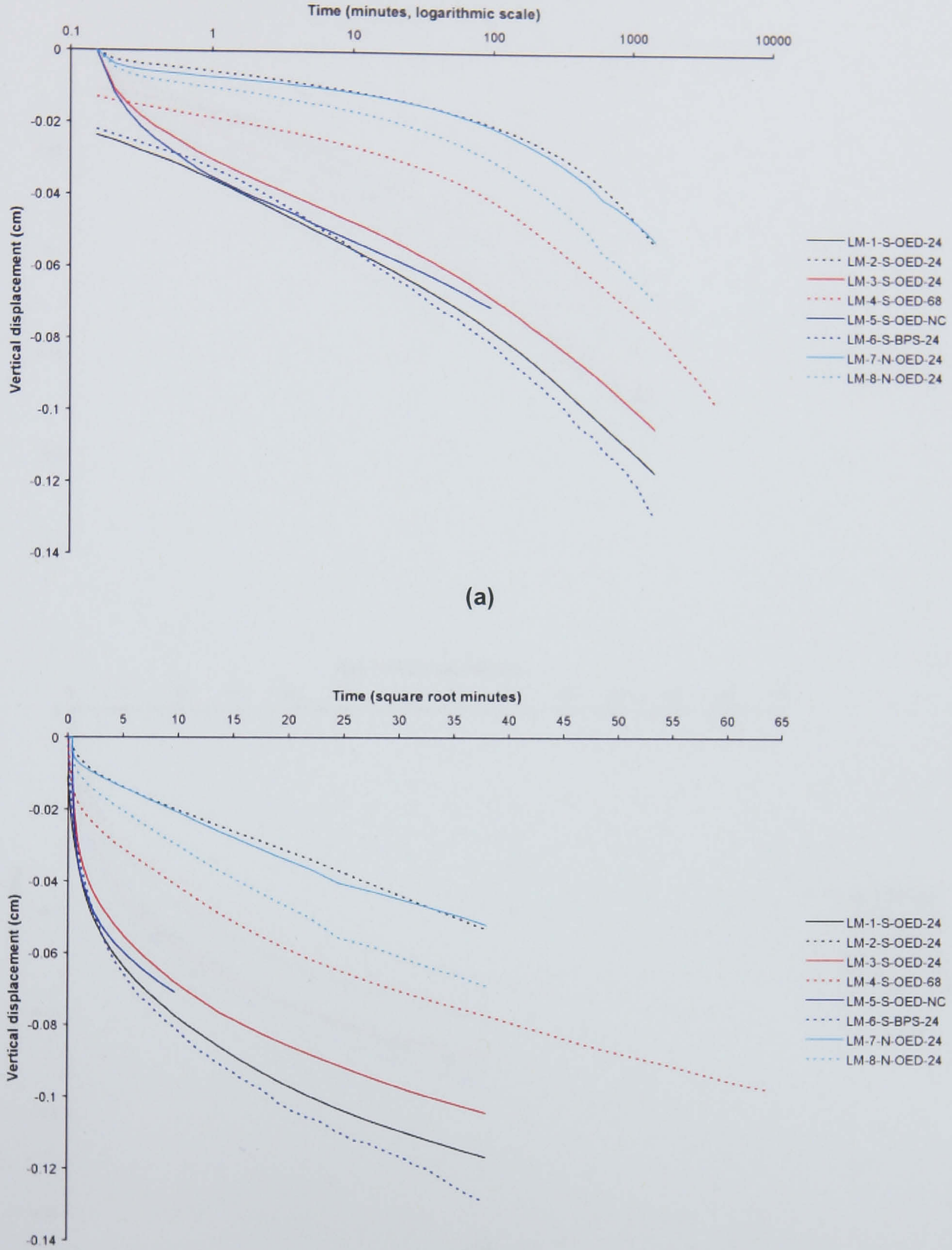

Figure 6.29 Time-vertical displacement plots for low marsh samples at an applied stress of 26 kPa (loading). (a) logarithmic time-vertical displacement (b) square-root time-vertical displacement.

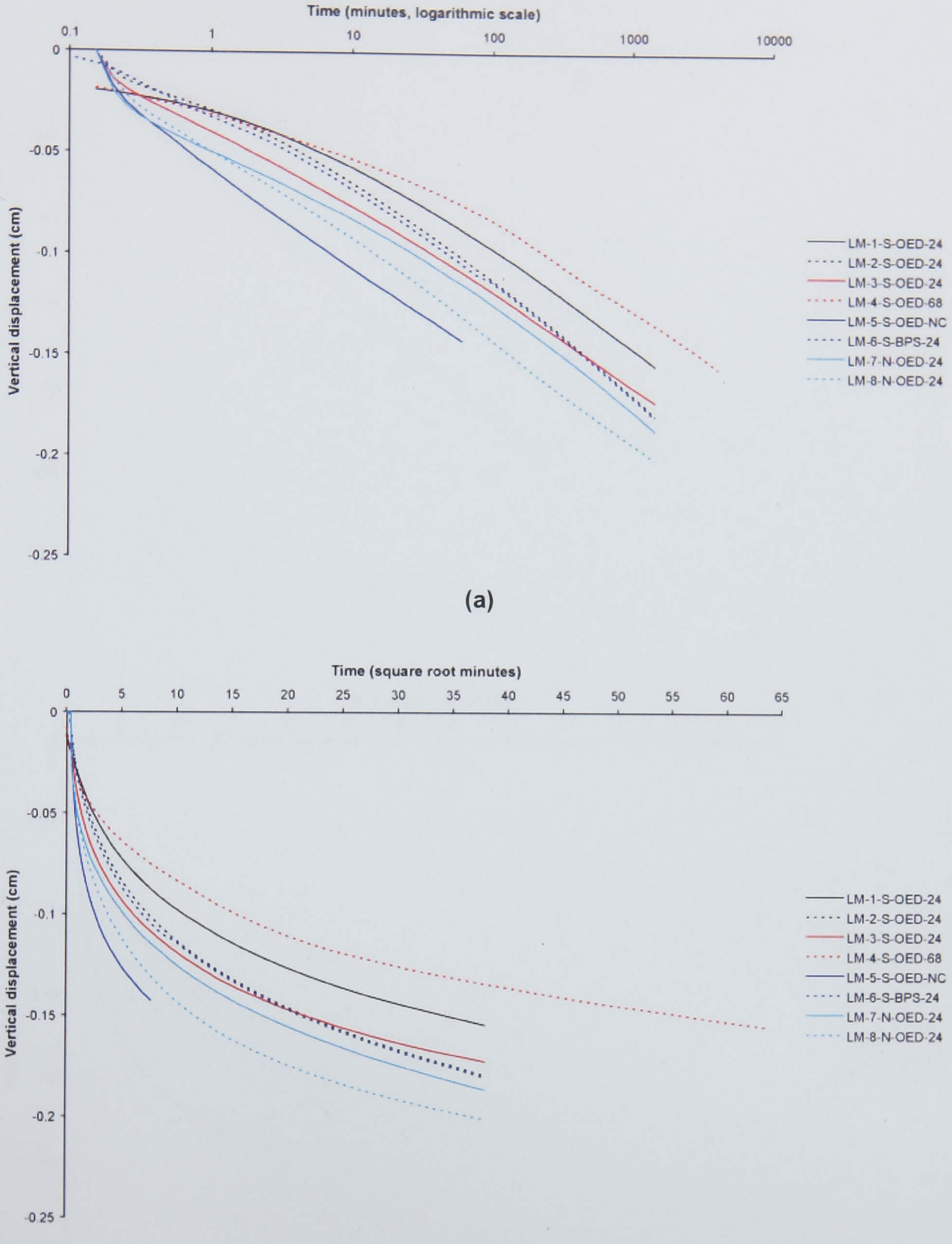

Figure 6.30 Time-vertical displacement plots for low marsh samples at an applied stress of 50 kPa (loading). (a) logarithmic time-vertical displacement (b) square-root time-vertical displacement.

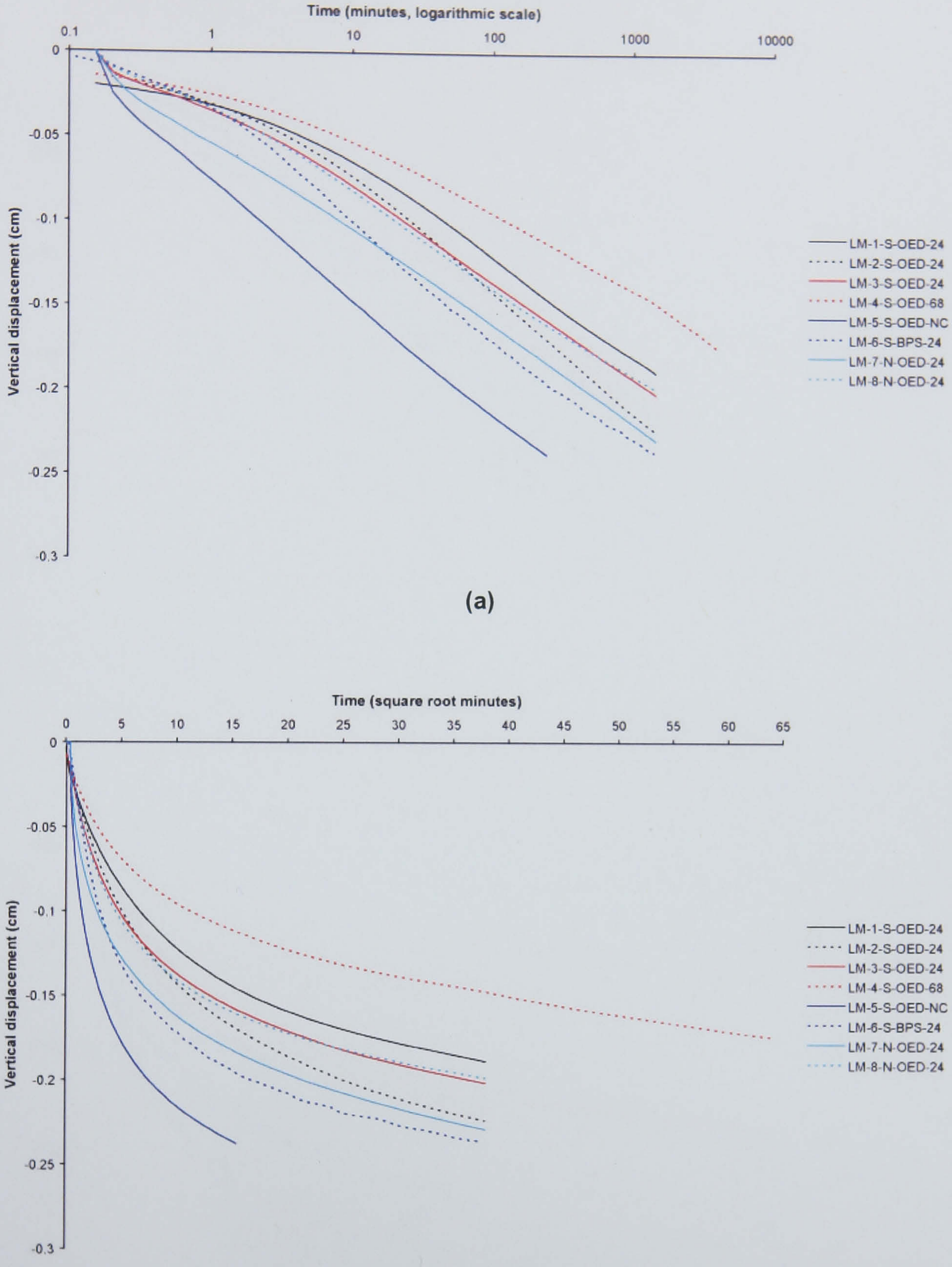

Figure 6.31 Time-vertical displacement plots for low marsh samples at an applied stress of 99 kPa (loading). (a) logarithmic time-vertical displacement (b) square-root time-vertical displacement.

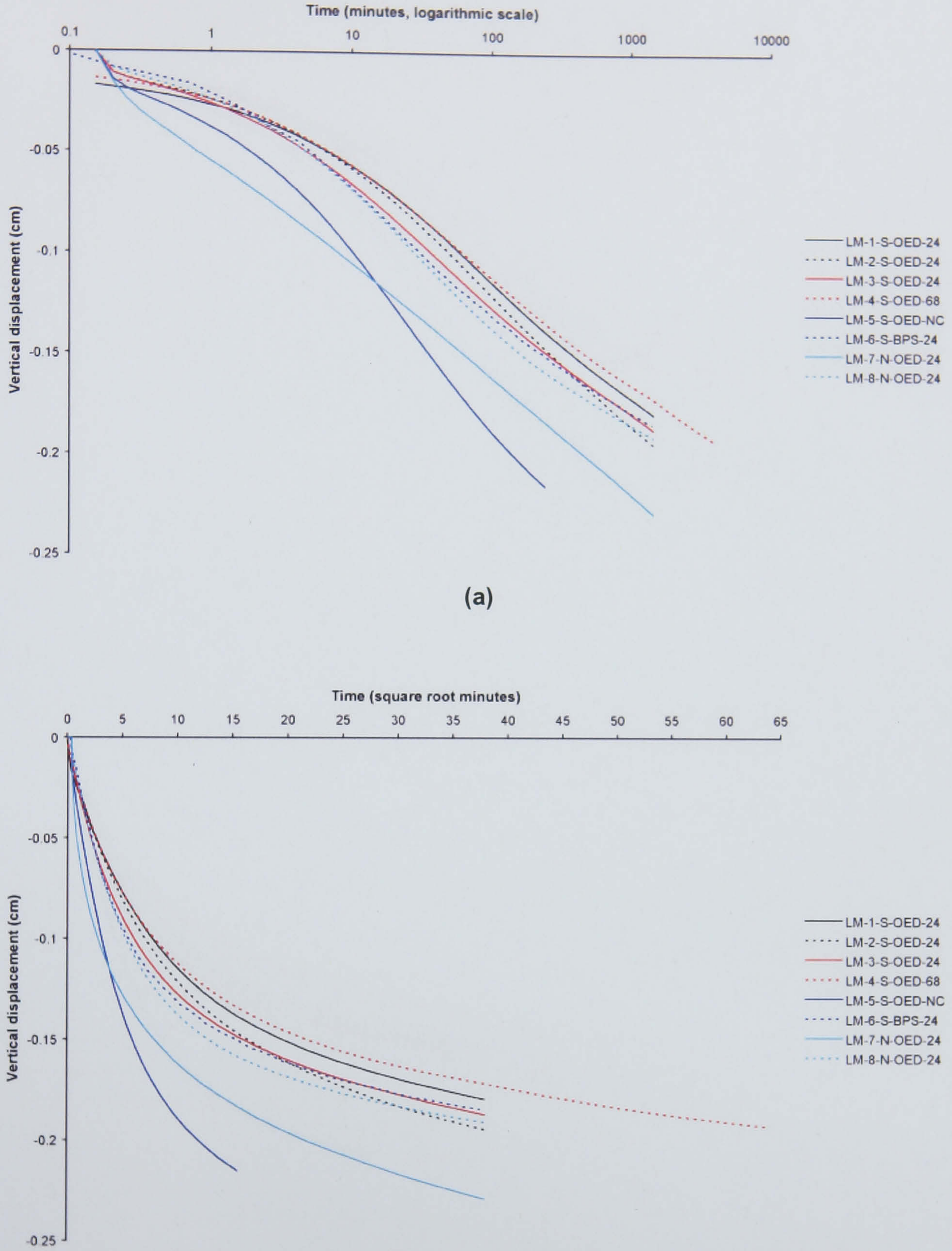

Figure 6.32 Time-vertical displacement plots for low marsh samples at an applied stress of 197 kPa (loading). (a) logarithmic time-vertical displacement (b) square-root time-vertical displacement.

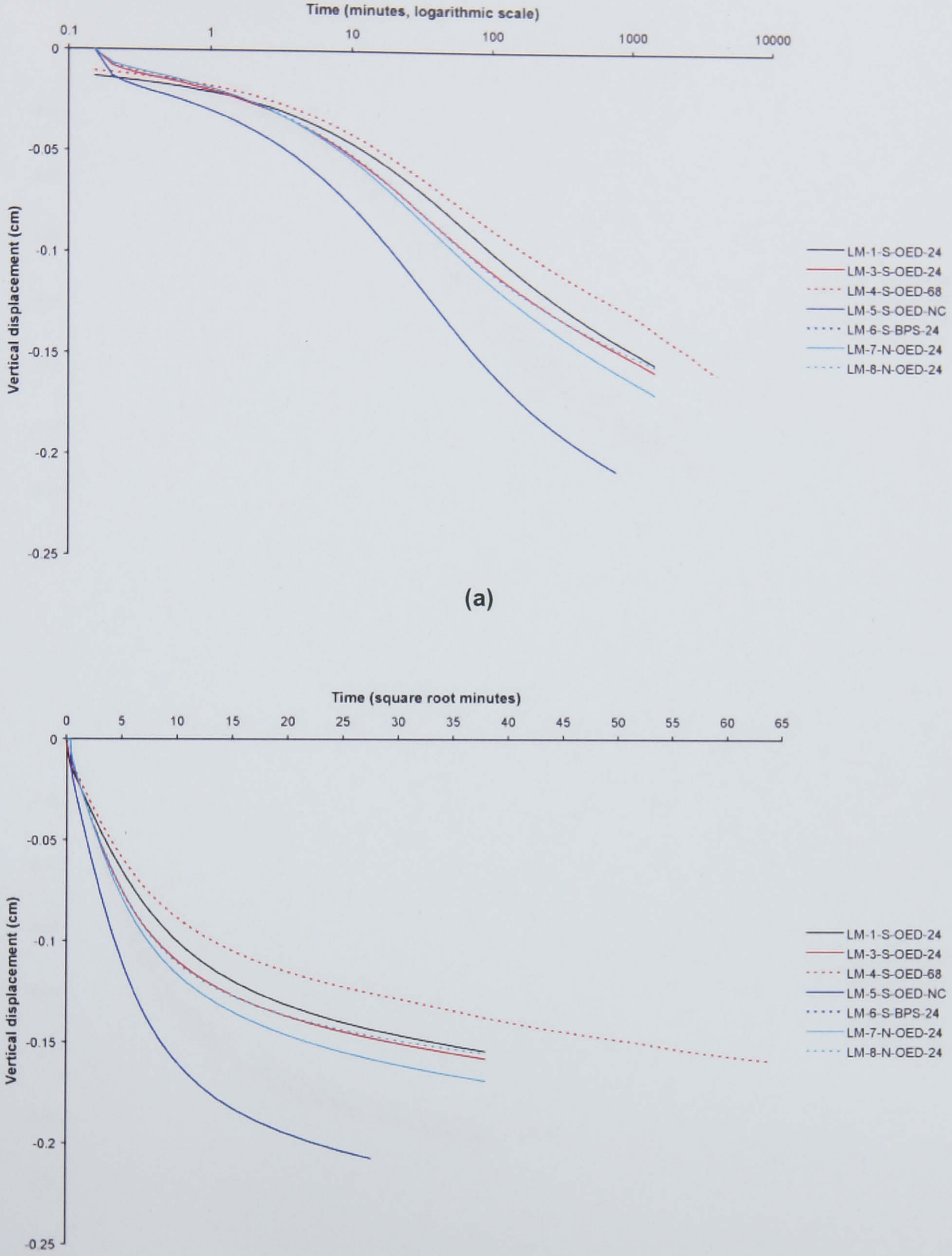

Figure 6.33 Time-vertical displacement plots for low marsh samples at an applied stress of 393 kPa (loading). (a) logarithmic time-vertical displacement (b) square-root time-vertical displacement.

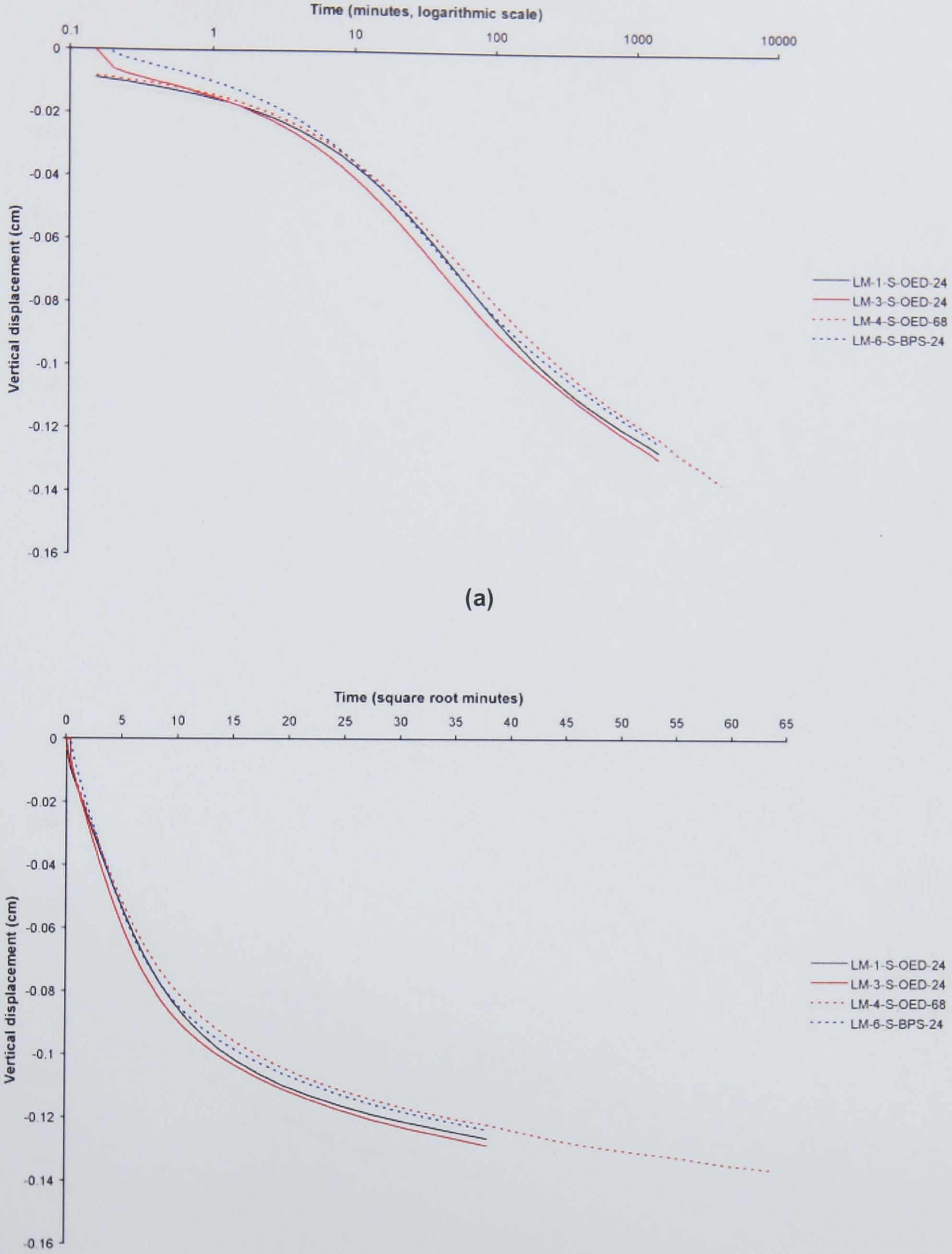

(a)

(b)

Figure 6.34 Time-vertical displacement plots for low marsh samples at an applied stress of 785 kPa (loading). (a) logarithmic time-vertical displacement (b) square-root time-vertical displacement.

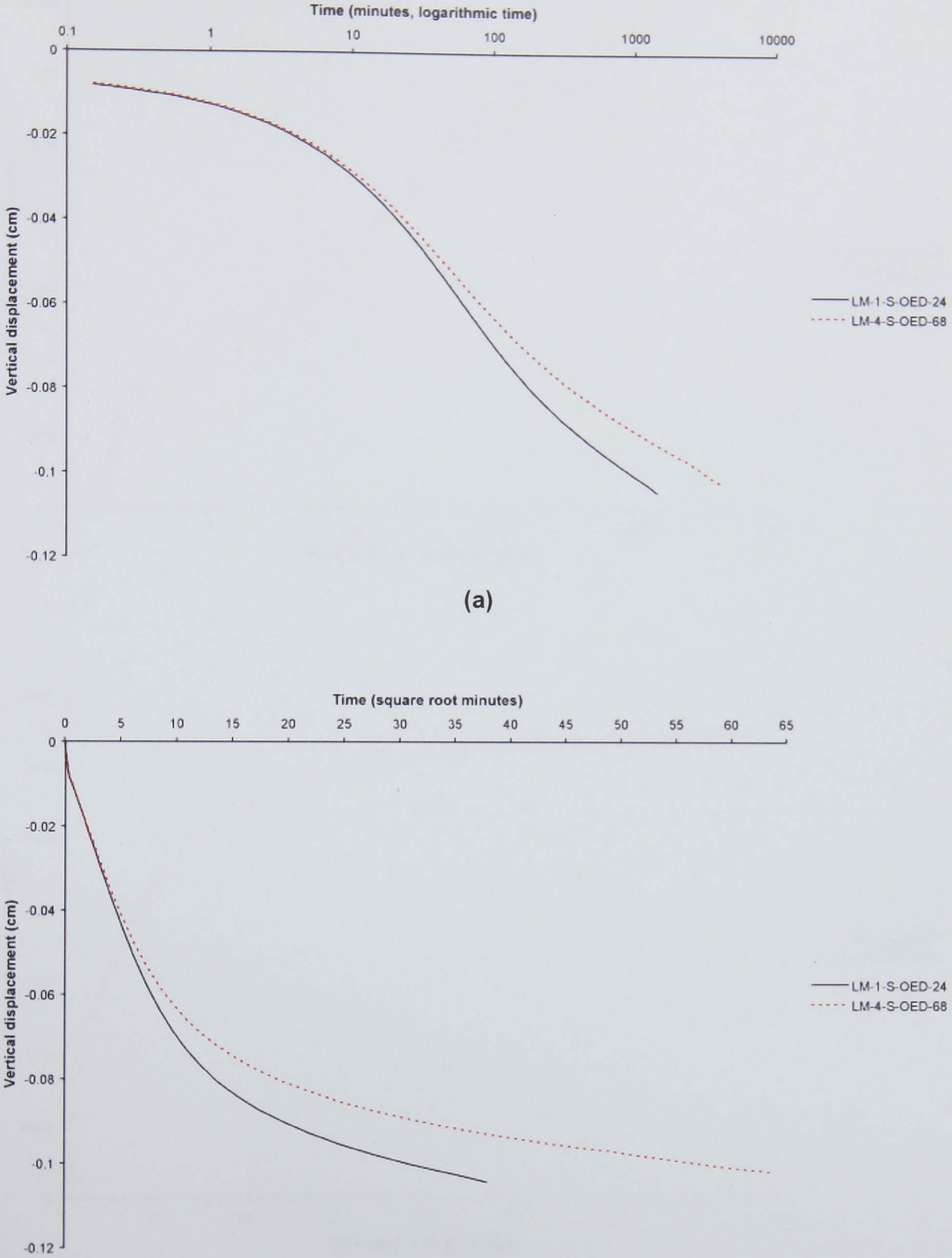

Figure 6.35 Time-vertical displacement plots for low marsh samples at an applied stress of 1570 kPa (loading). (a) logarithmic time-vertical displacement (b) square-root time-vertical displacement.

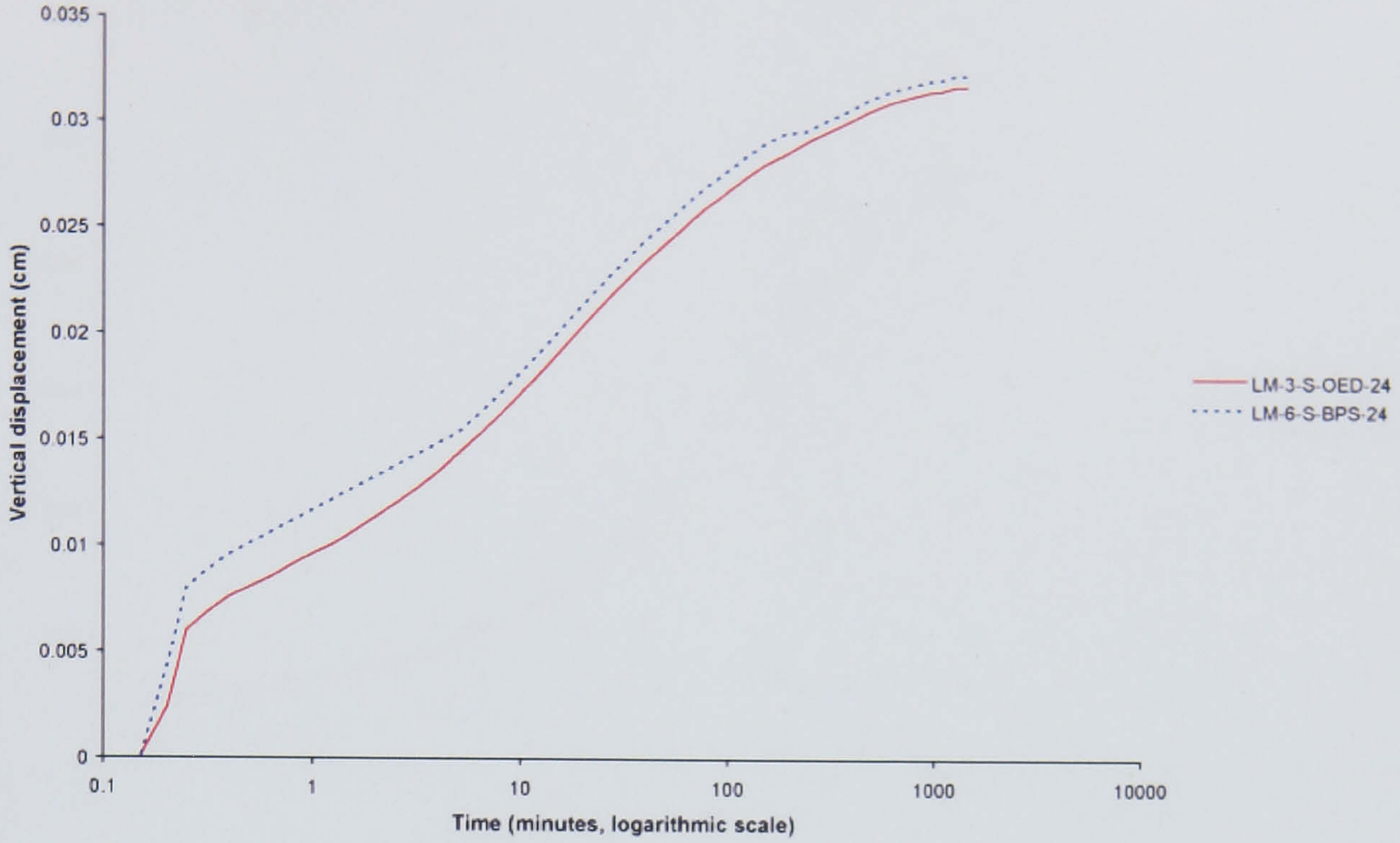

(a)

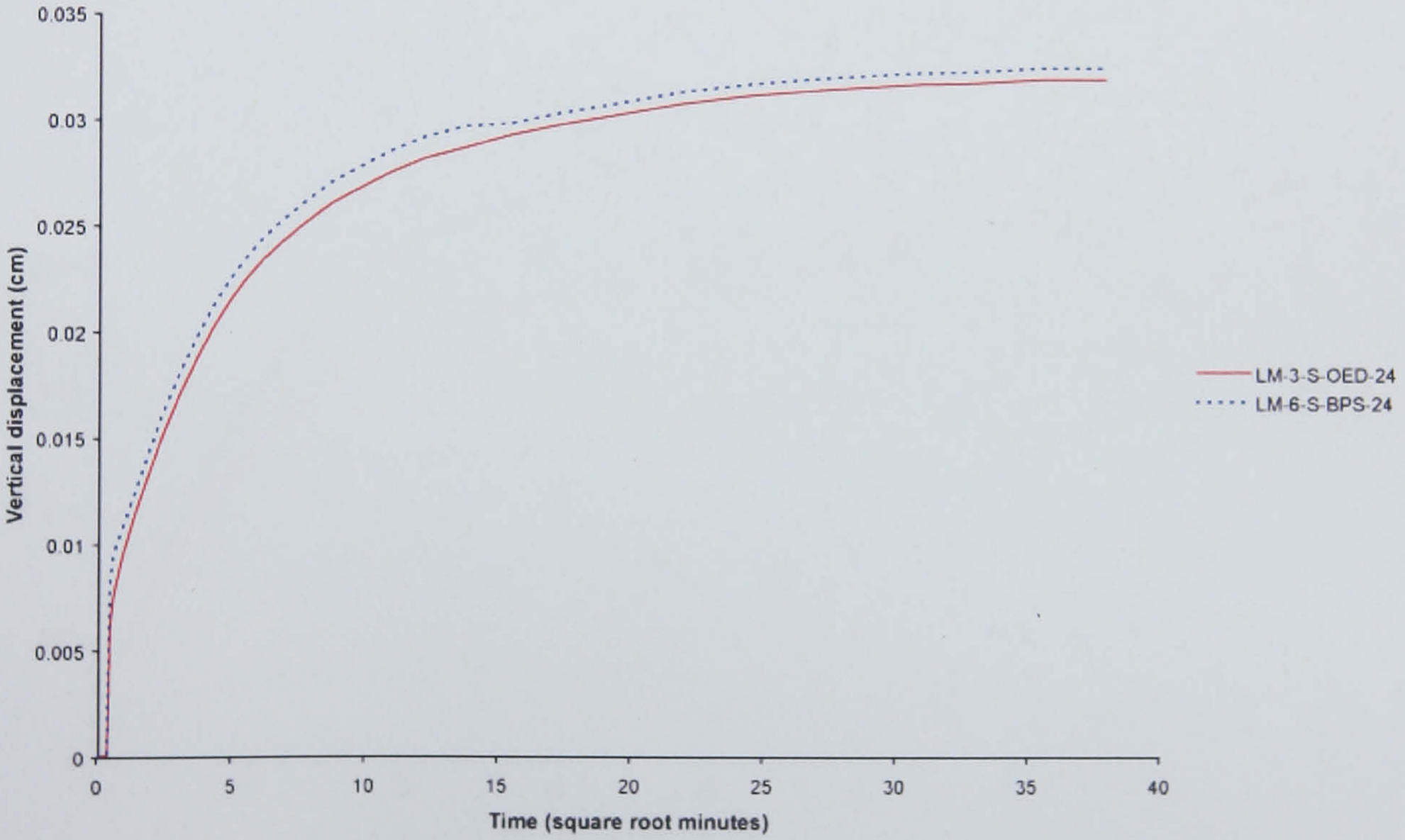

(b)

Figure 6.36 Time-vertical displacement plots for low marsh samples at an applied stress of 259 kPa (unloading). (a) logarithmic time-vertical displacement (b) square-root time-vertical displacement.

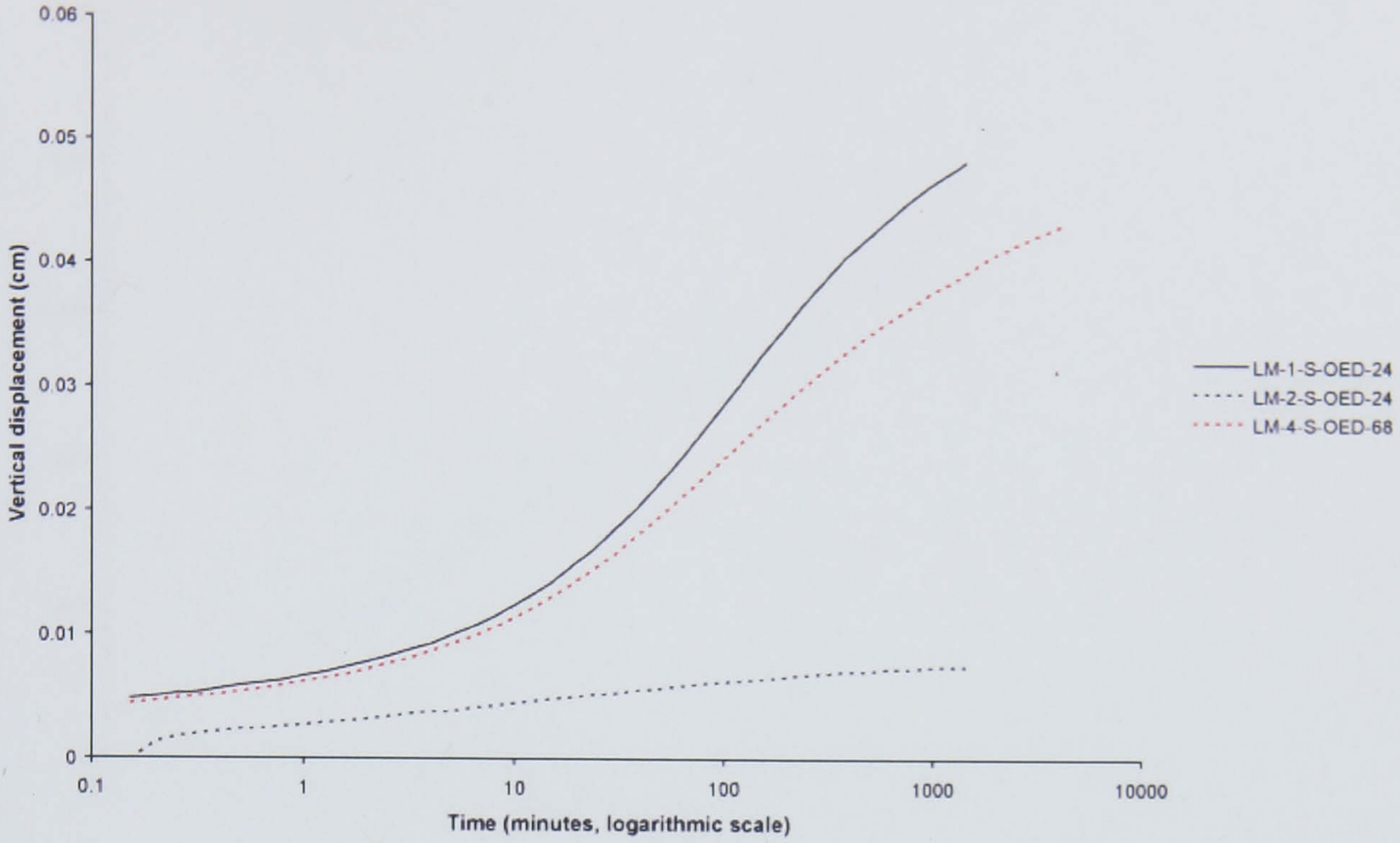

(a)

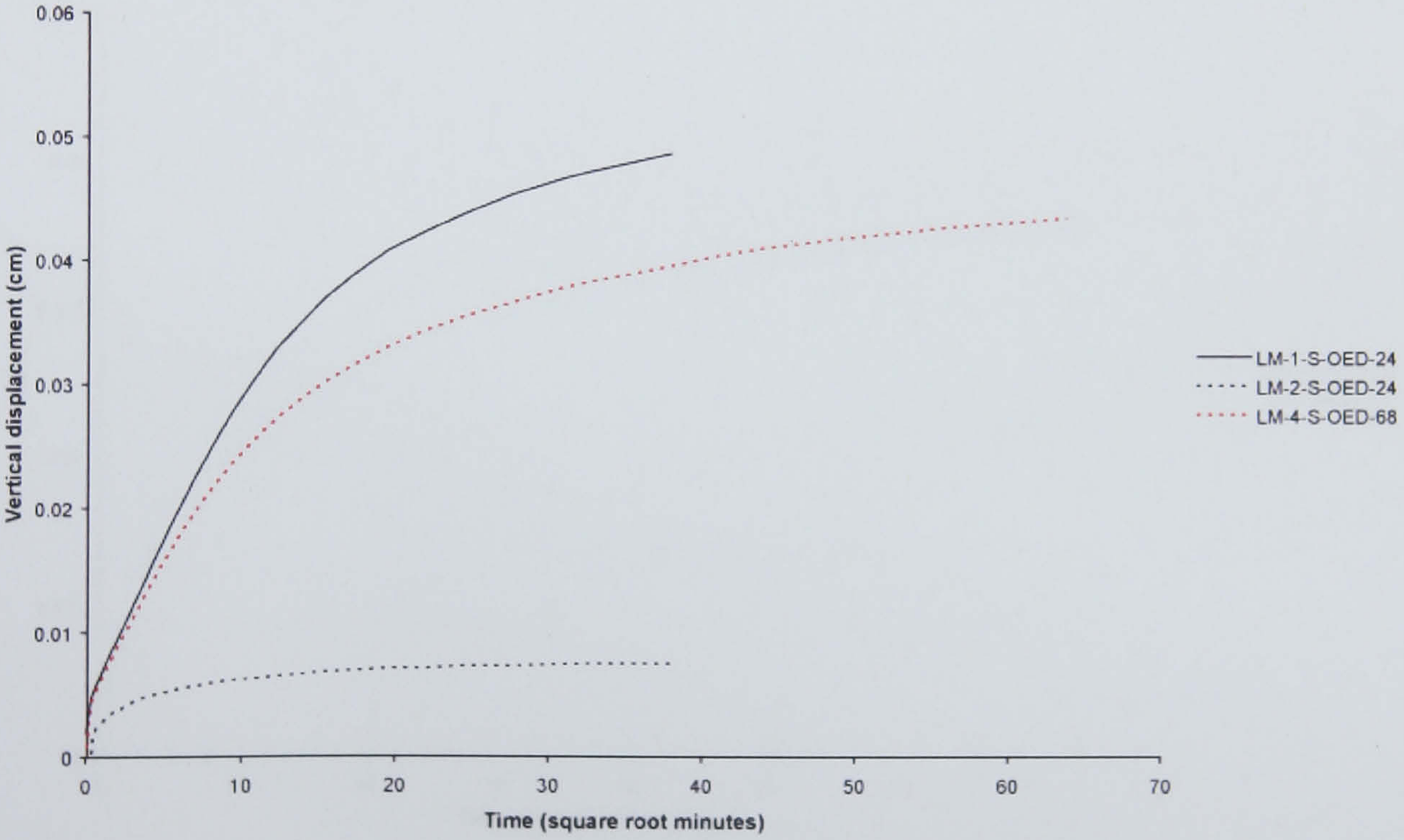

(b)

Figure 6.37 Time-vertical displacement plots for low marsh samples at an applied stress of 172 kPa (unloading). (a) logarithmic time-vertical displacement (b) square-root time-vertical displacement.

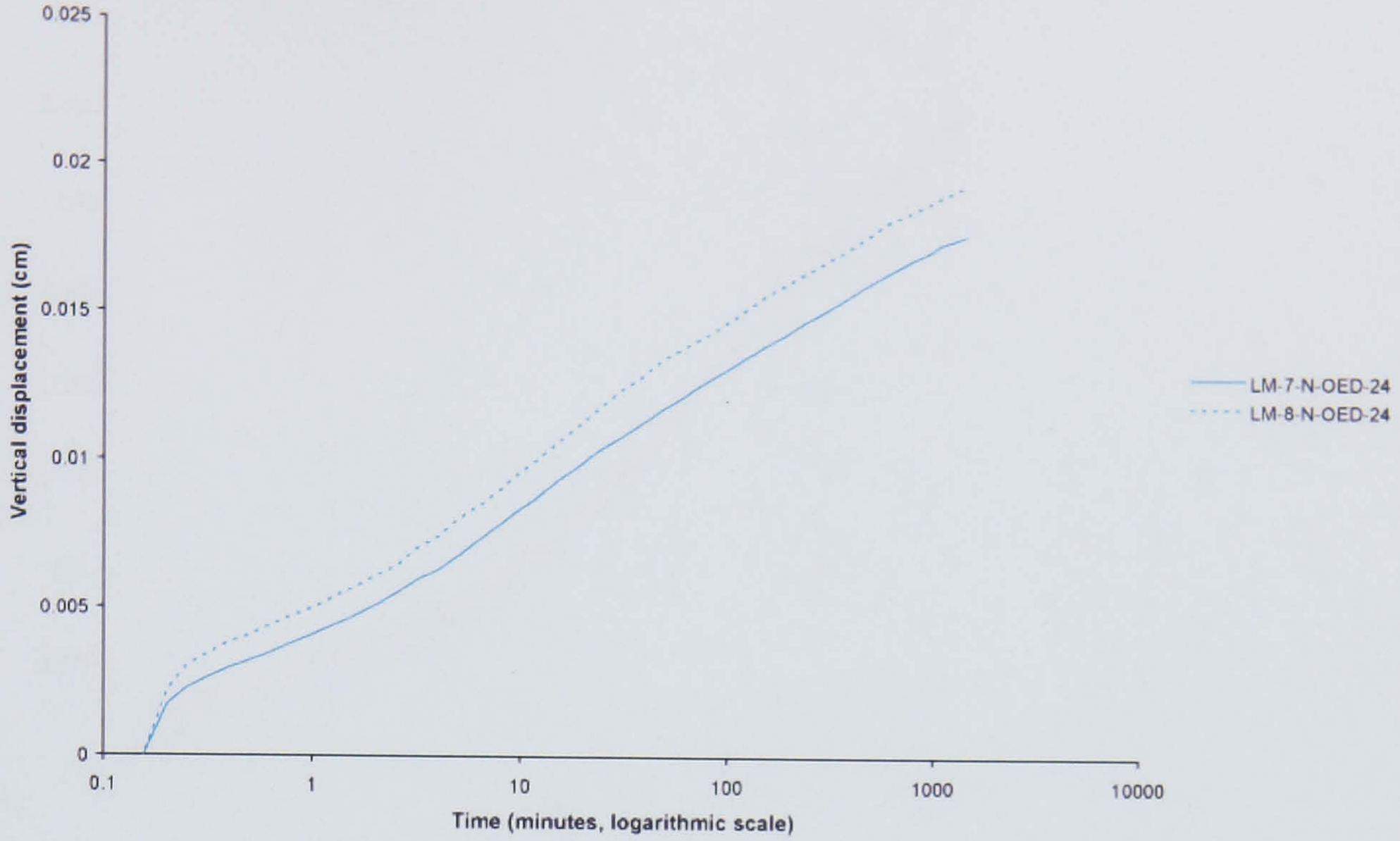

(a)

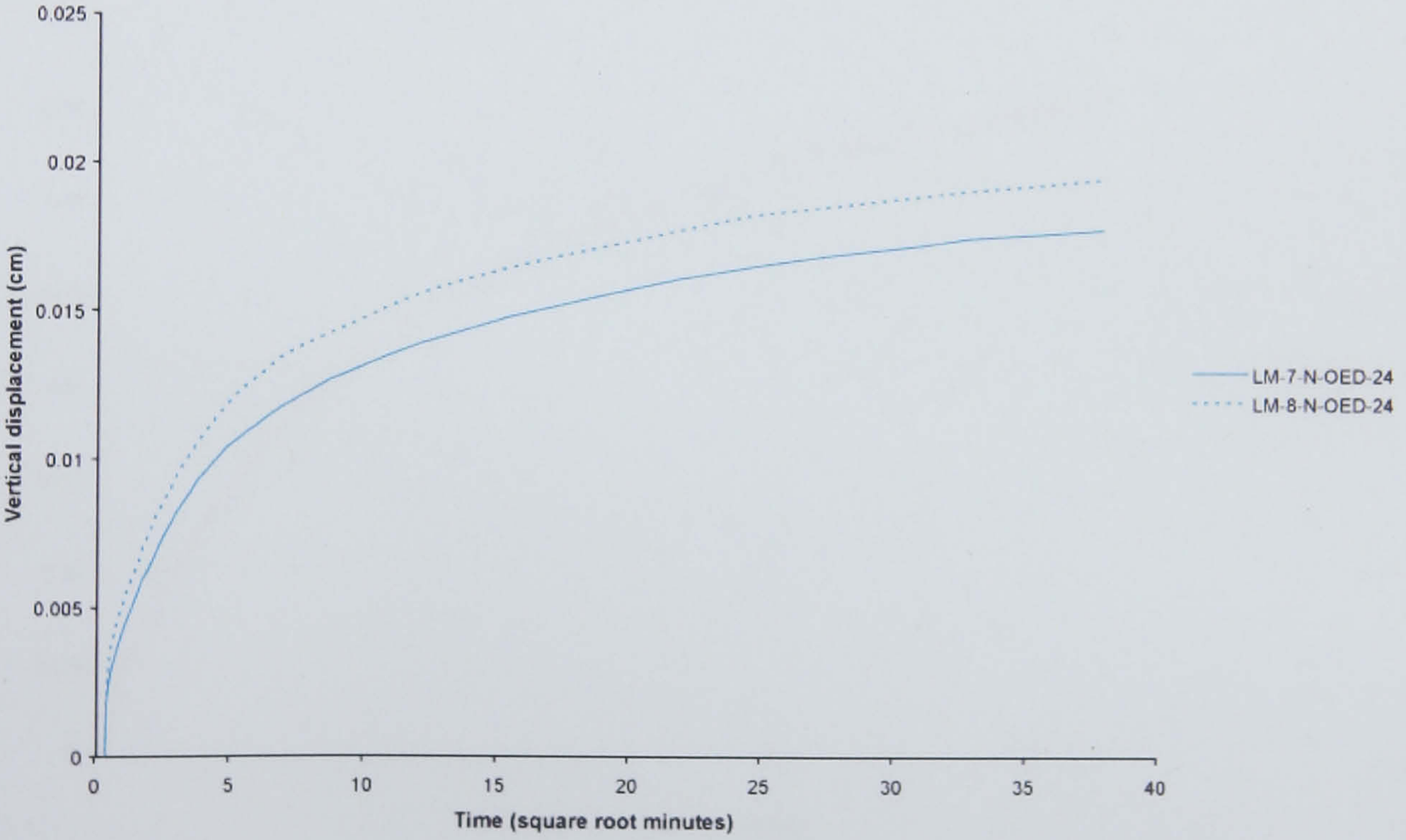

(b)

Figure 6.38 Time-vertical displacement plots for low marsh samples at an applied stress of 132 kPa (unloading). (a) logarithmic time-vertical displacement (b) square-root time-vertical displacement.

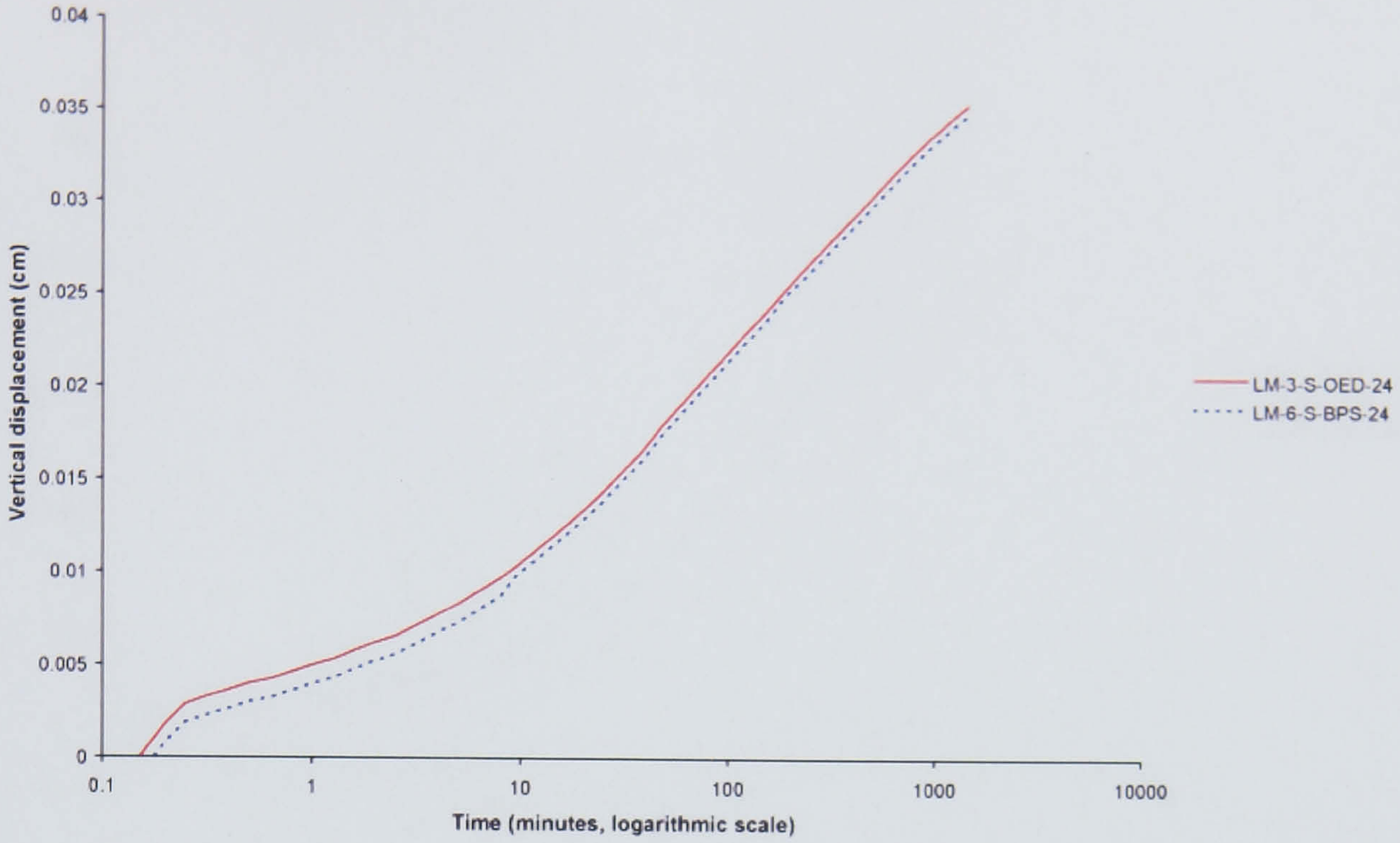

(a)

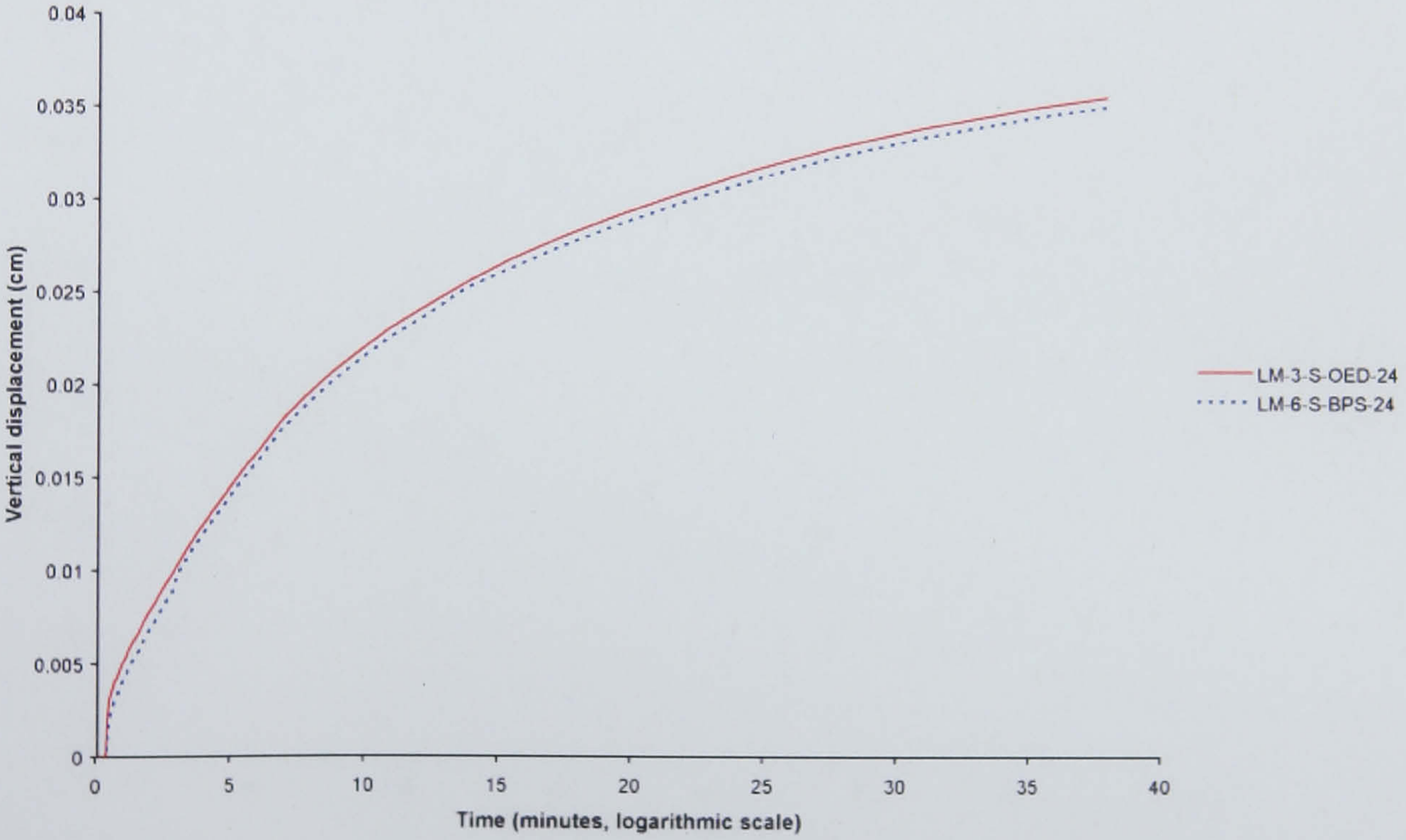

(b)

Figure 6.39 Time-vertical displacement plots for low marsh samples at an applied stress of 87 kPa (unloading). (a) logarithmic time-vertical displacement (b) square-root time-vertical displacement.

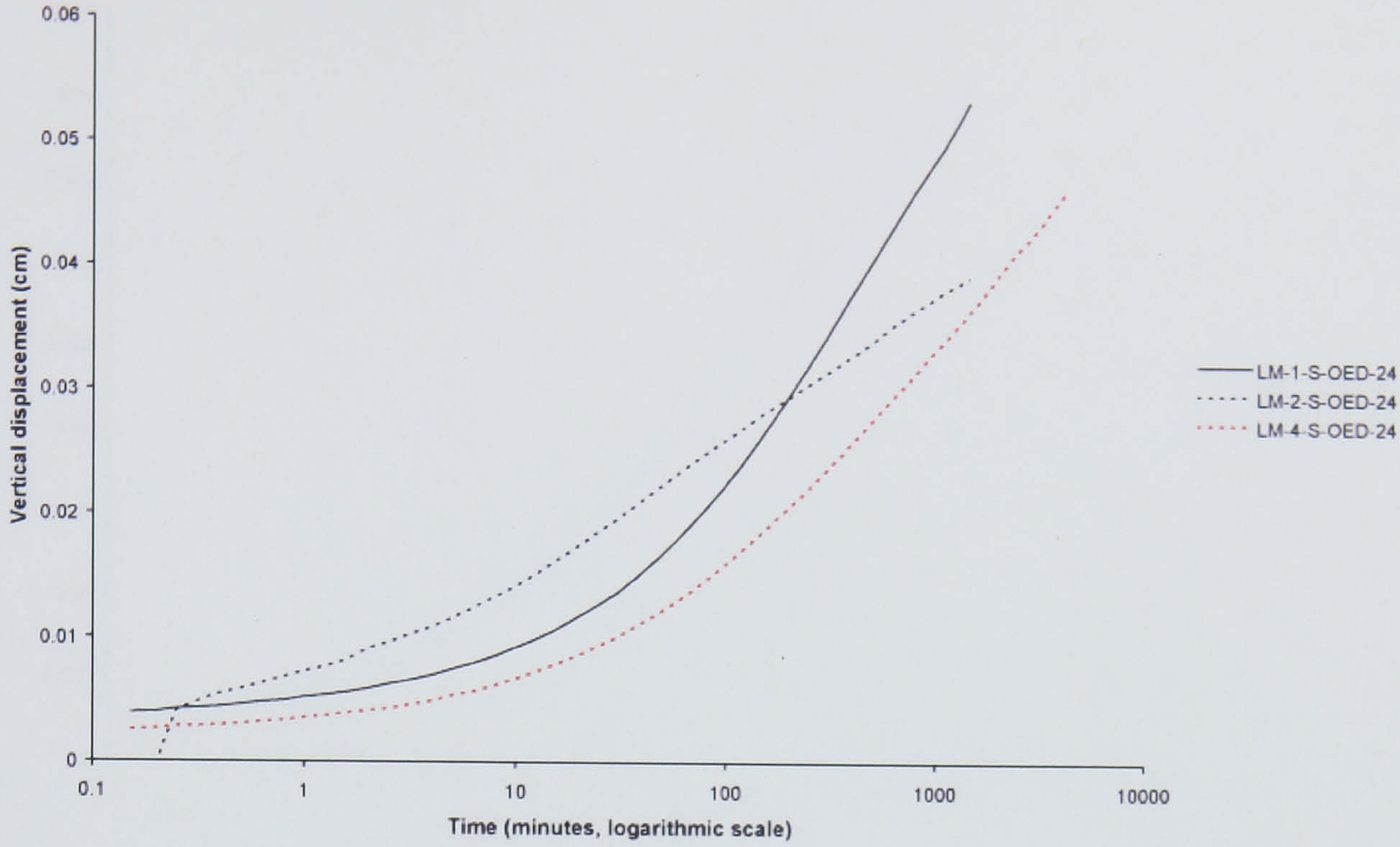

(a)

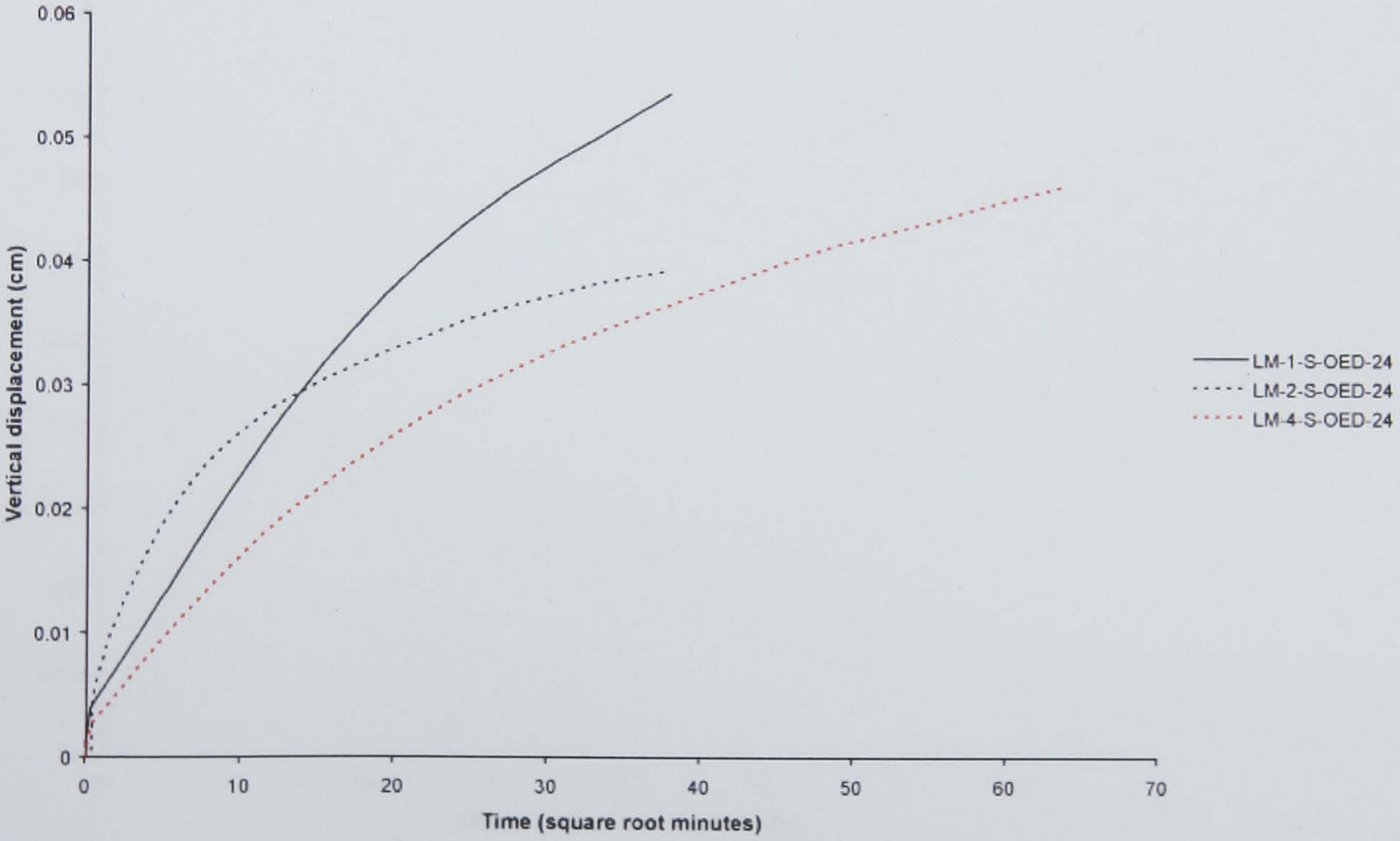

(b)

Figure 6.40 Time-vertical displacement plots for low marsh samples at an applied stress of 62 kPa (unloading). (a) logarithmic time-vertical displacement (b) square-root time-vertical displacement.

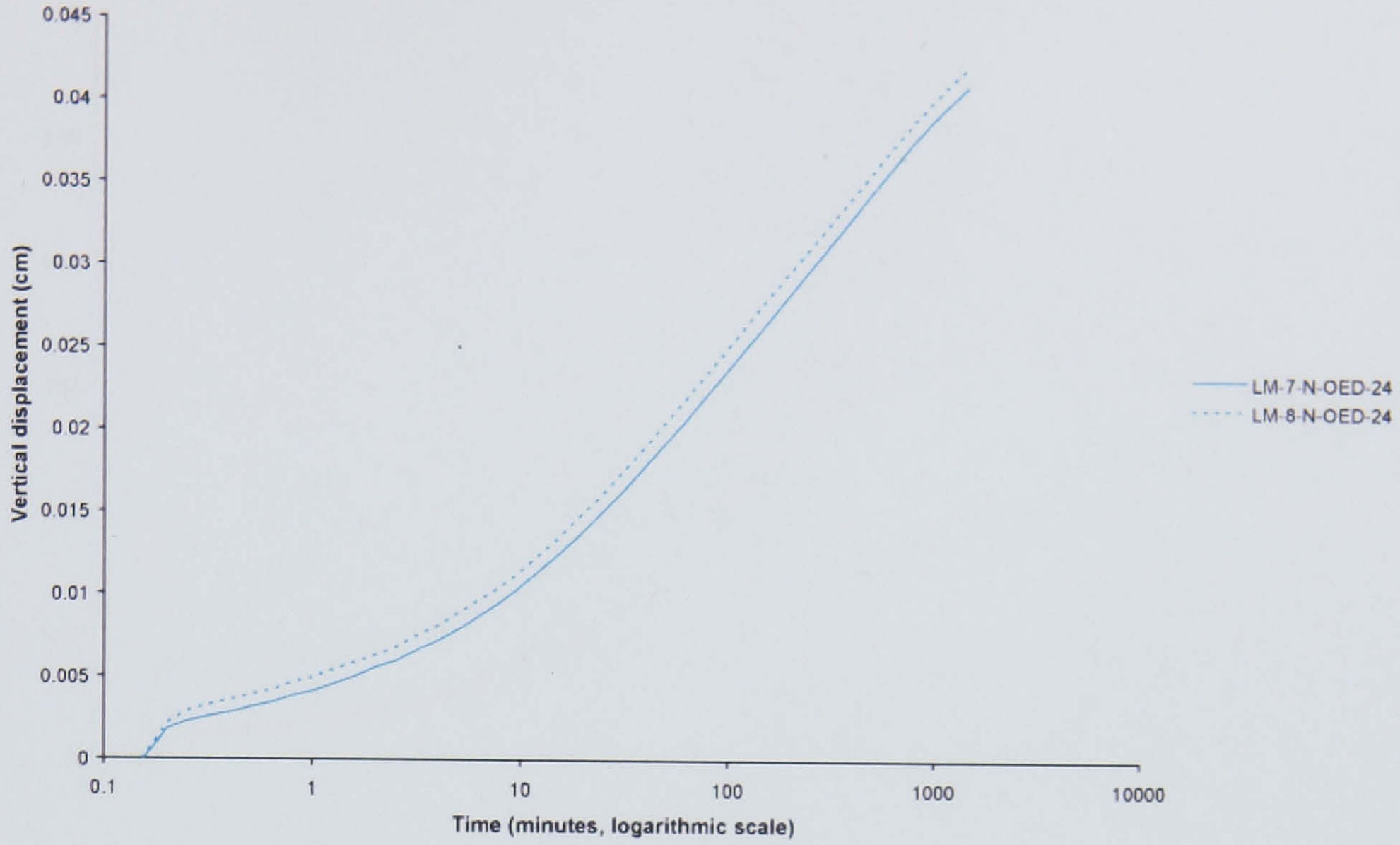

(a)

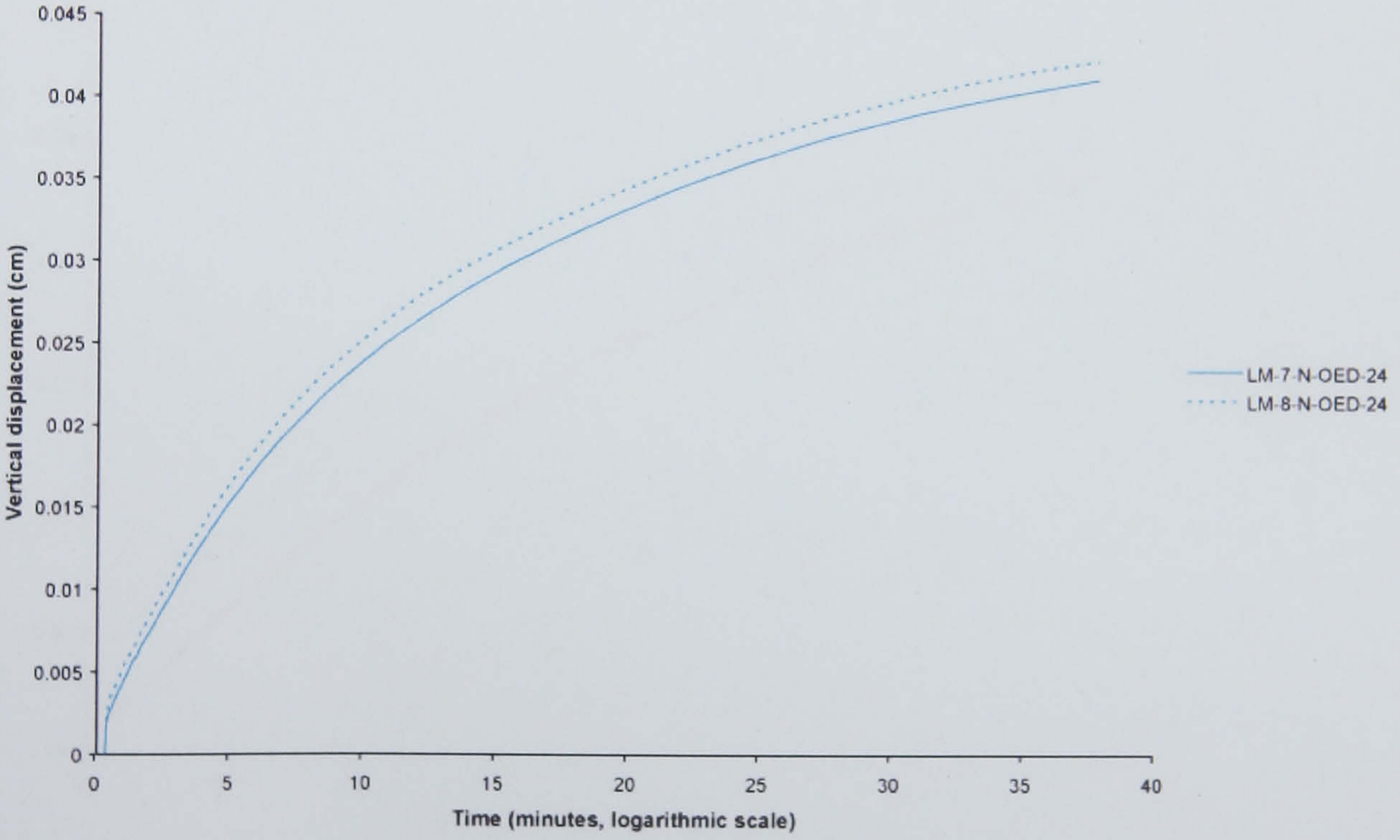

(b)

Figure 6.41 Time-vertical displacement plots for low marsh samples at an applied stress of 46 kPa (unloading). (a) logarithmic time-vertical displacement (b) square-root time-vertical displacement.

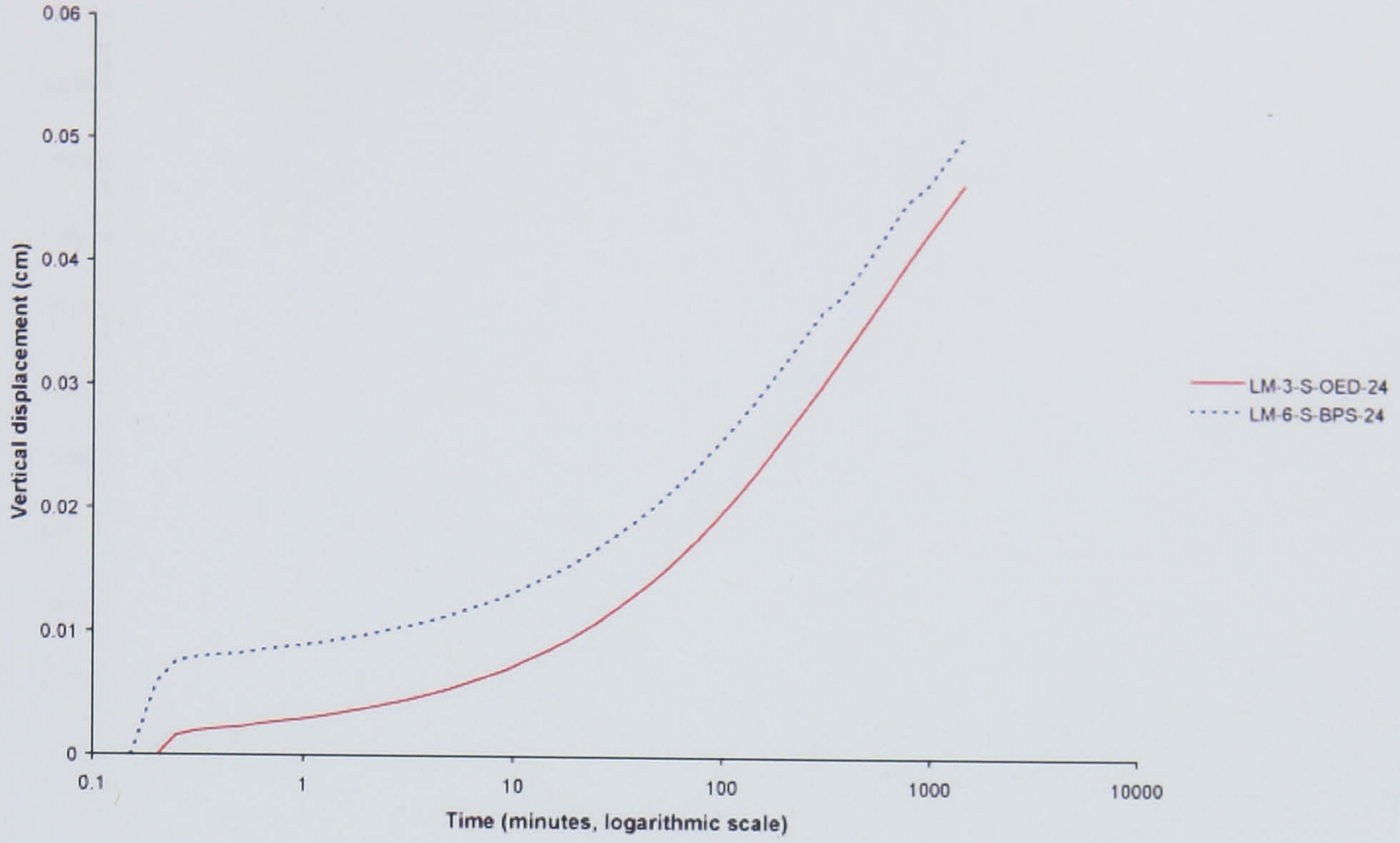

(a)

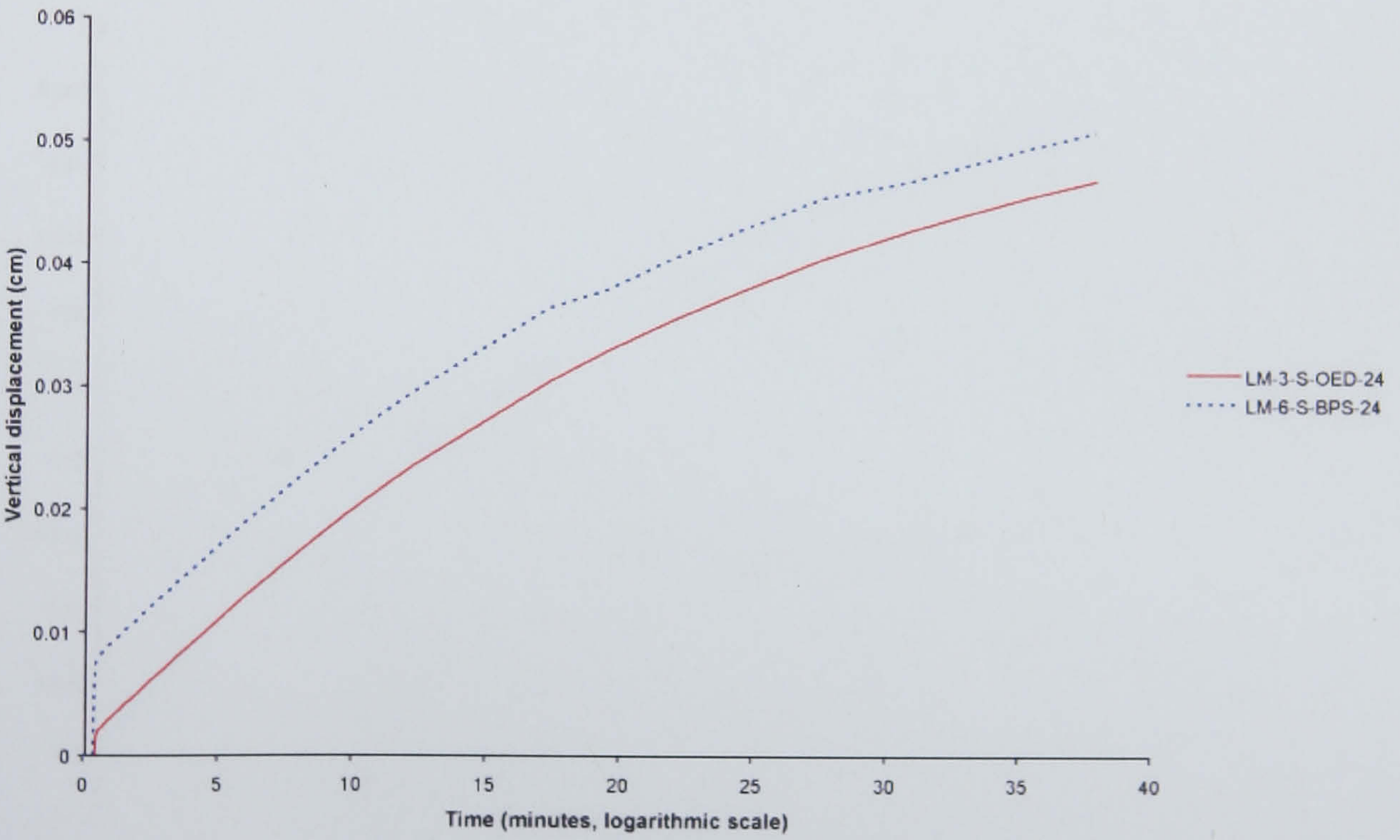

(b)

Figure 6.42 Time-vertical displacement plots for low marsh samples at an applied stress of 30 kPa (unloading). (a) logarithmic time-vertical displacement (b) square-root time-vertical displacement.

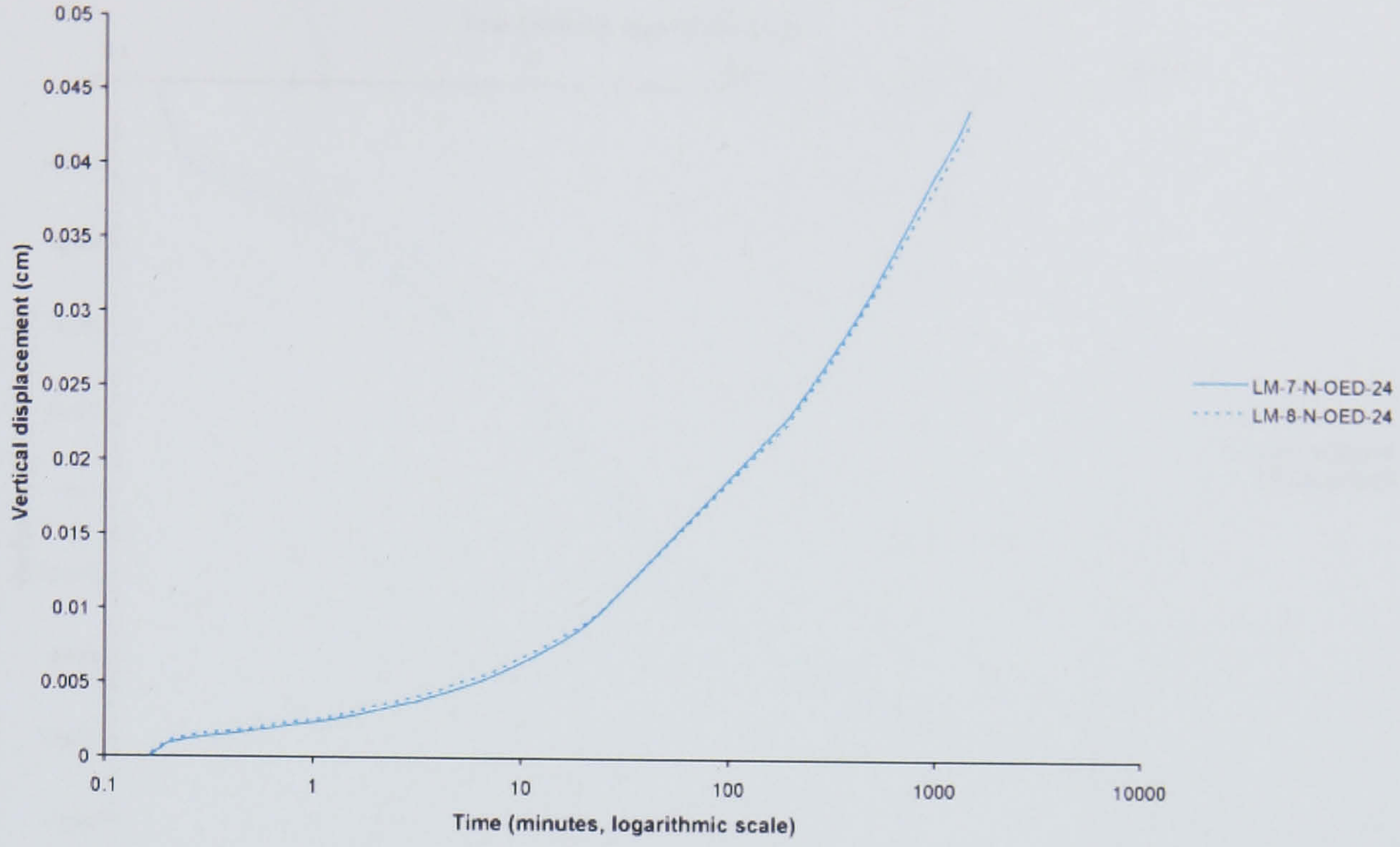

(a)

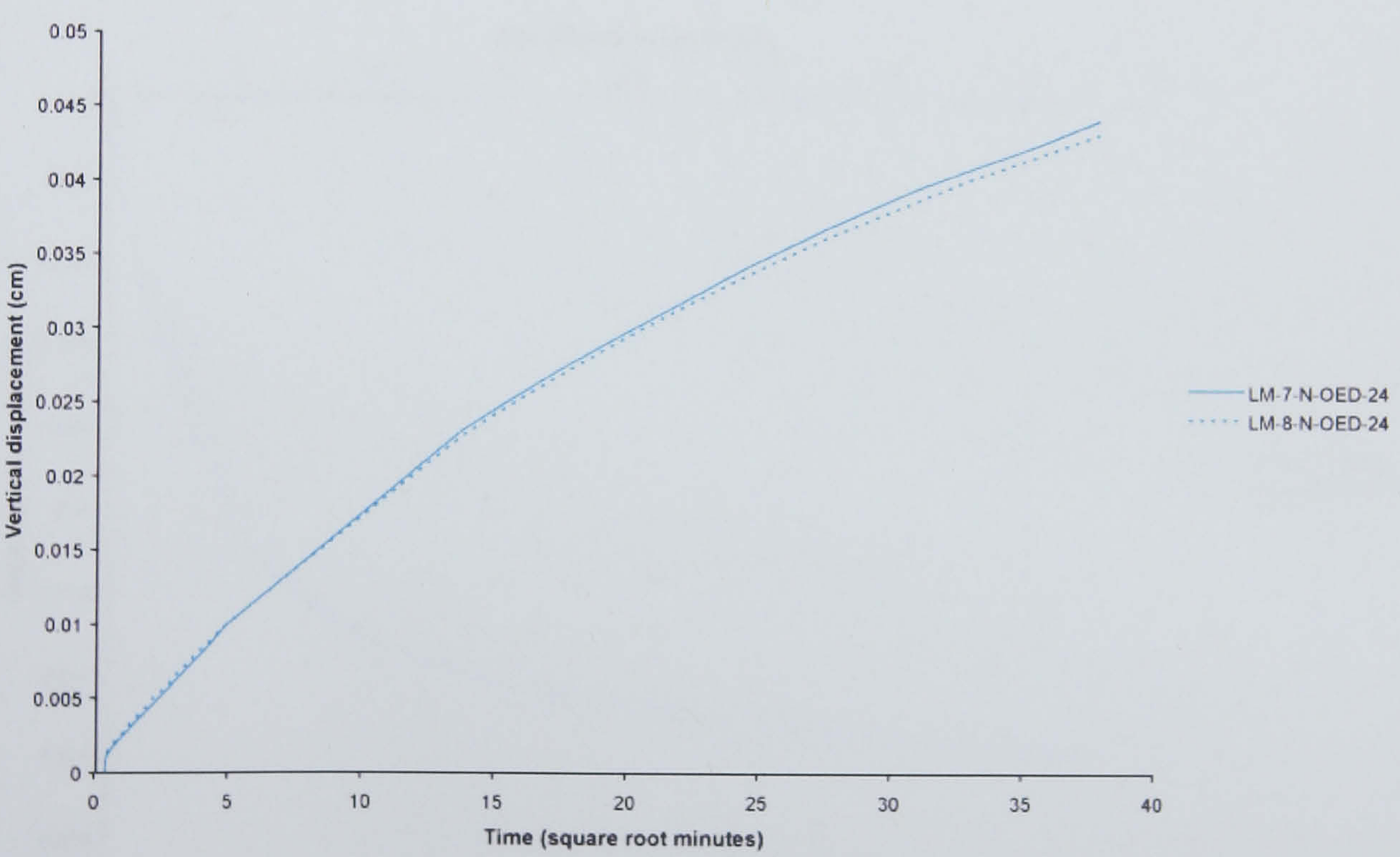

(b)

Figure 6.43 Time-vertical displacement plots for low marsh samples at an applied stress of 16 kPa (unloading). (a) logarithmic time-vertical displacement (b) square-root time-vertical displacement.

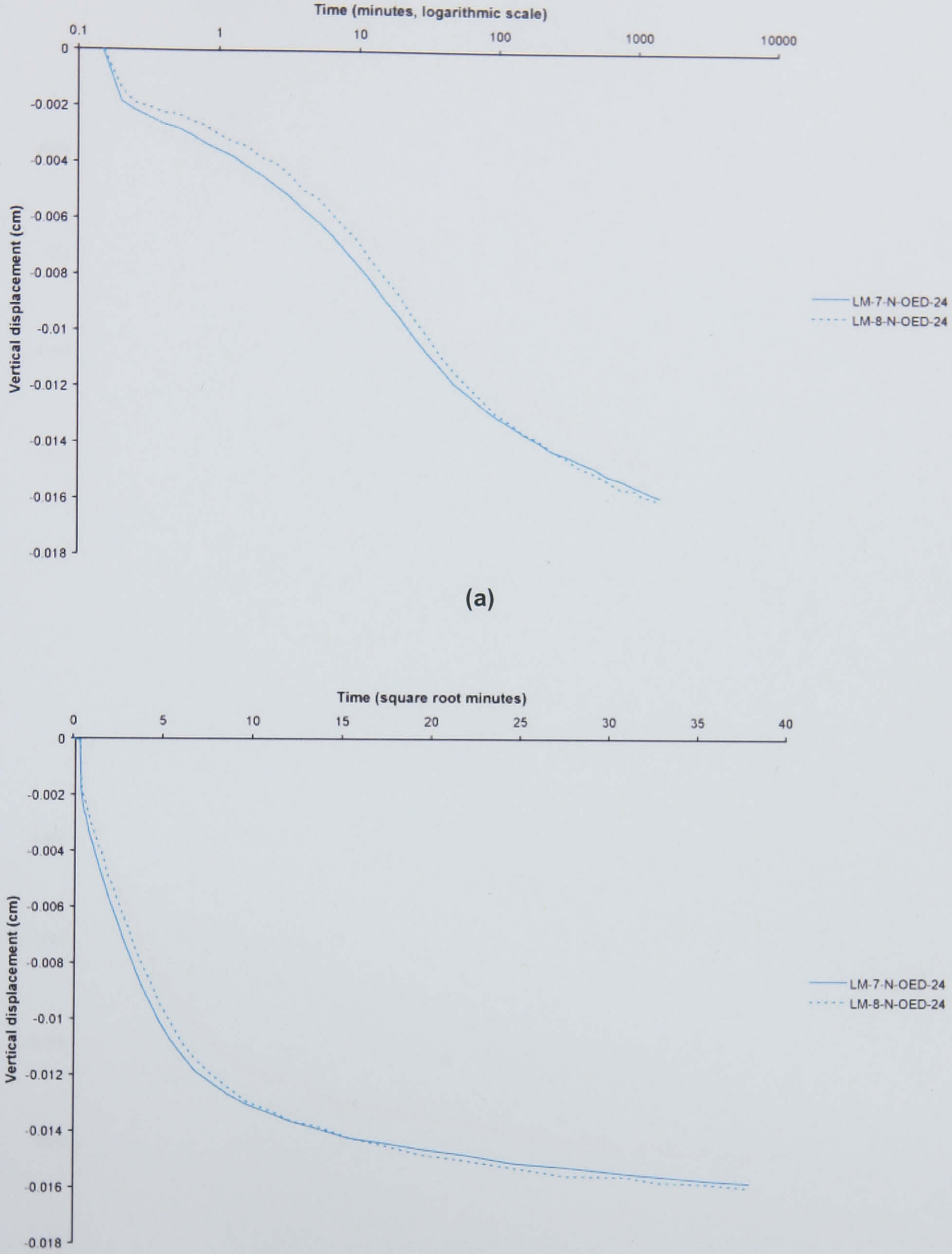

(a)

(b)

Figure 6.44 Time-vertical displacement plots for low marsh samples at an applied stress of 46 kPa (reloading). (a) logarithmic time-vertical displacement (b) square-root time-vertical displacement.

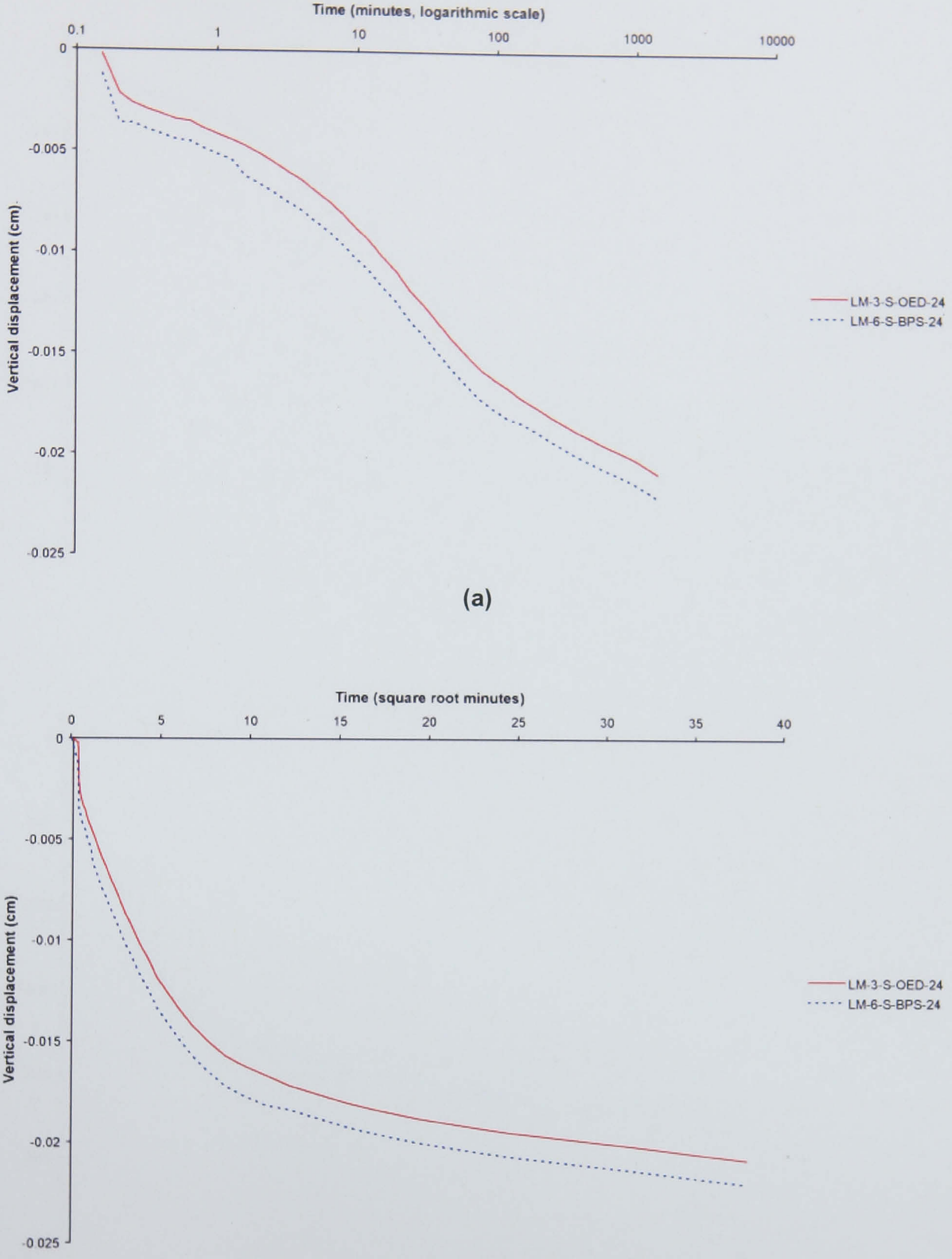

(a)

(b)

Figure 6.45 Time-vertical displacement plots for low marsh samples at an applied stress of 87 kPa (reloading). (a) logarithmic time-vertical displacement (b) square-root time-vertical displacement.

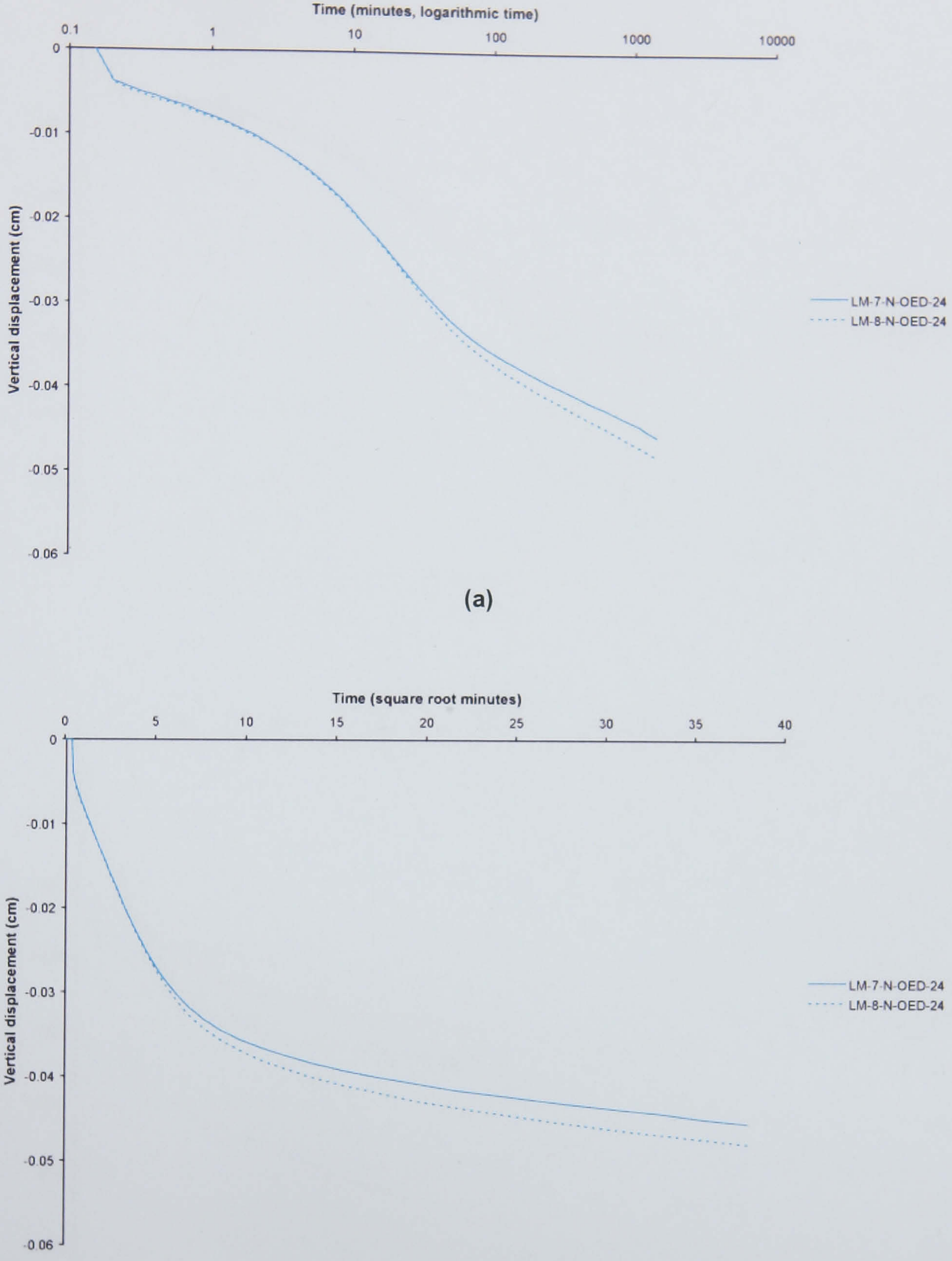

(a)

(b)

Figure 6.46 Time-vertical displacement plots for low marsh samples at an applied stress of 132 kPa (reloading). (a) logarithmic time-vertical displacement (b) square-root time-vertical displacement.

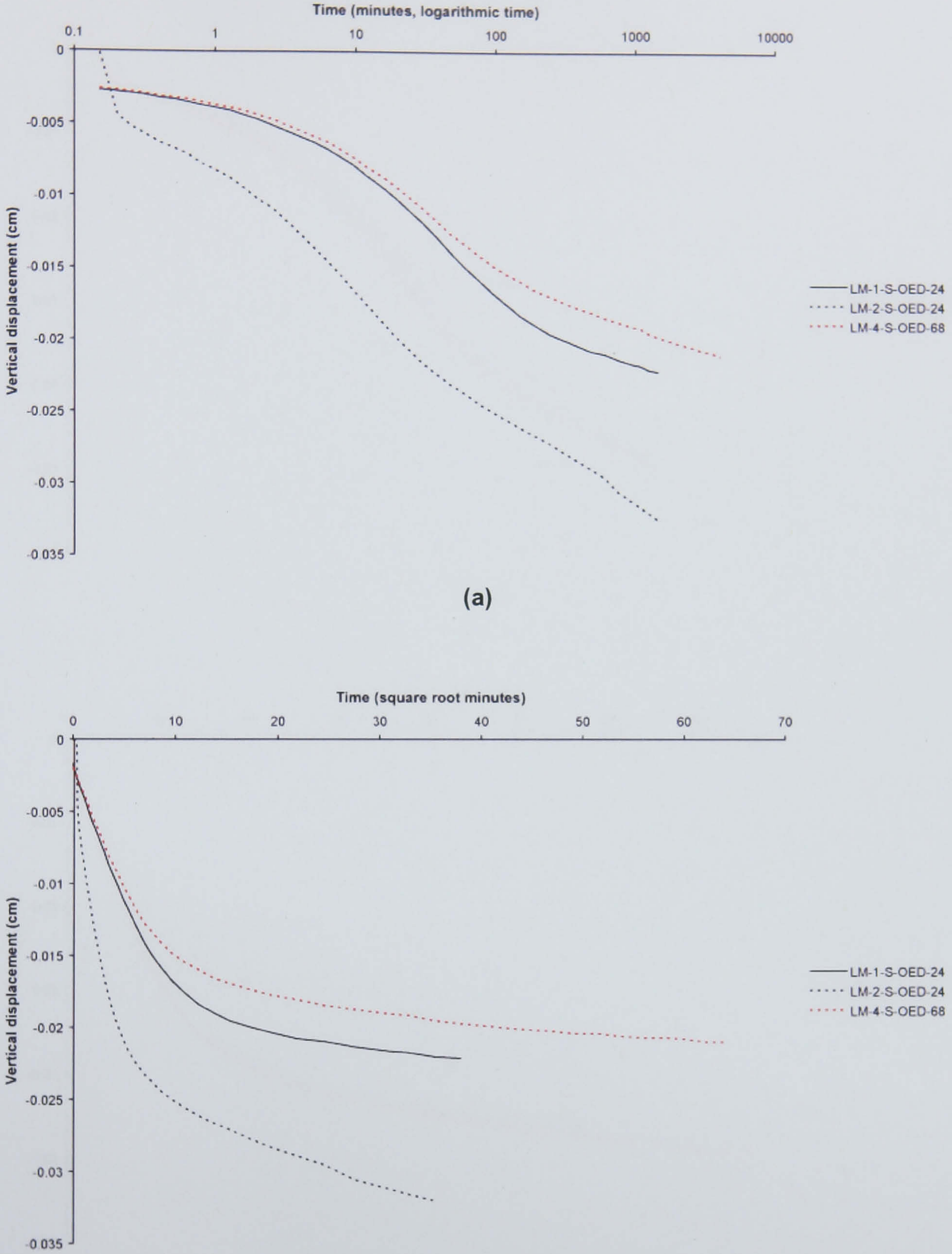

Figure 6.47 Time-vertical displacement plots for low marsh samples at an applied stress of 172 kPa (reloading). (a) logarithmic time-vertical displacement (b) square-root time-vertical displacement.

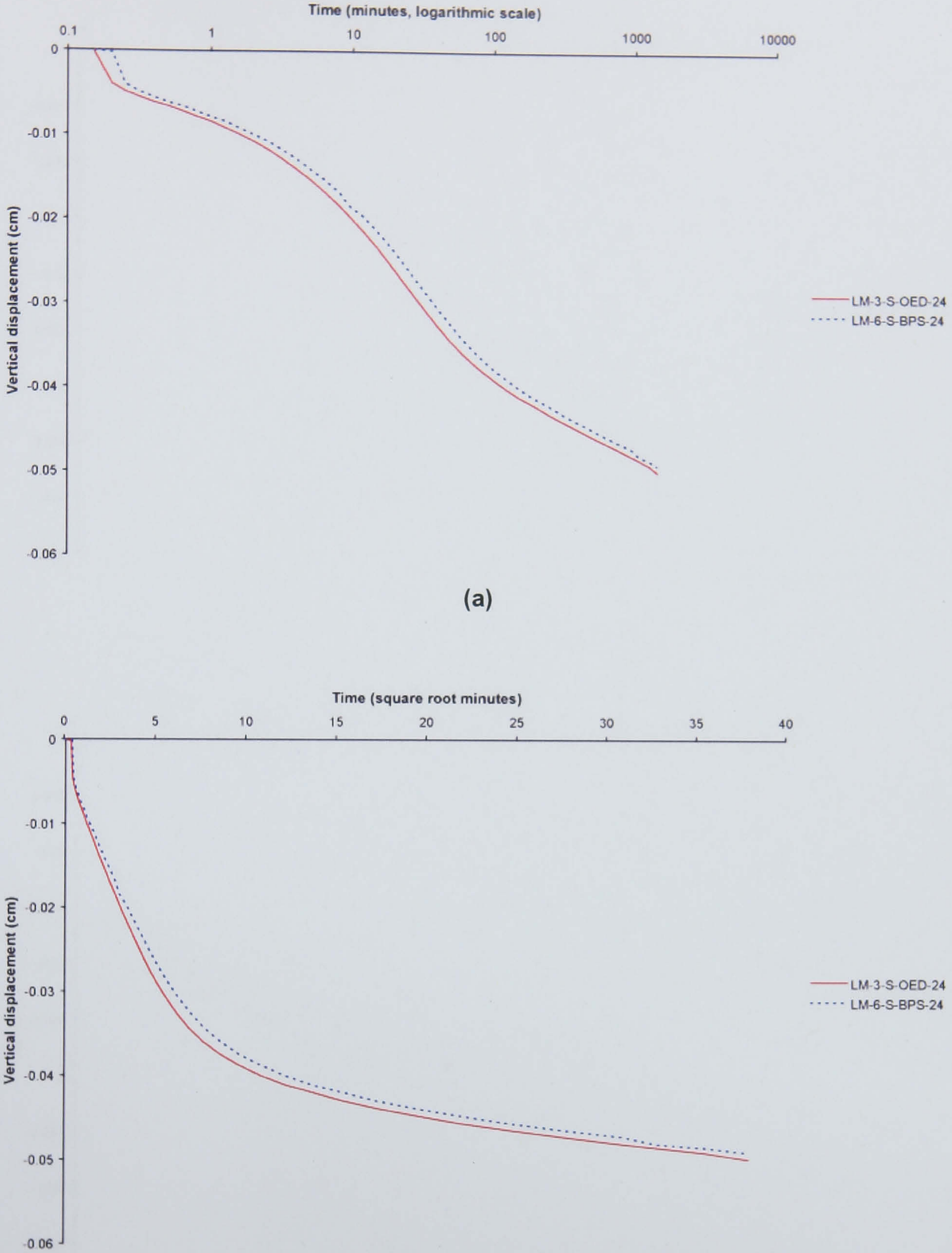

(a)

(b)

Figure 6.48 Time-vertical displacement plots for low marsh samples at an applied stress of 259 kPa (reloading). (a) logarithmic time-vertical displacement (b) square-root time-vertical displacement.

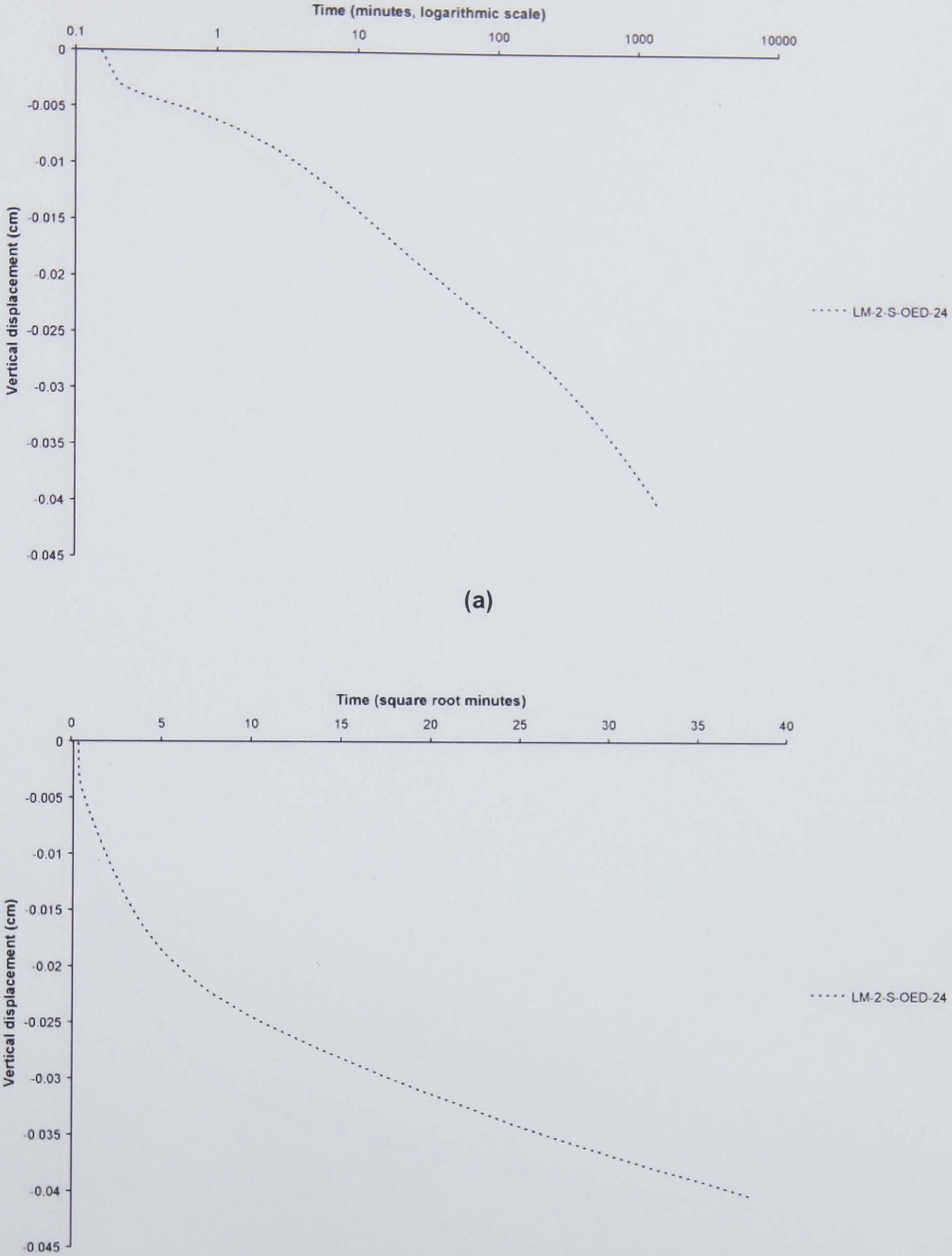

Figure 6.49 Time-vertical displacement plots for low marsh samples at an applied stress of 295 kPa (reloading). (a) logarithmic time-vertical displacement (b) square-root time-vertical displacement.

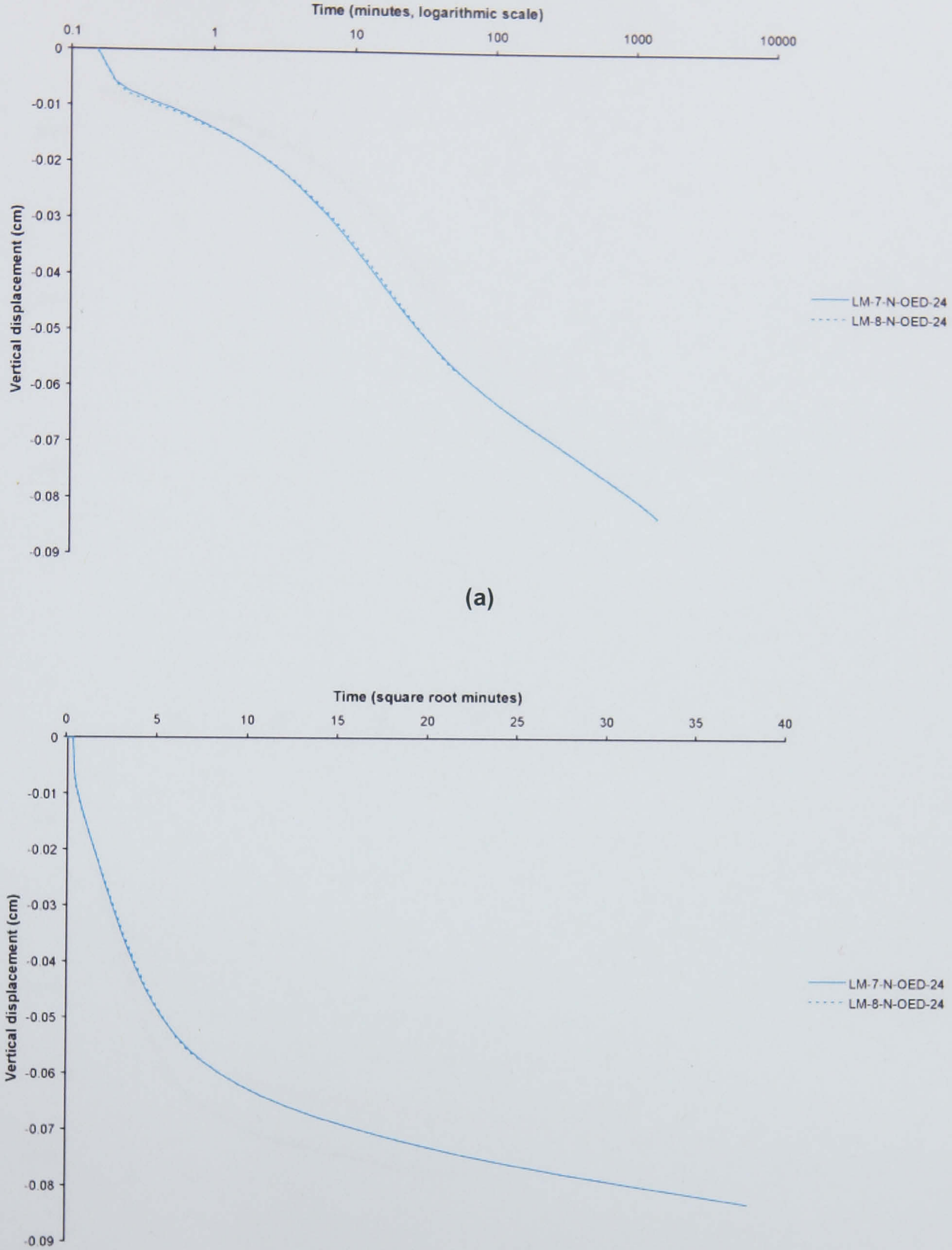

Figure 6.50 Time-vertical displacement plots for low marsh samples at an applied stress of 393 kPa (reloading). (a) logarithmic time-vertical displacement (b) square-root time-vertical displacement.

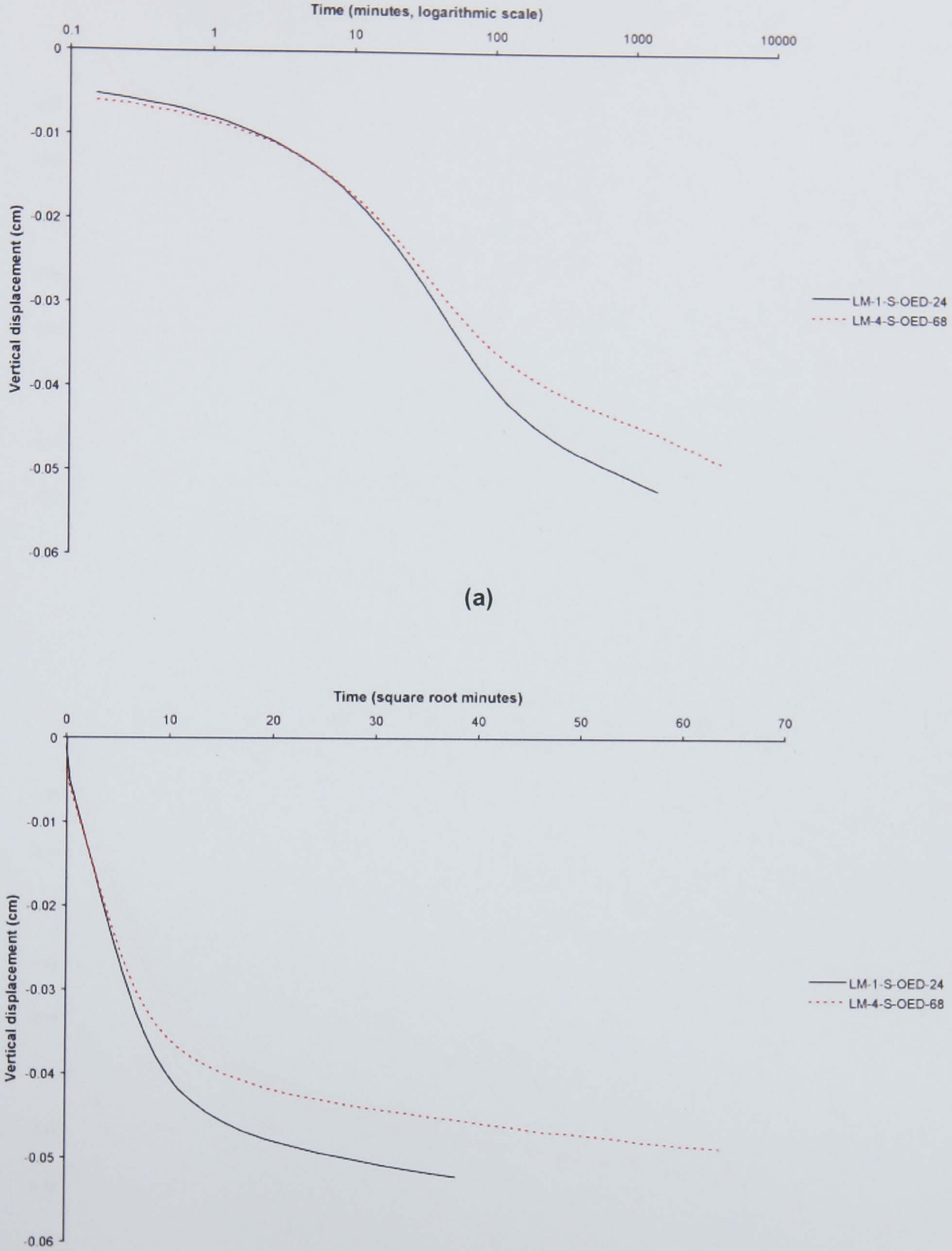

Figure 6.51 Time-vertical displacement plots for low marsh samples at an applied stress of 515 kPa (reloading). (a) logarithmic time-vertical displacement (b) square-root time-vertical displacement.

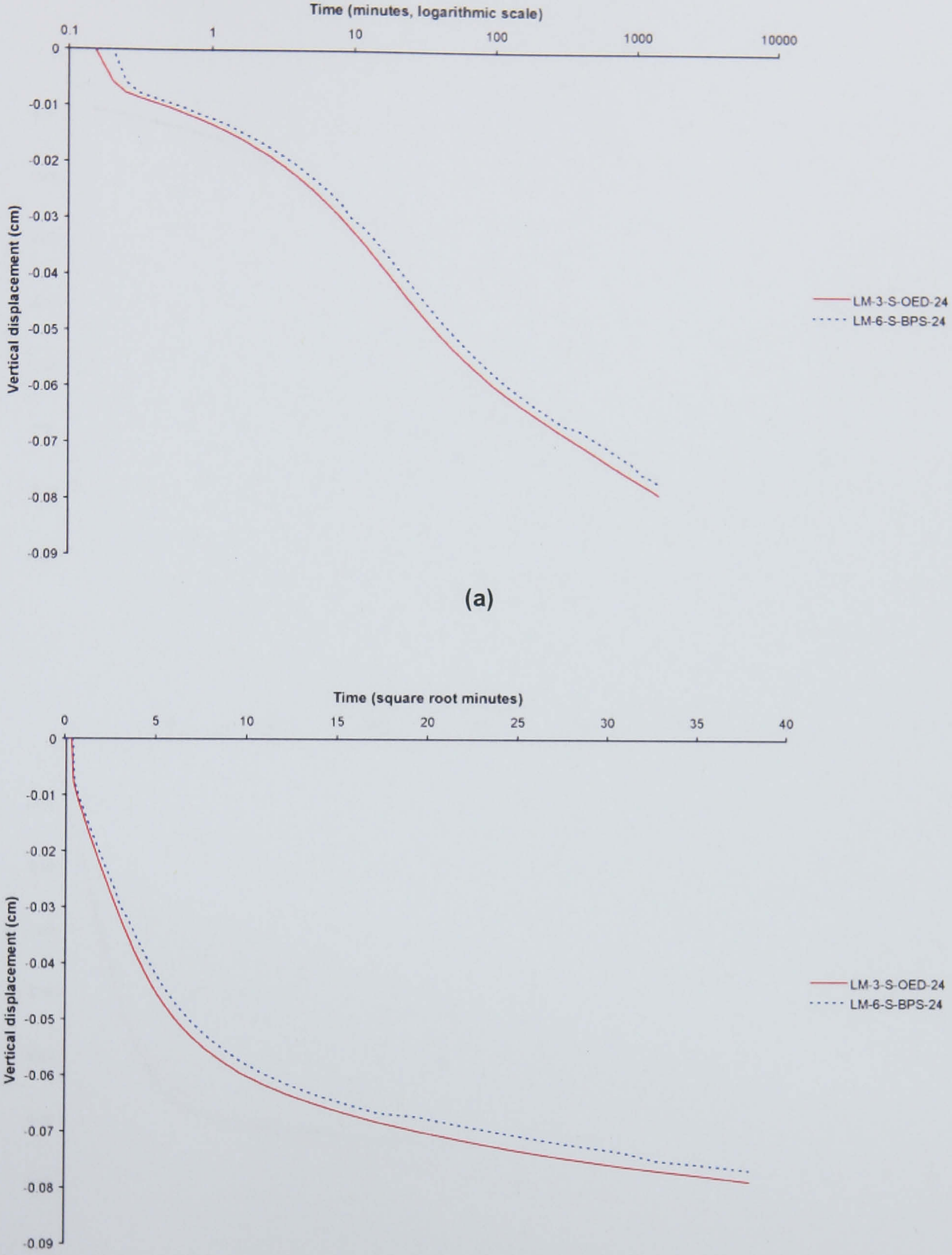

Figure 6.52 Time-vertical displacement plots for low marsh samples at an applied stress of 758 kPa (reloading). (a) logarithmic time-vertical displacement (b) square-root time-vertical displacement.

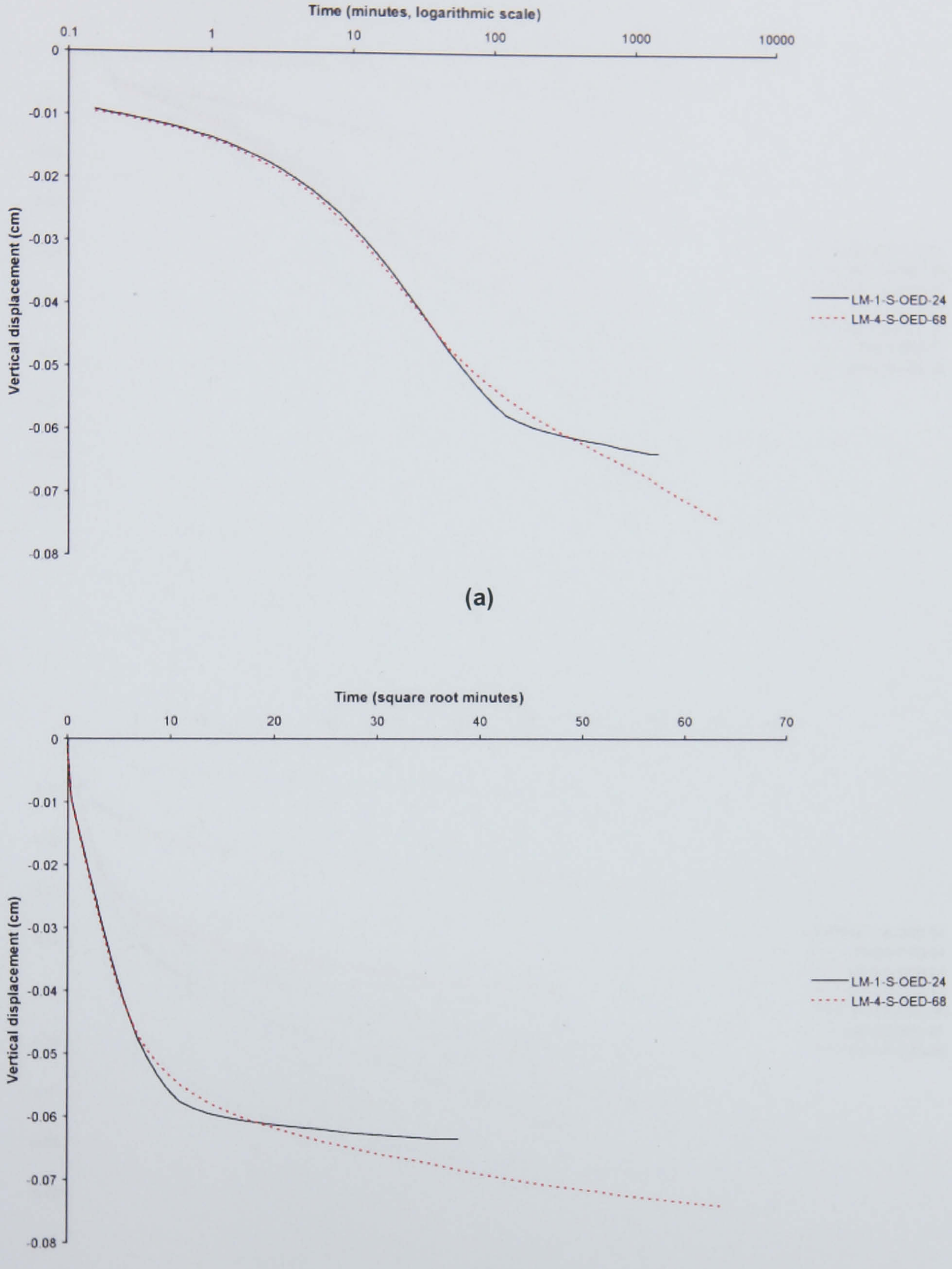

Figure 6.53 Time-vertical displacement plots for low marsh samples at an applied stress of 1570 kPa (reloading). (a) logarithmic time-vertical displacement (b) square-root time-vertical displacement.

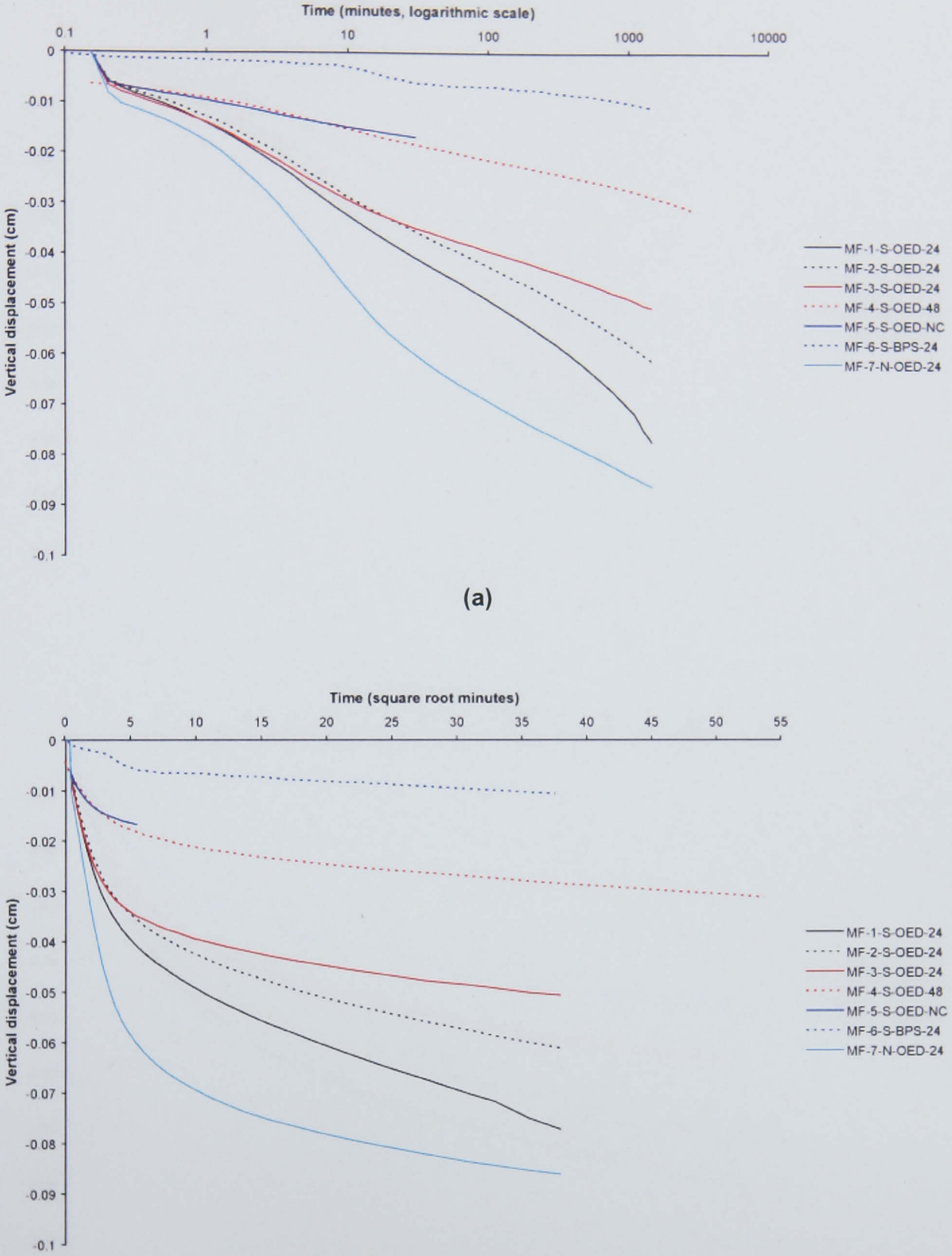

Figure 6.54 Time-vertical displacement plots for mudflat samples at an applied stress of 5 kPa (loading). (a) logarithmic time-vertical displacement (b) square-root time-vertical displacement.

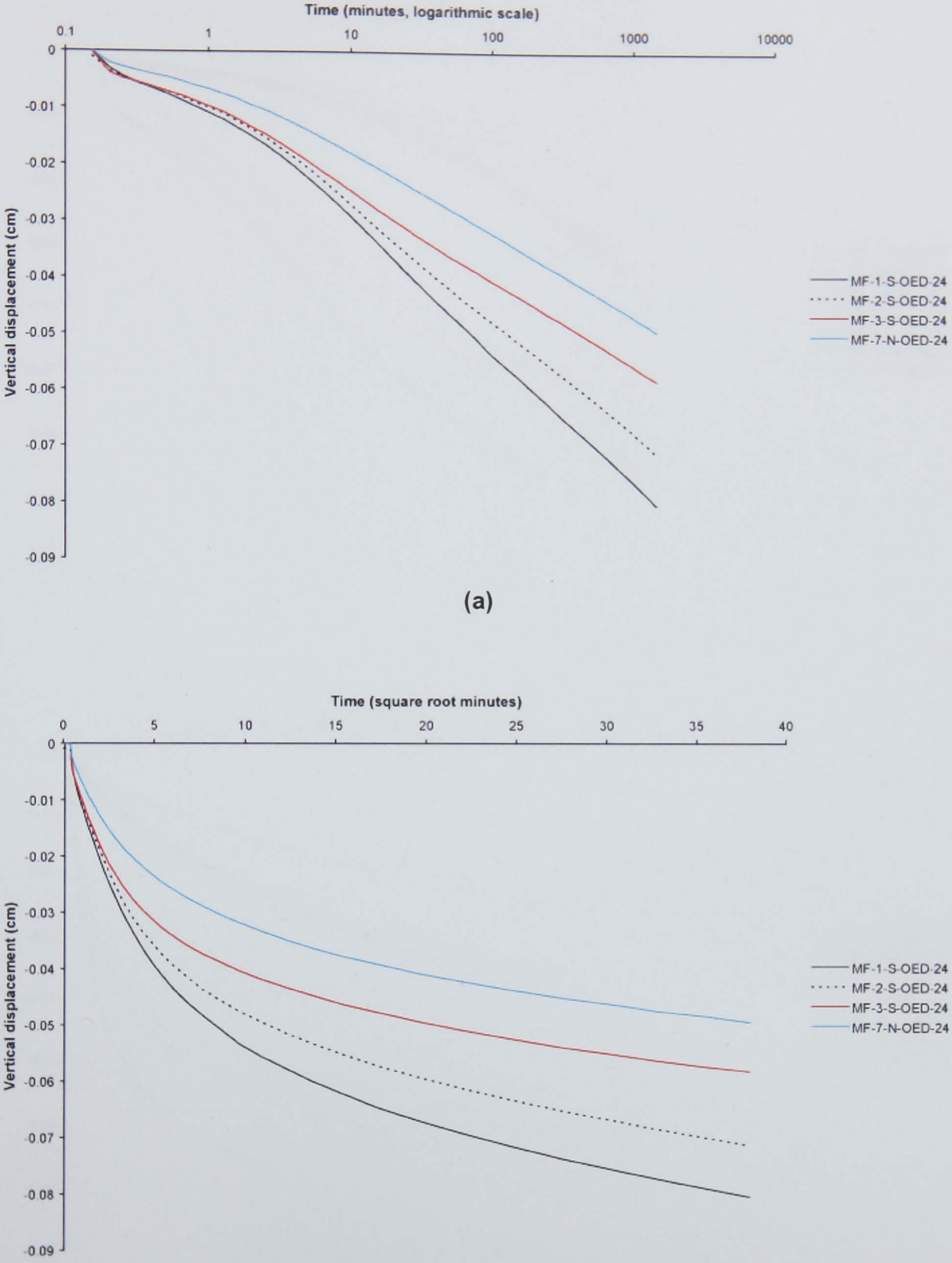

Figure 6.55 Time-vertical displacement plots for mudflat samples at an applied stress of 10 kPa (loading). (a) logarithmic time-vertical displacement (b) square-root time-vertical displacement.

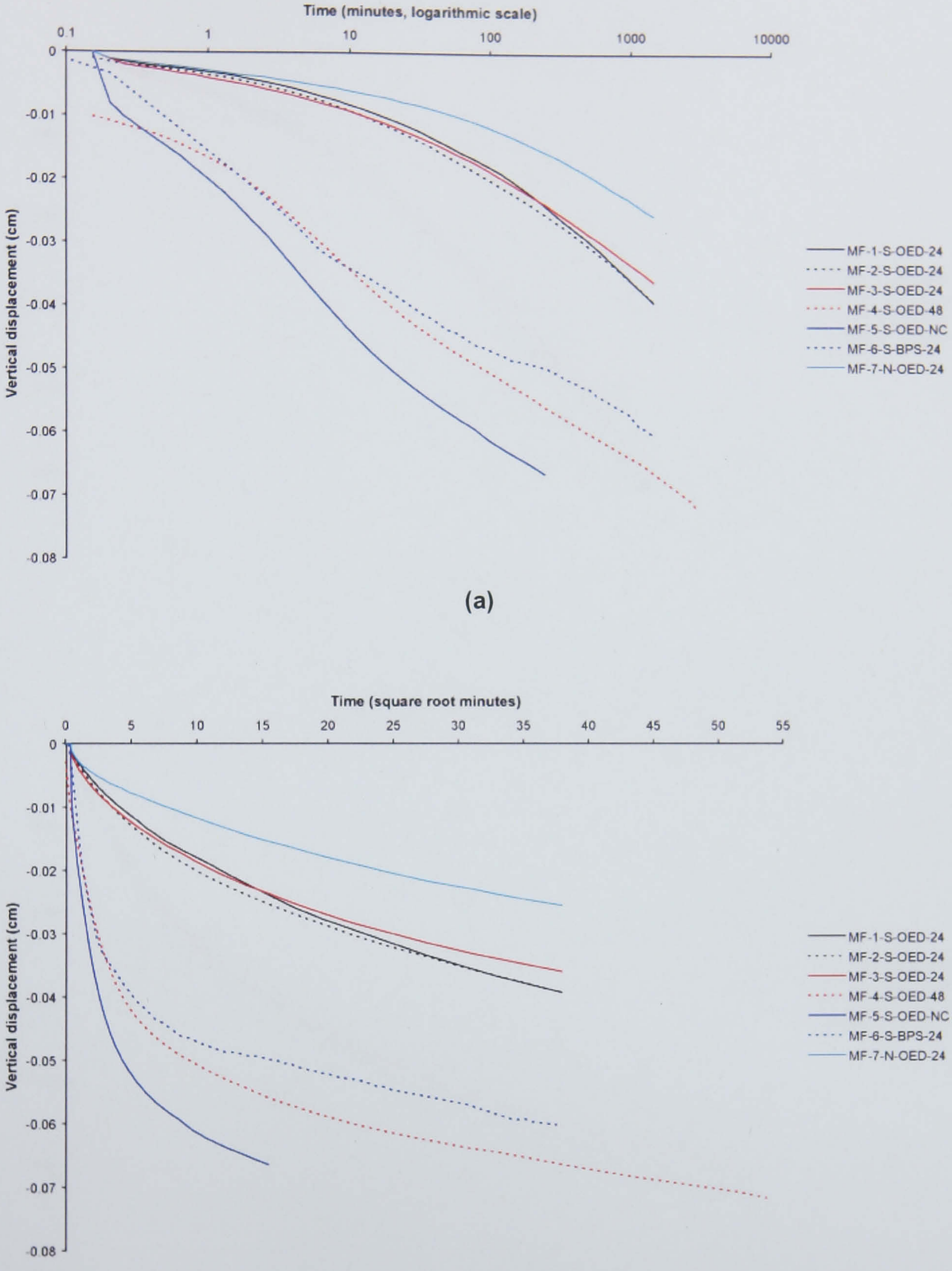

Figure 6.56 Time-vertical displacement plots for mudflat samples at an applied stress of 14 kPa (loading). (a) logarithmic time-vertical displacement (b) square-root time-vertical displacement.

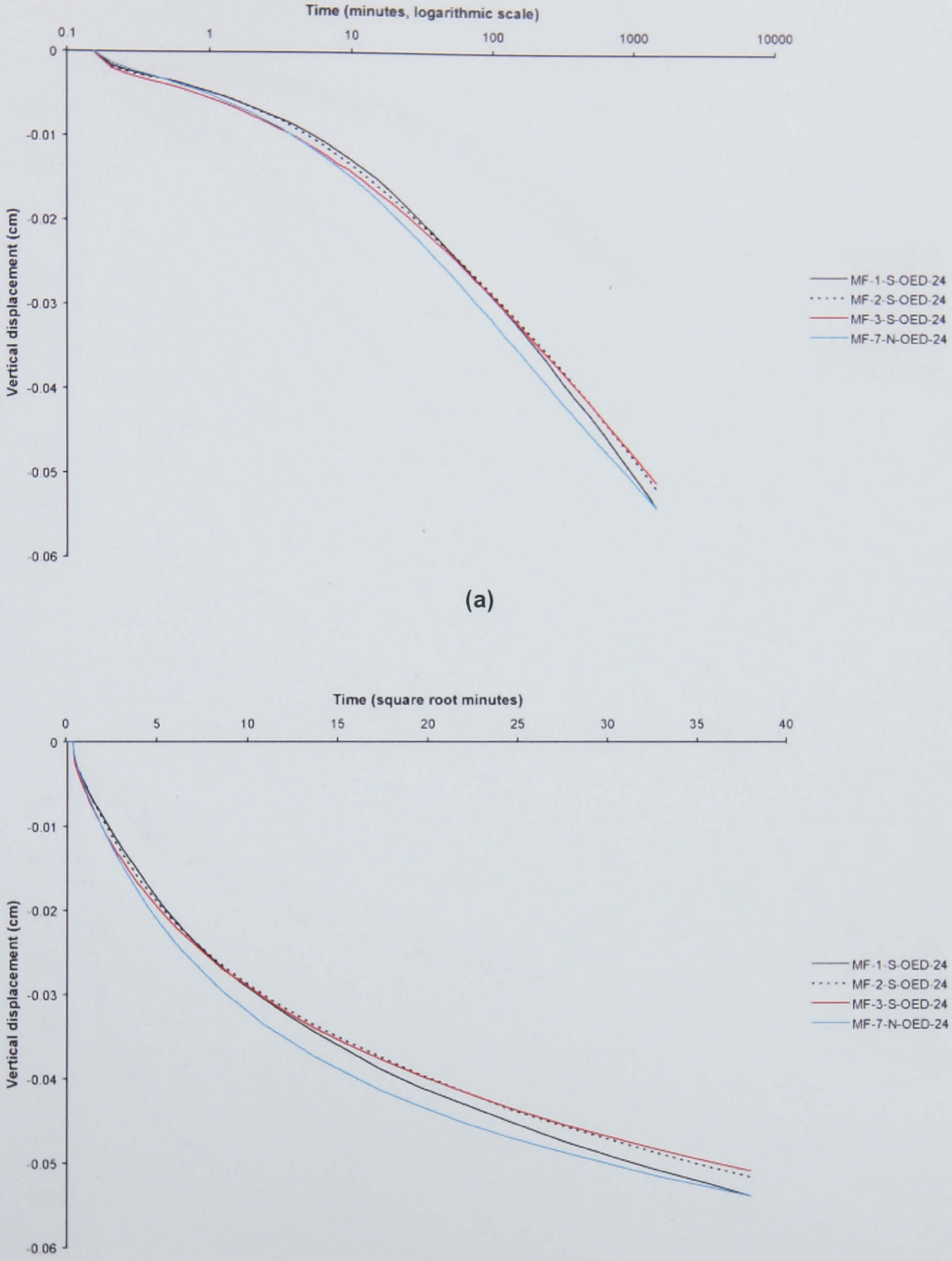

Figure 6.57 Time-vertical displacement plots for mudflat samples at an applied stress of 20 kPa (loading). (a) logarithmic time-vertical displacement (b) square-root time-vertical displacement.

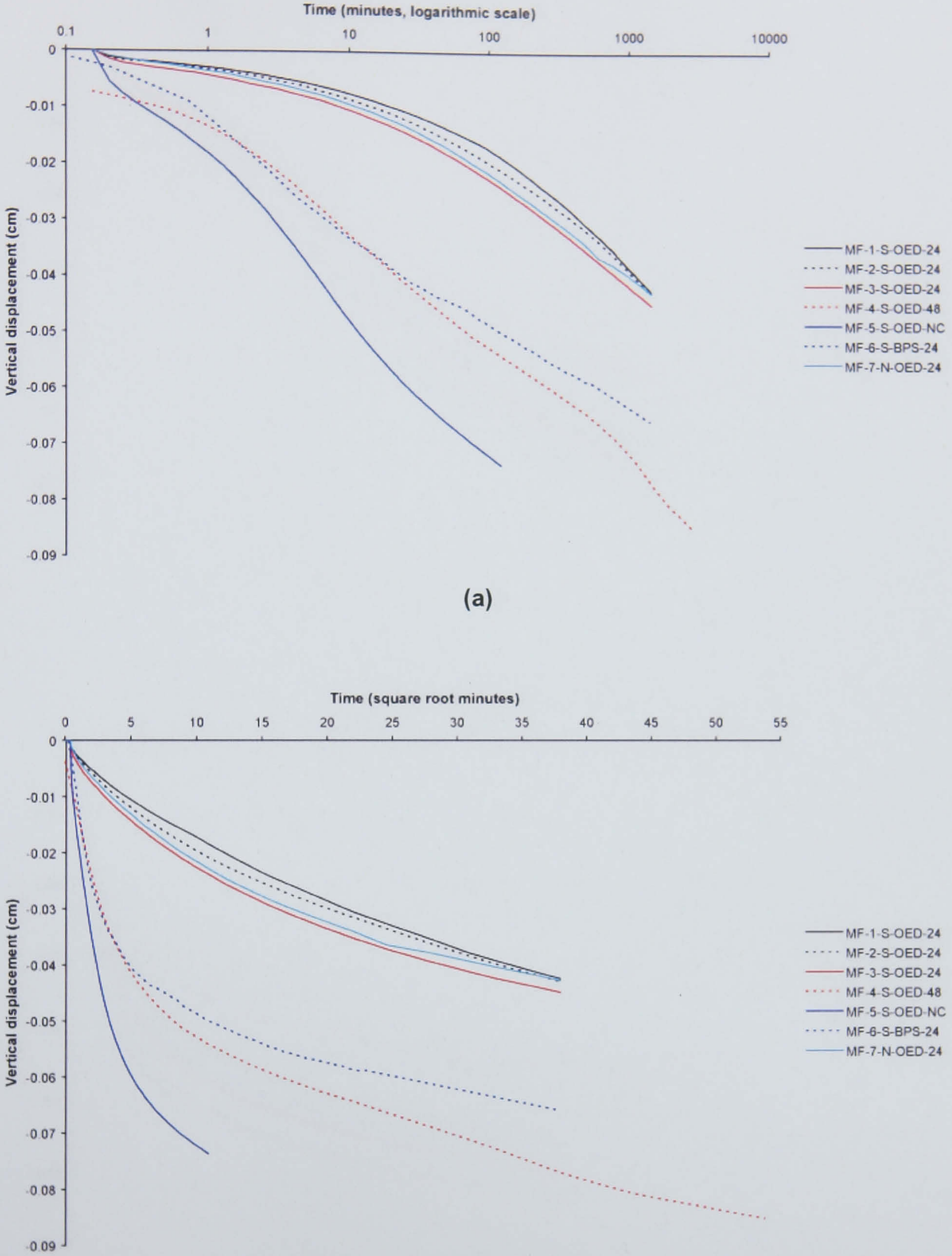

Figure 6.58 Time-vertical displacement plots for mudflat samples at an applied stress of 26 kPa (loading). (a) logarithmic time-vertical displacement (b) square-root time-vertical displacement.

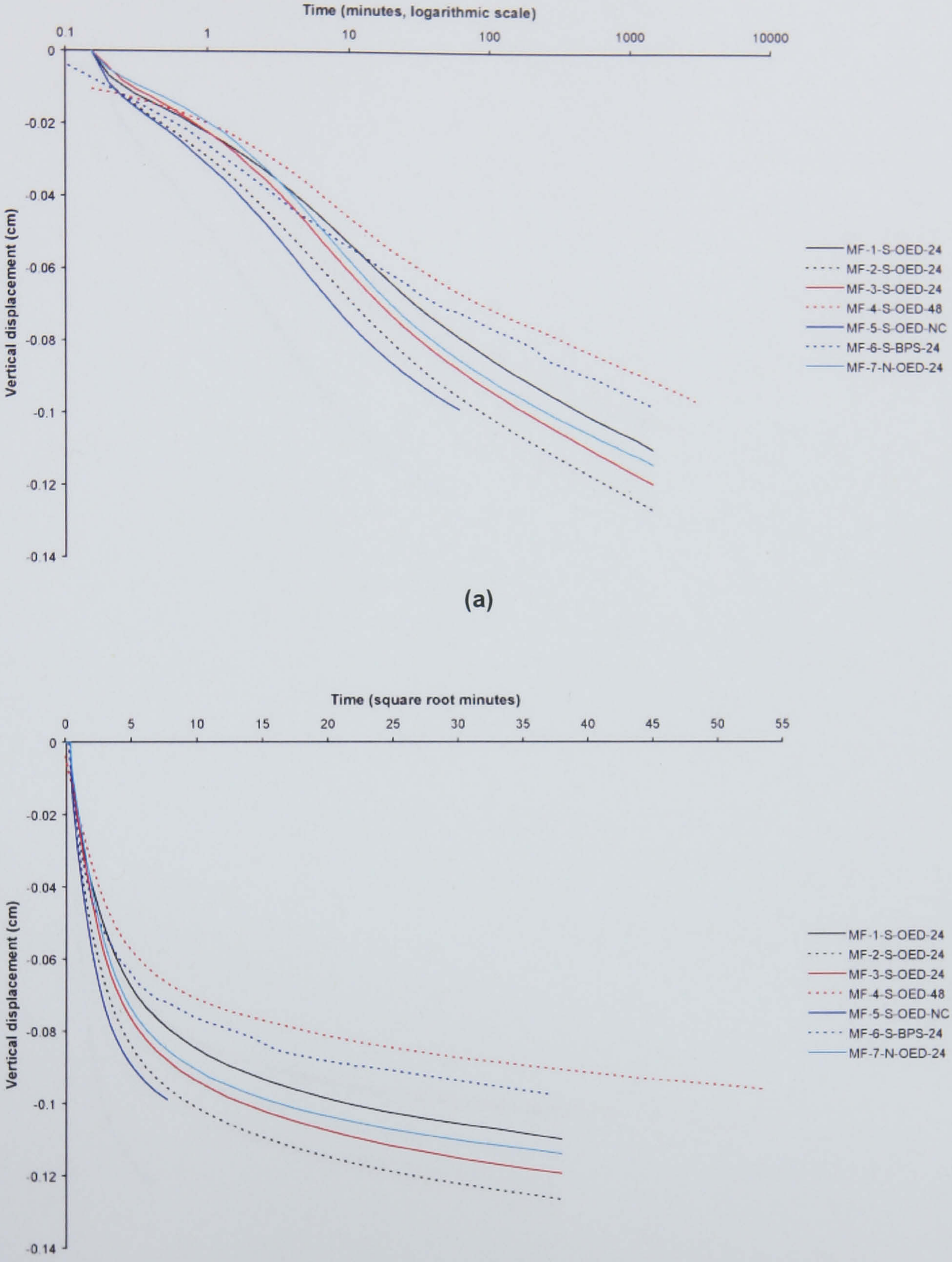

Figure 6.59 Time-vertical displacement plots for mudflat samples at an applied stress of 50 kPa (loading). (a) logarithmic time-vertical displacement (b) square-root time-vertical displacement.

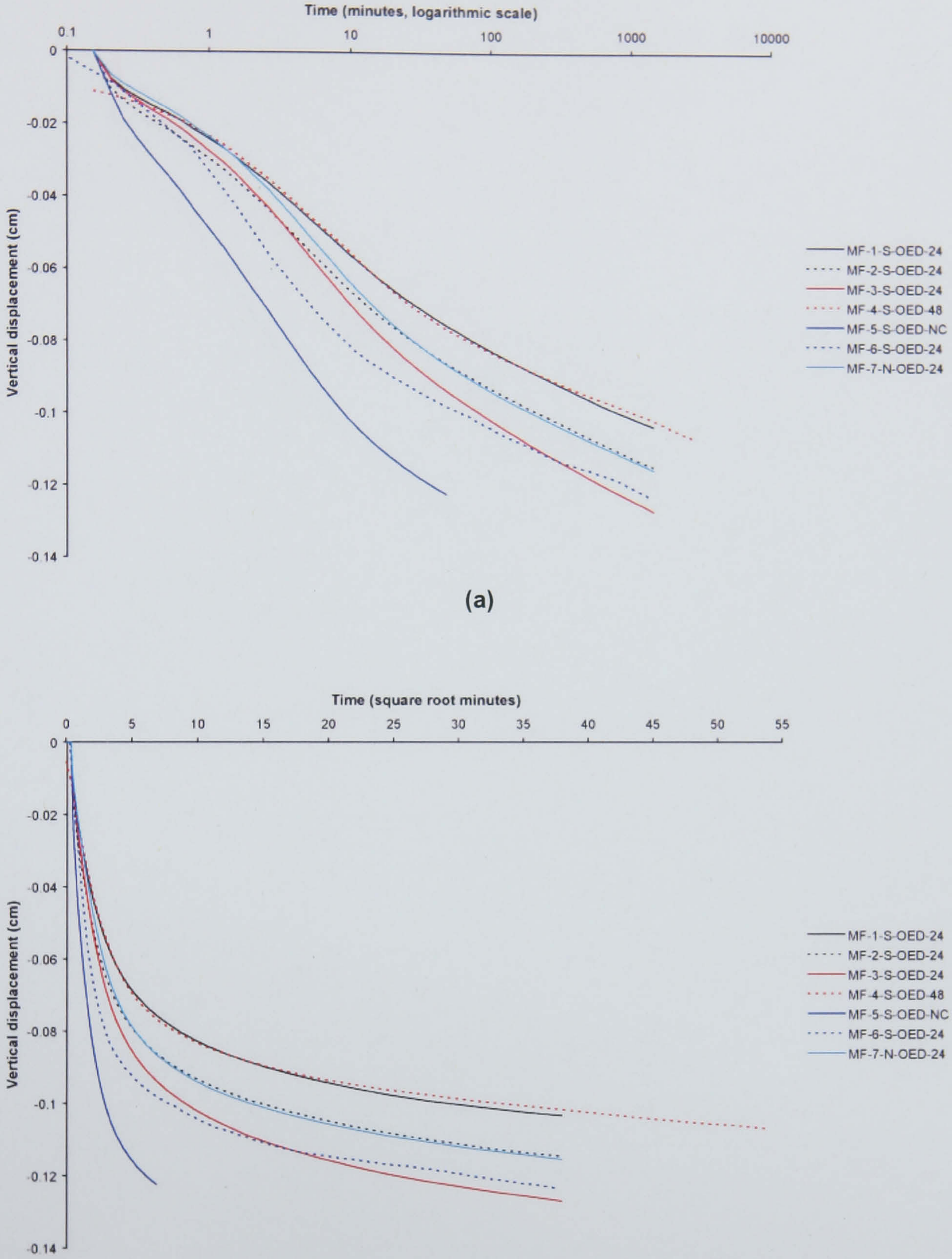

Figure 6.60 Time-vertical displacement plots for mudflat samples at an applied stress of 99 kPa (loading). (a) logarithmic time-vertical displacement (b) square-root time-vertical displacement.

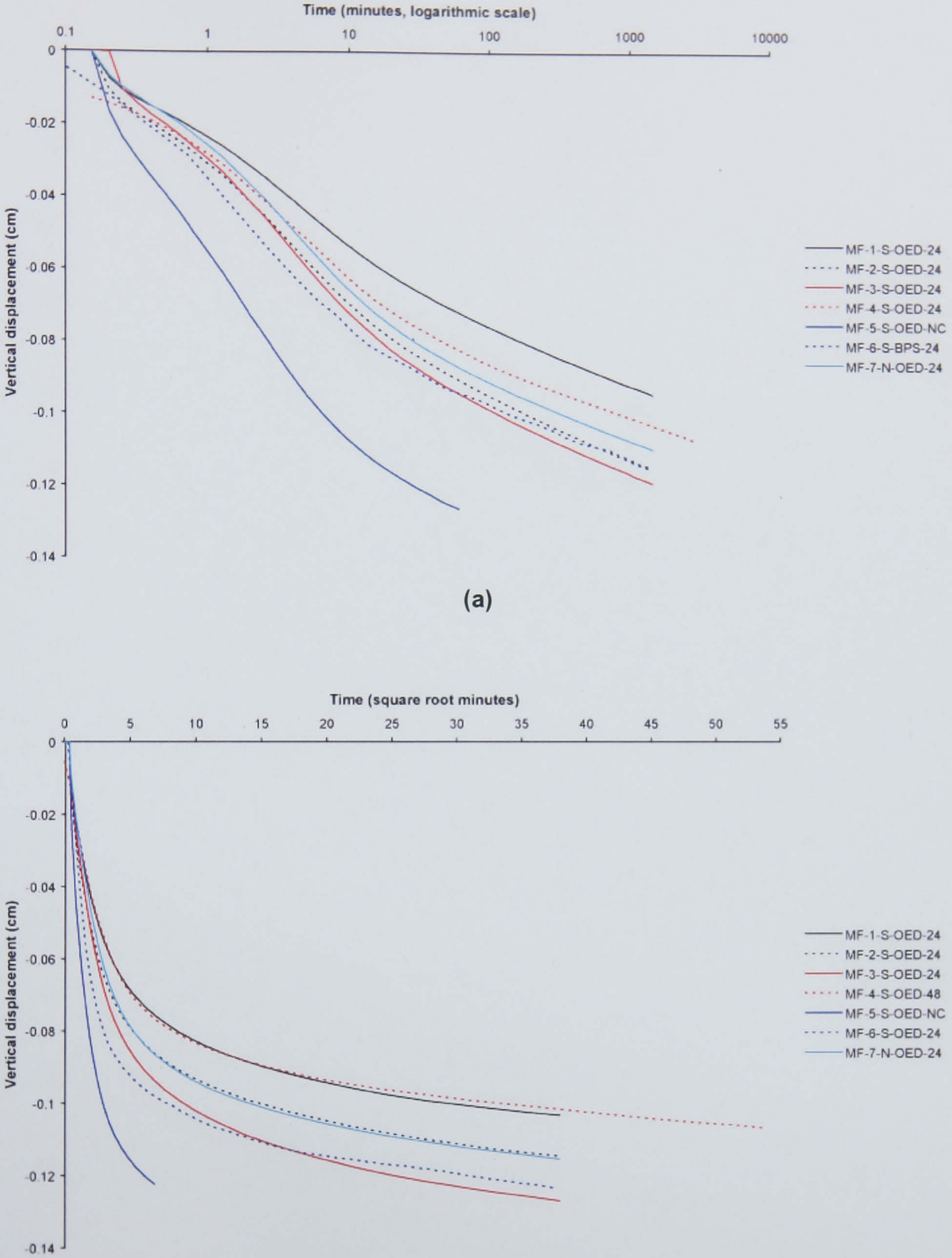

Figure 6.61 Time-vertical displacement plots for mudflat samples at an applied stress of 197 kPa (loading). (a) logarithmic time-vertical displacement (b) square-root time-vertical displacement.

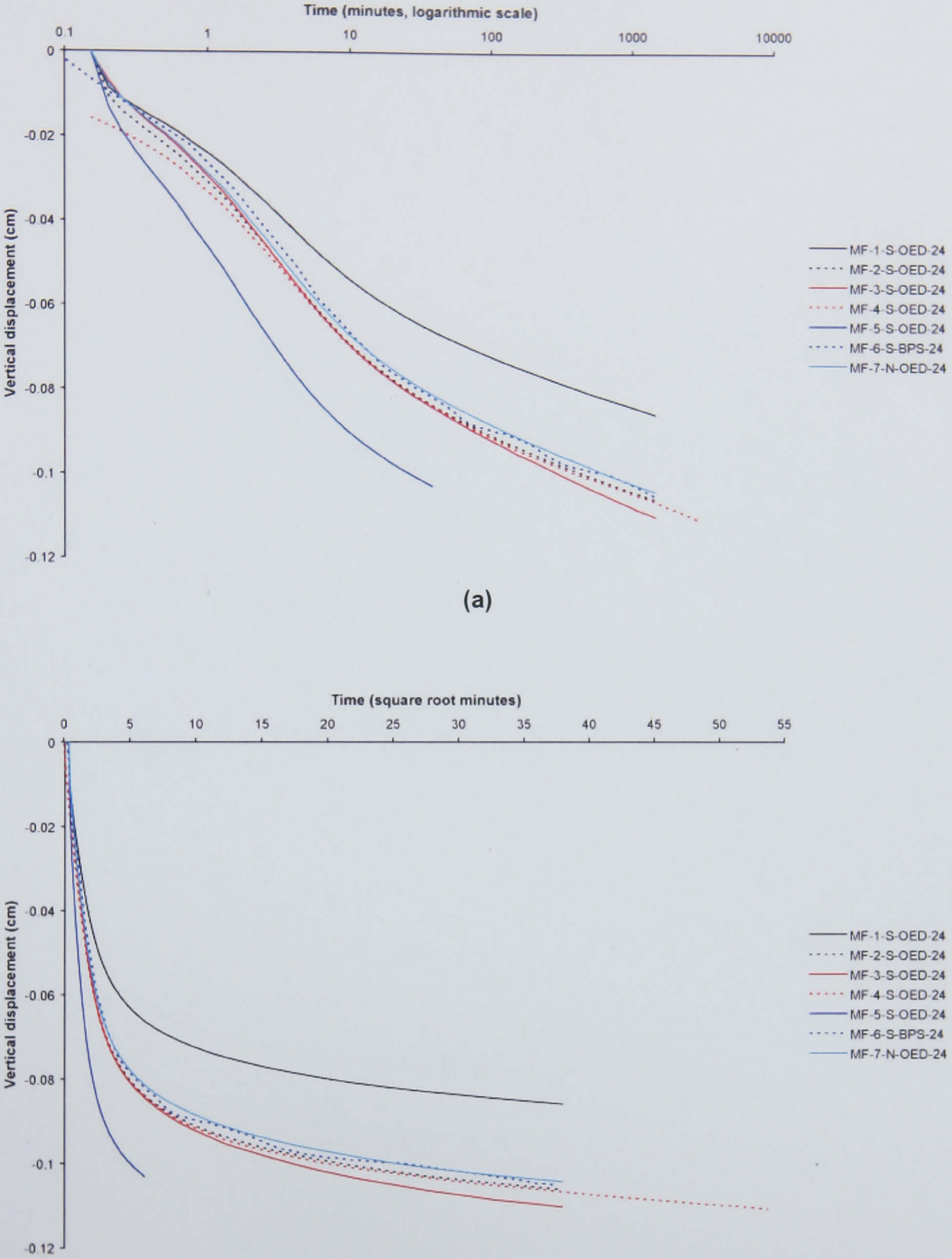

Figure 6.62 Time-vertical displacement plots for mudflat samples at an applied stress of 393 kPa (loading). (a) logarithmic time-vertical displacement (b) square-root time-vertical displacement.

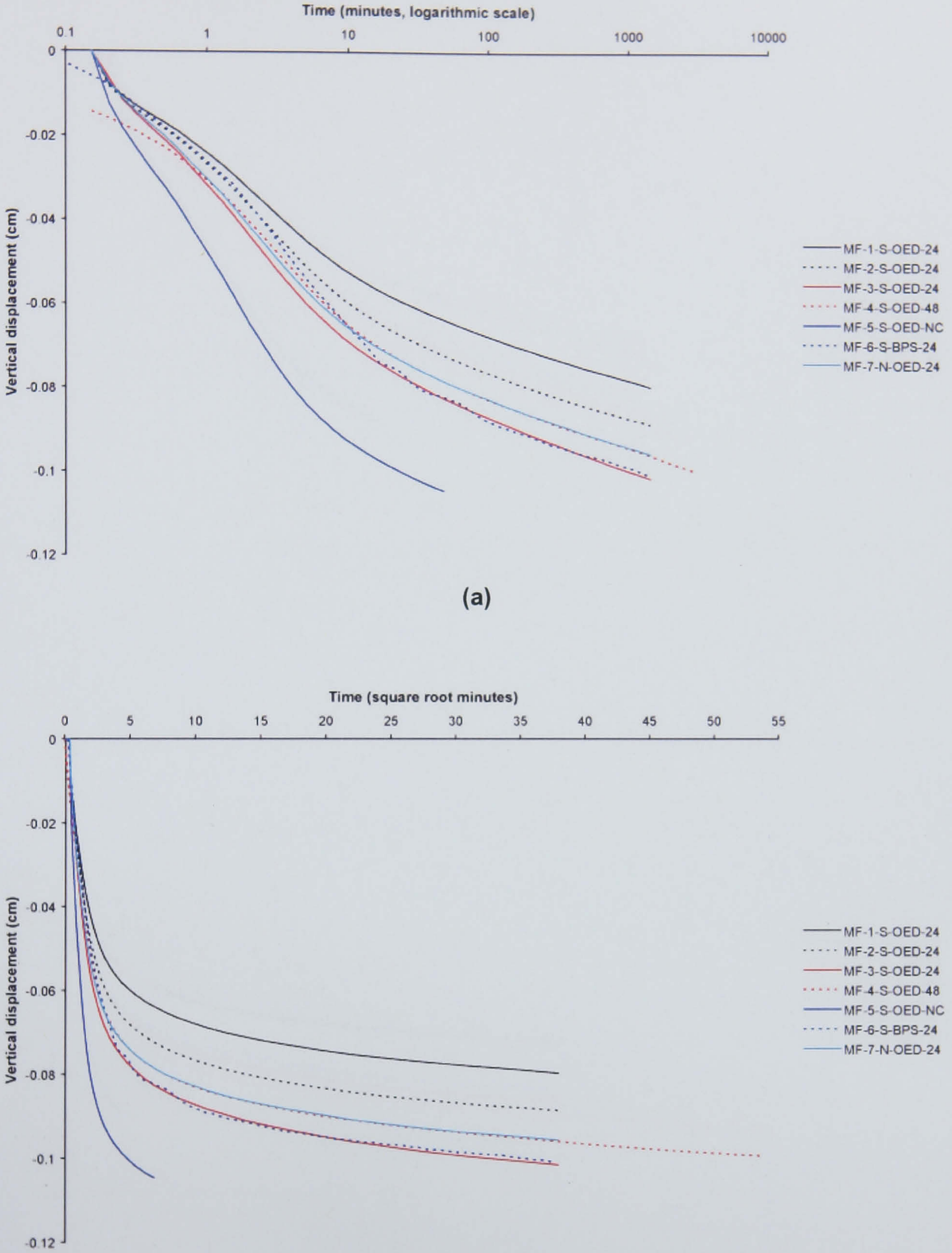

(a)

(b)

Figure 6.63 Time-vertical displacement plots for mudflat samples at an applied stress of 785 kPa (loading). (a) logarithmic time-vertical displacement (b) square-root time-vertical displacement.

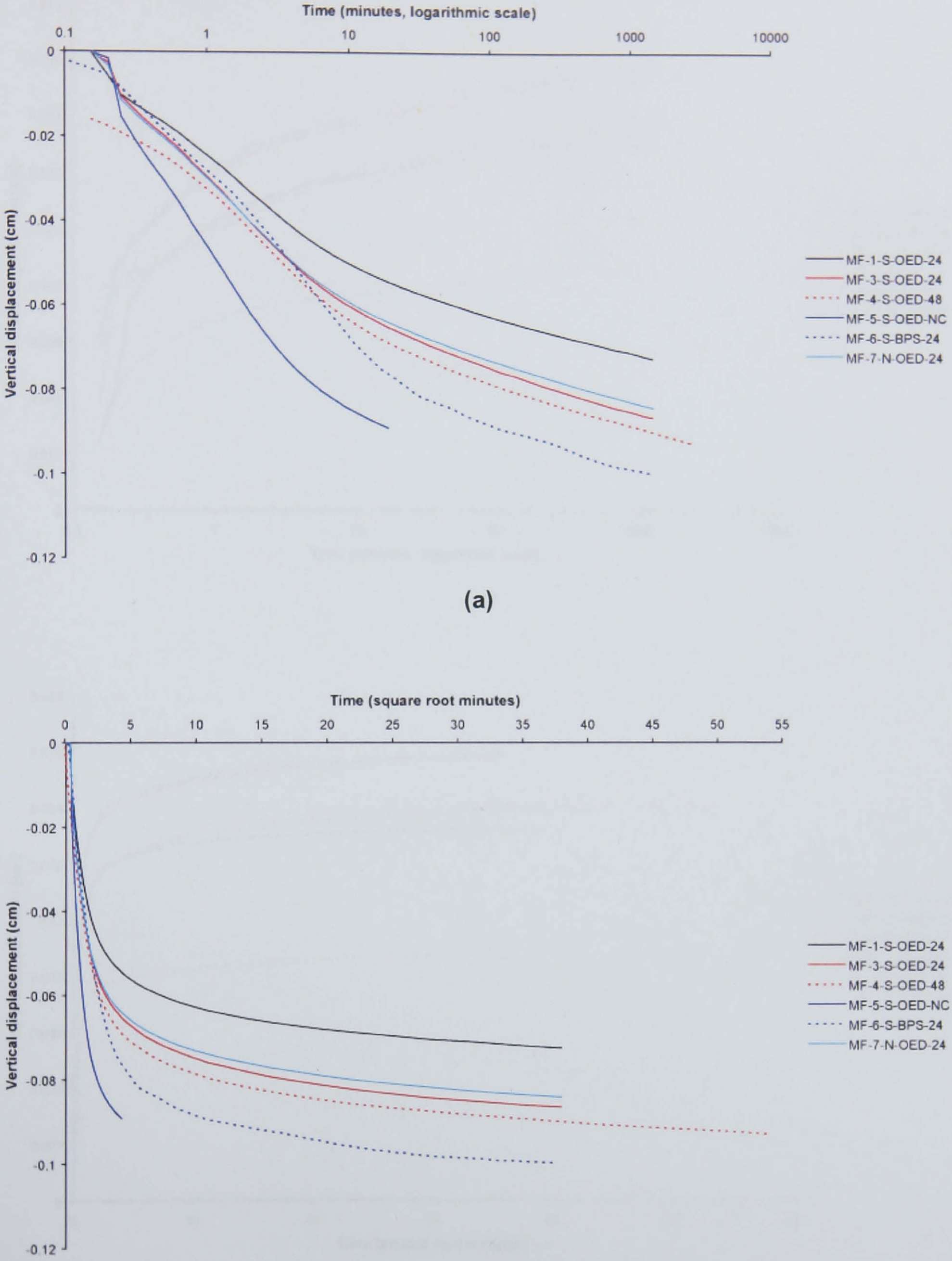

Figure 6.64 Time-vertical displacement plots for mudflat samples at an applied stress of 1570 kPa (loading). (a) logarithmic time-vertical displacement (b) square-root time-vertical displacement.

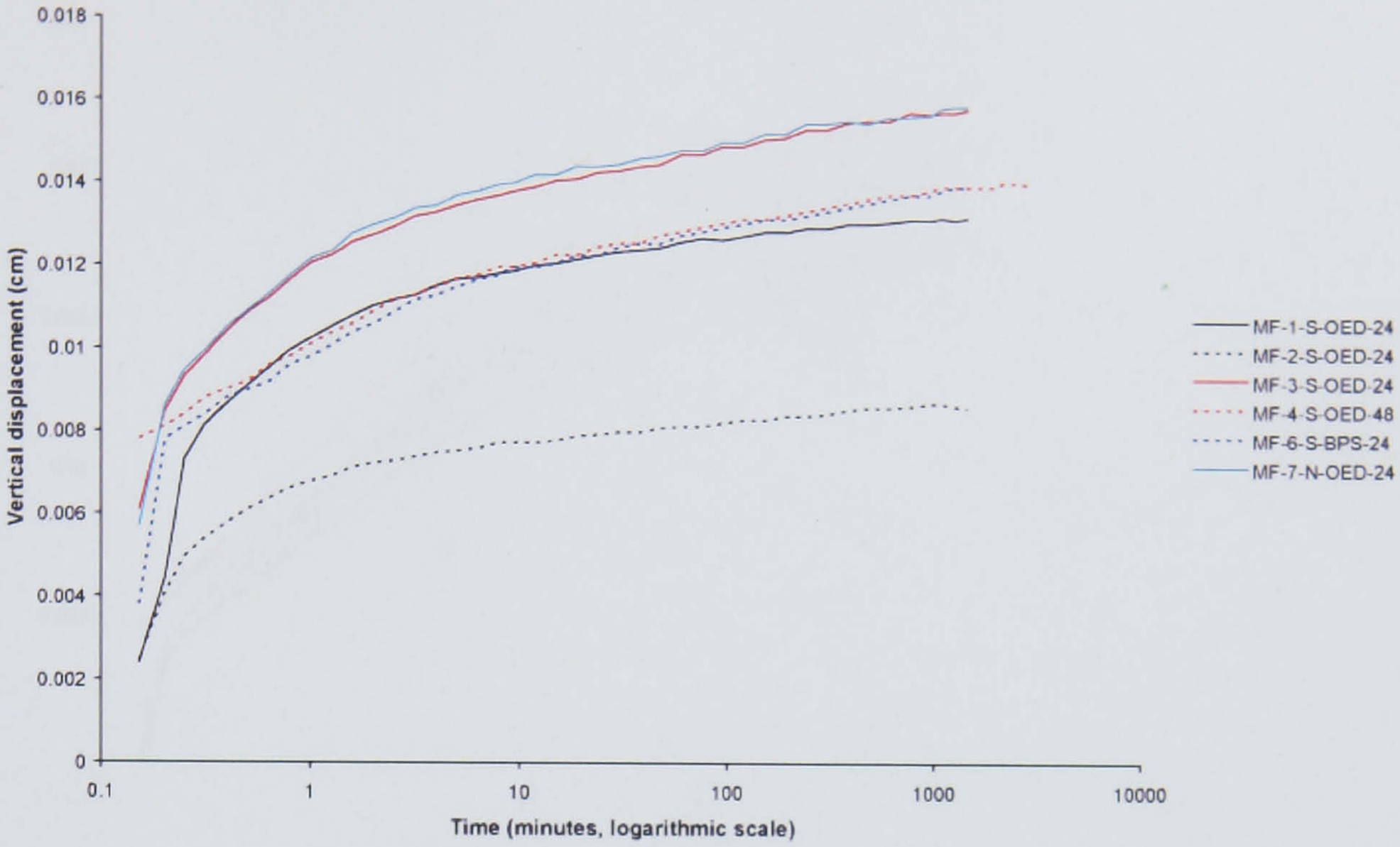

(a)

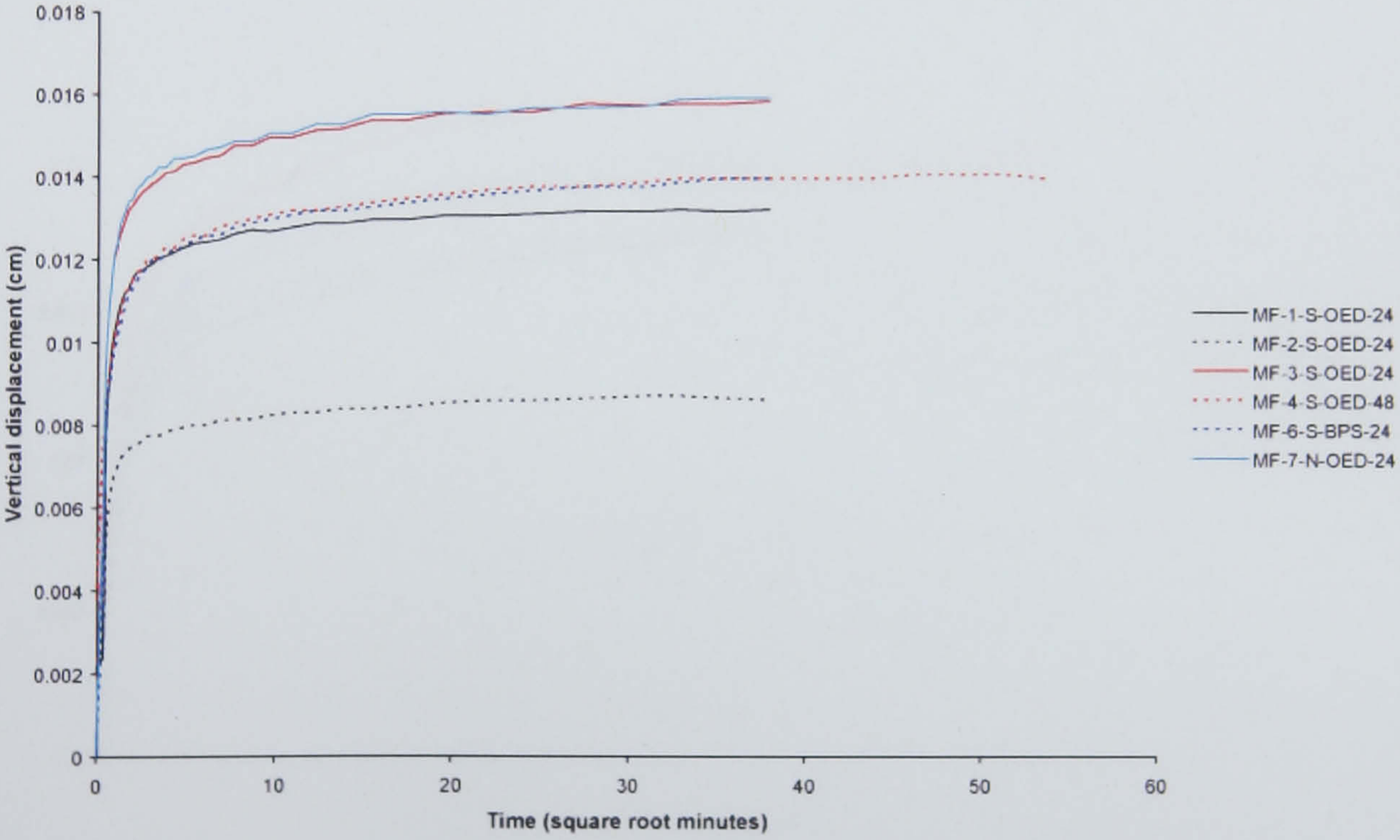

(b)

Figure 6.65 Time-vertical displacement plots for mudflat samples at an applied stress of 516 kPa (unloading). (a) logarithmic time-vertical displacement (b) square-root time-vertical displacement.

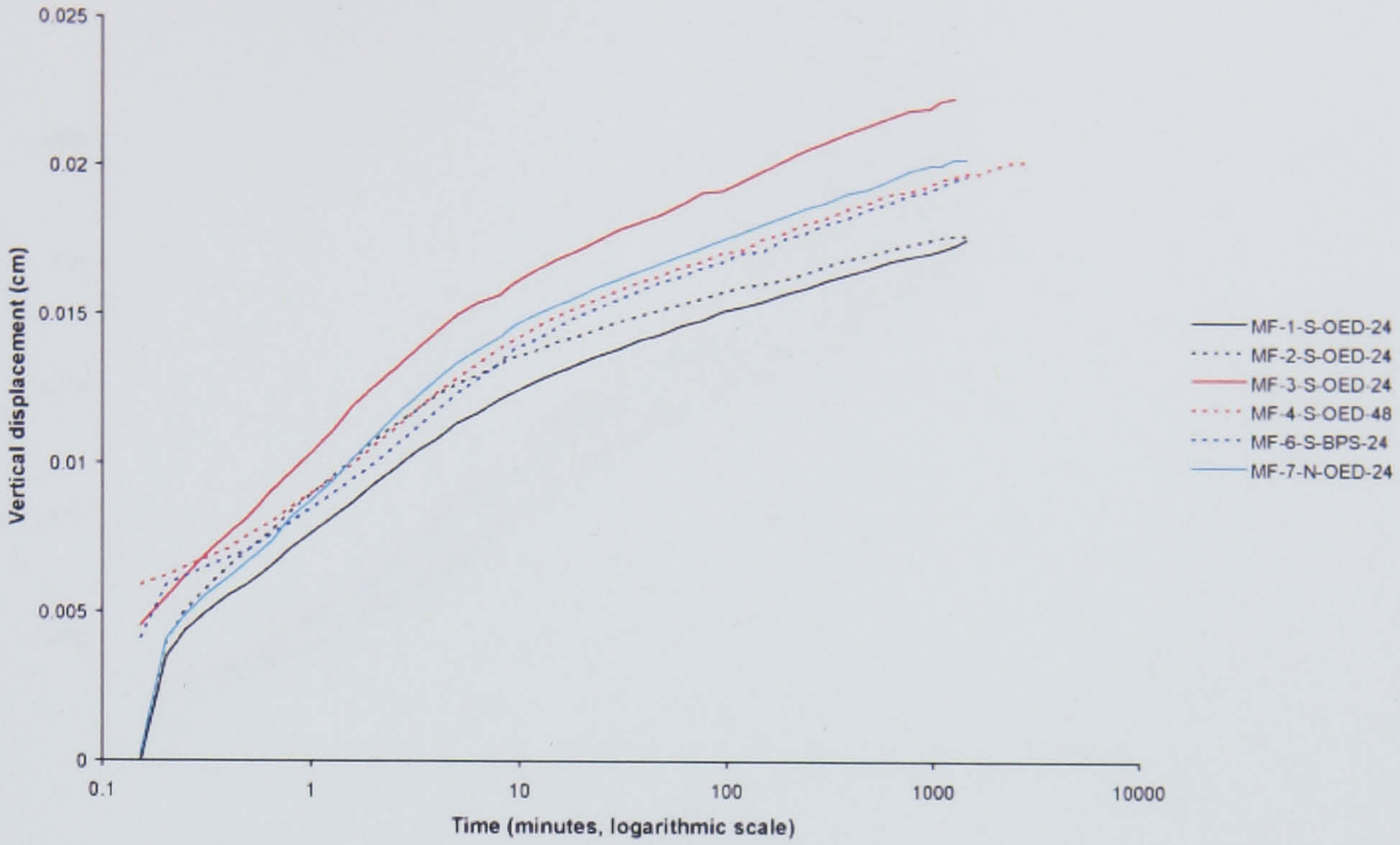

(a)

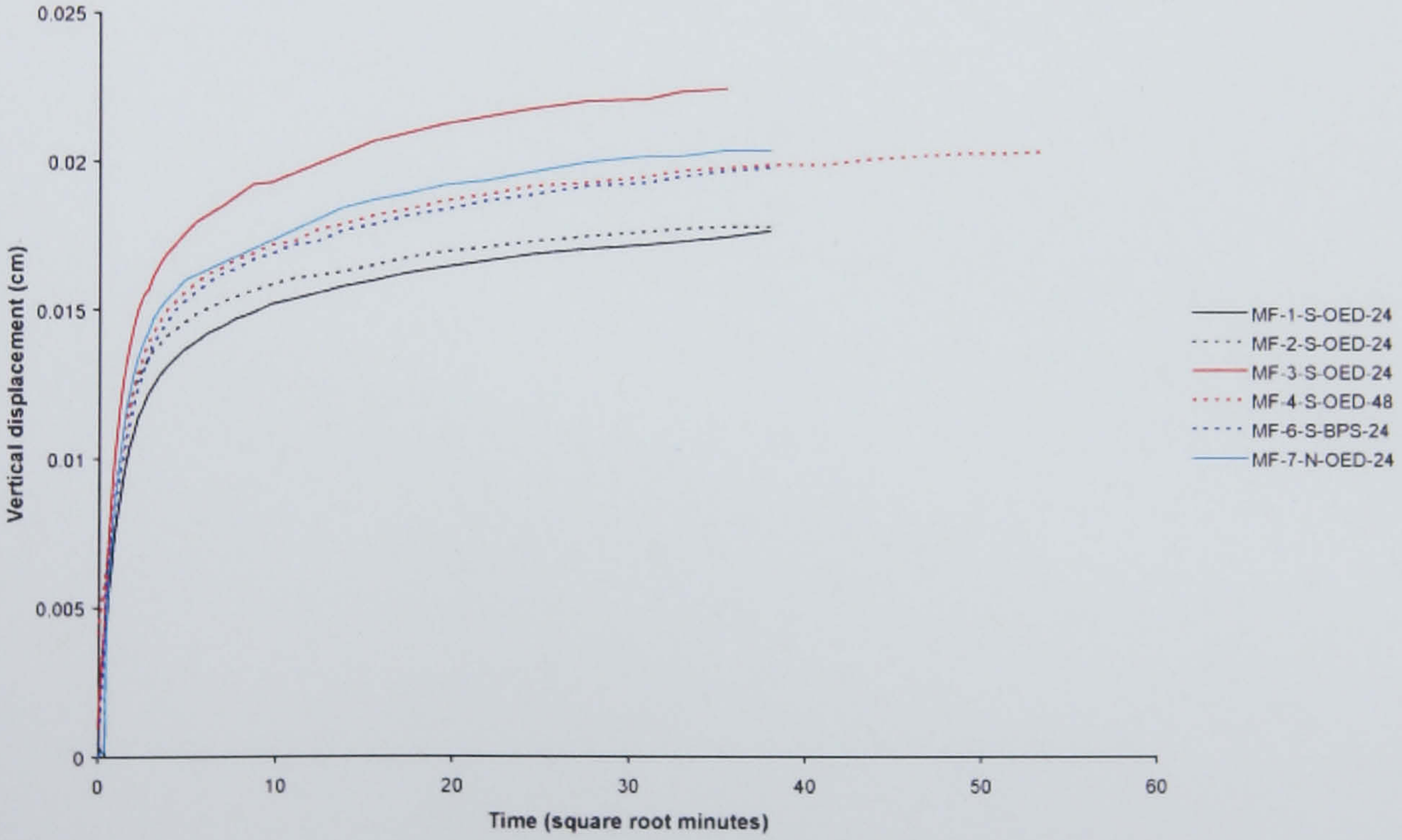

(b)

Figure 6.66 Time-vertical displacement plots for mudflat samples at an applied stress of 172 kPa (loading). (a) logarithmic time-vertical displacement (b) square-root time-vertical displacement.

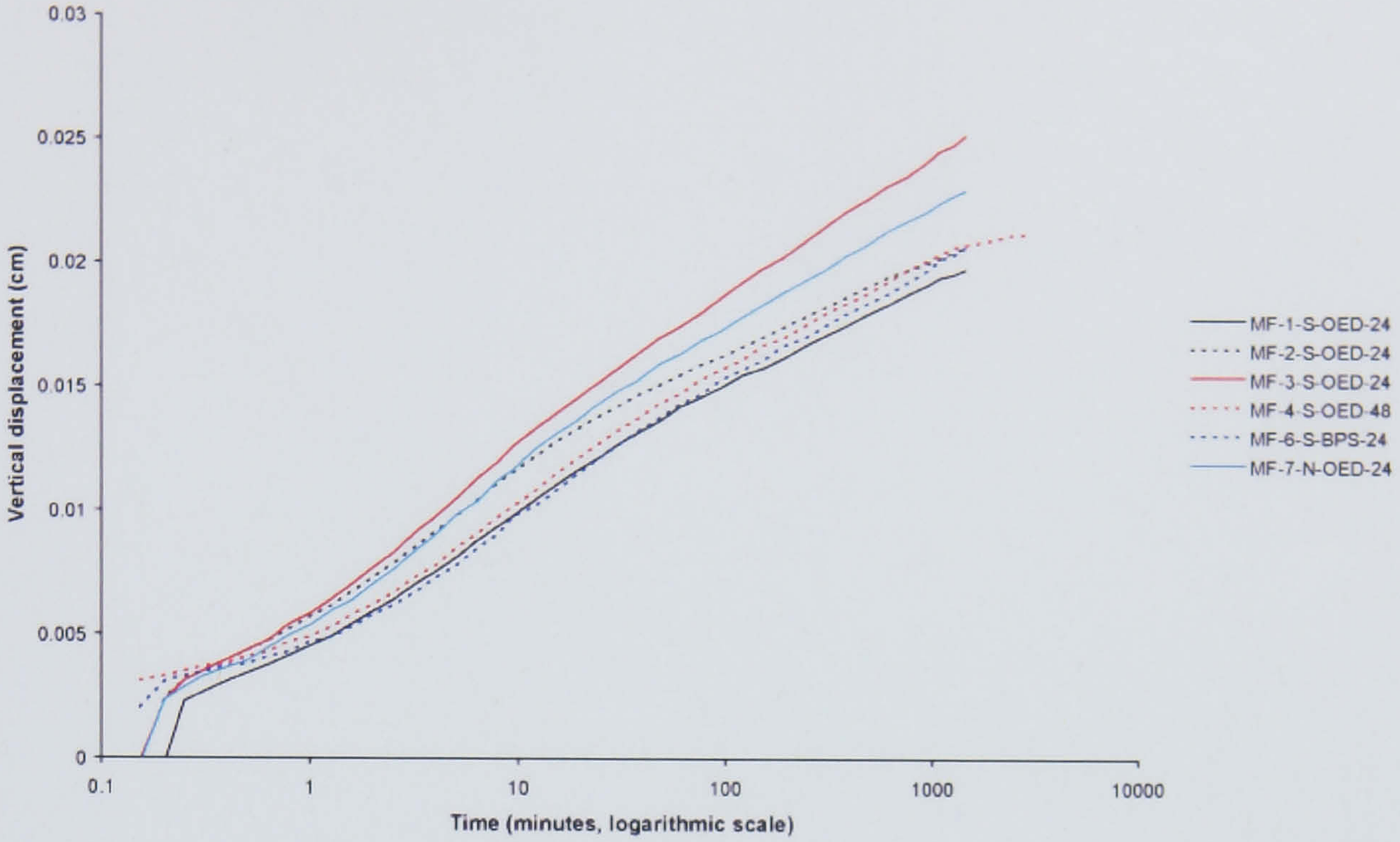

(a)

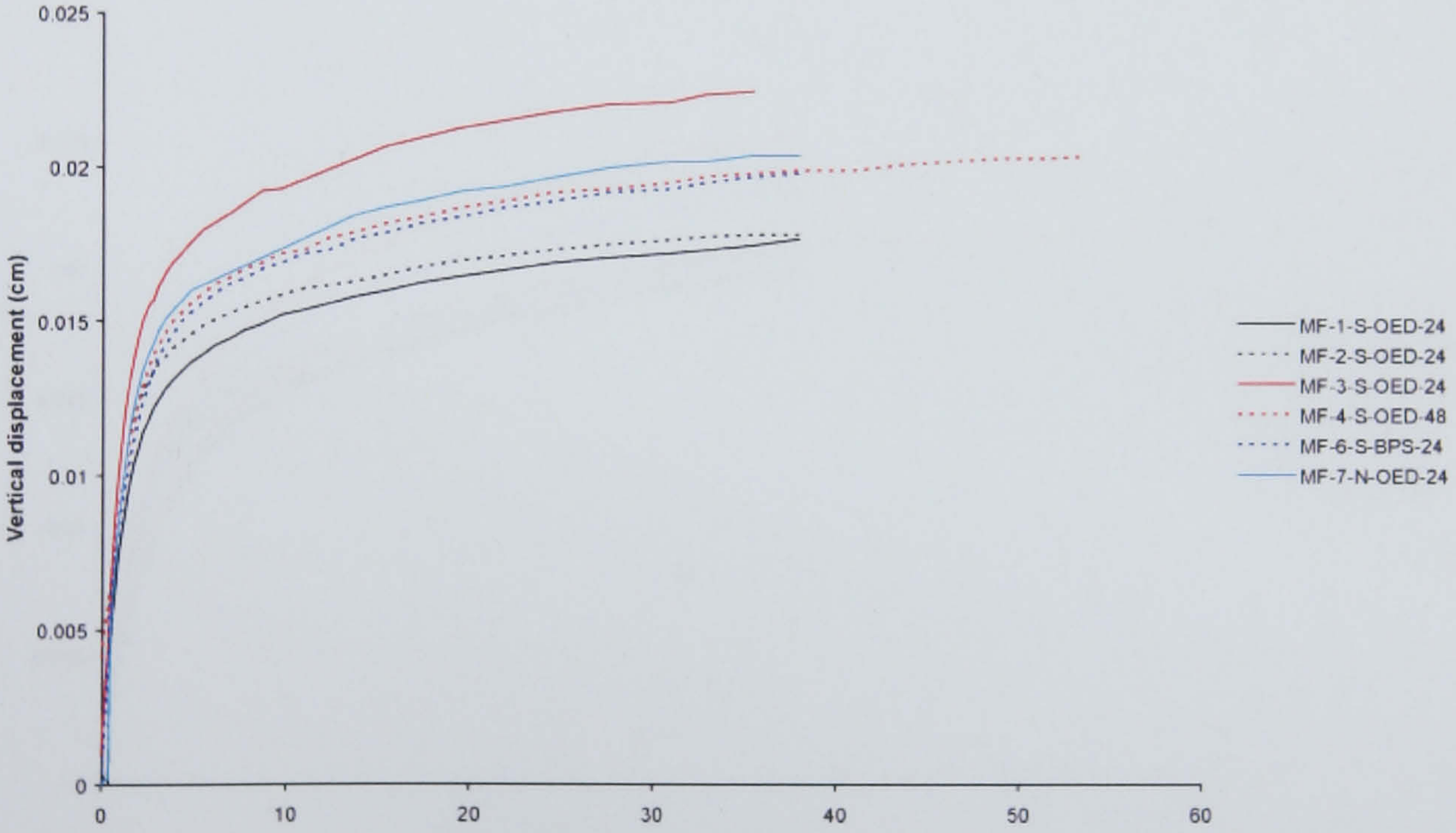

(b)

Figure 6.67 Time-vertical displacement plots for mudflat samples at an applied stress of 172 kPa (unloading). (a) logarithmic time-vertical displacement (b) square-root time-vertical displacement.

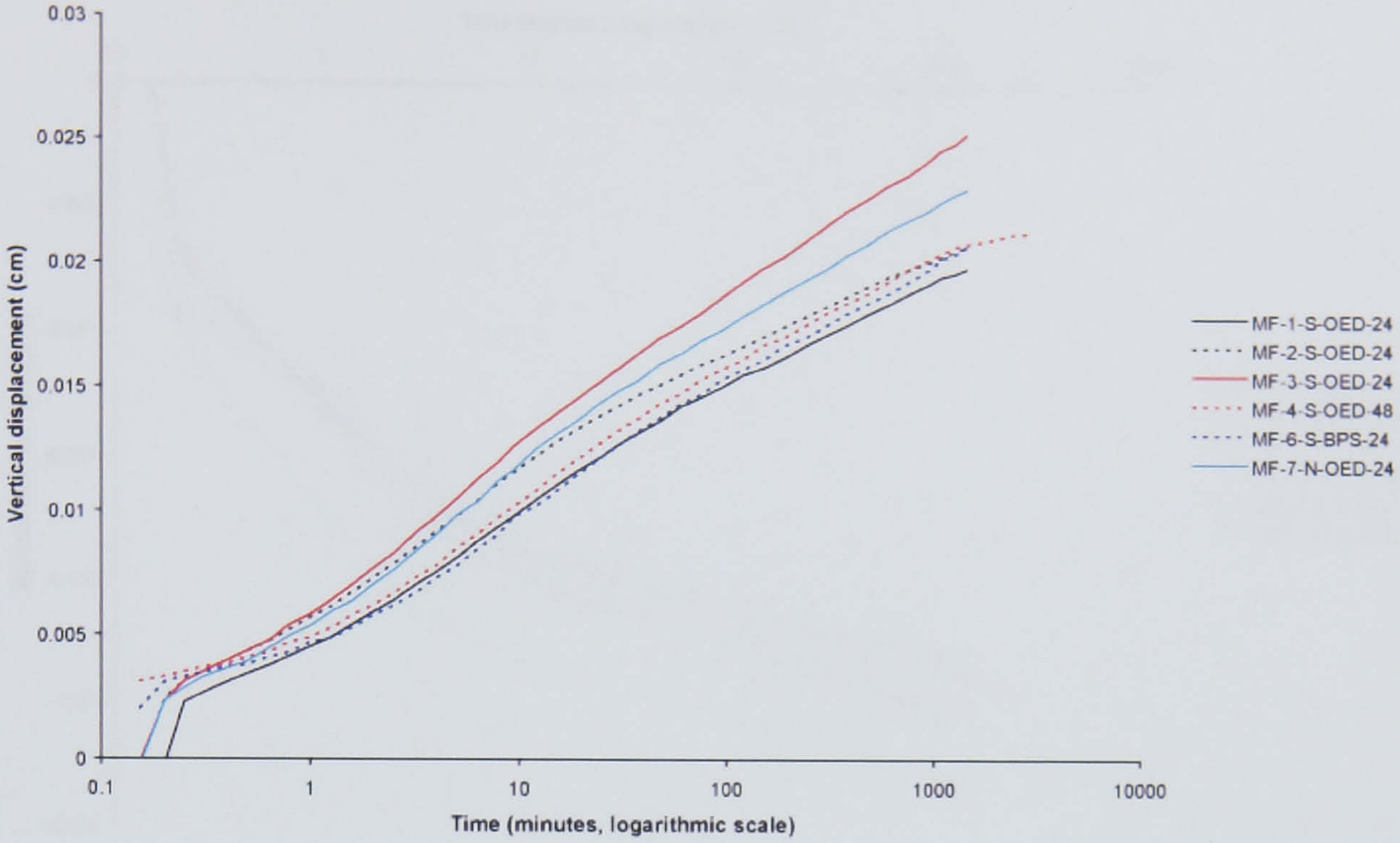

(a)

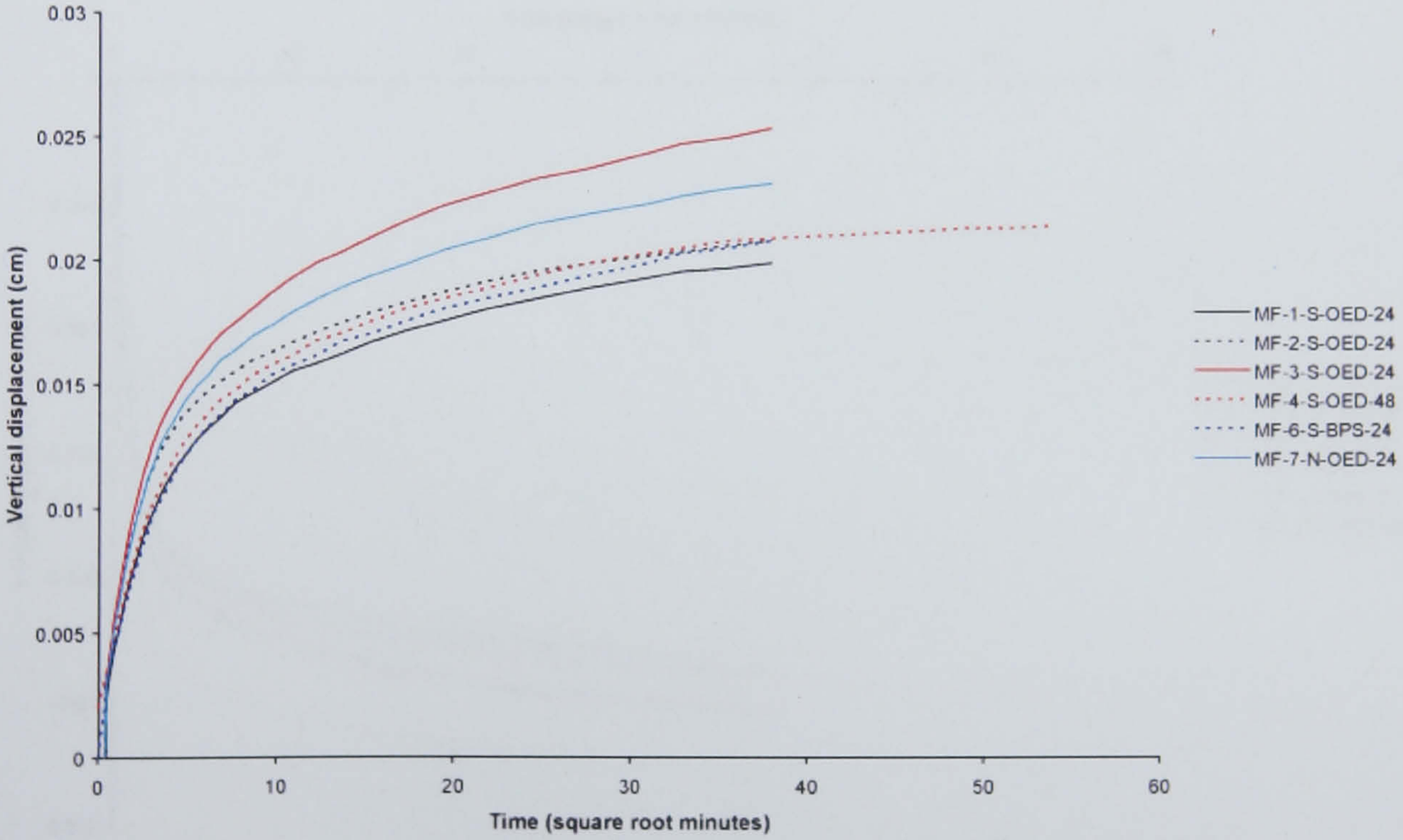

(b)

Figure 6.68 Time-vertical displacement plots for mudflat samples at an applied stress of 62 kPa (unloading). (a) logarithmic time-vertical displacement (b) square-root time-vertical displacement.

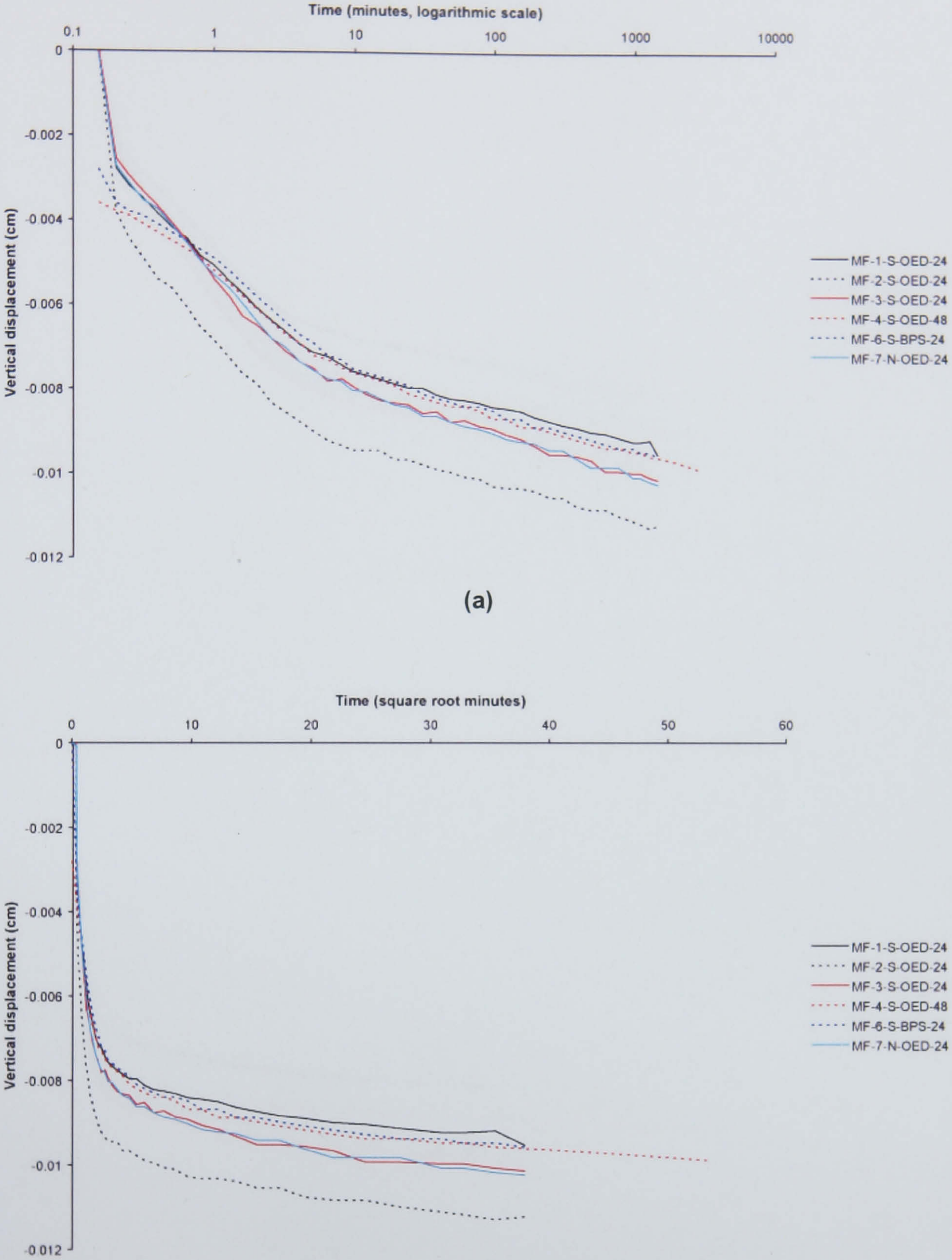

Figure 6.69 Time-vertical displacement plots for mudflat samples at an applied stress of 172 kPa (reloading). (a) logarithmic time-vertical displacement (b) square-root time-vertical displacement.

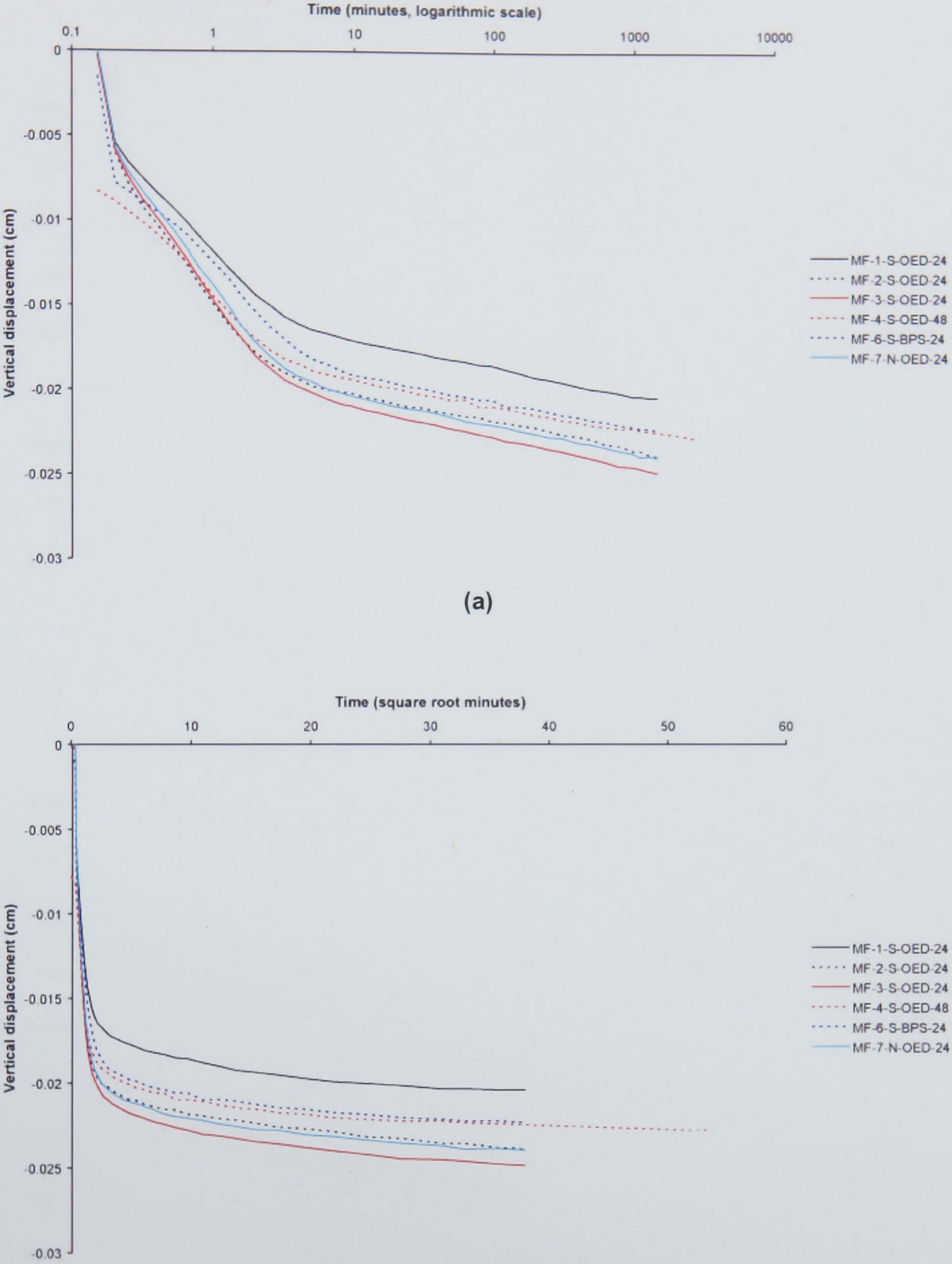

Figure 6.70 Time-vertical displacement plots for mudflat samples at an applied stress of 516 kPa (reloading). (a) logarithmic time-vertical displacement (b) square-root time-vertical displacement.

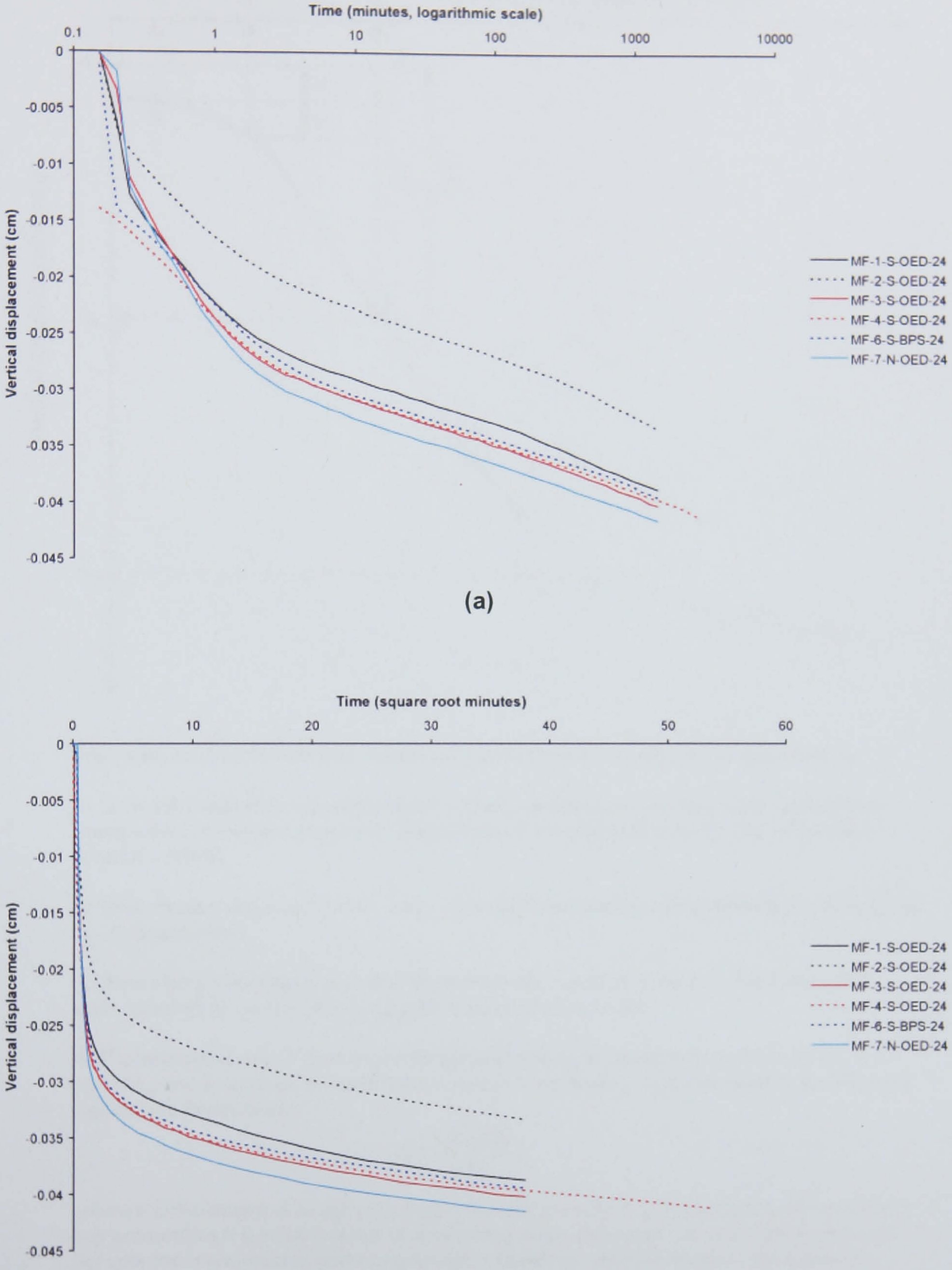

Figure 6.71 Time-vertical displacement plots for mudflat samples at an applied stress of 1570 kPa (reloading). (a) logarithmic time-vertical displacement (b) square-root time-vertical displacement.

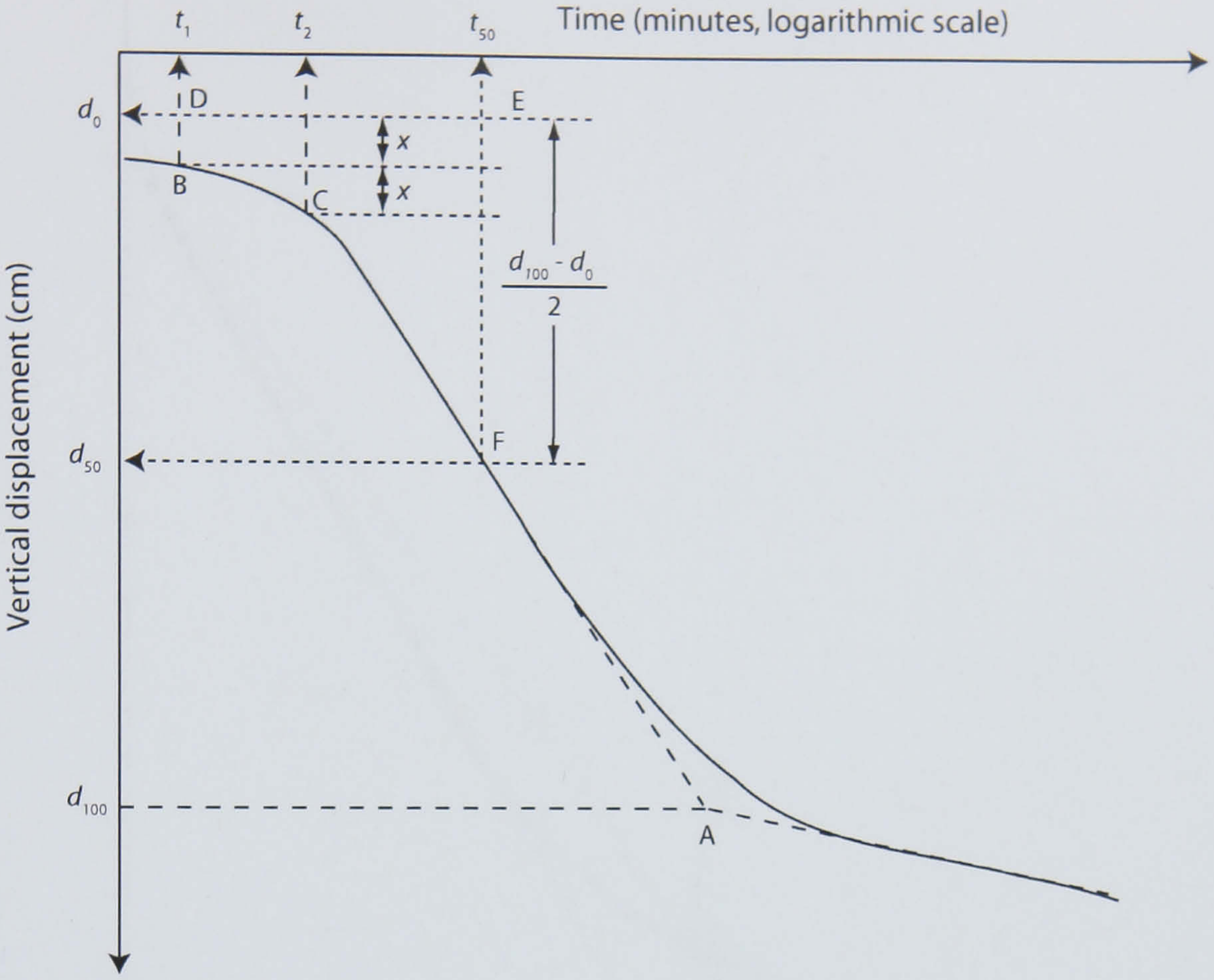

From a log time-settlement plot, the following constructions are required to determine c_v:

1. Extend the straight-line portions of the primary consolidation and secondary compression components to intersect at point A. The ordinate of A is represented by d_{100} (i.e. deformation when $U = 100$ %).

2. Select times t_1 and t_2 such that $t_2 = 4t_1$. Let the difference of specimen deformation during time $(t_2 - t_1)$ be equal to x.

3. Draw a horizontal line DE such that the vertical distance BD is equal to x. The deformation corresponding to the line DE is d_0 (i.e. deformation when $U = 0$ %).

4. The ordinate of point F on the vertical displacement curve represents the deformation at $U =$ 50 % (d_{50}) and its abscissa represents the corresponding time, t_{50}. t_{50} is then used in the following equation to determine c_v:

$$c_v = \frac{0.197H^2}{t_{50}}$$

where H is the longest drainage path during the load increment. For speciments drained at both top and bottom, H is equal to a half of the average heigh of the specimen during consolidation. For specimens undergoing one-way drainage, H equals the average height of the specimen.

All settlement prior to d_0 is designated as initial compression. All settlement following d_{100} is designated as secondary compression/creep.

Figure 6.72 The Casagrande curve-fitting method for determination of c_v, the coefficient of consolidation. Adapted from Das (1998) and Head (1988).

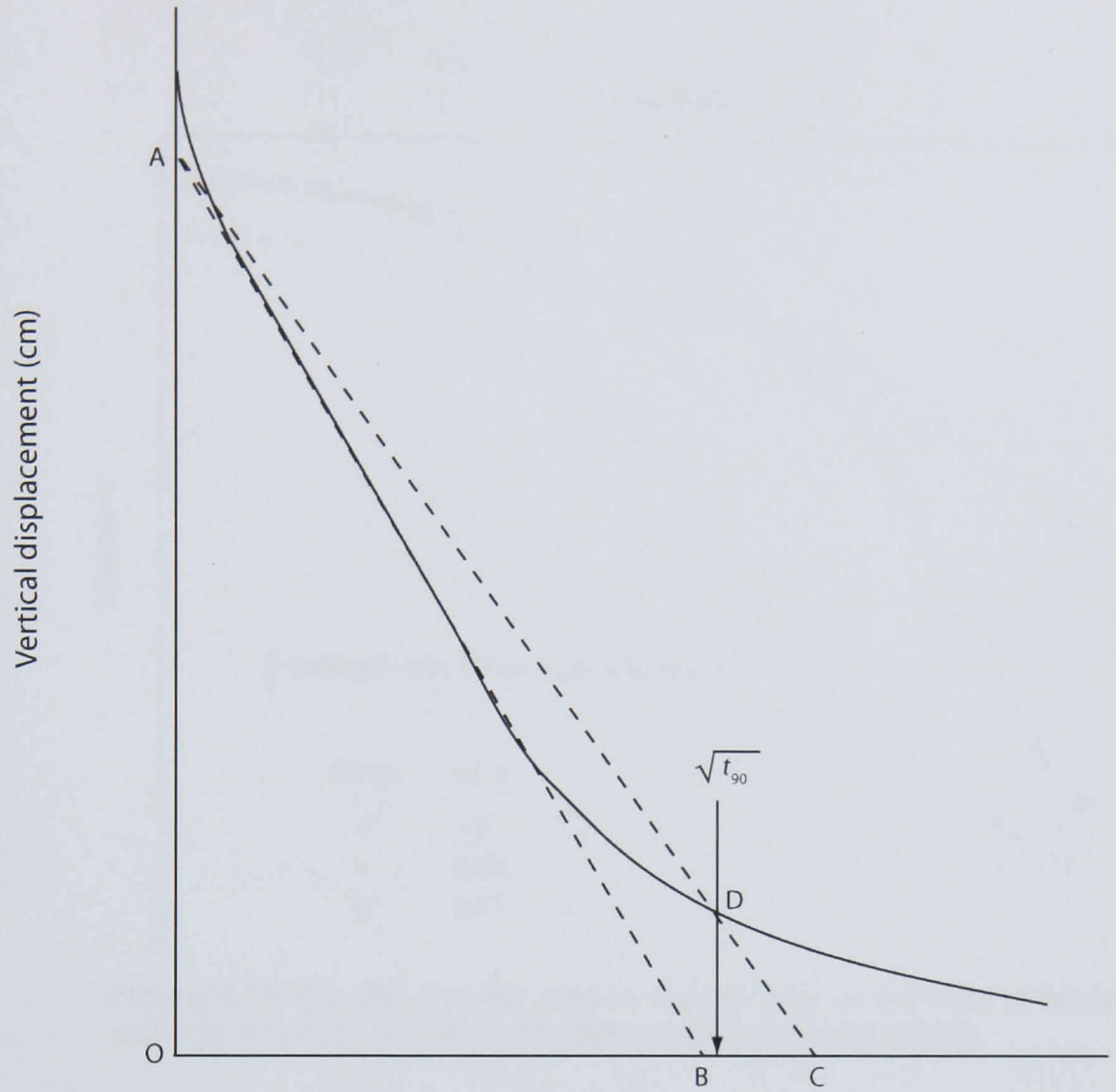

From a square root-time settlement plot, the following constructions are require to determine c_v:

1. Project the straight-line portion of the curve backwards to intersect the y-axis at point A. This represents the vertical displacement at which $U = 0$ %.

2. Draw a line AC such that OC = 1.15OB. The abscissa of point D (the intersection of AC on the consolidation curve) gives the square root of time of t_{90} (the time at which $U = 90$ %).

3. t_{90} can then be used in the following equation to determine c_v:

$$c_v = \frac{0.848H^2}{t_{90}}$$

where H is the longest drainage path during the load increment. For speciments drained at both top and bottom, H is equal to a half of the average heigh of the specimen during consolidation. For specimens undergoing one-way drainage, H equals the average height of the specimen.

Figure 6.73 The Taylor curve-fitting method for determination of c_v, the coefficient of consolidation. Adapted from Das (1998) and Head (1988).

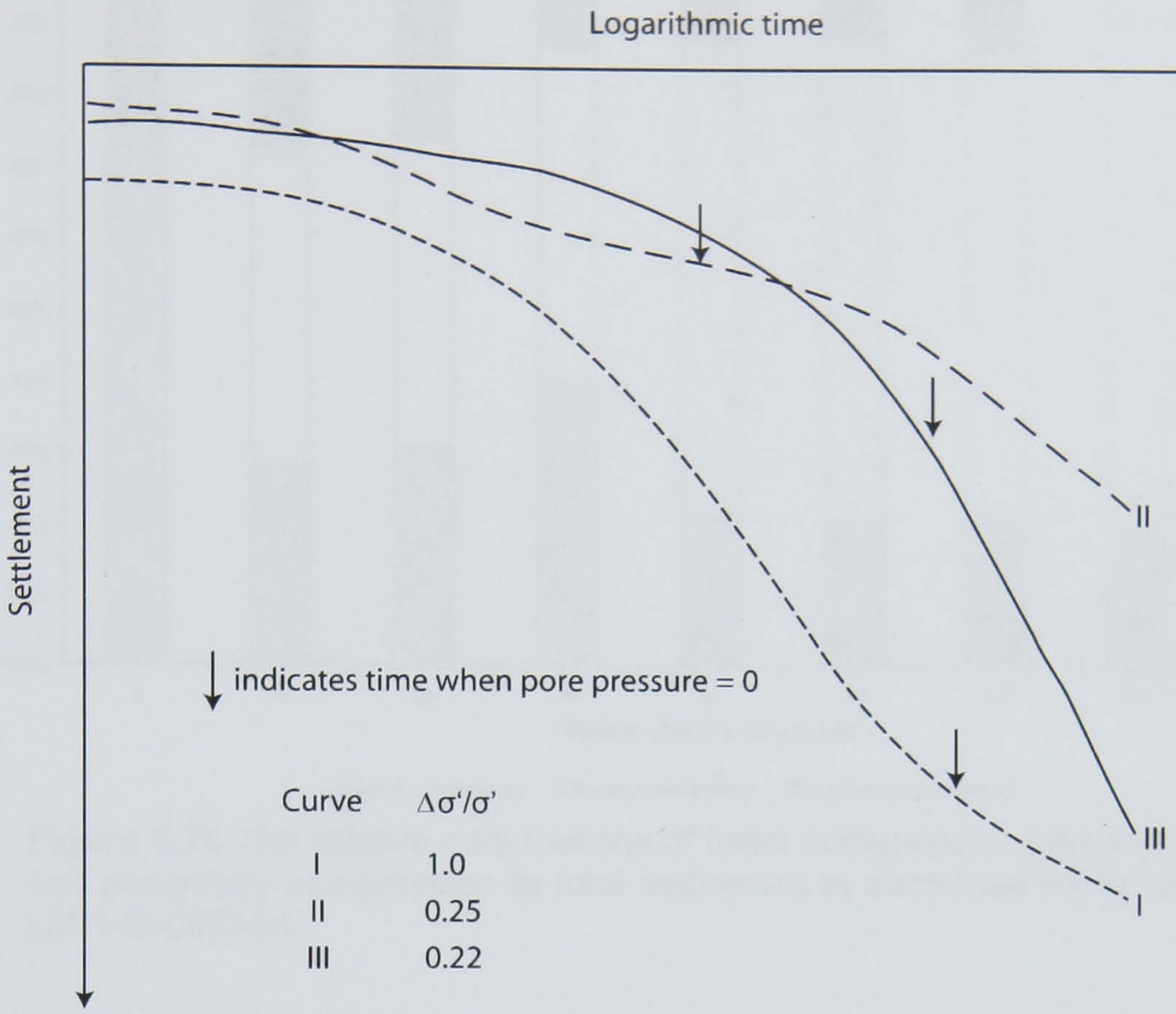

Figure 6.74 The effect of the load increment ratio on the form of logarithmic time-settlement curves. Adapted from Leonards and Girault (1961).

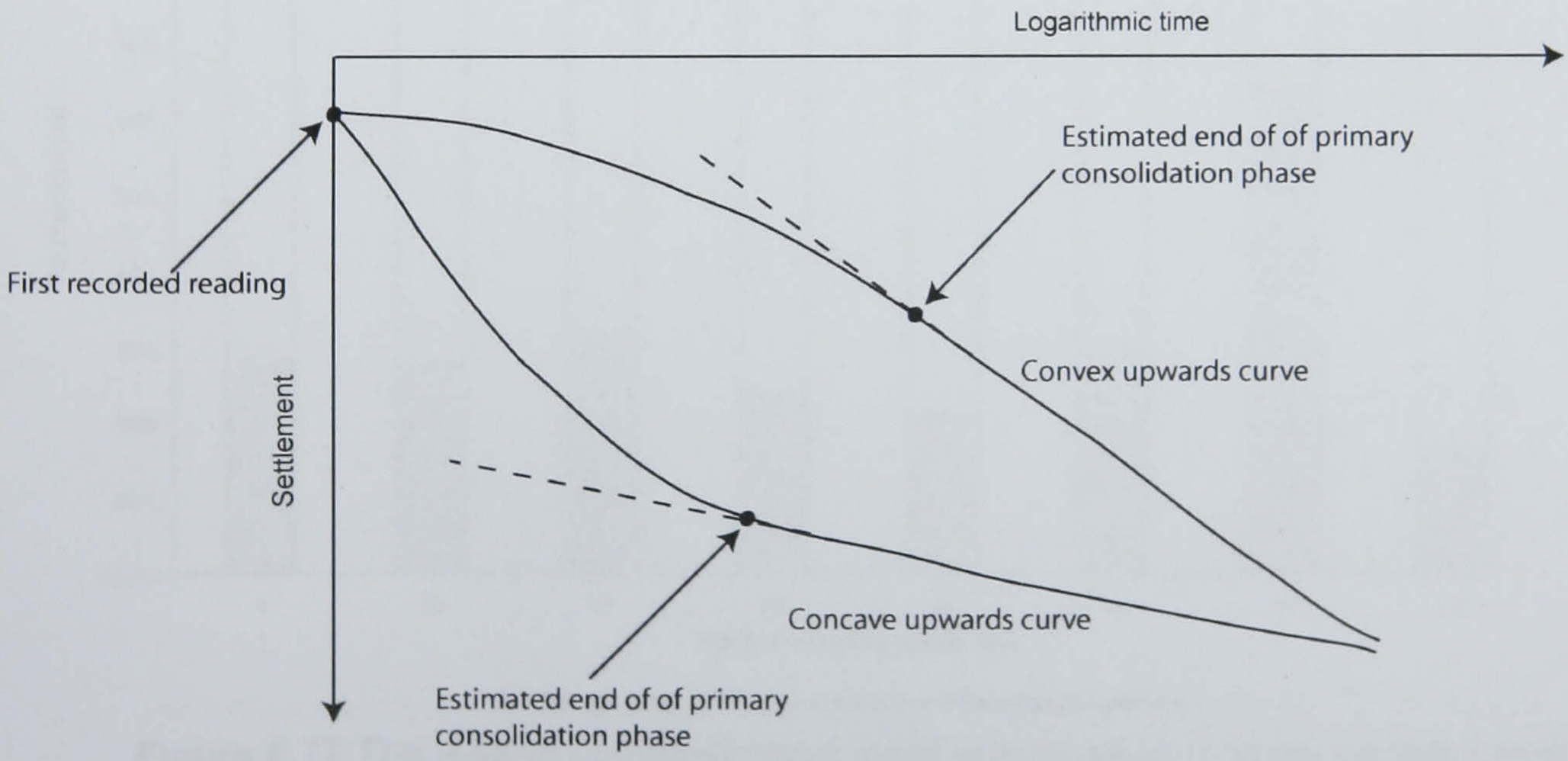

Figure 6.75 Graphical constructions for estimating the magnitude of initial compression and the time at which primary consolidation ceases. Adapted from Head (1988). See text for description.

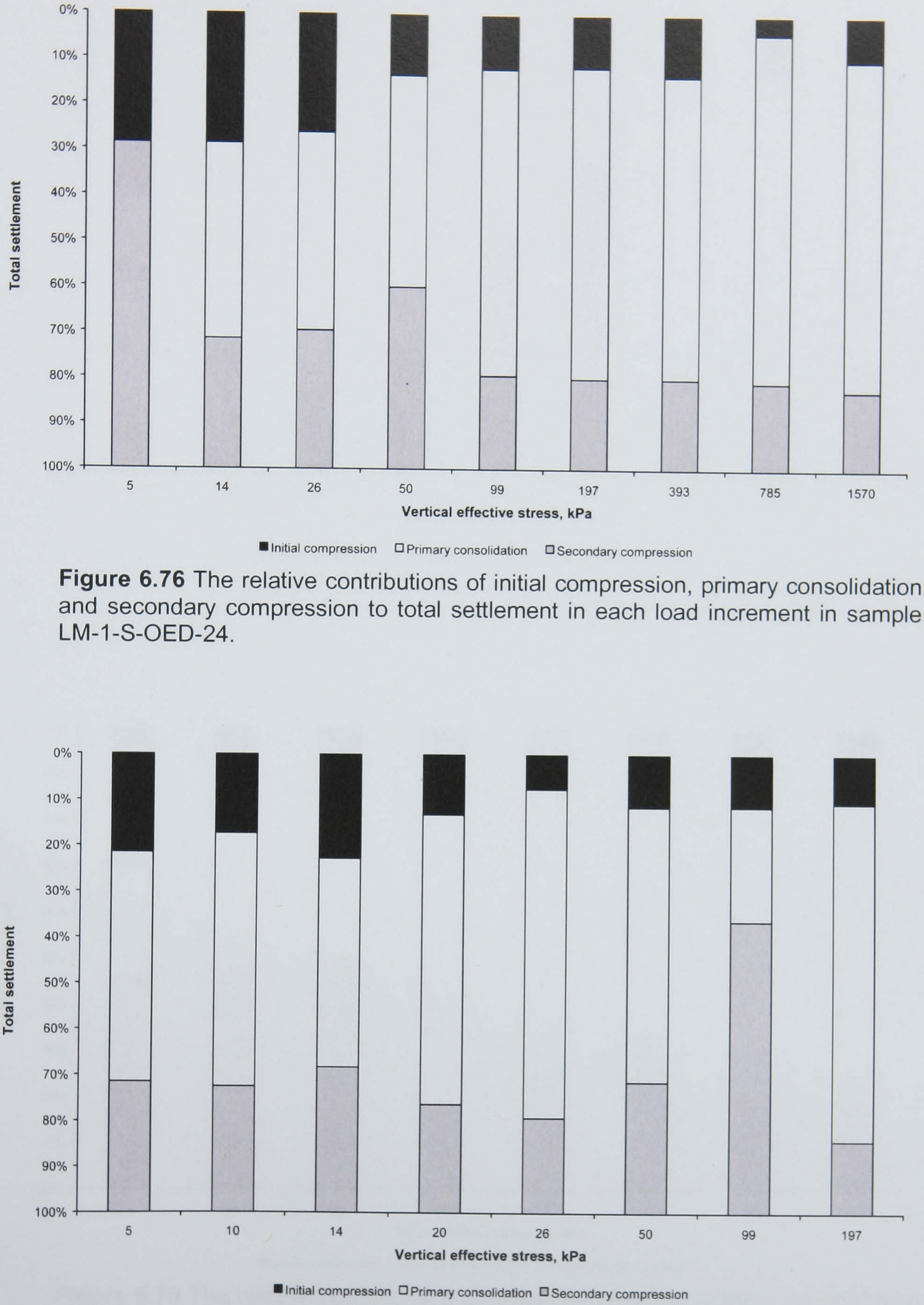

Figure 6.76 The relative contributions of initial compression, primary consolidation and secondary compression to total settlement in each load increment in sample LM-1-S-OED-24.

Figure 6.77 The relative contributions of initial compression, primary consolidation and secondary compression to total settlement in each load increment in sample LM-2-S-OED-24.

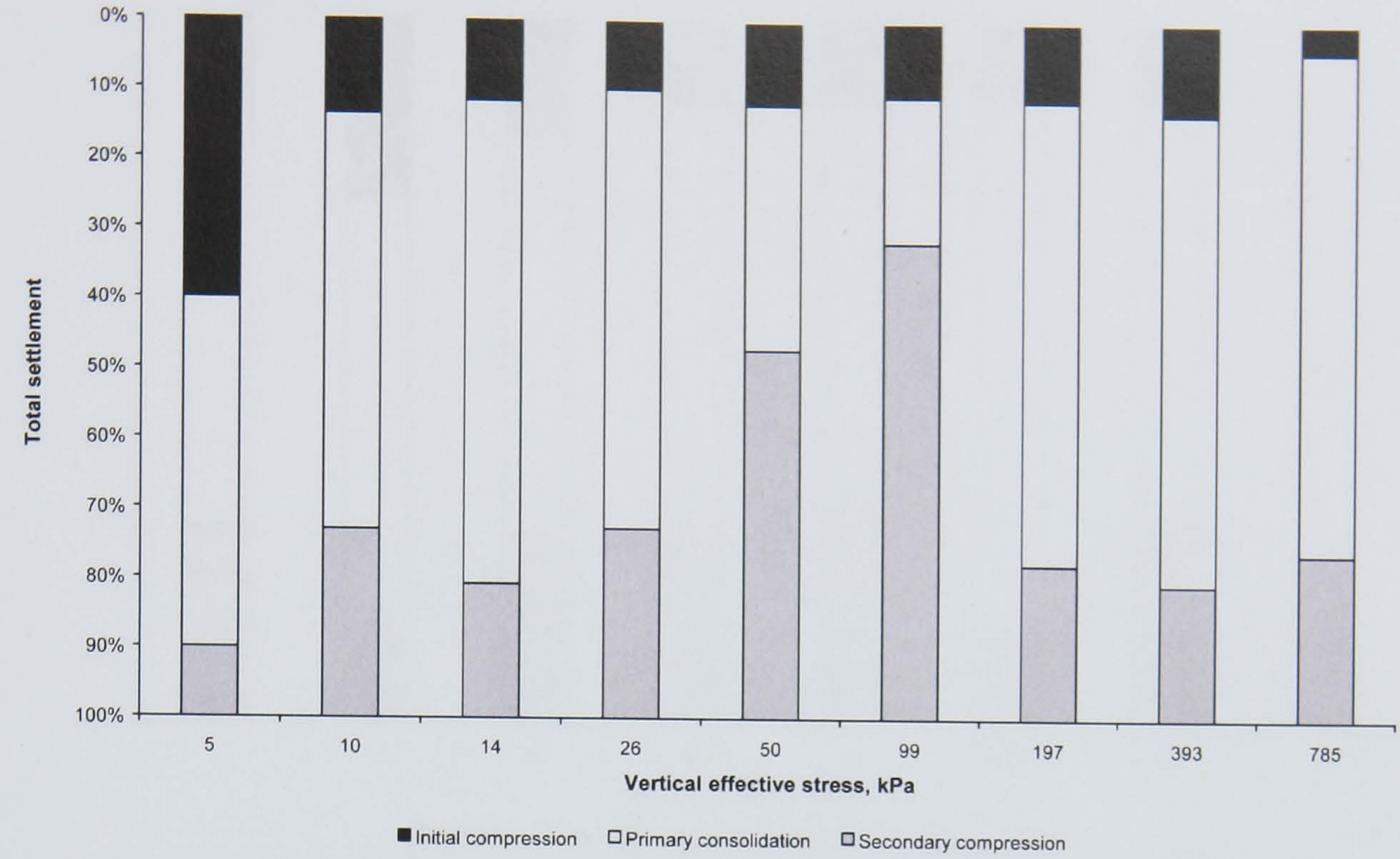

Figure 6.78 The relative contributions of initial compression, primary consolidation and secondary compression to total settlement in each load increment in sample LM-3-S-OED-24.

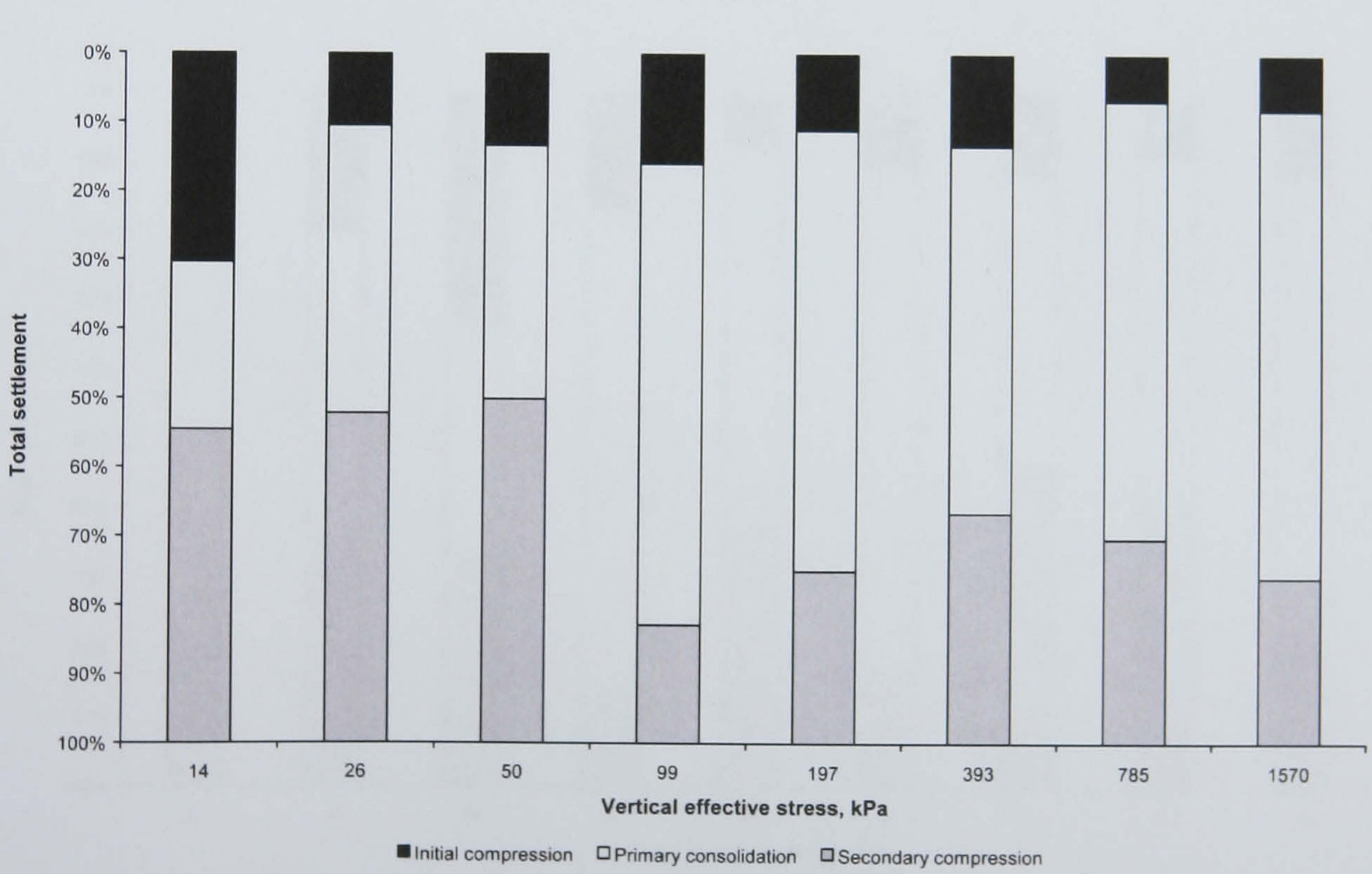

Figure 6.79 The relative contributions of initial compression, primary consolidation and secondary compression to total settlement in each load increment in sample LM-4-S-OED-68.

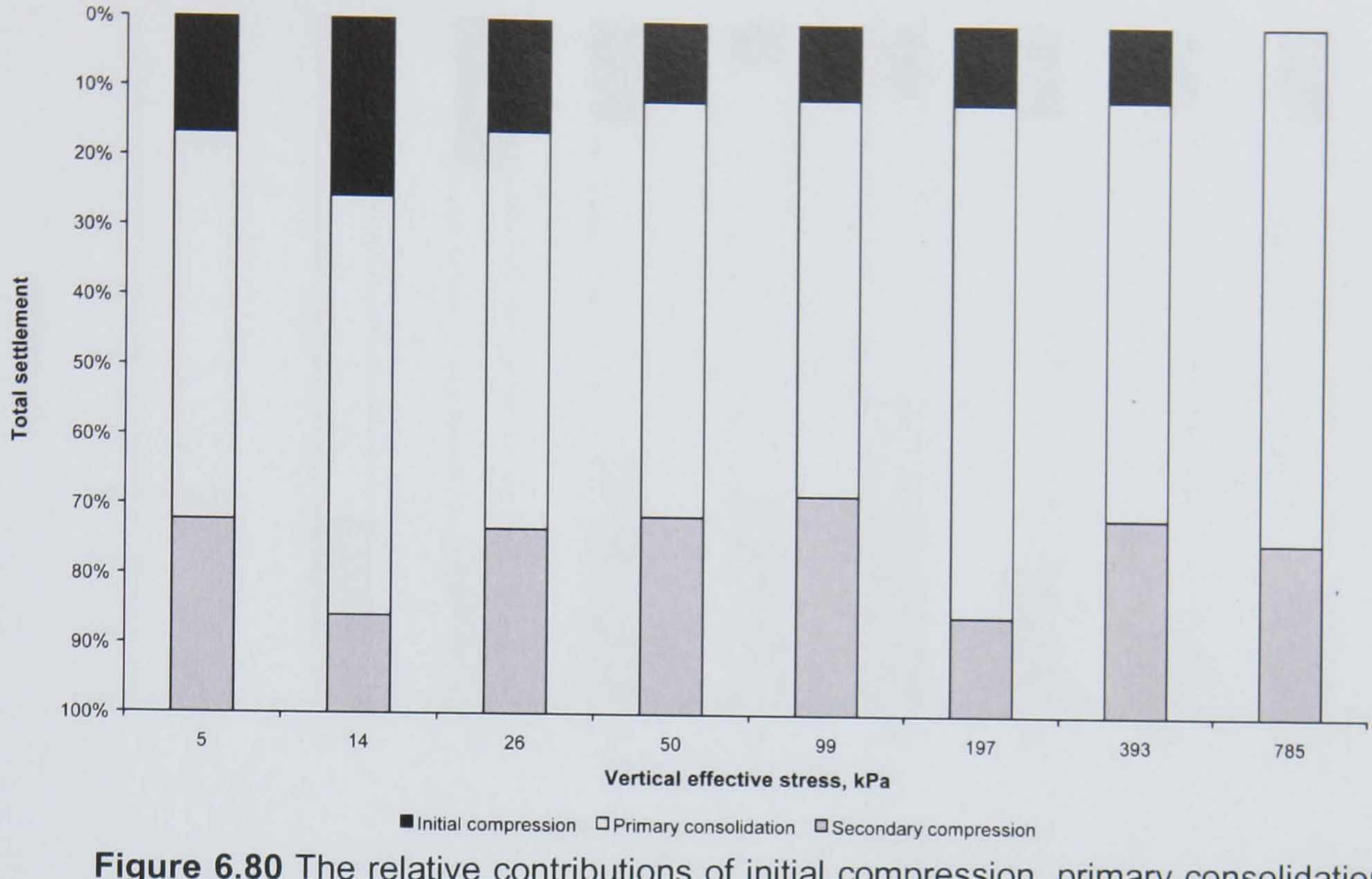

Figure 6.80 The relative contributions of initial compression, primary consolidation and secondary compression to total settlement in each load increment in sample LM-6-S-BPS-24.

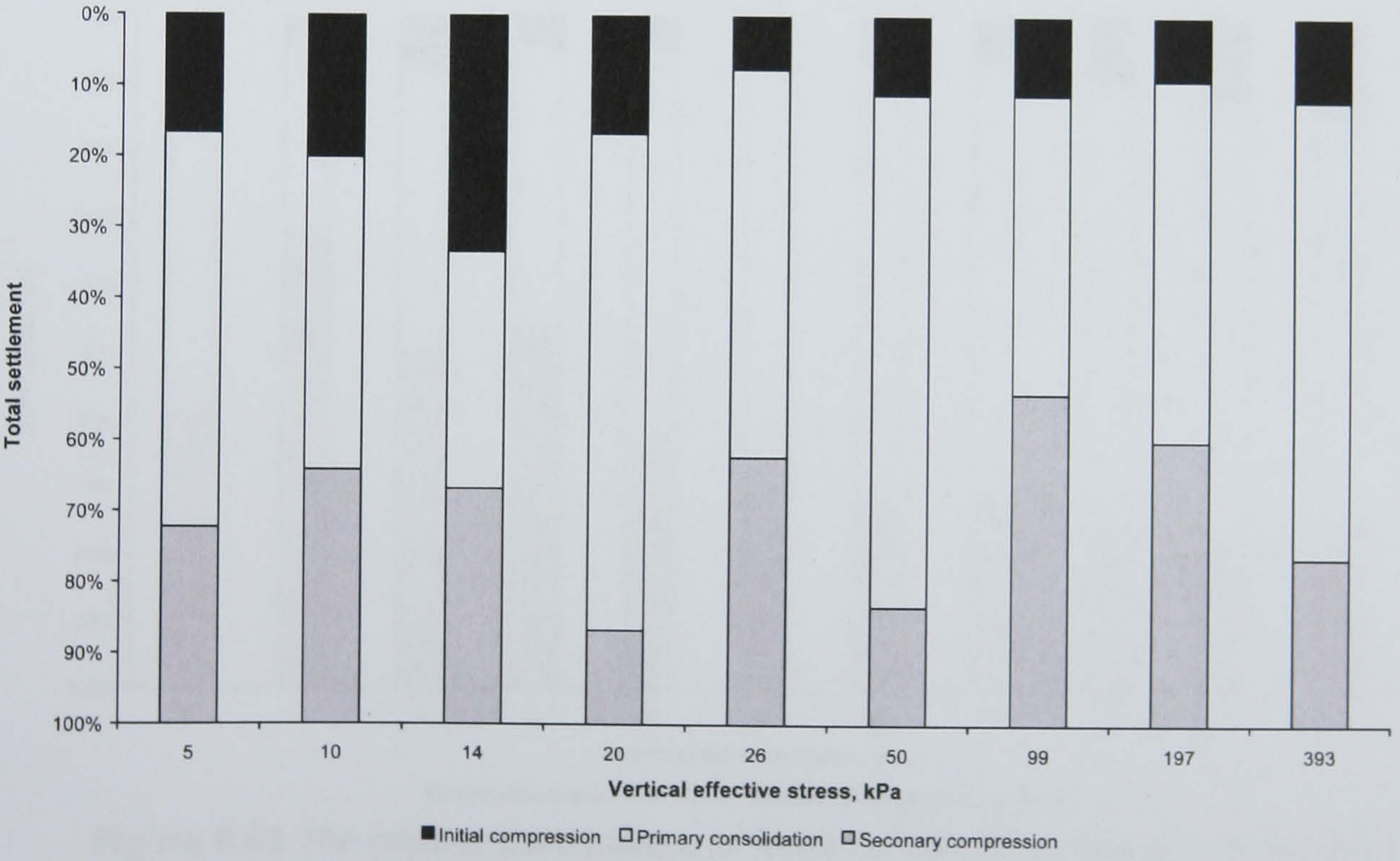

Figure 6.81 The relative contributions of initial compression, primary consolidation and secondary compression to total settlement in each load increment in sample LM-7-N-OED-24.

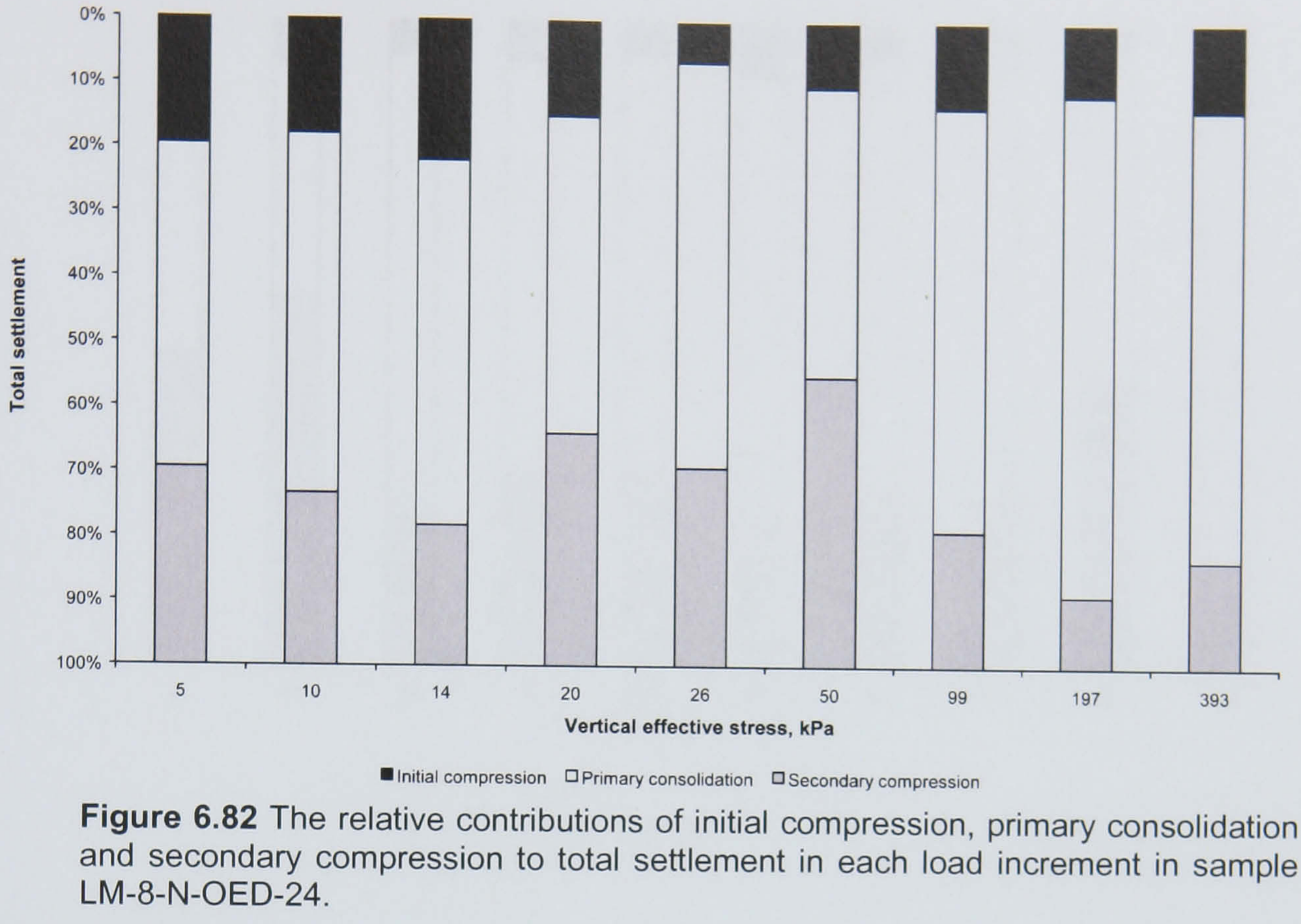

Figure 6.82 The relative contributions of initial compression, primary consolidation and secondary compression to total settlement in each load increment in sample LM-8-N-OED-24.

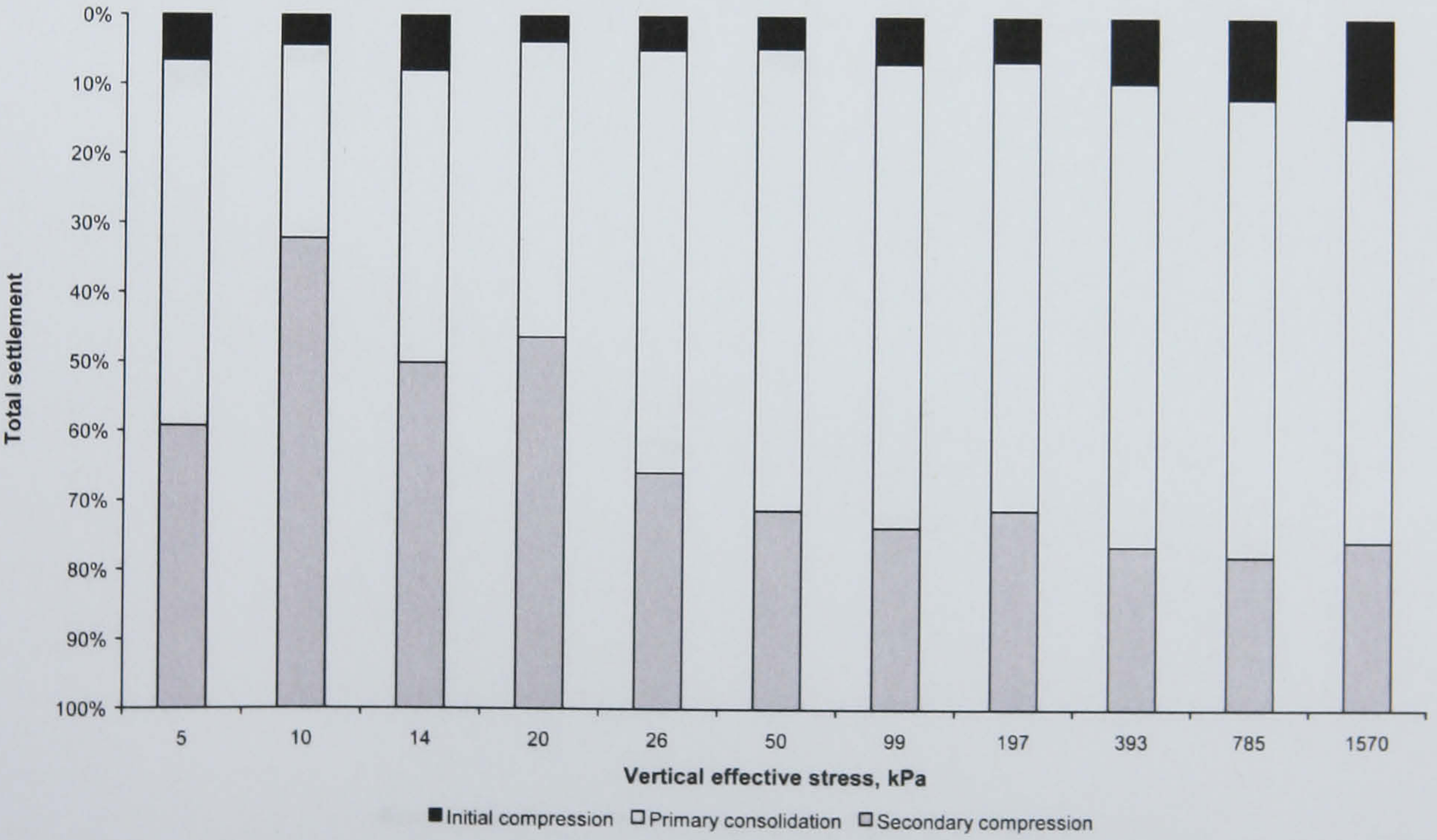

Figure 6.83 The relative contributions of initial compression, primary consolidation and secondary compression to total settlement in each load increment in sample MF-1-S-OED-24.

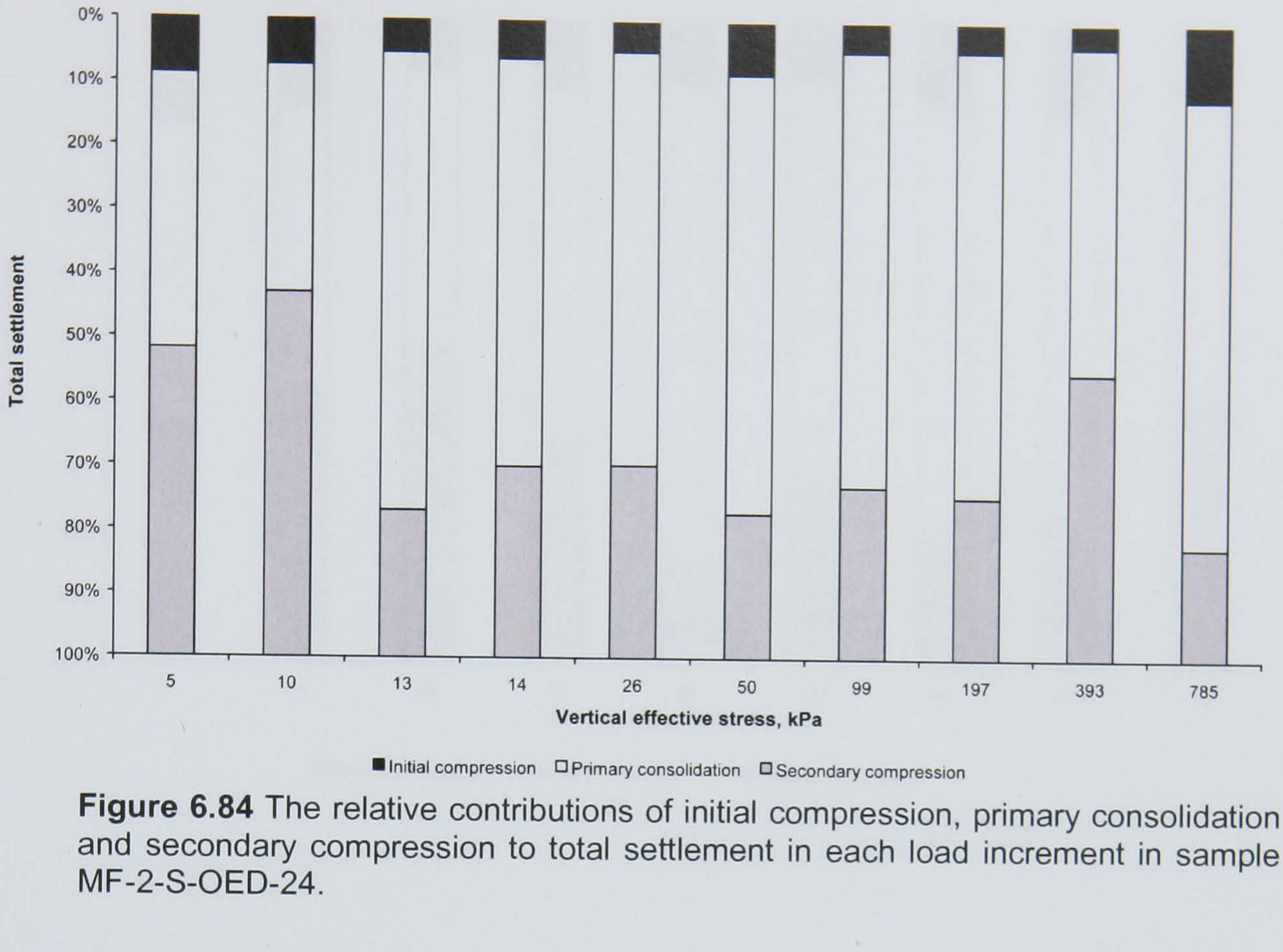

Figure 6.84 The relative contributions of initial compression, primary consolidation and secondary compression to total settlement in each load increment in sample MF-2-S-OED-24.

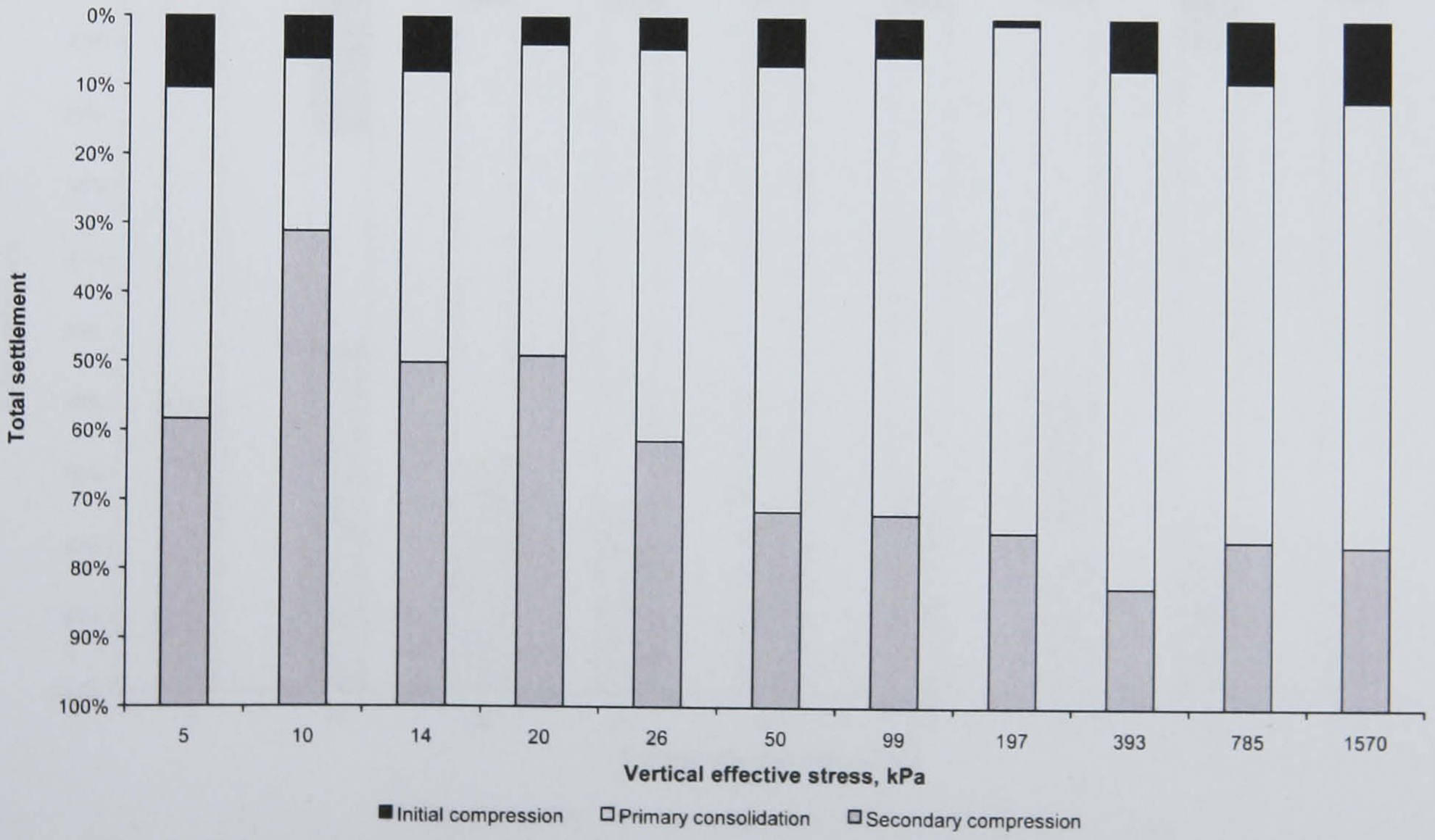

Figure 6.85 The relative contributions of initial compression, primary consolidation and secondary compression to total settlement in each load increment in sample MF-3-S-OED-24.

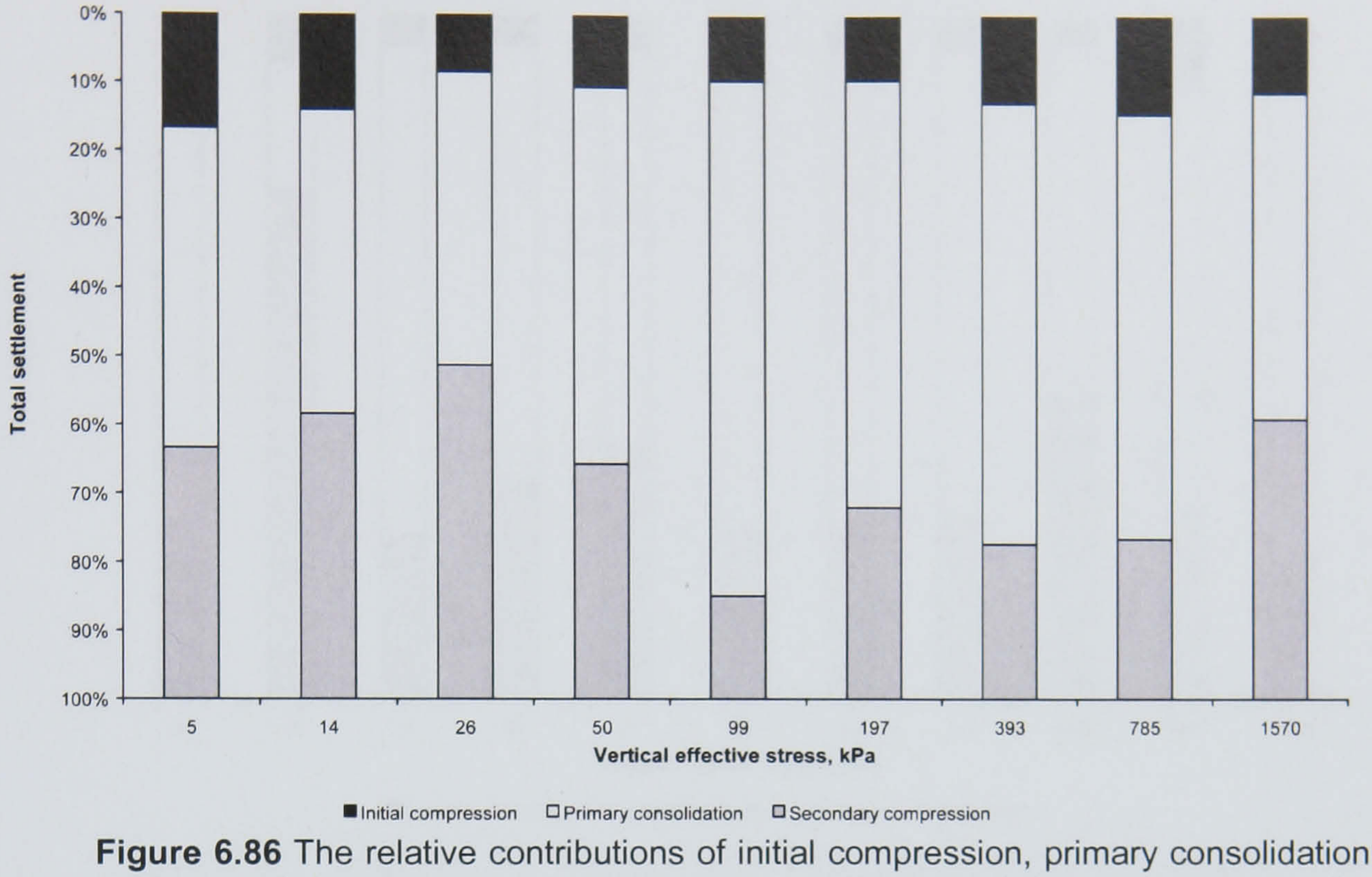

Figure 6.86 The relative contributions of initial compression, primary consolidation and secondary compression to total settlement in each load increment in sample MF-4-S-OED-48.

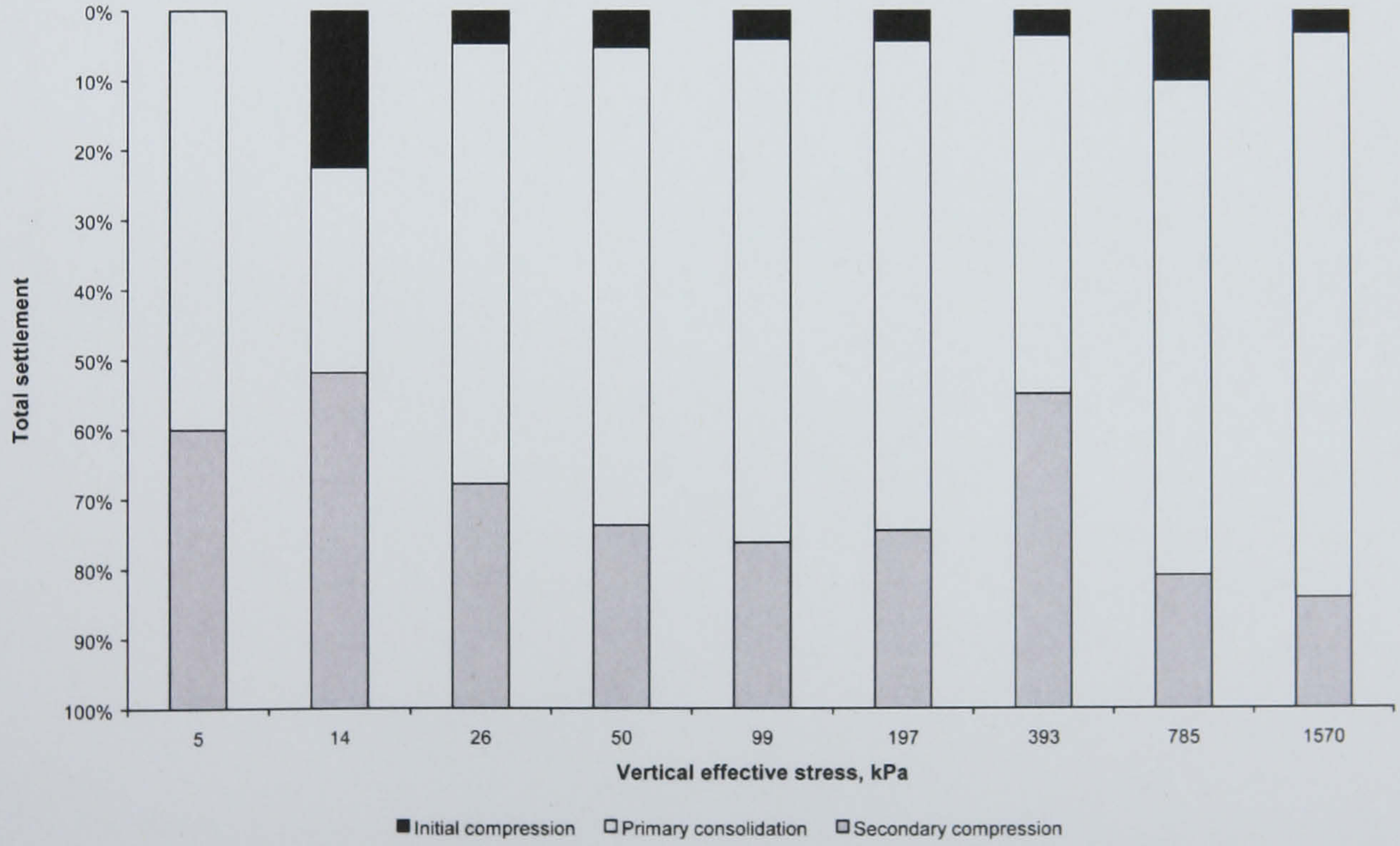

Figure 6.87 The relative contributions of initial compression, primary consolidation and secondary compression to total settlement in each load increment in sample MF-6-S-BPS-24.

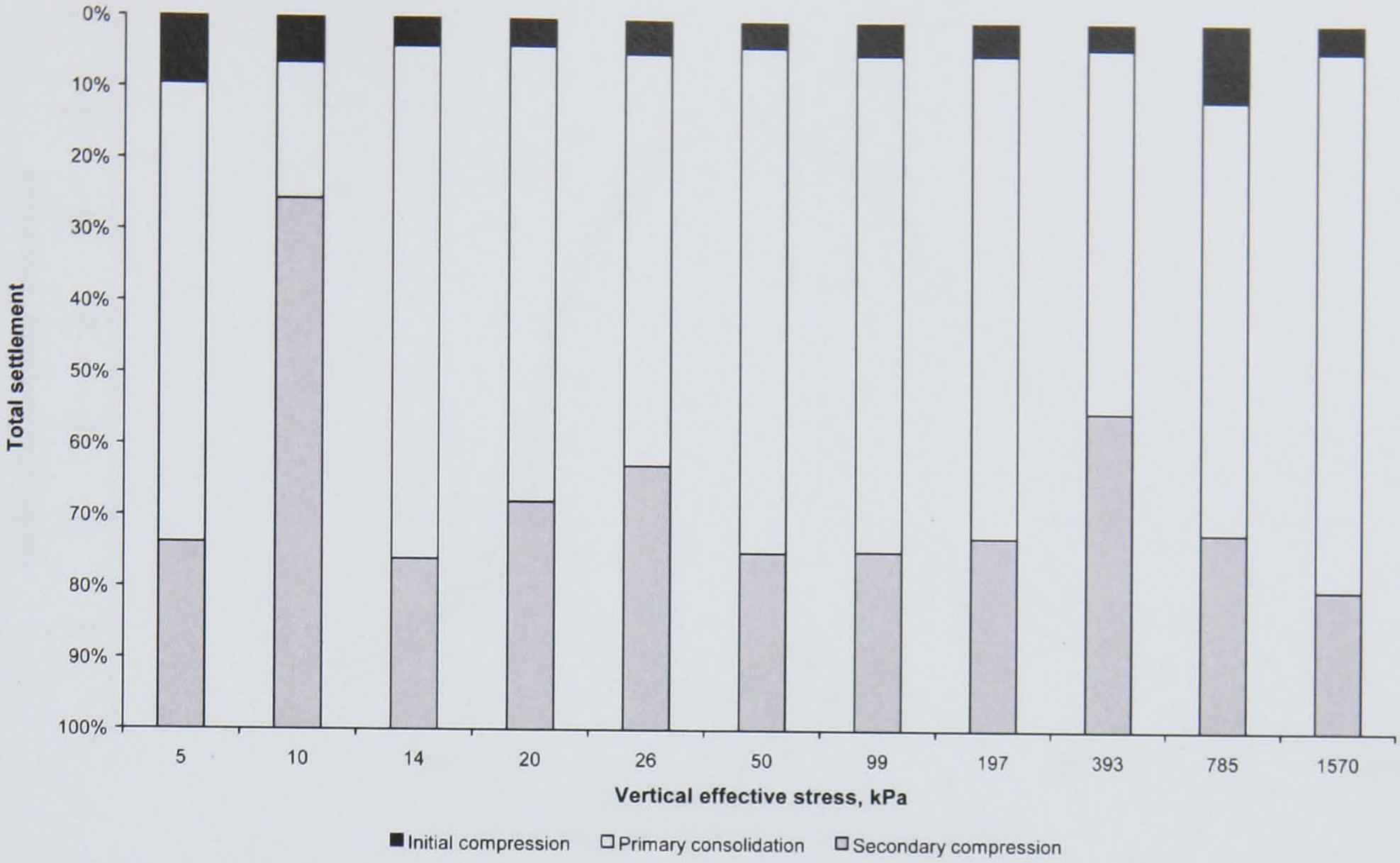

Figure 6.88 The relative contributions of initial compression, primary consolidation and secondary compression to total settlement in each load increment in sample MF-7-N-OED-24.

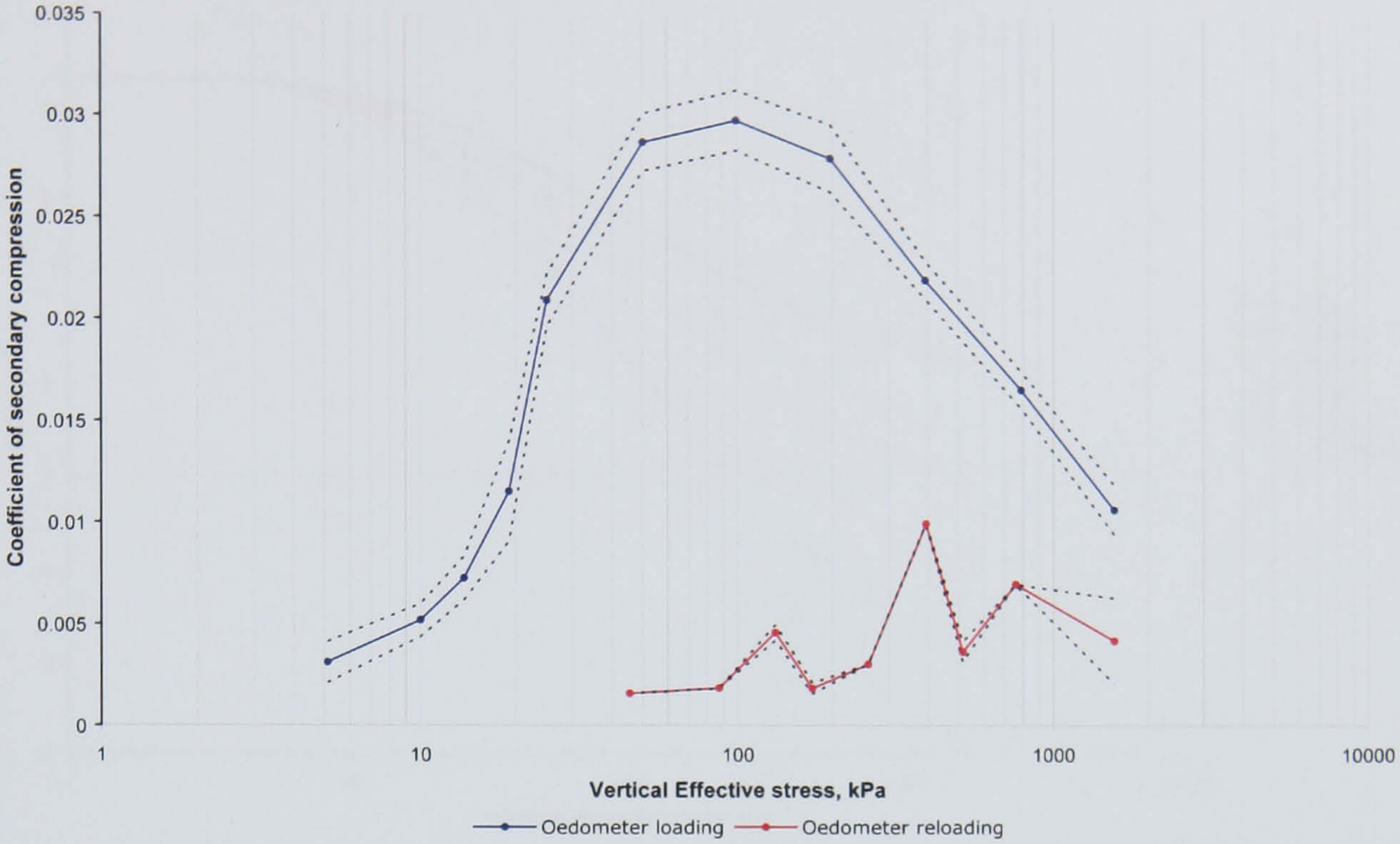

Figure 6.89 Variations in the coefficient of secondary compression with effective stress for the low marsh samples. Error margins are ± 1 standard error.

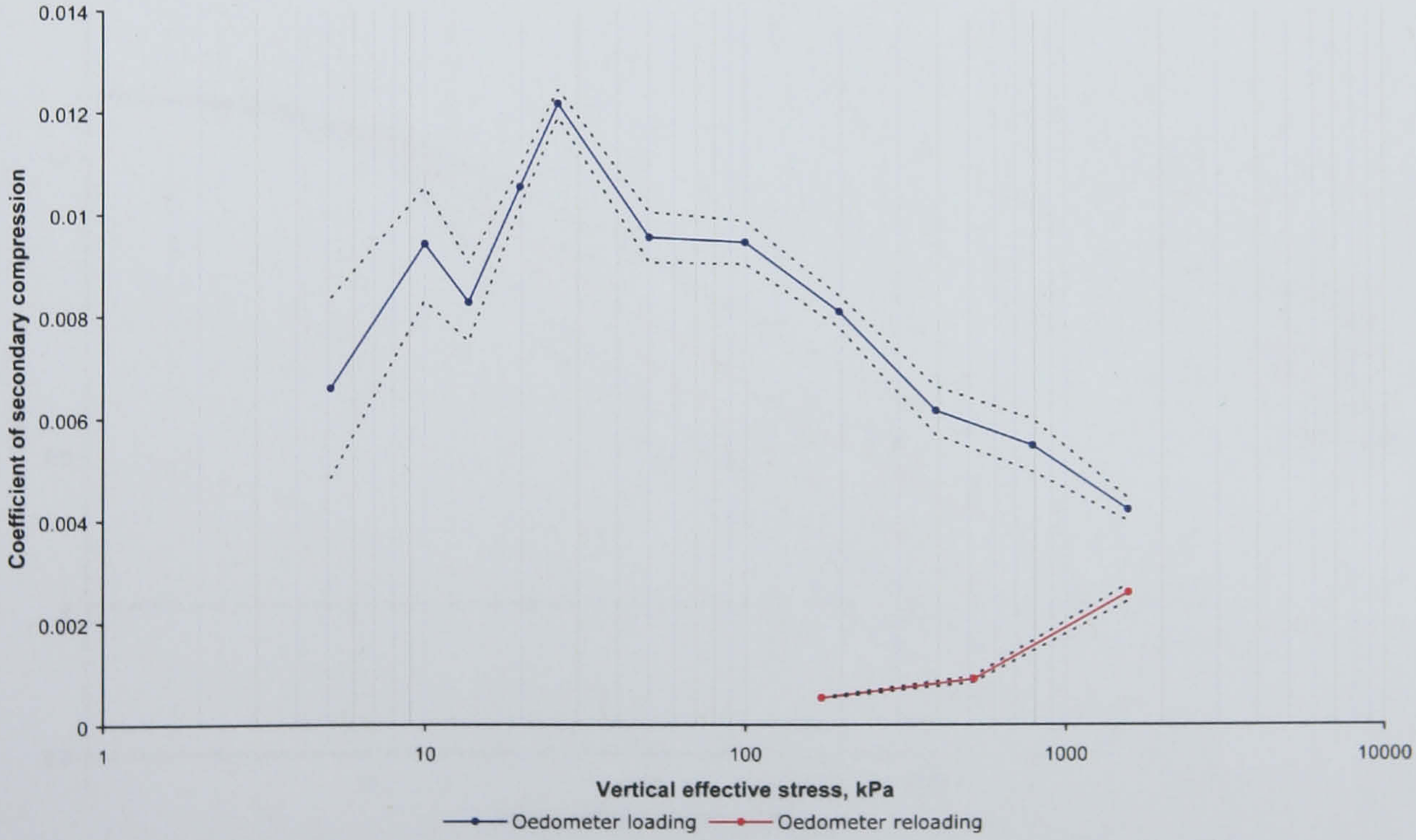

Figure 6.90 Variations in the coefficient of secondary compression with effective stress for the mudflat samples. Error margins are ± 1 standard error.

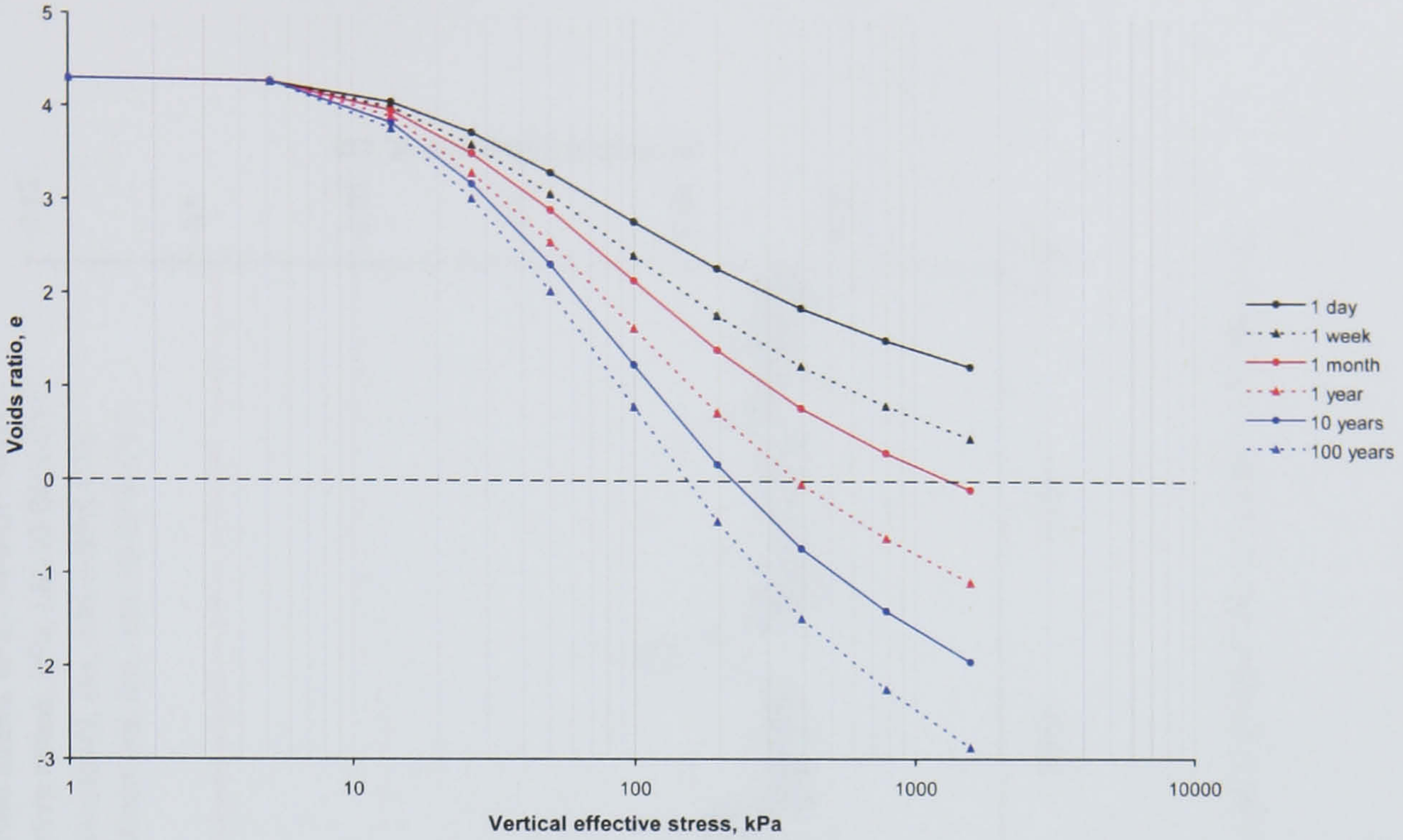

Figure 6.91 Predicted/theoretical variations in $e\log_{10}\sigma'$ plots for sample LM-1-S-OED-24 resulting from extended load increments and creep settlement.

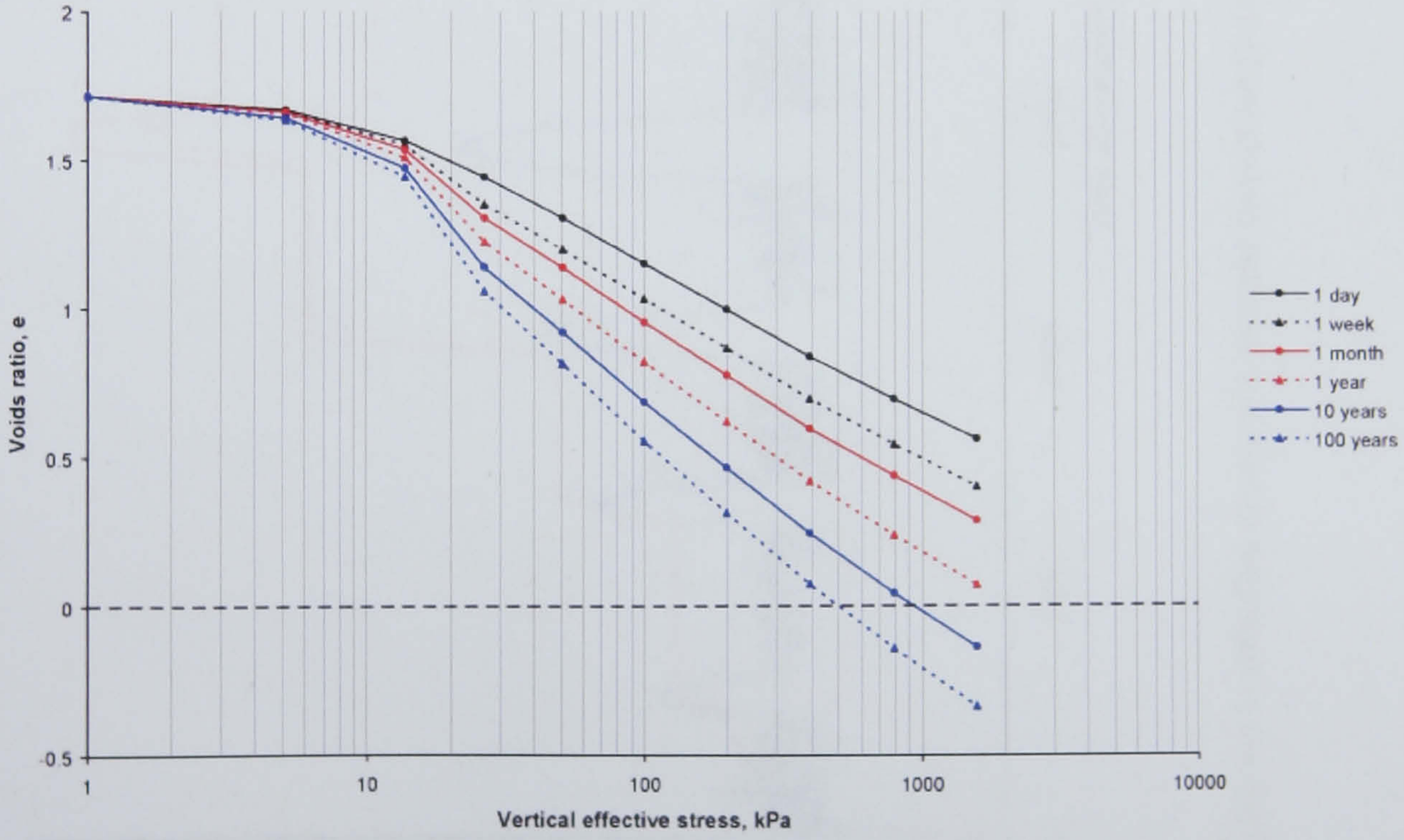

Figure 6.92 Predicted/theoretical variations in $e\log_{10}\sigma'$ plots for sample MF-4-S-OED-48 resulting from extended load increments and creep settlement.

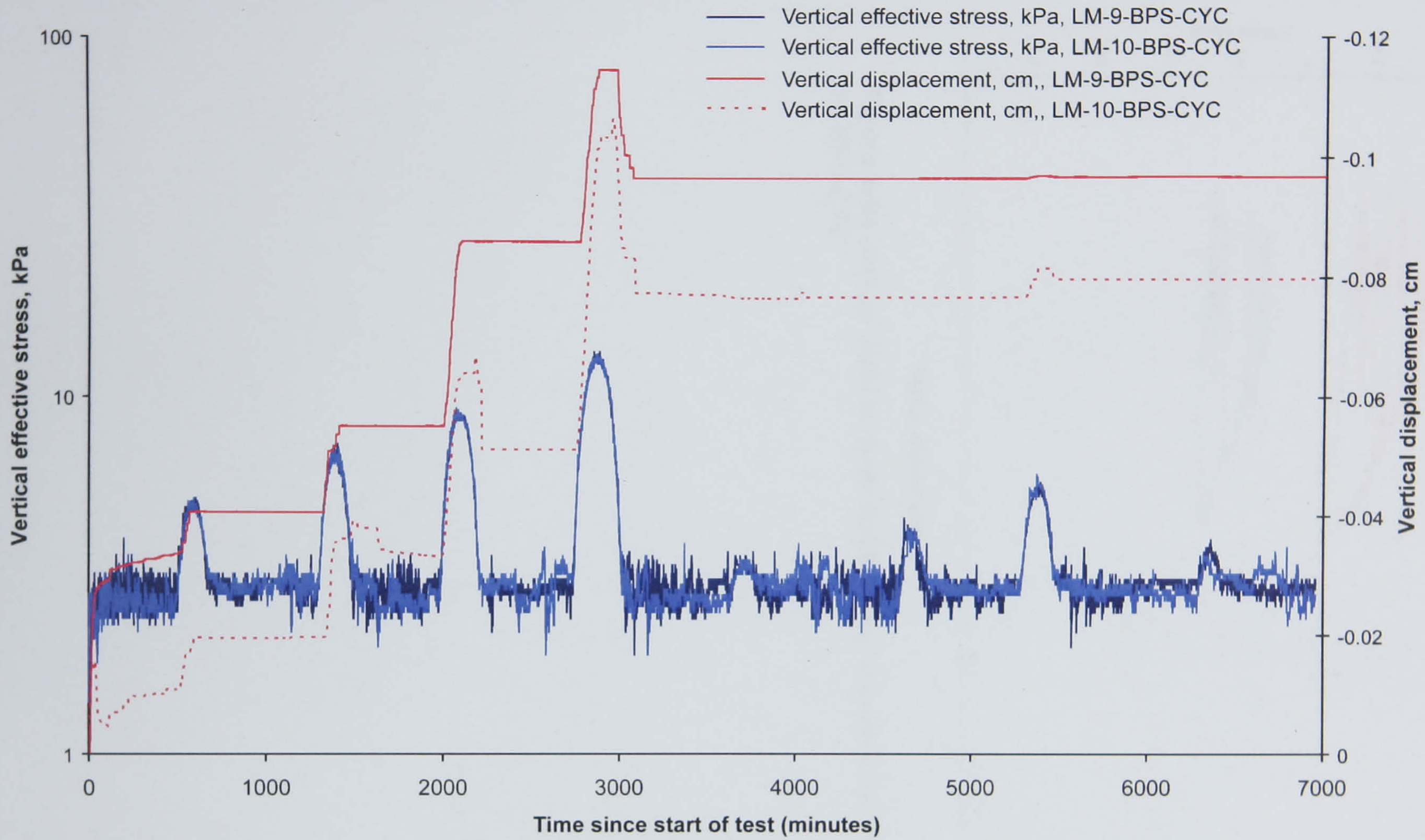

Figure 6.93 Variations in effective stress and vertical displacement over time in tests LM-9-BPS-CYC and LM-10-BPS-CYC.

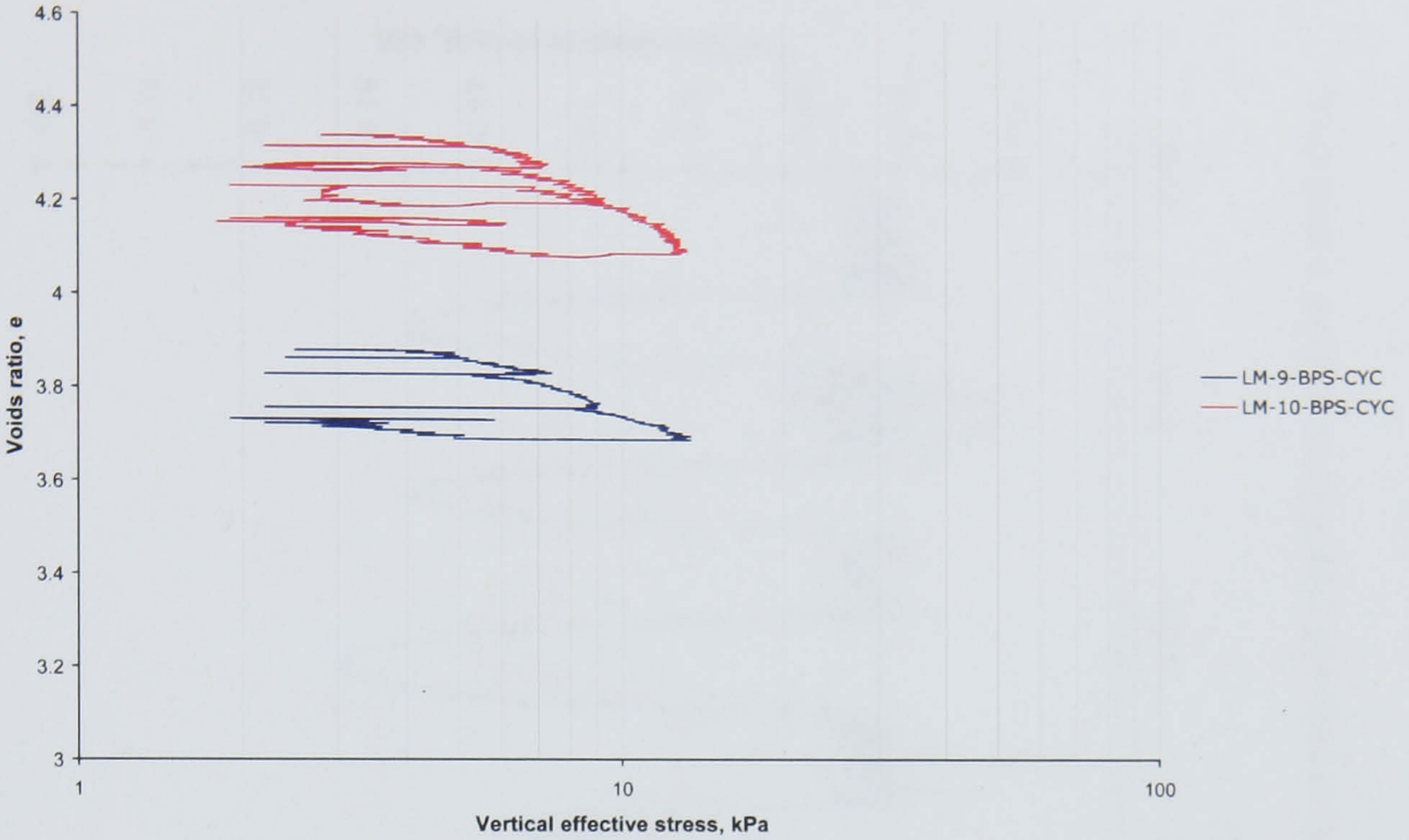

Figure 6.94 $e\log_{10}\sigma'$ plots of dynamically loaded samples LM-9-BPS-CYC and LM-10-BPS-CYC.

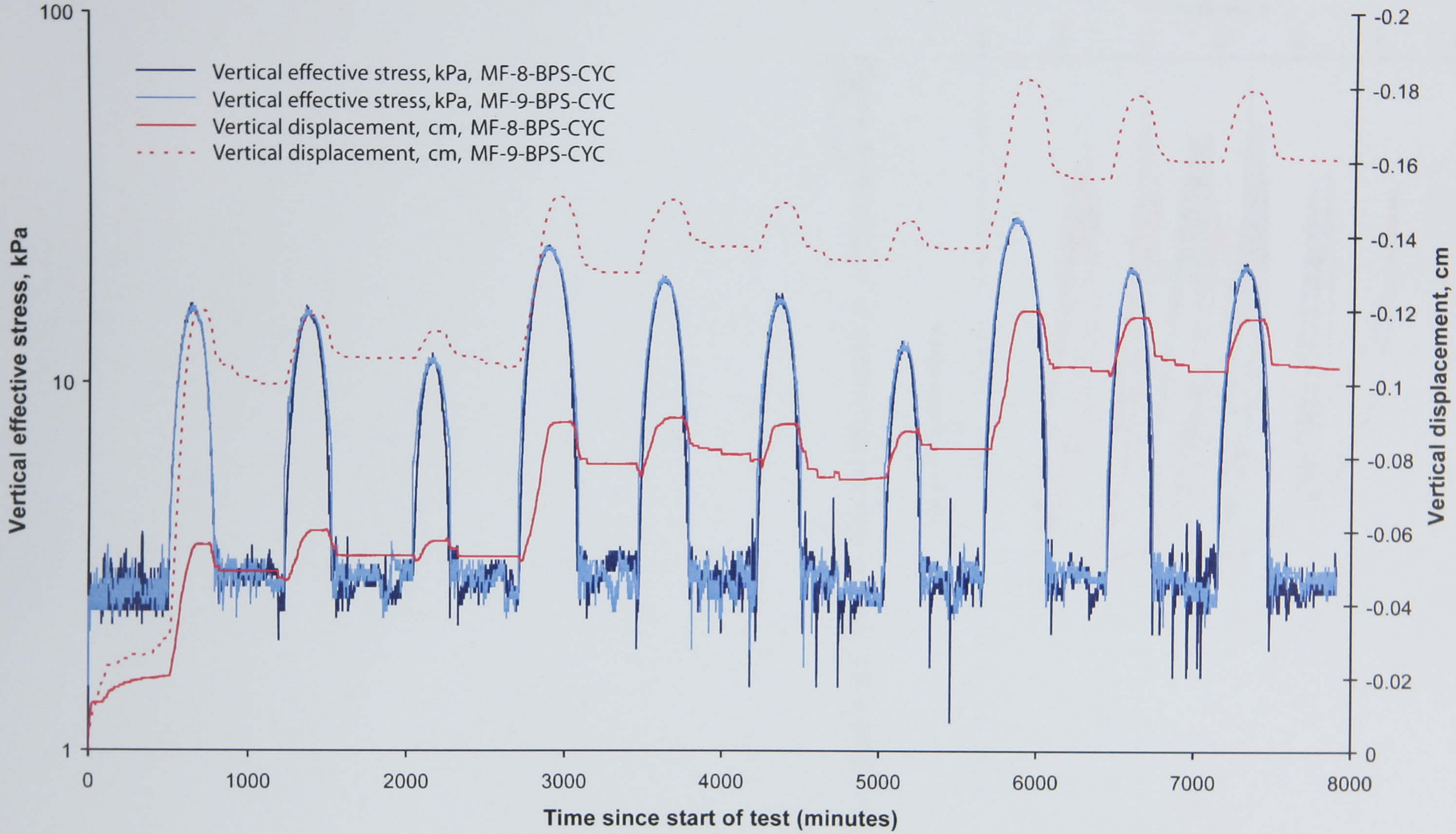

Figure 6.95 Variations in effective stress and vertical displacement over time in tests MF-8-BPS-CYC and MF-9-BPS-CYC.

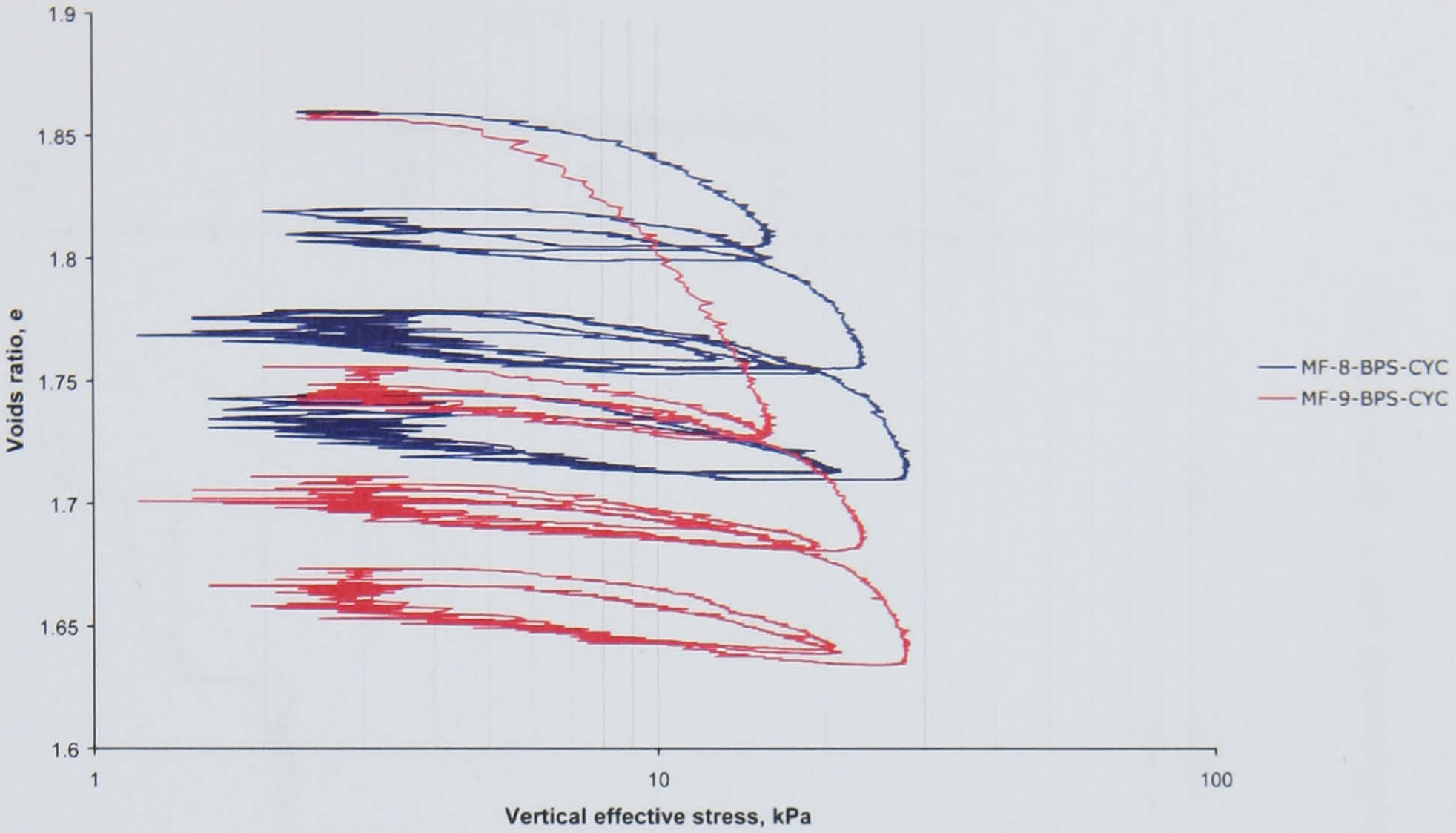

Figure 6.96 $e\log_{10}\sigma'$ of dynamically loaded samples MF-8-BPS-CYC and MF-9-BPS-CYC.

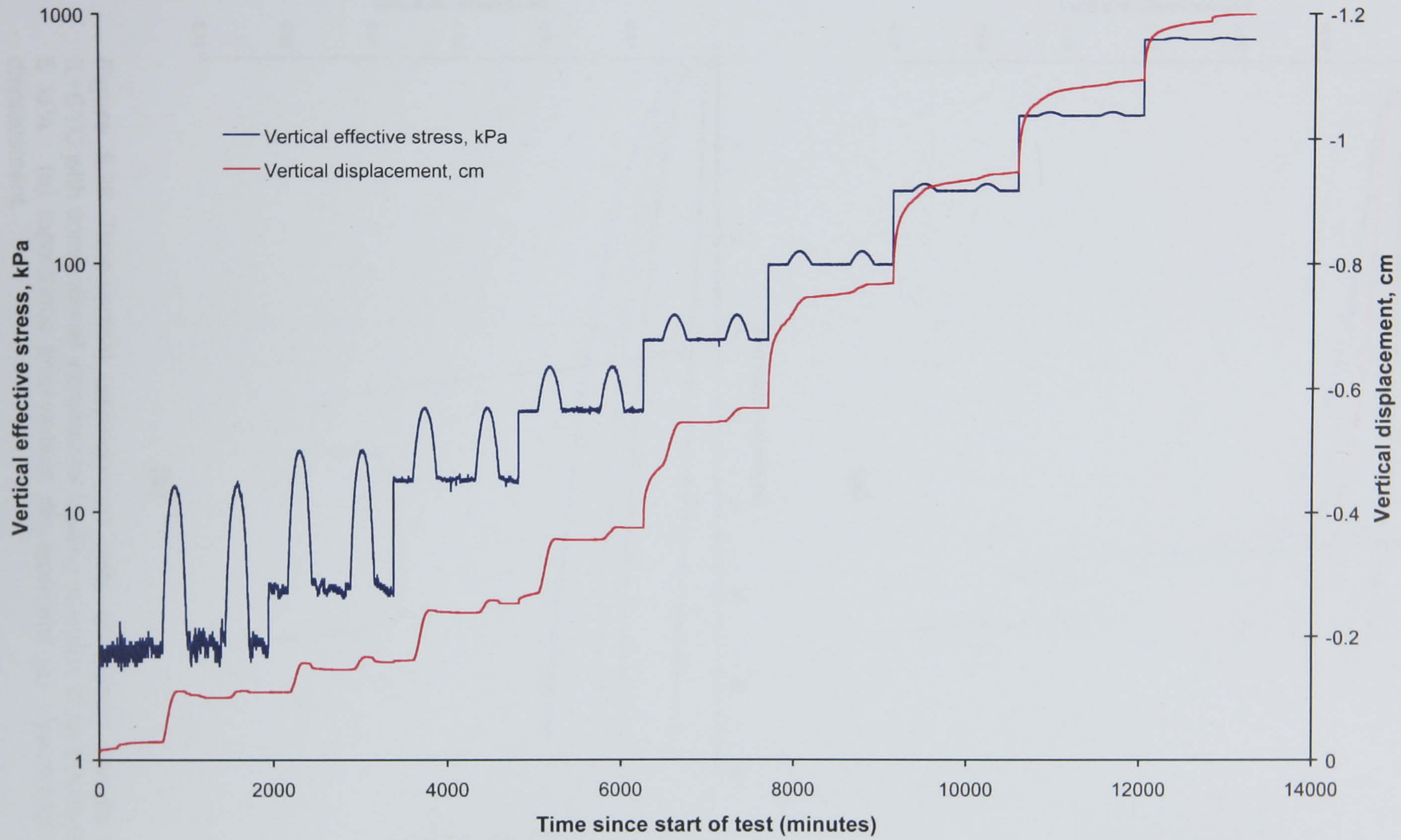

Figure 6.97 Variations in effective stress and vertical displacement over time in sample LM-11-BPS-IL+CYC.

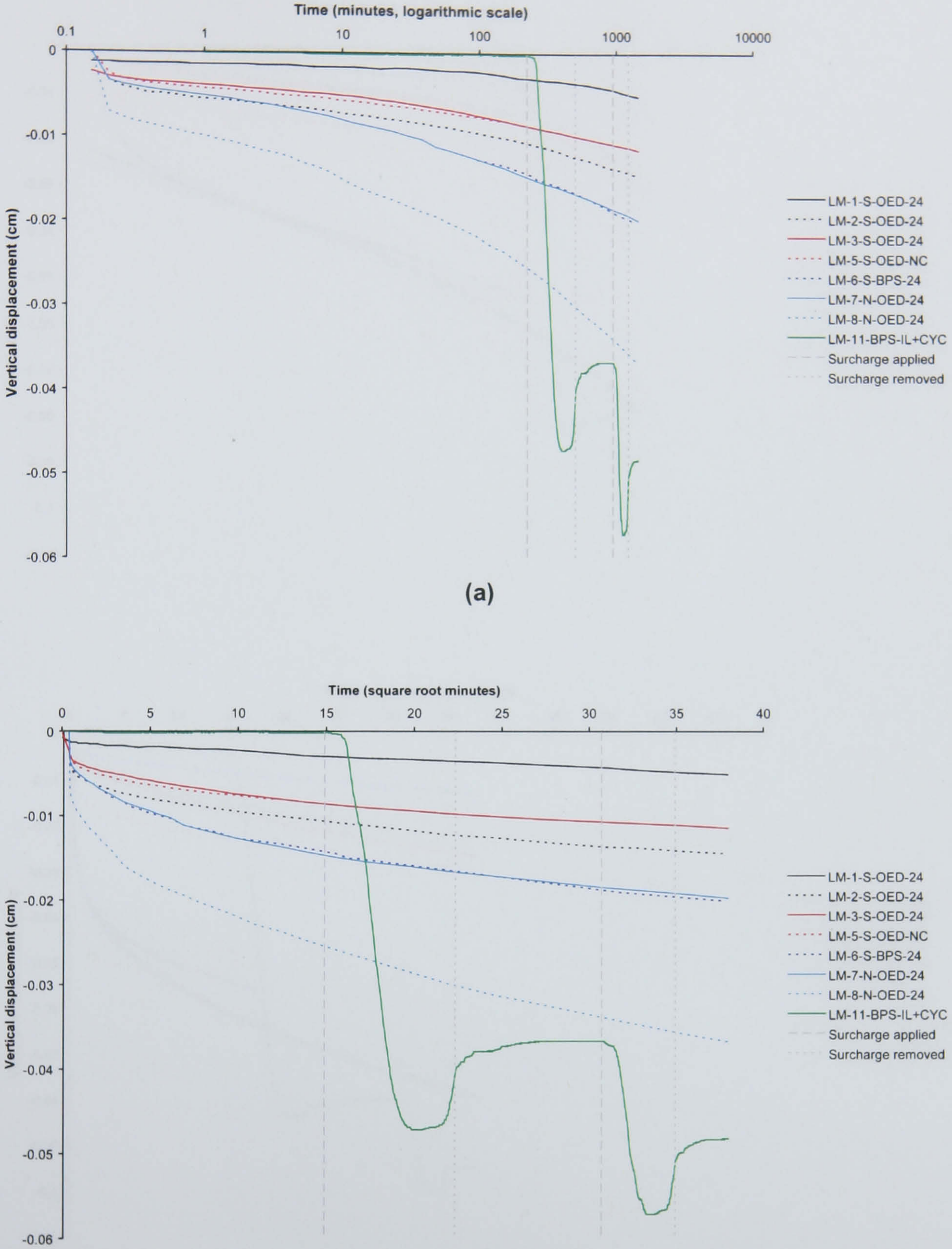

Figure 6.98 Time-vertical displacement plots comparing sample LM-11-BPS-IL+CYC with conventional incremental loading samples at an overburden stress of 5 kPa. (a) logarithmic time-vertical displacement (b) square-root time-vertical displacement.

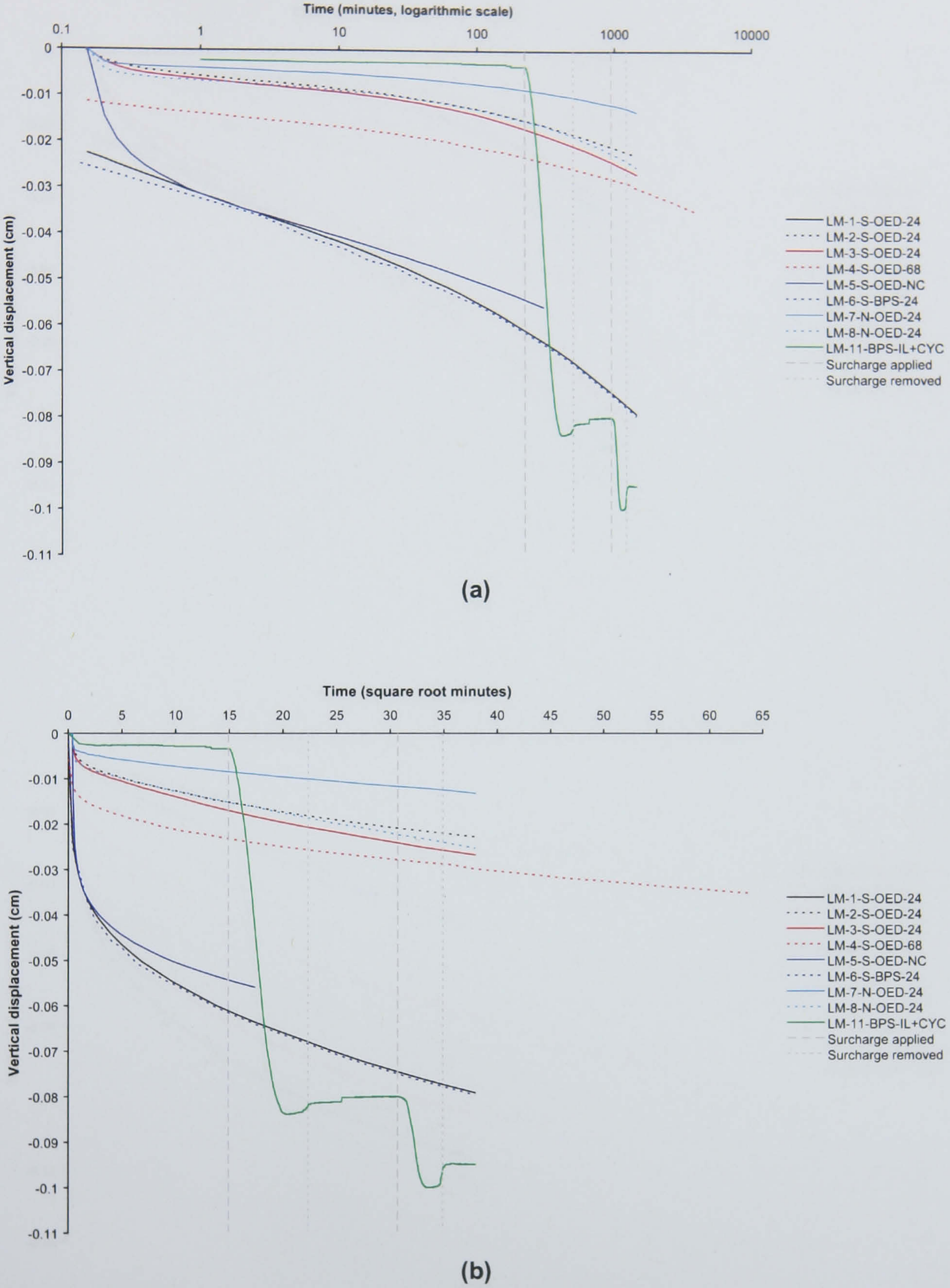

Figure 6.99 Time-vertical displacement plots comparing sample LM-11-BPS-IL+CYC with conventional incremental loading samples at an overburden stress of 14 kPa. (a) logarithmic time-vertical displacement (b) square-root time-vertical displacement.

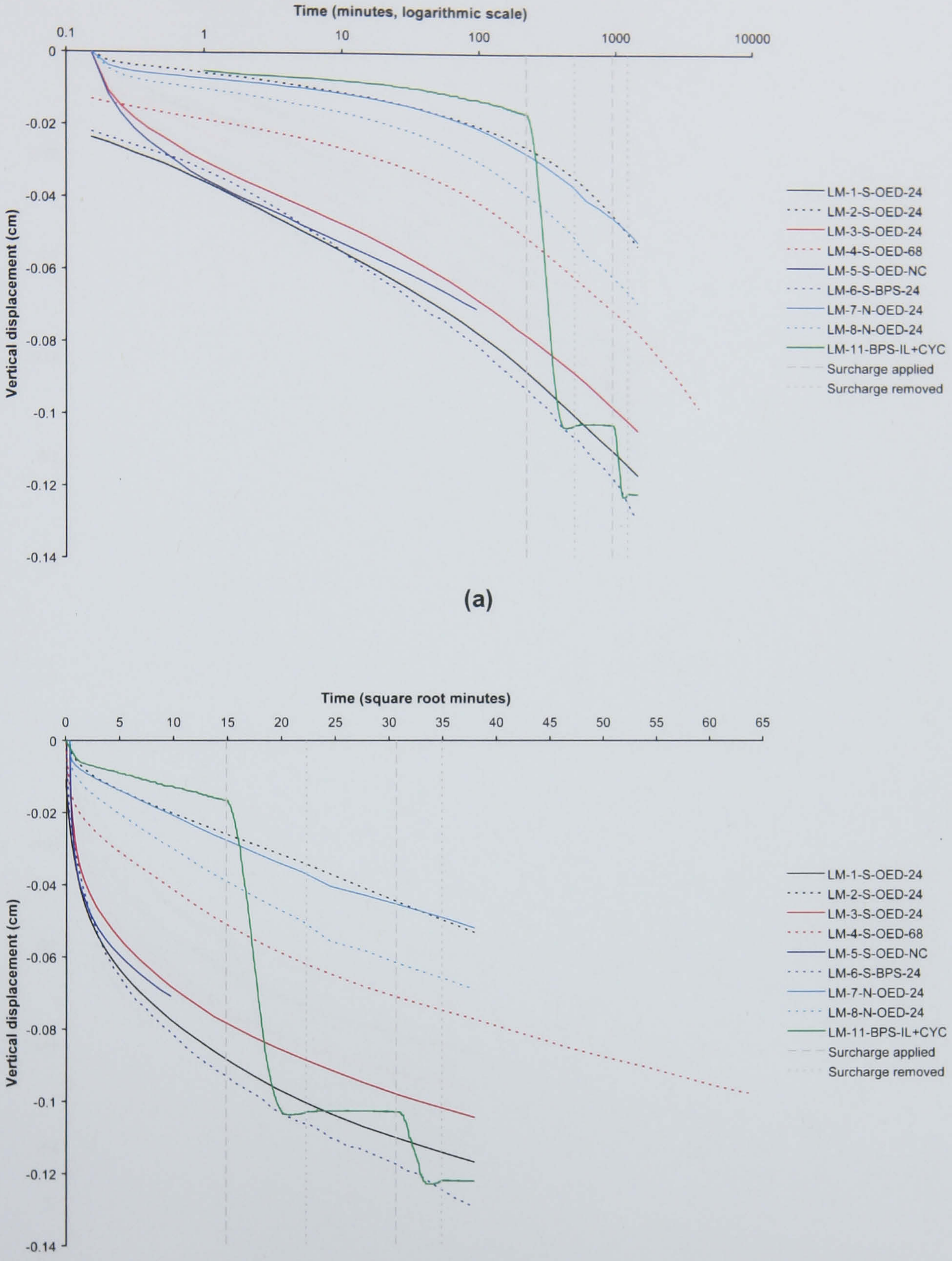

Figure 6.100 Time-vertical displacement plots comparing sample LM-11-BPS-IL+CYC with conventional incremental loading samples at an overburden stress of 26 kPa. (a) logarithmic time-vertical displacement (b) square-root time-vertical displacement.

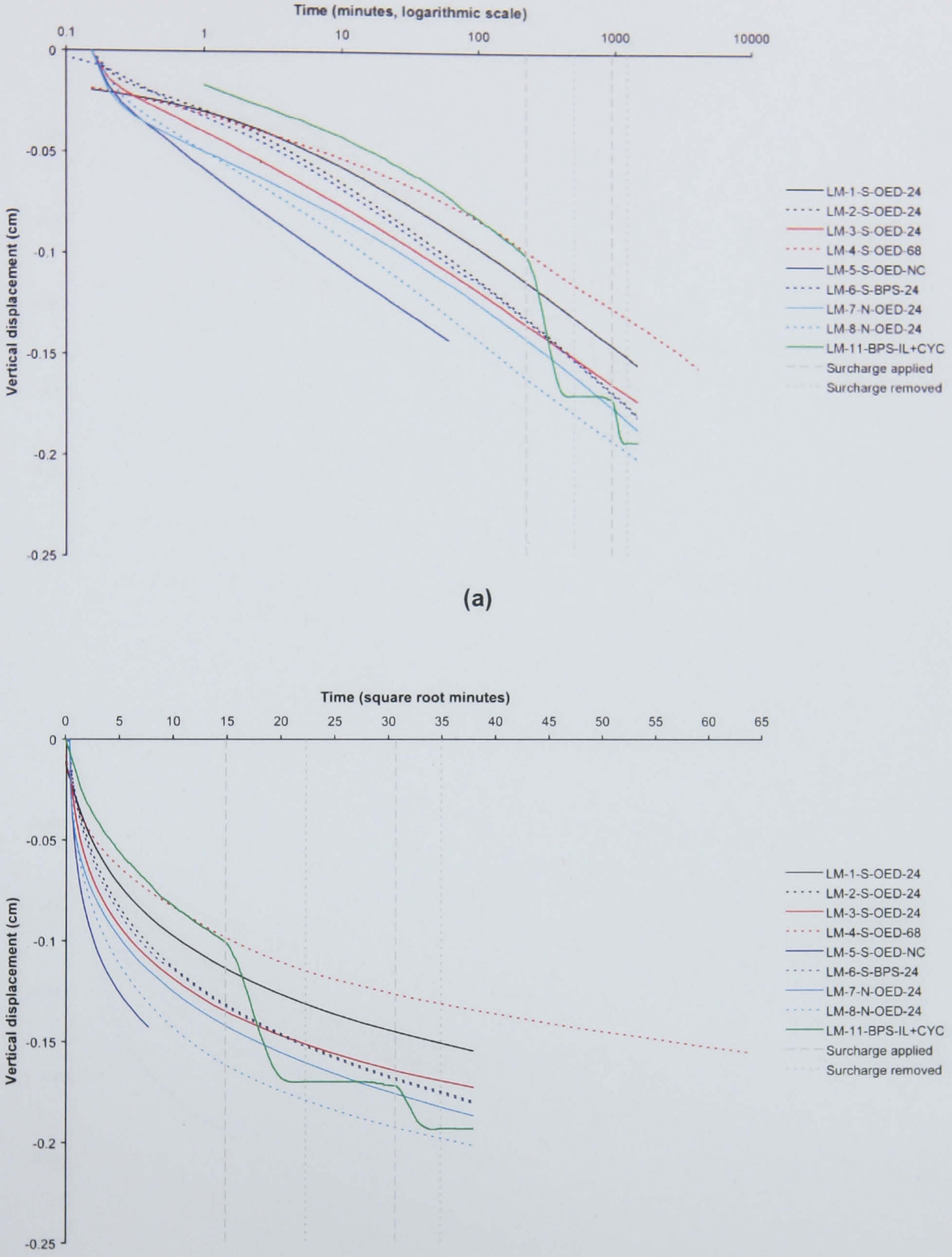

Figure 6.101 Time-vertical displacement plots comparing sample LM-11-BPS-IL+CYC with conventional incremental loading samples at an overburden stress of 50 kPa. (a) logarithmic time-vertical displacement (b) square-root time-vertical displacement

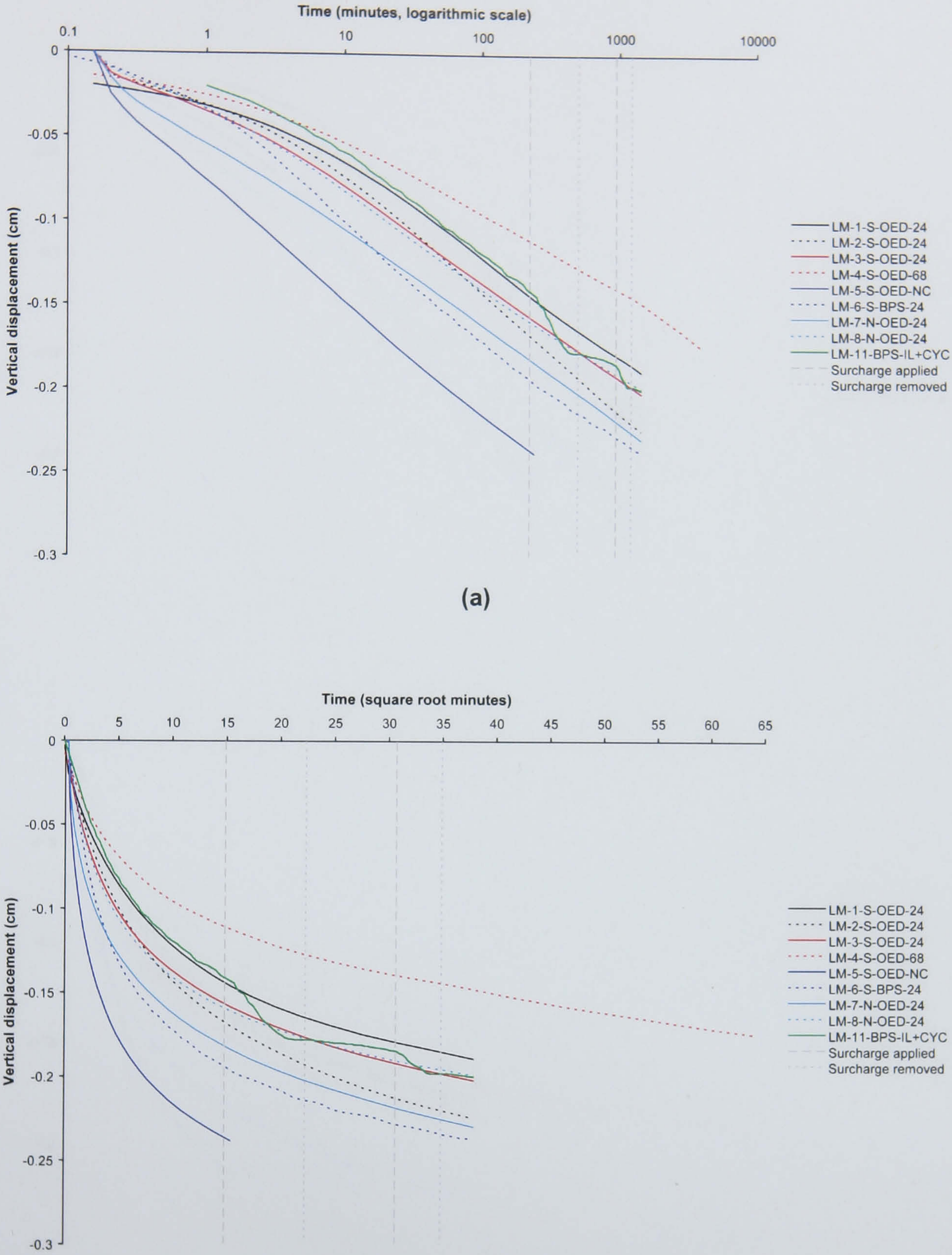

Figure 6.102 Time-vertical displacement plots comparing sample LM-11-BPS-IL+CYC with conventional incremental loading samples at an overburden stress of 99 kPa. (a) logarithmic time-vertical displacement (b) square-root time-vertical displacement.

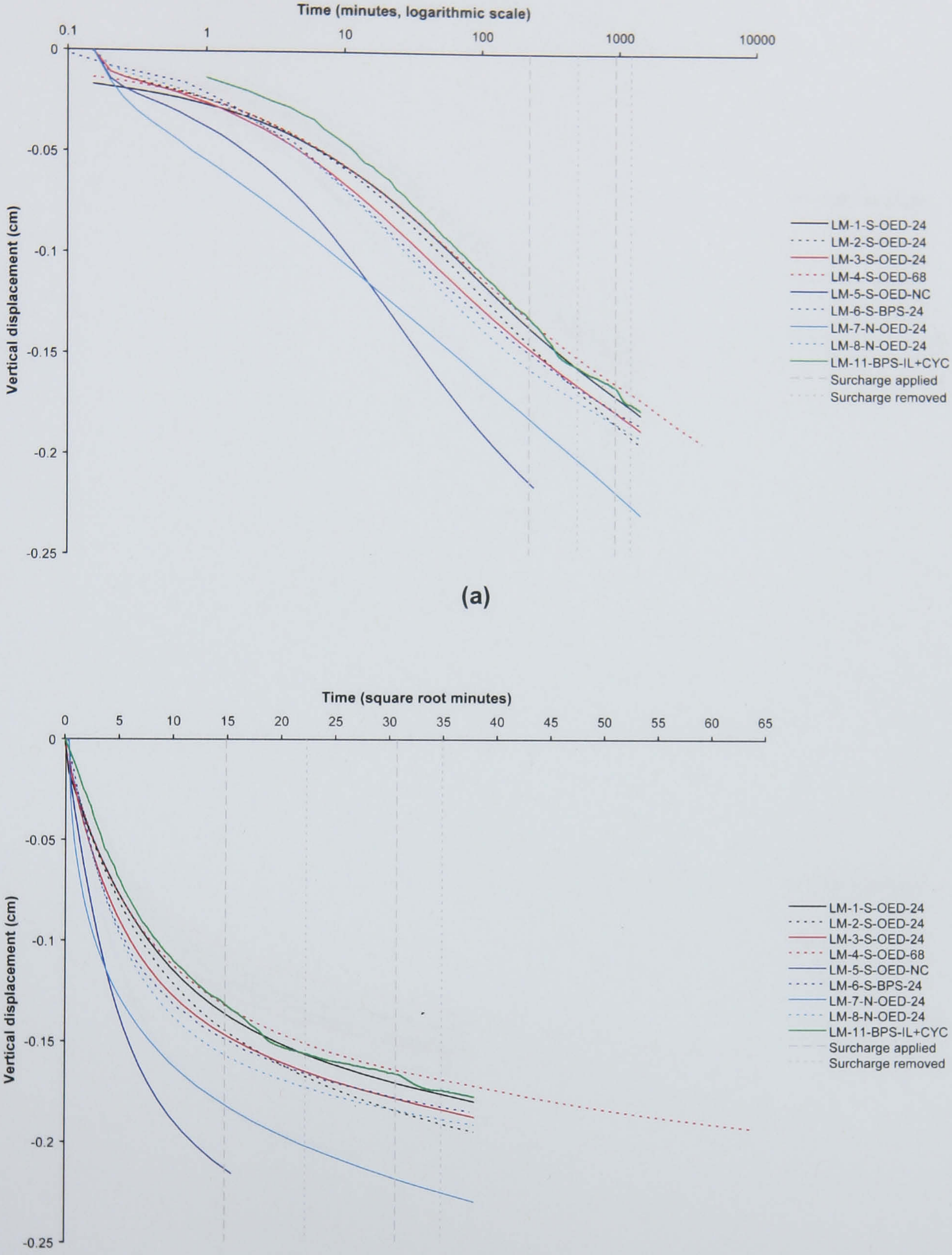

Figure 6.103 Time-vertical displacement plots comparing sample LM-11-BPS-IL+CYC with conventional incremental loading samples at an overburden stress of 197 kPa. (a) logarithmic time-vertical displacement (b) square-root time-vertical displacement.

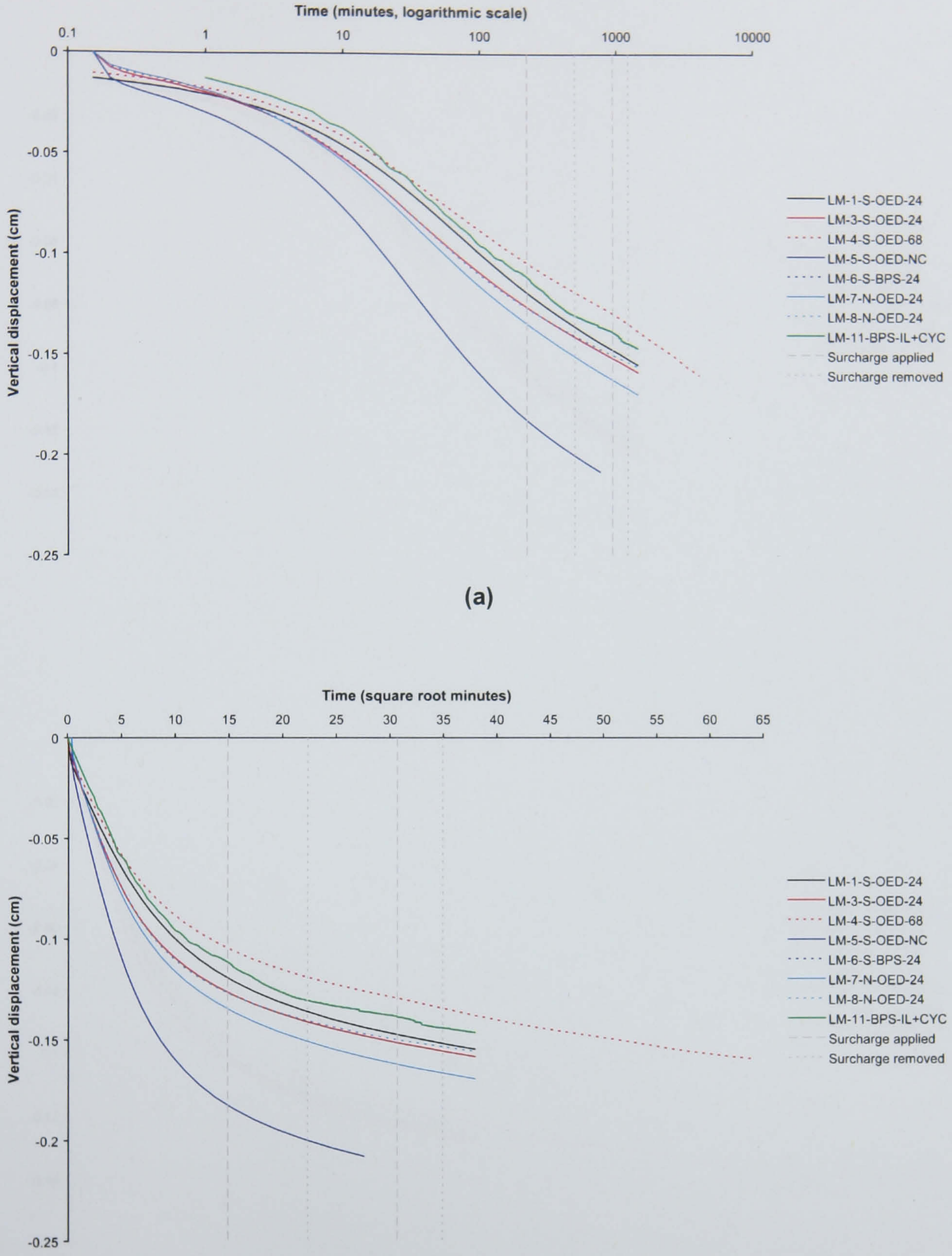

Figure 6.104 Time-vertical displacement plots comparing sample LM-11-BPS-IL+CYC with conventional incremental loading samples at an overburden stress of 393 kPa. (a) logarithmic time-vertical displacement (b) square-root time-vertical displacement.

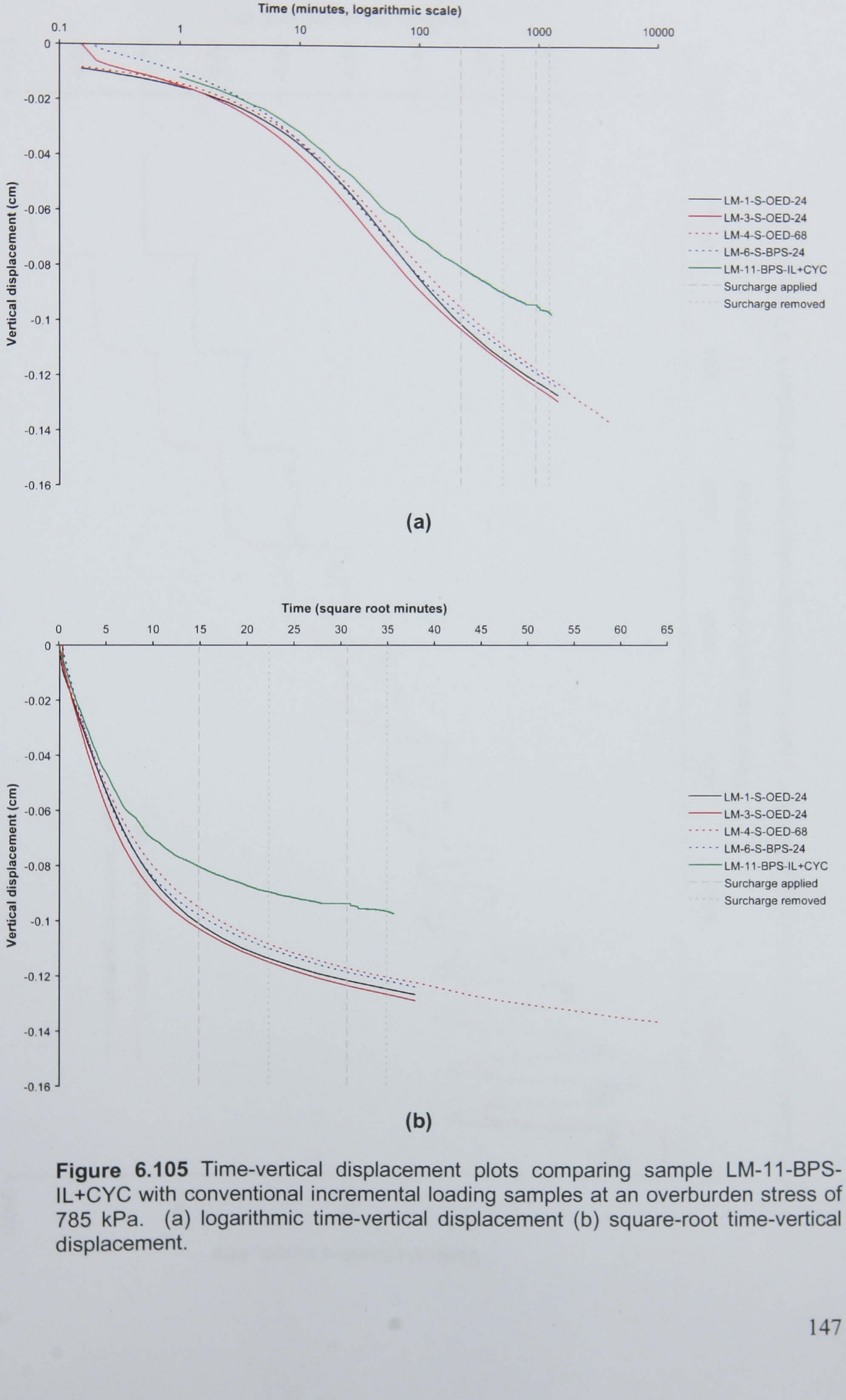

Figure 6.105 Time-vertical displacement plots comparing sample LM-11-BPS-IL+CYC with conventional incremental loading samples at an overburden stress of 785 kPa. (a) logarithmic time-vertical displacement (b) square-root time-vertical displacement.

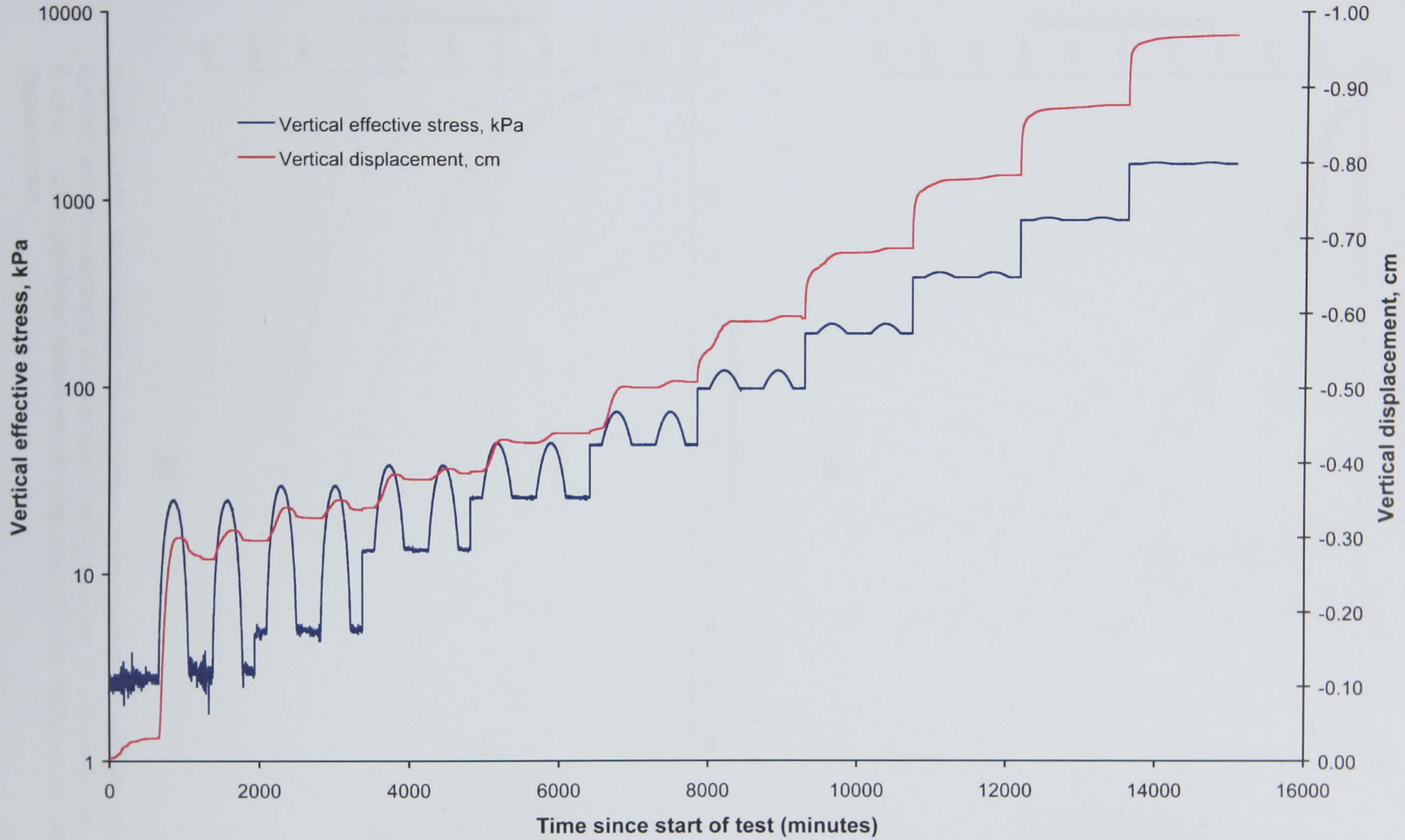

Figure 6.106 Variations in effective stress and vertical displacement over time in sample MF-10-BPS-IL+CYC.

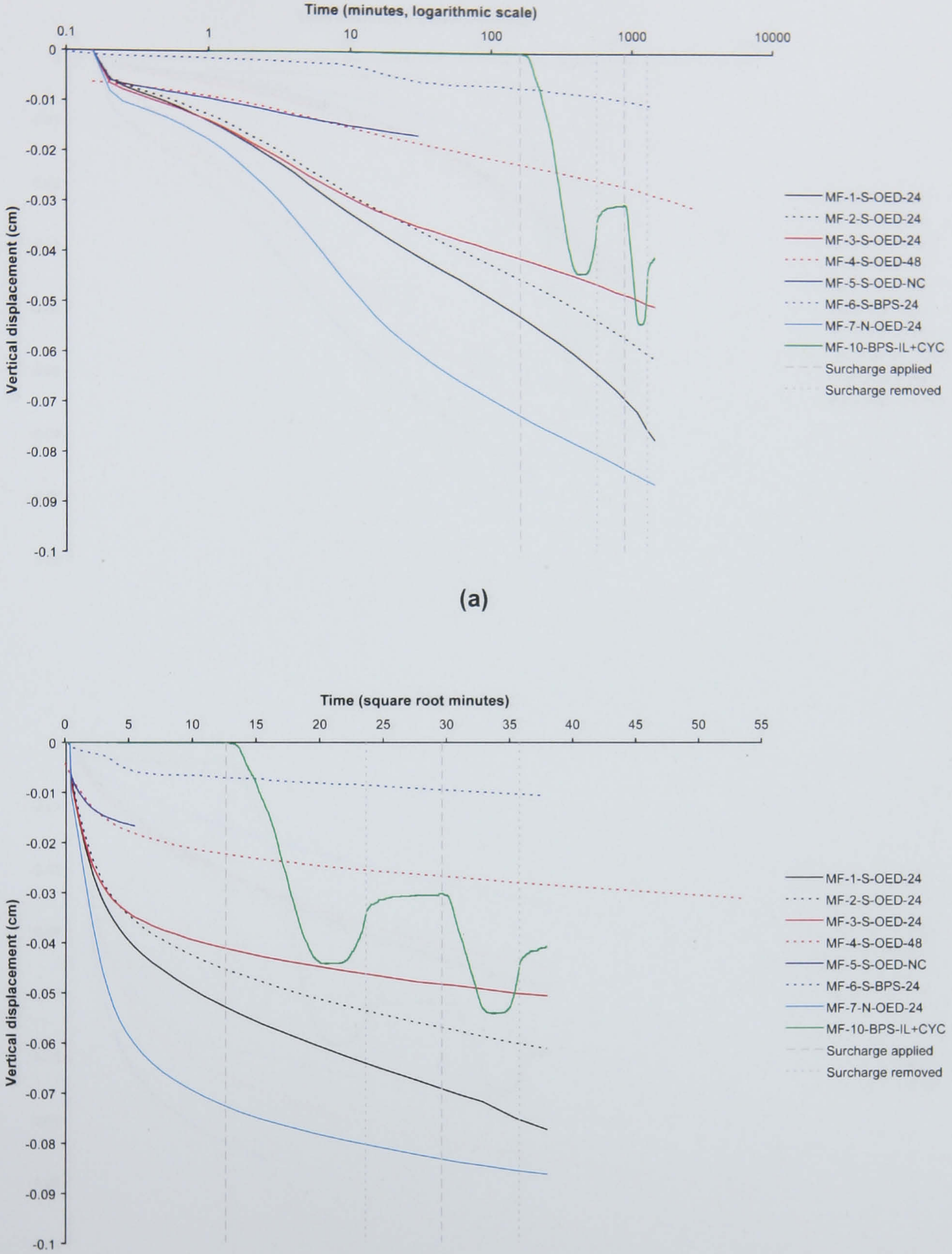

(a)

(b)

Figure 6.107 Time-vertical displacement plots comparing sample MF-10-BPS-IL+CYC with conventional incremental loading samples at an overburden stress of 5 kPa. (a) logarithmic time-vertical displacement (b) square-root time-vertical displacement.

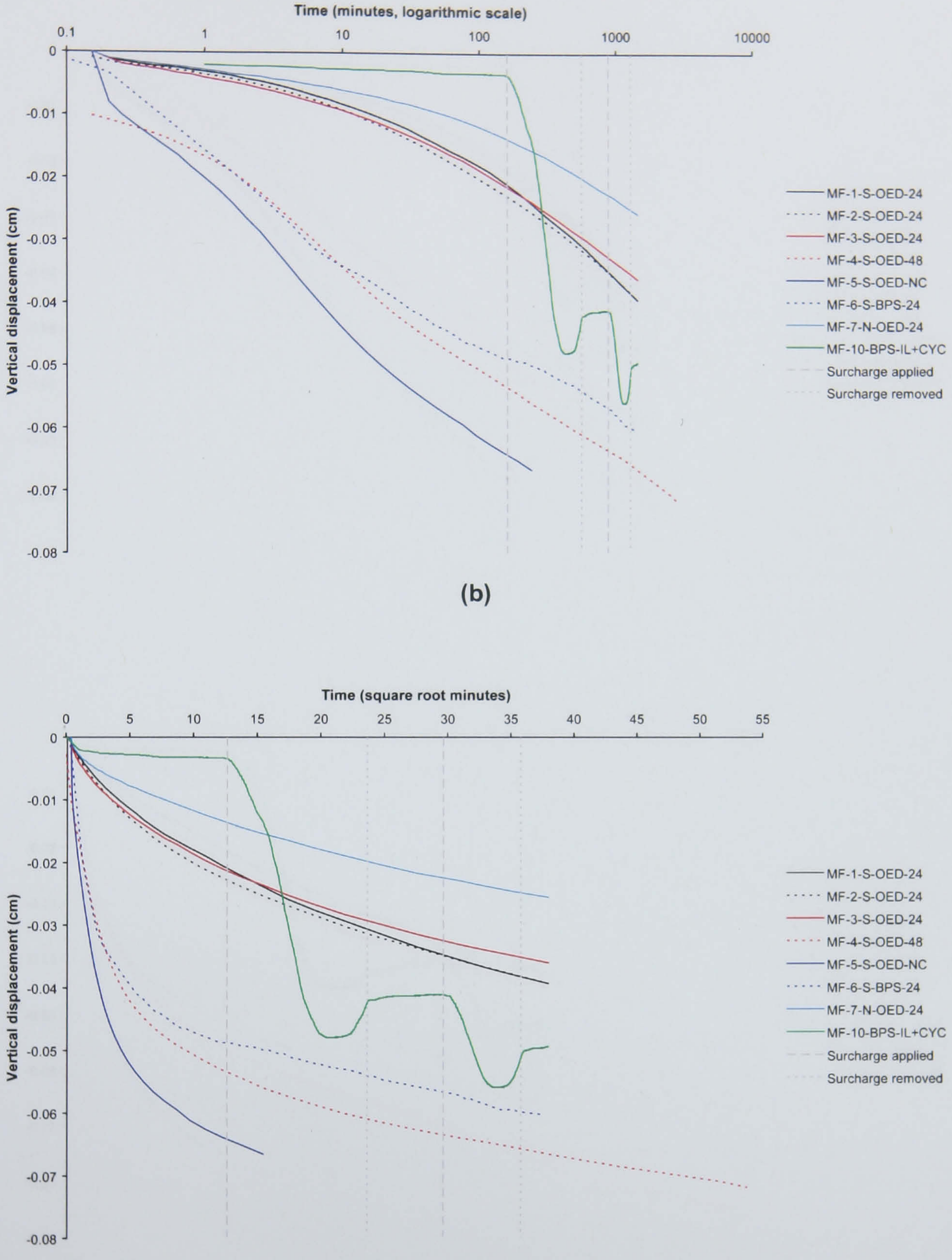

Figure 6.108 Time-vertical displacement plots comparing sample MF-10-BPS-IL+CYC with conventional incremental loading samples at an overburden stress of 14 kPa. (a) logarithmic time-vertical displacement (b) square-root time-vertical displacement.

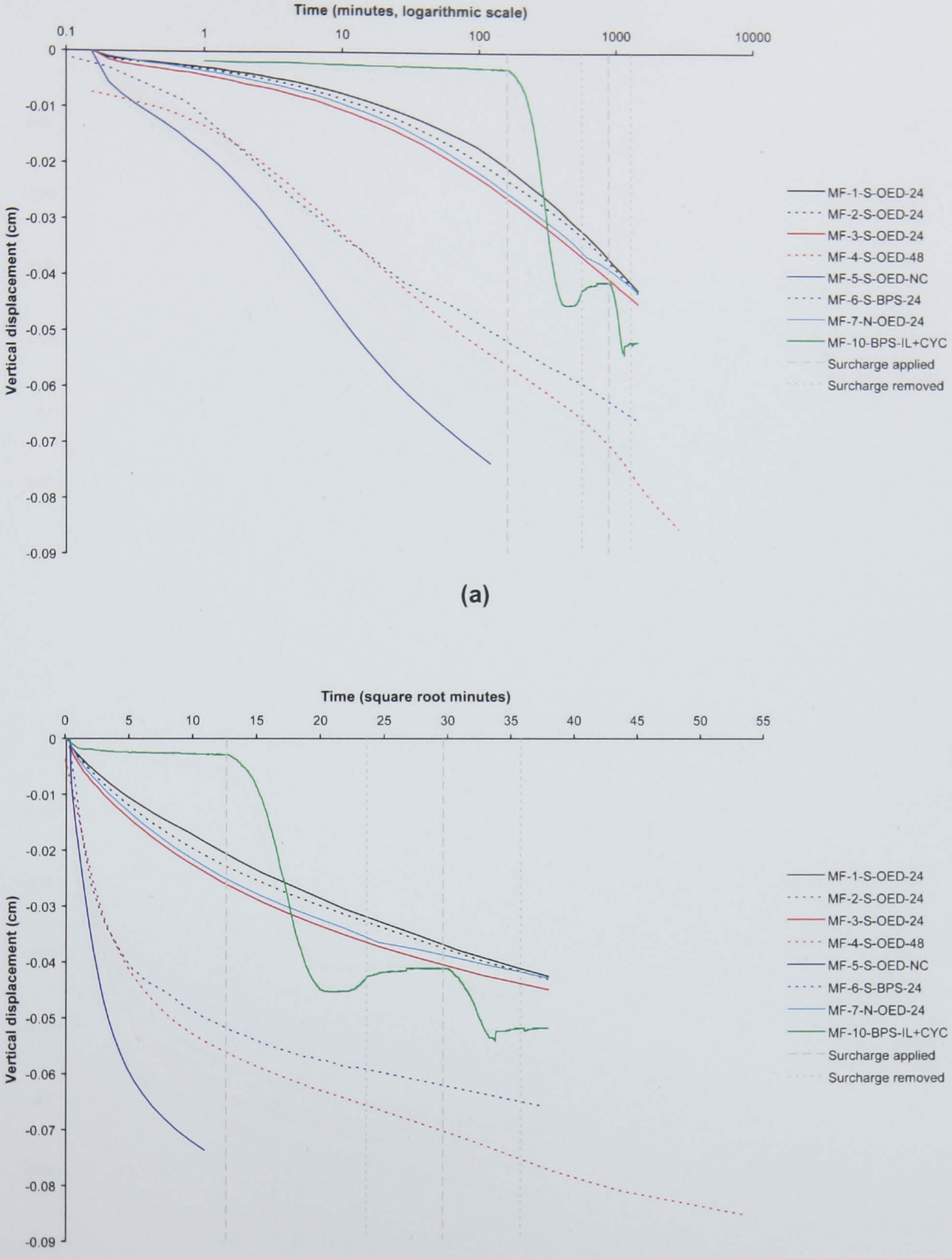

Figure 6.109 Time-vertical displacement plots comparing sample MF-10-BPS-IL+CYC with conventional incremental loading samples at an overburden stress of 26 kPa. (a) logarithmic time-vertical displacement (b) square-root time-vertical displacement.

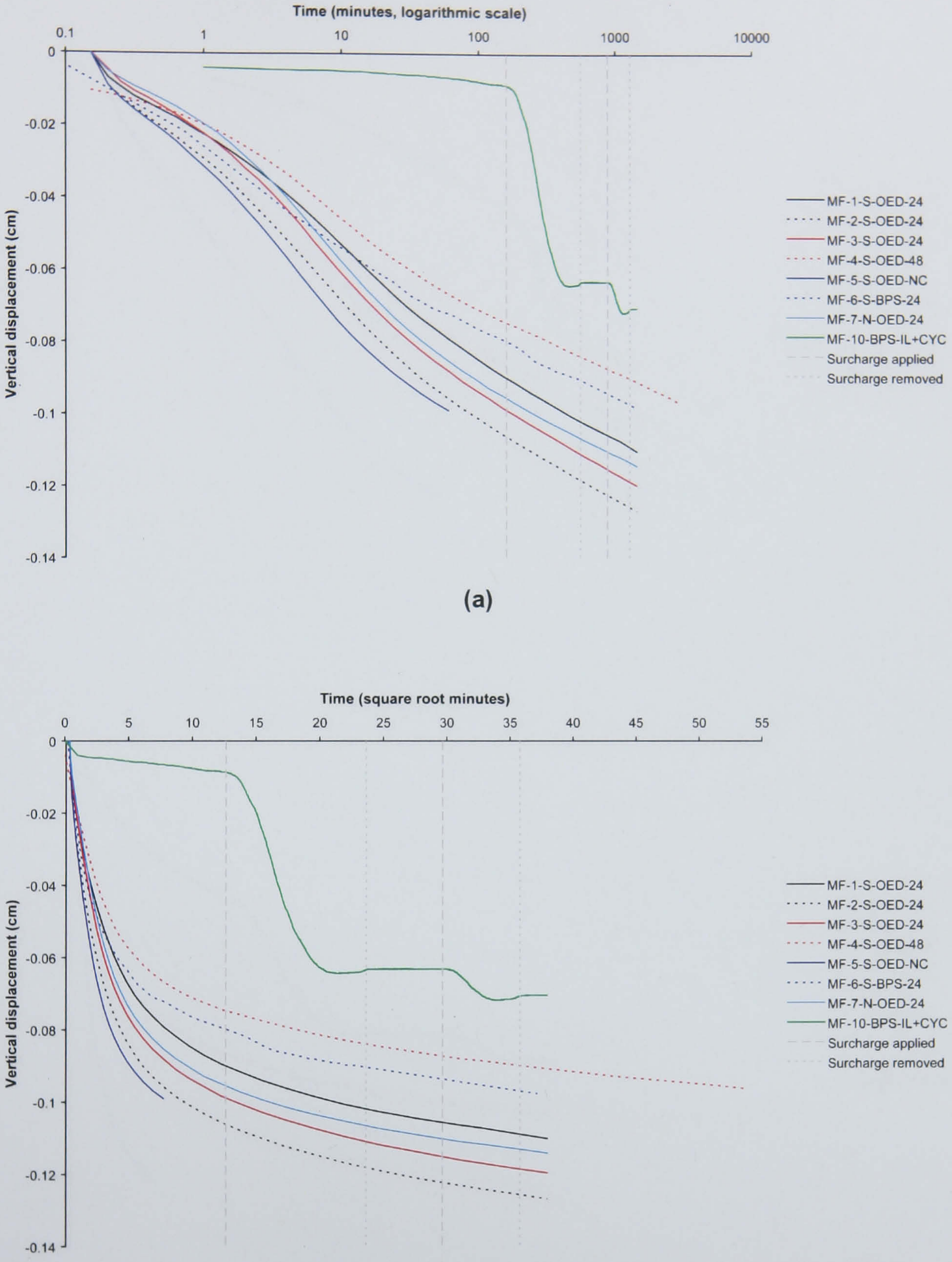

Figure 6.110 Time-vertical displacement plots comparing sample MF-10-BPS-IL+CYC with conventional incremental loading samples at an overburden stress of 50 kPa. (a) logarithmic time-vertical displacement (b) square-root time-vertical displacement.

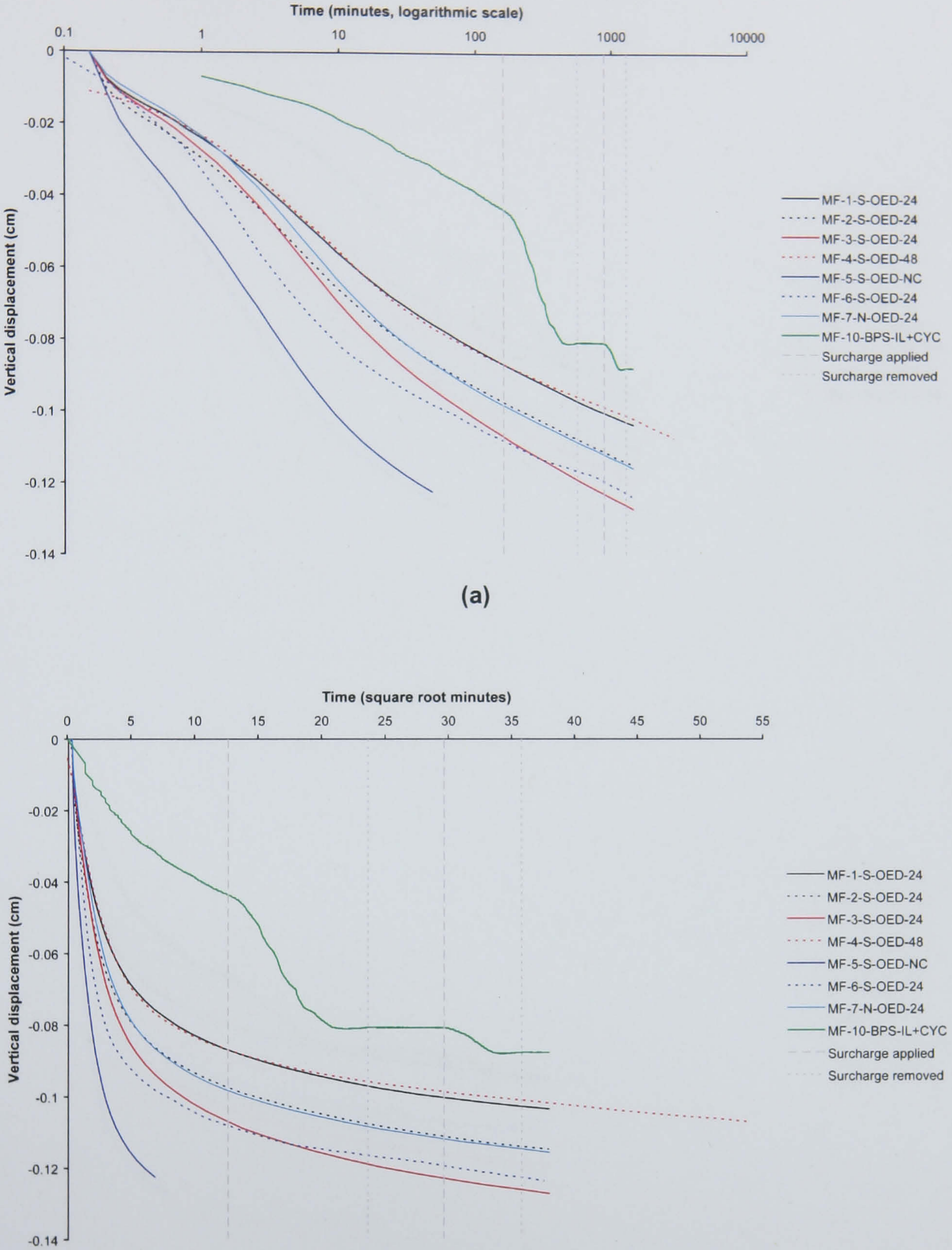

Figure 6.111 Time-vertical displacement plots comparing sample MF-10-BPS-IL+CYC with conventional incremental loading samples at an overburden stress of 99 kPa. (a) logarithmic time-vertical displacement (b) square-root time-vertical displacement.

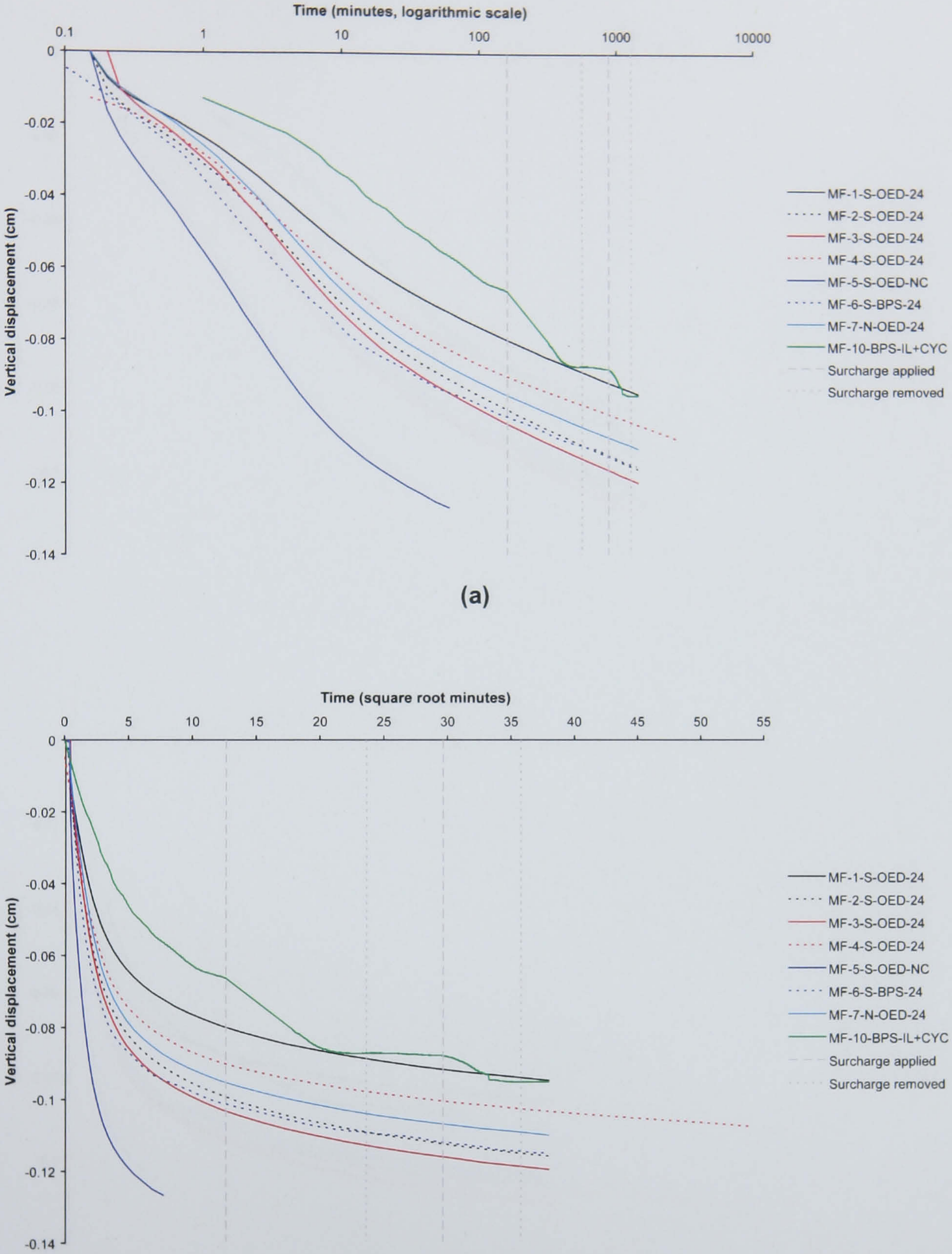

Figure 6.112 Time-vertical displacement plots comparing sample MF-10-BPS-IL+CYC with conventional incremental loading samples at an overburden stress of 197 kPa. (a) logarithmic time-vertical displacement (b) square-root time-vertical displacement.

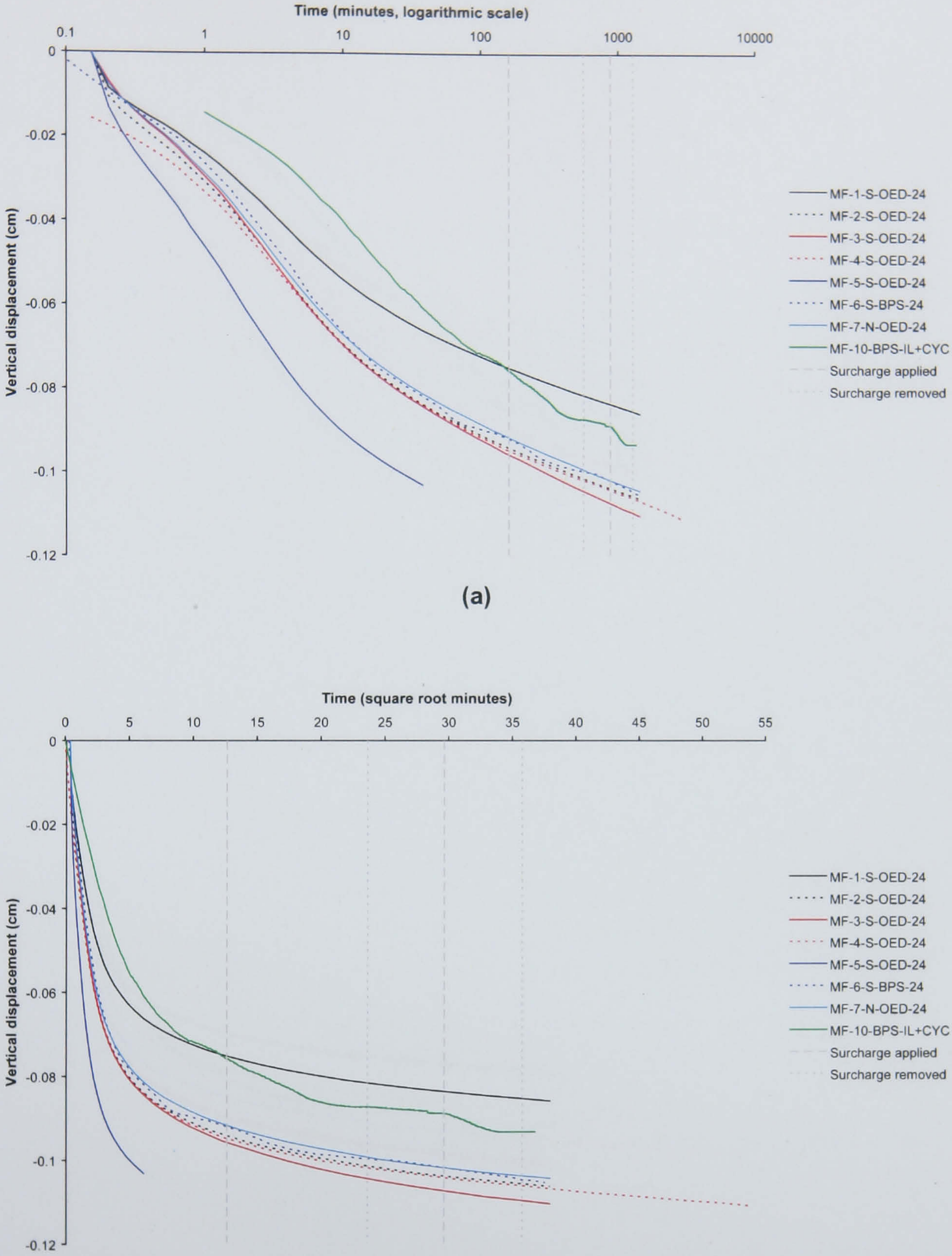

Figure 6.113 Time-vertical displacement plots comparing sample MF-10-BPS-IL+CYC with conventional incremental loading samples at an overburden stress of 393 kPa. (a) logarithmic time-vertical displacement (b) square-root time-vertical displacement.

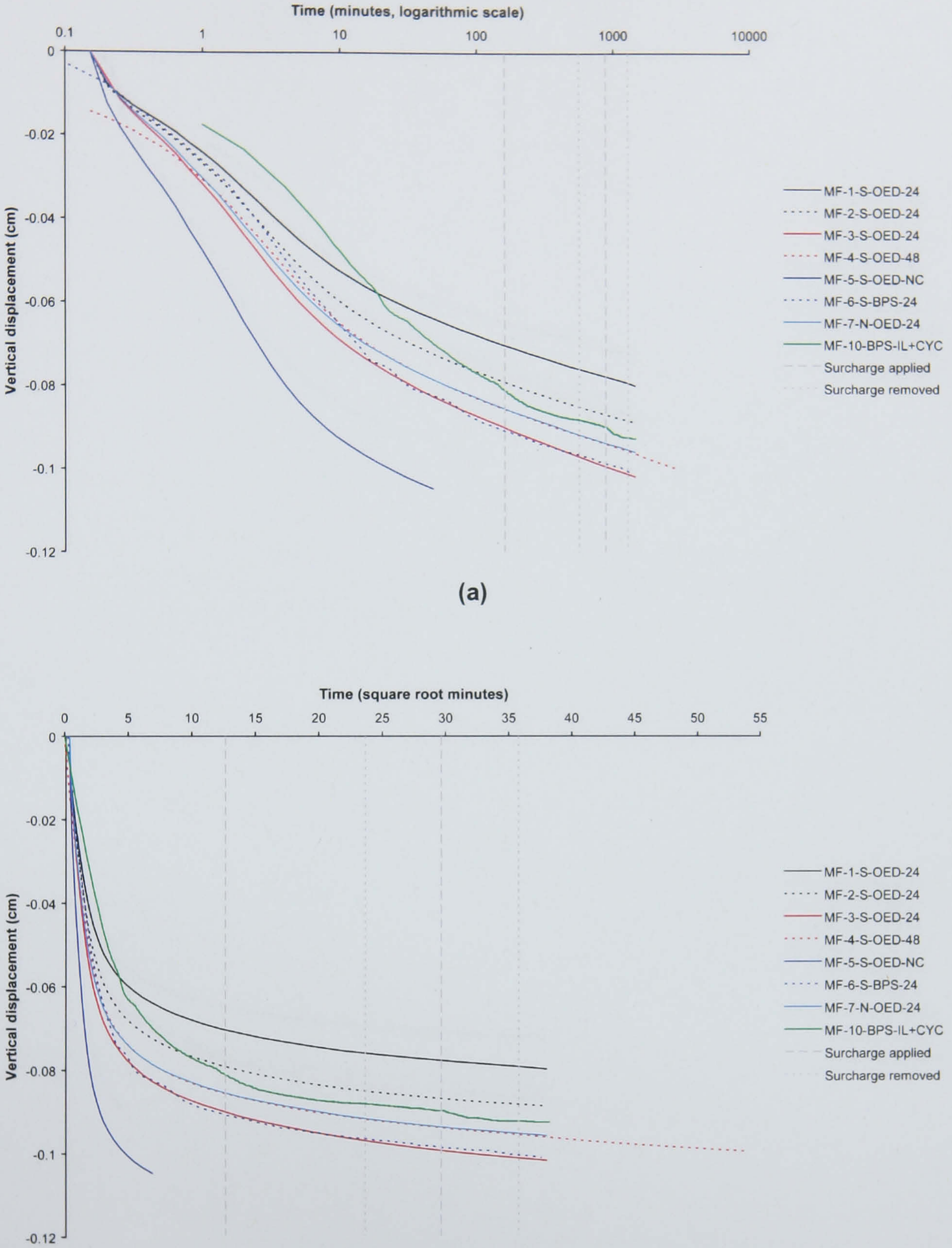

Figure 6.114 Time-vertical displacement plots comparing sample MF-10-BPS-IL+CYC with conventional incremental loading samples at an overburden stress of 785 kPa. (a) logarithmic time-vertical displacement (b) square-root time-vertical displacement.

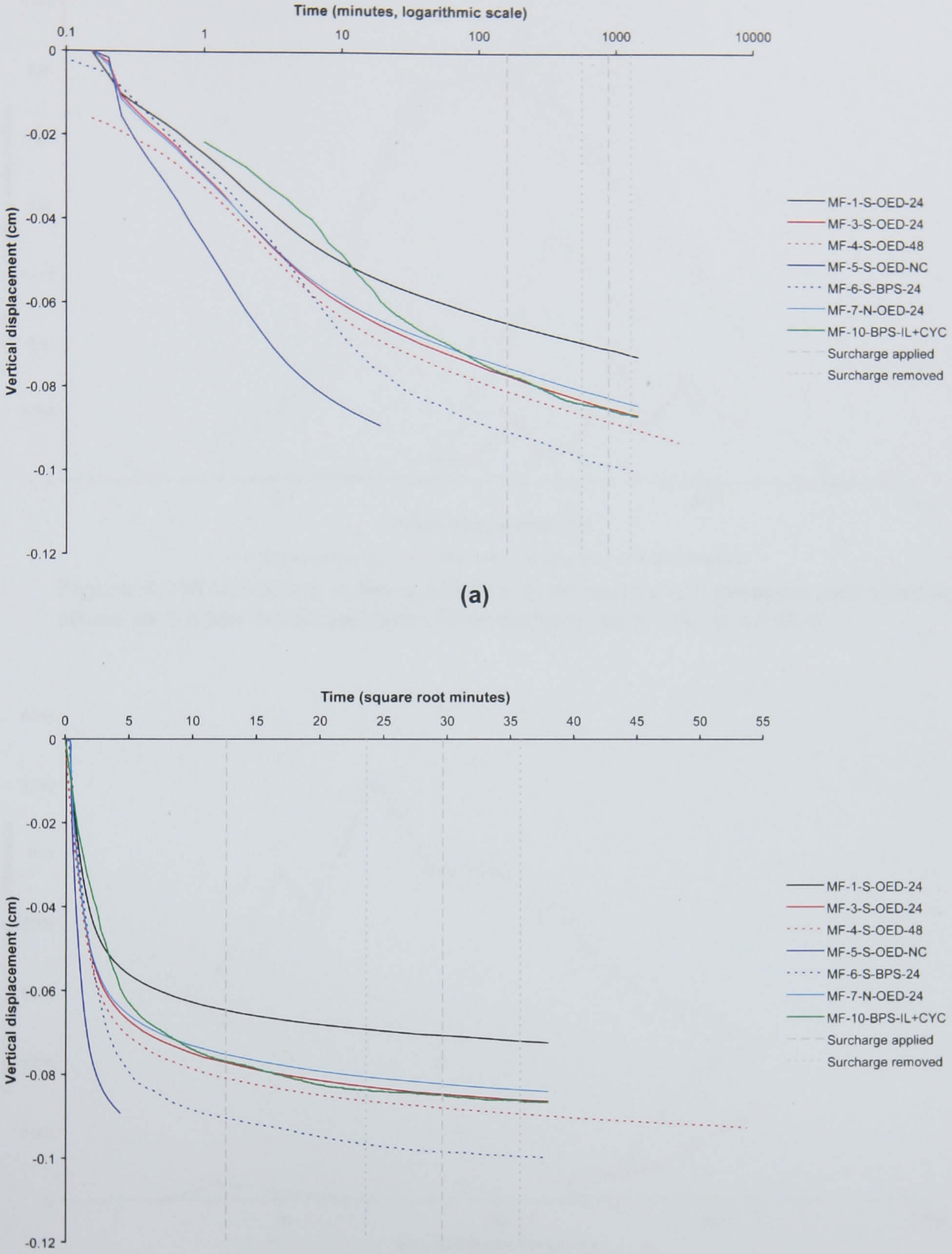

Figure 6.115 Time-vertical displacement plots comparing sample MF-10-BPS-IL+CYC with conventional incremental loading samples at an overburden stress of 1570 kPa. (a) logarithmic time-vertical displacement (b) square-root time-vertical displacement.

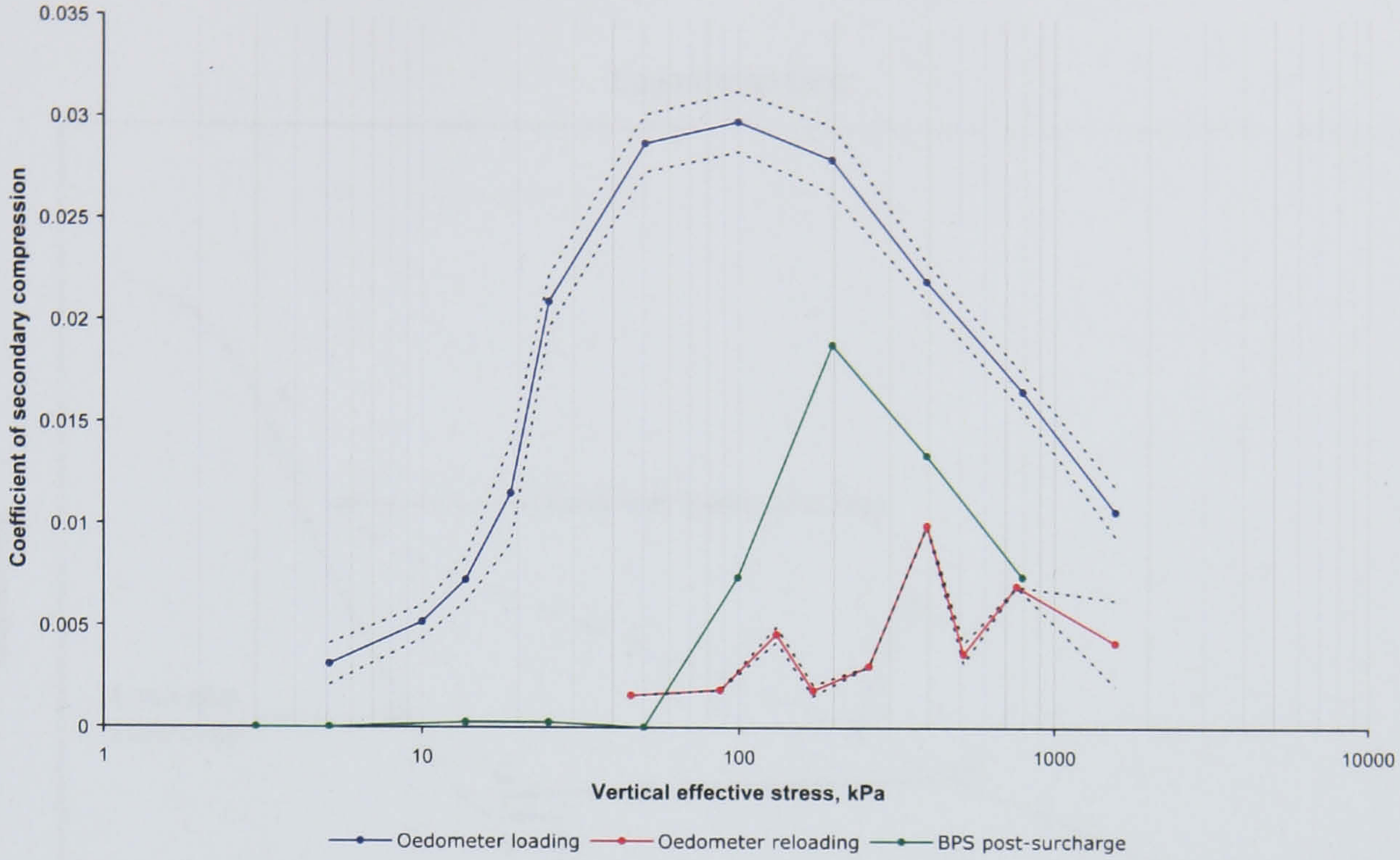

Figure 6.116 Variations in the coefficient of secondary compression with effective stress for the low marsh samples. Error margins are ± 1 standard error.

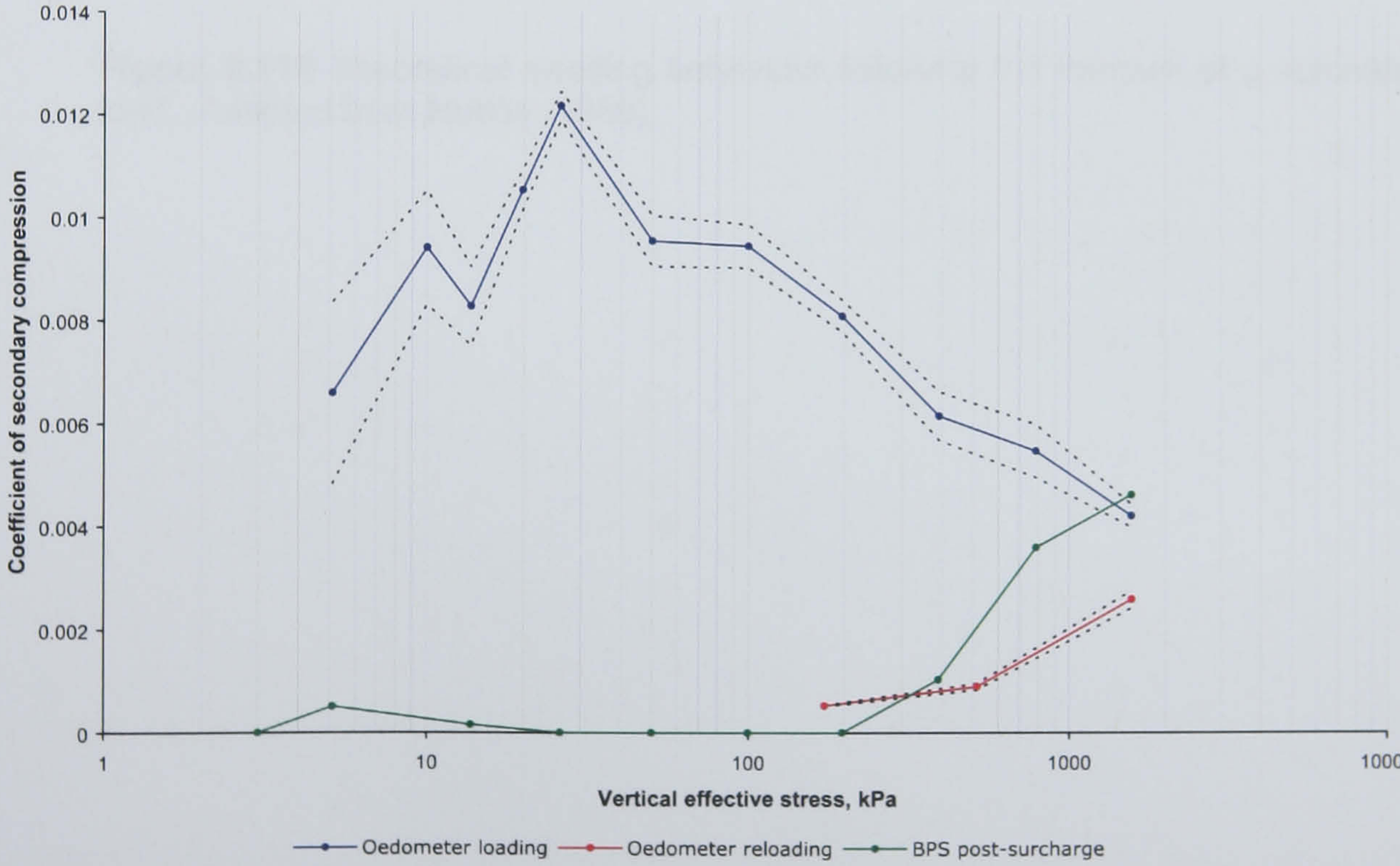

Figure 6.117 Variations in the coefficient of secondary compression with effective stress for the low marsh samples. Error margins are ± 1 standard error.

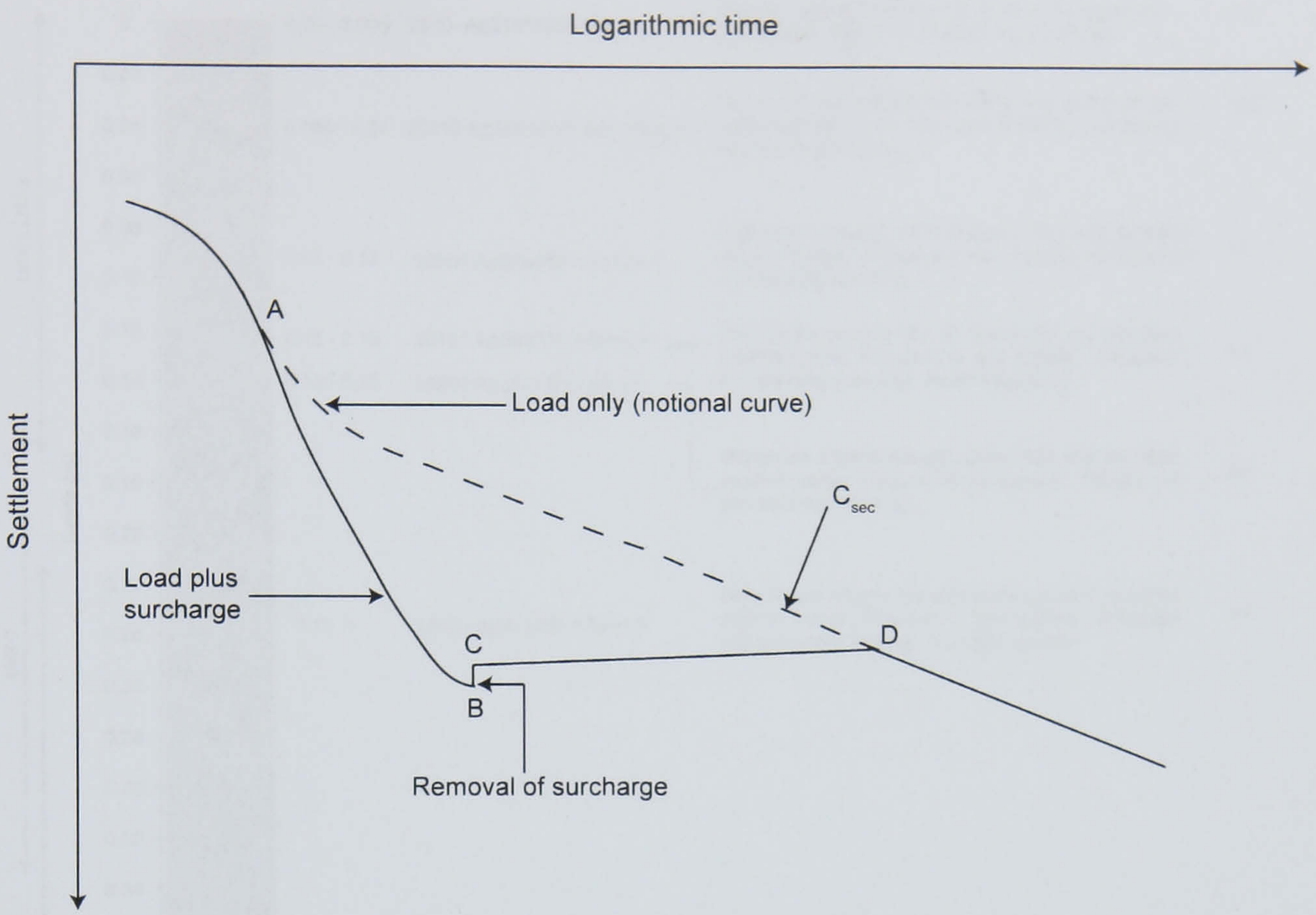

Figure 6.118 Theoretical swelling behaviour following the removal of a surcharge load. Adapted from Hobbs (1986).

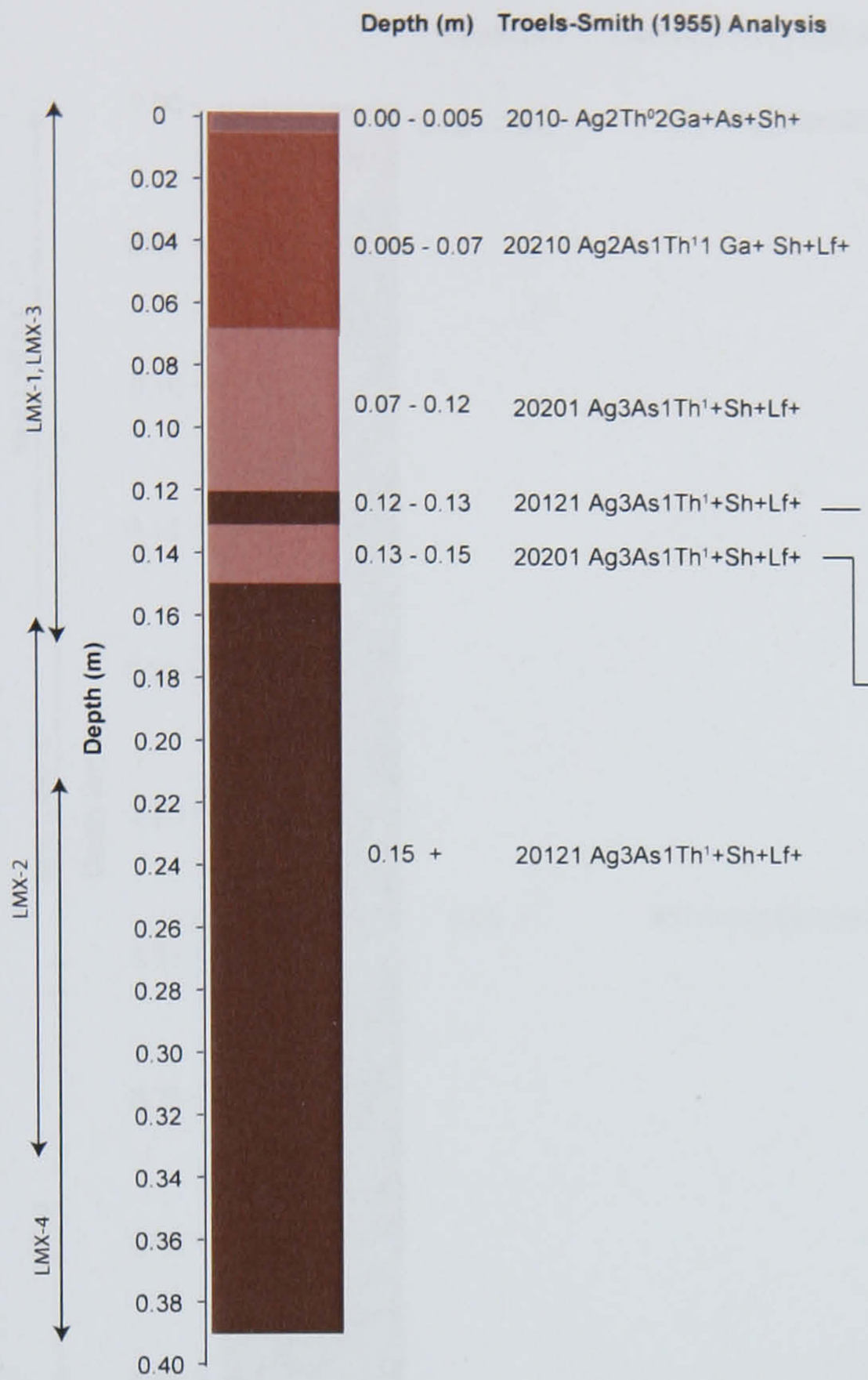

Figure 7.1 Stratigraphy of the sediment cores collected from the low marsh.

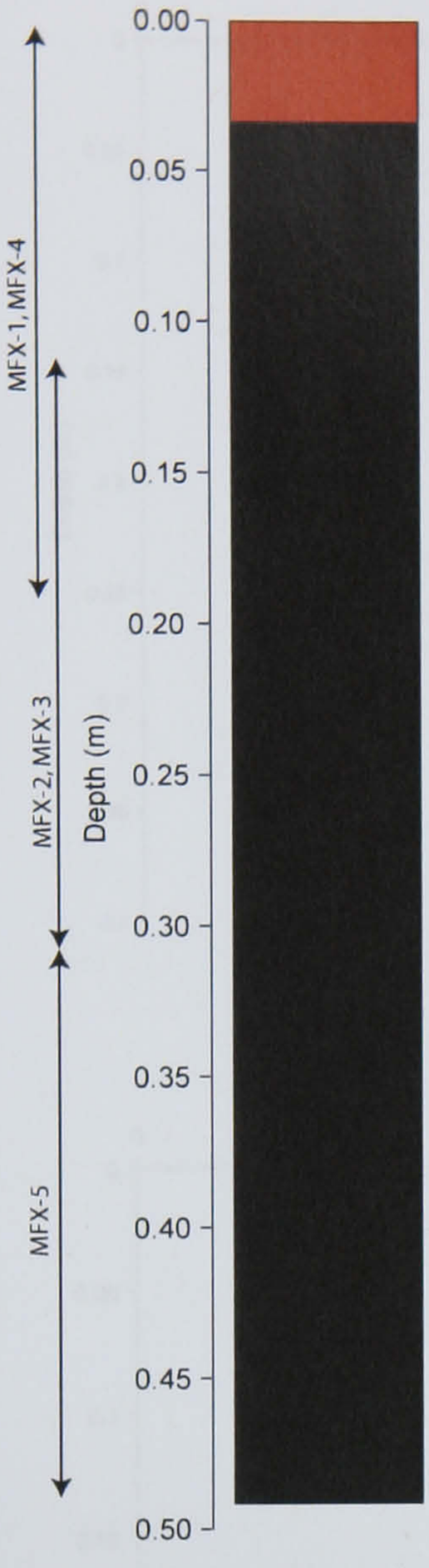

Depth (m)	Troels-Smith (1955) Analysis	Sediment Description	Lithological Unit
0.00 - 0.03	1011- Ag3Ga1As+	Light brown silt with some sand and clay. Oxidised zone with frequent bioturbation burrows.	M2
0.03 +	40110 Ag3Ga1As+Dh+	Dark black silt with some sand and clay. Reduced zone with occasional organic detritral matter.	M1

Figure 7.2 Stratigraphy of the sediment cores collected from the mudflat.

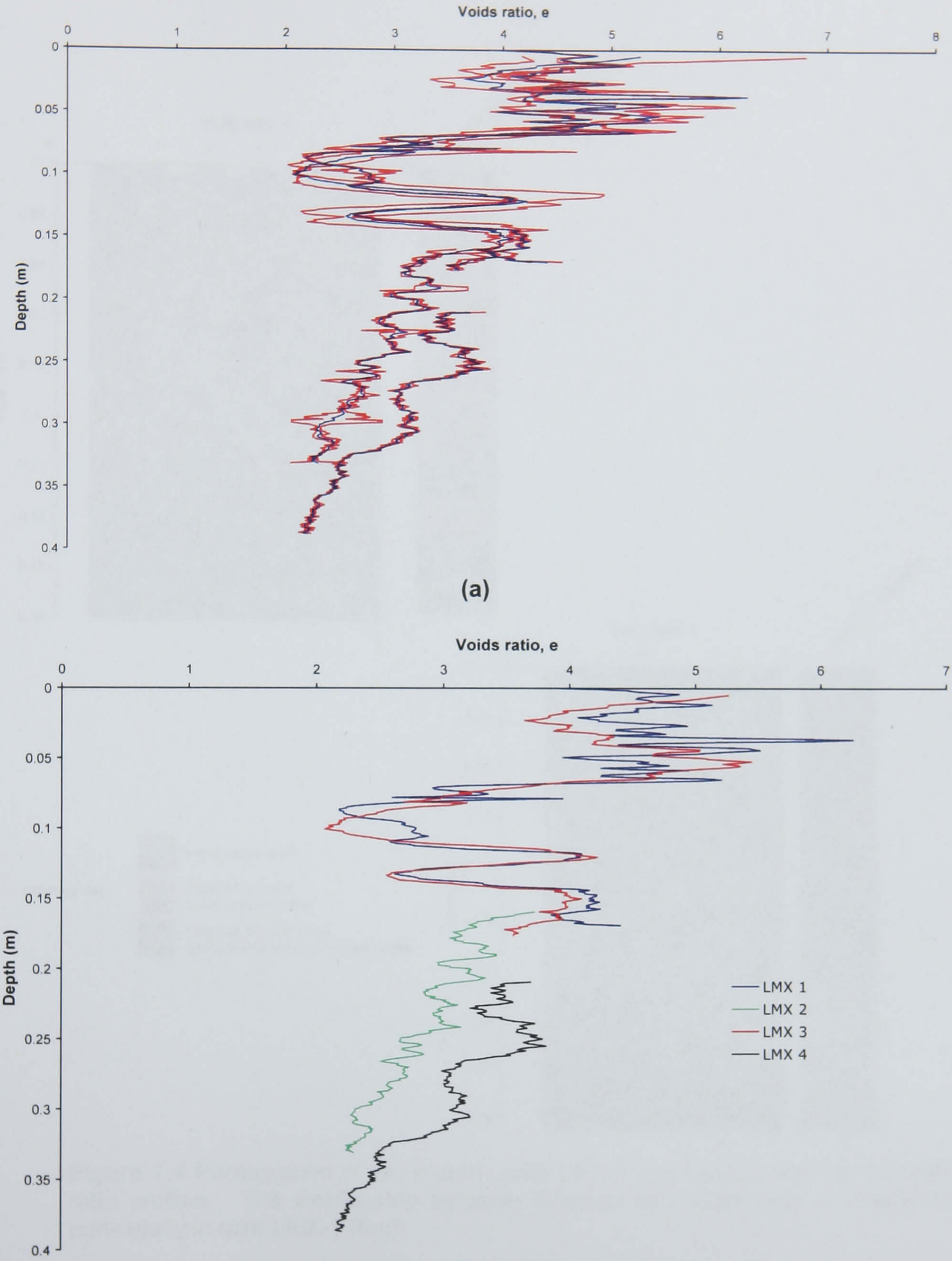

Figure 7.3 Voids ratio profiles of the low marsh cores with (a) and without (b) root squared error terms. 7.3 (b) also shows the replicability of voids ratio measurements between overlapping core samples.

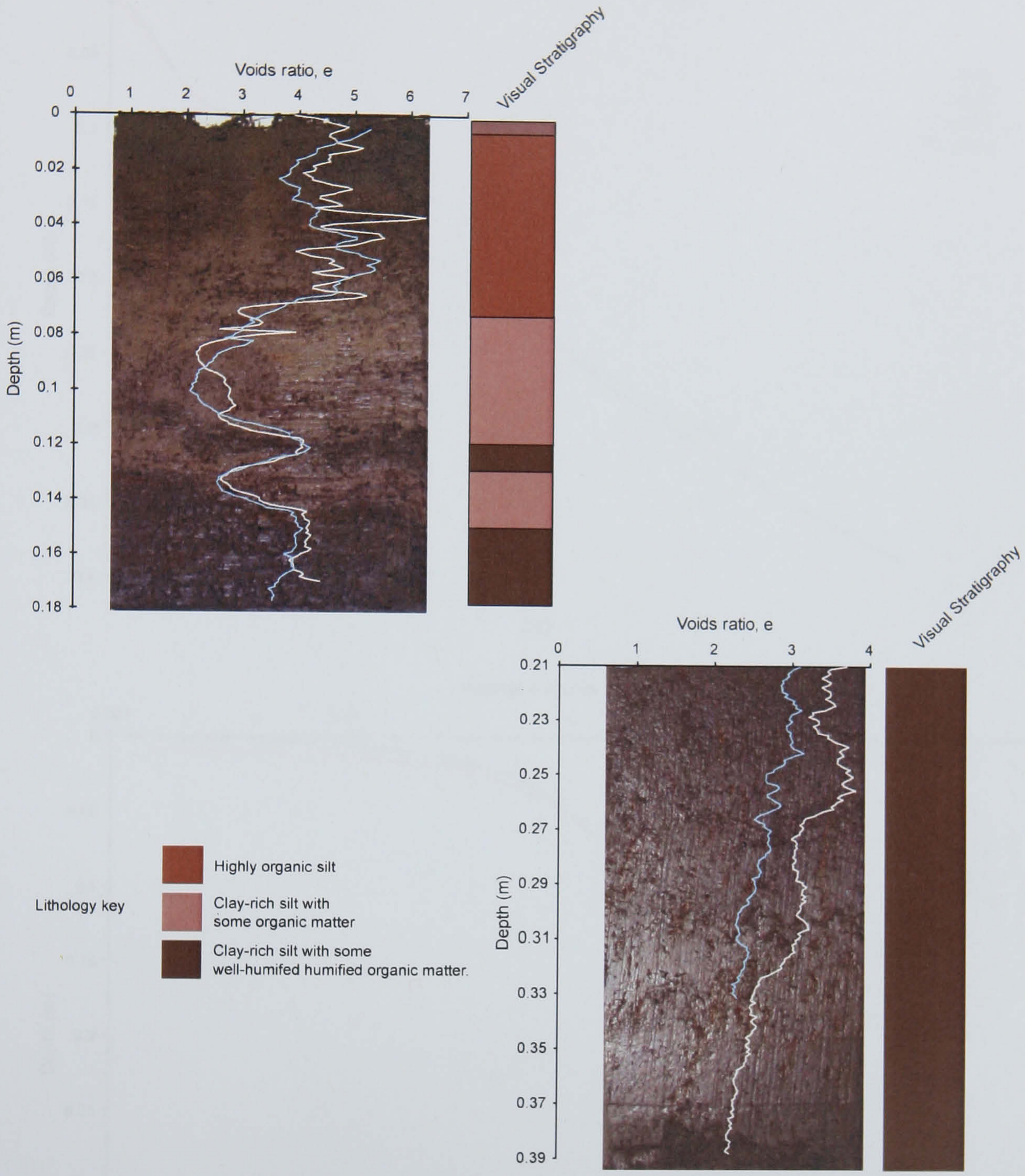

Figure 7.4 Photographs of low marsh cores LMX-1 and LMX-2, overlain by voids ratio profiles. The relationship between lithology and voids ratio is displayed, particularly in core LMX-1 (top)

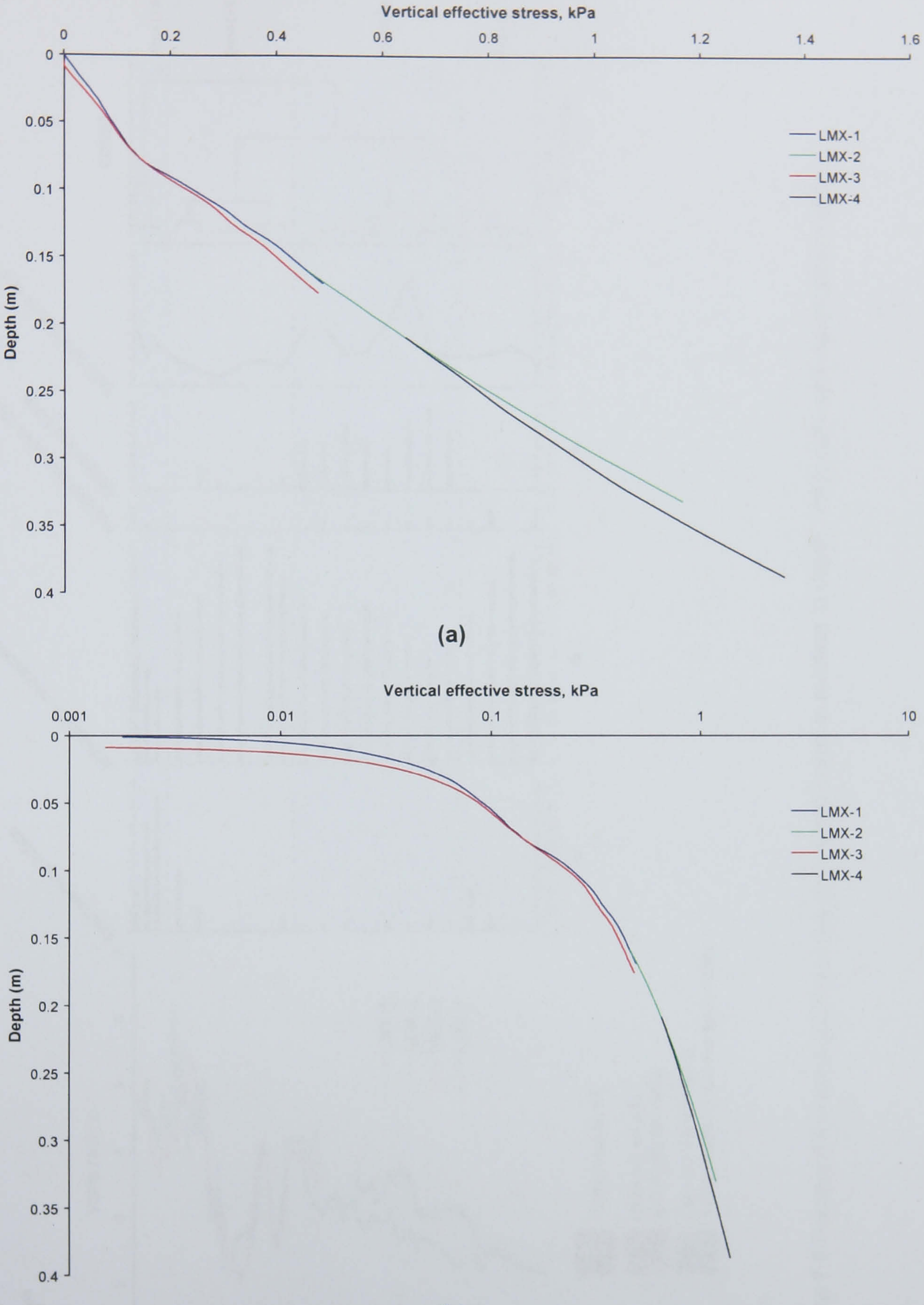

Figure 7.5 Depth variations of effective stress in the low marsh cores on (a) natural and (b) logarithmic scales.

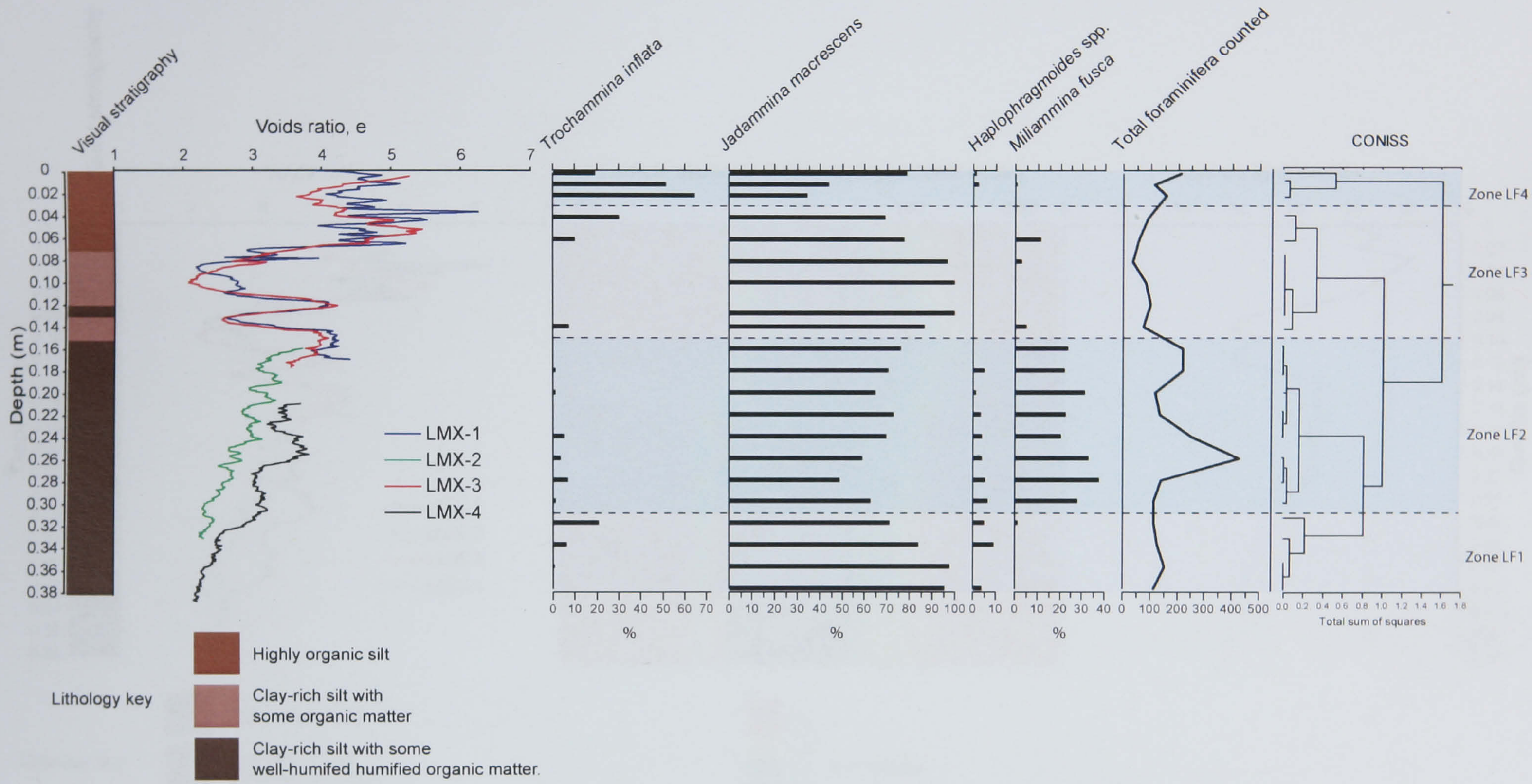

Figure 7.6 Foraminiferal stratigraphy of the low marsh cores in relation to depth, voids ratio and visual stratigraphy.

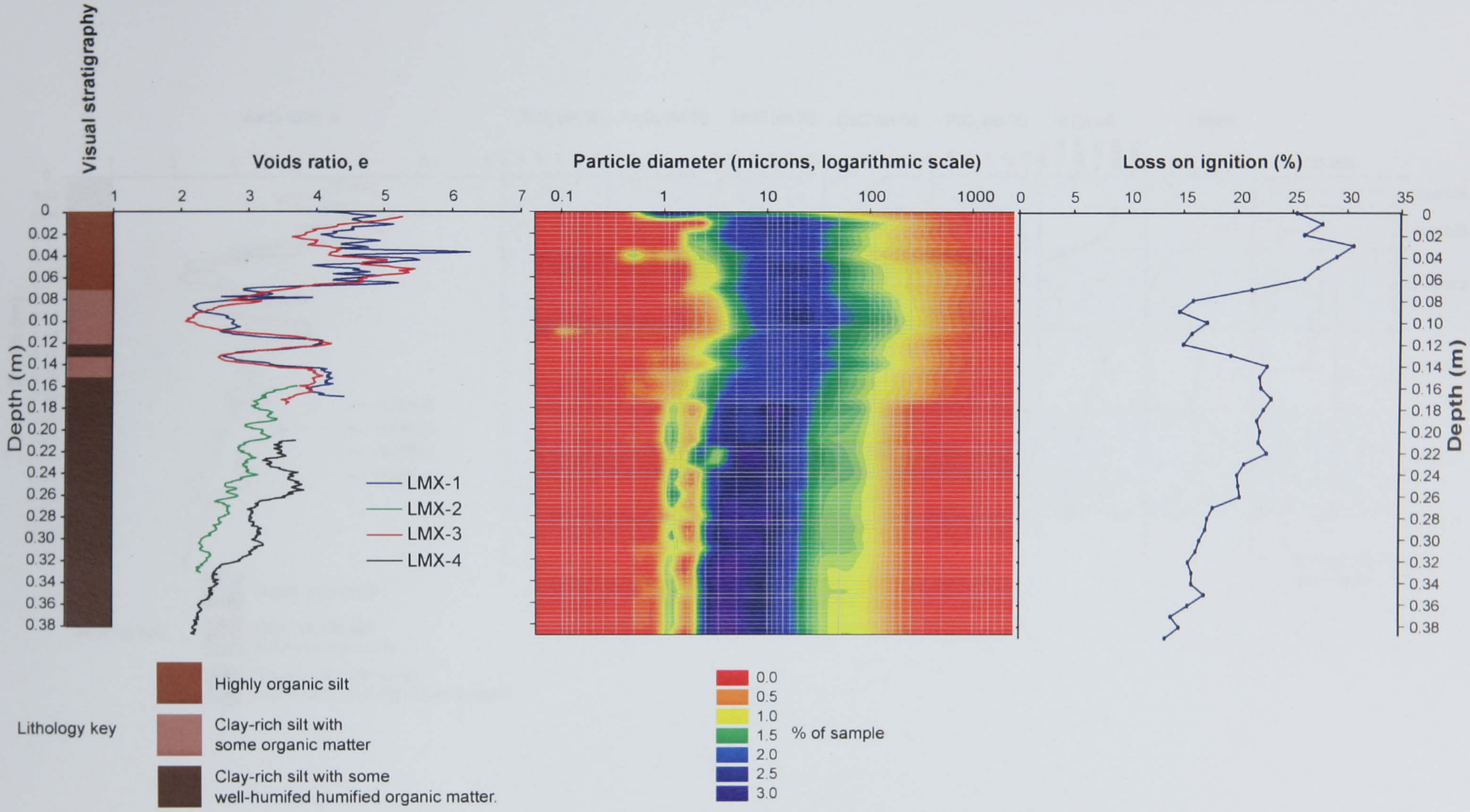

Figure 7.7 Lithostratigraphy of the low marsh cores in relation to depth, voids ratio and visual stratigraphy.

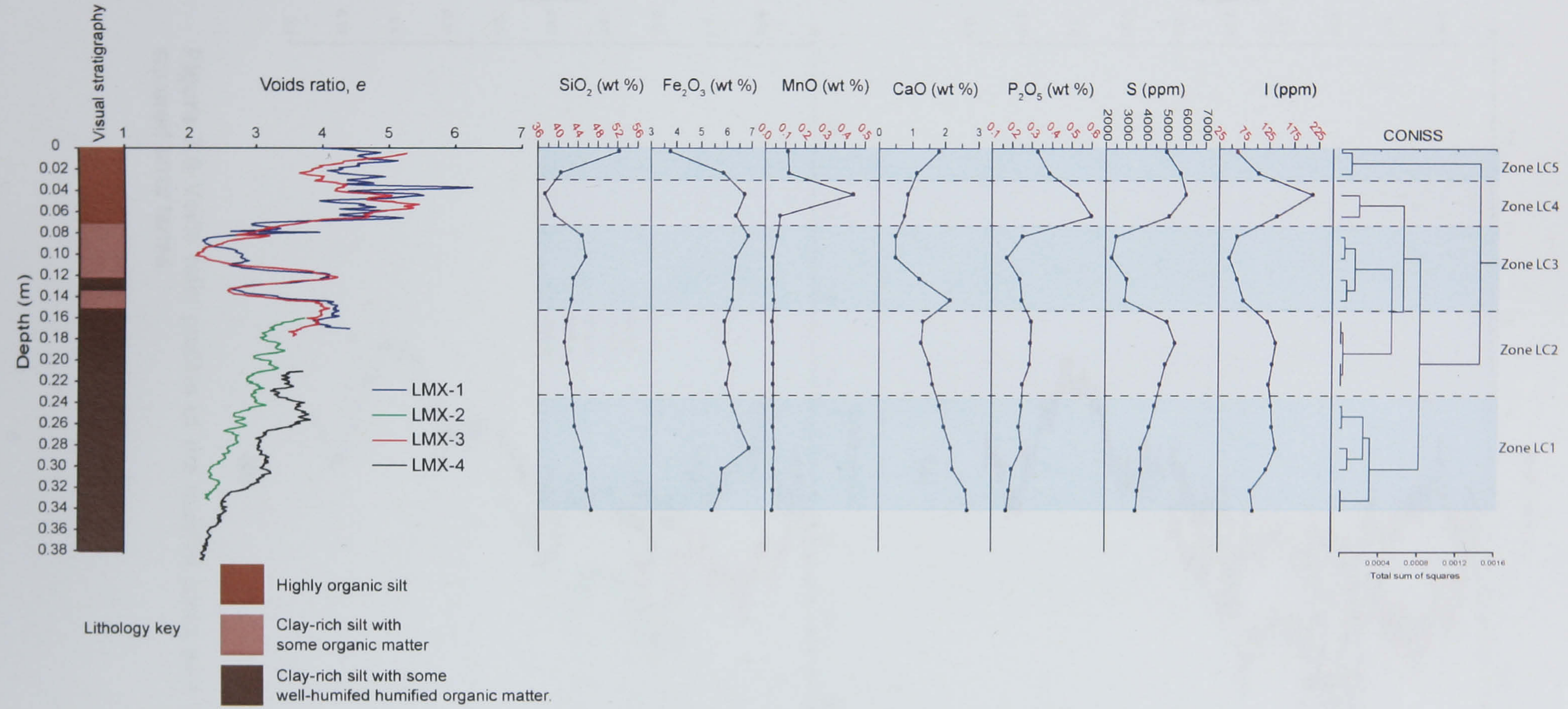

Figure 7.8 Chemostratigraphy of the low marsh cores in relation to depth, voids ratio and visual stratigraphy.

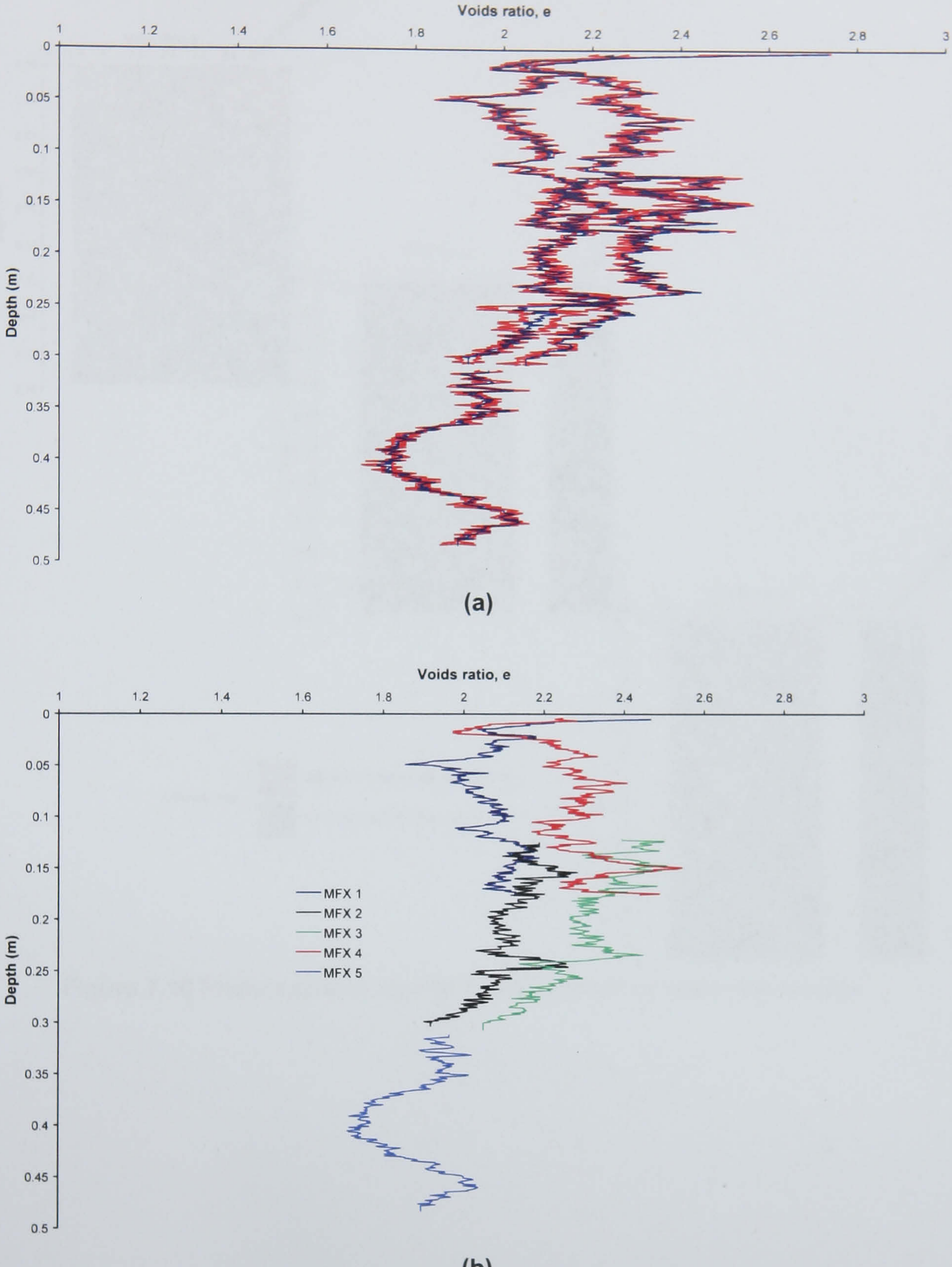

Figure 7.9 Voids ratio profiles of the mudflat cores with (a) and without (b) root squared error terms.

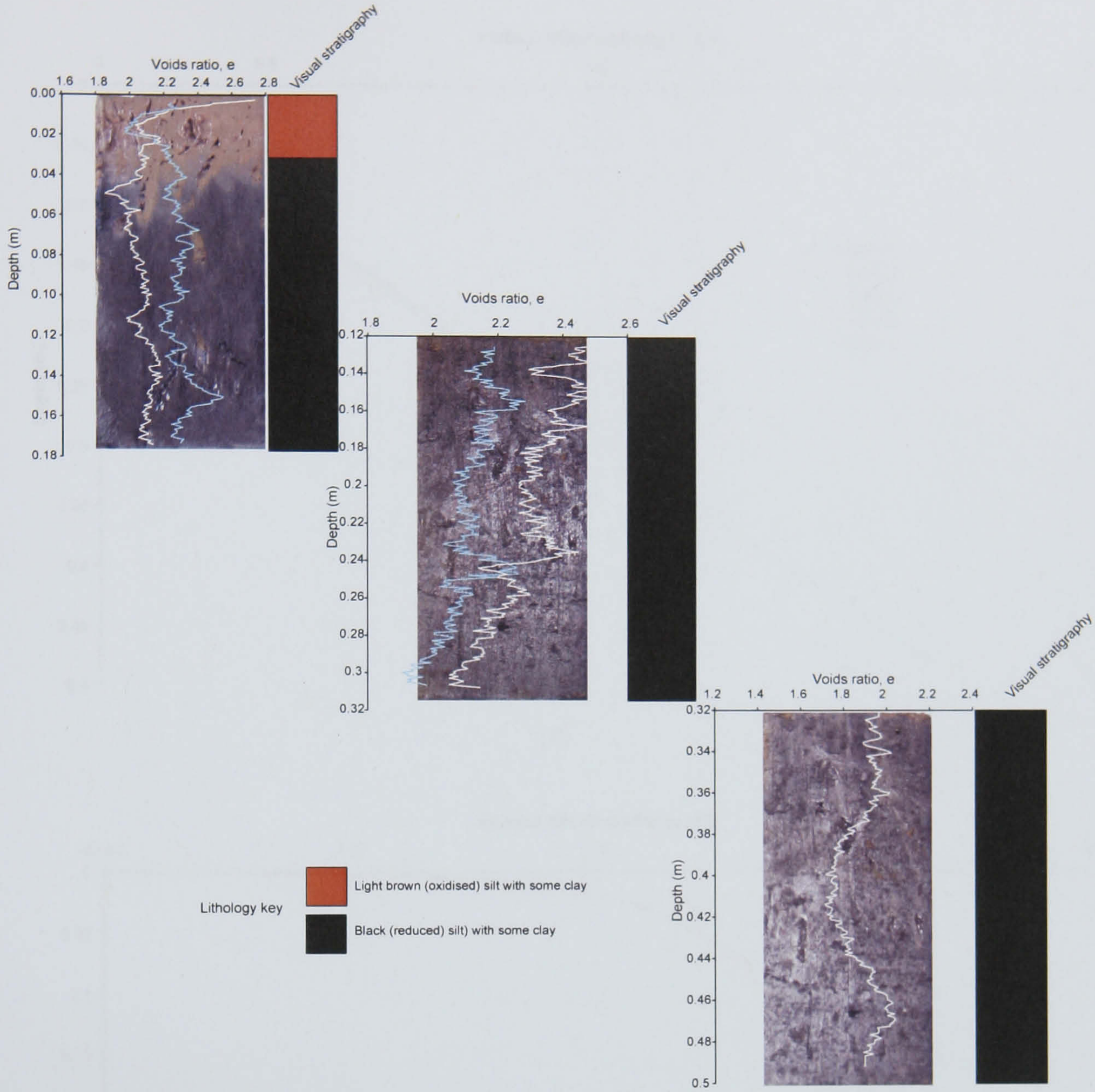

Figure 7.10 Photographs of mudflat cores, overlain by voids ratio profiles.

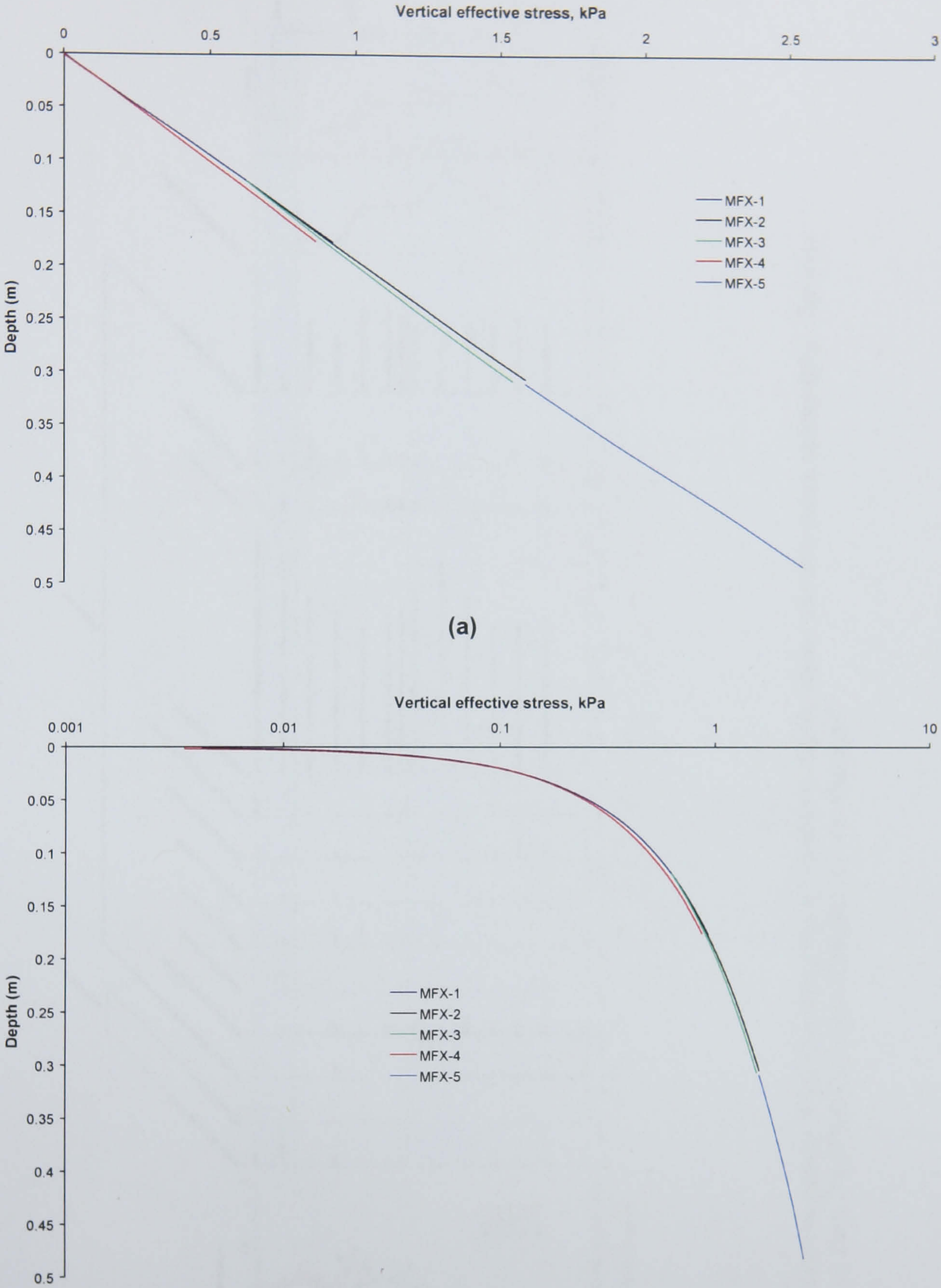

Figure 7.11 Depth variations of effective stress in the mudflat cores on (a) natural and (b) logarithmic scales.

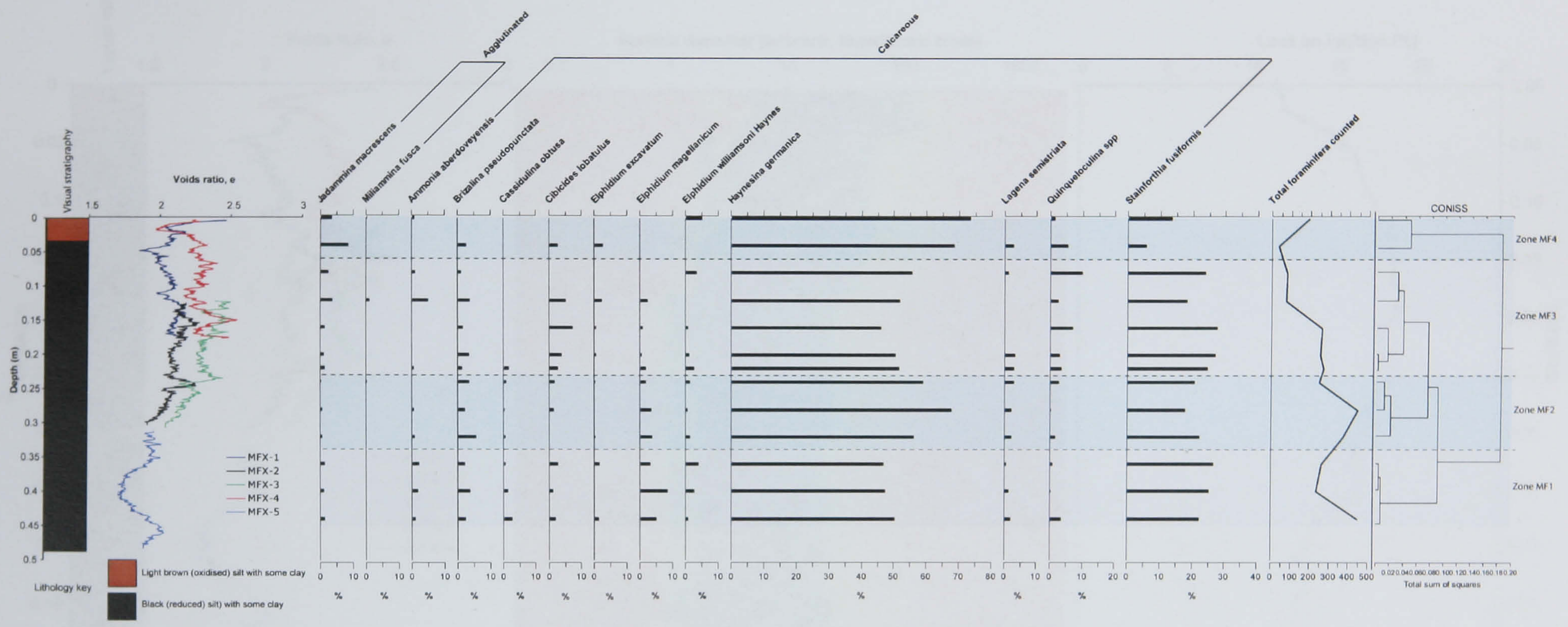

Figure 7.12 Biostratigraphy of the mudflat cores in relation to depth, voids ratio and visual stratigraphy. Species constituting less than 2% of the total assemblages are not displayed.

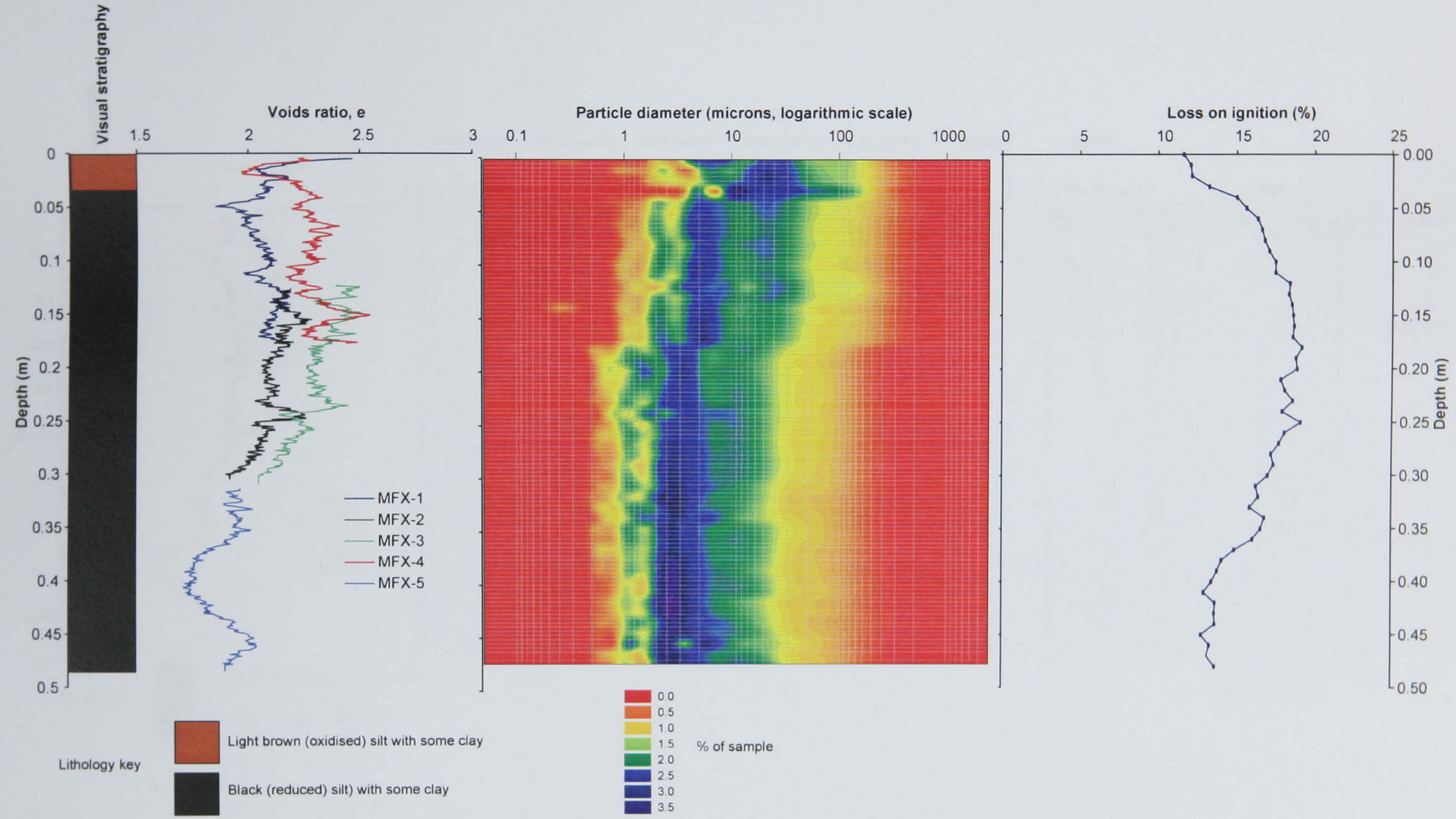

Figure 7.13 Lithostratigraphy of the mudflat cores in relation to depth, voids ratio and visual stratigraphy.

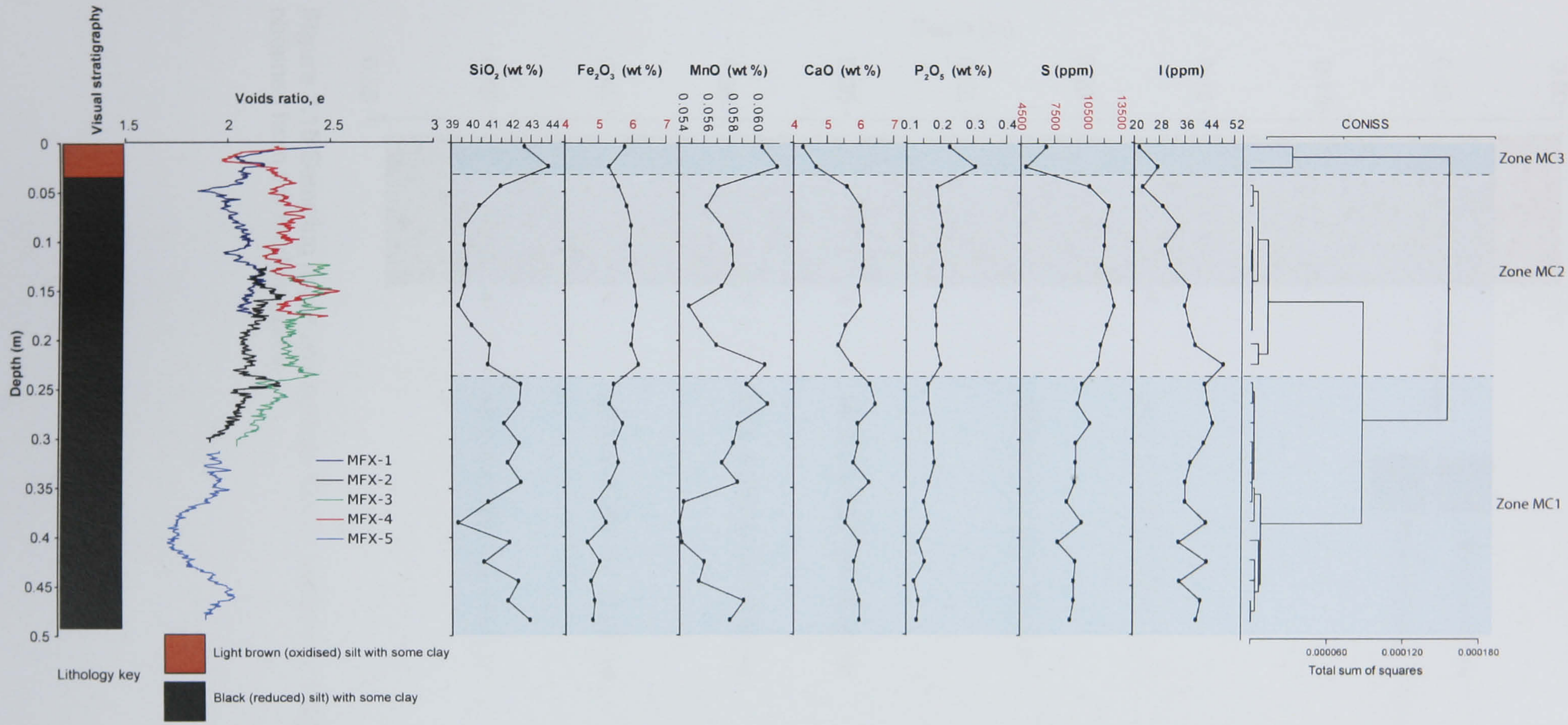

Figure 7.14 Chemostratigraphy of the mudflat cores in relation to depth, voids ratio and visual stratigraphy.

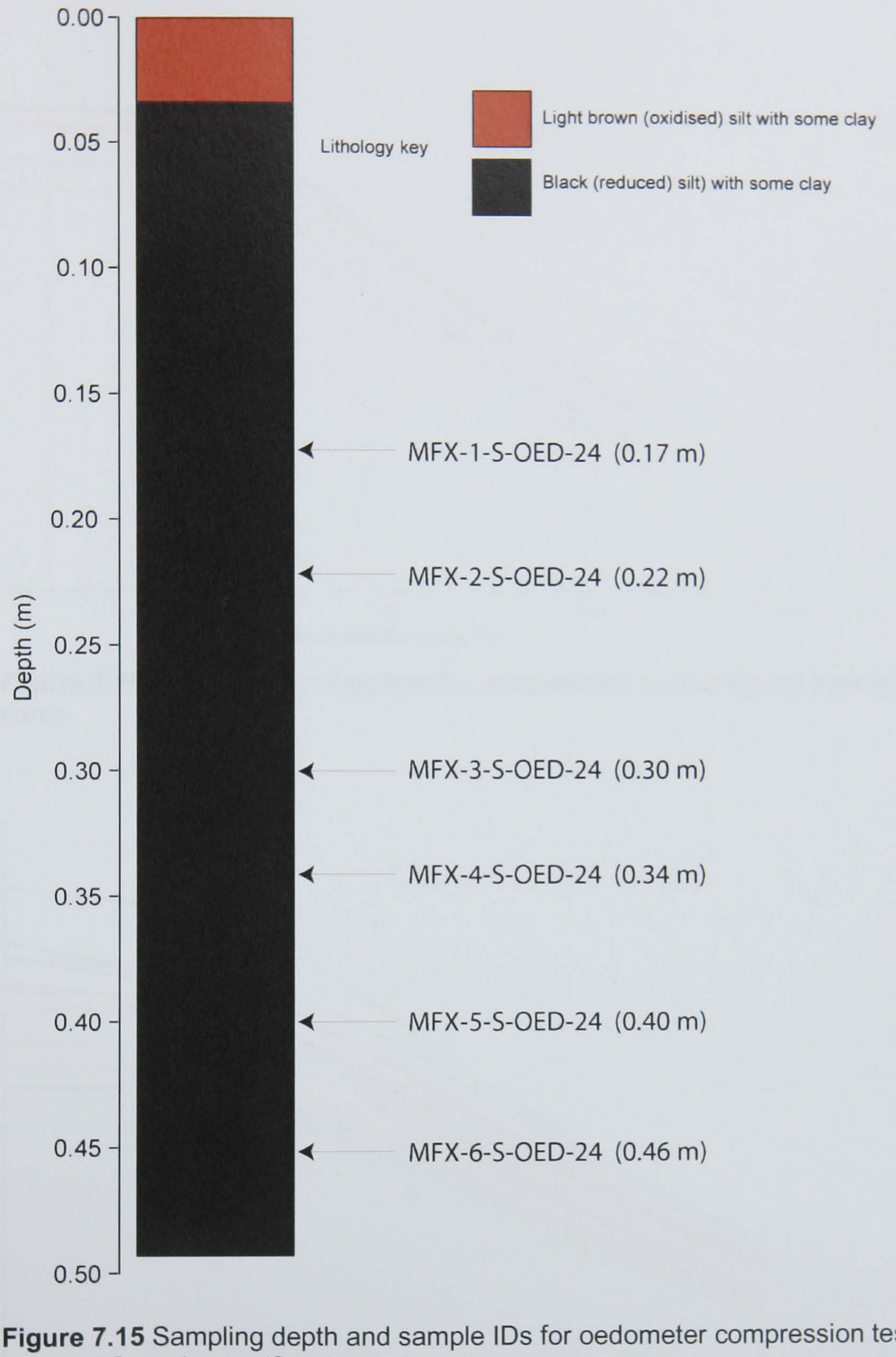

Figure 7.15 Sampling depth and sample IDs for oedometer compression tests obtained from the mudflat cores.

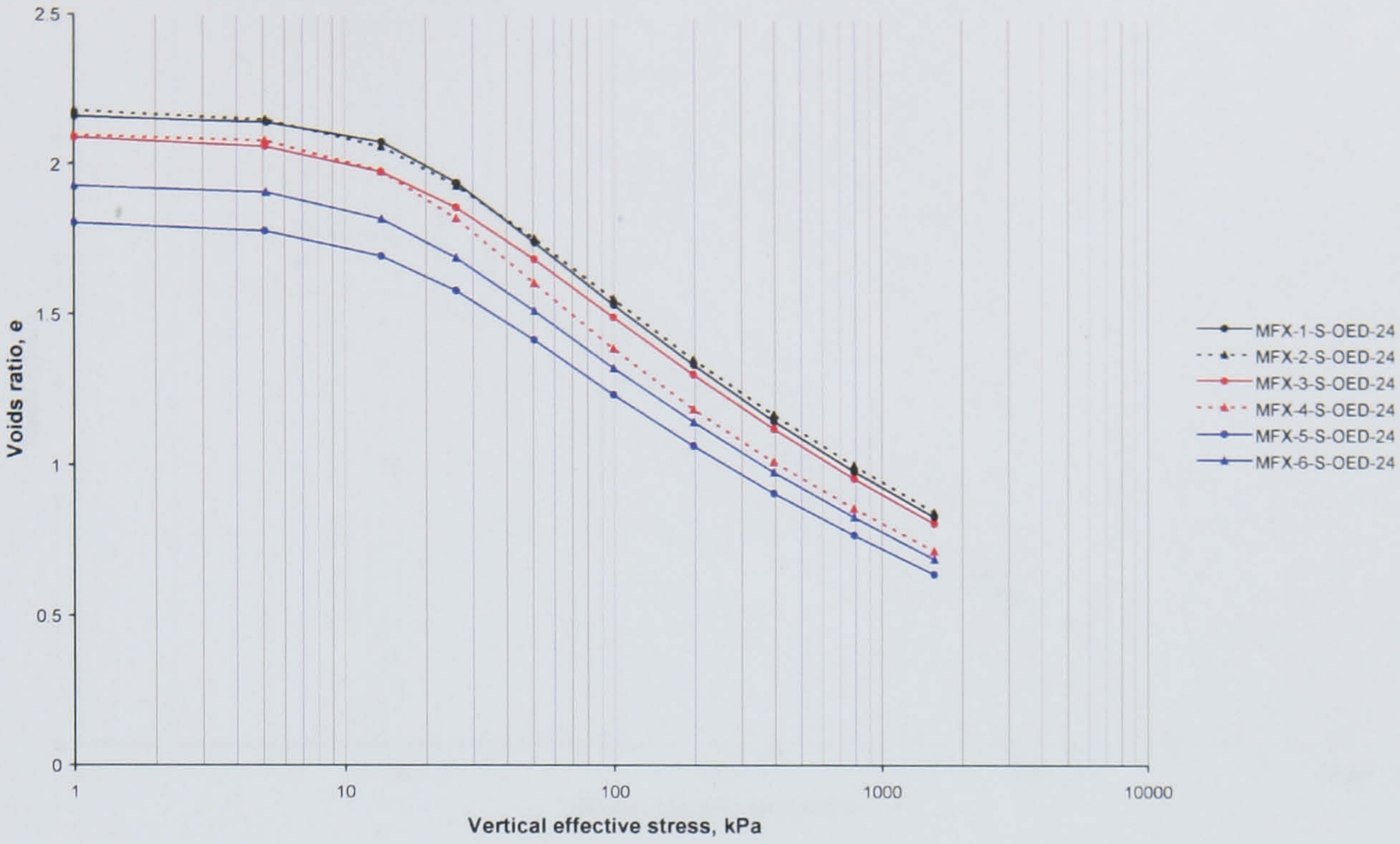

Figure 7.16 $e\log_{10}\sigma'$ plots of oedometer compression tests obtained from mudflat cores.

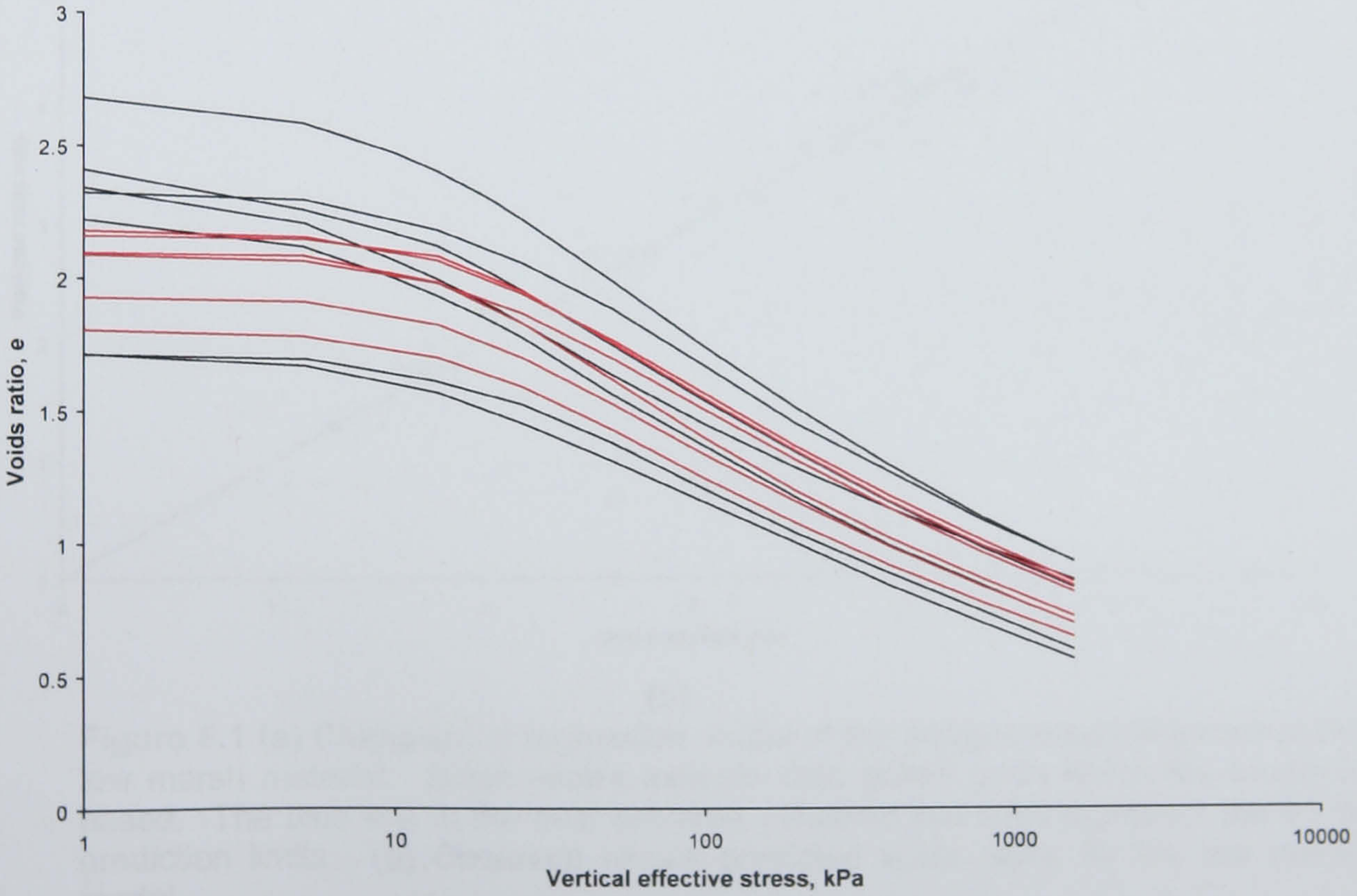

Figure 7.17 Comparison of $e\log_{10}\sigma'$ plots obtained from contemporary samples at the depositional surface (black lines) and from mudflat cores (red lines).

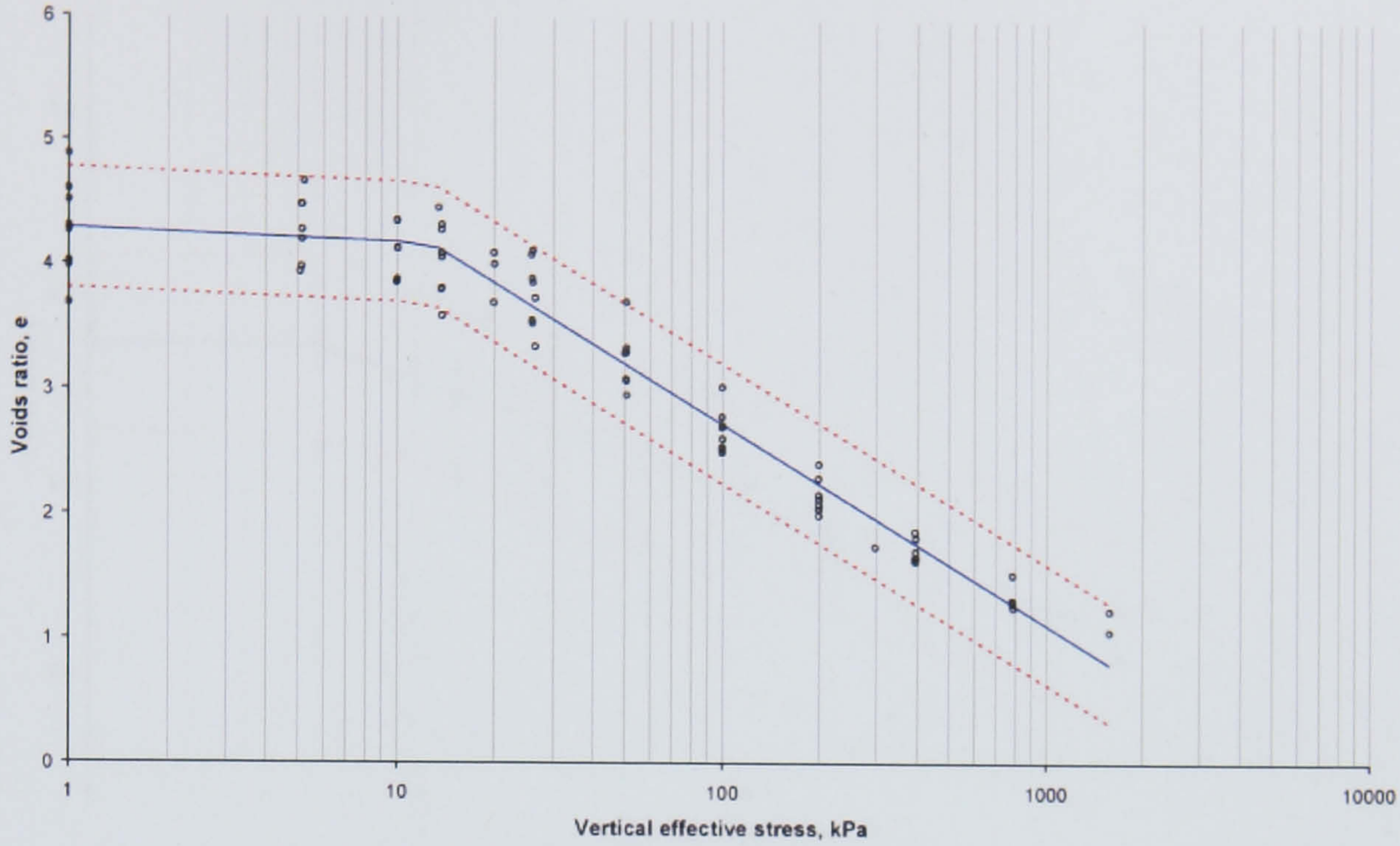

(a)

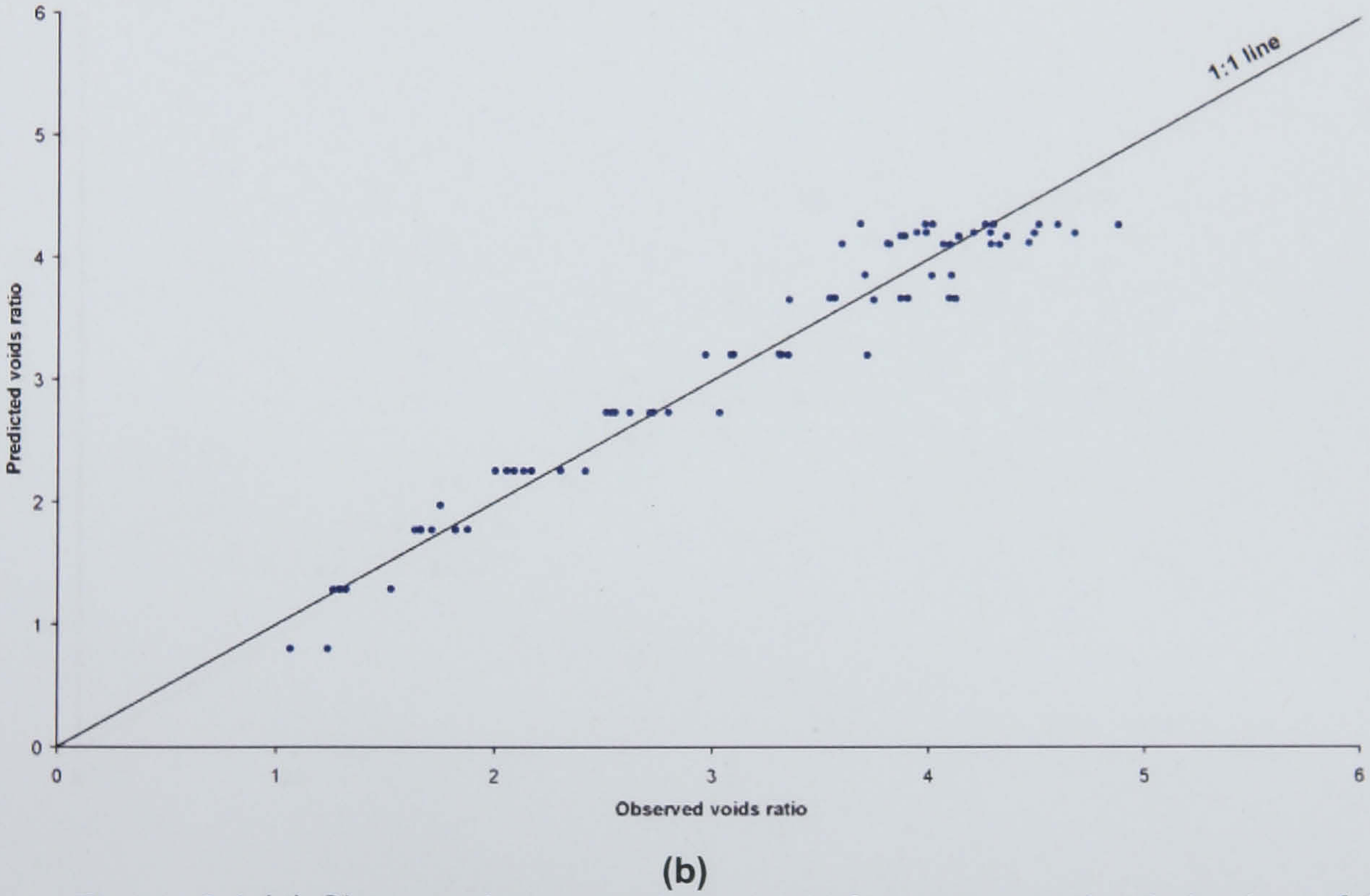

(b)

Figure 8.1 (a) Changepoint regression model of the compression behaviour of the low marsh material. Black circles indicate data points upon which the model is based. The blue line is the best estimate. Dashed red lines represent the 95 % prediction limits. (b) Observed versus predicted voids ratios for the low marsh model.

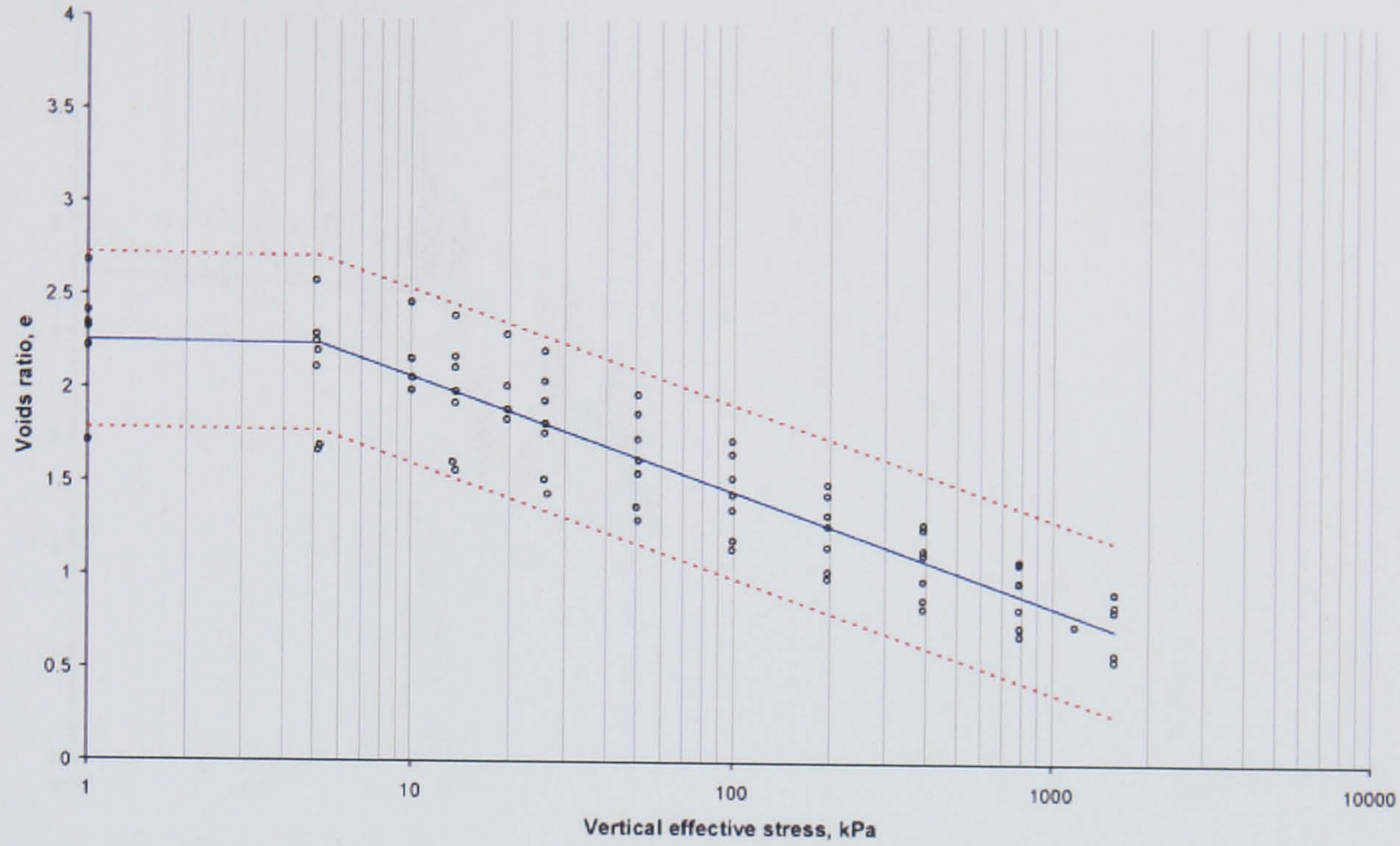

(a)

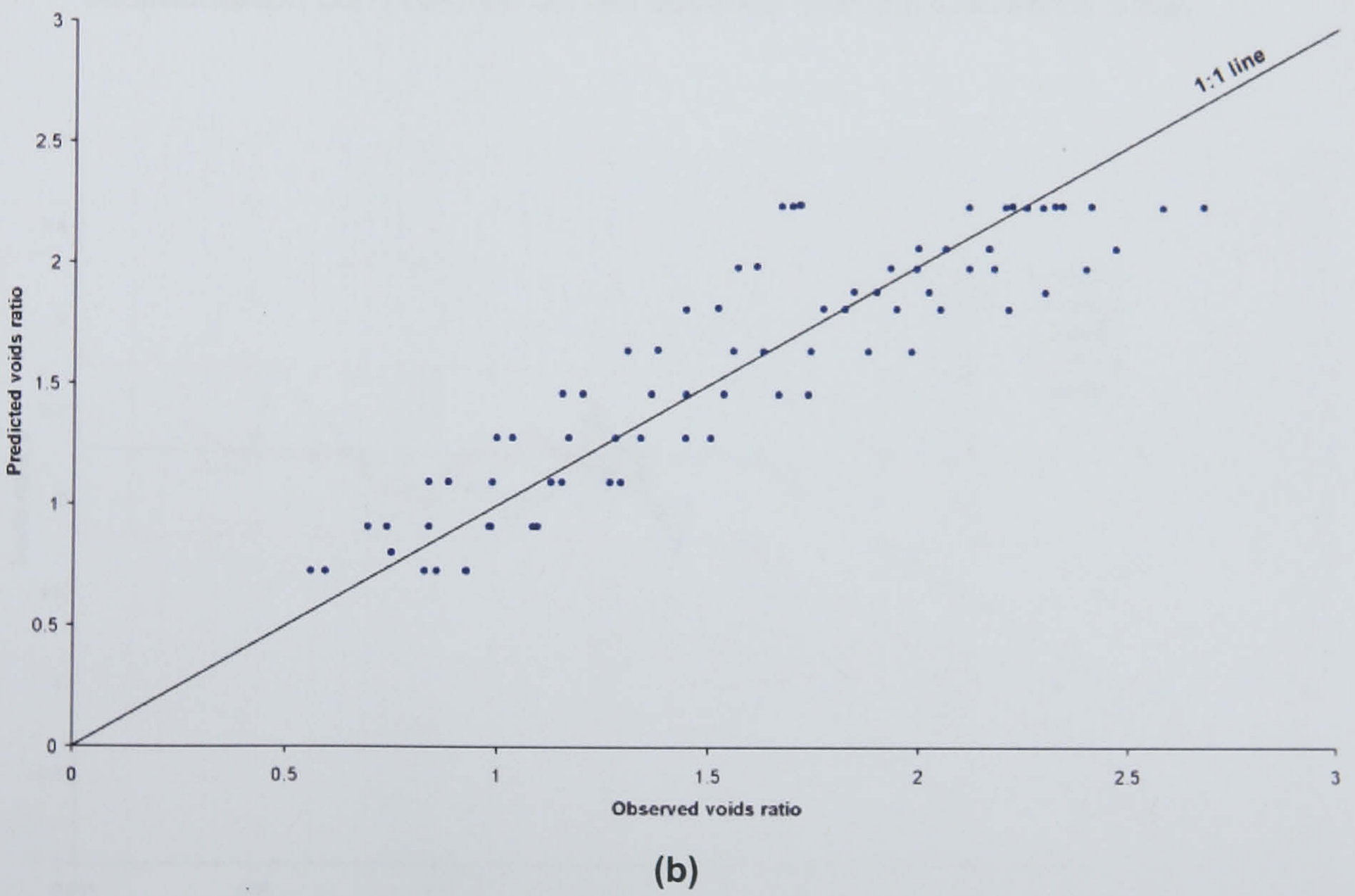

(b)

Figure 8.2 (a) Changepoint regression model of the compression behaviour of the low mudflat material. Black circles indicate data points upon which the model is based. The blue line is the best estimate. Dashed red lines represent the 95 % prediction limits. (b) Observed versus predicted voids ratios for the mudflat model.

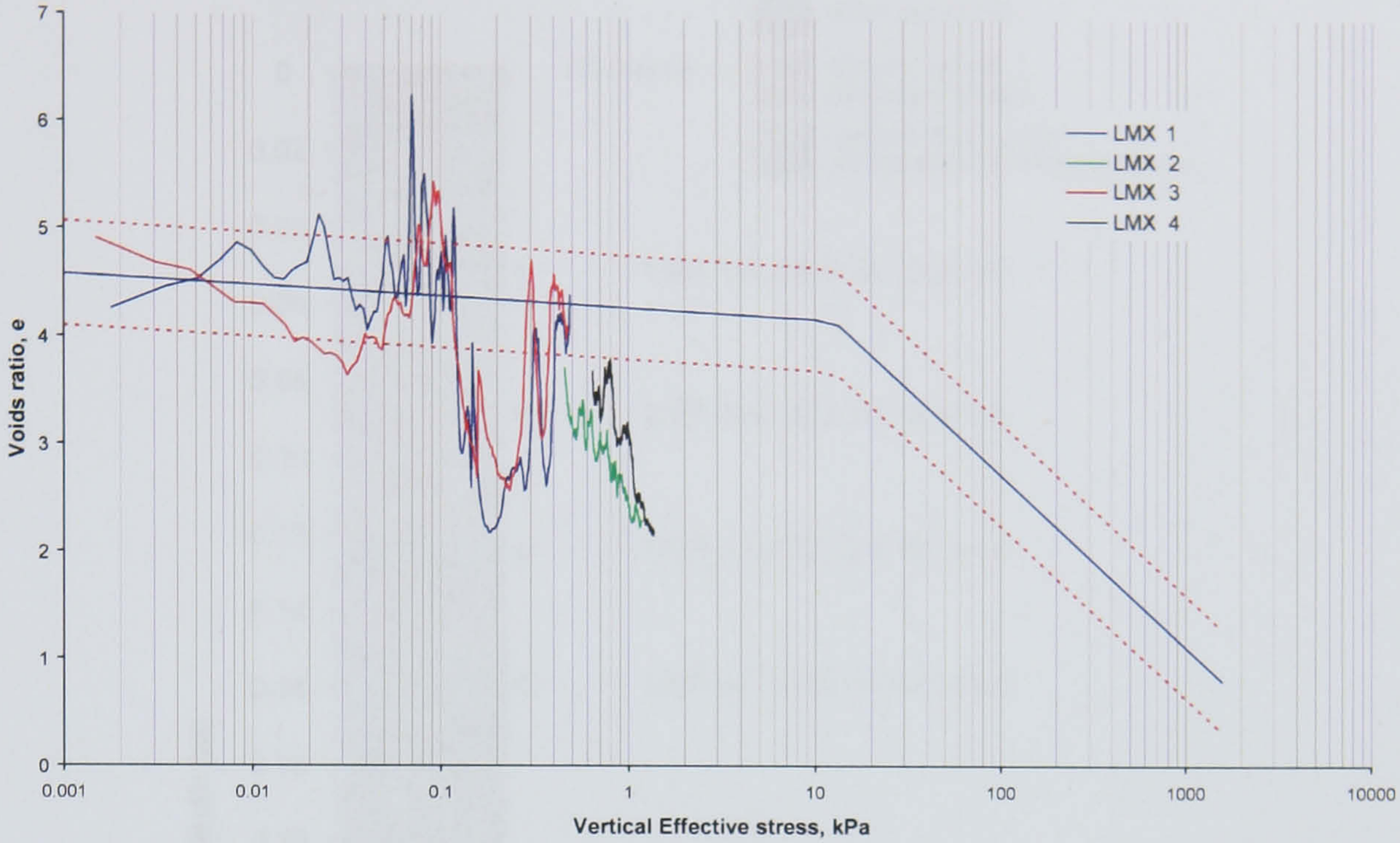

Figure 8.3 Comparison of the low marsh changepoint regression model with the sedimentation compression curves obtained from the low marsh cores.

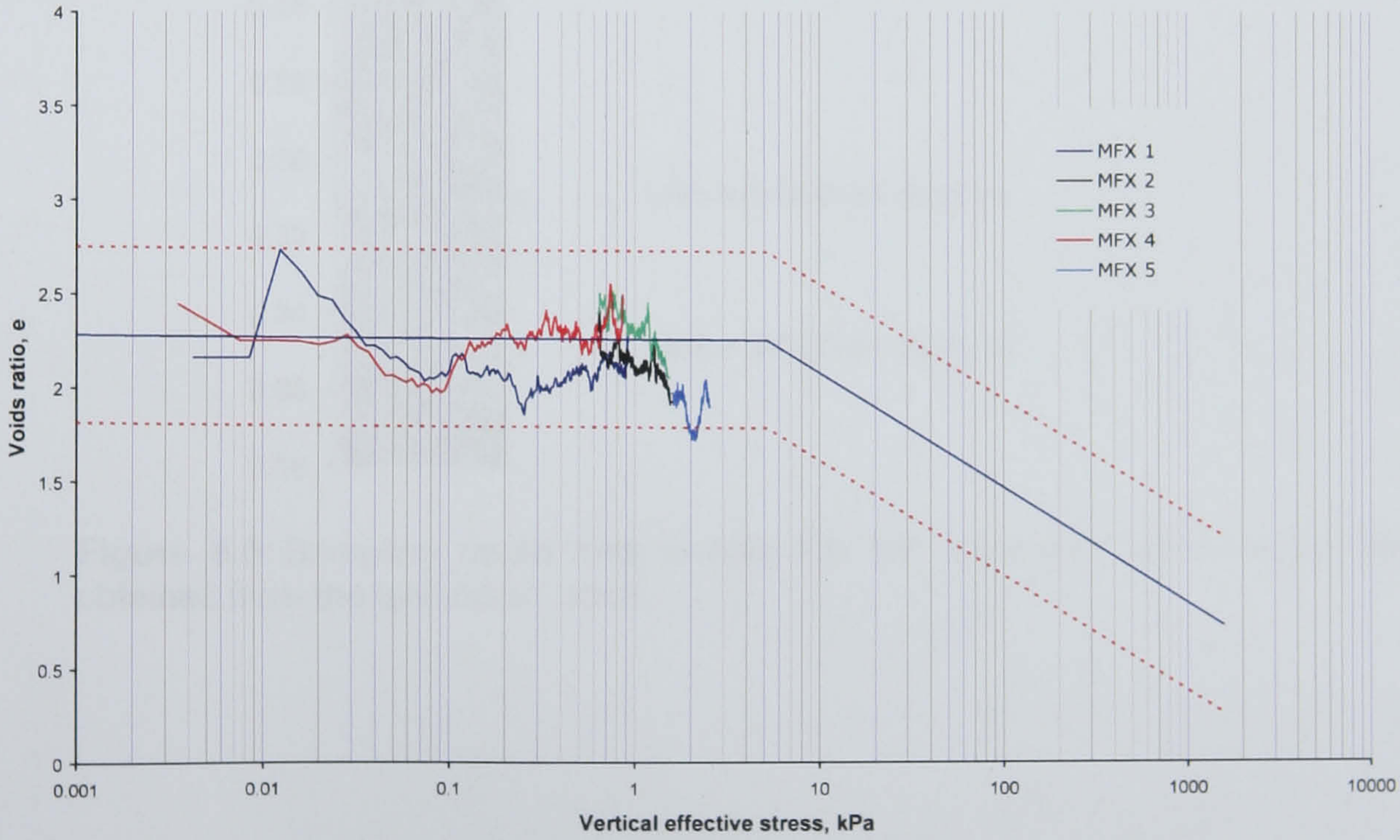

Figure 8.4 Comparison of the mudflat changepoint regression model with the sedimentation compression curves obtained from the mudflat cores.

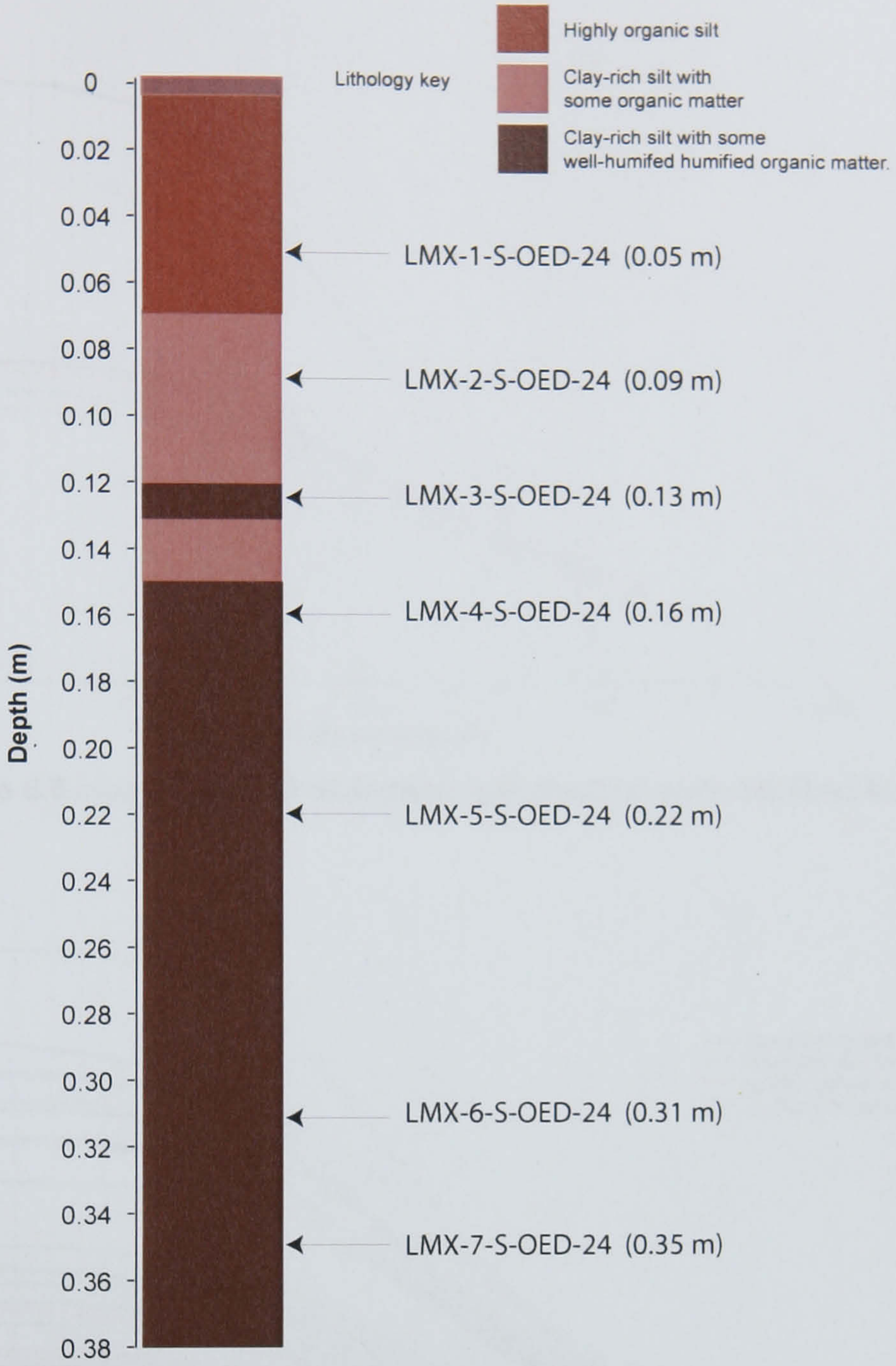

Figure 8.5 Sampling depth and sample IDs for oedometer compression tests obtained from the low marsh cores.

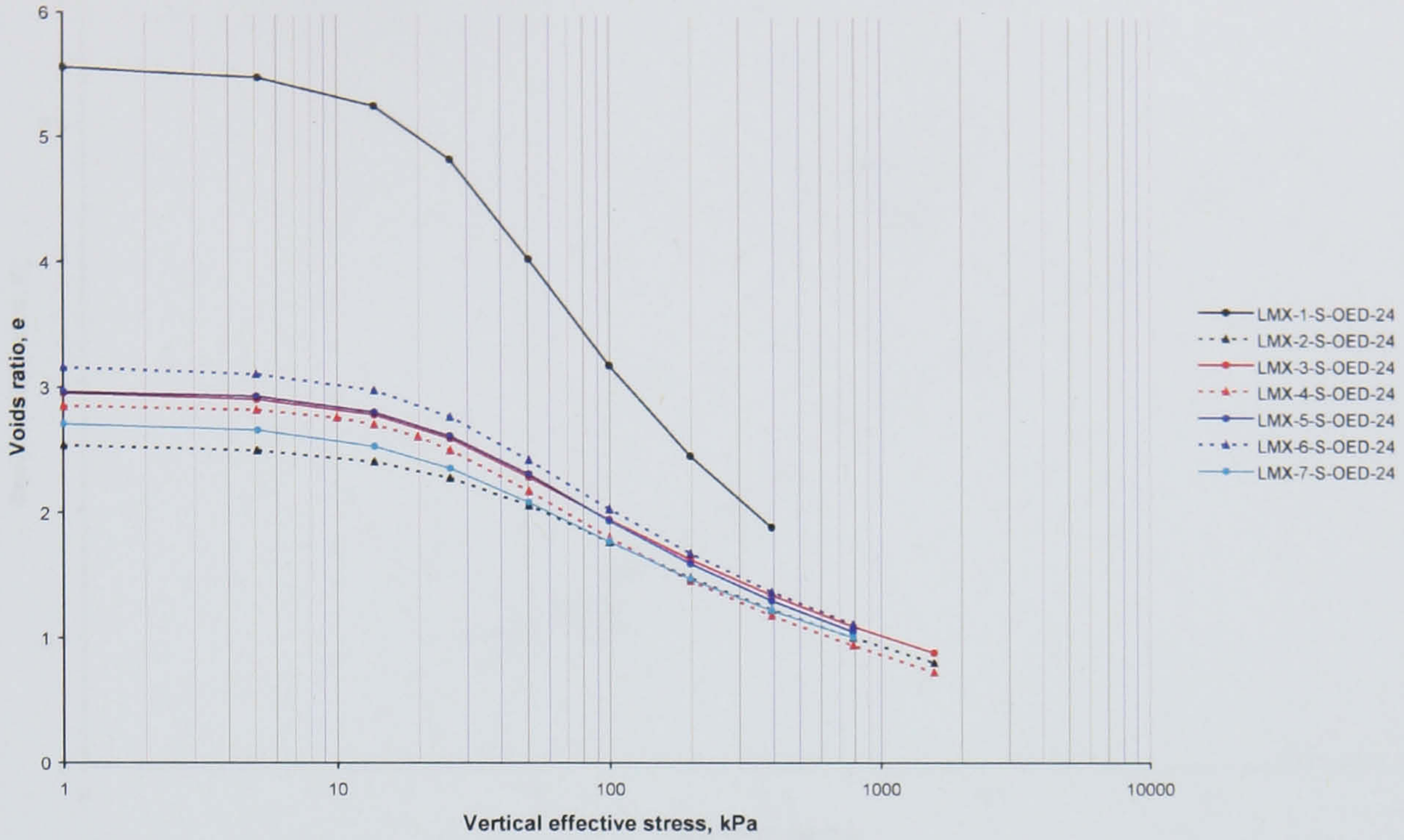

Figure 8.6 $e\log_{10}\sigma'$ plots of oedometer compression tests obtained from low marsh cores.

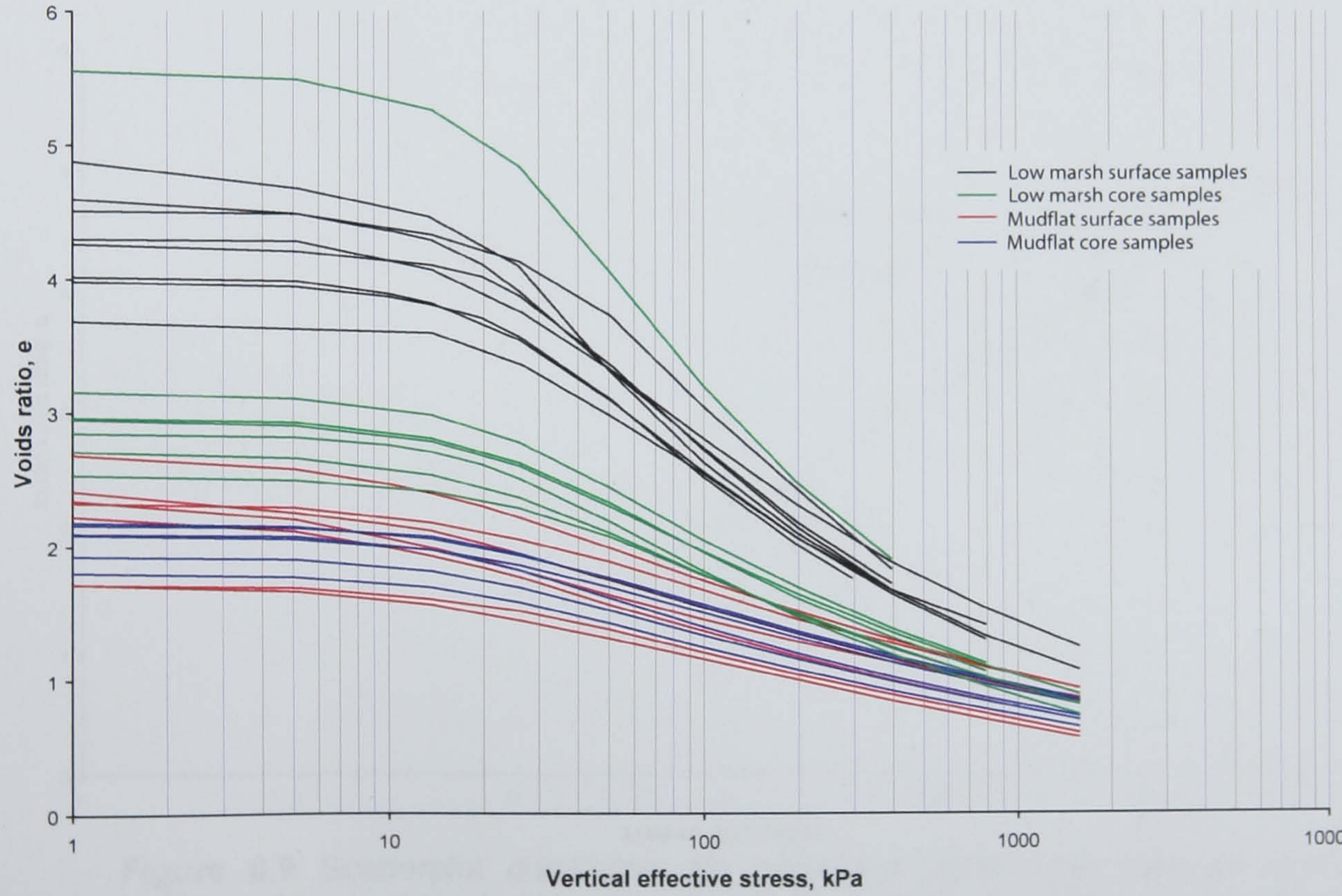

Figure 8.7 $e\log_{10}\sigma'$ plots of all increment loading tests.

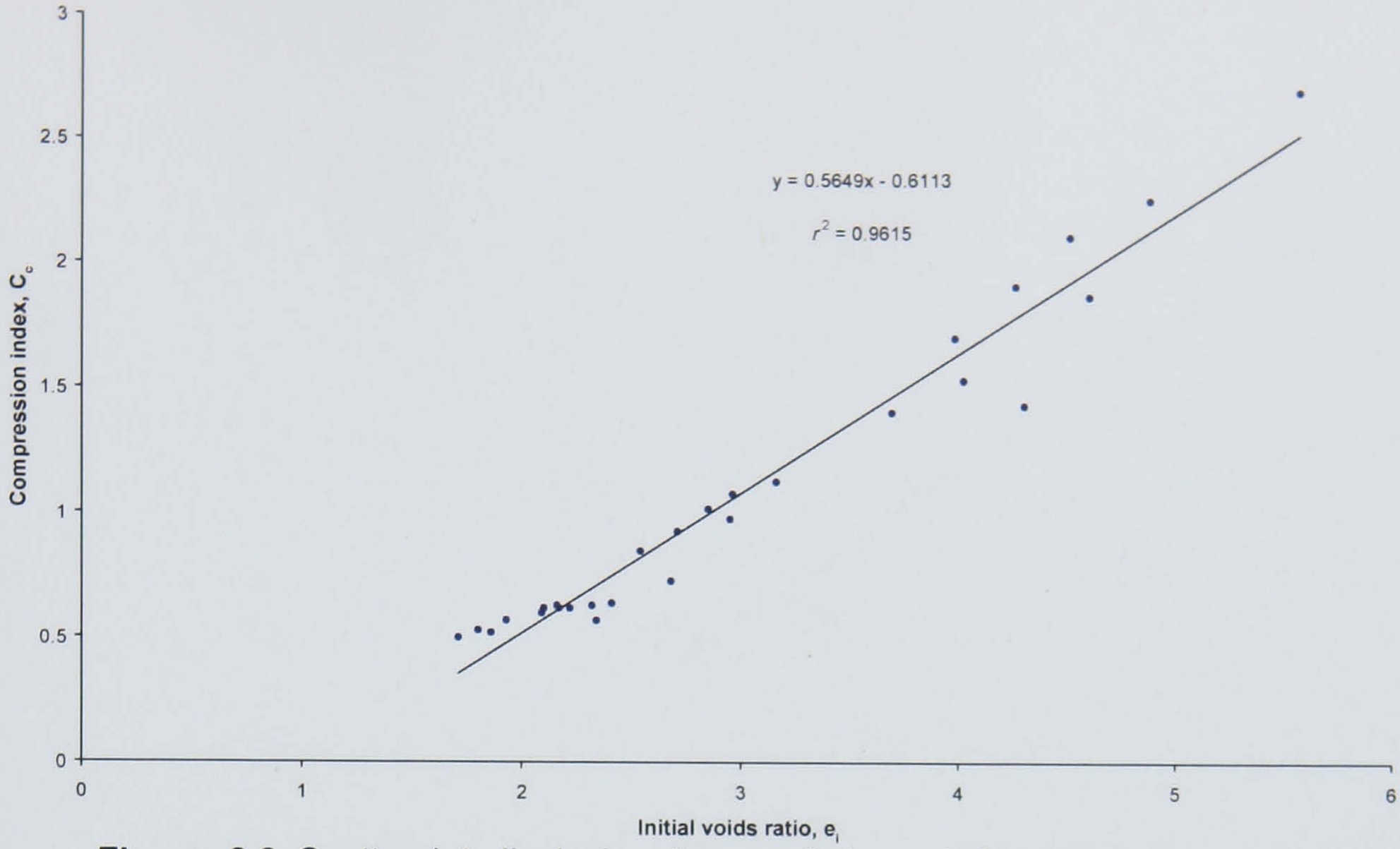

Figure 8.8 Scatterplot displaying the predictive relationship between the initial voids ratio and the compression index of all compression tests undertaken.

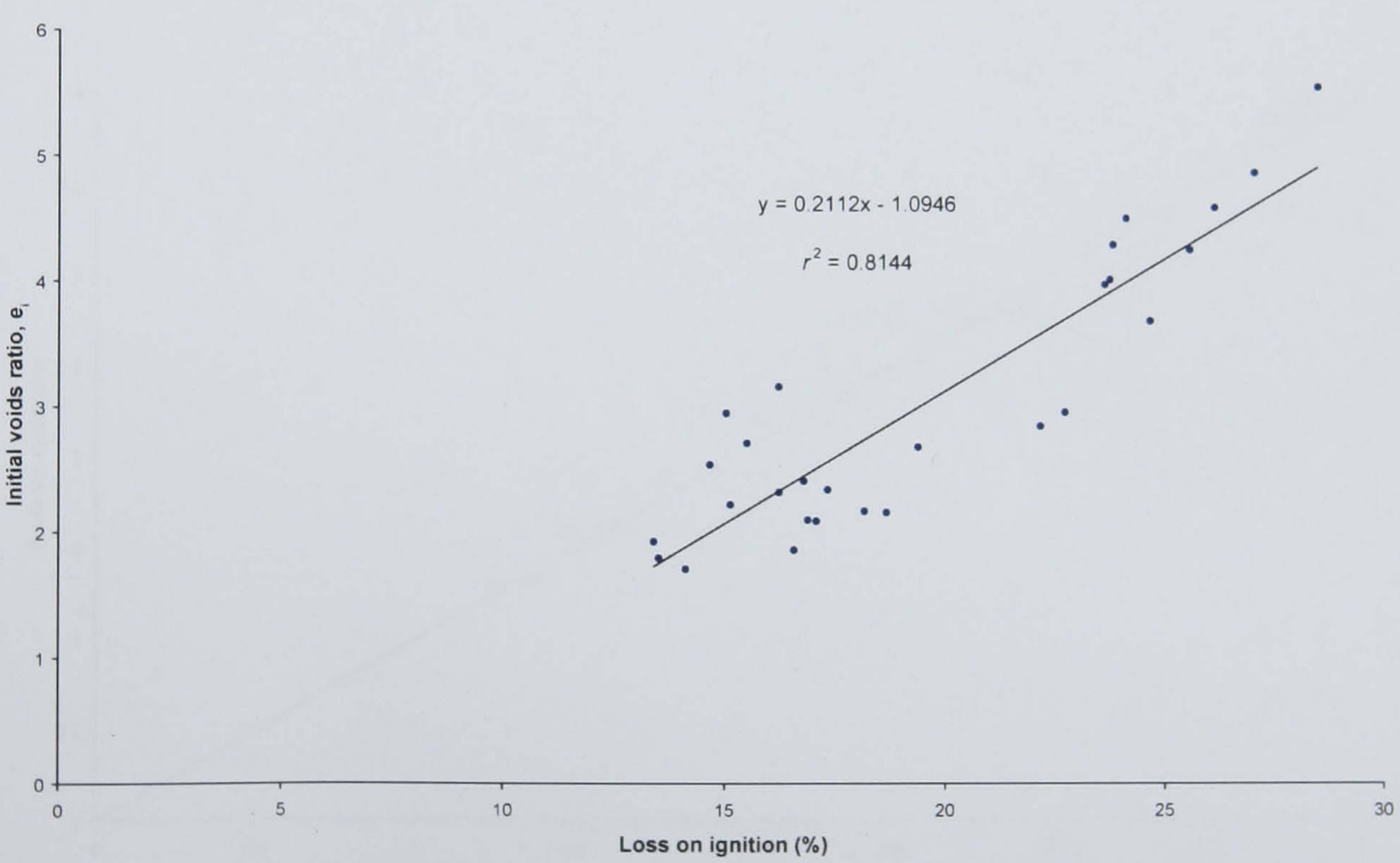

Figure 8.9 Scatterplot displaying the predictive relationship between loss on ignition values and the initial voids ratio of all samples tested for their compression behaviour.

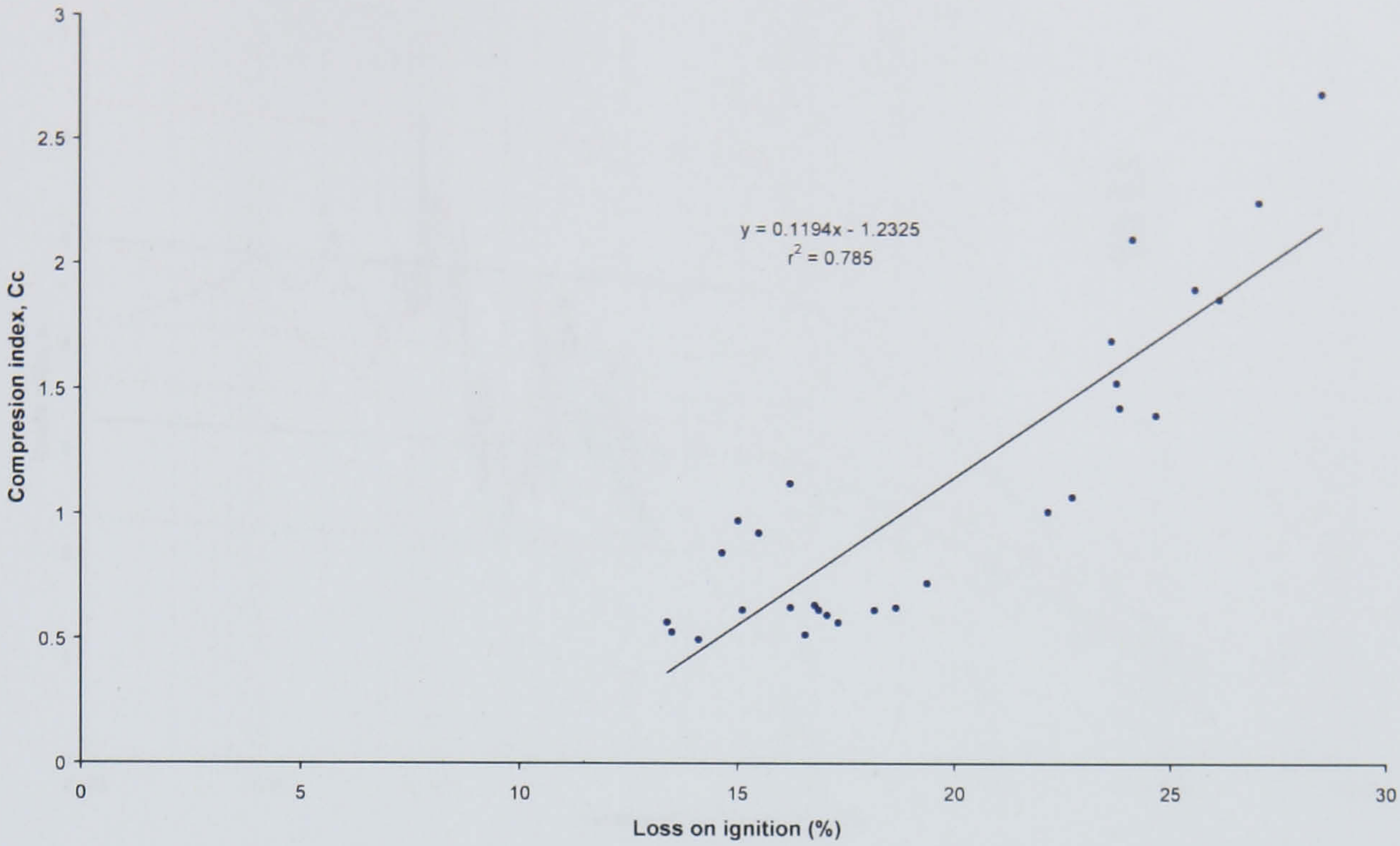

Figure 8.10 Scatterplot displaying the predictive relationship between loss on ignition values and the compression index for all samples tested for their compression behaviour.

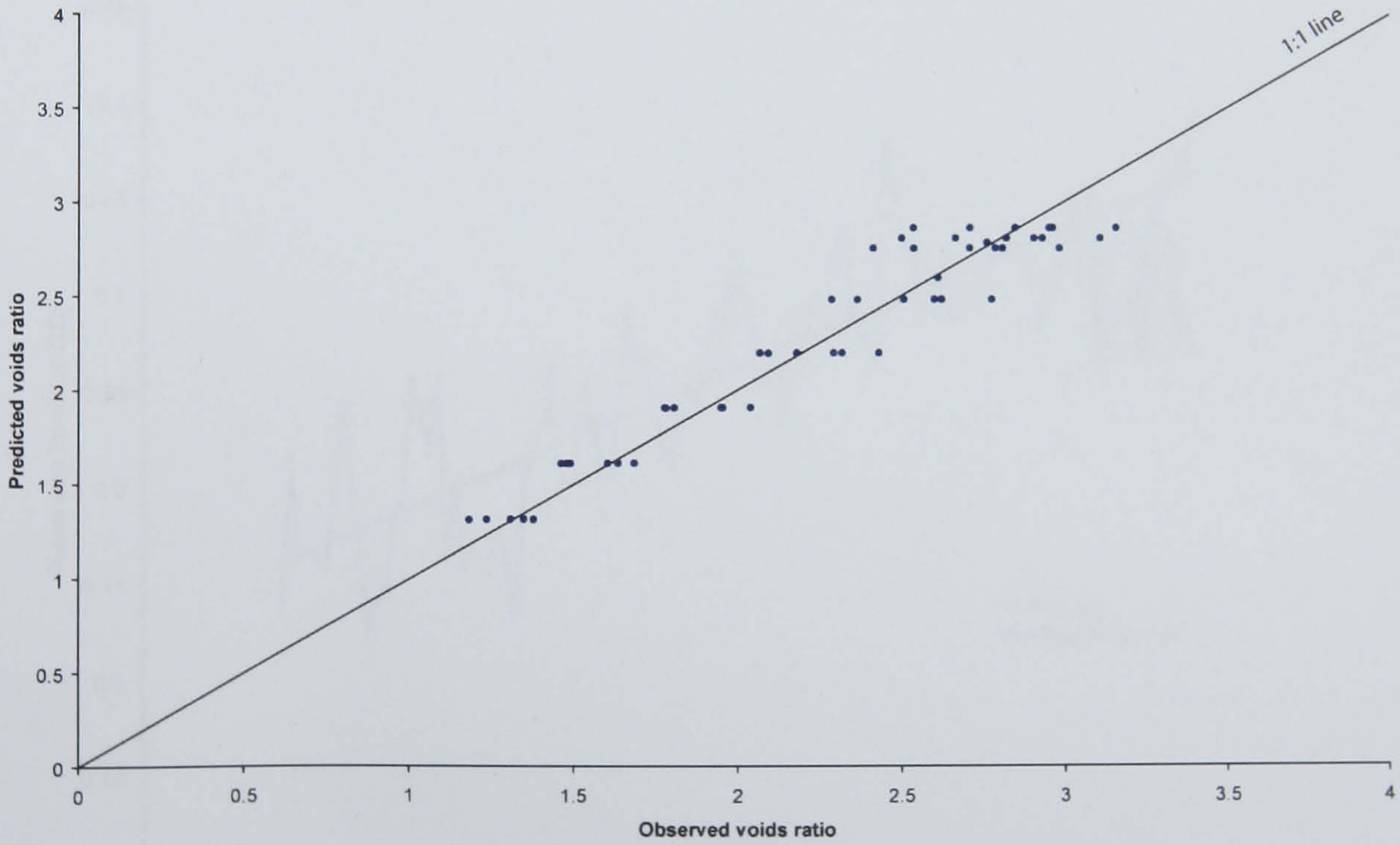

Figure 8.11 Observed versus predicted voids ratios for the 'Saltmarsh 1' model.

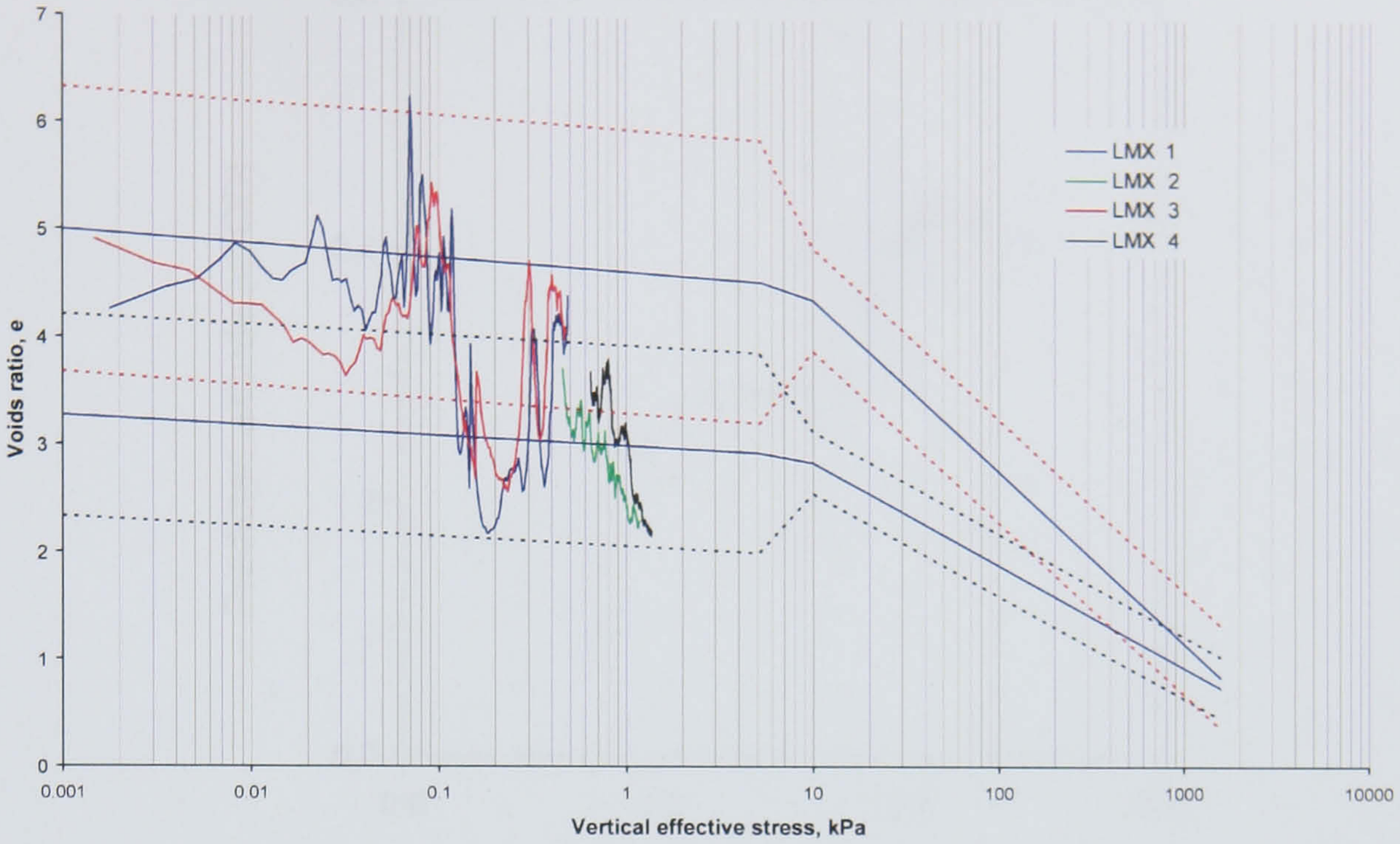

Figure 8.12 Comparison of the changepoint regression models (low marsh 2: dotted red error limits; saltmarsh 1: dotted error limits) with the sedimentation compression curves obtained from the low marsh cores.

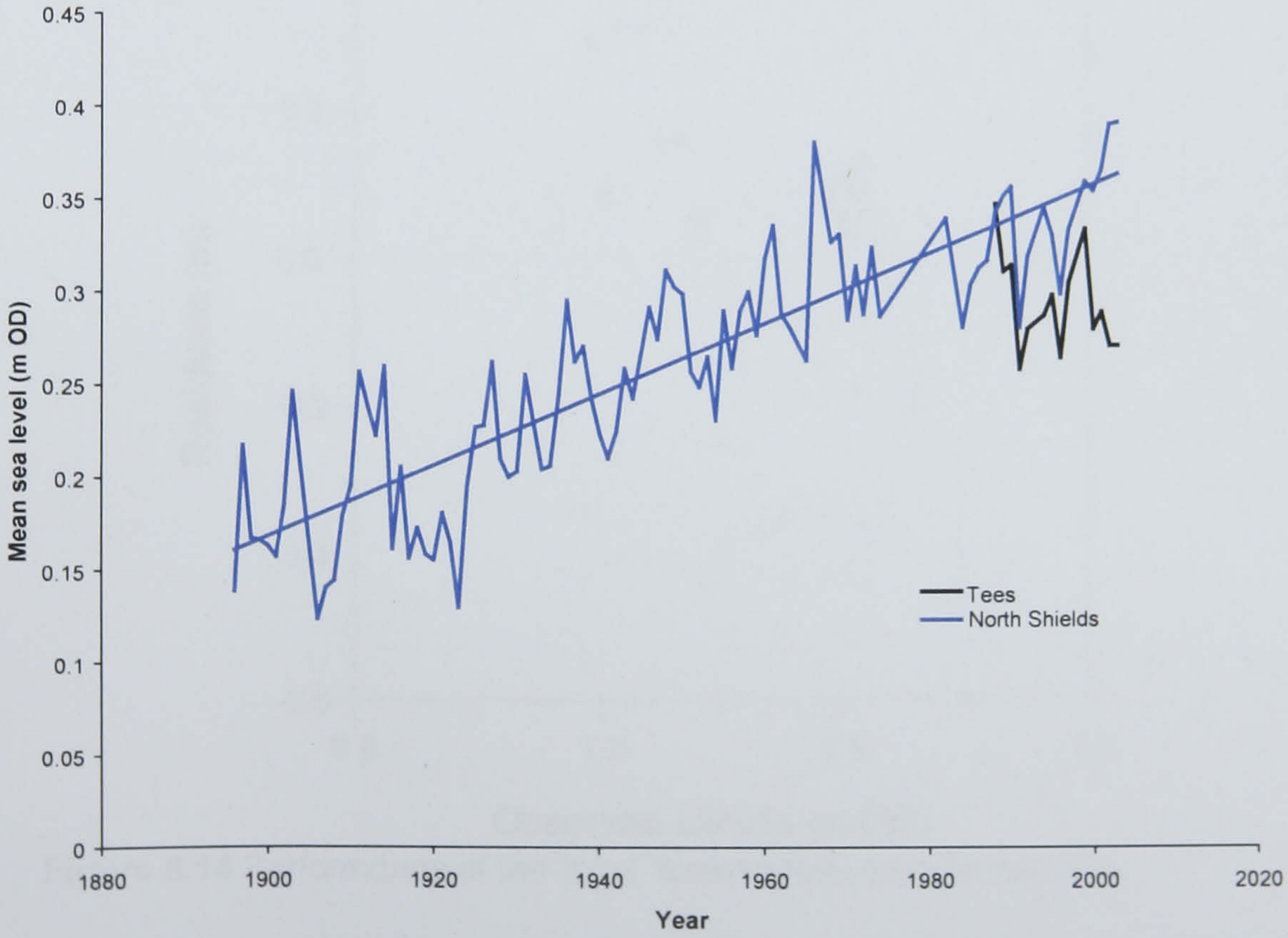

Figure 8.13 Tide gauge records from the Tees and North Shields.

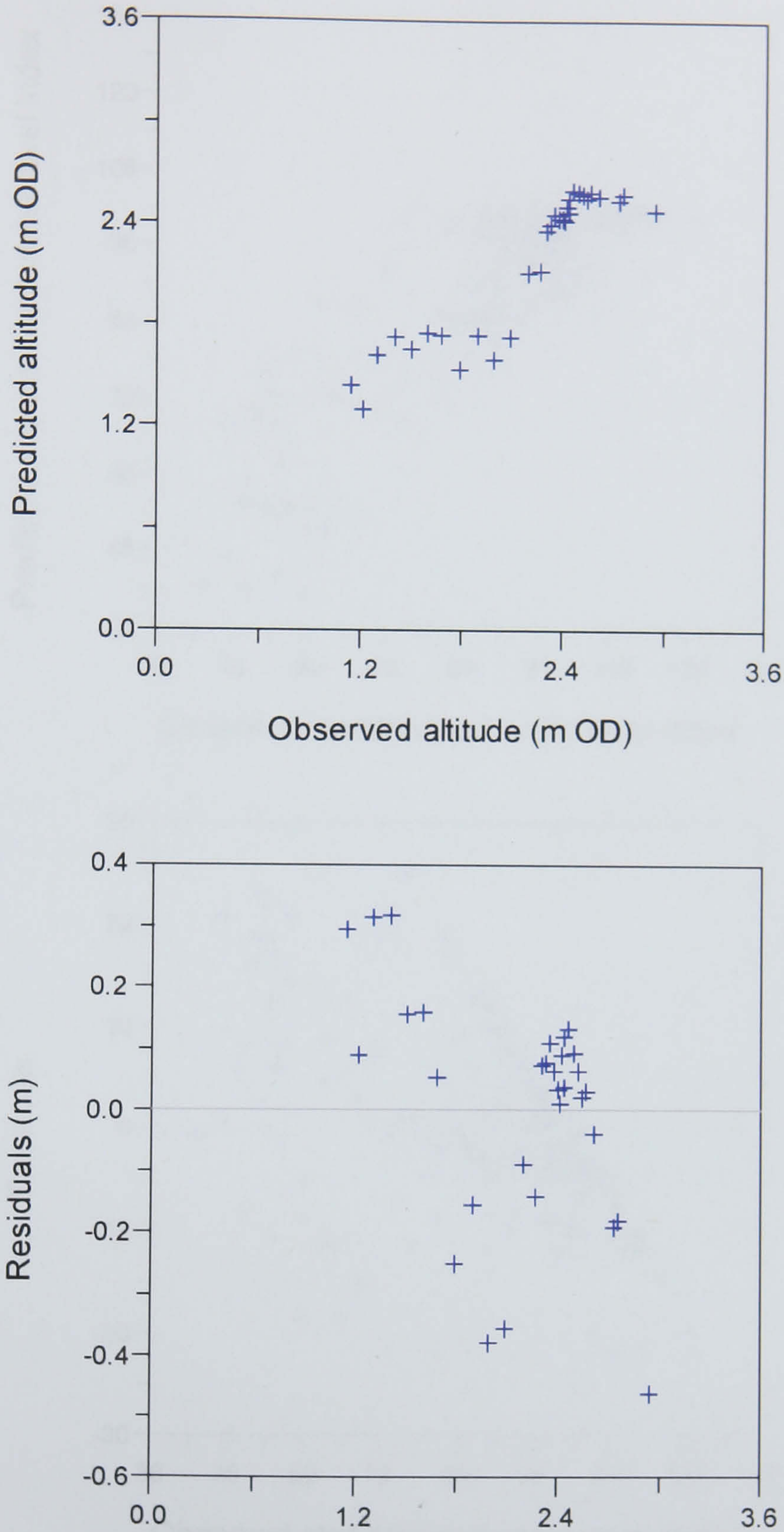

Figure 8.14 Performance of the 'local' foraminiferal transfer function.

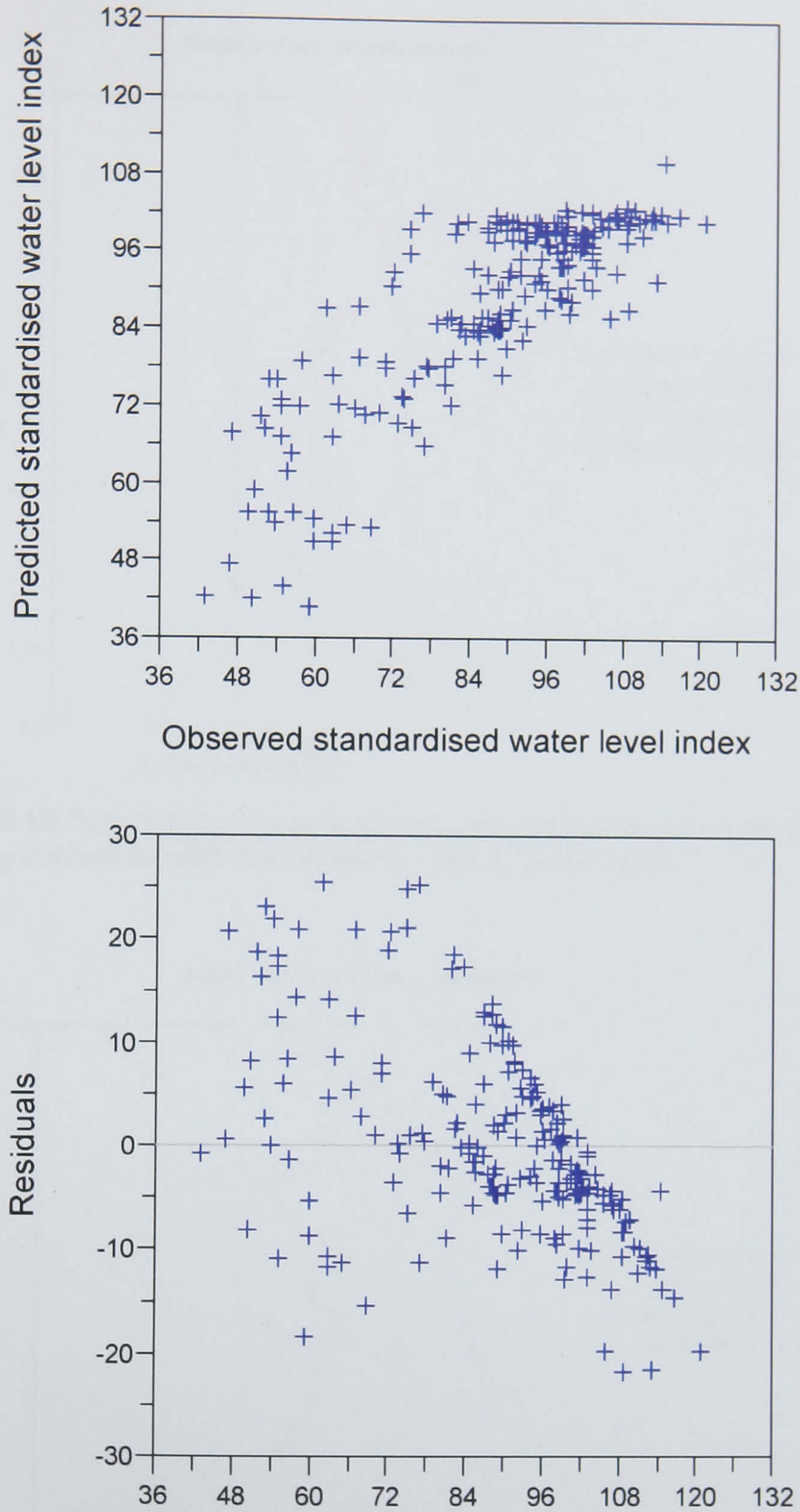

Figure 8.15 Performance of the 'national' foraminiferal transfer function.

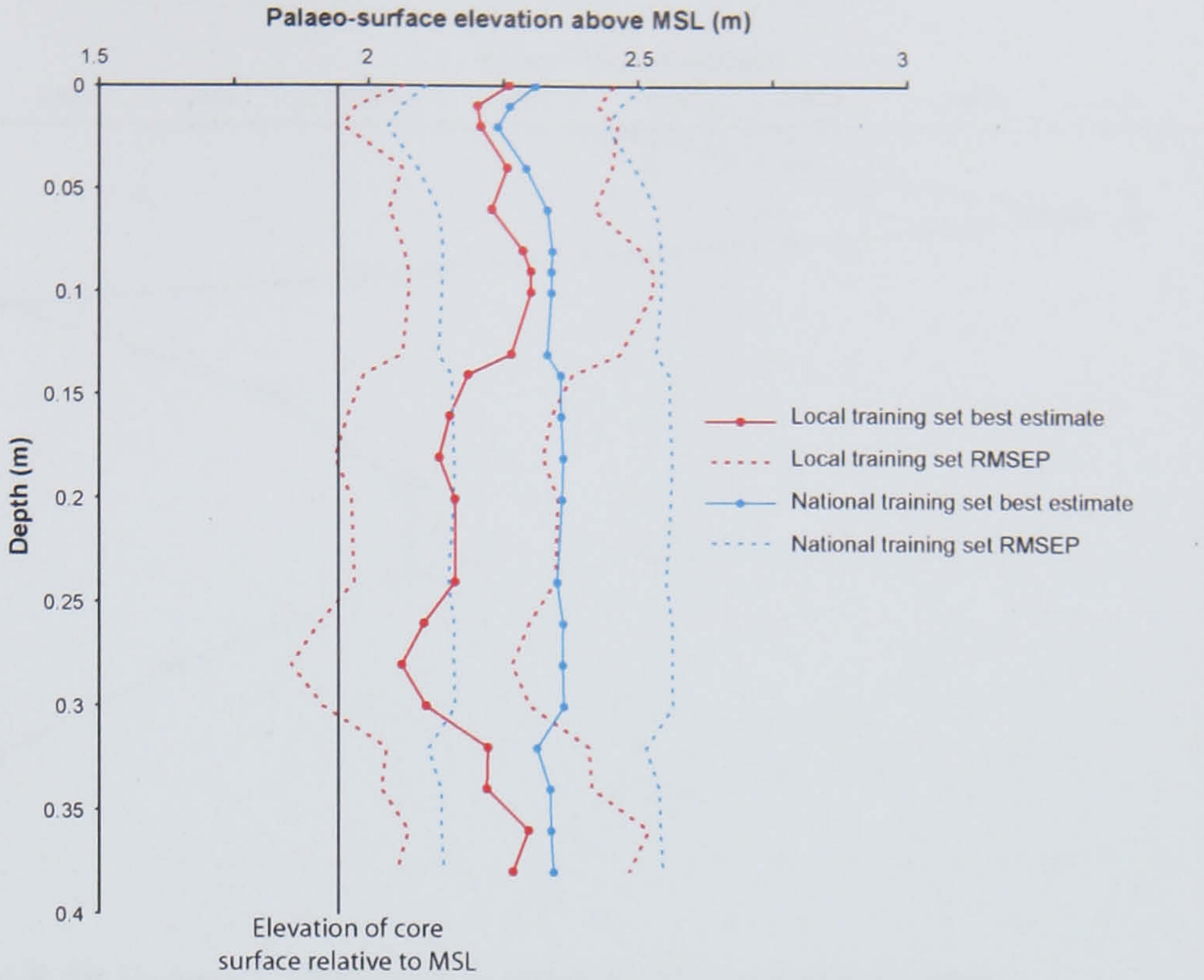

Figure 8.16 Output of the 'local' and 'national' foraminiferal transfer functions following calibration with the low marsh core assemblages.

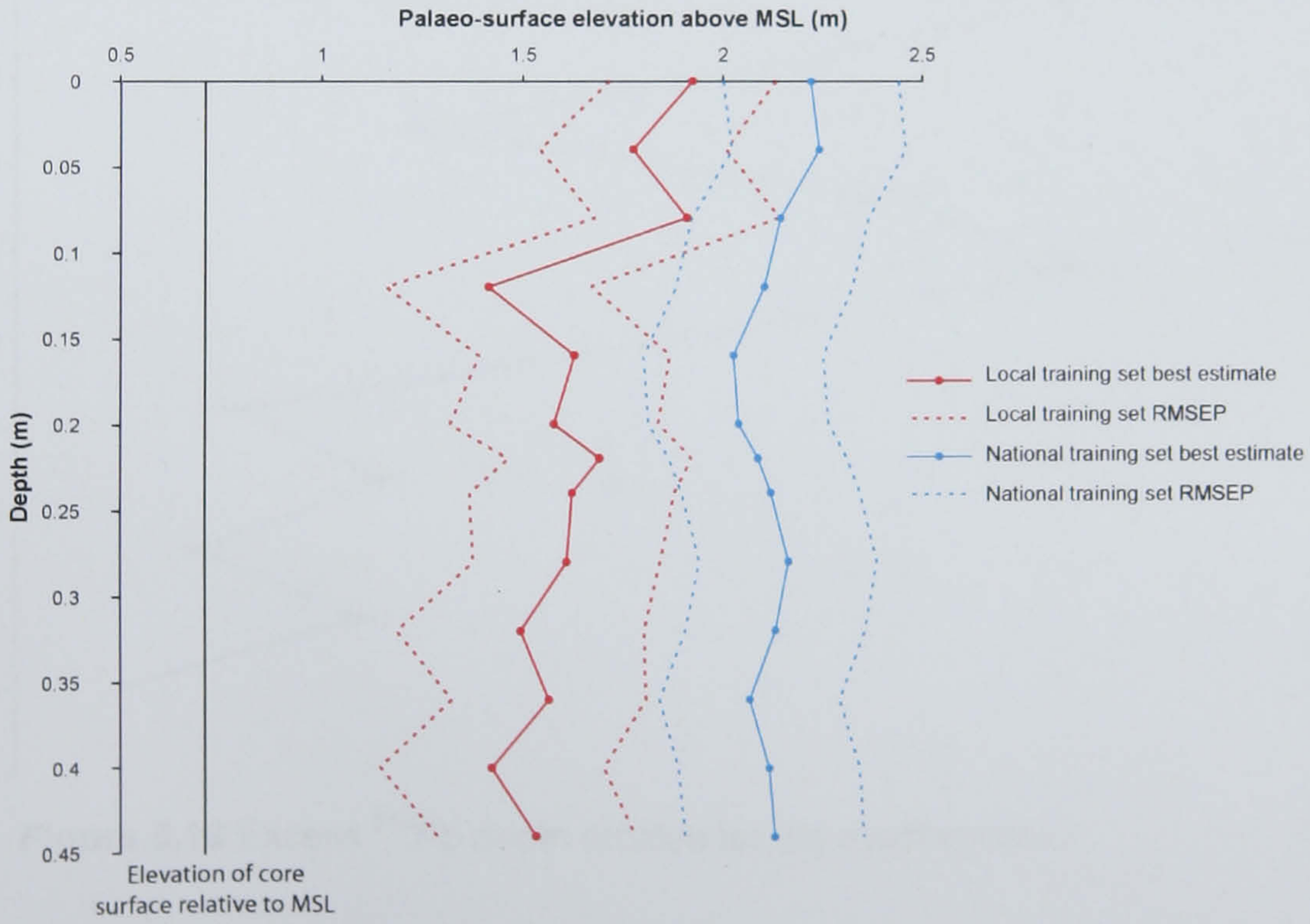

Figure 8.17 Output of the 'local' and 'national' foraminiferal transfer functions following calibration with the mudflat core assemblages.

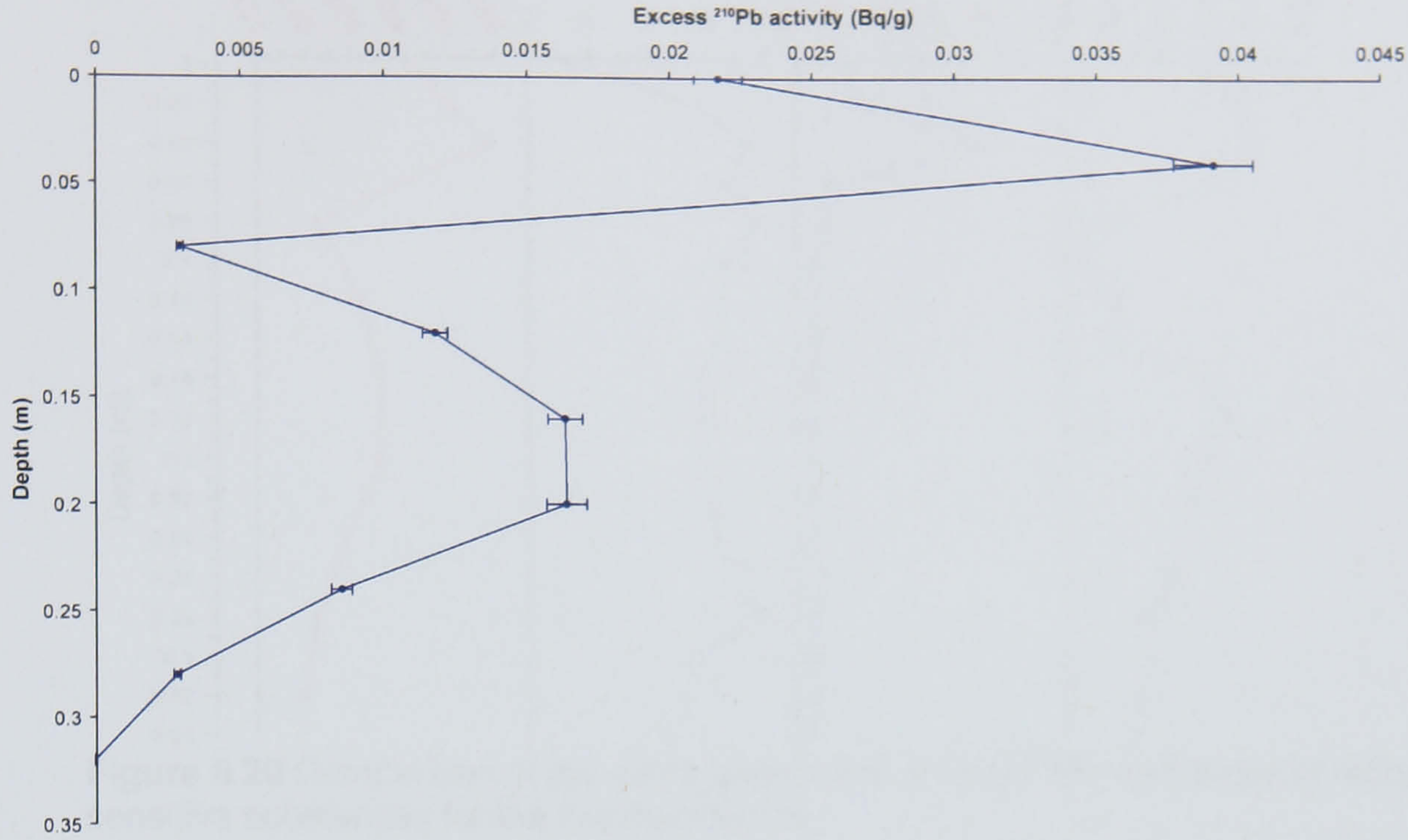

Figure 8.18 Excess ^{210}Pb depth profiles for the low marsh core.

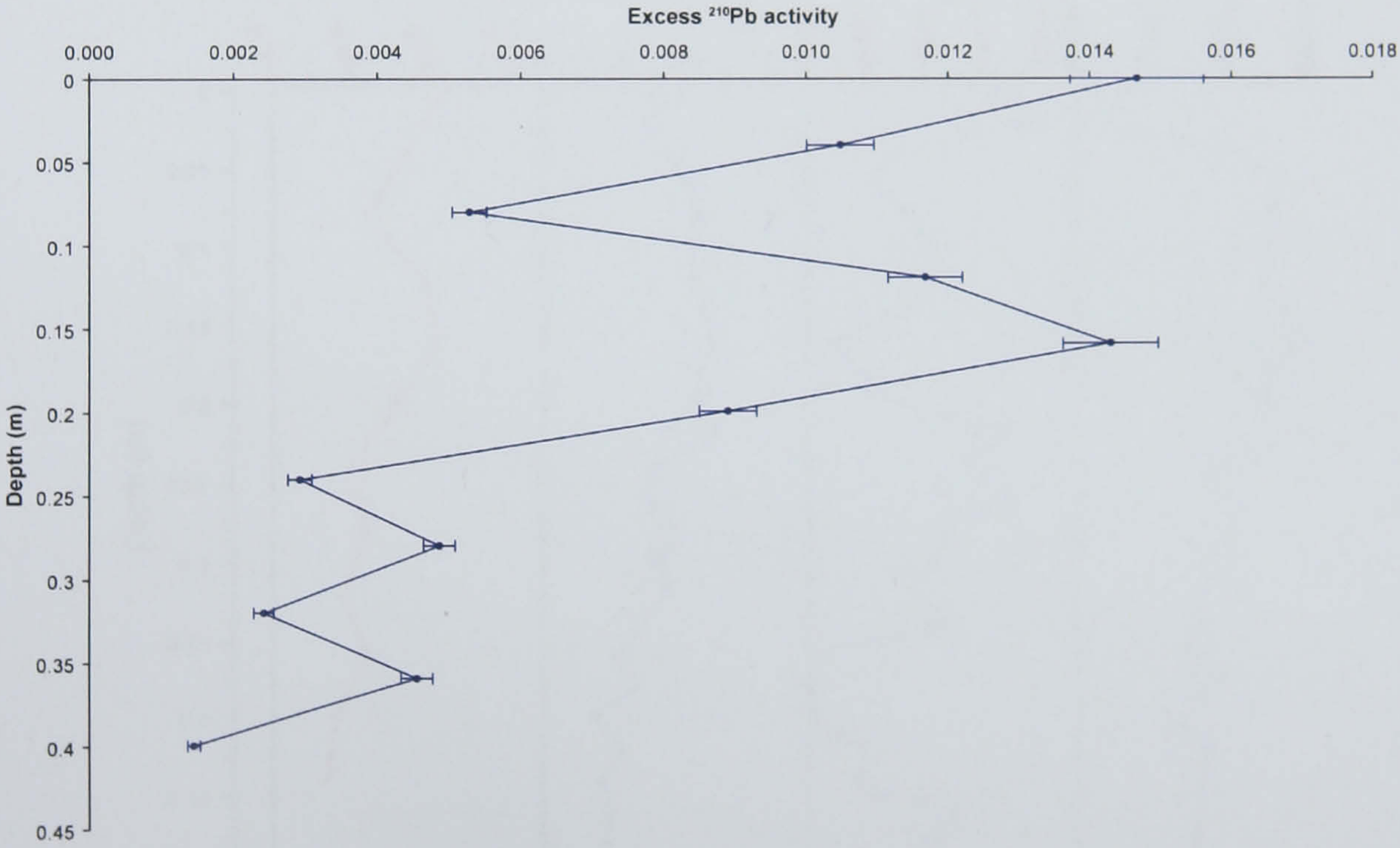

Figure 8.19 Excess ^{210}Pb depth profiles for the mudflat core.

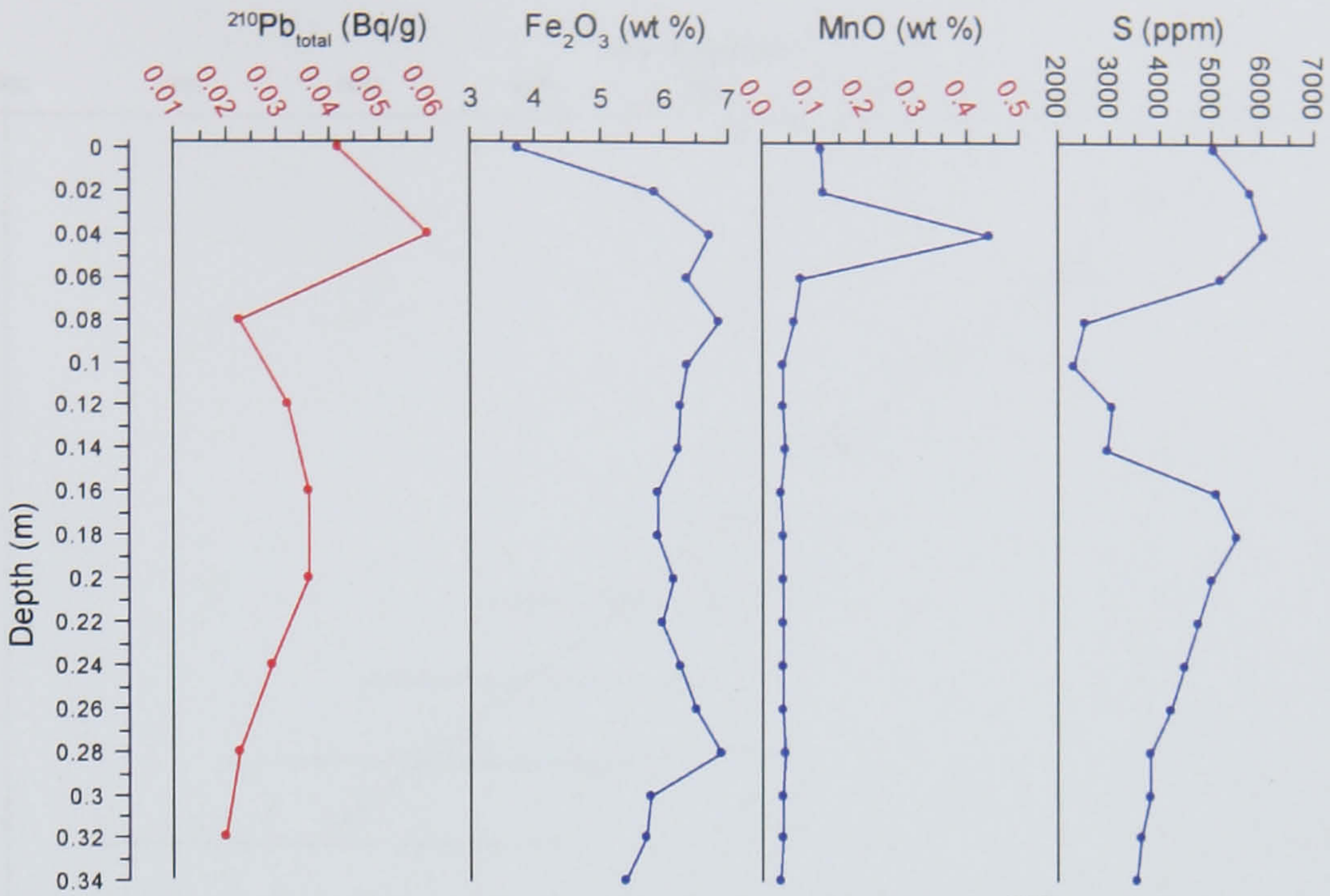

Figure 8.20 Comparison of the depth distribution of total ^{210}Pb with those of redox sensitive substances for the low marsh core.

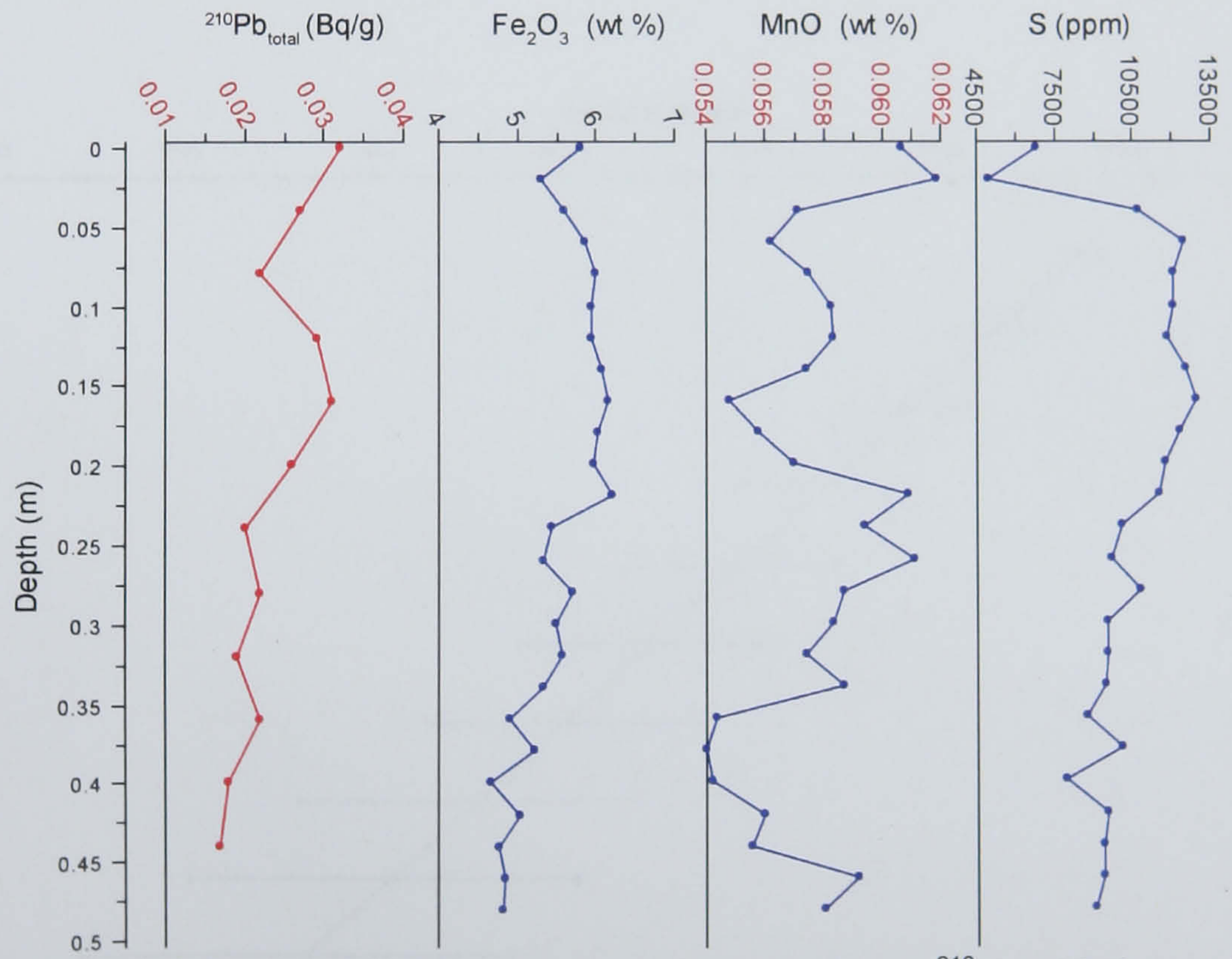

Figure 8.21 Comparison of the depth distribution of total ^{210}Pb with those of redox sensitive substances for the mudflat core.

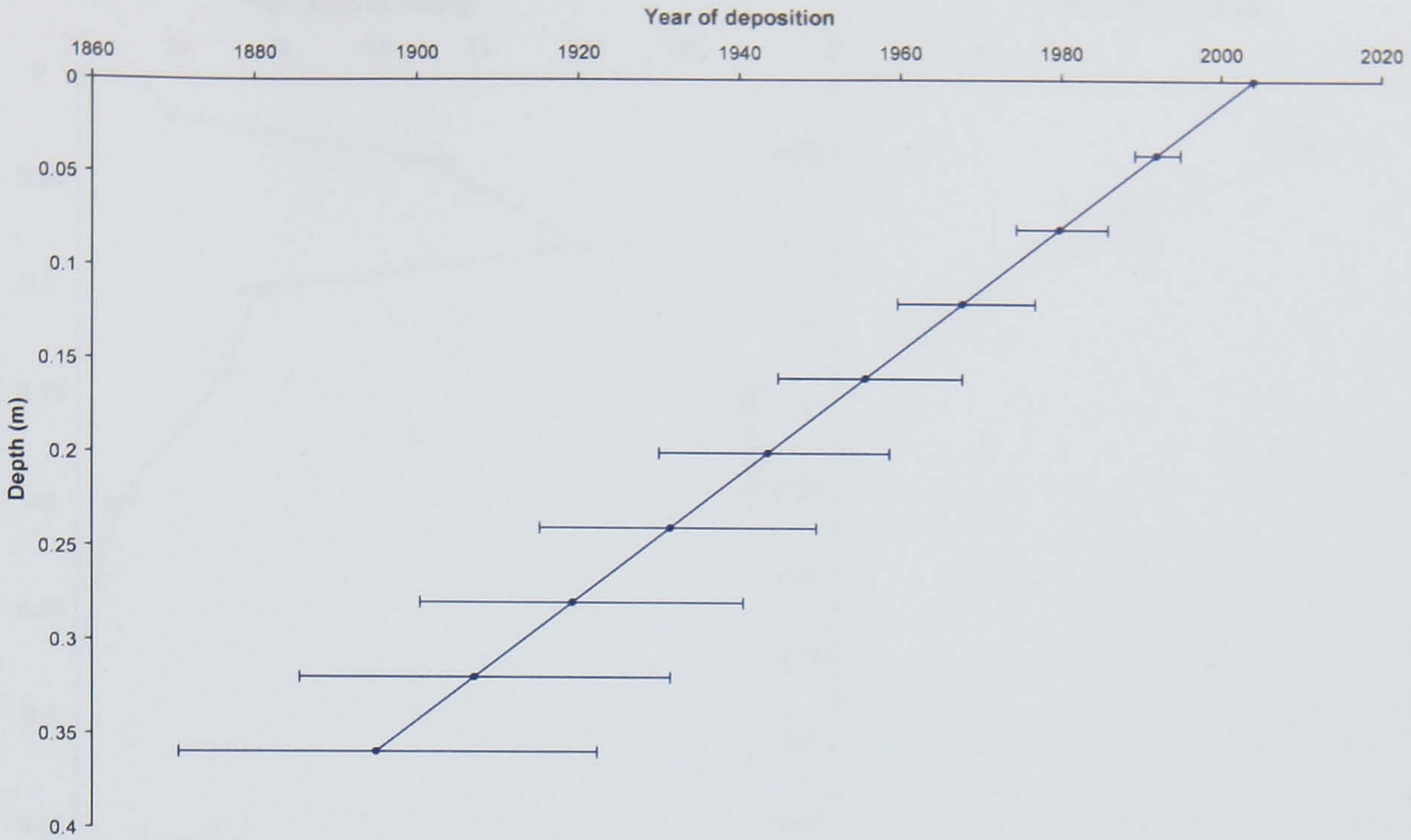

Figure 8.22 ^{210}Pb-derived age-depth model for the low marsh core. Error bars are 95 % confidence intervals.

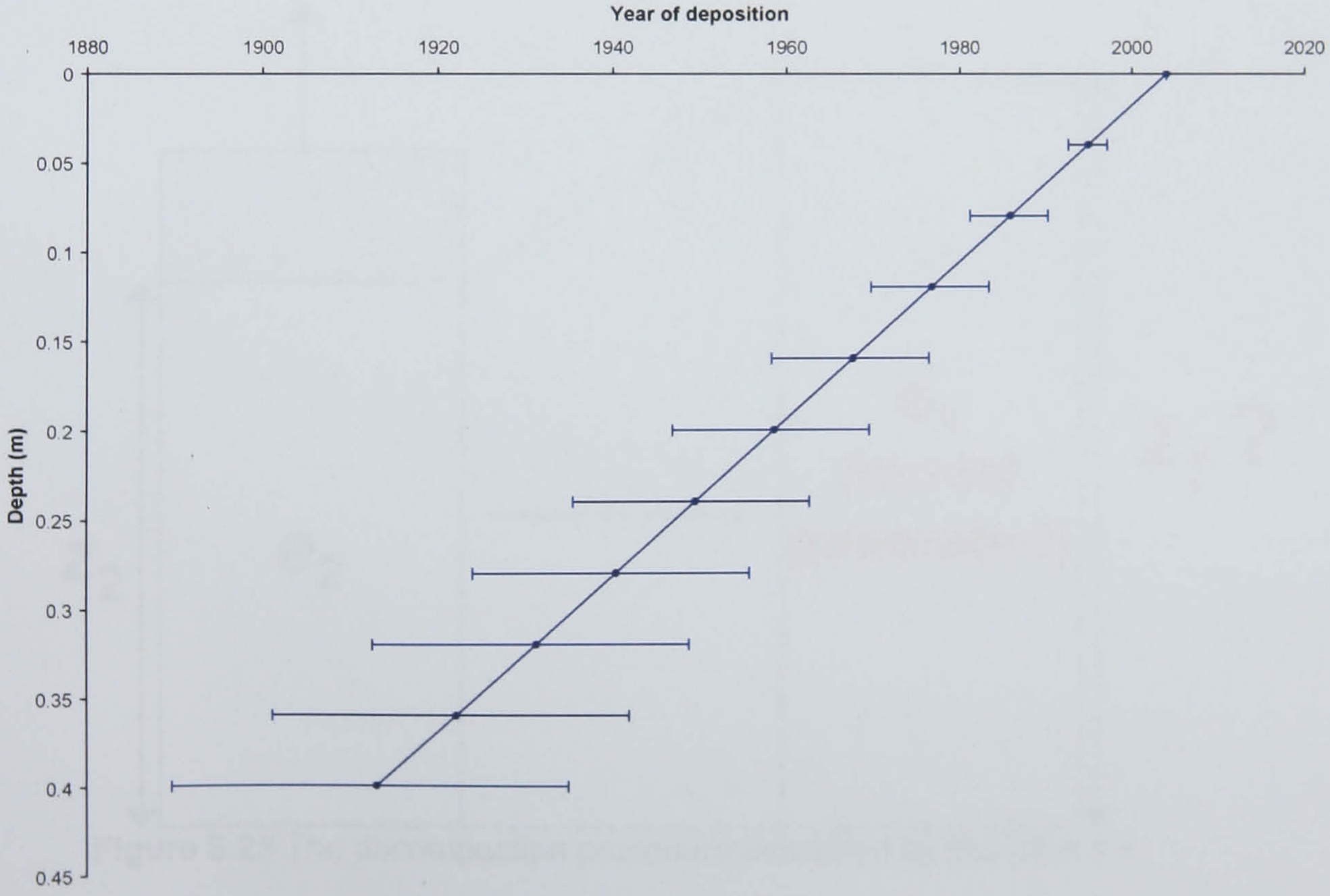

Figure 8.23 ^{210}Pb-derived age-depth model for the mudflat core. Error bars are 95 % confidence intervals.

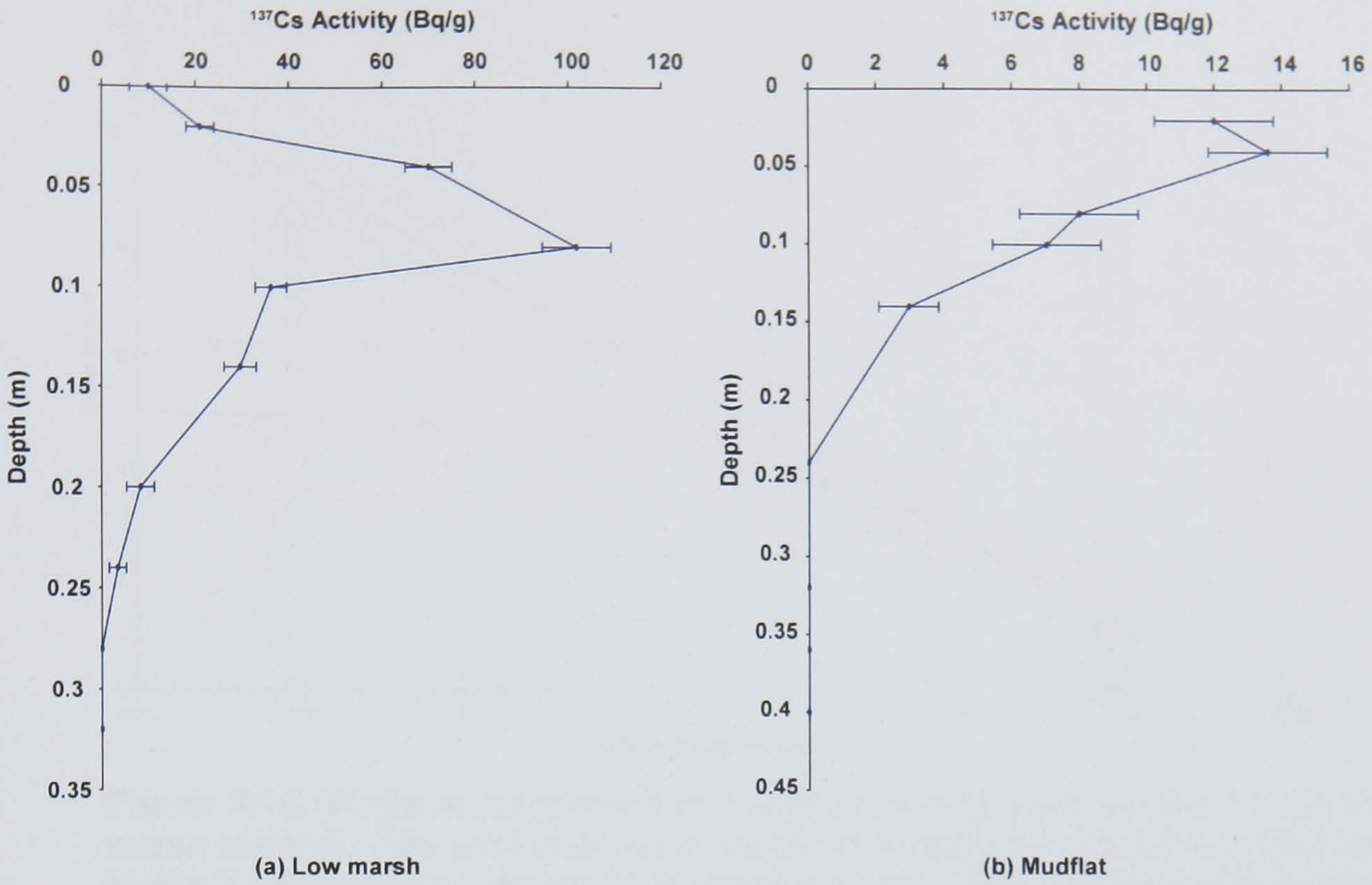

Figure 8.24 Distribution of ^{137}Cs with depth in (a) the low marsh and (b) mudflat cores.

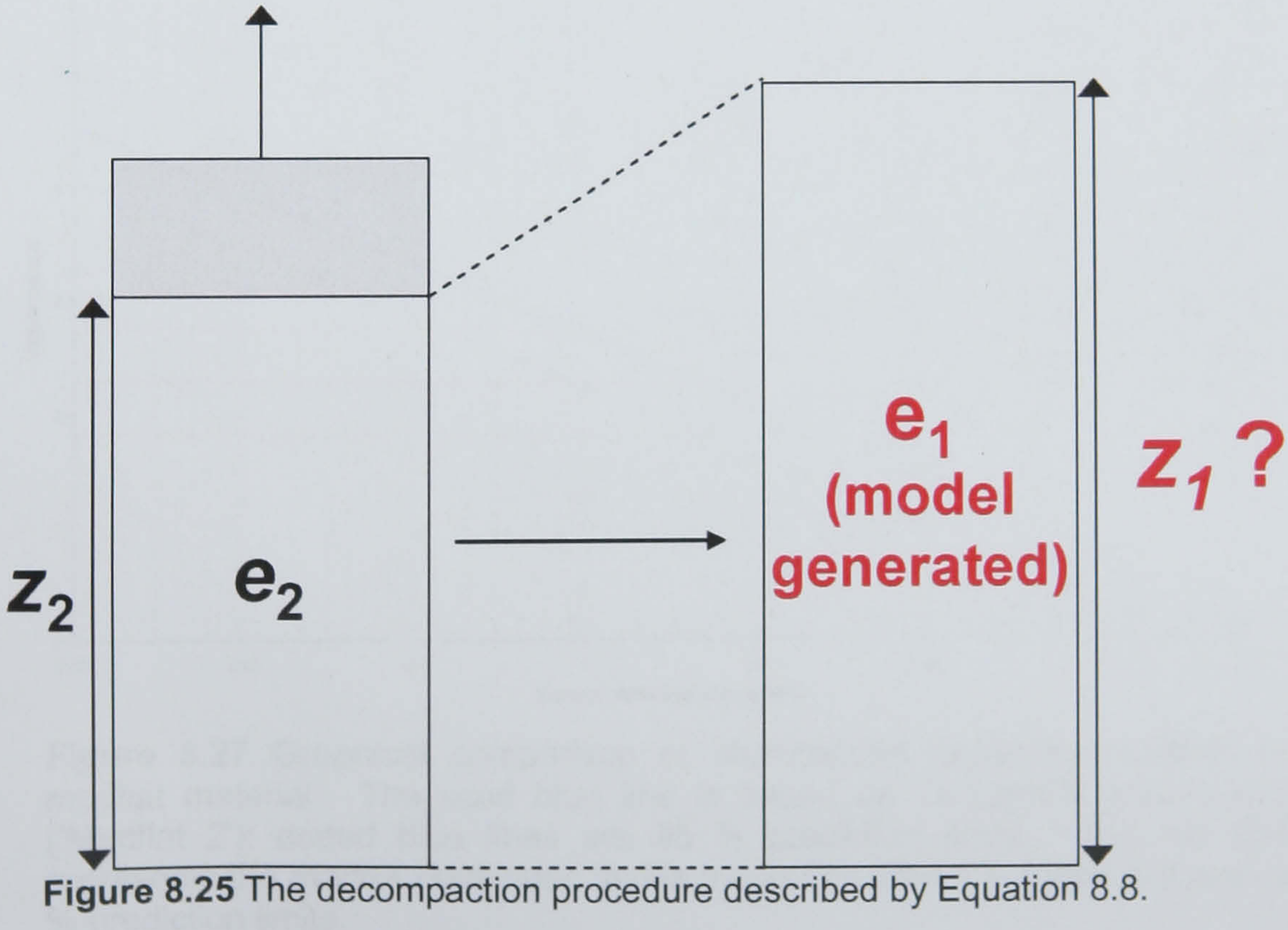

Figure 8.25 The decompaction procedure described by Equation 8.8.

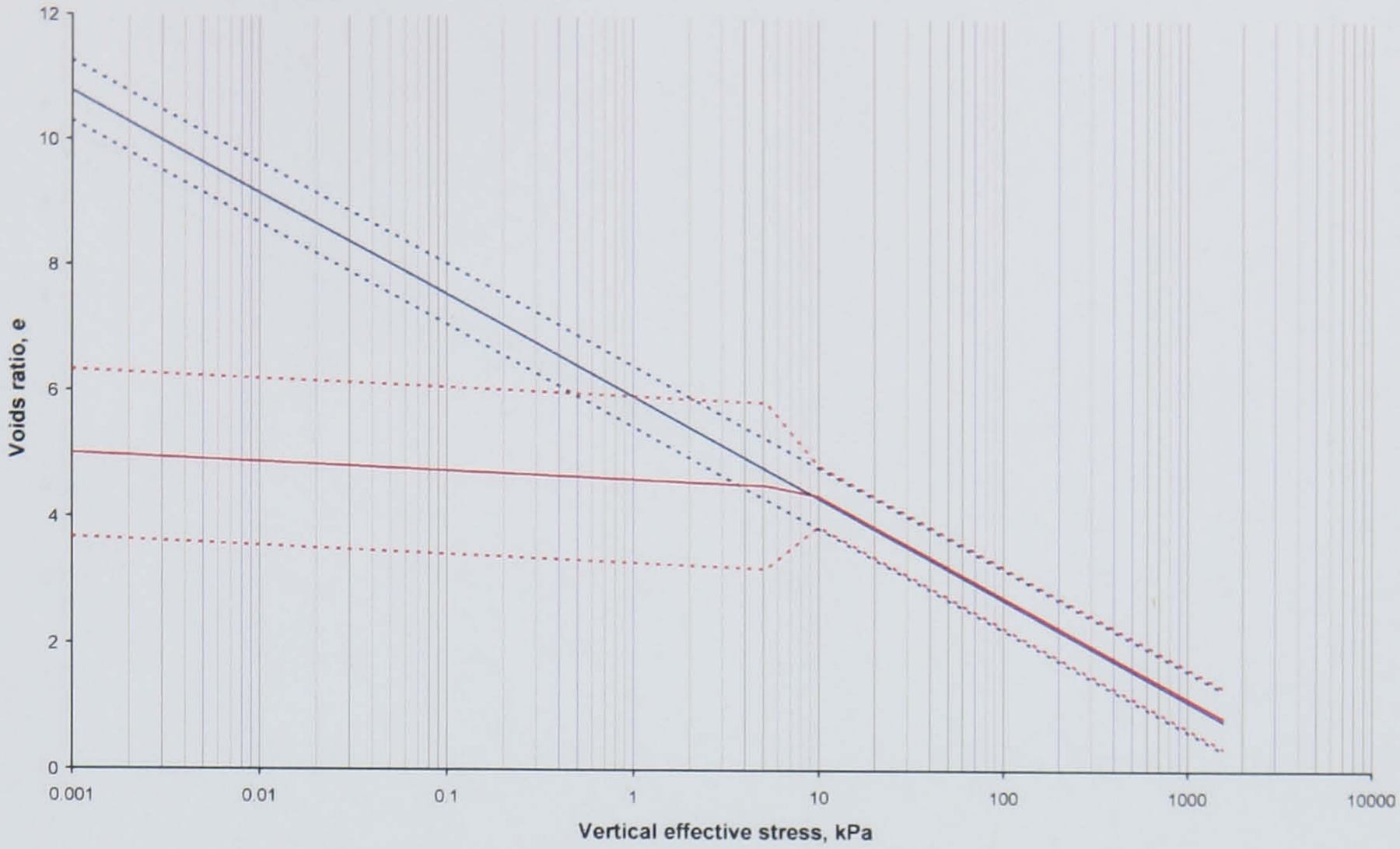

Figure 8.26 Graphical comparison of changepoint regression models for the low marsh material. The solid blue line is based on Terzaghi's compression law ('Low Marsh 3'); dotted blue lines are 95 % prediction limits. The red blue line represents the models developed in this thesis; dotted red lines are 95 % prediction limits ('Low Marsh 2').

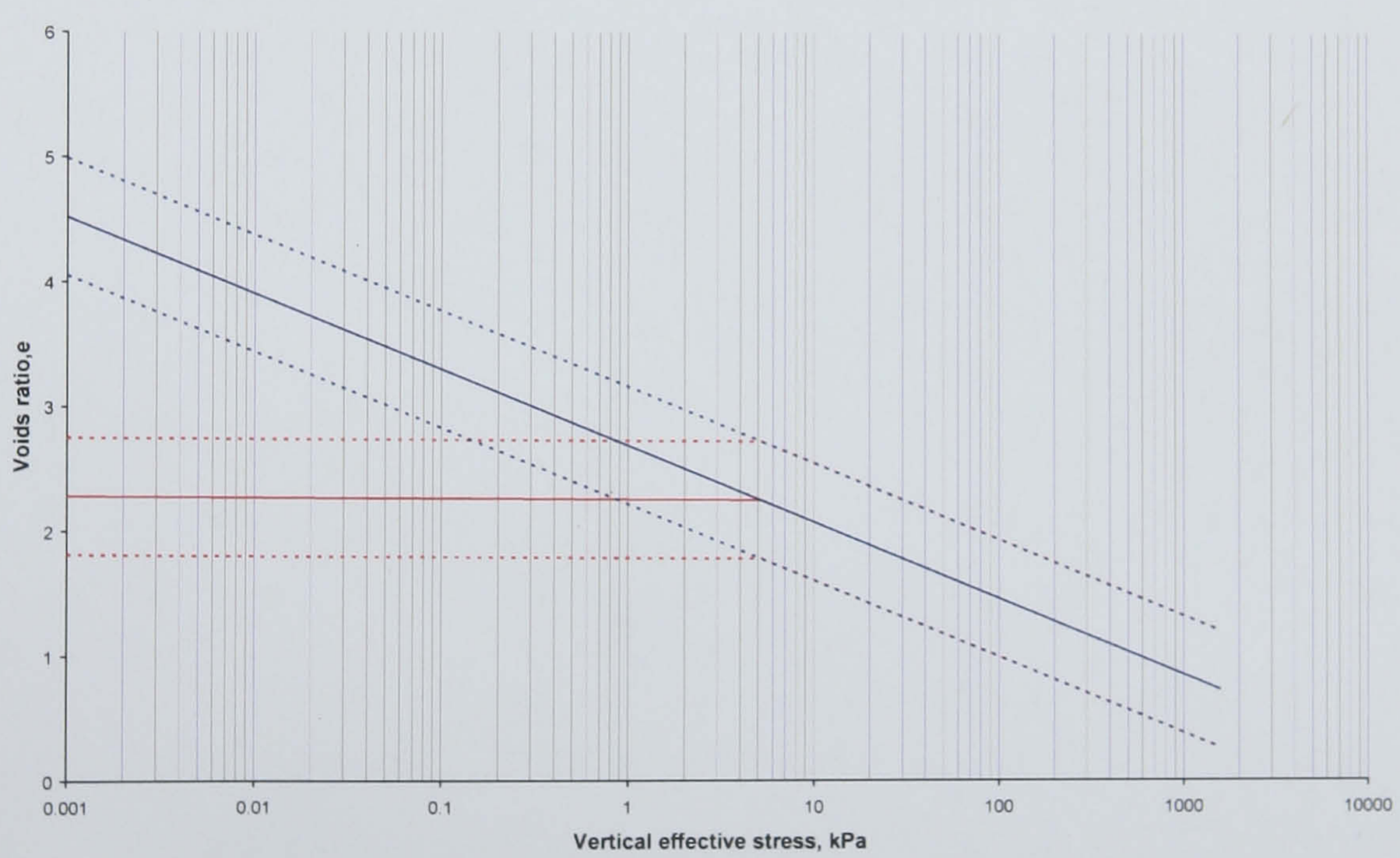

Figure 8.27 Graphical comparison of changepoint regression models for the mudflat material. The solid blue line is based on Terzaghi's compression law ('Mudflat 2'); dotted blue lines are 95 % prediction limits. The red blue line represents the models developed in this thesis ('Mudflat 1'); dotted red lines are 95 % prediction limits.

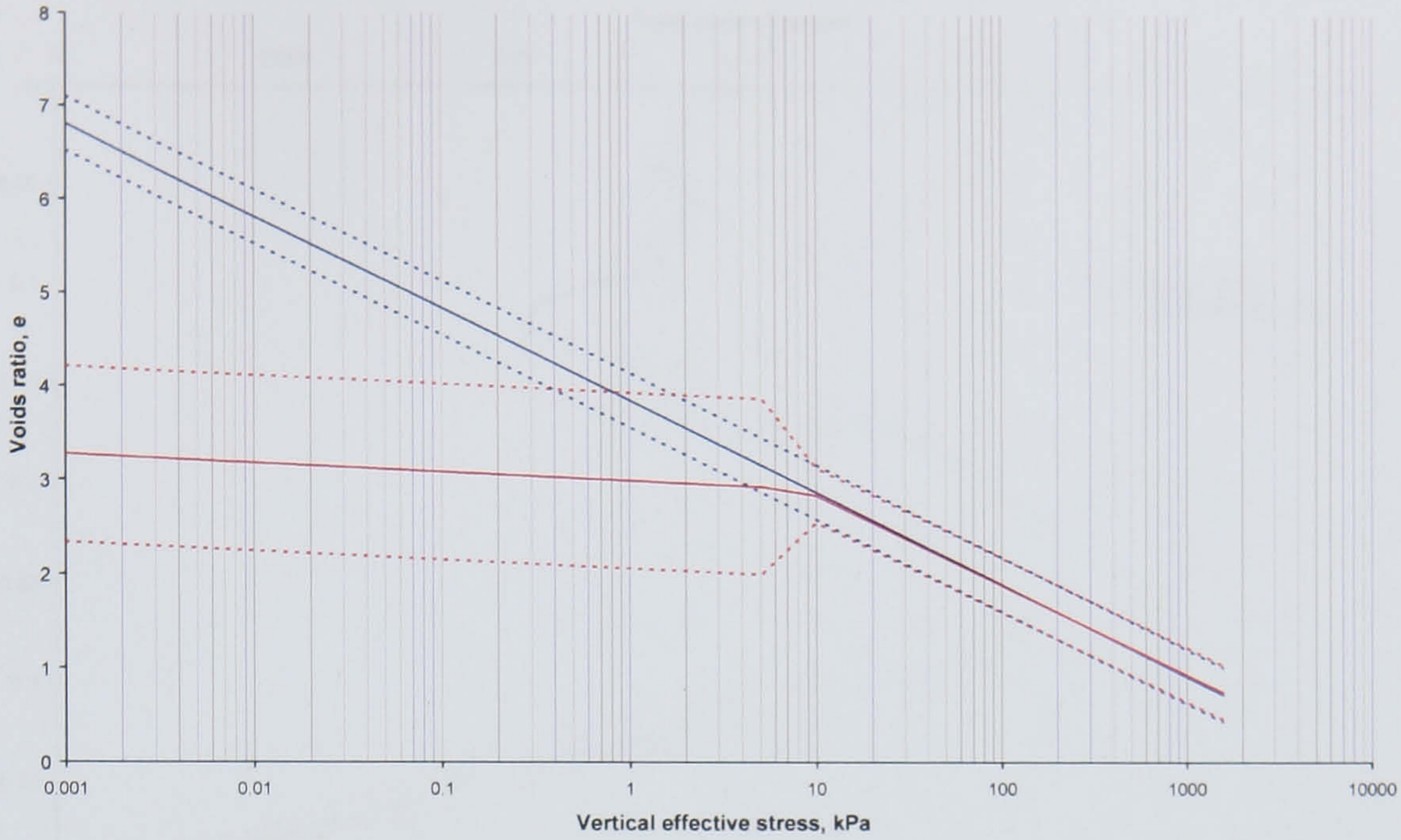

Figure 8.28 Graphical comparison of changepoint regression models for the 'saltmarsh' material. The solid blue line is based on Terzaghi's compression law ('Saltmarsh 2'); dotted blue lines are 95 % prediction limits. The red blue line represents the models developed in this study ('Saltmarsh 1'); dotted red lines are 95 % prediction limits.

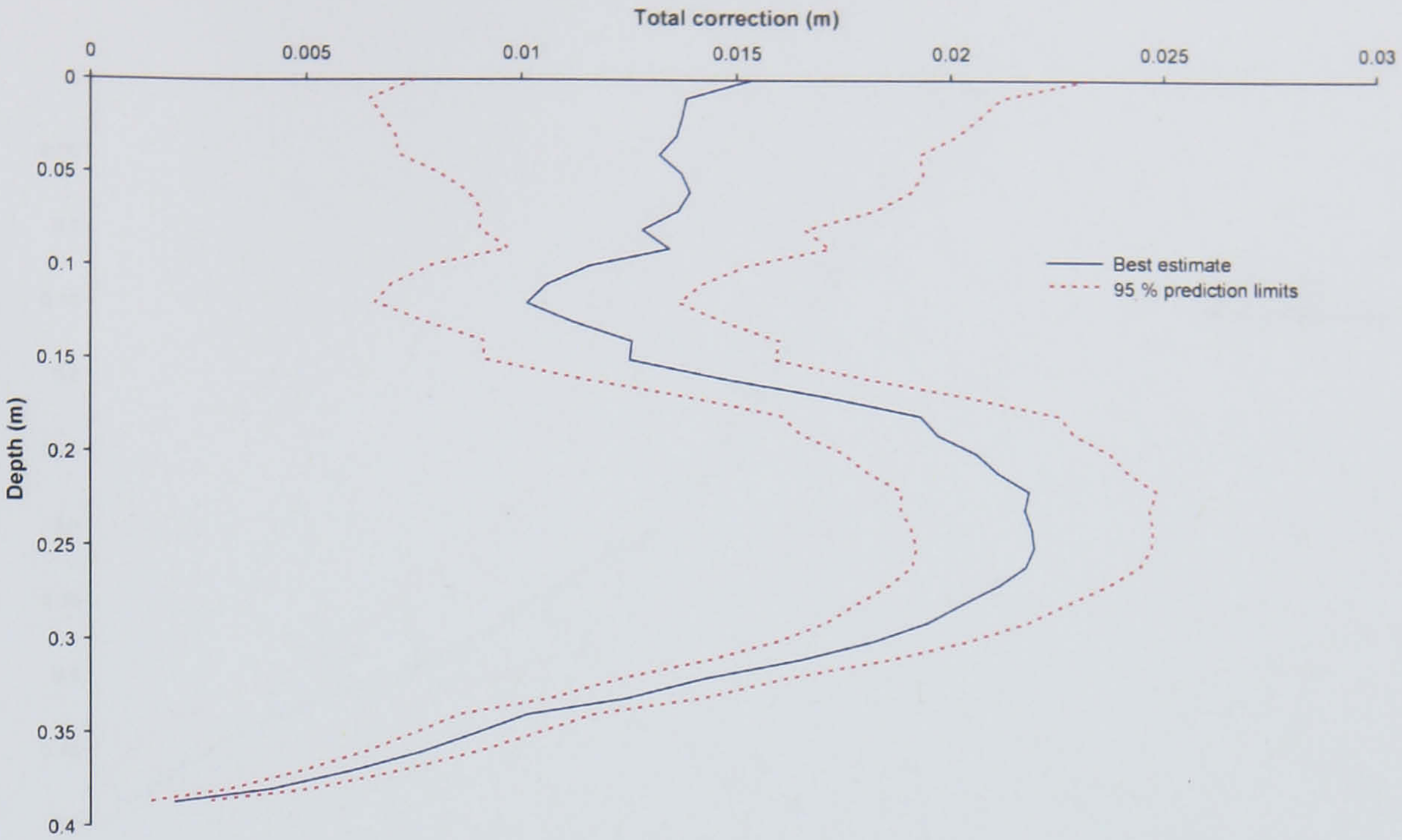

Figure 8.29 Decompaction corrections to be added to depths within the low marsh stratigraphic profile based on the 'new' models.

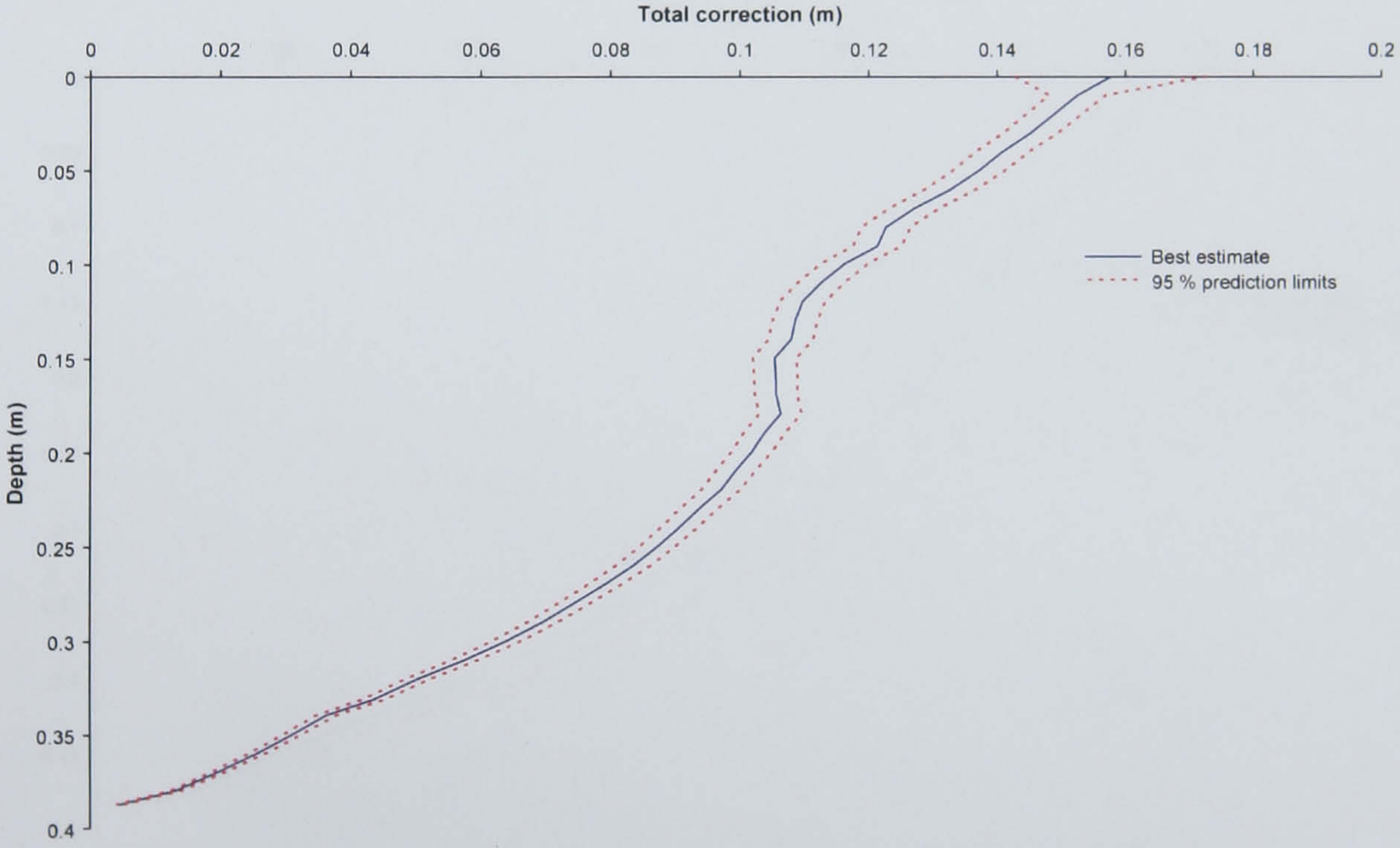

Figure 8.30 Decompaction corrections to be added to depths within the low marsh stratigraphic profile based on the Terzaghi models.

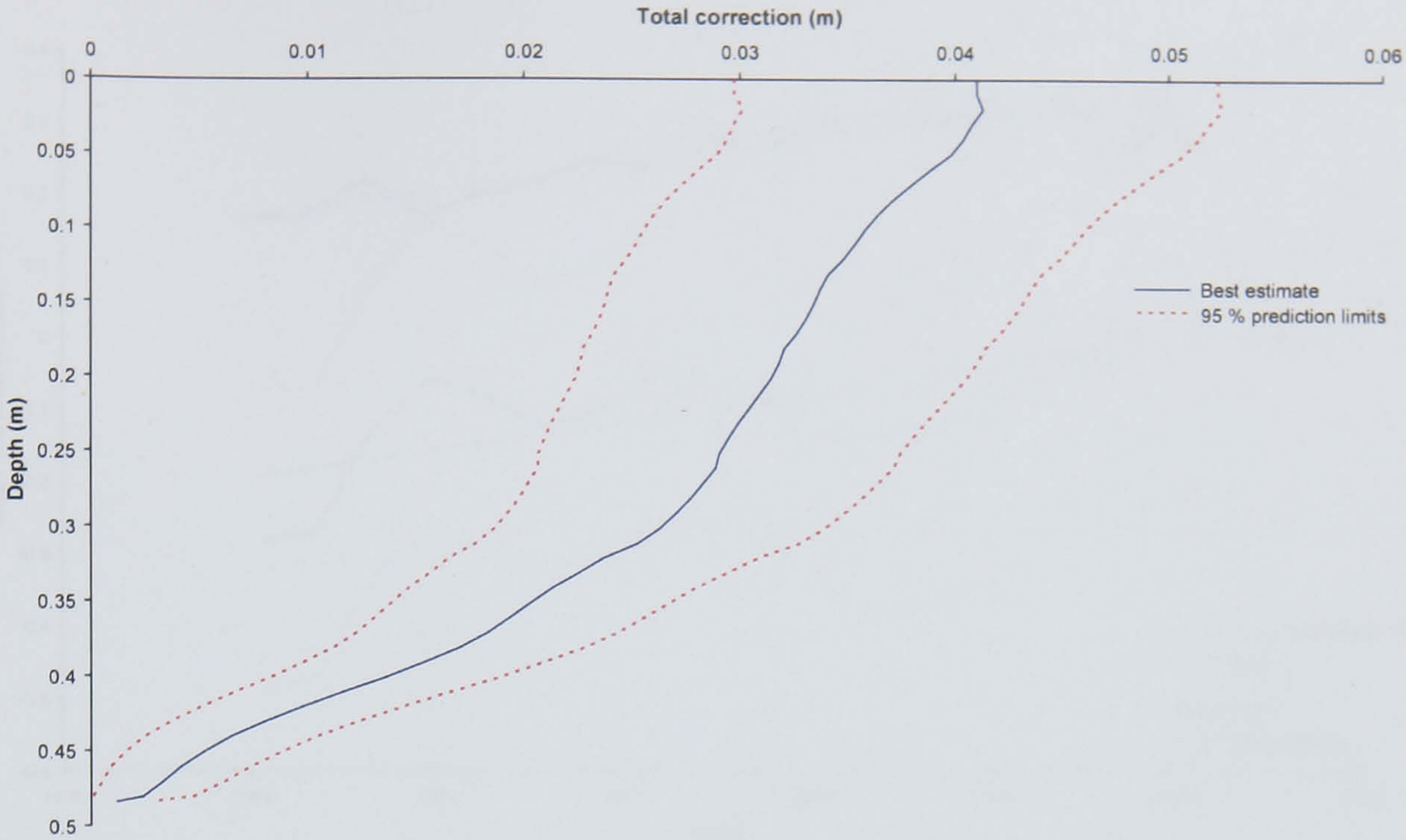

Figure 8.31 Decompaction corrections to be added to depths within the mudflat stratigraphic profile based on the 'new' models.

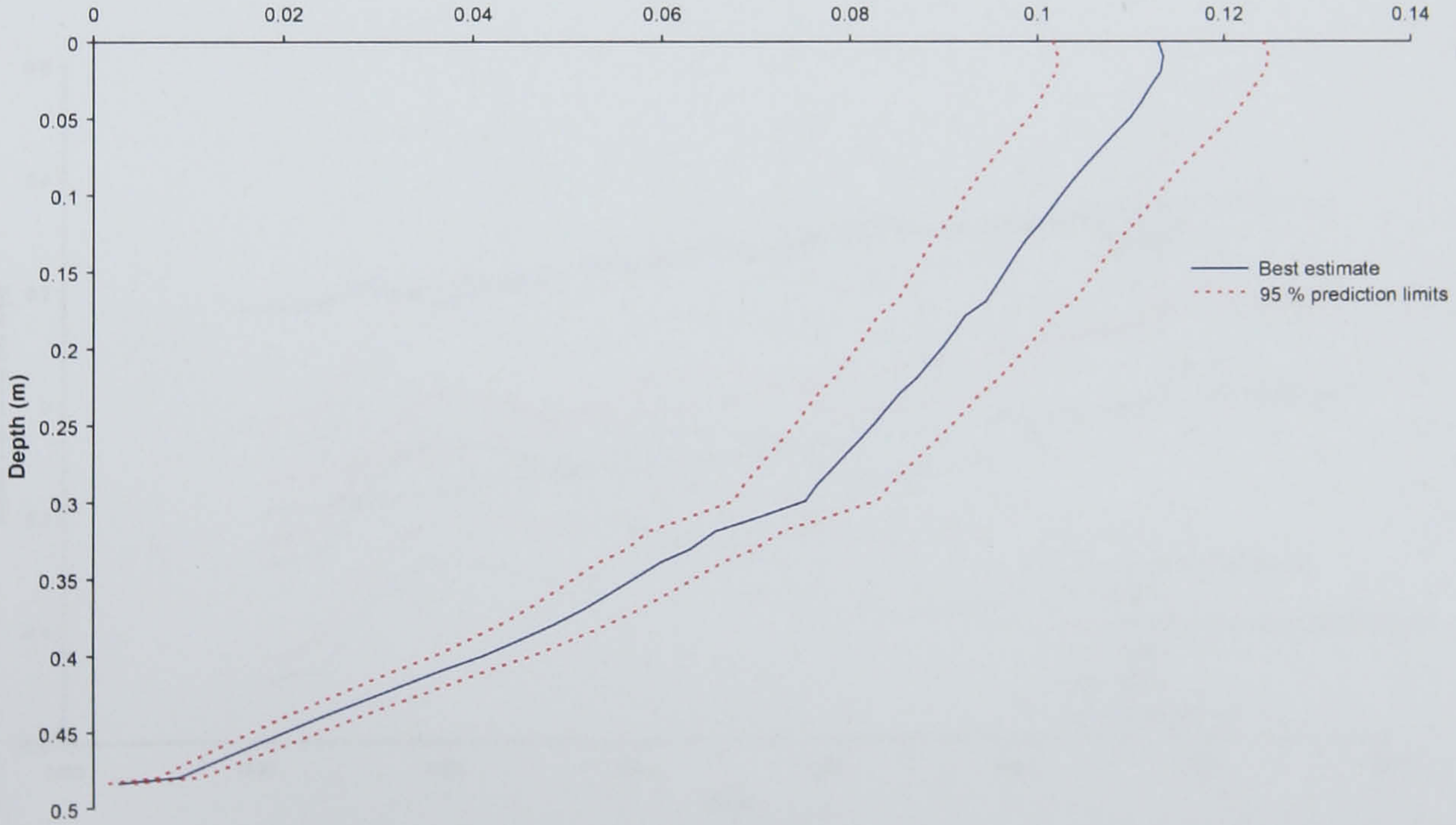

Figure 8.32 Decompaction corrections to be added to depths within the mudflat stratigraphic profile based on the Terzaghi models.

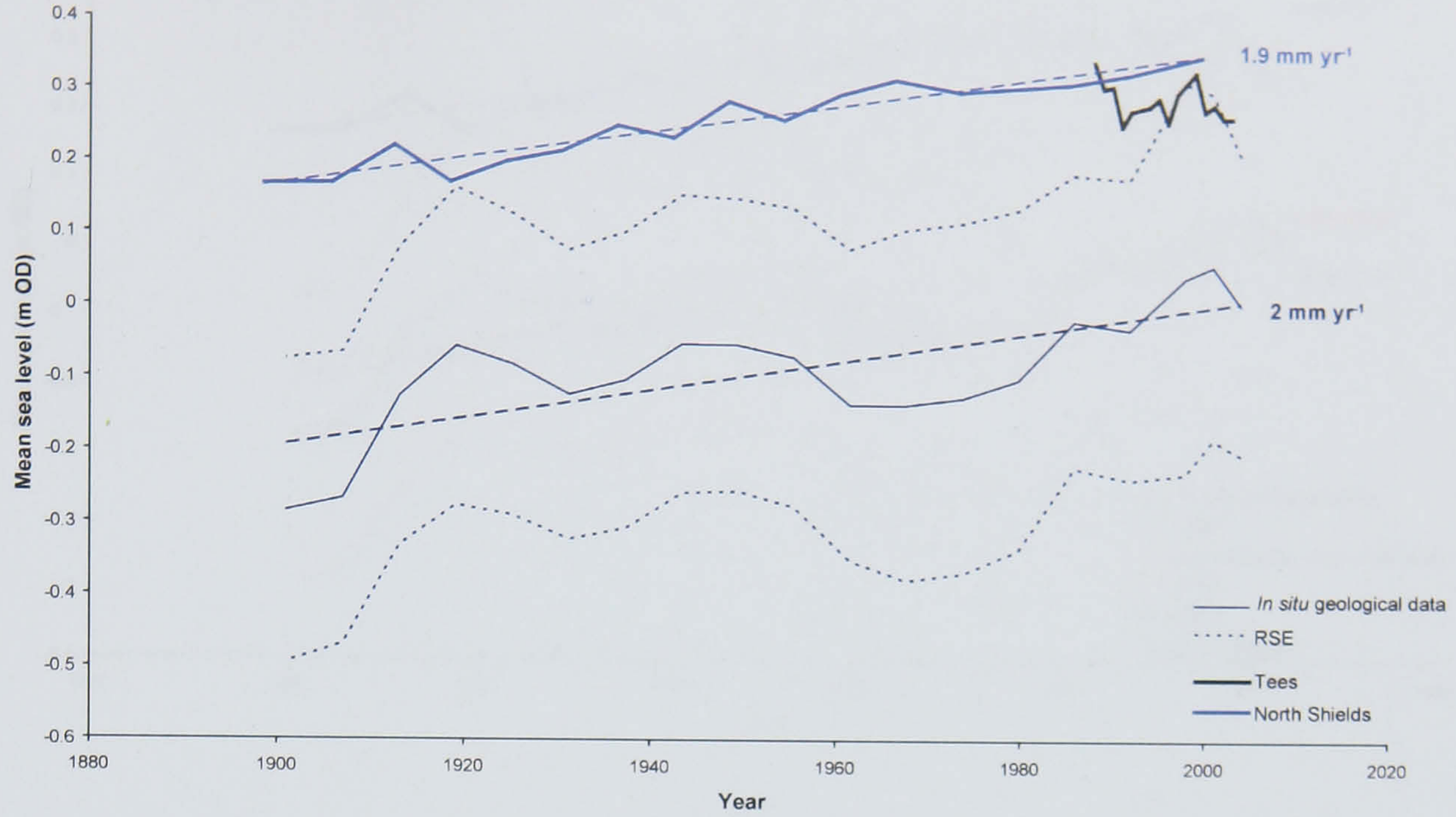

Figure 8.33 Reconstruction of the *in situ* (compacted) sea level curve obtained from the low marsh core and comparison with the North Shields and Tees tide gauge records.

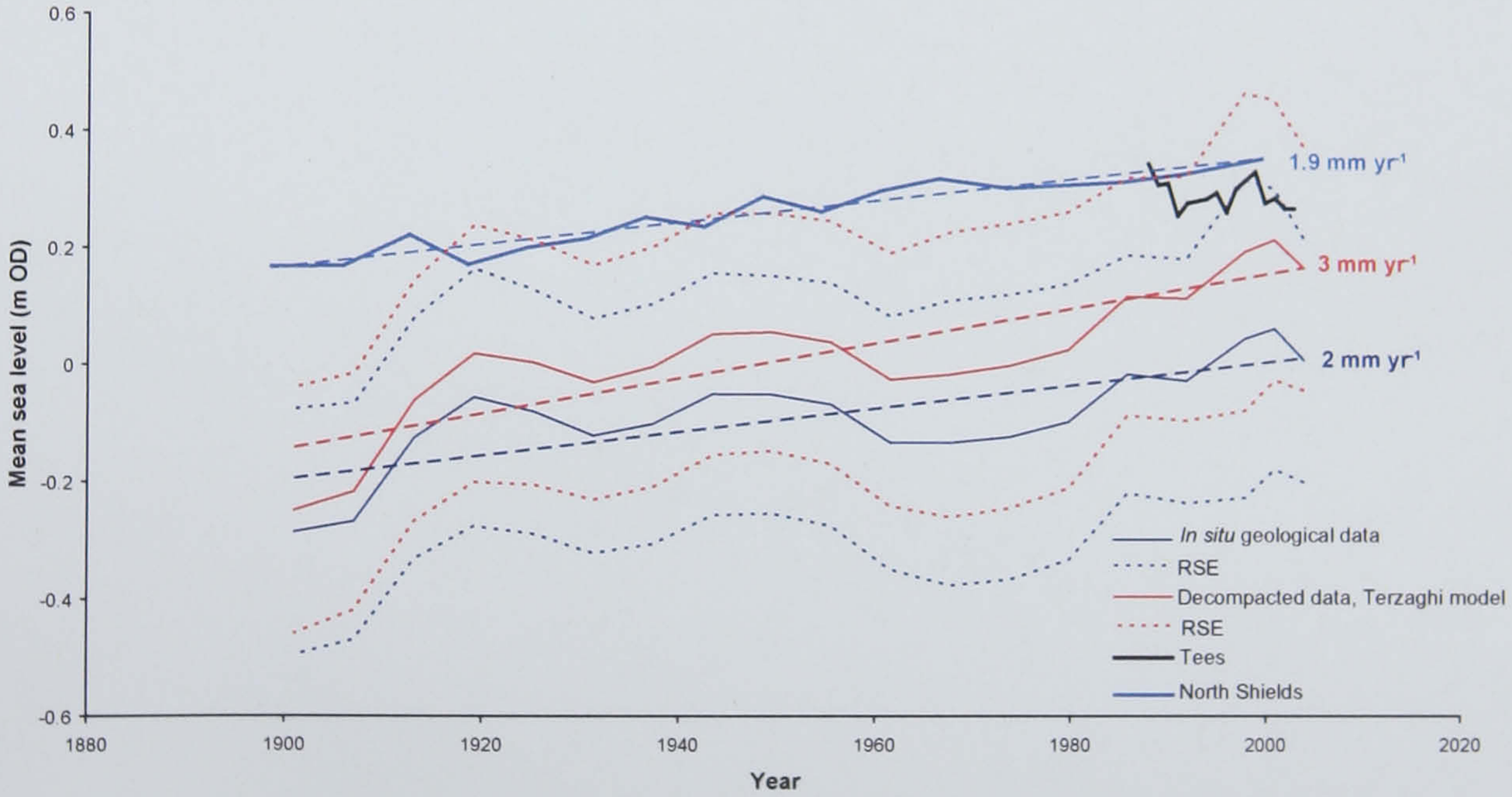

Figure 8.34 Reconstruction of the *in situ* (compacted) sea level curve obtained from the low marsh core and comparison with both the sea level curves decompacted using the Terzaghi compression models and the North Shields and Tees tide gauge records.

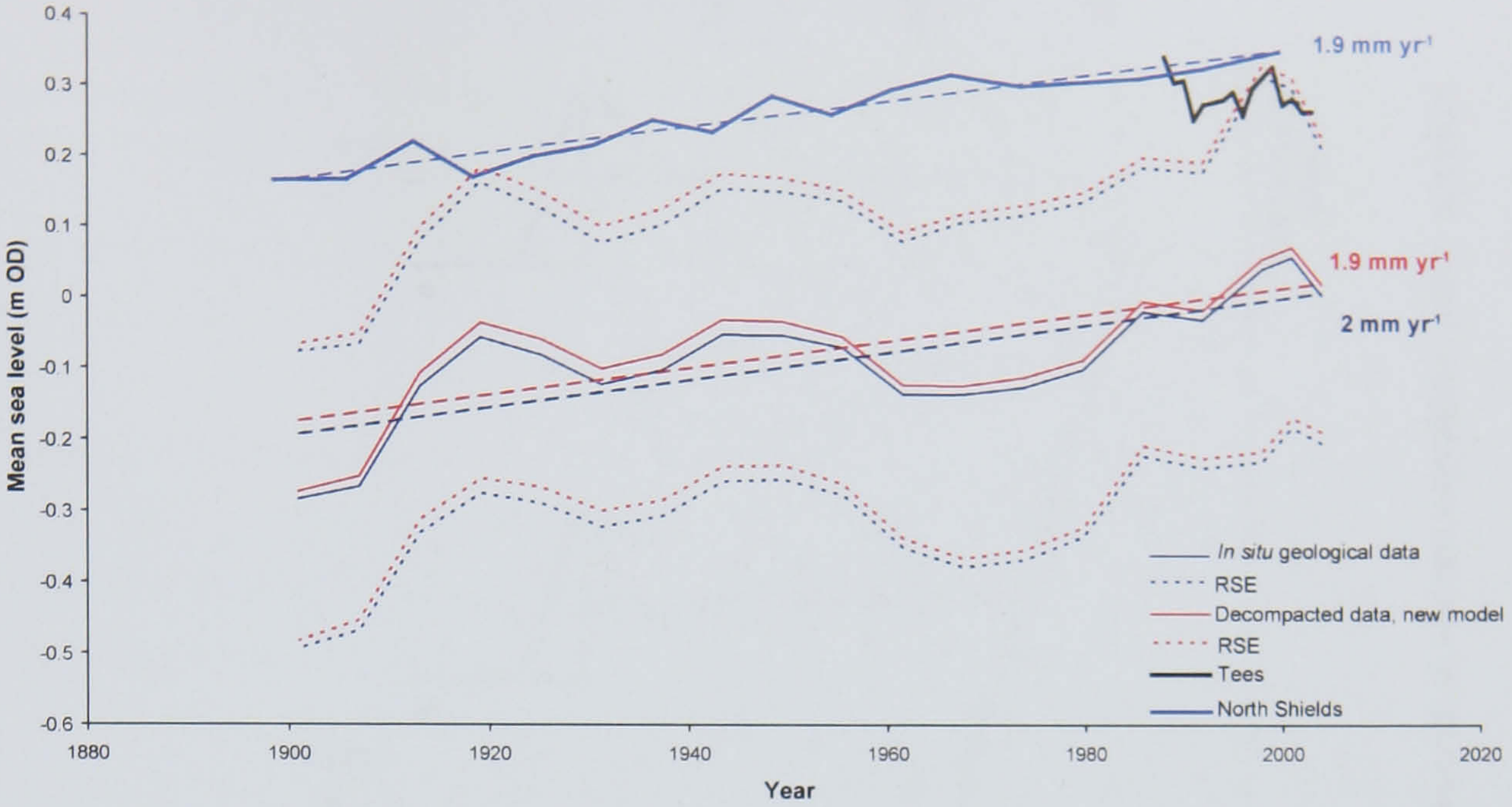

Figure 8.35 Reconstruction of the *in situ* (compacted) sea level curve obtained from the low marsh core and comparison with both the sea level curves decompacted using the 'new' compression models and the North Shields and Tees tide gauge records.

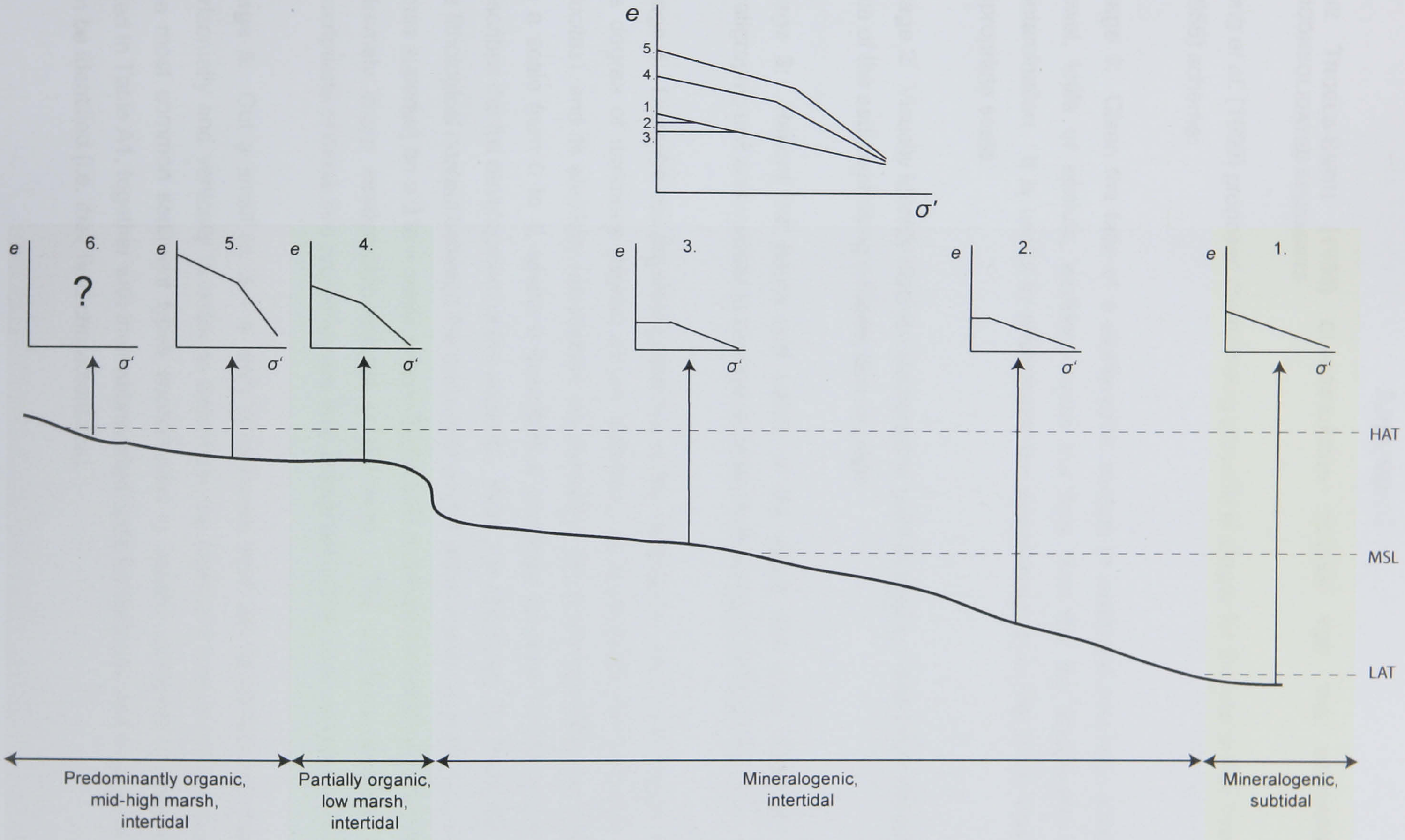

Figure 8.36 Hypothetical variations in $e \log_{10} \sigma'$ compression behaviour of sediments at various elevations within a typical contemporary northwest European intertidal zone.

APPENDIX I

THE TROELS-SMITH (1955) CLASSIFICATION SCHEME FOR THE DESCRIPTION OF UNCONSOLIDATED SEDIMENTS

Long *et al.* (1999) proposed the following procedural stages for the use of the Troels-Smith (1955) scheme:

Stage 1: Clean the face of a stratigraphic section or sediment core with a spade, flat trowel, knife or spatula, working across the face from the top downwards to avoid contamination. It is useful to photograph the sequence/core at this point, including an appropriate scale.

Stage 2: Visually identify discrete stratigraphic units or layers. Mark each of them on the face of the sediment using a blade, pins or pegs.

Stage 3: Record the depth and nature of the upper and lower boundary of each stratigraphic unit and number in ascending order from the base of the sequence.

Stage 4: Describe the physical properties of the sediments. Here information regarding the degree of darkness (*nigror*) of the sediment, its stratification (*stratificatio*), dryness (*siccitas*), and its elasticity (*elasticitas*) are recorded. Each physical attribute is measured on a scale from 0 to 4, where 0 describes a complete absence of the property and 4 describes the full development of the property. Next, it is necessary to record the nature of the lithological contact between the unit under examination and the one immediately above (*limes superior*) on a 0 to 4 scale, where 0 indicates a diffuse boundary and 4 indicates an extremely sharp stratigraphic contact (< 0.5 mm). The numbers obtained from the descriptions of these five properties are then presented in the order described above.

Stage 5: Cut a small (*c.* 3 – 4 cm^3) of sediment from the face/core and break open horizontally and vertically in order to determine the sediment composition and structure. The most common sediment types encountered in coastal stratigraphic sequences are listed in Table A1, together with their abbreviated code for field use and ways in which they can be identified (i.e. their field characteristics).

Table A1 A selective list of the most common sediment types recorded in coastal sediments (from Long *et al.*, 1999, after Troels-Smith, 1955).

Name	Code	Sediment type	Field characteristics
Argilla steatodes	As	Clay < 0.002 mm.	May be rolled into a thread ≤ 2 mm diameter without breaking.
Argilla granosa	Ag	Silt 0.06 – 0.002 mm.	Plastic when wet, hard when dry. Will not roll into thread without splitting. Will rub into dust on drying. Gritty on back of teeth.
Grana minora	Ga	Fine, medium and coarse sand (0.06 – 0.002 mm).	Crunchy between teeth. Lacks cohesion when dry. Grains visible to naked eye.
Grana majora	Gmaj	Fine, medium and coarse gravel (2 – 60 mm).	
Testae (molluscorum)	test.(moll)	Whole mollusc shells.	
Particulae testarum (molluscorum)	part.test.	Shell fragments.	
Substantia humosa	Sh	Humified organics beyond idenitification.	Fully disintegrated deposit lacking macroscopic structure, usually dark brown or black.
Turfa herbacea	Th^{0-4}	Roots, stems and rhizomes of herbaceous plants.	Can be seen vertically aligned or matted within sediment in growth position.
Turfa bryophytica	Tb^{0-4}	The protonema, rhizods, stems, leaves etc. of mosses.	Can be seen vertically aligned or matted within sediment in growth position.
Turfa lignosa	Tl^{0-4}	The roots and stumps of woody plants and their trunks, branches and twigs.	Can be seen vertically aligned or layered within sediment in growth position.
Detritus lignosus	Dl	Detrital fragments of wood and bark > 2 mm.	Non-vertical or random alignment, may be laminated, not in growth position.

Table A1 (continued)

Name	Code	Sediment type	Field characteristics
Detritus herbosus	Dh	Fragments of stems and leaves of herbaceous plants > 2 mm.	Non-vertical or random alignment, may be laminated, not in growth position.
Detritus granosus	Dg	Woody and herbaceous humified plant remains < 2mm > 0.1 mm that cannot be separated.	Non-vertical or random alignment, may be laminated, not in growth position.
Limus detrituosus	Ld^{0-4}	Fine detrital organic mud (particles < 0.1 mm).	Homogeneous, non-plastic, often becomes darker on oxidation and will shrink on drying.
Limus ferrugineus	Lf	Mineral and/or organic iron (III) oxide.	Forms mottled staining. Can be crushed between fingers. Often in root channels or surrounding Th.
Anthrax	Anth	Charcoal.	Crunchy black fragments.
Stirpes	Stirp	Tree stump.	
Stratum confusum	Sc	Disturbed stratum.	

In the Troels-Smith (1955) scheme, each layer is characterized by its components and physical properties. The components of the layer are recorded on a 4 point scale, where 1 is 25 % and 4 is 100 % of the layer. Thus, a peat which comprises 100 % herbaceous roots with attached stems and leaves (*turfa*) would be recorded as Th4, whereas a peat with 50 % clay and 50 % herbaceous stems and roots as As2 Th2. Additional minor components (< 25 %) which do not contribute to the main component totals can be recorded by a '+'. For organic deposits, the degree of humification is also recorded on a five point scale as a superscript from 0 (no humification) to 4 (totally humified). Hence, partly humified but distinct plant structures in peat comprising 100 % *turfa* would be described as $Th^{2}4$.

Stage 6: Finally, a written description of the sediment is added, providing any further descriptive information not already described, such as bedding structures.

APPENDIX II

ISOTOPIC DATA

Table A2 ^{210}Po and ^{210}Pb activity with depth in the sediment core obtained from the low marsh sampling altitude (2.26 m OD) employed in the sea level reconstruction in Chapter 8.

Depth (m)	^{210}Po activity (Bq/g)	Excess ^{210}Pb activity (Bq/g)	Excess ^{210}Pb activity error (%)
0.00	0.042	0.022	3.92
0.04	0.059	0.039	3.58
0.08	0.023	0.003	4.09
0.12	0.032	0.012	3.75
0.16	0.036	0.016	3.71
0.20	0.036	0.016	4.29
0.24	0.029	0.009	4.26
0.28	0.023	0.003	4.41
0.32	0.020	0.000	4.28

Table A3 ^{137}Cs activity with depth in the sediment core obtained from the low marsh sampling altitude (2.26 m OD) employed in the sea level reconstruction in Chapter 8.

Depth (m)	^{137}Cs activity (Bq/g)	^{137}Cs activity 2σ error (Bq/g)
0.00	10	4
0.02	21	3
0.04	70	5
0.08	102	7
0.10	36	3
0.14	30	3
0.20	8	3
0.24	3	2
0.28	0	0
0.32	0	0

Table A4 ^{210}Po and ^{210}Pb activity with depth in the sediment core obtained from the mudflat sampling altitude (1.06 m OD) employed in the sea level reconstruction in Chapter 8.

Depth (m)	^{210}Po activity (Bq/g)	Excess ^{210}Pb activity (Bq/g)	Excess ^{210}Pb activity error (%)
0.00	0.032	0.015	6.42
0.04	0.027	0.010	4.53
0.08	0.022	0.005	4.54
0.12	0.029	0.012	4.52
0.16	0.031	0.014	4.69
0.20	0.026	0.009	4.55
0.24	0.020	0.003	5.70
0.28	0.022	0.005	4.53
0.32	0.019	0.002	5.77
0.36	0.022	0.005	4.81
0.40	0.018	0.001	6.07
0.44	0.017	0.000	4.55

Table A5 ^{137}Cs activity with depth in the sediment core obtained from the mudflat sampling altitude (1.06 m OD) employed in the sea level reconstruction in Chapter 8.

Depth (m)	^{137}Cs activity (Bq/g)	^{137}Cs activity 2σ error (Bq/g)
0.02	12	2
0.04	14	2
0.08	8	2
0.10	7	2
0.14	3	1
0.24	0	0
0.32	0	0
0.36	0	0
0.40t	0	0

NOTES

The activity of supported (background) ^{210}Pb can be determined indirectly by measuring the activity of ^{226}Ra using gamma spectrometry; ^{226}Ra activity is assumed to represent supported ^{210}Pb activity. Excess ^{210}Pb activity was determined from the difference between total and supported ^{210}Pb activity. By definition, supported ^{210}Pb is in secular equilibrium with sedimentary ^{226}Ra and is equal to total ^{210}Pb activity at depths where excess ^{210}Pb is not measurable due to radioactive decay (I. Croudace, *pers. comm.*). In the low marsh core, the background activity of ^{226}Ra = 0.020 Bq/g. In the mudflat core, the background activity = 0.017 Bq/g.